

# **Forschungsbericht 2019-31**

## **Development and test of a UV lidar receiver for the measurement of wind velocities aiming at the near-range characterization of wake vortices and gusts in clear air**

Jonas Herbst

Deutsches Zentrum für Luft- und Raumfahrt  
Institut für Physik der Atmosphäre  
Oberpfaffenhofen

Dissertation  
an der Fakultät für Physik  
der Ludwig-Maximilians-Universität  
München

255 Seiten  
159 Bilder  
18 Tabellen  
233 Literaturstellen



DLR

Deutsches Zentrum  
für Luft- und Raumfahrt

Doppler-Wind-Lidar Empfänger, Michelson, Wirbelschleppen, Turbulenz, Simulation, Validierungsmessung

Jonas HERBST

(auf Englisch veröffentlicht)

Institut für Physik der Atmosphäre, DLR, Oberpfaffenhofen

**Entwicklung und Test eines UV-Lidarempfängers zur Windgeschwindigkeitsmessung für die kurzreichweitige Charakterisierung von Wirbelschleppen und Böen in klarer Luft**

Erweiterte Fassung der Dissertation, Ludwig-Maximilians-Universität München

DLR-Forschungsbericht 2019-31, 2019, 255 Seiten, 159 Bilder, 18 Tabellen, 233 Literaturstellen

Böen und Wirbelschleppen stellen heutzutage eine Hauptursache für Komfortminderungen, Zwischenfälle, und effizienzmindernde Strukturreserven im Flugverkehr dar. Konzepte zur automatischen Ausregelung dieser Turbulenzen, u.a. auf Reiseflughöhe, erfordern hochaufgelöste Windgeschwindigkeitsmessungen im Nahfeld in aerosolarmer Atmosphäre. Zu diesem Zweck wird in dieser Dissertation ein Lidarempfänger für einachsige Messungen entwickelt und getestet. Aus dem Vergleich bestehender Doppler-Wind-Lidar-Konzepte hinsichtlich der Anforderungen folgt ein streifenabbildendes, Michelson-Interferometer in Kombination mit einem schnellen Zeilendetektor. Durch monolithisches Design und Faserkopplung wird thermo-mechanische Stabilität erzielt. Das Konzept wird durch Berechnungen und Ende-zu-Ende-Simulationen evaluiert. Der Empfängerprototyp wird dann realisiert und im Labor charakterisiert. Erste bodengestützte Messungen im Frühjahr 2018 im Vergleich mit einem kommerziellen, kohärenten Lidar zeigen präzise, entfernungs aufgelöste Messungen, wobei auch systematische, zeitlich variable Fehler auftreten. Weitere Verbesserungen sind nötig um Wirbelschleppen aussteuern zu können.

Doppler wind lidar receiver, Michelson, wake vortices, turbulence, simulation, validation measurements

**Development and test of a UV lidar receiver for the measurement of wind velocities aiming at the near-range characterization of wake vortices and gusts in clear air**

Extended version of Doctoral Thesis, Ludwig Maximilian University of Munich

DLR-Forschungsbericht 2019-31, 2019, 255 pages, 159 figs., 18 tabs., 233 refs.

Gusts and wake vortices are a major cause of comfort degradations, incidents, and efficiency-reducing structure reserves in air traffic nowadays. Concepts for the automatic feed-forward control of these turbulences, i.a. during cruising flight, require highly-resolved near-range measurements of wind speeds in atmospheric regions with low aerosol concentrations. For this purpose a lidar receiver for uniaxial measurements is developed and tested in this thesis. A comparison of existing Doppler wind lidar concepts with respect to the requirements yields a fringe-imaging Michelson interferometer combined with a fast linear detector array. Monolithic design and fiber coupling aim at thermo-mechanical stability. The concept is evaluated through calculations and end-to-end simulations. The receiver prototype is then implemented and characterized in the laboratory. First ground-based measurements in spring 2018 are carried out in comparison to a commercial coherent lidar, revealing precise, range-resolved performance, whereby temporally variable systematic errors occur. Further improvements are necessary for alleviating wake vortex encounters.



---

# **Development and test of a UV lidar receiver for the measurement of wind velocities aiming at the near-range characterization of wake vortices and gusts in clear air**

Jonas Herbst

---



München 2018



---

# **Development and test of a UV lidar receiver for the measurement of wind velocities aiming at the near-range characterization of wake vortices and gusts in clear air**

**Jonas Herbst**

---

Dissertation  
an der Fakultät für Physik  
der Ludwig-Maximilians-Universität  
München

vorgelegt von  
Jonas Herbst  
aus Fürth

München, den 19.12.2018

Erstgutachter: Prof. Dr. rer. nat. Markus Rapp

Zweitgutachter: Prof. Dr. em. Wolfgang Zinth

Tag der mündlichen Prüfung: 5.04.2019

## Zusammenfassung

Diese Dissertation beschäftigt sich mit der Entwicklung und dem Test eines Empfängerprototyps für die einachsige Messung von Windgeschwindigkeiten in der Atmosphäre. Ein Lidarsensor auf Basis dieses Prototyps soll langfristig die Vision einer automatischen Ausregelung von Turbulenzen, Böen und Wirbelschleppen ermöglichen und so auf allen Flughöhen den Komfort verbessern, Unfällen vorbeugen, und zur Gewichtsreduktion im Flugzeugbau beitragen. Hierfür werden zunächst unterschiedliche direkte Doppler-Wind-Lidar (DWL) Empfängerkonzepte hinsichtlich der Sensoranforderungen dieser Anwendung theoretisch verglichen. Kriterien sind die Leistungsfähigkeit als spektraler Analysator, ihre Entfernungsauflösung, die Messbarkeit bei geringen Aerosolkonzentrationen, sowie der Überlapp in Nahdistanz, und ihre Komplexität. Auf Basis dieser Kriterien wird ein streifenabbildendes Verfahren beruhend auf einem Michelson-Interferometer ausgewählt, welches eine Kompensation der im Nahfeld auftretenden Winkelverteilungen ermöglicht. Der Überlapp in Nahdistanz (50 bis 300 m) und die Kombination mit einem schnellen Zeilendetektor erlauben die Messung an mehreren longitudinalen Messpunkten quasi gleichzeitig, und ohne Kenntnis des Partikelrückstreuverhältnisses. Das Konzept wird durch Berechnungen und End-to-end Simulationen evaluiert. Ein fasergekoppelter Aufbau wird konzipiert. Der Empfängerprototyp wird dann realisiert und charakterisiert. Ein monolithisches Michelson Interferometer soll thermomechanische Stabilität gewährleisten und wird hinsichtlich optimaler Leistungsfähigkeit spezifiziert und von einem Zulieferer gebaut. Das Interferometer wird dann in Bezug auf Streifenkontrast und Streifenform charakterisiert. Berechnungen und optische Simulationen zur Beleuchtung des Interferometers mit einer Multimodefaser und der Abbildung des linearen Interferenzstreifen auf ein Photomultipliertubearray werden durchgeführt und der Empfänger wird aufgebaut. Zu diesem Zweck werden Verstärkerelektroniken entwickelt, gebaut, und mit Analog-Digital-Wandler Karten kombiniert. Eine Multimodefaser wird in einer Kombination aus Experimenten und Simulationen hinsichtlich ihrer Scramblingeigenschaften zum Zweck der Biasreduktion und in Bezug auf Speckleeigenschaften zum Zweck der Specklerausunterdrückung untersucht. Für Validierungsmessungen wird ein Auswertalgorithmus der Interferenzstreifen entwickelt, welcher eine Korrektur der Beleuchtung des Interferometers beinhaltet. Für die Bestimmung der Streifenposition wird ein Downhill-Simplex-Algorithmus verwendet. Im Januar 2018 wurden mit dem aufgebaute Empfänger bodengestützten einachsige Windgeschwindigkeitsmessungen durchgeführt und mit Referenzmessungen eines kohärenten DWL (Windcube® 200S, Leosphere) verglichen. Es zeigt sich, dass die Horizontalmessungen beider Lidarsysteme eine hohe Korrelation von bis zu 0.89 aufweisen und dass der Prototyp Messungen mit einer Auflösung von 30 m in Entfernungen von 50 m und 76 m erlaubt. Allerdings zeigt sich auch ein entfernungsabhängiger systematischer Fehler von einigen m/s, dessen Zeitabhängigkeit durch eine Änderung der Beleuchtung hervorgerufen wird, und der korrigiert werden muss. Nach der Korrektur ist die relative Präzision beider Lidarsysteme um die 0.7 m/s für den Fall dass jeweils über ein halbe Sekunde gemittelt wird. Weitere vertikal orientierte Windgeschwindigkeitsmessungen im März 2018 erlauben langreichweitige (bis 900 m), entfernungs aufgelöste Messungen mit dem Empfängerprototyp. Ein Vergleich mit den Anforderungen für das Aussteuern von Wirbelschleppen mit einer erforderlichen Messrate von mehr als 45 Hz bei gleichzeitiger Messunsicherheit kleiner 1 m/s ergibt dass der Empfänger diesen Anforderungen noch nicht entsprechen kann. In Zukunft sind Verbesserungen der Effizienz des Empfängers, der Temperaturstabilisierung, sowie der Beleuchtungsfunktionskorrekturroutine erforderlich.

## Abstract

This thesis describes the development and test of a lidar receiver prototype for the uniaxial measurement of wind speeds in the atmosphere. An airborne lidar sensor based on this prototype may in the long run facilitate the vision of a feed-forward control of turbulence, gusts and wake vortices, in order to enhance comfort, prevent accidents, and reduce the weight of future aircraft constructions. For this purpose, different direct-detection Doppler Wind Lidar (DWL) receiver concepts are compared theoretically with respect to the sensor requirements of this application, i.e. with respect to the performance as spectral analyzer, range-resolution, measurement capability with low aerosol concentrations, overlap in the near-range (50 m to 300 m), and complexity. With respect to these criteria, a fringe-imaging Michelson interferometer is selected, which enables compensation of the angular distributions in the near-range. Full overlap in the near-range combined with a fast linear array detector permit wind speed measurements at multiple longitudinal measurement points quasi-simultaneously and without knowing the particle backscattering ratio. The concept is evaluated by calculations and end-to-end simulations. A fiber-coupled setup is conceptualized. The receiver prototype is then realized and characterized. A monolithic Michelson interferometer is to provide thermo-mechanical stability, and is specified according to optimal performance, and is built by an industrial supplier. The interferometer is then characterized with respect to interference fringe contrast and shape. Calculations and optical simulations of the multimode fiber-coupled illumination of the interferometer and of the imaging of the linear fringe on a photomultiplier tube array are carried through and the receiver is built up. For this purpose, amplifier electronics are designed, built, and combined with analog-to-digital converter cards. A frequency-tripled Nd:YAG laser is applied as transmitter. A multimode fiber is characterized in a combination of experiments and simulations with regard to its scrambling properties for reducing biases and with regard to its speckle properties for reducing speckle noise. For validation measurements a retrieval algorithm is developed, which entails a correction of the illumination of the interferometer. A fitting routine based on a Downhill-Simplex-Algorithm is applied for determining the shift of the interference fringes, yielding the Doppler frequency shift and the line-of-sight component of the wind speed. In late January 2018, ground-based, uniaxial wind speed measurements with the receiver prototype were carried out and are compared to referential measurements with a coherent DWL (Windcube<sup>®</sup>200S, Leosphere). It shows that horizontal measurements of both lidar systems yield a high correlation of up to 0.89 and that the prototype allows for wind speed measurements with a measurements resolution of 30 m at distances of 50 m and 76 m. However it shows as well that a range-dependent systematic error of several m/s exists, which has to be corrected. Its time-dependence is evoked by a long-term change of the illumination. After correction the relative precision of both lidar systems is around 0.7 m/s in case of respective averaging times of 0.5 s. Further vertically oriented wind speed measurements in March 2018 reveal that long-range (up to 900 m), range-resolved measurements can be done with the receiver prototype. A comparison with the requirements for the feed-forward control of wake vortices (i.e., a measurement update rate above 45 Hz and at the same time a measurement uncertainty of  $< 1$  m/s) yields that the receiver prototype does not currently meet those requirements. In the future, improvements of the efficiency, of the temperature stabilization, and of the illumination function correction routine are necessary.

# Contents

<b>1</b>	<b>Introduction</b>	<b>1</b>
1.1	Context . . . . .	1
1.2	State-of-the-art and mitigation strategies . . . . .	2
1.3	Objective and questions . . . . .	5
1.4	Structure of the thesis . . . . .	7
<b>2</b>	<b>Fundamentals</b>	<b>9</b>
2.1	Light Scattering in the atmosphere . . . . .	9
2.1.1	Scattering by molecules and aerosols . . . . .	9
2.1.2	Lidar equation and the optical Doppler effect . . . . .	11
2.2	Doppler wind lidar . . . . .	12
2.2.1	Coherent technique . . . . .	12
2.2.2	Direct-detection . . . . .	13
2.3	Mitigation of atmospheric disturbances for fixed-wing aircraft . . . . .	16
2.3.1	Wake vortices . . . . .	16
2.3.2	Clear-air turbulence and gusts . . . . .	17
2.3.3	Impact alleviation control of wake vortices and gusts . . . . .	18
2.4	History of wake vortex and turbulence detection lidars . . . . .	19
<b>3</b>	<b>Development of a Doppler wind lidar receiver</b>	<b>23</b>
3.1	Requirements on lidar transmitter and receiver . . . . .	23
3.2	Comparison of different coherent and direct-detection techniques . . . . .	24
3.3	Selected receiver principle . . . . .	29
3.3.1	Receiver overview: FWFIMI with fiber-coupled illumination . . . . .	30
3.3.2	The fringe-imaging Michelson interferometer as a spectral analyzer . . . . .	33
3.4	Design of a monolithic fringe-imaging Michelson interferometer . . . . .	37
3.4.1	Field-widening compensation . . . . .	37
3.4.2	Temperature tuning compensation . . . . .	40
3.4.3	Fabrication tolerances and instrumental contrast . . . . .	43
3.4.4	Fringe localization . . . . .	46
3.5	Characteristics of the actual physical receiver . . . . .	47
3.5.1	Specifications and characteristics of the FWFIMI . . . . .	48
3.5.2	General characterization of the interference fringe . . . . .	49
3.5.3	Receiver prototype and electronics . . . . .	55
3.5.4	Fiber induced speckle / modal noise . . . . .	63
3.5.5	Scrambling gain measurements of various fibers . . . . .	67
3.5.6	Illumination function determination procedure . . . . .	70
3.5.7	Interferometer temperature tuning and stability . . . . .	72
3.6	Laser transmitter characteristics . . . . .	74
<b>4</b>	<b>End-to-end simulation</b>	<b>77</b>
4.1	Prerequisites . . . . .	77
4.2	End-to-end simulation of horizontal wind speed measurements . . . . .	87
4.3	Estimation of the random error due to laser beam pointing fluctuations . . . . .	89

4.4	Estimation of biases due to illumination function deviations . . . . .	91
4.5	End-to-end simulation of vertical measurements with comparisons to CRB calculations and field-test measurements . . . . .	94
4.6	Lidar system scaling for improved performance . . . . .	95
<b>5</b>	<b>Field-tests of the lidar receiver on the ground</b>	<b>99</b>
5.1	Doppler wind lidar receiver prototype and measurement setup . . . . .	99
5.2	Development of a wind speed retrieval algorithm . . . . .	101
5.3	Validation measurements . . . . .	107
5.3.1	Moving hard target speed measurements . . . . .	107
5.3.2	Horizontal wind speed measurements . . . . .	109
5.3.3	Vertical wind speed measurements . . . . .	117
5.4	Discussion and Outlook . . . . .	123
<b>6</b>	<b>Summary</b>	<b>127</b>
<b>A</b>	<b>Background on field-test measurements of the AEROLI receiver</b>	<b>131</b>
<b>B</b>	<b>Lidar parameters</b>	<b>149</b>
B.1	Parameters of the Green-Wake project . . . . .	149
B.2	Results of the OWIDIA lidar sensitivity parameter study . . . . .	149
<b>C</b>	<b>Theoretical background</b>	<b>155</b>
C.1	Speckle . . . . .	155
C.2	Cramér-Rao lower bound of an ideal multichannel spectral analyzer . . . . .	161
C.3	Cramér-Rao bounds of real Doppler wind lidar receivers . . . . .	163
C.4	Influence of speckle on performance . . . . .	166
C.5	Plane wave propagation in fringe-imaging interferometers . . . . .	168
C.6	Analytical model of interference in Michelson interferometers . . . . .	173
C.7	Current amplifier model . . . . .	181
C.8	Mean wavelength estimators . . . . .	183
<b>D</b>	<b>Raytracing models and simulations</b>	<b>193</b>
D.1	Receiver front-end . . . . .	193
D.2	Monolithic fringe-imaging Michelson interferometer . . . . .	197
D.3	Receiver back-end . . . . .	202
D.4	Design of a two-lens optical scrambler . . . . .	205
<b>E</b>	<b>Specifications and test sheets of the Michelson interferometer</b>	<b>207</b>
<b>F</b>	<b>Equipment</b>	<b>215</b>
<b>G</b>	<b>Further fiber speckle measurements</b>	<b>223</b>
<b>H</b>	<b>Near-field and far-field scrambling measurements</b>	<b>227</b>
<b>I</b>	<b>Estimation of laser transmitter beam pointing fluctuations</b>	<b>233</b>
<b>J</b>	<b>Proposed green-UV dichroic mode for determining <math>R_b</math></b>	<b>235</b>



# 1 Introduction

## 1.1 Context

Wake vortices, gusts, and turbulence in clear air impose a major risk in commercial air transport ([Rossow and James, 2000](#); [Sharman, 2016](#)).

Wake vortices are an unavoidable complex artificial phenomenon accompanying any lift-generating, fixed-wing aircraft. Wake turbulence is constituted of a pair of coherent, counter-rotating vortices, which induce vertical air velocity fluctuations ([Gerz et al., 2002](#); [Breitsamer, 2011](#)).

Atmospheric turbulence designates irregular or disturbed flows in the atmosphere, which produce gusts and eddies, and which are caused by natural phenomena, such as storms and thunderstorms. Clear-air turbulence (CAT) is not caused by visible convection, and is often related to wind shear, especially between the core of a jet stream and the surrounding air, and to atmospheric gravity waves ([Sharman, 2016](#)). A (discrete) gust is a sudden, short duration ( $< 20$  s) increase of wind speed with peak to lull amplitudes of at least 9 knots ( $\approx 4.6$  m/s) (definition by the American Meteorological Society [AMS \(2018\)](#)).

If encountered by another aircraft, these types of turbulence can cause unexpected rolling moments, vertical acceleration, or abrupt changes of altitude, and structural dynamic loads upon the aircraft ([Sharman, 2016](#)), which may result in damage to the plane or injuries to the passengers ([Tvaryanas, 2003](#)).

For U.S. accidents between 1987 and 2011, 13% of the accidents can be attributed to CAT, and 7% to wake turbulence ([Evans, 2014](#)) with around 70 wake related accidents in total. [Evans \(2014\)](#) attributed another 24% of the accidents to low altitude wind shear, gusts, microbursts or turbulence (LWT), which occurred primarily during take-off, approach and landing. Wake related accidents happened during all flight phases, but mostly during take off and descent, while CAT is mainly a cruise flight and descent phenomenon.

Wake vortex encounter events (WVE) in the en-route phase of the flight and related accidents are still rather rare events. 73 wake induced incidents above 5000 ft, 27 of whom occurred above flight level FL285 (= 28,500 ft or 8687 m above mean sea level for the international standard atmosphere (ISA)) have been reported in Europe between 2009 and 2012 ([Hoogstraten et al., 2015](#)).

One such recent spectacular event was an incident which transpired on January 7, 2017 over the Arabian sea during cruise flight (at FL340  $\approx$  10360 m above sea level), when a Bombardier challenger 604 jet passed 300 m underneath an Emirates Airbus 380 and hit its wake (15 NM behind), the pilot lost control, the jet flipped upside down, rolled, and plunged 8700 ft before the pilot could flare out the aircraft ([BFU, 2017](#)). Typical for such accidents, passengers who were not seat-belted were thrown against the seats and ceiling and suffered serious or minor injuries. The jet had to be discharged.

The standard 1000 ft vertical separation in RVSM (Restricted Vertical Separation Minima) ([BFU, 2017](#)) was maintained, although it had been noted in a special safety case for the A380-800, that at cruise speed wake vortices sink into the flight path 10 to 20 NM behind and 1000 ft below the generator aircraft under calm atmospheric conditions ([EU-ROCONTROL, 2006](#)).

Similar wake turbulence related accidents with injuries were reported for example in 2008 ([TSB, 2008](#)), 2011 ([CIAIAC, 2011](#)), and 2001 ([NTSB, 2001](#)), or incidences even lead

to an aircraft crash, e.g. (*NTSB*, 2004, 1994).

Turbulence appears to be the leading cause of passenger injuries (*Sharman*, 2016). According to the FAA, between 1980 and 2008, 234 turbulence events with 298 serious injuries were reported, two thirds of which occurred at altitudes above 30000 ft (*FAA*, 2018). Apart from that, the comfort of air travel is reduced by the “bumpiness” felt.

The annual increase of passenger volume in the last ten years is around 4% (*IATA*, 2015) with only minor reductions due to global crisis, and lets await similar growth rates in the future, and thus an increased number of artificial wake turbulence sources and an increased number of (en-route) wake turbulence encounters.

Likewise, natural turbulence, such as CAT is likely to increase due to global warming as was estimated using climate model simulations, making predictions on a time scale of 50 years (*Williams and Joshi*, 2013; *Storer et al.*, 2017).

Simulations analyzing the encounter probability on the basis of surveillance data, suggest that wake vortex encounters will increase in the future (*Hoogstraten et al.*, 2015), due to increased traffic, a more heterogeneous fleet (e.g., very light and very heavy jets, drones), different operation schemes of SESAR2020 (*SESAR*, 2015), less dispersion of the flight tracks, and reduced separation minima (*Melgosa Farrés et al.*, 2017). The risk of wake vortex encounters is mainly influenced by the weight of the generating aircraft, the encounter geometry, and atmospheric conditions (*Hoogstraten et al.*, 2015). Furthermore, estimated annual expansion of the tropical region of one degree of latitude (*Reichler*, 2009) due to global warming, may lead to an increased average tropopause height in European airspace, which may increase en-route wake vortex related encounters, because of lower vortex decay rates below the tropopause (*Hoogstraten et al.*, 2015).

## 1.2 State-of-the-art and mitigation strategies

Today’s traditional risk reducer in case of wake vortex turbulence is a standard minimum distance of travel between any two planes, which is chosen according to the aircrafts’ maximum takeoff weights (*ICAO*, 2016) with special guidelines for heavy aircraft, for instance the Airbus A380 (*ICAO*, 2008), such that the vortices have safely decayed or subsided before the encounter. The guidelines are voluntary, and can be country specific, so that in the U.S.A. slightly different rules defined by the FAA (*FAA*, 2014) apply.

Wake vortex decay rate is a matter of the vortex strength, the stratification of the atmosphere, the turbulence-kinetic-energy dissipation rate, and the advection with horizontal and vertical wind (*Schumann and Sharman*, 2014). Typical decaying times are in the order of a few minutes. In some cases current separation standards defined by the ICAO (*ICAO*, 2016) could not be sufficient, although studies such as *Schumann and Sharman* (2014) show, that they are often too conservative. Within the RECAT-EU (wake vortex re-categorization) framework (*Rooseleer and Treve*, 2018) wing geometry, A380 flight tests, and wake decay models are taken into account. Future separation plans include weather conditions and specific aircraft pairings.

In terms of gusts and turbulence, the standard measures are to consider maximum loads and an additional safety factor in the design of aircraft structures. Another applied method is to go to a defined “safe air airspeed” in the presence of turbulence. Both strategies are effective, however, they reduce efficiency by an increase of mass or by longer flight durations (*Fezans et al.*, 2017).

Enforcing safety and providing comfort in a future of increased air traffic, increased natural turbulence, and reduced separation minima could be a problem, because this would often require precise knowledge about the turbulent regions ahead, and possibly fast counteracting measures, in order to eliminate the risk of incidents and accidents, especially as complexer guidelines may lead to an increased human error rate. In the same way, a reduction of the safety margins in aircraft design is not possible without a better prediction of loads caused by turbulence.

During cruise flight, especially in clear-air atmosphere, onboard weather radars cannot detect turbulence nowadays (*Airbus*, 2007). Recent radars provide some turbulence detection functionality in the presence of clouds and precipitation (*Baynes and Tyrdy*, 2014).

During the starting and landing phase, plates installed on the ground could be used to increase the decay rate of wake vortices (*Holzäpfel et al.*, 2016).

In case of wake turbulence, approaches have been researched to influence the vortex strength and decay of the generator aircraft with the help of passive spoilers or triangular flaps, splines or tail wings, and active methods, which involve moving and oscillating flaps or synthetic jets (*Schwithal*, 2017). Another research branch is focused on the influence on the encountering aircraft. In this case the aim is to reduce the risk of wake vortex encounters. One way is related to the prediction of likely wake vortex locations using various prediction models, such as “P2P” (*Holzäpfel*, 2006). An example, for a tested system, which combines prediction, avoidance, and awareness is the Wake Encounter Avoidance and Advisory (WEAA) system, developed by DLR, successfully tested on the research aircraft ATRA, performing small scale evasions of wake vortex encounters (*Bauer et al.*, 2014).

Another way is to sense the forces induced by the wake vortex (or turbulence). Future possibilities could include a direct feedback to the forces of the wake vortex on the aircraft by new flight controller routines, examined by *Looye et al.* (2012), or the remote sensing of the disturbances caused by wake vortices and turbulence. Remote sensing in the far-range (several km distant) could be used to circumvent the turbulent region (first option). This approach requires long warning lead-times and a reliable detection of the wake vortex or turbulence.

Alternatively, the consequences of flying through these areas could be attenuated, using prior knowledge about the disturbance ahead (second option). Automatic alleviation and control of wake vortices, however requires relatively high resolution measurements of the wind field in the near-range (typically 50 m to  $\approx 300$  m) ahead of the aircraft (*Ehlers et al.*, 2015; *Ehlers and Fezans*, 2015; *Schwithal*, 2017).

*Schwithal and Fezans* (2016) deem a full-scan update rate of the wind field measurement of 5 to 10 Hz appropriate for their concept of wake impact alleviation control to work reasonably well in the near-range, at a range of 60 m ahead of the aircraft. For wake vortex alleviation a wind speed measurement accuracy  $<1$  m/s, a high density of measurement points with at least nine measurement directions, and a spatial resolution in the order of 20 to 30 m, are further requirements. The control concept includes a wake identification algorithm, which allows one to reconstruct the wake vortex disturbance, and alleviates its impact by specific control commands compensating for the determined disturbance. After a computation time of 200 ms for the first identification of the wake vortex, the control system continuously (typical sampling time in the order of 20 ms (*Schwithal and Fezans*, 2016)) countervails the disturbances on the basis of the determined wake vortex model.

Note that the disturbance reconstruction step allows the anticipation of the disturbances

at locations where no measurement was made (or not yet), leading to rather complex relationships between the sensor measurements (location, orientation, and quality) and the disturbance rejection capability. Actuator time delays, which are assumed to be 100 ms, are compensated by predicting the wake vortex impact on the aircraft for a moment 100 ms in the future (*Schwithal and Fezans, 2016*). The simulated system works acceptably on “young” vortices (up to 48 s after initiation), which are not too much deformed (*Schwithal, 2017*). According to *Schwithal (2017)*, deformation models, e.g., by *Münster (2011)* could however be included to improve performance, i.e., to increase the reduction of the wake-induced bank angle for moderately and strongly deformed wake vortices.

*Schwithal (2017)* estimates that the system would most likely allow for an aircraft spacing reduction from current minimum separation standards (*ICAO, 2016*) to minimum radar separation.

Loads due to gusts and turbulence could be applied to a similar alleviation and control scheme (*Fezans et al., 2017*), which would possibly allow for lighter aircraft and a higher comfort. Provided that a suitable Doppler wind lidar (DWL) sensor existed, which is currently not the case, a higher alleviation performance, compared to prior alleviation approaches (see e.g., *König and Hahn (1990)*, *Zeng and Moulin (2010)*), would be possible (*Fezans et al., 2017*). *Fezans et al. (2017)* tested their scheme on an analytical 1-cosine vertical gust, using a free-form wind field model. Conical scanning of the DWL lidar line-of-sight direction at ranges between 65 m and 300 m ahead of the aircraft model, assuming a measurement accuracy standard deviation of the measured velocities of 1.5 m/s, was simulated, allowing for a reconstruction of the gust. Free-form wind field models consist of a mesh of wind field vectors surrounding the airplane, and are necessary due to the stochastic nature of turbulence, and when no particular turbulence model structure may be assumed (*Fezans and Joos, 2017*). Scanning is necessary, because the most important turbulence velocity component for loads is the vertical one, which affects local lift via a local modification of the angle of attack. The Feedforward Gust Load Alleviation controller, in combination with a feedback controller, yielded promising results (*Fezans and Joos, 2017*).

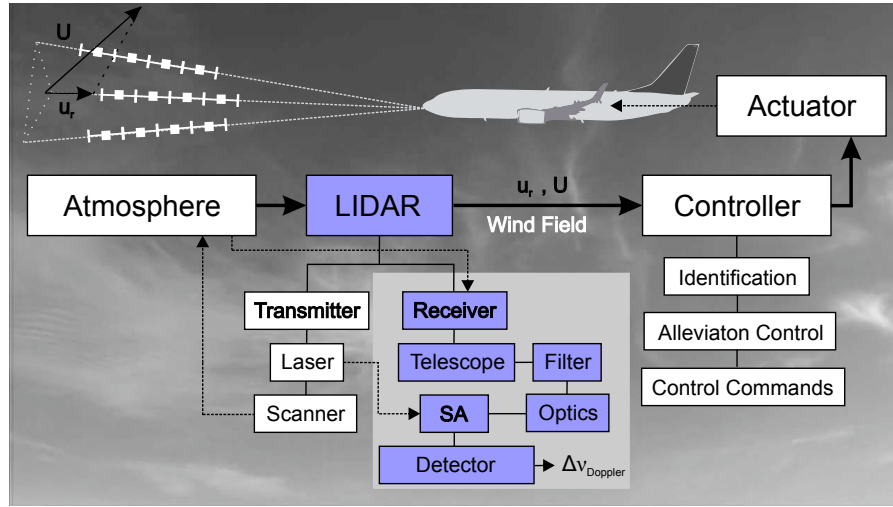
Such a generalized mitigation strategy including a suitable Doppler Wind Lidar (DWL) sensor could be the key to increasing aircraft efficiency by an optimization of aircraft structures to the really occurring loads induced by natural turbulence, or by reducing the separation minima (*ICAO, 2016*), which are necessary due to (artificial) wake turbulence.

Fig. 1.1 shows a conceptual scheme of such a turbulence alleviation system including the necessary Aeronautics Lidar (AEROLI) DWL sensor.

The DWL includes a high power transmitter and a receiver with a spectral analyzer (SA) and a detector to determine the Doppler frequency shift ( $\Delta\nu_{Doppler}$ ) of light scattered by molecules and/or aerosols moving with the wind, along the line-of-sight (LoS) of the laser beam, which is scanned vertically and horizontally in order to sample the required portion of the wind field.

Efforts have been undertaken to develop and flight-test DWL sensors to mitigate turbulences. A forward-looking lidar sensor (direct-detection DWL) was developed by Airbus (*Schmitt et al., 2007*) and was tested during the “Aircraft Wing with Advanced Technology Operation” (AWIATOR) FP5 EC-project (*Rabadan et al., 2010*). This DWL sensor proved the practicality of low spatial resolution wind field measurements, verified against true air speed at cruise flight levels in the near-range in four measurement directions at a distance of 60 m.

JAXA developed and tested a coherent DWL for the detection of turbulence several



**Figure 1.1:** Concept for the alleviation of atmospheric disturbances by feed-forward control including an Aeronautics Lidar Doppler Wind Lidar (AEROLI-DWL) sensor concept.

kilometers ahead of an aircraft in cruise flight (*Inokuchi et al., 2016*), which would be needed to implement an avoidance strategy. In this case wind speed variances are determined as a measure of turbulence intensity.

These systems are however not suitable for above described alleviation and control schemes, comparing them to requirements estimated by *Schwithal (2017)*. In case of the AWIATOR DWL, the main reasons are the low concentration of aerosols, the low densities of molecules at cruise flight altitudes, as well as systematic biases, which make high speed wind measurements an intricate endeavor. Major deficiencies of the AWIATOR DWL are also its low spatial resolution (four wind field component measurements at a single distance ahead of the aircraft) and its low measurement accuracy of 1 to 1.5 m/s during flight tests (*Rabadan et al., 2010*).

In case of coherent detection DWL systems (e.g., *Inokuchi et al. (2016)*) the low spatial and temporal resolution (25 m to 150 m,  $> 1$  s) are major problems. Moreover, the reliance on high enough aerosol concentrations necessary for accuracies  $\sigma(u_r) < 1$  m/s, provides an inherent, unacceptable risk of failure of any feed-forward control system equipped with a coherent DWL. The system should work independent of the flight level and of the weather conditions, i.e., also under clear-air conditions, and on cruise flight level. No studies specifying high enough aerosol concentrations for a close to 100% reliability of a coherent DWL, on cruise flight level in a feed-forward control scenario, exist to the present day.

Accordingly, no DWL receiver, meeting the requirements for the reliable alleviation of atmospheric disturbances by feed-forward control during flight, is implemented nowadays.

### 1.3 Objective and questions

The general objective of this thesis is to develop and test a receiver prototype for the unidirectional measurement of wind speeds in the atmosphere. The prototype should provide range-resolved high accuracy radial wind speed measurements ( $\sigma(u_r) < 1$  m/s) at near-range distances ( $\approx 50$  m to 300 m), independent of the aerosol backscattering signal, with high update rates on the order of  $> 45$  Hz. A thorough evaluation of these requirements would necessitate airborne test measurements, which is far beyond the frame of this

work. Therefore, in this work a receiver is developed and the corresponding AEROLI-DWL (Aeronautics Lidar – Doppler Wind Lidar) is tested on the ground, and theoretical performance predictions and the measurement results are compared with the requirements for the feed-forward control of wake vortices in clear air.

Specifically, within this work the following questions are evaluated:

**1.1) What are the most promising state-of-the-art Doppler wind lidar receiver techniques for this application and how do they compare?**

This question is dealt with by a literature study, comparing different direct detection Doppler wind lidar (DWL) concepts. These techniques can be compared with respect to theoretical performance using so-called performance factors, which compare their performance to an ideal spectral analyzer. Further important criteria, are range-resolution, performance at cruise flight level (i.e., in low particle concentration environments), applicability of full overlap in the near-range, eye-safety, speckle noise behavior, and bias suppression. A further important factor is realization in terms of device complexity.

**1.2) Which technique for wind measurements on cruising altitude is especially suited and realizable?**

This question is answered using a comparison of the performance factors, and other criteria defined above. Theoretical performance calculations of the selected technique are used to estimate the performance on cruise flight level, and to study influences of particle concentration, temperature, and background sunlight. Raytracing simulations are applied to estimate the geometrical requirements, i.e., the required field-of-view for total overlap in the near-range, and the consequent requirement on the spectral analyzer with respect to incident angular distributions of the received light. A plane wave propagation method is used to evaluate the performance of different spectral analyzers with respect to these angular distributions. End-to-end simulations are used to verify the selected fringe-imaging Michelson concept against theoretical performance calculations under different conditions.

**2.1) Can such a Doppler wind lidar receiver prototype be built up and characterized?**

The selected receiver concept is realized, designing the spectral analyzer of the selected direct-detection DWL receiver concept. The monolithic Michelson interferometer is designed using a combination of calculations and optical simulations, and is specified with an optimized free spectral range (FSR), with field-widening compensation, with temperature tuning compensation, and according to the requirements for a high instrumental contrast, as a Rayleigh-Mie receiver with pure molecular scattering capability. The interferometer is manufactured by an industrial supplier in Canada. Proper optics such as lenses, multimode fibers, and optomechanics are integrated into a prototype setup, aiming at thermomechanical stability. A combination of manufacturer measurements and test setups are used to verify the specifications. A linear fast photomultiplier tube array (PMTA) is selected as detector, and amplifier electronics are developed and built, to fit to the selected analog-to-digital converter boards. Algorithms for data acquisition with the PMTA are developed. Speckle noise and bias suppression with the help of a fiber-coupled setup are evaluated using a combination of speckle contrast measurements, a speckle noise simulation model,



and a combination of measurements and simulations to estimate laser beam pointing bias suppression. All the components are combined to yield a UV direct-detection Doppler wind lidar receiver prototype.

## **2.2) To what extent can the lidar receiver concept be validated by first ground-based wind speed measurements?**

This question is answered by deploying the lidar prototype including the WALES/DELICAT laser transmitter, and the AEROLI receiver inside a container with one line-of-sight (LoS) measurement direction on the Oberpfaffenhofen apron. A coherent detection DWL (Windcube® 200S by Leosphere) is installed, pointing into the same direction with additional anemometers located next to the LoS until the beam is dumped at 115 m horizontal distance. A horizontal alignment of both lidars is used to measure the turning speed of a moving hard target, and to measure the horizontal winds, during several measurement days, during day and night. Vertical alignment of the line-of-sights is applied to measure vertical wind speeds range-resolved up to altitudes of 900 m, which are compared between both instruments in order to verify the functionality of the AEROLI receiver.

## **2.3) Which requirements with respect to wake vortex alleviation control does the receiver prototype fulfill?**

This question is evaluated with results of end-to-end simulations using required LoS update rates implied by a lidar parameter study ([Schwithal, 2017](#)) for wake vortex alleviation and control, comparing them to the results of the field-test measurements.

# **1.4 Structure of the thesis**

This thesis is structured in a way, that the reader is introduced at first to the fundamentals of light scattering in the atmosphere ([2.1](#)), of Doppler wind lidars (DWL, [2.2](#)), to concepts for the DWL-sensor-based mitigation of wake vortices and gusts in clear-air ([2.3](#)), and to the history of lidar-based detection of wake vortices and turbulence ([2.4](#)).

Chapter [3](#) is dedicated to the development of the DWL receiver. Starting from requirements for wake vortex alleviation and control ([3.1](#)) based on the work of [Schwithal \(2017\)](#), a comparison of suitable existing direct-detection receiver techniques ([3.2](#)) is undertaken. Then, in section [3.3](#) an overview of the selected receiver concept based on a fringe-imaging Michelson interferometer, as spectral analyzer, is provided and its performance is evaluated theoretically. The following section ([3.4](#)) is dedicated solely to the design of a monolithic, field-widened fringe-imaging Michelson interferometer (FWFIMI) with partial temperature compensation, and with optimized specifications yielding high instrumental contrasts. The next section ([3.5](#)) describes the characterization of the FWFIMI and the realization of a fiber-coupled receiver, including optics and electronics. Next, measurements of speckle noise and scrambling gains of multimode fibers for random error reduction and bias reduction are described. Moreover, this section involves the development of a procedure for determining the illumination function of the receiver, and measurements of its temperature tuning and stability. At last, the laser transmitter used in this work is presented ([3.6](#)).

Chapter [4](#) describes the performed end-to-end simulation of the AEROLI receiver for the measurement of wind speeds. Prerequisites ([4.1](#)) include mean wavelength estimators

and their systematic biases, the modeling of noise, of cross-talk, laser-frequency jitter, and analog-to-digital conversion. These models are applied to simulations of horizontal measurements (4.2), to an estimation of the bias due to laser beam pointing fluctuations (4.3), and to an estimation of the bias due to illumination function deviations (4.4). Vertical measurements are simulated, as well (4.5). Finally, the wind speed measurement performance of improved receivers is estimated using Cramér-Rao bound calculations (4.6).

Having evaluated the performance theoretically, field-tests with the AEROLI receiver and with a Leosphere Windcube<sup>®</sup> 200S, performed in January and March 2018 are detailed in chapter 5. This chapter contains four sections, describing the settings and measurement setups (5.1), the steps of the wind speed retrieval algorithm (5.2), and the measurements as such (5.3). The field-test measurements are subcategorized into moving hard target measurements, horizontal wind speed measurements, and vertical wind speed measurements. The last section (5.4) contains a discussion of the measurements and a comparison with the requirements for wake vortex alleviation and control, followed by an outlook.

Further important fundamentals underlying this work are treated in the appendix of this thesis. Chapter A contains background information on the field-test measurements. Chapter B provides more detailed information on lidar sensor requirements and on the lidar parameters study (Schwithal, 2017). Chapter C describes important theoretical background, i.e., on speckle (C.1), on the Cramér-Rao bound of an ideal spectral analyzer (C.2) and of real DWL receivers (C.3), and on the influence of speckle on performance (C.4). Furthermore, a plane wave propagation model to estimate the field-widening performance of fringe-imaging interferometers (C.5) and an analytical model of interference in fringe-imaging Michelson interferometers (C.6) are described. The theoretical background chapter also provides information on the current amplifier model used during the development of the electronics (C.7), and a description of the mean wavelength estimators (C.8) applied in the end-to-end simulation chapter. Additional chapters treat the raytracing models and simulations used to design the interferometer and the receiver (D), the specifications of the FWFIMI (E), and the equipment used in the receiver and during testing (F). Further fiber speckle measurements (G), and near- and far-field scrambling measurements (H) are attached. Laser beam pointing fluctuations of the applied transmitter are estimated experimentally in appendix I. Finally, in appendix J a green-UV dichroic mode for measuring particle backscattering ratios, and the prospective performance of the receiver at a wavelength of 532 nm, are discussed.



## 2 Fundamentals

### 2.1 Light Scattering in the atmosphere

#### 2.1.1 Scattering by molecules and aerosols

This section recounts some important properties of laser light backscattered by molecules and aerosols in the atmosphere.

The atmospheric backscattering spectrum has two distinct features. A broad molecule peak (FWHM  $\approx 4$  GHz) due to Rayleigh-Brillouin scattering, as well as rotational and vibrational Raman scattering and a thin peak due to light scattered from aerosols/hydroparticles moving with the ambient wind. The aerosol peak is broadened by turbulence (see section 2.3.2, FWHM  $\approx 38$  MHz). There is an additional broadening contribution due to the laser (FWHM  $\approx 0.16$  GHz) (see, e.g., [Weitkamp \(2005\)](#) or [Witschas \(2012\)](#)).

This atmospheric backscattering spectrum can be modeled with the help of altitude-dependent temperature  $T$ , pressure  $p$ , and particle concentration data.

In case of [Collis and Russell \(1976\)](#) the molecular backscattering coefficient is inferred from molecule density data using  $p$  and  $T$  as function of altitude  $H$ , using  $\beta_{mol} = N_g \cdot d\sigma_R(\pi)/d\Omega$ , where  $N_g = p(H)/(R_{air}T(H)m_{air})$  is the number of air molecules per volume,  $d\sigma_R(\pi)/d\Omega = (550/\lambda_L[\text{nm}])^4 \cdot 5.45 \cdot 10^{-32}$  is the differential Rayleigh scattering cross section at scattering angle  $\theta = \pi$  per average gas molecule in  $\text{m}^2/\text{sr}$ ,  $R_{air} = 287.058 \text{ J kg}^{-1} \text{ K}^{-1}$  is the specific gas constant of (dry) air, and  $m_{air} = 4.811 \cdot 10^{-26} \text{ kg}$  is the average mass of an air molecule. Molecular backscattering cross sections can be derived from fundamental equations ([Miles et al., 2001](#)). [Bucholtz \(1995\)](#) includes the dispersion of the refractive index of air, the anisotropy of the air molecules, and the dispersion of the depolarization factor of air, to yield approximately the same results.

Particles or aerosols are assumed to be of spherical shape, such that backscattering from these particles can be considered purely elastic and without depolarization (i.e., Mie theory ([Mie, 1908](#)) applies) ([Wriedt, 2012](#)). Values of the particle backscattering coefficients  $\beta_{aer}$  are scaled from values determined by [Vaughan et al. \(1995\)](#) at  $10.6 \mu\text{m}$ , using  $\beta_{aer} = \beta_{aer}[10.6\mu\text{m}] \cdot (10.6/\lambda_L[\mu\text{m}]) \cdot (-0.104 \cdot \ln(\beta_{aer}[10.6\mu\text{m}])) - 0.62$ .

Fig. 2.1 provides median, lower and upper quartiles of the backscattering coefficients of molecules and aerosols as a function of altitude.  $R_b$  is the particle backscattering ratio given by  $R_b = 1 + \beta_{aer}/\beta_{mol}$  (plotted on the right side of Fig. 2.1).

Different models are used to calculate the spectra of light scattered in the atmosphere. The Knudsen model is a simple analytic model strictly valid only for thin gases, which is presented here for simplicity. The Knudsen model is a coarse approximation of the TentiS6 model ([Tenti et al., 1974](#)) or its approximation in the kinetic regime by three Gaussians - the ‘‘G3 model’’ ([Witschas, 2011](#)).

The Knudsen models describes the molecular scattering spectral shape  $I_{mol}(\nu)$  by a Gaussian. It can be combined with a Gaussian aerosol scattering peak  $I_{aer}(\nu)$ , convolved with

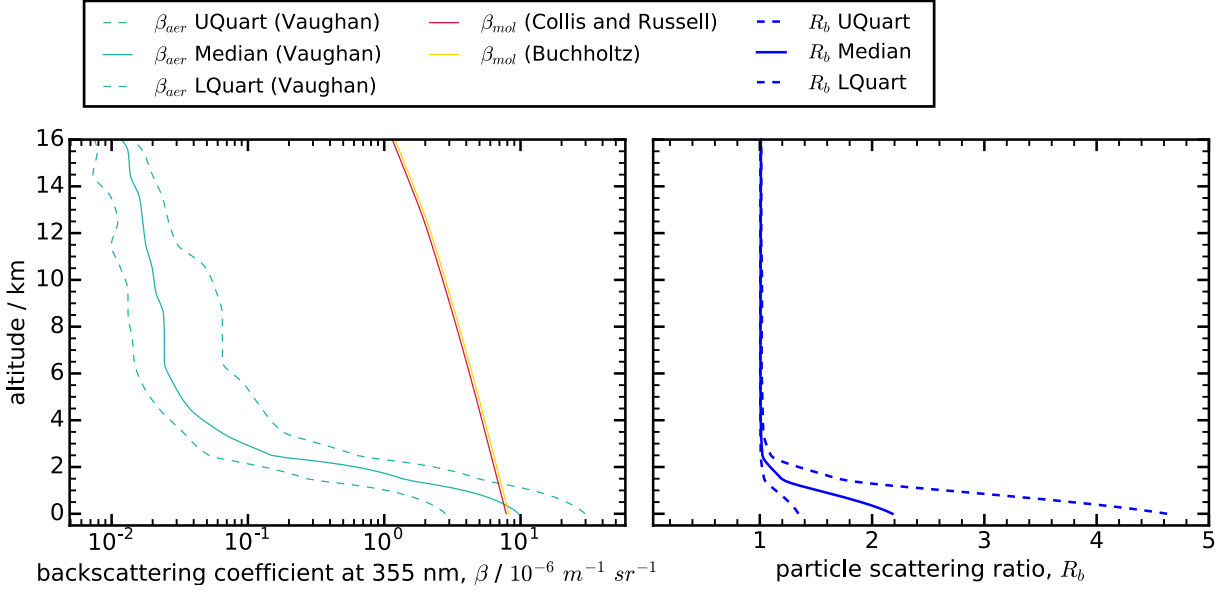


**Figure 2.1:** Left: Altitude-dependent backscattering coefficients of molecules ( $\beta_{mol}$ ) for two models (Collis and Russell (*Collis and Russell, 1976*), Buchholtz (*Buchholtz, 1995*)) assuming a mid-latitude standard (MLS) atmospheric model, and  $\beta_{aer}$  of aerosols at a laser wavelength ( $\lambda_L$ ) of 355 nm (derived from *Vaughan et al. (1995)* data for 10.6 SI), given here as lower and upper 25% (LQuart, UQuart) quartile, and median. Right: Dependence of the particle backscattering ratio  $R_b$  on altitude.

the Gaussian-shaped laser spectrum  $I_L(\nu)$ :

$$I(\nu) = [I_{mol}(\nu) + I_{aer}(\nu)] * I_L(\nu) = \frac{1}{R_b} \frac{1}{\sqrt{2\pi}\sigma_G} \exp \left[ - \left( \frac{\nu - \nu_c}{\sqrt{2}\sigma_G} \right)^2 \right] + \left( 1 - \frac{1}{R_b} \right) \frac{1}{\sqrt{2\pi}(\sigma_L^2 + \sigma_w^2)} \exp \left[ - \left( \frac{\nu - \nu_c}{\sqrt{2}\sqrt{\sigma_L^2 + \sigma_w^2}} \right)^2 \right]. \quad (2.1)$$

The backscattered light is shifted in frequency by  $\Delta\nu_D = \nu_c - \nu_L$ , here  $\nu_L$  is the frequency of the laser and  $\nu_c$  is the Doppler-shifted central frequency (see section 2.1.2).

$\sigma_G = (\sigma_{Ray}^2 + \sigma_L^2)^{1/2}$  is the standard deviation in Hz of the Rayleigh-Laser spectrum, whereby  $\sigma_{Ray} = 2/\lambda_L [(k_B T N_A)/m_{air}]^{1/2}$  is the standard deviation in Hz of the Rayleigh spectrum, where  $k_B$  is the Boltzmann constant,  $N_A$  the Avogadro constant and  $T$  the air temperature in the scattering volume.

$\lambda_L$  is the wavelength of the laser.  $\sigma_L = \Delta\nu_L/\sqrt{8\ln 2}$  is the standard deviation [Hz] of the Gaussian laser line shape, where  $\Delta\nu_L$  is the laser linewidth (FWHM) [Hz].

$\sigma_w = \sqrt{4/3}/\nu_L \cdot u_{r.m.s.}$  is the Doppler broadening (see *Measures (1992)*) due to the r.m.s. wind speed  $u_{r.m.s.}$ . Assuming isotropy,  $u_{r.m.s.}$  is equal to the vertical speed fluctuations  $\sigma(w)$ . Typical, conservative values of  $u_{r.m.s.}$  at flight level are  $\approx 5$  m/s (derived from energy dissipation rates using expressions by *Cornman et al. (1995)*; *Weinstock (1981)*) ( $\sigma_w \approx 6.8$  fm, i.e., 16.3 MHz) for moderate turbulence (*ICAO, 2010*).  $\sigma_w$  is about 10% as broad as the WALES laser transmitter lineshape (see section 3.6), and is therefore negligible.

The width of the peaks of the atmospheric backscattering spectra and their relative area are important in terms of temporal coherence, influencing phenomena such as atmospheric speckle (see appendix C.1) and Doppler wind lidar design (see chapter 3.3.2).

Exemplary molecular spectra calculated with the Knudsen and the TentiS6 model (top) and a Gaussian spectral peak of laser light backscattered from aerosols (bottom) are shown in Fig. 2.2(a). Fig. 2.2(b) provides altitude-dependent normalized spectral shapes, using the TentiS6 model and a Gaussian for aerosols and realistic values of  $T$ ,  $p$ , and  $R_b$ .

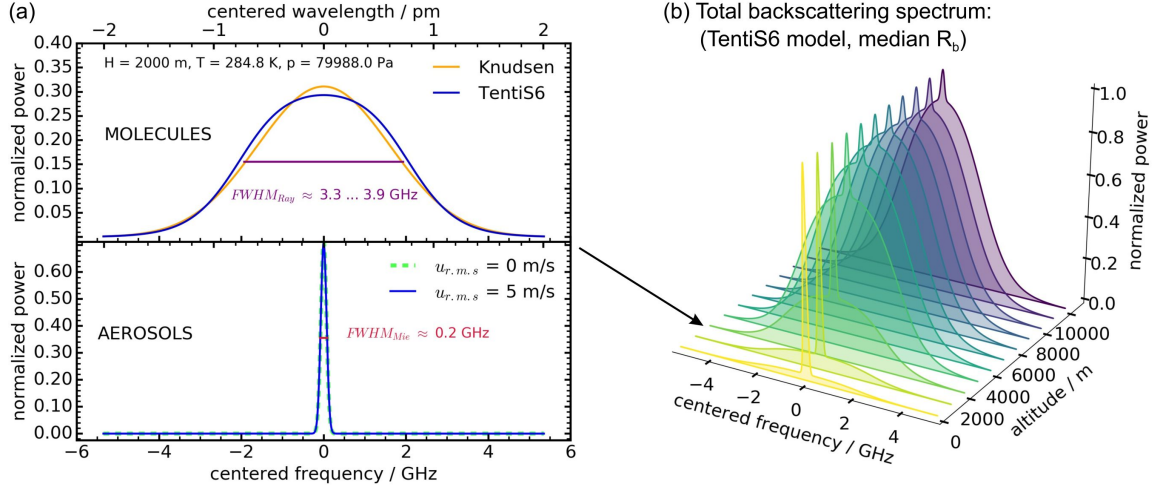


**Figure 2.2:** (a) Top: Spectral shape of laser light backscattered by molecules (Knudsen model of eq. 2.1 and the Kinetic Tenti S6 model (Tenti et al., 1974)), and by aerosols (bottom) in terms of centered frequency and centered wavelength. (b) Altitude dependence of the overall normalized spectral shape due to the altitude dependent relative number density of molecules and aerosols in the atmosphere.

In reality the extinction-to-backscatter ratio (lidar ratio,  $S_P$ ) and the particle linear depolarization ratio (LDR) of particles in the atmosphere are highly dependent on their type and shape, and there is large variability (Groß et al., 2015). A lidar ratio ( $S_P$ ) of 50 sr is a good estimate.

### 2.1.2 Lidar equation and the optical Doppler effect

#### Lidar equation

The amount of backscattered light received by the lidar can be calculated with the single-scattering lidar equation (Measures, 1992)

$$n_p(\nu_L, R) = E_L \frac{\Delta R}{h\nu_L} \frac{A_{tel}}{R^2} O(R) \eta_R \eta_T \beta \exp\left(-2 \int_0^R \alpha dr\right), \quad (2.2)$$

where  $n_p$  is the number of received photons, which is used here as a means to quantify the amount of backscattered light without making any assumption on its nature (see, e.g., Mishchenko (2014)).  $\nu_L$  is the frequency of the laser transmitter.  $R$  is the distance [m] of the light scattering volume in front of the telescope.  $\Delta R$  is the length of the range gate.  $E_L$  is the transmitted energy of one laser pulse with pulse duration  $\tau_p$ .  $h = 6.626 \cdot 10^{-34}$  Js is Planck's constant.  $A_{tel}$  is the receiver telescope area.  $O(R)$  is the range-dependent overlap function.  $\eta_R$  and  $\eta_T$  are the receiver and transmitter loss factors.  $\beta = \beta_{mol} + \beta_{aer}$  is the total backscattering coefficient.  $\alpha = \alpha_{mol_s} + \alpha_{mol_a} + \alpha_{aer}$  is the overall atmospheric extinction coefficient [1/m]. The molecular extinction coefficient is given by  $\alpha_{mol_s} = (8\pi/3) \cdot \beta_{mol}$  (Measures, 1992). Molecular absorption  $\alpha_{mol_a}$  is assumed to be zero everywhere.

### The optical Doppler effect

The received light can be shifted in frequency due to the optical Doppler effect. If scattering centers (molecules and aerosols in the air) and the receiver are moving with respect to each other with a velocity  $u$  (equal to the mean wind speed), and if the light emitted by the transmitter has a wavelength  $\lambda_L$ , the Doppler shift can be calculated by

$$\Delta\nu_D = \frac{2u \cos(\psi)}{\lambda_L}, \quad (2.3)$$

whereby  $\psi$  is the angle between the wind direction and the line-of-sight of the laser beam for monostatic conditions, and  $u \cdot \cos(\psi)$  is the radial wind velocity  $u_r$  ([Henderson et al., 2005](#)).

## 2.2 Doppler wind lidar

The term “lidar” stems from (“Light Detection And Ranging”). It is nowadays often used synonymously for laser radar (“ladar”). Doppler wind lidars (DWL) are a subcategory of lidars used for wind speed measurements, whereby the radial wind speed  $u_r$  is deduced from a Doppler shift measurement of light scattered back from molecules and aerosols ([Henderson et al., 2005](#); [Werner, 2005](#)). In the following the working principles of the two fundamental types of DWL, so-called “coherent” detection DWLs and “incoherent” direct-detection DWLs are summarized.

### 2.2.1 Coherent technique

The working principle is shown schematically in Fig. 2.3(a). In coherent DWL-systems with heterodyne detection both the return signal (scattered by aerosols) and the pulsed or continuous laser transmitter (LT) are optically mixed with a local oscillator (LO) with fixed offset frequency  $\nu_{\text{offset}}$  (offset locked with a phase lock loop (PLL)) and imaged onto high-speed detectors at the atmospheric signal output (DA) and the reference output (DR). The higher frequency component (carrier frequency) is the known fixed offset frequency  $\nu_{\text{offset}}$ . The pulse-to-pulse frequency jitter component of  $\nu_{\text{offset}}$  between LT and LO is determined from detector DR. The Doppler shift of the moving particles  $\Delta\nu_{\text{aerosol}}$  is determined from the lower frequency (RF) component (envelope) of the sinusoidally modulated signal, i.e., from the mean frequency of the resulting beat frequency spectrum ( $\nu_{\text{beat}}$ ) of the signal compared to the reference. The spectra are obtained e.g. by a fast Fourier transform (FFT). The axial wind speed component  $u_r(R)$  is then inferred from  $\Delta\nu_{\text{aerosol}}$ . The spectral width can be used to get information on the turbulence  $\sigma_{u_r}(R)$ , often called Doppler spectral width (DSW) (see, e.g., [Smalikho et al. \(2005\)](#)). The laser frequency  $\nu_{\text{laser}}$  is typically at 1.5  $\mu\text{m}$  to 1.6  $\mu\text{m}$ , 2  $\mu\text{m}$ , and 10.6  $\mu\text{m}$  depending on the laser technology, because in the infrared the ratio of the aerosol to the molecular backscatter coefficient is adequate.

Besides this down-conversion from the optical band (THz) to the RF band (MHz), the optical mixing amplifies the signal (heterodyning gain). This allows for near-quantum limited efficiency and for long-range detection of wind speeds in atmospheric regions containing aerosols, which is in general guaranteed at low and medium flight levels and near- to mid-range distances (ten to hundreds of meters). At higher altitudes, e.g., typical cruise flight level of 30 kft to 40 kft, the carrier-to-noise ratio (CNR) decreases due to lower particle

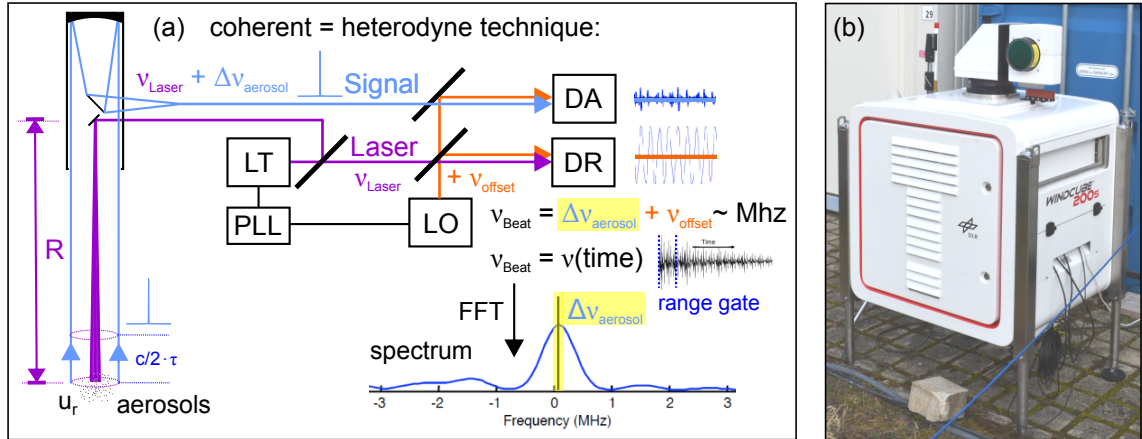


**Figure 2.3:** (a) Principle of coherent Doppler wind lidar (DWL) technique, (b) Commercial coherent detection DWL system (“Windcube® 200S”) used for reference measurements in this work.

densities (see section 2.1.1), reducing the precision of Doppler shift ( $\Delta\nu_{\text{aerosol}}$ ) determination and the maximum range  $R_{\text{max}}$ . The CNR is the height of the spectral peak above the shot noise floor in the spectral domain, or simply the ratio of the mean squared heterodyne signal photocurrent  $\langle i_h^2 \rangle$  to the receiver noise current  $\langle i_n^2 \rangle$  in the temporal domain. An adequate concentration of aerosols is necessary, because the mixing requires high temporal coherence of the return signal, i.e., a small spectral width of the signal (see section 2.1.1), and a narrow bandwidth (few MHz) of the laser. Furthermore, high transverse (spatial) coherence is required for an optimum mixing efficiency, which can be ensured by reducing the illuminated area of the target as much as possible (focusing the laser beam at the mean measurement distance), rendering the speckle grain size at the receiver as large as possible (application of the Van Cittert-Zernike theorem, see also appendix C.1). The interested reader finds more information for example in [Banakh and Smalikho \(2013\)](#) and [Henderson et al. \(2005\)](#).

In this work a commercial coherent detection DWL-system “Windcube® 200S” by Leosphere (developed in cooperation with ONERA) (Fig. 2.3(b)) is used as reference instrument. It operates at  $1.54\mu\text{m}$  with an internal laser power of 5 W, and a pulse width of 100 ns. It has a minimum accumulation time of 0.5 s, a range resolution of 25 m, a nominal range of 40 m to 6000 m, and is specified with a radial wind speed accuracy of  $<0.5\text{ m/s}$  (no details on range-dependence and on atmospheric conditions are provided), within a radial wind speed range of  $-30\text{ m/s}$  to  $30\text{ m/s}$  ([Leosphere, 2016](#)).

### 2.2.2 Direct-detection

The direct-detection techniques are all those DWL methods, where the Doppler shift is determined via direct spectral analysis, i.e., the Doppler shift is determined from the amount of light transmitted through filters of a spectral analyzer. The spectral analyzer is in general an interferometer (e.g., Fabry-Pérot, Fizeau, Michelson, or Mach-Zehnder). An overview of various direct-detection techniques is shown in Fig. 2.4. If laser wavelengths below  $1\mu\text{m}$  (in the visible and ultra-violet) are used, the molecular backscattering signal is strong, and wind speeds can be measured based on pure molecular backscattering signals, aerosol signals or a combination of these two.

The most popular frequency analyzer is the Fabry-Pérot interferometer (FPI), mainly



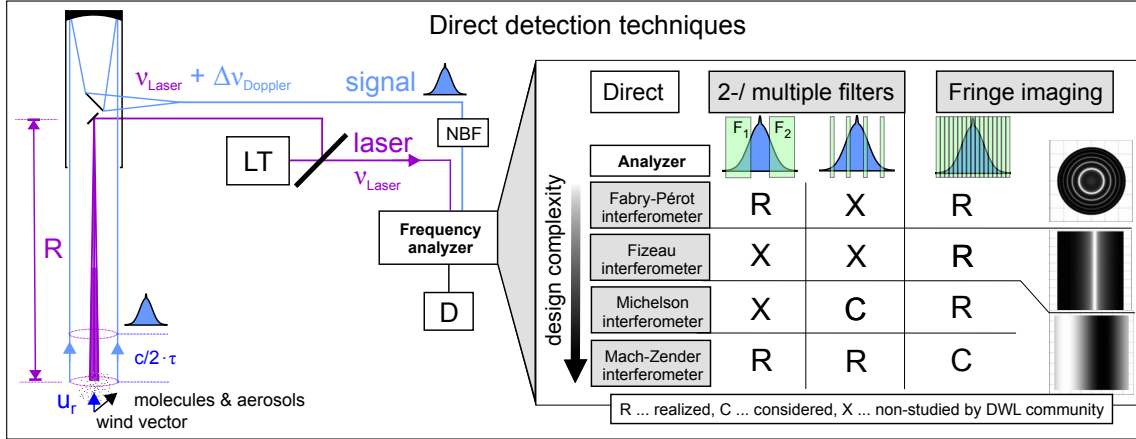


**Figure 2.4:** Concept of a Direct-detection receiver with different spectral analyzers / interferometers (Fabry-Pérot, Fizeau, Michelson, Mach-Zehnder) used in two-/ multiple filter and fringe-imaging methods.

due to the relative ease of fabrication. A Fabry-Pérot etalon consists of two plan-parallel mirrors of reflectance  $R$  at distance  $h_g$ . Two types of methods can be distinguished: two-/ multiple-filters and fringe-imaging.

The two-filter or double-edge technique (DE) is based on two Fabry-Pérot interferometers with different optical path lengths ( $h_{g1}$  and  $h_{g2}$ ) that determine the frequency of maximum transmission. The frequency-dependent transmission function of an FPI is periodic over the free spectral range ( $FSR = c/(2h_g)$ ) and Airy-shaped due to multiple interference (for details on etalon theory see, e.g., [Hernandez \(1986\)](#); [Vaughan \(1989\)](#)). The Doppler shift is determined by the ratio of transmission through these filters. The transmission through the filters strongly depends on the shape of the light scattering spectra as the instrument function is a convolution with the spectrum of the backscattered light (see section 2.1.1). That is why this method requires the knowledge of  $H$ ,  $T$ ,  $p$ , and  $R_b$ .

ADM Aeolus ([Durand et al., 2005](#)) and its airborne demonstrator (A2D) ([Lux et al., 2018](#)) are very prominent examples of the application of the double-edge technique. The Atmospheric Dynamics Mission ADM Aeolus is an ESA mission launched on August 22, 2018, with the aim of measuring altitude profiles of horizontal wind speeds from ground to stratosphere during a period of three years, in order to improve weather and climate predictions.

There is also a double-edge technique which consists of a single-channel all-fiber FPI, and a dual frequency laser pulse, positioned at the rising and falling edges of this channel ([Shangguan et al., 2017](#)). This concept could reduce complications caused by manufacturing requirements, precise alignment and environmental influences, when using a free-space FPI.

In practice, the required separation of the molecular and aerosol channels, e.g., used in the ALADIN instrument of ADM Aeolus ([Durand et al., 2005](#)), can only be circumvented by the use of multiple filters (MF) or of the fringe-imaging technique (FI).

The principle of fringe-imaging relies on the imaging of the interference pattern of an interferometer on a position-sensitive detector array. The frequency shift between a laser reference and an atmospheric Doppler-shifted signal can be determined from the difference of the spatial irradiance distributions on the detector channels.

A distinction can be made between multi-wave and two-wave interference. The most

common multi-wave interferometer is the Fabry-Pérot interferometer (FIFPI). When properly illuminated with divergent light, the produced interference fringes are rings. In this way every frequency component has a unique radial position within the annular fringe pattern imaged on a 2D detector. The rings radii change as the light is Doppler shifted. Here again the irradiance distribution on the detector (instrument function) is the convolution of the backscattering spectrum with the Airy-shaped transmission function of the FPI etalon. From the change of the shape of the instrument function, it is theoretically possible to infer the coupled parameters temperature  $T$ , and the particle back-scattering ratio ( $R_b$ ) (Cézard, 2008). It is a general feature of all cited fringe imaging techniques, that no knowledge of the particle backscattering ratio  $R_b$  is required for the determination of the Doppler shift induced change in position of the interference fringe. The FIFPI was the method of choice both in the AWIATOR project (Schmitt et al., 2007) and the Green-Wake project (Rees, 2014), which both aimed at detecting turbulence and wake-vortices (for details see section 2.4).

Another FI technique, which theoretically allows likewise the simultaneous determination of  $u_r$ ,  $T$ , and  $R_b$  (see, e.g., Witschas et al. (2016)), is the Fizeau fringe-imaging technique (FIFI). The Fizeau is a modified FPI with inclined mirrors, such that a linear fringe with a deformed Airy shape is obtained, which can be optimized choosing proper system parameters (McKay, 2002). In ADM Aeolus a FIFI is used in the aerosol channel (Paffrath, 2006). The advantage of the linear fringe is, that it can be imaged relatively easy onto fast, linear detector arrays. A major disadvantage is the strong sensitivity of the fringe shape on the incidence angle (see, e.g., Novak et al. (2011)) as well as contrast loss with extended, high étendue sources (see also appendix C.5).

The field-widening compensation necessary for high étendue sources can be achieved with two-wave interferometers, namely with the Mach-Zehnder interferometer and the Michelson interferometer. Compensation can be achieved with a glass plate (CP) inside one of the arms (as described as early as in 1941 (Hansen, 1941), see appendix C.6, Hilliard and Shepherd (1966)).

Liu and Kobayashi (1996) proposed to use a Mach-Zehnder interferometer in a direct-detection DWL, using a two-channel differential discrimination method (DMZ), similar to the DE technique using the FPI, only that the transmission function is cosine-shaped. An all-fiber two-channel Mach-Zehnder frequency discriminator for an aerosol Doppler wind lidar was verified, recently (Wang et al., 2017). The DMZ-method requires, however, like the DE-method a knowledge of  $R_b$  and  $T$ .

Bruneau considered a four-channel-based free-space version (QMZ) with polarization multiplexing achieved by using a quarter-wave plate (QWP) and polarizing beamsplitters (PBS) (Bruneau, 2001), and an equivalent field-widened fringe-imaging Mach-Zehnder interferometer with inclined mirrors (FIMZ) (Bruneau, 2002), both optimized for Rayleigh scattering, but applicable without knowledge of any particle backscattering ratio  $R_b$ .

Bruneau and Pelon (2003) showed that the concept can be used to measure wind speeds. An application of this principle is the Optical Autocovariance Wind Lidar (OAWL) (see Grund et al. (2009); Tucker et al. (2018)), with a different field-widening approach, using cat's-eye mirrors.

Multiple filters can be created with a Michelson interferometer, as well. Schwiesow and Mayer (1995) presented a concept of a modified Michelson interferometer with either a three stepped mirror or polarization division with quarter-wave plates to measure the autocovariance function at three points for wind speed measurements.

*Cézard* (2008) considered a dual fringe-imaging Michelson interferometer (FIMI) technique with inclined mirrors for the measurement of the wind speed and of other air parameters (temperature, scattering ratio, density) (*Cézard et al.*, 2009a). In case of the FIMI, a quasi-linear, cosine-shaped fringe is obtained, due to an angle of inclination  $\theta$  between its two mirrors. When the frequency of the incident light is Doppler-shifted, the Fourier transform of the signal power spectrum, i.e., the autocorrelation (produced by the FIMI) is shifted in phase, being observable as a positional shift of the fringe (*Cézard et al.*, 2009b). The fundamentals of this technique are detailed in section 3.3.2.

Iodine-vapor (incoherent) Doppler wind lidars using absorption bands of iodine, instead of an interferometer, as (edge) filters (*Liu et al.*, 1997) are used for ground-based measurements of atmospheric wind speeds at day and night (see, e.g., *Liu et al.* (2007)), and are limited to a laser wavelength of 532 nm.

Direct-detection techniques in general do not require accurate wavefront-matching and allow for large-aperture receivers, which are often complex in design and continuously necessary calibration (*Henderson et al.*, 2005). Furthermore direct-detection can be performed in the UV, with low-noise high gain PMTs, APDs or cooled CCDs being available. Background light noise is reduced in the UV compared to the IR. The solar background is in general blocked using a narrow-band filter (NBF). Most importantly direct-detection techniques can be designed to work with pure molecular backscattering signals. An in-detail comparison of the presented techniques is provided in section 3.2.

Section 2.4 provides an overview of the history of the usage of coherent and direct-detection Doppler wind lidars for the detection of wake vortices and turbulence.

## 2.3 Mitigation of atmospheric disturbances for fixed-wing aircraft

### 2.3.1 Wake vortices

Wake vortices are the unavoidable companions of the lift generated by the finite wings of an aircraft. Lift is generated when there is a pressure difference between the upper and the lower side of the wing.

The circulation  $\Gamma$  (bound vortex) cannot abruptly end at the wing tips, but forms tow tip or trailing (free) vortices in the wake of the wing (see, e.g., *Kundu and Cohen* (2004), *Ginevsky and Zhelannikov* (2009)). This principle of wake vortex production is shown schematically in Fig. 2.5(a).

A wake vortex evolves in three stages: Wake formation, a stable phase, and vortex decay. Formation occurs up to between 15 and 20 wing spans behind the aircraft. In the stable zone, which stretches up to 150 wing spans, depending on the atmospheric conditions, two approximately straight vortex tubes are formed.

Vertical velocity profiles of two-dimensional wake vortex flow fields perpendicular to the tubes can be generated with a number of simple analytical models (e.g., *Burnham and Hallock* (1982), where  $b = \frac{r_c^2 + r^2}{r}$ , whereby  $r$  is the distance from the vortex core and  $r_c$  is the core radius). Similar profiles as shown in Fig. 2.5(b) are obtained, with different peak velocities depending on the model used (overview provided by *Gerz et al.* (2002), e.g.). The induced vertical velocity  $\omega = \frac{\Gamma}{2\pi b}$  forces the wake vortex downwards. Typical descent speeds of commercial aircraft are within a range of 1 m/s to 2 m/s with the wake vortices



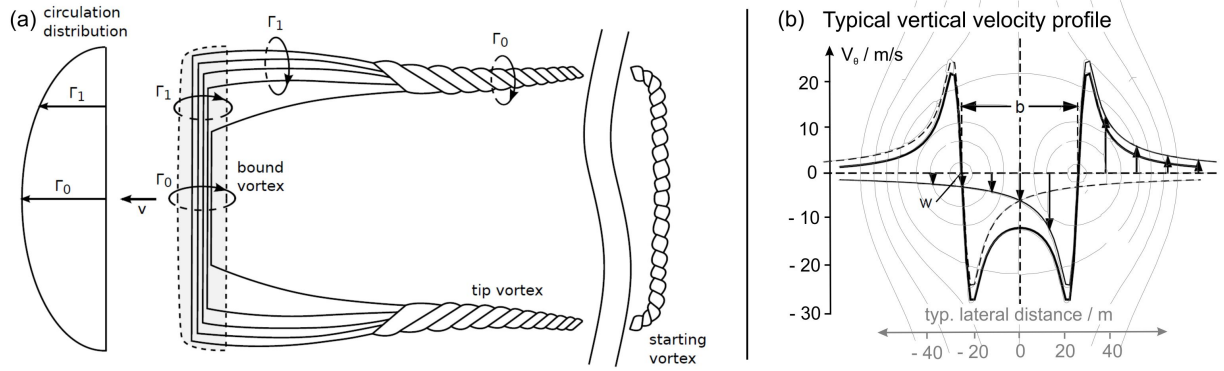


**Figure 2.5:** (a) Circulation of a wing and its wake (based on [Kundu and Cohen \(2004\)](#)). (b) Schematic vertical velocity profile of a wake vortex pair with a typical induced vertical velocity  $w$  and a vortex separation  $b$  (based on [Holzäpfel \(2005\)](#)).

sinking downwards several hundred meters ([Holzäpfel, 2005](#)).

At longer ranges the vortex tubes lose their straight form and break down, whereby vortex rings (induced by Crow Instabilities ([Crow, 1970](#))) can be formed under certain atmospheric conditions ([Crow and Bate, 1976](#)) before break-down in an unstructured way. The first phase (diffusion decay) is due to internal diffusion and stretching of the wake vortices. The second phase (rapid decay) is influenced by temperature stratification, which induces a rebound of the wake vortex back to flight level, and by turbulent friction processes. Higher magnitudes of stratification and turbulence enforce earlier decay and a faster decrease of circulation ([Holzäpfel, 2003](#)).

Interaction of a following aircraft with the wake vortex may result in increased structural dynamic loads, in a loss of altitude or climb rate, or in an increase of the bank angle, which may induce a rolling motion and a loss of control of the aircraft (aircraft-induced “turbulence”) ([Sharman, 2016](#)).

### 2.3.2 Clear-air turbulence and gusts

There are various types of natural turbulence that may affect an aircraft. Natural sources are convection in clouds (CIT), including storms and thunderstorms, and at low-level, convection and strong winds influenced by the terrain (LLT) ([Sharman, 2016](#)).

Clear-air turbulence (CAT) is all turbulence, which cannot be associated with visible convection, e.g., due to convection in clear-air (near-cloud turbulence - NCT, e.g., [Lane et al. \(2012\)](#)). The main energy sources are vertical wind shear produced by jet streams and atmospheric gravity waves ([Vinnichenko, 1980](#)), this includes mountain wave turbulence (MWT), i.e., gravity wave breaking giving rise to turbulence above and behind mountains in stably stratified flow (see, e.g., [Strauss et al. \(2015\)](#)). CAT typically occurs in the upper troposphere and lower stratosphere (UTLS).

CAT like any turbulence is inherently three-dimensional, nonlinear, non-isotropic, and decays, accompanied by an energy cascade, which redistributes its spatial scales. Assuming homogeneity and isotropy, Kolmogorov’s 5/3-law (K41) ([Kolmogorov, 1941](#)) and the von Kármán spectrum ([Von Kármán, 1948](#)), and other models provide spectral representations of the inertial subrange (domain of pure energy transfer) and of extended spatial scale regimes, linking them to the energy or eddy dissipation rate ( $\epsilon$ ), which is a measure of the intensity of turbulence experienced by an aircraft ([Sharman, 2016](#)).

The energy dissipation rate ( $\epsilon$ ) may be predicted by numerical weather prediction forecasts (e.g., [Frehlich and Sharman \(2004\)](#)).

An aircraft's transfer function (acceleration over vertical velocity  $w$  as a function of spatial scales) may be computed, which shows, that a typical aircraft may be affected by turbulent interaction mainly in the inertial subrange.

Fig. 2.6(a) shows a von Kármán spectrum with  $k^{-5/3}$  dependence within the inertial subrange, and contains exemplary transfer functions of a transport aircraft ([Vrancken, 2018](#)) based on calculations by [Cornman et al. \(1995\)](#).

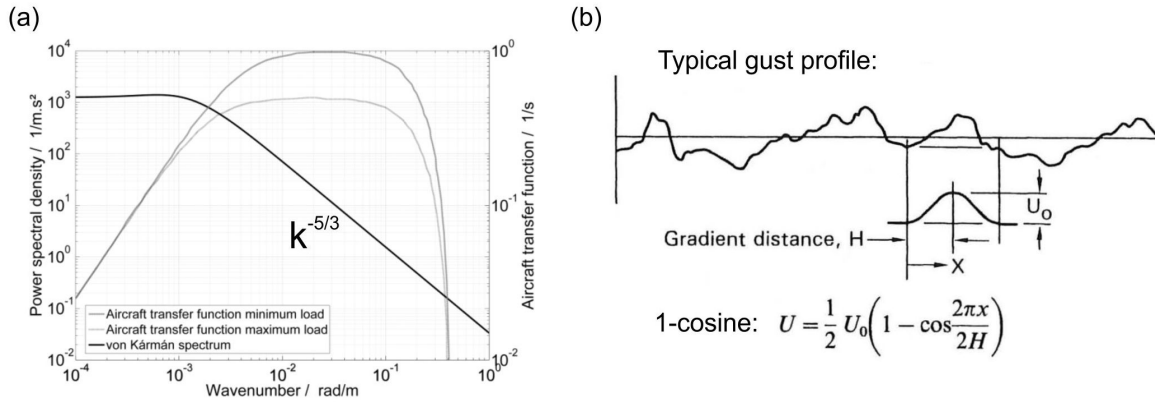


**Figure 2.6:** (a) Von Kármán spectrum with Kolmogorov's 5/3-law dependency within the inertial subrange and aircraft transfer functions for different loads calculated by [Cornman et al. \(1995\)](#) ([Vrancken, 2018](#)). (b) Typical gust profile and 1-cosine idealization ([Hoblit, 1988](#)).

Fig. 2.6(b) provides a typical velocity profile of a gust. Often simplified models such as the shown 1-cosine model are used to describe “single” gusts.

For an aircraft flying at high speed the main effect of clear-air turbulence and of gusts is lift (felt as a “bumpyness”), while axial and sideways drag are often neglectable. The effect of this turbulent lift is nearly ten times higher than the effect due to a change of the apparent airspeed ([Hoblit, 1988](#)), and increases with altitude and airspeed.

The ICAO classifies clear-air turbulence (CAT) into “Light” ( $EDR = [0.1, 0.4] \text{ m}^{2/3}\text{s}^{-1}$ ), “Moderate” ( $EDR = [0.4, 0.7] \text{ m}^{2/3}\text{s}^{-1}$ ), and “Severe” ( $EDR > 0.7 \text{ m}^{2/3}\text{s}^{-1}$ ) according to  $EDR = \epsilon^{1/3}$  ([ICAO, 2010](#)).

$EDR$  can also be directly linked to the CAT vertical velocity fluctuations (see, e.g., [Cornman et al. \(1995\)](#); [Weinstock \(1981\)](#)). CAT and gusts may induce increased structural dynamic loads on the aircraft, and may cause passenger discomfort and anxiety.

### 2.3.3 Impact alleviation control of wake vortices and gusts

In the following, concepts are recounted, which make use of theoretical DWL measurements to define control commands to minimize the impact of disturbances caused by wake vortices and gusts.

A typical impact alleviation (forward-feedback) control workflow for wake vortices and CAT / gusts is shown in Fig. 2.7.

The concept was first implemented for wake vortices by [Fischenberg \(2013\)](#), and fully-integrated developed by [Ehlers et al. \(2015\)](#) (Online Wake IDentification and Impact Alleviation - OWIDIA). Recently, an approach applying the same concept for gusts was published by [Fezans and Joos \(2017\)](#) (Gust Load Alleviation using REmote WInd SENSors

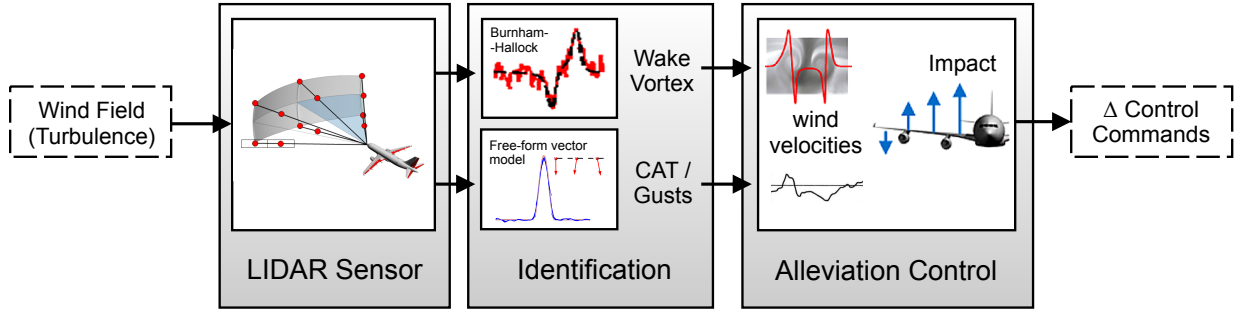


**Figure 2.7:** Workflow of wake vortex and gust impact alleviation control (based on [Fezans et al. \(2017\)](#)).

- GLAREWISE). The three main steps are lidar sensor measurements, identification of the disturbance, and impact alleviation.

The measurement step entails a Doppler wind lidar (fundamentals in section 2.2) to sample the wind field in short distance in front of the aircraft by scanned line-of-sight (LoS) wind speed measurements.

In the identification step, the missing information of wind field components perpendicular to the LoS and of all wind field components at further positions, is reconstructed, based on an algorithm, which identifies a certain disturbance model (i.e., Burnham-Hallock in case of wake-vortices, see section 2.3.1) from the measured, disturbance-induced wind field components ([Ehlers et al., 2015](#)). In case of gusts a mesh-based free-form wind field model is used ([Fezans et al., 2017](#)).

The parameters of the models are estimated by minimizing a cost function, which compares the “measured” (estimated) with the simulated LoS velocities (e.g., based on Large Eddy Simulations (LES) ([Schwithal, 2017](#))). The default or preconditioned initial parameters are optimized using a Maximum-Likelihood approach or gradient methods, provided that the measured LoS velocities let await a disturbance (“activation criterion”). The final parameters undergo a plausibility check.

In the third step, the reconstructed disturbances (i.e., vertical velocity profiles) are passed to client systems and are combined with additional data provided by the Air Data Inertial Reference Unit (ADIRU), to compute wing load profiles and forces (e.g., lift and rolling moment) acting on the aircraft. Control commands are computed to compensate for the turbulence-induced aircraft reaction.

Schwithal and colleagues used simulations of this OWIDIA system for a sensitivity study of lidar parameters, in order to estimate optimal parameters of a future lidar ([Ehlers and Fezans, 2015](#)), which may ensure optimal wake impact alleviation performance. The results of this study ([Schwithal, 2017](#)), and its assumptions on the lidar, are summarized at the beginning of chapter 3.1 and in appendix B.2. These findings are temporary, because many aspects of DWL measurements, e.g., noise behavior, scanning operation, and spatial averaging, are simplified and further iterations are required.

## 2.4 History of wake vortex and turbulence detection lidars

Today, there are many implementations of Doppler Wind Lidars (DWL), which could possibly be used for wake vortex and turbulence detection. A distinction is made in the following between ground-based and airborne measurements.

## Ground-based measurements

Coherent detection Doppler Wind Lidar (C-DWL) systems have been used extensively for crosswind and wind shear measurements at airports (e.g., at Hong Kong International Airport ([Chan and Lee, 2012](#))), as well as for the ground-based detection and characterization of wake vortices and turbulence.

One of the first measurements of wake wake vortices in Germany, using a C-DWL based on a cw-CO<sub>2</sub>-laser, date back to 1991, when vortex properties of a large variety of landing aircraft were studied at Frankfurt/Main Airport ([Köpp, 1994](#)).

Another example is a study of wake vortices of large transport aircraft carried out during the EC project C-Wake, using cw and pulsed C-DWL at Tarbes airfield (see, e.g., [Harris et al. \(2002\)](#)). DLR used a pulsed, 2- $\mu$ m C-DWL working with a Tm:LuAG laser, at a measurement range of 500 m to 1100 m ([Köpp et al., 2004](#)). ONERA and QinetiQ applied cw-CLs, based on 10- $\mu$ m-CO<sub>2</sub>-lasers ([Köpp et al., 2005](#)).

During the EU project MFLAME (Multifunction Future Laser Atmospheric Measuring Equipment) wake vortices were detected axially with a 2- $\mu$ m C-DWL in March 2000 at Toulouse airport ([Keane et al., 2002](#)). The beam was scanned sinusoidally with measurement ranges between 400 m and 2 km, measuring at 20 range gates of 75 m length each.

In 2007 a 1.5- $\mu$ m pulsed fiber C-DWL, developed by ONERA, was used for ground-based lateral wake vortex measurements of departing aircraft within the EC project CREDOS (Crosswind - Reduced Separations for Departure Operations) at Frankfurt airport ([Dolfi-Bouteyre et al., 2009a](#)). The lidar was based on a 50  $\mu$ J/15 Hz MOPA (Master Oscillator Power Amplified) laser transmitter. Its maximum measurement range was 400 m.

In FIDELIO, ONERA applied its 1.5- $\mu$ m fiber C-DWL with a 120  $\mu$ J/12 kHz MOPA laser and conducted ground-based wake vortex detection up to 1.2 km range at Orly airport ([Dolfi-Bouteyre et al., 2009b](#)).

Furthermore, C-DWL have been regularly used for wind turbine wake measurements, e.g., using three ground-based, long-range, scanning C-DWLs ([Wildmann et al., 2018](#)).

C-DWL have also been applied to ground-based studies of atmospheric turbulence. The large probing volume and low temporal resolution of C-DWL, inducing spatial and temporal averaging of the turbulence, provide major challenges for deducing turbulence information from raw lidar data (see, e.g., a review of measurements of the last 30 years by [Sathe and Mann \(2013\)](#)). Because these effects are very hard to correct, lidars have not yet been accepted for (natural) turbulence measurements. [Dors et al. \(2011\)](#) used a direct-detection DWL to estimate the eddy dissipation rate  $\epsilon$  from the radial velocity spectrum, assuming isotropy, accompanied by balloon-borne thermal probes, with major limitations due to lidar instrumental noise and range-averaging effects. Alternatively,  $\epsilon$  could be estimated from the width of the Doppler spectrum (e.g., [Banakh et al. \(2010\)](#)), the line-of-sight radial velocity structure function (e.g., [Smalikho et al. \(2005\)](#)), or the radial velocity azimuthal structure function (e.g., [Kristensen et al. \(2012\)](#)). However, all these techniques more or less require a combination with an isotropic turbulence model, and are limited by noise, by the sampling rate, by spatial averaging, and by the requirement of scanning. That is, evaluation algorithms using only raw lidar data (no turbulence models) would have to be developed and lidar technology would have to be improved, for the reliable determination of quantities describing natural turbulence, such as  $\epsilon$  ([Sathe and Mann, 2013](#)).

### Airborne measurements

Airborne measurements of turbulence and wake vortices, using coherent detection lidars are far more challenging. The major challenge is the lower particle density at high altitude (see section 2.1), reducing the carrier-to-noise ratio. A wake vortex alleviation or avoidance system should work with high ( $\approx 99.9\%$ ) availability, also at cruise flight level. Additional challenges are the compactness, light-weighted, vibration-save and low maintenance requirements on standardized lidar sensors for this purpose. The development activity of airborne C-DWL systems and its validation for this purpose, considering above difficulties, appears to be pursued not fervently enough. Therefore, it is difficult to make predictions about the availability of airborne C-DWL for high-altitude wind speed measurements.

Nevertheless, a few C-DWL systems for the detection of wake vortices and turbulence have been developed and have been flown on aircraft.

During the EC project I-Wake (2002-2005) airborne axial wake measurements have been carried out with a modified MFLAME-lidar (C-DWL) with a maximum measurement range of 2360 m, using a 2- $\mu\text{m}$  diode-pumped Tm:LuAG laser installed on the NLR Citation II aircraft (*Douxchamps et al.*, 2009).

During the European AWIATOR (Aircraft Wing with Advanced Technology OpeRation) project, vertical downward wake vortex measurements were carried out with the DLR 2- $\mu\text{m}$  C-DWL, installed at the DLR research aircraft Falcon 20, which flew 900 m above the wake-generating aircraft ATTAS (*Rahm et al.*, 2007).

JAXA (Japan Aerospace Exploration Agency) developed and tested different forward-looking C-DWL sensors for long-range airborne turbulence measurements. Their C-DWL systems are fiber-based, pulsed, working at a wavelength of 1.5  $\mu\text{m}$ , and using different laser transmitters. The measurement range of the first prototype was one nautical mile (NM). The measurement resolution was 150 m (*Kameyama et al.*, 2007). By increasing the laser power the range was increased to 3 NM (5.6 km) at low altitude (*Inokuchi et al.*, 2009). The sensor was installed on the JAXA Beechcraft Model 65 research aircraft, and measured airspeed at 450 m to 600 m ranges with a standard deviation of 0.63 m/s and at 900 m to 1050 m with a standard deviation of 0.7 m/s. Increasing the laser power further allowed to increase maximum measurement range to 5 NM at high cruise flight altitudes (12,200 m), using a Gulfstream II, and the successful detection of air-turbulence at an altitude of 3,200 m in 2014, based on the DSW method (*Inokuchi et al.*, 2014). The system is developed and optimized further (*Inokuchi et al.*, 2016) for measurements at cruise flight level, several km ahead, during the Boeing 2018 ecoDemonstrator program.

These very recent measurements show the high potential of using coherent systems for turbulence detection at high altitudes. Nevertheless, they do not provide statistics on the reliability in low particle density regions, and for highly resolved, near-range measurements with high update rates.

Another example of clear-air turbulence detection at large distances (15 km) are flight tests undertaken during the EU project DELICAT (DEMonstration of LIdar based Clear Air Turbulence detection), using a pulsed UV lidar, with a different measurement principle. The system did not measure LoS wind speeds (like a Doppler wind lidar), but measured density fluctuations, due to the vertical movement of turbulent air masses (*Vrancken et al.*, 2016).

Above systems appear well-suited for a timely warning of turbulence, such that the turbulent region may be avoided. A different concept is alleviation control (see section 2.3.3, which requires high density measurements of the wind field in close range to the



aircraft (see section 3.1 and appendix B), and a very high reliability during cruise flight independent of aerosol concentrations.

These preconditions favor direct-detection DWL systems, which can be designed to work independently of aerosol concentration, i.e., fringe-imaging and multi-channel based methods (see section 2.2.2).

The single, and most promising example, is a fringe-imaging Fabry-Pérot based, Rayleigh-Mie UV DWL, that was flight tested during the AWIATOR project, with main focus on clear-air turbulence (*Schmitt et al., 2007*; *Rabadan et al., 2010*). UV wavelengths favor molecular backscattering and can be built eye-safe. The direct DWL had one single measurement range of 50 m and a scanner allowing for four LoS measurement directions and a LoS update rate of 60 Hz (total: 15 Hz). It was installed on a Airbus A340-300 aircraft, allowing for measurements at cruise altitude (39000 ft) in four directions with a rectangular scan pattern under different atmospheric conditions including clear-air, clouds, and rain. Standard deviations of 1 to 1.5 m/s of the measured line-of-sight (LoS) velocity were achieved, verified by true airspeed, and proved the validity of the approach. Presently, these values are not considered sufficient for wake-vortex alleviation control ((*Schwithal, 2017*), see appendix B.2).

Another UV-imaging lidar for wake vortex detection, based on a fringe-imaging Fabry-Pérot interferometer, was developed during the EC project “GreenWake” (2008 – 2012). The ground-based validation of the developed DWL (*Rees, 2014*) was a failure, without proven scientific output. A short description of the system and of its parameters is provided in appendix B.1.

The failure in validating the “GreenWake”-DWL illustrates the high challenges faced, when developing a direct-detection DWL. Furthermore, it demonstrates the high efforts required for the quasi-instantaneous measurement of wind speeds at multiple range gates, using the fringe-imaging Fabry-Pérot concept with a two-dimensional detector.

These two examples of AWIATOR and GreenWake highlight the necessity for a different direct-detection Doppler Wind Lidar concept, which allows for the range-resolved, near-range measurement of radial wind speeds at multiple measurement points at once.

## 3 Development of a Doppler wind lidar receiver

This section describes the development of the DWL receiver starting from its respective requirements for wake vortex and gust alleviation control (section 3.1) over a spectral analyzer comparison (section 3.2), and method selection (section 3.3). The selected fringe-imaging Michelson interferometer (FIMI) is described (section 3.3.2), the integrated concept of a fiber-coupled setup is introduced (section 3.3.1), and a monolithic, field-widened Michelson (FWFIMI) (section 3.4) is designed. The proposed setup is realized and its components are described and characterized (section 3.5).

### 3.1 Requirements on lidar transmitter and receiver

#### Requirements for wake vortex alleviation control

For wake vortex alleviation control several requirements on the lidar receiver were defined during the Green-Wake project (see appendix B.1). Important results of a lidar parameter study for wake vortex alleviation by *Schwithal* (2017), using the OWIDIA framework (see 2.3.3) are summarized in appendix B.2. A related technique can be applied for the alleviation of gusts and turbulences (*Fezans et al.*, 2017).

The lidar system and alleviation control system parameters show complex interdependencies and have to be studied in a complex simulation framework for optimizing its performance (*Schwithal*, 2017). Nevertheless it is possible to estimate certain key requirements of the lidar transmitter and receiver necessary for wake alleviation control. These required ranges of the lidar system parameters are listed in Tab. 3.1.

**Table 3.1: Estimated requirements of a lidar sensor for wake vortex alleviation control**

Requirement	Value
Geometry	forward-looking
Scanning directions	$> 9, 10^\circ$ vertical, $16^\circ$ to $40^\circ$ horizontal
Range	$\approx 60$ m to 150 m or 300 m (near-range)
Longitudinal measurement points	$\geq 1$
Blur depth / range gate length	$\leq 30$ m
Altitude	up to FL400 ( $> 12100$ m)
Range of wind velocity	$\pm 25$ m/s
LoS velocity accuracy	$< 1$ m/s
Total scan update rate	2.5 Hz to 10 Hz
Line-of-sight (LoS) update rate	$> 45$ Hz to 270 Hz (geometry dependent)

These requirements on the lidar sensor should allow adequate reconstruction of the wind field in the near-range in front of the aircraft, which is necessary for wake vortex and gust alleviation control.

### Transmitter

The transmitter light beam should be eye-safe and should provide enough backscattered signal to analyze Doppler shifts range-resolved, with several longitudinal range gates, and with the required accuracy. These requirements favor pulsed systems.

For direct-detection receivers, the transmitter should provide a high Rayleigh scattering signal. Ultraviolet (UV) wavelength ( $\lambda$ ) systems are a good choice, because these can be designed eye-safe beyond a certain acceptable distance (e.g., [Behrendt et al. \(2011\)](#)), and because of the Rayleigh scattering scaling with  $\lambda^{-4}$  (see, e.g., [Miles et al. \(2001\)](#)).

The power requirement depends on the receiver principle, the required range, and the signal-to-noise ratio. The according laser power should be of  $> 2$  W order of magnitude according to direct-detection receiver simulations. Average power, repetition rate, and pulse energy are interdependent and should be optimized for maximum signal-to-noise ratio (SNR) and speckle suppression (see section 4.1). The development of an optimum transmitter depends thus on receiver selection, and is not within the scope of this work.

### Receiver

The lidar receiver should fulfill the requirements listed in Tab. 3.1. These are requirements which favor systems with the capability to detect several longitudinal range gates simultaneously. Transceiver arrangements or large telescope field-of-views are thus required for maximum overlap at all these distances, together with fast detectors. The receiver should work with the required precision at all altitudes, i.e., for a broad range of air densities and aerosol concentrations. At last, the receiver should be largely insensitive to sun background light and to bias, e.g., due to laser beam pointing fluctuations or temperature fluctuations, which should be minimized or be constant.

Additionally both transmitter and receiver should be compact, light-weight, highly reliable, and thermomechanically stable for future airborne implementations.

## 3.2 Comparison of different coherent and direct-detection techniques

This section compares several direct-detection DWL receivers and evaluates the question which requirements of section 3.1 can be fulfilled, respectively. The following comparisons provide a basis for the decision on the receiver scheme detailed in section 3.3. Parts of this section are based on [Herbst and Vrancken \(2016\)](#).

### Coherent detection

Coherent Doppler Wind Lidars (C-DWL) should work well in near- to mid-range applications, where despite of low aerosol concentrations, the backscattered signal is high enough for an adequate carrier-to-noise ratio (CNR). Coherent detection seems to be highly promising and especially suited for the detection of wake vortices and small scale turbulent structures in close range (few tens to several hundreds of meters) ([Vrancken, 2016](#)), as was shown by [Rahm et al. \(2007\)](#) and [Douxchamps et al. \(2009\)](#).

A narrow linewidth of the received signal, and therefore backscatter of the laser pulses by aerosols, is required for coherent detection. However, an argument often used in the



past is, that a sufficiently high aerosol density is not available in all global regions and at higher flight levels (30 kft to 40 kft) (e.g., [Rabadan et al. \(2010\)](#), [Hirschberger \(2013\)](#)). This means, that the maximum range can be limited and higher integration times are needed.

A further limitation is often, that many (airborne) pulsed coherent systems generate long pulses (typ.  $\geq 400$  ns), resulting in a relatively poor longitudinal ( $\Delta R = 75$  m ([Douxchamps et al., 2009](#)),  $\Delta R = 150$  m ([Inokuchi et al., 2014](#))) resolution.

In C-DWL systems the accuracy and temporal resolution can be increased by averaging over  $n$  pulses, because  $SNR \propto \sqrt{n}$ . That is why [Inokuchi et al. \(2014, 2016\)](#) optimized their C-DWL for high altitudes by using high pulse energies (1.9 mJ, 3.3 mJ) and high repetition rates (4 kHz, 1 kHz), yielding line-of-sight update rates between 1 Hz and 5 Hz.

The development of a coherent airborne lidar system with  $\Delta R < 30$  m and radial wind speed measurement accuracy of  $\sigma(u_r) < 1$  m/s at distances of 50 m to several hundred meters at cruise flight altitude, with a LoS update rate of 45 Hz to 90 Hz has not been undertaken yet, but may be achievable.

## Direct-detection

Due to the ubiquitous uncertainty of aerosol backscatter availability, we focus on the development of a direct-detection UV DWL receiver, which works with pure molecular backscattering signal, and which allows for a high longitudinal resolution down to few meters. As was shown in section 2.2.2, there exists a great variety of established and proposed direct-detection DWL techniques, employing different spectral analyzers. Hence, the aim of the next paragraphs is to compare these techniques and spectral analyzers with respect to their potential as a wake vortex and gust alleviation control lidar sensor.

### 1. Theoretical performance

The first criterion used here for comparison is the magnitude of penalty factors for wind speed measurements with respect to an ideal spectral analyzer (ISA). An ideal spectral analyzer is constituted of an infinite amount of channels, sampling the spectrum with Dirac-type transmission functions. Additionally, in an ISA, there is no loss of information, energy, or spectral content. The Cramér-Rao lower bounds (CRB) are the lowest achievable standard deviations of an unbiased estimator. The CRB of an ISA for the measurement of wind speed assuming a pure Rayleigh signal is given by  $\epsilon = \gamma / \sqrt{2N_{ISA}}$  (derived in appendix C.2 for the interested reader) with  $\gamma = \sqrt{2k_B T / m}$ , whereby  $N_{ISA}$  is the total number of photoelectrons detected by the spectral analyzer,  $m$  is the molecular mass of air,  $k_B$  is Boltzmann's constant, and  $T$  is the absolute atmospheric temperature.

A “real-world” physical (unbiased) spectral analyzer (like a fringe-imaging Michelson interferometer (FIMI)) mixes the photons spatially and spectrally and therefore underperforms compared to the ISA. Tab. C.1 in appendix C.3 lists penalty factors for various DWL techniques, which vary between 1.7 (dual channel Mach-Zehnder) and 4.4 (Dual fringe-imaging Michelson). Coherent lidars yield penalty factors above two due to speckle (as detailed in appendix C.4). In total these are similar orders of magnitude, such that the penalty factors with respect to an ISA are not considered decisive for method selection.

## 2. Measurement geometry and angular performance

Another criterion is the applicability in fiber-coupled setups. Fiber coupled setups have the advantage that biases due to laser beam tilt can be reduced by means of optical scrambling in multimode fibers (see sections 3.5.5 and 4.3). Relatively large-core multimode fibers are required if the measurement range shall be in the near-range (50 m to several hundred meters), because this near-range detection results in relatively large, range-dependent angular distributions. Raytracing simulations are performed in the following to estimate the magnitude of these angular distributions. Thereafter, the effect of these angular distributions on fringe-imaging Fabry-Pérot, Fizeau, and Michelson interferometers is evaluated.

A monostatic, coaxial, free-beam setup is considered, where laser beam, telescope, interferometer and detector are on the same optical axis. In this case, the range dependence manifests mainly in a varying angular distribution and width of the illumination, due to the shift of the focus of the telescope.

This front-end receiver including an exemplary Newtonian telescope (15 cm diameter, focal length of 0.75 m) and lenses to collimate and couple the light into a multimode fiber. The front-end receiver is modeled with sequential raytracing using raytracing software (ZEMAX) (see appendix D.1 for a detailed description).

A graphical representation of the front-end receiver model is shown in Fig. 3.1(a). We assume a coaxial arrangement of the laser beam with divergence  $\Theta$  of  $150 \mu\text{rad}$  and a collimated laser beam diameter ( $2w_0$ ) of 13 mm at a range  $R = 0$ . The values of  $\Theta$  and  $w_0$  are not decisive for the outcome of the simulation.

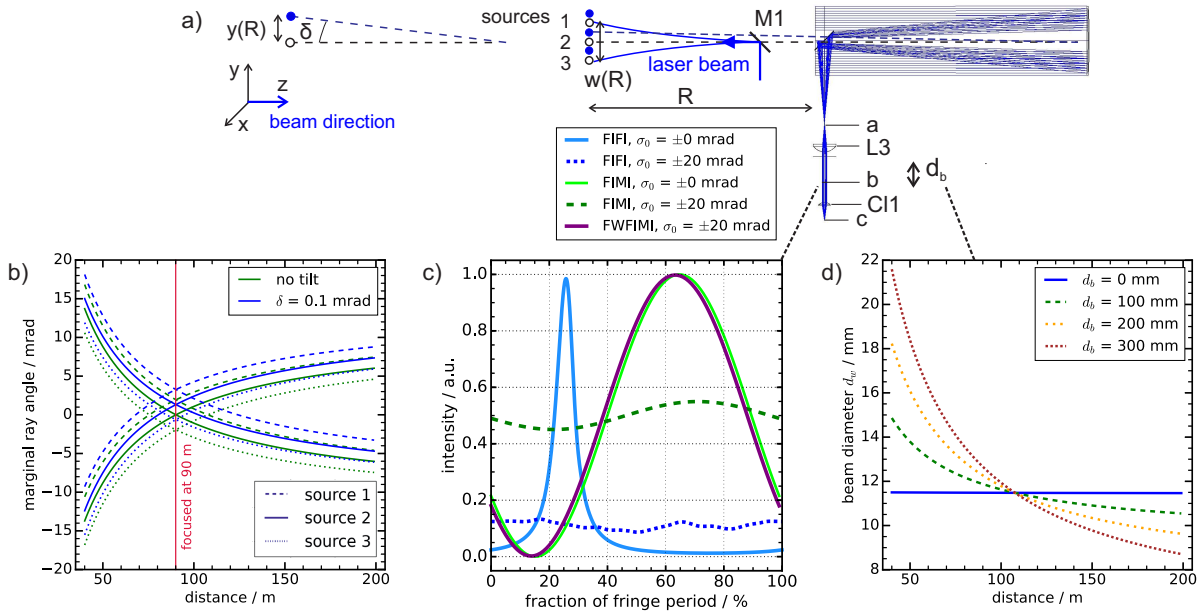


**Figure 3.1:** (a) Ray-tracing layout of a Newton telescope with three point sources (1, 2, 3) at distance  $R$  and planes  $a$ ,  $b$ , and  $c$ . (b) Marginal ray angles as a function of  $R$  without tilt ( $\delta = 0$ , green) and with a tilt of the laser beam ( $\delta = 0.1$  mrad, blue) at position  $b$ . (c) Angular sensitivity of fringe shapes of a fringe-imaging Fizeau interferometer and of a fringe-imaging Michelson interferometer, the latter with and without field widening for collimated light and incidence angle distributions of  $\rho_0 = [-20, 20]$  mrad (flat-top). For better visibility, the fringes for angular distributed light have been shifted in the  $x$ -direction. (d) Illumination beam diameter as a function of distance  $R$  for different distances  $d_b$ .

The maximum angles  $\rho'$  (marginal ray angle) of the angular distribution are evaluated

as a function of distance  $R$ , at position  $b$  (for the three point sources in Fig. 3.1(a), 1: dashed, 2: continuous and 3: dotted line) and are shown in Fig. 3.1(b).

The angular distribution is range-dependent and varies for this configuration between  $\pm 2$  mrad and  $\pm 17$  mrad (green lines in Fig. 3.1(b)). Minimum marginal angles are obtained for  $R = 90$  m, because the position of lens  $L3$  is set for quasi-collimation at this distance. At  $R = 50$  m the angular distribution is  $\pm 12$  mrad, i.e., within the interval  $[-12, 12]$  mrad.

For these angular distributions of the incident light, the fringe shape stability of a fringe-imaging Fizeau interferometer (FIFI) and a Michelson interferometer (FIMI) with and without field-widening can be compared exemplarily.

Following the description by [Novak et al. \(2011\)](#) for a FIFI, multiple plane waves are propagated along their propagation vectors. The plane waves are reflected and refracted in the interferometers. Their phases are recorded and they are superimposed in a plane. The intensities are summed up along the direction parallel to the linear fringes. In case of the FIMI the beam splitter is completely omitted. The model is described in appendix C.5. The obtained interference fringe shapes are shown in Fig. 3.1(c) for a FIFI and for a FIMI without and with field-widening (FWFIMI, i.e., the optical path length difference is made largely independent of the angle of incidence, see section 3.4.1) for collimated light and for light with incidence angles  $\rho_0$  of  $[-20, 20]$  mrad. The illumination diameter  $d_w$  is set to 10 mm. The net inclination angle is  $17.75 \mu\text{rad}$ , such that one fringe period is imaged. The FIFI mirrors have exemplary values of reflectivity ( $R$ ) of 80%, and separation of 7.5 mm. For the FIMI and FWFIMI optimal parameters described in sections 3.3.2 and 3.4.1 are used.

In case of the FIFI the fringe shape is strongly dependent on the angular distribution. The finesse and the contrast decrease rapidly with increasing  $\rho'$ . No fringe can be obtained for  $\rho_0 = [-20, 20]$  mrad. For the uncompensated FIMI the contrast is reduced, while the cosine shape is preserved. The contrast of the FWFIMI is insensitive to the angular distribution (purple line in Fig. 3.1(c)). The same results as for the FWFIMI could be obtained for the field-widened fringe-imaging Mach-Zehnder interferometer (FWFIMZ).

The fringe-imaging Fabry-Pérot interferometer (FIFPI) produces circular fringes instead of linear fringes. A variation of the angle does not change the instrumental contrast, but the number of rings (interference maxima). In case of  $\rho_0 = [-20, 20]$  mrad, a wavelength of 355 nm,  $R = 0.7$ , and a spacing  $h_g$  of 6.5 mm eight fringe order are obtained (see Fig. C.5 in appendix C.5, [Hirschberger and Ehret \(2011\)](#)).

The field-widening only compensates the angular distribution, i.e., conserves the instrumental contrast, and not the off-set in position or tilt of the illuminating beam. Fluctuating values of the laser beam pointing (tilt) angle  $\delta$  can be caused by thermomechanical instabilities of the laser transmitter (see section 3.6). In this case (blue lines in Fig. 3.1(b),  $\delta = 0.1$  mrad) the angular distribution gets an offset of  $\gamma \cdot \delta = 1.32$  mrad, where  $\gamma$  is the angular magnification of the telescope.

The range-dependence of the illumination manifests in a varying beam diameter  $d_w$  (Fig. 3.1(d) and angular distribution, see appendix D.1), which could be accounted for by range-dependent calibration. A configuration with two lenses to image the focal plane of the collimating lens on the entrance of the FIMI, would minimize this range dependence (i.e.,  $d_b = 0$  in Fig. 3.1(d)), however this free-beam setup provides no compensation for biases induced by shifts of the illumination due to laser beam tilt fluctuations.

The actual shift of the illumination on the detector depends on the imaging optics used (e.g., appendix D.1). Such a shift of the illumination will introduce an error on the

determined wind speed. The tilt  $\delta$  results in a lateral shift at the position of the focus of the telescope primary mirror (a) and after the collimating lens (b in Fig. 3.1(a)). If the FIMI is positioned in b, the illumination of the FIMI depends on  $R$  and  $\delta$ .

The offset in y-direction at surface b, due to the tilt  $\delta$ , is  $\tan(\gamma\delta)d_b$ , where  $d_b$  is the distance between the focal plane of the collimating lens and surface b. The interference fringe is displaced on the detector by at least  $\Delta y_d = \tan(\gamma\delta)(d_b + d_z)$ , here  $d_z$  is the distance between the entrance of the FIMI and the detector. Physical geometry constraints of the setup (see appendix D.3) impede small values of  $d_z$ . Assuming one fringe period is imaged ( $N_p = 1$ ) with  $d_w = 10$  mm,  $d_b = 200$  mm, and  $d_z = 140$  mm according to eq. 3.1 and eq. 3.3 of section 3.3.2, a tilt of  $\delta = 1$   $\mu$ rad causes an estimated positional fringe shift  $\Delta y_d$  of 4.5  $\mu$ m on the detector. The values of  $d_b$ ,  $d_z$  and  $d_w$  can be slightly different in a real setup. Anticipating that the phase sensitivity  $S$  defined in section 3.3.2 is 3.3 mrad/(m/s) for an FSR of 10.7 GHz and a wavelength of 355 nm, we see that a wind speed of 1 m/s gives a shift of 1/1900 of the imaged fringe period width  $d_w$ . Comparing this to the  $y_d = 1/2228 \cdot d_w$ , a bias of 0.9 m/s is estimated. Two lenses of equal focal length  $f$  at distance  $2f$  can be used to image the focal plane of the collimating lens on the entrance of the FIMI (i.e.,  $d_b = 0$ ). In this case the estimated bias for  $\delta = 1$   $\mu$ rad is  $0.4 \text{ m s}^{-1}$ . This order of magnitude of bias could severely degrade measurement performance, as can be seen with respect to the results and discussion of section 4.

A way to reduce the range dependence of  $d_w$  and the influence due to laser beam tilt fluctuations is the already mentioned fiber-coupled setup. The effectiveness of the suppression of this spatial (angular) information, is called “scrambling”, and depends on the type of multimode fiber being used (e.g., its core shape, see section 3.5.5). In case of perfect scrambling solely the fiber core diameter determines the angular distribution of the light in the far-field behind the fiber, e.g.,  $\rho_0 = [-21, 21]$  mrad in case of a quadratic-core fiber diameter of 600  $\mu$ m (see eq. C.35 in appendix C.5). Accordingly, a field-widening compensation is necessary in the fiber-coupled case, as well.

### 3. General comparison of direct-detection techniques

The two-filter based techniques, Double-edge Fabry-Pérot (DFP) and Dual-channel Mach-Zehnder (DMZ) have good theoretical performances, but they are sensitive to the Rayleigh-Mie backscattering ratio ( $R_b$ , see Fig. 2.1) and require inversion of the lidar signal to correct this (Bruneau, 2001).

The fringe-imaging Fabry-Pérot technique (FIFPI) is complicated by the evaluation of circular fringe patterns (Hirschberger and Ehret, 2011) or the complexities of circle-to-line converters (Wu et al., 1994). In case of averaging over 20 circular noisy fringe patterns imaged on 2D CCD detector with 960 x 780 Pixels, it has been shown by simulations, that for a measurement distance of 56 m, and a range gate length of 10 m, the bias and standard deviation of the LoS wind speed component is about 2 m/s (Hirschberger and Ehret, 2011). For an unknown, fluctuation center of the rings, caused in reality by laser beam pointing fluctuations, Hirschberger and Ehret (2011) obtained biases  $< 7$  m/s, and according values of  $\sigma(u_r)$  of  $\approx 3$  m/s. Hirschberger (2013) concludes that these measurement accuracies are not high enough, and that the evaluation takes too long for real-time measurements. Furthermore, the 2D interference pattern prohibits multiple quasi-simultaneous measurement points along the LoS. A fast gated, intensified CDD ( $\approx 180$  ns long gate, frame rate: 60 Hz) is required to reduce the range gate length to 30 m (Rabadan et al., 2010), and multiple CCD detectors are needed for multiple longitudinal measurement points (such as

in the Green-Wake DWL ([Rees, 2014](#)).

The fringe-imaging Fizeau interferometer (FIFI) provides linear fringes, allowing for the use of fast, linear, UV-sensitive detectors, and thus for multiple measurement points along the LoS. However, the fringe shape is very sensitive to the incident angular distribution (see Fig. C.7 in appendix C.5, or, e.g., [McKay \(2002\)](#)) and does require collimated light (see Fig. 3.1(c)), what impedes range-dependent measurements in the near-range (50 m to 300 m).

This is not the case with field-widened Michelson and Mach-Zehnder interferometers. The QMZ and FIMZ techniques have very low penalty factors and do not require knowledge of the scattering ratio. The penalty factor for the FIMI is  $\sqrt{2}$  to two times the penalty factor for the FIMZ (see Tab. C.1). The first  $\sqrt{2}$  factor arises because half of the light is back-reflected (see factor F, eq. 3.3). An additional  $\sqrt{2}$  factor occurs if the interferometer is designed for a single linear polarization. The light guided through a multimode fiber is depolarized. The light has to be polarized prior to illuminating the interferometer, whereby half of the signal goes astray.

The FPI transmits a fraction  $(1 - R)/(1 + R)$  of solar background light in comparison to 0.5 and 1.0 in case of the FIMI and the FIMZ. Solar background radiance can however be reduced by an additional narrow-band transmissive filter, i.e., an interference filter (e.g., an FPI etalon).

The reduction of laser-telescope misalignment biases favors a fiber-coupled setup with optical scrambling, which also simplifies range-resolved detection, due to more similar range-dependent angular distributions.

Possible candidates are thus the FIMI, the FIMZ and the QMZ, which may all be field-widened, and which do not require knowledge of the particle backscattering ratio  $R_b$ .

The QMZ ([Bruneau et al. \(2013, 2015\)](#)) and its close derivate the optical autocovariance lidar (OAWL) ([Hardesty et al., 2018](#)) have already been flight-tested and are rather established techniques (considered for space missions ([Tucker et al., 2016](#); [Mariscal et al., 2018](#))), while the FIMI and the FIMZ, have not yet been applied for airborne DWL measurements.

The fringe-imaging Michelson interferometer (FIMI) is a simpler special case of the FIMZ (as shown theoretically by [Bennett and Kahl \(1953\)](#)), because only one beamsplitter and one linear detector are required instead of two each for the FIMZ. This reduction of complexity leads us to see the FIMI as a well-suited alternative.

Furthermore, the manufacturing of monolithic, field-widened Michelson interferometers (FWFIMI) is an established technique (see, e.g., the solid wide-field Michelson (SWFM) interferometer ([Title and Ramsey, 1980](#))) and companies such as LightMachinery Inc., Canada are specialized in their manufacture (see, e.g., [Liu et al. \(2012\)](#)).

For these reasons a fiber-coupled, monolithic, field-widened, fringe-imaging Michelson interferometer (with inclined mirrors) (FWFIMI) is selected as spectral analyzer for the receiver ([Herbst and Vrancken, 2016](#)). The complete receiver concept is described in the next section.

### 3.3 Selected receiver principle

This chapter presents the selected fiber-coupled receiver concept (section 3.3.1) and explains fundamentals of the fringe-imaging Michelson interferometer as a spectral analyzer (section 3.3.2). Within this chapter content of [Herbst and Vrancken \(2016\)](#) is used.



### 3.3.1 Receiver overview: FWFIMI with fiber-coupled illumination

The DWL receiver concept is depicted in Fig. 3.2. The Doppler wind lidar (DWL) consists of the laser transmitter, the front-end part of the receiver, the back-end part of the receiver, and fiber components linking front-end and back-end. The front-end part serves for collecting the backscattered light, sun-filtering, and fiber coupling. The back-end part is dedicated to the spectral analysis. The laser transmitter is the WALES/DELICAT transmitter (described in section 3.6).

The receiver front-end consists of a Newtonian telescope, a lens to collimate the received light and a mirror to guide the light towards the narrow-band filter (IF) for blocking sunlight. The light is then reflected by a polarizing beamsplitter cube (PBSC) and coupled into the (scrambling) fiber components. A small part of the transmitter light (reference) is delayed by guiding it through another multimode fiber and is combined through the same PBSC into the same fiber components (1. option) or with a 3:1 coupler (2. option).

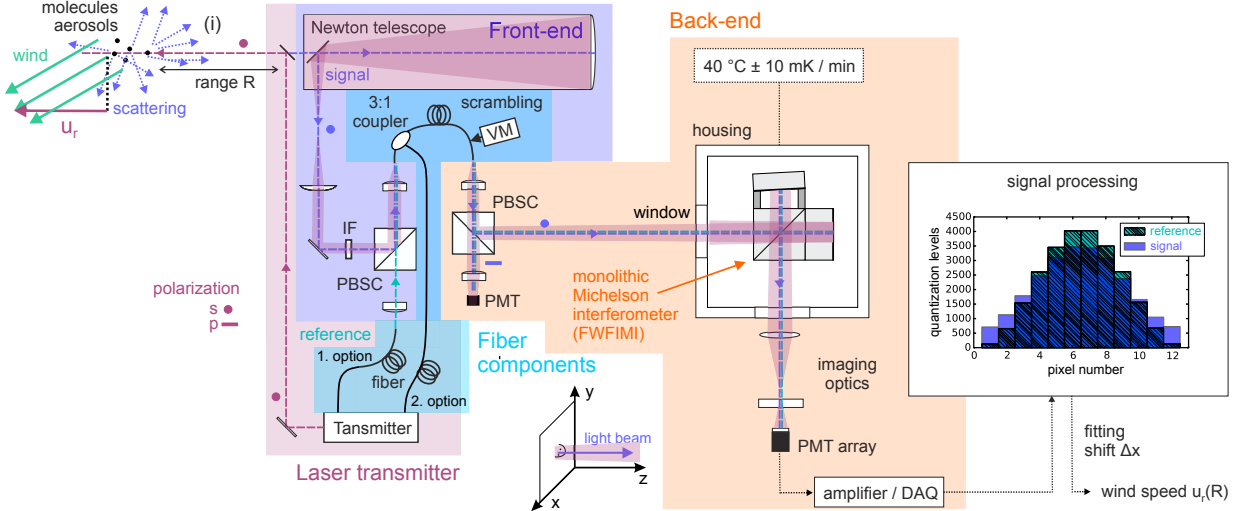


**Figure 3.2:** Receiver and DWL concept setup comprised of laser transmitter, receiver front-end, receiver back-end, and fiber components. Its realization can be seen in section 3.5.3 (receiver) and section 3.6 (transmitter) (modified figure of *Herbst and Vrancken (2016)*).

A large-core, multimode “scrambling” fiber with a quadratic core with a diameter (edge length) of 600  $\mu\text{m}$  provides several advantages compare to free-beam illumination.

1. The fiber acts as a field aperture, limiting the FOV of the telescope. Larger core sizes provide larger field-of-views and therefore a larger region of full overlap (see appendix D.1), which is needed for range-resolved measurements in the near-range (50 m) up to several hundred meters distance.
2. A larger core size leads to a higher detector size to speckle grain size ratio (see appendix G), which facilitates more effective spatial averaging of speckle noise (see section 3.5.4) compared to a free-beam illumination (atmospheric speckle, see appendix C.1). A small vibration motor (VM) can be used to vibrate the “scrambling” fiber for (additional) temporal speckle reduction (see section 3.5.4).
3. The fiber provides optical scrambling, whereby quadratic fibers provide a higher degree of scrambling (than circular shapes, see section 3.5.5) and the near-field is shaped quadratically, which simplifies imaging on rectangular detectors (see section 3.5.3).

On the other hand, a larger core-size requires a higher degree of field-widening of the spectral analyzer located behind the fiber, because even if the light is quasi-collimated after

the fiber the maximum angle of the angular distribution in the far-field (see eq. C.35) is significantly too high for uncompensated (Michelson) interferometers, such that the instrumental contrast is effectively zero (see Fig. 3.1 and see appendix C.6, Fig. C.15).

Therefore, the spectral analyzer of the receiver back-end is laid out as a field-widened, fringe-imaging Michelson interferometer (FWFIMI). The mirrors of the Michelson interferometer are inclined in x-direction (see Fig. 3.2) in order to provide a quasi-cosine shaped linear fringe varying along the x-axis. The light from the multimode fiber may then be either quasi-collimated (far-field illumination) or the image of the fiber-end is imaged through the Michelson interferometer on the detector (near-field illumination, see section 3.5.3) by shifting the lens accordingly behind the fiber. The light is guided through another PBSC, and the s-polarized half of the unpolarized light, resulting from the propagation in the MM-fiber, is guided towards the FWFIMI. The other p-polarized part is imaged onto a single PMT for power measurements for the purpose of calibration and alignment (overlap). Thus, the depolarization of the light in the MM-fiber is the major disadvantage of using MM-fibers, especially if the coating of the (cubic) beamsplitter of the FWFIMI requires perfect s-polarization (see section 3.4.3). The distance between the PBSC and the FWFIMI is selected such that the aperture diameter of the illumination ( $d_{\text{illum}}$ ) is approximately 10 mm.

The FWFIMI with inclined mirrors is designed such that exactly one period of the vertically (quasi s-) oriented linear fringe can be imaged with the help of imaging optics (i.e., a biconvex lens and a cylindrical lens) onto the linear photomultiplier tube array (PMTA). Both the atmospheric signal light (blue in Fig. 3.2) and the delayed reference light (turquoise in Fig. 3.2) produce currents in the twelve selected PMTA channels, which are converted by the amplifier into voltages (analog detection) and then into digital values by the analog-to-digital converter (ADC) of the data acquisition (DAQ).

As the radial wind speed  $u_r$  along the line-of-sight (LoS) of the laser beam changes, the fringes of reference and signal are shifted in position ( $\Delta x$ ) with respect to each other and the wind speed  $u_r(R)$  can be determined for different ranges  $R$  quasi-simultaneously by applying a mean-frequency estimator (e.g., a fit) to the respective fringe signals.

Fig. 3.3 shows a sketch of the DWL receiver concept developed in this work, summarizing several aspects of the above description.

The concept's performance could optionally be enhanced by a factor of  $\sqrt{2}$  by employing the FWFIMI in a 2°-tilted configuration, and by imaging the back-reflected interference fringe (second channel) on a second linear detector (*Herbst and Vrancken, 2016*). A ray-tracing model of this option is shown in appendix D.3. This two-channel option may be established after the single-channel version (Fig. 3.2) has been validated. Tab. 3.2 lists important properties of the DWL receiver.

A detailed list of the DWL receiver's components and their efficiencies is provided in appendix F. The estimated total efficiency of the receiver is 2.7% (Tab. F). A description of the built-up receiver is provided in section 3.5.3.

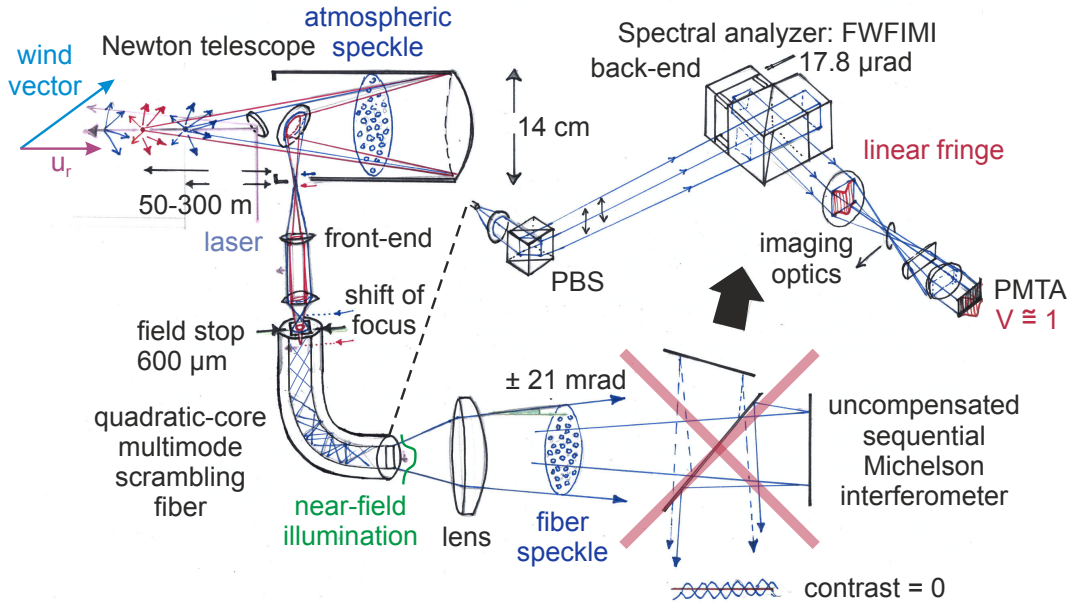


**Figure 3.3:** Aeronautics Lidar – Doppler Wind Lidar (AEROLI – DWL) receiver concept. The most important aspect is a compensation for field-angles in the near-range, yielding high instrumental contrasts ( $V \approx 1$ ). Therefore, an uncompensated sequential Michelson interferometer should be replaced by a field-widened, monolithic version providing thermomechanical stability. The stability of the illumination provided by suitable fiber components in a fiber-coupled setup is intended to reduce additional random measurement errors caused by atmospheric speckle and laser beam pointing fluctuations. A fiber-coupled setup with full overlap in the near-range, in combination with linear fringes with a high instrumental contrast, and a fast linear PMTA, allow for range-resolved wind speed measurements in the near-range.

**Table 3.2:** Important properties of the DWL receiver.

Transmitter (DELICAT)	(see section 3.6)
wavelength	$\lambda_L = 354.84 \text{ nm}$ (844.87 THz)
Pulse energy	$< 8 \text{ mJ}$
Repetition rate	100 Hz
Receiver front-end (RFE)	(see hardware in section 3.5.3)
Newton telescope	$D = 14 \text{ cm}$ , $f_1 = 750 \text{ mm}$ , $D_2 = 40 \text{ mm}$
measurement range	50 m to several hundred meters
Sunlight filter, FWHM, T	Materion, 0.5 nm at 354.85 nm, $T = 88\%$
Fiber components	(see section 3.5.3 and appendix F)
Optical scrambling fiber	$NA = 0.22$ , $L = 10 \text{ m}$ , $D = 600 \mu\text{m}$ , quadratic core
Receiver back-end (RBE)	(see hardware in section 3.5.3)
FIMI FSR	10.7 GHz ( $\approx 6.8 \cdot \sigma_{Ray}$ ) (see section 3.3.2)
Detector	analog, linear PMTA (16 channels, $QE \approx 40\%$ )
Efficiency	$\leq 2.7\%$ (see appendix F, Tab. F.4)
Range gate length	$\Delta R \approx 30 \text{ m}$

In the next section, the fringe-imaging Michelson interferometer is discussed as a spectral analyzer and important design features are concluded from this description. The most important feature is the free spectral range (FSR) of 10.7 GHz.



### 3.3.2 The fringe-imaging Michelson interferometer as a spectral analyzer

The following description is based on fundamental work carried out by [Fortunato \(1997\)](#), [Bruneau \(2002\)](#), and [C  zard et al. \(2009a\)](#), who provided descriptions of fringe-imaging in the FIMI, of the FIMZ, and a feasibility analysis of the FIMI as a DWL, respectively. It also contains parts of [Herbst and Vrancken \(2016\)](#).

As can be inferred analytically (see appendix C.6), the monochromatic transmission function (TF) of a Michelson interferometer with inclined (ideally planar) mirrors (along  $x$ , see Fig. C.10(a)) is cosine-shaped, varies in space along the  $x$ -axis, and is constant along the  $y$ -direction. The TF can be written as

$$I(x, \nu) = F \cdot I_0 [1 + V \cos(\phi)] = F \cdot I_0 \left[ 1 + V \cos \left( \frac{2\pi\nu}{c} \cdot (OPD_0 - 2\theta x) \right) \right], \quad (3.1)$$

where the linear interference fringes of equal thickness are aligned perpendicular to the  $x$ - and parallel to the  $y$ -axis.  $\phi$  is the fringe phase and  $\nu$  is the frequency of the monochromatic light.  $OPD_0$  is the fixed optical path length difference between the arms. Assuming dispersion-free media in the interferometer arms,  $OPD_0$  is equal to  $c/FSR$ , where  $FSR$  is the free spectral range. The  $FSR$  is the width of one fringe period in [Hz].  $\theta$  is the angle of inclination in  $x$ -direction rotated about the  $y$ -direction.  $\theta$  creates a linear variation of  $OPD_0$  within the illuminated area of width  $x_w$ .  $\theta$  determines the amount of periods  $N_p$  of the TF. To image exactly  $N_p$  fringe periods,  $\theta$  must equal  $N_p \lambda_L / (2x_w)$ . The prefactor  $F = 0.5$  accounts for half of the light being reflected by the Michelson interferometer. The reflected intensity function (RF) is phase-shifted by  $\pi$  with respect to the TF.

$V$  is the instrumental interference contrast, its contributions are a beamsplitter ratio factor  $V_{BS}$  (see eq. C.43), the pixel factor  $V_{pix}$  (see eq. C.45), and factors due to wide-field illumination with maximum angle  $\rho_{max}$ :  $V_{wf}$  in the uncompensated case (see eq. C.58) and in the field-widening compensated case, i.e., when a glass plate is inserted in one of the arms (see eq. C.66, eq. C.69) or in case of a monolithic field-widening design (see eq. C.70). An additional contribution  $V_{loc}$  can occur when the plane of localization of the fringe is not properly imaged onto the detector plane (see eq. C.56). The total instrumental contrast for monochromatic light is thus given by

$$V = V_{BS} \cdot V_{pix} \cdot V_{wf} \cdot V_{loc}. \quad (3.2)$$

$V$  amounts to approximately 99%, for a proper system design, i.e., a beamsplitter ratio near to 50:50, a number of pixels  $P > 12$  for  $N_p = 1$ , a field-widening design (see section 3.4.1), and optimal imaging of the plane of localization (see section 3.4.4).

The instrument function for laser light is the convolution of the lineshape of the laser with the transmission function (TF). The instrument function for received atmospheric light ( $I_F$ ) is the convolution of the atmospheric backscattering spectrum (Knudsen model, see eq. 2.1) with the TF (eq. 3.1).  $I_F$  can be written analytically ([C  zard et al., 2009a](#)) as

$$I_F(x, \nu) = F \cdot I_0 [1 + W(T, R_b) \cos(\phi + \Delta\phi)]. \quad (3.3)$$

The resulting interference pattern is shifted in phase by  $\Delta\phi = 4\pi/(FSR \cdot \lambda_L)u_r$  with

$\lambda_L = c/\nu$  and has a reduced global fringe contrast  $W(T, R_b) = V \cdot G(FSR, T, R_b)$ , where

$$G(FSR, T, R_b) = \exp \left[ -2 \left( \frac{\pi \sigma_L}{FSR} \right)^2 \right] \cdot \left( \frac{1}{R_b} \exp \left[ -2 \left( \frac{\pi \sigma_{Ray}(T)}{FSR} \right)^2 \right] + \left( 1 - \frac{1}{R_b} \right) \right). \quad (3.4)$$

The LoS wind speed  $u_r$  is determined by measuring the phase shift  $\Delta\phi$  between a reference instrument function and a Doppler frequency-shifted received instrument function, which are both imaged sequentially on the position-sensitive detector.

By applying a fit to eq. 3.3,  $\Delta\phi$  can be determined independently of  $G$ , i.e., without knowledge of  $R_b$ .  $G$  depends on the spectral width of the laser  $\sigma_L$ , on the free spectral range ( $FSR$ ), on the particle backscattering ratio ( $R_b$ ) and on the standard deviation of the Gaussian-shaped Rayleigh peak  $\sigma_{Ray}(T)$ , and thus on the absolute temperature  $T$ .  $G$  is a measure of temporal coherence of the backscattered light and the FIMI can be considered a temporal coherence analyzer (C  zard *et al.*, 2009a). That is, a FIMI with a specific  $FSR$  measures through  $G(FSR)$  a small segment of the envelope of the temporal coherence function (degree of first-order coherence), which is the Fourier transform of the respective backscattering spectrum. This is an application of the Wiener-Khintchine theorem, stating that for wide-sense stationary random processes of zero mean the power spectrum is equal to the Fourier transform of the autocorrelation (Born and Wolf, 1980). When the TentiS6 model is used instead of the Knudsen model (see Fig. 2.2) different values of  $G(FSR)$  are obtained, this however does not induce a bias of the determined phase shift, due to the symmetry of the atmospheric backscattering spectrum (C  zard *et al.*, 2009a).

A penalty factor  $\kappa_{u_r}$  can be defined, which compares the Cram  r-Rao bound, i.e., the lowest possible standard deviation of a spectral analyzer (see appendix C.2, and C.3) for the measurement of radial wind speed of the fringe-imaging Michelson interferometer (FIMI,  $\epsilon_{FIMI}$ ) with an ideal spectral analyzer (ISA, eq. C.20). That is eq. C.22 can be written in terms of  $FSR$ :

$$\kappa_{(u_r)FIMI} = \frac{\epsilon_{FIMI}}{\epsilon_{ISA}} = \frac{d_c FSR}{\sqrt{2}c} \left( 1 - \sqrt{1 - V^2 \exp \left[ -8 \left( \frac{c}{d_c FSR} \right)^2 \right]} \right)^{-\frac{1}{2}}. \quad (3.5)$$

Where  $d_c = \sqrt{2}c/(\pi\sigma_{Ray}(T))$  is the coherence length of the Rayleigh signal. For higher values of the  $FSR$ , the fringe phase sensitivity  $S_e = 4\pi/(FSR \cdot \lambda_L)$  in [rad/(m/s)] with respect to the Doppler shift is lower. For lower values of the  $FSR$  the fringe contrast is reduced and the efficiency of the determination of the fringe phase decreases.

Here, the  $FSR$  is optimized for the ‘‘worst case’’ condition, where no aerosols contribute to backscattering ( $R_{b_{vop}} = 1$ ). ‘‘vop’’ signifies the atmospheric conditions the device is optimized for. In this case, the contrast factor  $G$  is equal to 66% (assuming  $V = 1$ ).

In Fig. 3.4(a)  $\kappa_{u_r}$  is plotted as a function of the  $FSR$  at  $T_{vop} = 273$  K for  $R_{b_{vop}} = 1$ , for  $V = 1$ , and for  $V = 0.6$  (dashed line). The plot includes contrast factors  $G(FSR)$  for  $R_b = 1$  (green), and for  $R_b = 2$  (magenta) and the phase sensitivity  $S_e(FSR)$  (black).

The optimum  $FSR$  value of  $10.7$  GHz  $\approx 6.8 \times \sigma_{Ray}$  (at  $R_{b_{vop}} = 1$ ,  $T_{vop} = 273$  K) is found at the minimum:  $\kappa_{u_r} = 4.4$  (dotted vertical line).

While for an ideal spectral analyzer  $N_{tot} = 8 \times 10^4$  signal photons are necessary for a precision of  $u_r$  of  $\sigma(u_r)$  of 1 m/s, a FIMI (with  $\kappa_{u_r} = 4.4$ ) requires 20 times more signal photons to bring  $\epsilon_{FIMI}$  to the same value as  $\epsilon_{(u_r)ISA}$  (see eq. C.20).

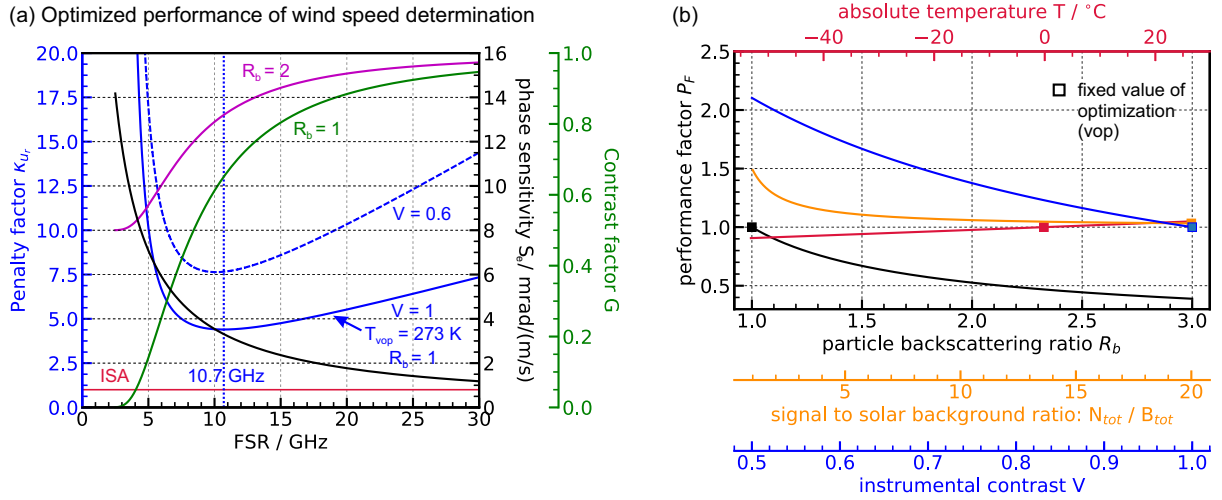


**Figure 3.4:** (a) Penalty factor of wind speed measurement  $\kappa_{ur}$  (blue), contrast factor  $G(FSR)$  (green:  $R_b = 1$ , magenta:  $R_b = 2$ ), and phase sensitivity  $S_e$  (black, independent of  $T$ ,  $R_b$ ,  $V$ ) as a function of  $FSR$  for  $T = 273$  K,  $R_b = 1$  at a wavelength of 355 nm. (b) Sensitivity study: Performance factors  $P_F$  as a function of  $R_b$ ,  $T$ ,  $N_{tot}/B_{tot}$ , and  $V$ , which compare the CRBs at the varied parameter with the CRB at the fixed parameters of optimization, i.e.,  $R_{bvop} = 1$ ,  $T_{vop} = 273$  K,  $N_{tot}/B_{tot} = \infty$  ( $B_{tot} = 0$ ), and  $V = 1$  (fixed values marked by squares).

### Theoretical performance of the FIMI with respect to atmospheric conditions

Cézard *et al.* (2009a) showed in a sensitivity study for two FIMI interferometers with  $OPD_1 = 28$  mm and  $OPD_2 = 10$  cm, for the measurement of  $u_r$ ,  $T$ , and  $R_b$ , that when  $R_b$  increases the global contrast increases thus producing lower penalty factors of  $u_r$ , and, that a decrease of temperature by 40 K reduces  $\kappa_{ur}$  by 10% (Cézard, 2008). The results of a similar sensitivity study (for only one FIMI with  $FSR = 10.7$  GHz) are shown in Fig. 3.4(b), whereby the performance factor  $P_F = \epsilon_{FIMI}/\epsilon_{FIMI_{vop}}$  is shown in dependence of the particle backscattering ratio  $R_b$ , of the absolute temperature  $T$ , of the solar background ratio  $N_{tot}/B_{tot}$  (whereby  $N_{tot}$  is the number of received signal photons, and  $B_{tot}$  is the number of solar background photons), and of the instrumental contrast  $V$ . One of these parameters is varied respectively, while the other parameters are kept constant (those constant values, which are the values of the above optimization, i.e., “vop”, are marked by squares in Fig. 3.4(b)). The corresponding equation of CRB is derived using eq. C.24 in appendix C.3 and inserting it into eq. C.18 and using eq. C.13 (see appendix C.2).

Best measurement performance of wind speed measurement is thus expected at low temperatures  $T$ , at high scattering ratios  $R_b$ , suppressed solar background  $B_{tot}$ , and high instrumental contrast  $V$ .

The altitude-dependent performance factors  $P_F$  can be estimated, using the median values of the atmospheric model provided in Fig. 2.1, inserting them into eq. C.29. The results of this sensitivity study are provided in Fig. 3.5(a). Fig. 3.5(b) shows CRB values as a function of range and altitude for IR pulse energies of 267 mJ (DELICAT transmitter, see section 3.6) with a repetition rate of 100 Hz equal to the line-of-sight update rate, a total receiver efficiency of 2.7%, exactly one fringe period imaged, and pure molecular scattering ( $R_b = 1$  at all altitudes).

A CRB value of one (obtained with  $\approx 1.6 \times 10^6$  photons incident on the FIMI) would give a measurement precision of radial wind speeds  $u_r$  of 1 m/s. The CRB increases linearly as a function of range. The steepness of this increase is altitude dependent, due to the varying

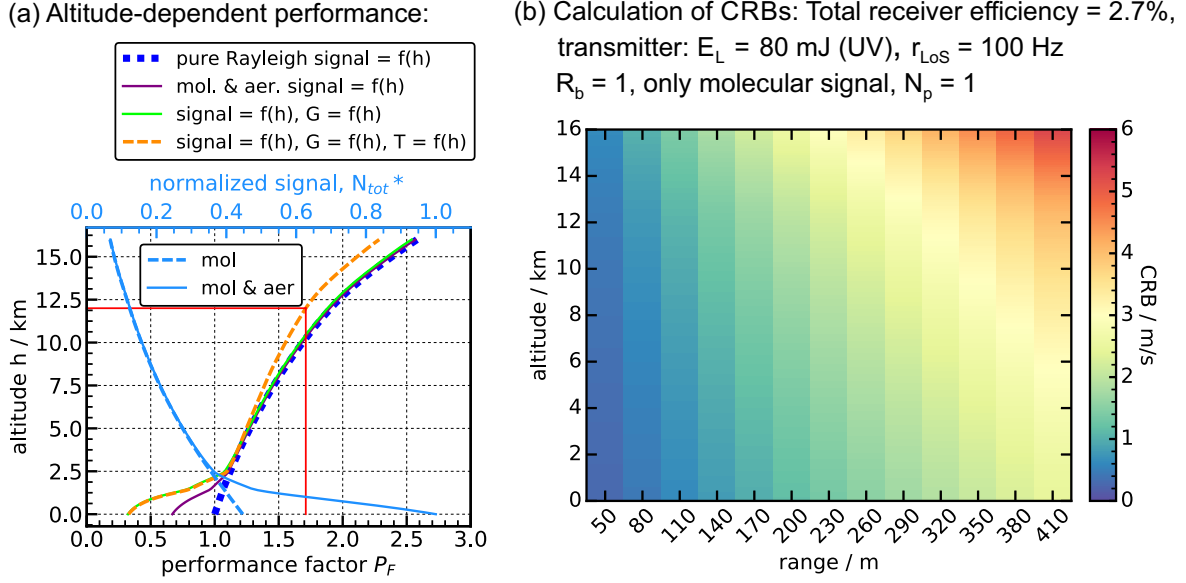


**Figure 3.5:** (a) Altitude-dependent performance factor  $P_F$  for pure Rayleigh signal (blue), including aerosols (purple), altitude-dependent atmospheric contrast factor  $G$  (lime), and altitude-dependent temperature  $T$  (orange), using atmospheric models (see Fig. 2.1), and solving eq. C.29, assuming  $V = 1$ . (b) Typical estimated CRB values for an FIMI receiver with a total efficiency of 2.8%, assuming pure Rayleigh scattering, and pulse energies  $E_L$  of 270 mJ (IR, i.e., 80 mJ at 355 nm, similar to the DELICAT transmitter, see section 3.6) and a LoS update rate ( $r_{LoS}$ ) of 100 Hz, i.e.,  $N_p = 1$  number of pulses averaged. Detection losses are not considered (see section 4).

density of air molecules ( $\rho$ ), aerosol concentration (i.e., values of  $R_b$ ) and its influence on the number of backscattered photons and on the atmospheric contrast factor  $G$ , which also depends on  $T$ . The CRB value does not take into account noise sources apart from (dominant) shot noise. Further noise contributions can be laser beam pointing fluctuations (see appendix I), and speckle noise (see appendix C.1, and section 3.5.4). An estimation of the performance including speckle noise is provided in section 4.

This sensitivity study shows that, provided the total receiver efficiency, the laser power, and the instrumental contrast ( $V = 1$ ) are high enough, radial wind speeds ( $u_r$ ) can be measured with acceptable performance under all atmospheric conditions ( $\rho$ ,  $T$ ,  $R_b$ ) with an FIMI with an  $FSR$  of 10.7 GHz optimized for pure Rayleigh scattering ( $R_b = 1$ ) and for medium temperatures of  $T = 273$  K.

The detailed, physical design of a fringe-imaging Michelson interferometer (FWFIMI), assuring a high instrumental contrast  $V$ , is described in the next section.

### 3.4 Design of a monolithic fringe-imaging Michelson interferometer

This section describes the development of the monolithic, field-widened and partly temperature tuning compensated FIMI (FWFIMI), and is largely based on [Herbst and Vrancken \(2016\)](#).

As detailed in appendix C.6 (see Fig. C.15), a monolithic FIMI that consists of glass components, that are connected by optical contact bonding or with glue, may provide a higher degree of field-widening compensation than a sequential FIMI. Furthermore, a monolithic FIMI may provide a higher degree of thermomechanical stability.

Exactly one fringe period ( $N_p = 1$ ) shall be imaged on the detector to maximize both the modulation depth of the fringes and the number of pixels per fringe period.  $N_p < 1$  would reduce the contrast of the fringe pattern, while  $N_p > 1$  would reduce the signal-to-noise ratio (SNR) per pixel of the detector. The width of the illuminating beam  $d_w$  shall be 10 mm. This width is of the same order of magnitude as the width of the linear detector (see appendix F) in the proposed setup (see Fig. 3.2), what simplifies the imaging of the fringe on this detector. Assuming a wavelength of the laser ( $\lambda_L$ ) of 354.84 nm, and using eq. 3.1, the ideal net inclination angle  $\theta$  between the mirrors is thus 17.74  $\mu\text{rad}$ .

#### 3.4.1 Field-widening compensation

As pointed out above, the term field-widening (FW) refers to the ability of an interferometer to accept angular distributed light without reduction of fringe contrast, i.e., a FWFIMI is compensated for a larger beam étendue. Field-widening makes the *OPD* on the first order independent of the incident angle ( $\rho_0$ ). The FW compensation requires a special solution for the refractive indices and lengths of the arms of the Michelson interferometer. The compensation can only be achieved for a fixed *FSR* at a selected tilt angle (in this work:  $\theta_t = 2^\circ$ ), with respect to the incident light. Tilted illumination of the FWFIMI at  $\theta_t = 2^\circ$  may allow to simultaneously detect the transmitted and the reflected interference patterns (as shown schematically in Fig. 3.6, see also: Fig. D.15 in D.3), what may increase theoretical performance by a factor of  $\sqrt{2}$  (see appendix C.3). As is shown below, a compensation for  $\theta_t = 2^\circ$  is also suitable for  $\theta_t = 0^\circ$ , which is the configuration chosen in this work in order to keep the overall setup as simple as possible. In Section 3.3.2 an ideal *FSR* of 10.7 GHz for wind speed measurements was determined. In a dispersion-free interferometer the optimum optical path difference ( $OPD_{opt}$ ) is thus 28 mm. In order to achieve field-widening, the refractive indices of arm one ( $n_1$ ) and arm two ( $n_2$ ) have to be different. This requires in general the use of at least two different optical glasses for the interferometer arms or one arm made of air and one of glass.

The latter option is selected here, because it offers an important refractive index difference  $\Delta n$ , which minimizes the lengths of the interferometer arms, and thus reduces temperature sensitivity ([Title, 2013](#)), and leaves the option of pressure tuning the fringe position. Apart from the required spacers it keeps the instrument simple.

A schematic of the (monolithic) fringe-imaging Michelson interferometer (FWFIMI) illuminated at a tilt angle ( $\theta_t$ ) of  $2^\circ$  is shown in Fig. 3.6.

$n_1, n_2, d_1, d_2$  are the absolute refractive indices and lengths of the interferometer arms.  $n_0 = n_a$  is the refractive index of air.  $\rho_0, \rho_1$  and  $\rho_2$  are the angles of incidence and refraction in the respective media.  $\theta_t$  is the mean incident angle of the quasi-collimated

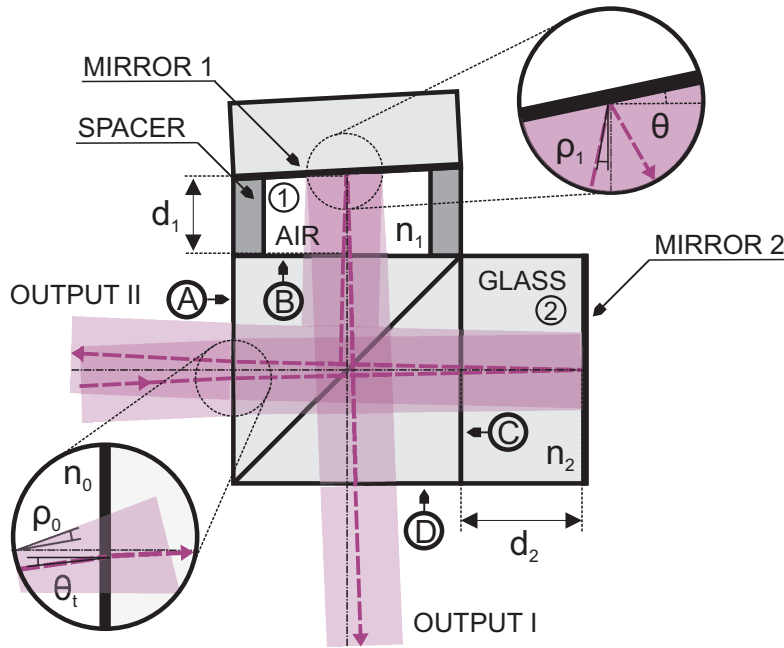


**Figure 3.6:** Monolithic fringe-imaging Michelson interferometer (FWFIMI) tilted by  $2^\circ$  with air arm (1) and glass arm (2). This figure was taken from [Herbst and Vrancken \(2016\)](#).

light beam with angular distribution  $\rho_0 = \pm 21$  mrad (full width of an assumed flat-top angular distribution of  $[-21, 21]$  mrad for a  $600 \mu\text{m}$  quadratic-core fiber, see eq. C.35). In the scheme a perfectly collimated beam is drawn for simplicity. In the following considerations, the cubic non-polarizing beamsplitter is omitted due to symmetry.

The optical path difference  $OPD$  can be expressed as a function of the ray angles  $\rho_1$  and  $\rho_2$  in the interferometer arms in the following way:

$$OPD = n_1 d_1 (\cos(\rho_1) + \cos(\rho_1 \pm 2\theta)) - 2n_2 d_2 \cos(\rho_2) \quad (3.6)$$

Seeing that  $\cos(2\theta) = 1 - 1.6 \cdot 10^{-10}$  we can set  $\theta$  equal to 0. Using Snell's law:  $n_0 \sin(\rho_0) = n_1 \sin(\rho_1) = n_2 \sin(\rho_2)$ , using  $\cos(\rho) = (1 - \sin^2(\rho))^{1/2}$  and expanding  $\sin(\rho_0)$ , one obtains the expressions (eq. 3.7 and eq. 3.8 after expansion) for the optical path difference ( $OPD$ ) as a function of the angle of incidence ( $\rho_0$ ) ([Title and Ramsey, 1980](#)):

$$OPD(\rho_0) = 2n_1 d_1 \sqrt{1 - \frac{\sin^2(\rho_0)}{n_1^2}} - 2n_2 d_2 \sqrt{1 - \frac{\sin^2(\rho_0)}{n_2^2}} \quad (3.7)$$

$$OPD(\rho_0) = 2(n_1 d_1 - n_2 d_2) - \sin^2(\rho_0) \left( \frac{d_1}{n_1} - \frac{d_2}{n_2} \right) - O(\rho_0^4) - \dots \quad (3.8)$$

The first term in eq. 3.8 is the  $OPD$  at the central incident angle  $\theta_t = 0^\circ$  and is called fixed optical path difference ( $OPD_0$ ).

For field-widening the 2nd order term  $w$  is set to zero (field-widening condition):

$$w = \frac{d_1}{n_1} - \frac{d_2}{n_2} = 0 \quad (3.9)$$

If the Michelson interferometer is tilted by the tilt angle  $\theta_t$  with respect to the incident



light, the expressions for  $OPD_0$  and  $w$  are (Cheng *et al.*, 2015):

$$OPD_0(\theta_t) = 2 \left[ n_1 d_1 \sqrt{1 - \frac{\sin^2(\theta_t)}{n_1^2}} - n_2 d_2 \sqrt{1 - \frac{\sin^2(\theta_t)}{n_2^2}} \right] \quad (3.10)$$

$$w(\theta_t) = \frac{d_1}{\sqrt{n_1^2 - \sin^2(\theta_t)}} - \frac{d_2}{\sqrt{n_2^2 - \sin^2(\theta_t)}} \quad (3.11)$$

In order to determine the optimum arm lengths  $d_{1opt}$  and  $d_{2opt}$  for field-widening, this system of equations (3.10, 3.11) has to be solved, where  $OPD_0(\theta_t) = OPD_{opt}$  and  $w(\theta_t) = 0$ . We choose to optimize the arm lengths for a tilt angle  $\theta_t$  of  $2^\circ$ . This allows for the option of a second detector in back-reflection (output II, Fig. 3.6). In this way, the CRB of the Michelson interferometer can be reduced by a factor between  $\sqrt{2}$  and 2 (see Tab. C.1). The interference pattern of output II is shifted by  $2(\delta_T + \delta_R) = \pi$  with respect to output I, where  $\delta_T$  and  $\delta_R$  are the phase shifts of transmittance and reflectance of the beamsplitter.

The preferred glass material is fused silica (FS), because of its high transmission in the UV. The refractive index of the FS glass  $n_{gr}$  at wavelength  $\lambda$  [μm] relative to air at  $T_0$  and  $p_0$  is calculated with the Sellmeyer equation (SCHOTT, 2007):

$$n_{gr}(\lambda) = \sqrt{1 + B_1 \frac{\lambda^2}{\lambda^2 - C_1} + B_2 \frac{\lambda^2}{\lambda^2 - C_2} + B_3 \frac{\lambda^2}{\lambda^2 - C_3}} \quad (3.12)$$

Where  $B_1, B_2, B_3, C_1, C_2, C_3$  are the Sellmeyer coefficients. In eq. 3.10 and eq. 3.11  $n_2$  is equal to the absolute refractive index of glass  $n_{ga}(\lambda_L) = n_{gr}(\lambda_L) \cdot n_a$ .  $n_1$  is equal to  $n_a$  at the reference temperature ( $T_0$ ) of  $22^\circ\text{C}$ , which is the temperature during fabrication. See eq. 3.16 for the calculation of the absolute refractive index of air ( $n_a$ ) at  $T_0$ . The field-widening compensation can only be done for one wavelength. Setting  $OPD_{opt}$  equal to 28 mm, and solving the system of equations 3.10, and 3.11 the optimal arm lengths are obtained, neglecting dispersion.

Wavelength dispersion of the glass arm, modifying the  $FSR$ , has to be considered. This is done by calculating the  $OPD$  as a function of wavelength by inserting eq. 3.12 into eq. 3.10.  $OPD(\lambda)$  is put into the Michelson transmission function (eq. 3.1). The correct values of  $d_{1opt}, d_{2opt}$  are determined by an iterative optimization process.  $OPD_{opt}$  is varied until one fringe period exactly spans 10.7 GHz. The resulting value of  $OPD_{opt}$  is 26.149 mm.

The change of  $OPD$  as a function of the incident angle  $\Delta OPD(\rho_0) = OPD_0 - OPD(\rho_0)$  is a measure of the quality of the field compensation. Fig. 3.7 depicts the change of the optical path difference  $\Delta OPD(\rho_0)$  in wavelengths ( $\lambda = \lambda_L$ ) for FIMIs field-widened for  $\theta_t$  values of  $0^\circ$  and  $2^\circ$  (vertical lines mark the mean incidence angle) and for the case of an ordinary MI with the same  $FSR$  (10.7 GHz).

Typical angular distributions of  $\rho_0 = \pm 16$  mrad or  $\pm 21$  mrad are thus compensated by this field-widening compensation of the FWFIMI. The obtained interference fringe contrast as a function of the maximum value of  $\rho_0$  can be evaluated using eq. C.70–C.72, as is shown in Fig. C.15 of appendix C.6. The analytical model by Fortunato (1997), presented in appendix C.6, was applied by Cézar (2008) to calculate the parameters of a glass plate for the field-widening compensation in a sequential FIMI (see eq. C.66). His results including the effect of the plate beamsplitter (see eq. C.69) are shown in Fig. C.15 for comparison. The symmetric, cubic beamsplitter of the FWFIMI in combination with optimum values



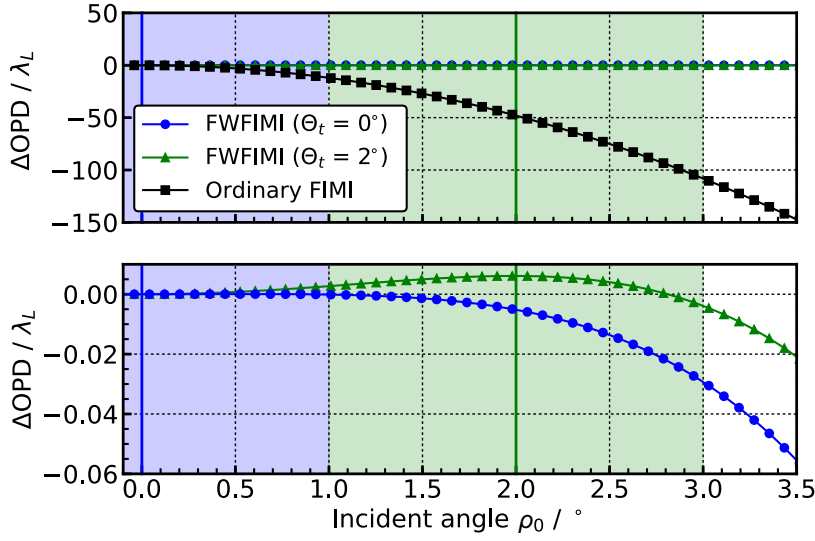


**Figure 3.7:** OPD change in wavelengths as a function of incident angle for FWFIMI field-widened for  $\theta_t = 0^\circ$  and  $2^\circ$  and uncompensated FIMI. Vertical lines mark the respective tilt angle ( $\theta_t$ ). Colored areas mark ranges of  $\theta_t \pm 1^\circ$ . This figure is taken from [Herbst and Vrancken \(2016\)](#).

$d_{1opt}$  and  $d_{2opt}$  allows for field-widening compensation up to  $\rho_0 = \pm 30$  mrad with an instrumental contrast  $V \approx 1$ , while the compensated sequential FIMI is characterized by a contrast reduction for  $\rho_0 > \pm 4$  mrad.

The optimized lengths of the air arm and the glass arm of the FWFIMI for  $\theta_t = 2^\circ$  turn out to be  $d_{1opt} = 11.076$  mm and  $d_{2opt} = 16.360$  mm (see appendix E and Tab. 3.3).

### 3.4.2 Temperature tuning compensation

This section is dedicated to the compensation of temperature-induced shifts of the fringe position during measurements, i.e., during the time needed for numerical averaging over several pulses. These shifts are a consequence of the change of the fixed optical path difference ( $OPD_0$ ) with temperature due to changes of the refractive index and due to thermal expansion of the glass substrate.

The FWFIMI can be more easily temperature-stabilized at elevated operational temperatures (here  $40^\circ\text{C}$ ). The temperature tuning rate  $R_T$  is the shift of the fringe spectral position in Hz per Kelvin. Low values of  $R_T$  minimize temperature-induced biases of the estimated radial wind speed  $u_r$ .  $R_T$  is mainly determined by the spacer material used in the air arm. The spacer material should be optimized for small temperature-tuning. The goal in this section is to find such a spacer material.

Thermal compensation requires the derivative of  $OPD_0$  with respect to temperature being close to zero:

$$\begin{aligned}
 \frac{\partial OPD_0(\theta_t)}{\partial T} &= 0 \\
 &= 2 \left[ \alpha_1 d_1 (n_1^2 - \sin^2(\theta_t))^{\frac{1}{2}} + \beta_1 n_1 d_1 (n_1^2 - \sin^2(\theta_t))^{-\frac{1}{2}} \right] \\
 &\quad - 2 \left[ \alpha_2 d_2 (n_2^2 - \sin^2(\theta_t))^{\frac{1}{2}} + \beta_2 n_2 d_2 (n_2^2 - \sin^2(\theta_t))^{-\frac{1}{2}} \right]
 \end{aligned} \tag{3.13}$$

Where  $\alpha_k = (1/d_k)\partial d_k/\partial T$  is the coefficient of linear thermal expansion (CTE) of the material  $k$ , and  $\beta_k = \partial n_k/\partial T$  is the thermal coefficient of the refractive index.  $n_1$  and  $n_2$  are the absolute refractive indices of air and glass. This condition (eq. 3.13) can be fulfilled by choosing a material for the air arm spacer with an optimized CTE (denoted  $\alpha_1$ ). The ideal value of  $\alpha_1$  is determined in the following. For the calculations the values of  $d_{1opt}$  and  $d_{2opt}$ , determined in Section 3.4.1 are assumed. The CTE of fused silica ( $\alpha_2$ ) is  $0.51 \cdot 10^{-6} \text{ K}^{-1}$ .

The thermal coefficient of fused silica ( $\beta_2$ ) may be calculated with the derivative of the Sellmeyer equation with respect to temperature ([SCHOTT, 2008](#)):

$$\frac{dn_{ga}(\lambda_L, T)}{dT} = \frac{n_2^2(\lambda_L, T_0) - 1}{2n_2(\lambda_L, T_0)} \cdot \left( D_0 + 2D_1\Delta T + 3D_2\Delta T^2 + \frac{E_0 + 2E_1\Delta T}{\lambda_L^2 - \lambda_{TK}^2} \right) \quad (3.14)$$

Where  $n_2(\lambda_L, T_0)$  is the refractive index of the glass at the laser wavelength  $\lambda_L$  in  $[\mu\text{m}]$ , obtained with the Sellmeyer equation at the reference temperature ( $T_0$ ) of  $22^\circ\text{C}$ .  $\Delta T = T - T_0$  is the temperature difference versus  $T_0$ .  $D_0, D_1, D_2, E_0, E_1$  are the thermal dispersion coefficients of the glass and  $\lambda_{TK}$  is the average effective resonance wavelength in  $[\mu\text{m}]$  for the thermo-optic coefficients (see, e.g., [Ghosh \(1997\)](#)). The change of the absolute refractive index  $\Delta n_{ga}(\lambda_L, \Delta T)$  may be calculated by integrating eq. 3.14.

The absolute refractive index of the glass at temperature  $T$  is  $n_{ga}(\lambda_L, T) = n_{ga}(\lambda_L, T_0) + \Delta n_{ga}(\lambda_L, \Delta T)$ .

The thermal coefficient of air ( $\beta_1$ ) and refractive index of air  $n_a(\lambda_L, T, P)$  ([SCHOTT, 2008](#)) are calculated by

$$\beta_1 = \frac{dn_a(\lambda_L, T)}{dT} = -0.00367 \cdot \frac{n_a(\lambda_L, T, p) - 1}{1 + 0.00367 \frac{1}{^\circ\text{C}} \cdot T}, \quad (3.15)$$

$$n_a(\lambda_L, T, p) = 1 + \frac{n_a(\lambda_L, 15^\circ\text{C}, p_0) - 1}{1 + 3.4785 \cdot 10^{-3} \frac{1}{^\circ\text{C}} (T - 15^\circ\text{C})} \frac{p}{p_0} \lambda_L^2, \quad (3.16)$$

where  $p_0 = 0.101325 \cdot 10^6 \text{ Pa}$  is the standard pressure at  $20^\circ\text{C}$ .  $n_a(\lambda_L, T, p)$  is the absolute refractive of index of air at the air pressure  $p$  and at the temperature  $T$  in  $^\circ\text{C}$ .  $\lambda_L$  is the laser wavelength in  $[\mu\text{m}]$ .

With  $n_1/\sqrt{n_1^2 - \sin^2(2^\circ)}$  being 1.0003, one may set  $\theta_t$  equal to  $0^\circ$  in eq. 3.13 in the following, for simplicity. Two variants of temperature tuning are possible. The first is temperature tuning with constant air density (“TTCD”, i.e.,  $\beta_1 = 0$ ) as in the case of isochoric heating when the FIMI is enclosed in a sealed container. We can set  $n_a = 1$ , from which follows, that  $n_{ga} = n_{gr}$ . The second is temperature tuning at constant air pressure (“TTCP”). TTCP occurs when the container is not sealed. Inserting the field-widening equation into the temperature compensation condition we obtain, in case of TTCD and TTCP, the following results for the optimized CTE values of the spacers for CD and CP, respectively:

$$\alpha_{1CD} = n_{gr}^2 \left( \frac{1}{n_{gr}} + \alpha_2 \right) \quad (3.17)$$

$$\alpha_{1CP} = \frac{n_{ga}(T_{op})}{(n_a(T_{op}))^2} \cdot \beta_2 + \frac{(n_{ga}(T_{op}))^2}{(n_a(T_{op}))^2} \cdot \alpha_2 - \frac{1}{n_1} \cdot \beta_1 \quad (3.18)$$

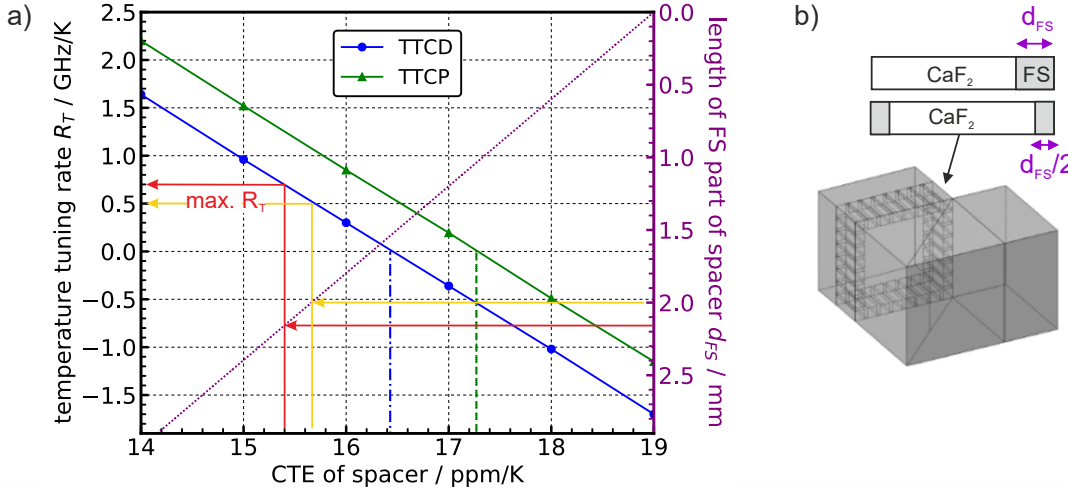


**Figure 3.8:** (a) Temperature tuning rate for tuning modes: constant density (TTCD) and constant pressure (TTCP) as a function of the CTE of the spacer and according length of the FS part of a composite spacer made of silica and calcium fluoride. A red arrow indicates the specified maximum values of  $R_T$  and  $d_{FS}$ . The yellow arrow shows an exemplary lower  $R_T$  for a smaller value of  $d_{FS}$ . (b) 3D-model of the FWFIMI with composite spacers in the air arm. This figure is gathered from [Herbst and Vrancken \(2016\)](#).

The ideal CTE values of the spacers for zero temperature tuning are  $\alpha_{1CD} = 16.4$  ppm/K for constant density in our case, and  $\alpha_{1CP} = 17.3$  ppm/K for constant pressure tuning.

To evaluate  $R_T$  for different values of the spacers' CTE one can use the absolute refractive indices of glass and air and the arm lengths  $d_k(T) = d_k(T_0)(\alpha_k \Delta T + 1)$  to determine the fixed  $OPD$  values at temperatures  $T_1$  and  $T_2$  close to the intended temperature of operation of  $40^\circ\text{C}$ . These fixed  $OPD$  values are then used to calculate the Michelson transmission functions at  $T_1$  and  $T_2$ . The transmission function (eq. 3.1) is evaluated over the frequency range of one  $FSR$  for  $T_1 = 40^\circ\text{C}$  and  $T_2 = 41^\circ\text{C}$  for TTCD and TTCP for different values of the spacer CTE. In each case the temperature tuning rate is determined from the shift between the transmission functions at  $T_1$  and  $T_2$ . The temperature tuning rate is plotted in Fig. 3.8(a), as function of the CTE of the spacers for both TTCD and TTCP.

The respective ideal CTE values  $\alpha_{1CD}$  and  $\alpha_{1CP}$  are highlighted (dotted lines). Assuming  $\alpha_1 = \alpha_2 = 0.51$  ppm/K,  $R_T$  would be higher than one  $FSR/[1\text{ K}]$ . Fabricating the spacers of the same material as the glass arm is therefore no option. Copper with  $CTE_{Cu} \approx 17$  ppm/K and calcium fluoride ( $CTE_{CaF_2} = 19$  ppm/K) are suitable materials. [Mahadevan et al. \(2004\)](#) used a copper ring spacer glued to a BK7 beam splitter with UV cure epoxy. Stability issues and thermal drift were reported later, and were explained with shear stresses due to the large CTE difference between copper and BK7 ([Wan et al., 2011](#)). A concept applied by [Harlander and Englert \(2013\)](#) is to fabricate column spacers of calcium fluoride ( $\text{CaF}_2$ ) with relatively small cross section in order to minimize the thermal stresses. The  $\text{CaF}_2$  can be glued to fused silica (FS) components with UV cure epoxy.

Furthermore the spacer columns can be fabricated as a composite of fused silica (FS) and  $\text{CaF}_2$ . In this way the net CTE of the spacers can be tuned by  $CTE_C = j \cdot CTE_{FS} + (1 - j) \cdot CTE_{CaF_2}$ , where  $j$  is the length fraction of glass in the composite. The glass part length  $d_{FS}$  is  $j \cdot d_2$ . Fig. 3.8(a) shows  $d_{FS}$  as a function of  $CTE_C$  (violet dotted line).

The minimized ideal CTE values ( $\alpha_{1CD}$ ,  $\alpha_{1CP}$ ) require a polished glass part thickness ( $d_{FS}$ ) smaller than 2 mm, what is hard to achieve. TTCD tuning mode is selected because it

allows to seal the Michelson compartment for protection and pressure tuning, and because the tuned CTE value is closer to  $\alpha_{1CD}$ . A 3D-model of such a interferometer can be seen in Fig. 3.8(b).

For measurements the interferometer will be heated up from fabrication temperature (22 °C) to operation temperature (40 °C) at constant density. In case of TTCD,  $\beta_1$  is zero and  $\alpha_1$  is assumed to be 15.5 ppm/K (not the optimum 16.4 ppm/K), because of fabrication limits of the thickness of the fused silica parts of the spacers. The change of the air arm length  $\Delta d_1$  for  $\Delta T = 18$  K is 3.1  $\mu\text{m}$ , while  $\Delta d_2$  is 0.15  $\mu\text{m}$ . The change of the arm lengths is compensated by reducing the initial air arm length by 3  $\mu\text{m}$ . One may ignore the thermal coefficient of the fused silica slice ( $\beta_2$ ). This is a fair approximation. The change of the  $FSR$  over a temperature range of 20 K is thus achieved to be smaller than 0.2%.

The finally specified maximum temperature tuning rate ( $R_T$ ) of the FWFIMI is less than 700 MHz/K (see appendix E and Tab. 3.3).

### 3.4.3 Fabrication tolerances and instrumental contrast

For a realistic evaluation of the expected performance, fabrication tolerances and their influence on the instrumental contrast  $V$ , and therefore on the performance, have to be considered. In the following, some of the important parameters of the FWFIMI are studied in a sensitivity analysis to determine specifications of the fabrication tolerances of these parameters.

#### Arm Lengths and Refractive Index Tolerances

First, the influence of arm length tolerances on the instrumental contrast is considered.

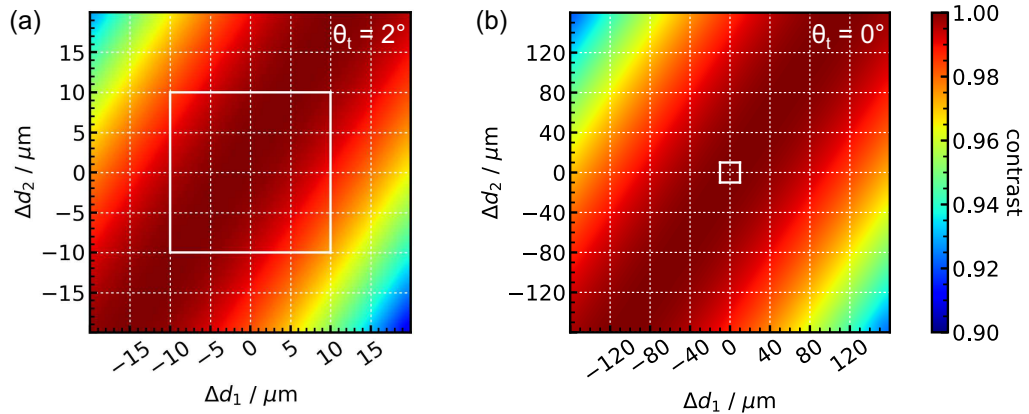


**Figure 3.9:** Global contrast for angular distributed light incident on an FWFIMI, where the arm lengths  $d_1$  and  $d_2$  are varied around the ideal values for mean angles of incidence of  $\theta_t = 2^\circ$  (a) and  $\theta_t = 0^\circ$  (b), assuming a flat-top angular range of  $\rho_i$  of  $\theta_t + [-16, 16]$  mrad. Tolerances are indicated by white squares. This figure is retrieved from [Herbst and Vrancken \(2016\)](#).

The  $OPD$  is calculated for a systematic variation of  $d_1 + \Delta d_1$  and  $d_2 + \Delta d_2$  in eq. 3.7 for the angle-dependent  $OPD$  for different incident flat-top angular distributions ( $\rho_i = \theta_t + [-16, 16]$  mrad). The according transmission functions are calculated using eq. 3.1 for each configuration (pair of  $d_1$  and  $d_2$ ) at a temperature of 40 °C. The transmission functions for different  $\rho_i$  are summed up to yield the global transmission function for the angular distribution. The contrast of the global fringe pattern is determined for each configuration.

In these calculations dispersion is neglected. The contrast is plotted in Fig. 3.9(a) and (b) as a function of  $\Delta d_1$  and  $\Delta d_2$  for  $\theta_t = 2^\circ$  and  $\theta_t = 0^\circ$  (see also eq. C.70).

In case of  $\theta_t = 2^\circ$  a tolerance for the arm lengths  $\Delta d$  of  $\pm 10 \mu\text{m}$  (see white rectangle) may reduce the global fringe contrast in the worst case to 97%. A tilt of  $0^\circ$  of the FWFIMI decreases the sensitivity of field-widening to the arm length tolerances. For  $\theta_t = 0^\circ$  the contrast is always equal to one within  $\pm 10 \mu\text{m}$ . A reduction of the angular distribution  $\rho_i$  decreases the sensitivity, as well. However, in section 3.2 it was observed that a required FOV of 4 mrad results in values of  $\rho_i$  on the order of at least  $[-16, 16]$  mrad. Even higher values of  $\rho_i$  may be obtained in a fiber-coupled setup (see eq. C.35).

Similar considerations may be performed for the refractive index of the glass arm. It has a refractive index consistency of one part in 2000. The reduction of contrast due to such a variation of  $n_g$  is less than 0.2%.

### Net Surface Accuracy

The fringe shape is sensitive to deviations of the net contour of the mirrors from planarity. Here this deviation is considered to be a radial curvature - an assumed worst case. The effect on the fringe shape is modeled with non-sequential raytracing in ZEMAX (see appendix D.2, scheme in Fig. 3.10(a)).

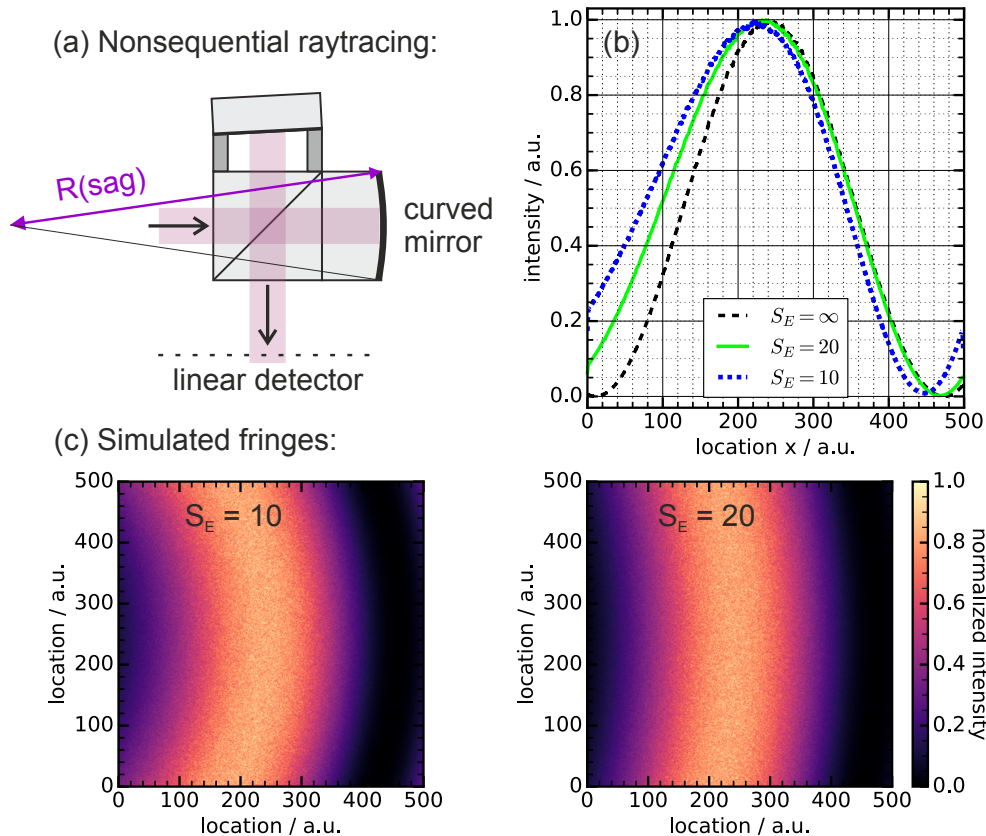


**Figure 3.10:** Effect of net surface radial curvature on fringe shape: (a) Scheme of the non-sequential raytrace. (b) Integrated fringe shapes of an ideal (straight) fringe ( $S_E = \infty$ ) and of the simulated fringes (c) for radial surface errors of  $S_E = 10$  (left) and  $S_E = 20$  (right).

According to ISO 10110 contour accuracy is given for the test wavelength  $\lambda$  of 633 nm. We consider here surface errors  $\lambda/S_E$  with  $S_E = \infty$ ,  $S_E = 20$ , and  $S_E = 10$ . The surface



sag is then:  $sag = 0.00063 \text{ mm}/S_E$ . The radius of curvature is  $R(sag) = (0.25d_C^2 + sag^2)/(2sag)$ , where  $d_C = 19 \text{ mm}$  is the defined clear aperture of the FWFIMI.

Fig. 3.10(c) shows the fringe shapes obtained by coherent raytracing with a collimated, quadratic-shaped, uniform illumination of wavelength  $\lambda_L = 354.84 \text{ nm}$  and  $d_w = 10 \text{ mm}$ , through an FIMI, where the net radius of curvature of the mirrors is  $R(sag)$ . The final shape of the fringe on a linear detector is obtained by summation of all pixels along the y-direction (Fig. 3.10(b)). The y-axis is normalized to the intensity of the planar (straight) case.

As the net surface curvature increases, the fringe is curved increasingly. Its summation in y-direction results in an asymmetrical (skewed) fringe with reduced contrast. In case of  $S_E = 10$  the contrast is reduced by 1.7%. In case of  $S_E = 20$ , the reduction of contrast is 0.5%. In contrast to this simplified scheme, surface irregularities depend on the manufacturing process and may be random, and far from radial. The actual fringe shape has to be measured and the fit model of the evaluation process should be adapted.

## Coatings

The quality of the multilayer dielectric coatings applied to the interfaces of the FWFIMI determine the instrumental fringe contrast  $V$  and the efficiency of the FWFIMI, as well. We consider a dielectric beamsplitter coating with a reflectivity of  $50\% \pm 2\%$  at  $355 \text{ nm}$  for s-polarized light at incident angles of  $45^\circ \pm 2^\circ$ . The term splitting ratio refers to the ratio of the luminous light intensity transmitted ( $I_T = tI_0$ ) and reflected ( $I_R = rI_0$ ) by the beamsplitter coating. Here  $I_0 = E_0^2$  is the luminous light intensity of the input beam, and  $t$  and  $r$  are the intensity transmission and reflection coefficients of the beam splitter, where  $t + r = 1$ . The total intensity  $I_{tot}$  at the FIMI mirrors, where the interference pattern is localized (see: section 3.4.4), can be written as

$$I_{tot} = \left| \sqrt{r}E_0 + \sqrt{t}E_0 \exp(j\phi) \right|^2 = I_0[1 + V_{BS} \cos(\phi)]. \quad (3.19)$$

Here  $\phi$  is the phase, and  $V_{BS} = 2 \cdot \sqrt{rt}$  is the maximum contrast due to the repartition of energy by the beam splitter in the two arms of the FIMI. In case of  $r = 0.52$  and  $t = 0.48$ ,  $V_{BS}$  amounts to 99.9%. The reflectance for p-polarized light is low ( $\approx 5\%$ ). For pure p-polarized light  $V_{BS}$  would be  $\approx 44\%$  (see appendix E). The reason for this is, that at incident angles of  $45^\circ$  (close to Brewster's angle) dielectric coatings are very polarizing. Alternatively, metal based coatings could be used, however due to absorption at  $355 \text{ nm}$  ( $\approx 15\%$  for Al-coatings), durability would be a concern (Miller, 2018).

This major disadvantage of cubic beamsplitters could be circumvented by using hexagonal beamsplitters, which allow for incident angles of  $30^\circ$ , and could allow splitting ratios of 35:65 for s- and p-polarized light (i.e.,  $V_{BS} \approx 95\%$ ) (Miller, 2018). However these beamsplitters are more sophisticated to build, are impacting the overall optical layout, and are more expensive. Such interferometers with a hexagonal BS have been successfully implemented (see, e.g., the Michelson interferometer of the SHIMMER instrument on STPSat-1 (Harlander et al., 2003)). Here, a polarizing element in front of the FIMI should guarantee that the incident light is s-polarized in order to ensure a high instrumental contrast.

The instrumental contrast may depend, as well, on the anti-reflection coatings applied to the surfaces of the beamsplitter. Due to imperfect AR coatings, the reflected signal will interfere with the primary signal and will be visible as a background due to the high

intensity difference for a Michelson interferometer used as spectral discrimination filter (*Liu et al.*, 2012). Calculations estimating the influence of multiple reflections in wide-angle Michelson interferometers (without mirror inclination) on the intensity distribution have also been undertaken by *Ward et al.* (1985). Here, a non-sequential raytracing model of the FWFIMI (see appendix D.2) is used to estimate the influence of the reflectivity of the surfaces A, B, C and D of the FWFIMI (see Fig. 3.6) on the interference fringe shape. The simulations show that the interference fringe shape and contrast depend on the illumination condition (e.g., collimated or divergent), and that for a reflectivity of the AR-coating of  $R_{AR} < 0.5\%$  there is no significant contrast reduction (see Fig. D.11 and Fig. D.12 in appendix D.2). When no coating is applied ( $R_{AR} = 4\%$ ) the contrast may be reduced by several percent.

The surfaces A, B and D shall be anti-reflection coated with  $R_{AR} = 0.1\%$ , in order to maximize transmission efficiency, and to reduce stray light and ghost images.

### Mirror Inclination Angle

The net inclination angle between the mirrors ( $\theta$ , Fig. 3.6) is specified with  $17.8 \pm 1 \mu\text{rad}$ . The according number of imaged fringe periods ( $N_p$ ) is  $1 \pm 0.06$ . In case of  $N_p = 0.94$  the contrast is reduced by 2%, because less than one fringe period is imaged. In this case an increase of the illuminating beam diameter  $d_w$  to 10.6 mm would correct  $N_p$  back to one.

#### 3.4.4 Fringe localization

Up to now the étendue of the illumination was considered in terms of field-widening, but not for fringe-imaging simulations. Actually, the illumination can be viewed as an extended disk made up of incoherent point sources (plane waves after collimation). Each point source produces a “nonlocalized” fringe pattern, where the visibility (contrast) is unity everywhere and only depends on the relative intensities of the two waves made to interfere. The actual fringe pattern is the incoherent superposition of these elementary “nonlocalized” fringe patterns. The mutual displacement between the patterns and therefore the visibility of the global fringe pattern depends on the location of the imaging plane (because of the beam divergence) and may vary between 0 and 1. Such fringes are called “localized”. An analytical description for the case of a FIMI is given by *Fortunato* (1997) (see appendix C.6, where the fringe localization is described by a Bessel function  $J_0$ , see eq. C.56, and see *Wyant* (1978); *Simon and Comastri* (2004) in terms of the Van Cittert-Zernike theorem).

Here, a more practical approach is applied. Fringe localization is simulated in the sequential mode of ZEMAX (see appendix D.2, Fig. D.9). The layout of the FWFIMI model is shown in Fig. 3.11 (right inset). The arm lengths and refractive index values are set to the ideal ones determined in section 3.4.1.  $\theta_t$  is set to zero. A number of rays with an angular distribution of  $[-16, +16]$  mrad in the x- and y-direction are traced through the monolithic FWFIMI. The screen can be shifted in z-direction towards the inclined mirror of the air arm ( $d_z < 0$ ) and further away from the exit surface ( $d_z > 0$ ). For every pair of rays a pair of plane waves is constructed at the location of incidence on the imaging plane. The interference of each pair of plane waves is calculated on a two-dimensional grid in the x-y plane at a position  $d_z$  to produce the “nonlocalized” fringe patterns. Their incoherent sum gives the global fringe patterns for different values of  $d_z$ .

Fig. 3.11 shows global fringe pattern profiles (left inset) for increasing values of  $d_z$  and their contrast  $V_{loc}$  as a function of  $d_z$ .



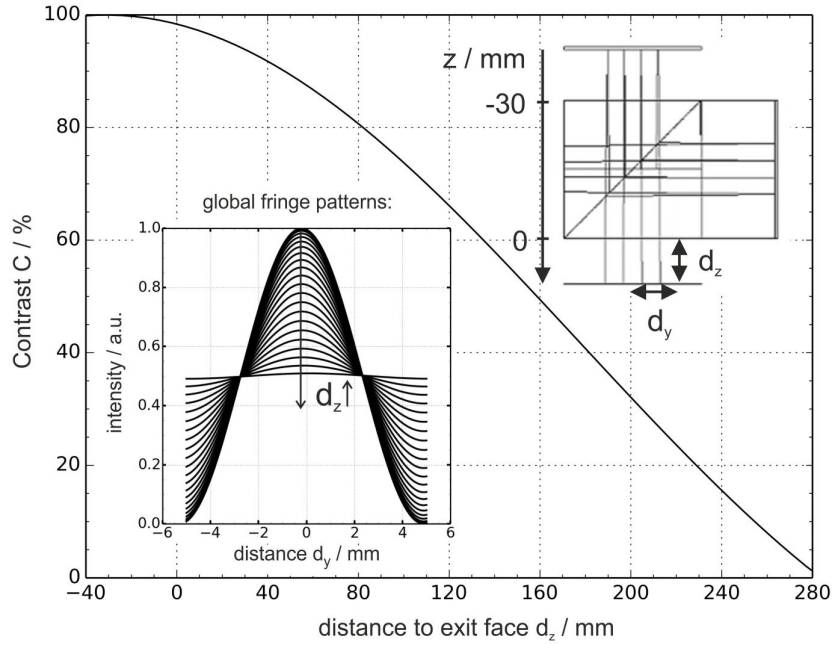


**Figure 3.11:** Instrumental contrast factor ( $V_{loc}$ ) as a function of the distance ( $d_z$ ) from the exit face of the FWFIMI.  $V_{loc}$  is given by  $|\text{sinc}(a)|$  with  $a = 2k\theta\rho_{max}(\epsilon_p - 10 \text{ mm})$ , i.e., by the Fourier transform of  $[-\rho_{max}, \rho_{max}]$  (see appendix C.6). Inset: Global fringe patterns for different  $d_z$  and raytracing layout of the FWFIMI (*Herbst and Vrancken, 2016*).

$V_{loc}$  contributes to the instrumental contrast  $V$  (eq. 3.2) of the TF (eq. 3.1).  $V$  is the product of all the contrast reducing contributions detailed in chapter 3.4.3. The fringes are localized close to the mirrors of the FWFIMI. In order to maximize the visibility and the measurement performance, an imaging system is required, projecting the fringe localization plane on the detector plane, being located at positive values of  $d_z$  outside the sealed compartment. Alternatively, the mirror inclinations of the FWFIMI and the mean incidence angle could be designed such that the localization plane is located at the detector plane. This solution however would increase the complexity of the FWFIMI and would reduce the flexibility of the instrument with respect to different detector types.

This section (3.4) described the design of a fringe-imaging Michelson interferometer (FWFIMI) with field-widening compensation and with partly temperature-tuning compensation. Tolerances of the interferometer arm lengths, of net surface accuracy, and of the beamsplitter coatings and AR coatings have been treated. The issue of fringe localization was illustrated. The resulting specifications are shown in appendix E and in Tab. 3.3 of the next section.

The FWFIMI is characterized and concepts for a possible receiver setup are developed in the following sections.

### 3.5 Characteristics of the actual physical receiver

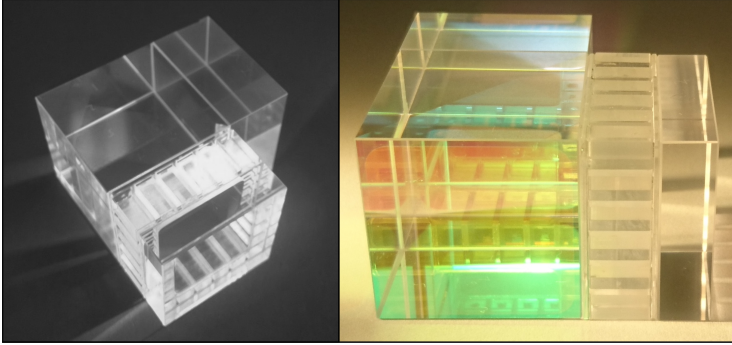
The assembled receiver yields optical properties, which cannot be fully anticipated through calculation and simulation. This section describes the physical receiver and experimental optical characterizations of the receiver's components. Firstly, the characteristics of the manufactured monolithic Michelson interferometer (FWFIMI) are described.

### 3.5.1 Specifications and characteristics of the FWFIMI

Complete specifications and a test report provided by the manufacturer are included in appendix E. Here the main characteristics are reproduced for comparison with measured features of later sections.

Photographs of the manufactured interferometer and a schematic drawing are shown in Fig. 3.12(a) and (b).

(a) Photographs of the assembled interferometer



(b) Schematic drawing

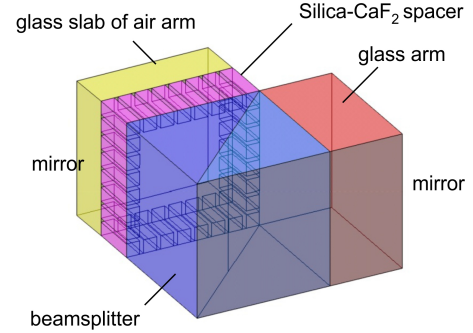


**Figure 3.12:** (a) Photographs of the assembled interferometer<sup>1</sup>, (b) Schematic drawing.

Important specifications of the FWFIMI<sup>1</sup> and the characteristics of the manufactured FWFIMI are summarized in Tab. 3.3. Some “measured” values of the manufactured FWFIMI in Tab. 3.3 are based on calculations using other measured parameters.

**Table 3.3:** The most important specifications of the FWFIMI and reported values after manufacture (see appendix E).

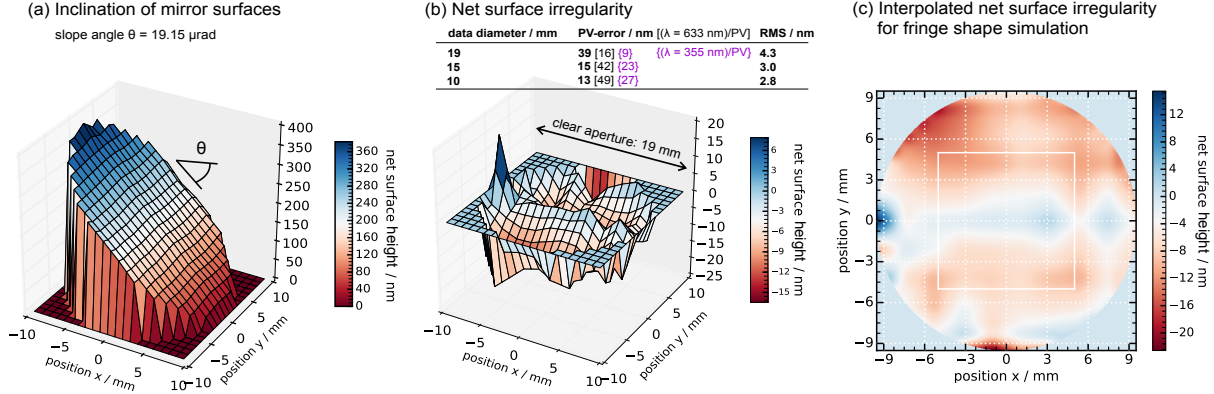
Requirement	Specification	Measured value
Edge length	30 mm	30 mm
$OPD_0$	26.149 mm at 22°C	26.165 mm at 22°C (calculated)
$FSR$	10.7 GHz	10.69 GHz (calculated)
Clear aperture (CA)	19 mm	19 mm
Aperture of illumination	10 to 15 mm	10 to 15 mm
Air arm length	11.076 mm $\pm$ 10 $\mu$ m	11.075 mm
Glass arm length	16.360 mm $\pm$ 10 $\mu$ m	16.363 mm
Net wedge	17.8 $\mu$ rad $\pm$ 1 $\mu$ rad	19.1 $\mu$ rad
Net surface irregularity	$\lambda/20$ ( $\lambda = 633$ nm)	39 nm PV (over CA)
Cubic beamsplitter ratio	48% T at 355 nm	48% T at 355 nm
AR coatings	0.1% R at 355 nm	<0.1% R at 355 nm
Temperature tuning rate	<700 MHz/K	477 MHz/K (calculated)
Temperature range	10 °C to 50 °C	10 °C to 50 °C

Fig. 3.13 shows the results of phase measurements carried out on the Michelson interferometer after final assembly by LightMachinery Inc. (by scanning a collimated laser beam). The inclination angle  $\theta$  is determined to be 19.1  $\mu$ rad (see Fig. 3.13(a)).

The net surface irregularity after subtraction of the slope angle  $\theta$  is determined over circular measurement areas of 19 mm, 15 mm, and 10 mm diameter (see Fig. 3.13(b)).

<sup>1</sup> manufactured by LightMachinery Inc., Nepean, Ontario K2E7L2, Canada

The Peak-to-Valley (PV) error is given by the difference between maximum and minimum net surface height value within the measurement area. The root-mean-square error (RMS) is the standard deviation of the net surface height values within the measurement area.



**Figure 3.13:** Measured mirror inclination angle (a) and net surface irregularity (b) based on a phase measurement procedure carried out by LightMachinery Inc. after final assembly. (c) Top-view of the interpolated net surface irregularity used for fringe shape simulations. The proposed location of the illumination is marked by a white box.

The inclination angle  $\theta$  is larger than the specified  $17.8 \pm 1 \mu\text{rad}$ . A way to mitigate this is to reduce the aperture of the illumination ( $d_w$ ) by 0.7 mm. The net surface irregularity over the specified clear aperture of 19 mm, after several re-polishing actions, turns out to be 39 nm (PV), i.e.,  $\lambda/16$  with  $\lambda = 633 \text{ nm}$ . This is outside the specified value of  $\lambda/20$ . The illumination aperture is intended to be smaller than 15 mm in diameter. In this case the irregularity is 15 nm (PV), i.e.,  $\lambda/42$  provided that the interferometer is illuminated in a centered way. For this reason, the FWFIMI was accepted with these characteristics. Fig. 3.13(c) contains an on top view of the interpolated net surface irregularity, which is used to estimate the resulting fringe shape by non-sequential raytracing simulations in the next section.

### 3.5.2 General characterization of the interference fringe

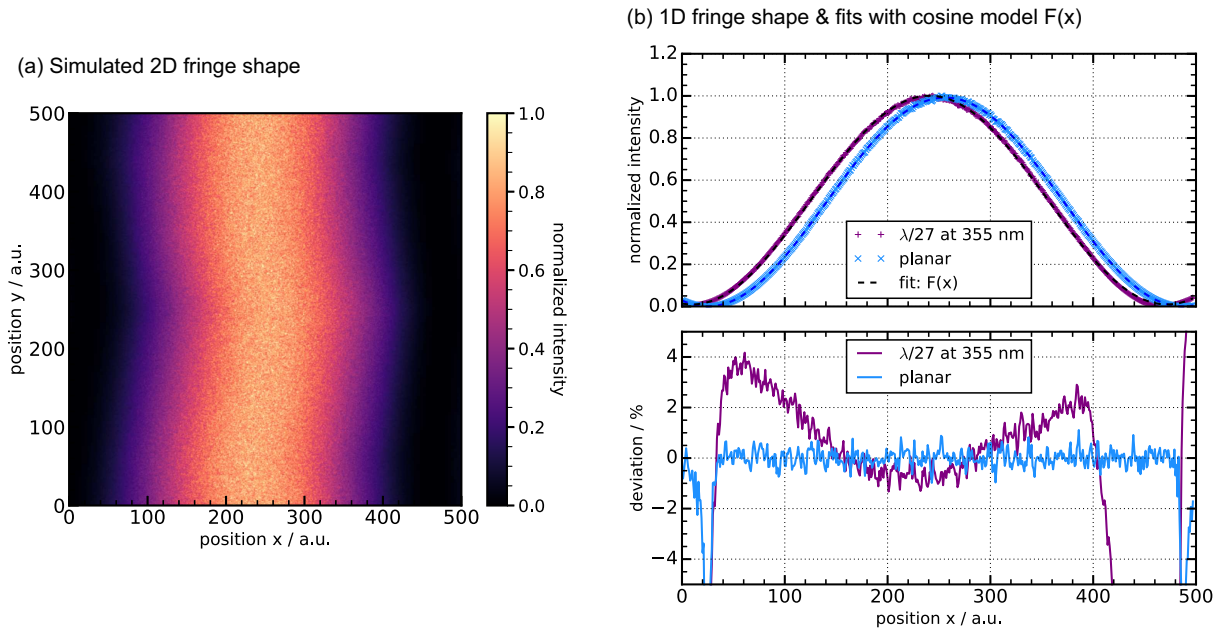
The actual instrument's fringe properties differ from the theoretical ones due to the non-ideal manufacturing process. The purpose of this section is to summarize the results of the fringe characterization. Important properties are the fringe shape, the free spectral range, the number of periods imaged, and the instrumental contrast.

Fig. 3.14 shows the results of a non-sequential fringe shape simulation (see appendix D.2) using the net surface irregularity of Fig. 3.13(c) and assuming central illumination of the area marked by a white square in Fig. 3.13(c). The 2D fringe-shape (Fig. 3.14(a)) is curved as compared to the ideal linear fringe shape.

Fig. 3.14(b) contains the 1D fringe shapes, obtained by summation along the y-axis. Fitting is performed with a fit model of the form

$$F(x) = p_A (1 + p_W \cos((2\pi/d_w)N_{\text{periods}}x - p_{\Delta\phi})) + p_B, \quad (3.20)$$

for both the realistic and the ideal fringe shape.  $p_A$ ,  $p_W$ ,  $p_{\Delta\phi}$ , and  $p_B$  are fit parameters for amplitude, contrast, phase shift, and background.  $d_w$  is the diameter of the illumination, and  $N_{\text{periods}} = 1.078$  is the number of imaged fringe periods. The realistic fringe (Fig. 3.14)



**Figure 3.14:** (a) Simulated 2D fringe shape using non-sequential raytracing (see appendix D.2) and the interpolated net surface irregularity of Fig. 3.13(c). (b) Fit to 1D fringe shape (shape of (a) summed along y-axis) with a simple cosine fit model (see eq. 3.20).

shows some deviations from the ideal fringe shape. The deviations between the simulated fringes and the fit model are largest in the vicinity of the fringe minima in both cases, what is likely due to artificial noise (random distribution of rays hitting the detector) within the coherent non-sequential raytracing simulation.

In the following, the aim is to measure the actual fringe shape of the lidar receiver. For this purpose a UV continuous-wave (cw) laser (Cobolt™ Zouk, see appendix F) is collimated with two beam expanders. Collimation is verified with a shearing interferometer. As depicted in the scheme of Fig. 3.15, the interference fringe shape is always the product of the illumination function and the instrument function (i.e., the fringe shape obtained for flat, homogeneous illumination). Fig. 3.16(a) shows a photograph of the FWFIMI fixed inside an invar (FeNi36) cage. The interference pattern intensity is visualized by fluorescence on a sheet of paper in Fig. 3.16(b) or can be evaluated quantitatively with a CMOS-sensor located at the respective position.

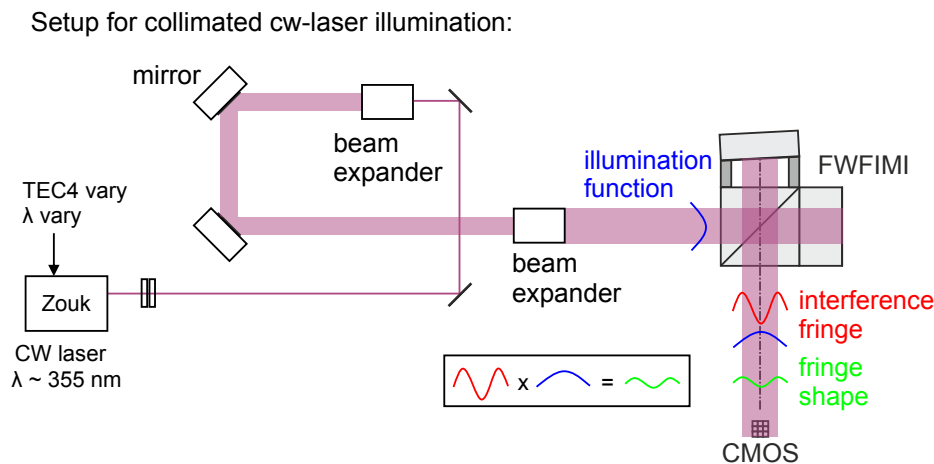


**Figure 3.15:** Schematic illumination of interferometer with collimated cw laser.

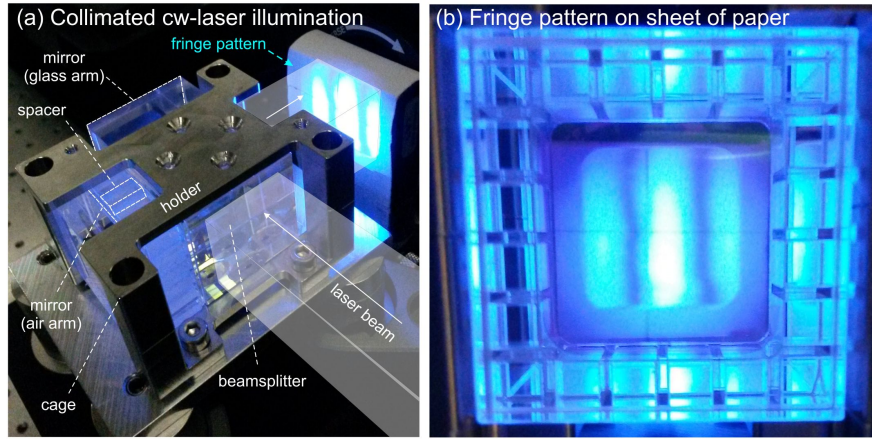


**Figure 3.16:** Photographs of illuminated interferometer fixed by an invar cage (a) and fluorescent 2D-fringe on a sheet of paper (b).

Extracting the fringe-shape is a challenge if the illumination function is not precisely known. The wavelength of the cw-laser is tuned through the entire *FSR* to get access to the illumination function and thereby to the fringe shape. This is performed by changing the cavity length via the temperature of a thermal element within the Zouk laser, what affects also the power and the intensity profile of the laser. The receiver is fiber-coupled, therefore the evaluation of the reference fringe is carried out in a fiber-coupled setup, as well. A free-beam setup (see Fig. 3.15) has the disadvantage that the laser-beam and therefore the illumination function on the interferometer fluctuates due to air-convection, even in the lab.

A fiber-coupled receiver entails a considerable étendue (angular distribution of  $\pm 16$  mrad to  $\pm 21$  mrad for a 600- $\mu\text{m}$ -core fiber, see eq. C.35) of the illumination incident on the Michelson interferometer. A collimated free-beam setup does not provide this angular distribution. Moreover, the imaging optics, needed because of fringe-localization (see section 3.4.4), and because of the need to shape the illumination in order to image it on the final photomultiplier tube array, may also affect the fringe shape.

A schematic setup used for fiber-coupled illumination of the interferometer with the cw-laser (1) or with a UV-LED (2) (see appendix F) is depicted in Fig. 3.17.

Setup for fiber-coupled illumination of the Michelson interferometer

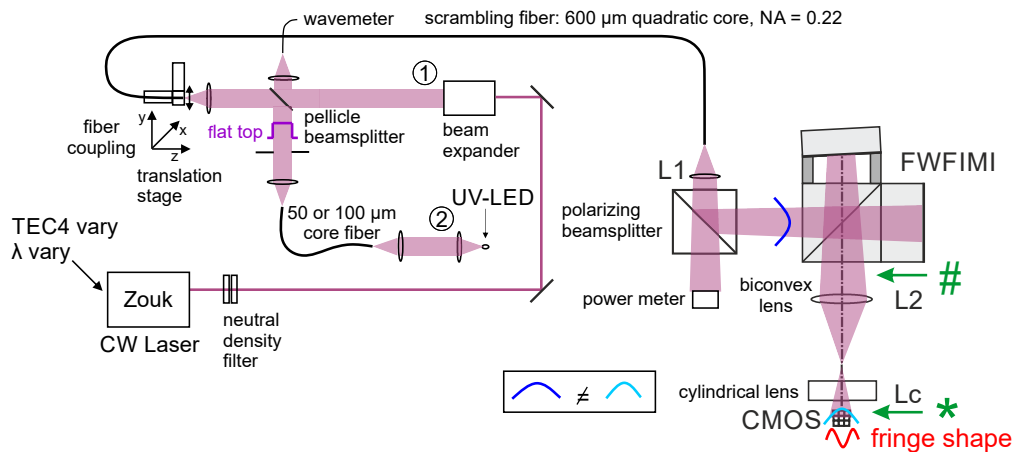


**Figure 3.17:** Schematic illumination of interferometer with a fiber-coupled cw laser (1) or LED (2).



The expanded laser beam (1) is coupled into a 600  $\mu\text{m}$  quadratic-core, multimode fiber (SQ WF 600x660/990/1400N (CeramOptec), see appendix F), and lens L1 is positioned such that the near-field of the fiber is imaged onto the plane of the CMOS camera sensor. Lens L2 images the plane of localization on the sensor plane. The cylindrical lens (Lc) compresses the illumination in vertical direction. Alternatively, the laser beam (1) may be blocked, and a UV-LED (2), which is expanded and guided through a small core fiber for beam-shaping, is again collimated and coupled into the same multimode fiber. Such a configuration may be used to determine the illumination function with the help of incoherent UV light, without producing an interference fringe. A further option for a fast determination of the illumination function would be an interferometer design allowing to block one of the mirrors of the interferometer during illumination with laser light. This is, however, not possible with the current monolithic design.

As the interferometer is illuminated with quasi-coherent laser light a fringe pattern appears, which depends also on the location of the sensor plane (see Fig. 3.18). In all the images a near-field imaging configuration is used.

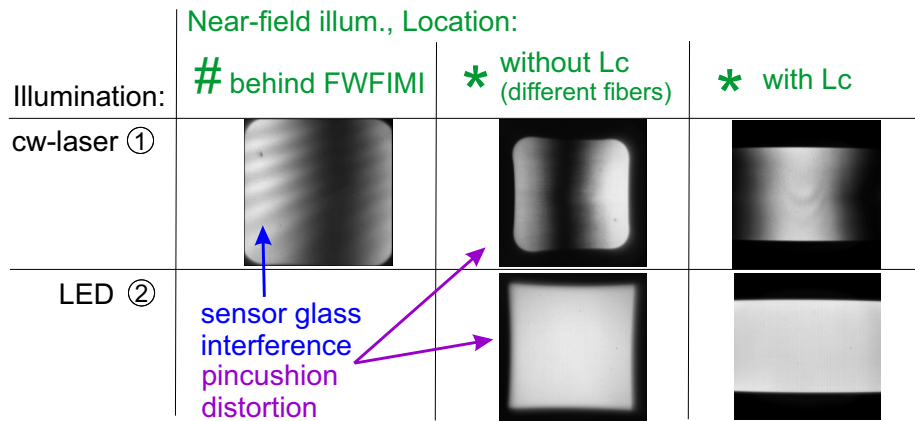


**Figure 3.18:** Exemplary CMOS images obtained with near-field illumination configuration with influence of the imaging lenses. CMOS sensor placed behind the FWFIMI in front of lens L2 (see Fig. 3.17, location marked by “#”), or behind the lens L2 at location “\*” with and without a cylindrical lens (Lc).

In Fig. 3.18 quadratic-core fibers are used. Therefore, the illumination aperture is quadratically shaped. Interferences visible as linear stripes or rings are superimposed, which are produced by interference with the CMOS sensor glass window without AR-coating. When the detection plane is positioned behind the biconvex lens (L2), pincushion distortion becomes visible for both laser and LED illumination. Pincushion distortion is a purely geometric defect, occurs in axis rotational systems, and means that the image magnification increases with the distance from the optical axis (see, e.g., *Gross et al. (2007)*). Raytracing simulations yield that the main aberrations in this setup are spherical aberration, coma, astigmatism, and distortion (see Fig. D.14 of appendix D.3), mainly due to the numerical aperture of the fiber and the physical extension of the multimode fiber core, providing a high étendue, and due to the biconvex lens L2.

To sum up, the fringe shape is affected by the net surface irregularity of the fabricated FWFIMI. The integrated fringe profile is no longer an ideal cosine function. Furthermore, the fringe shape may be affected by aberrations of the imaging optics between the FWFIMI and the detector. These aberrations may be corrected by a more complicated optics scheme.

This option is, however, avoided here in favor of a simple setup. The effects on the fringe shape are challenging to quantify experimentally, especially when the illumination function affecting the fringe shape, is not known.

The setup described in Fig. 3.17 is used in the following for the determination of instrumental contrast and free spectral range ( $FSR$ ) of the interference fringe. This characterization requires a determination of the illumination function for the correction of the fringe shape, because only after correction, a fit can be applied to determine the contrast and the shift in position of the fringe. At the same time, this study shows, that the fringe shape may change when the fringe position changes.

A wavemeter (WS-7, HighFinesse GmbH) and a powermeter are installed in order to monitor frequency changes of the cw-laser, when it is tuned by varying the laser cavity length (temperature), and to track the variations of laser power. The cw-laser is run in nominal constant power mode at 12 mW. Fig. 3.19(a) summarizes the raw data. The cavity temperature is increased linearly, inducing a frequency change of the cw-laser, measured with the wavemeter. For every frequency step a 2D image (similar to the configuration “\* with Lc” in Fig. 3.18 is recorded with the CMOS camera. Every thus recorded 2D fringe pattern is summed along the y-direction to obtain the uncorrected 1D fringe profile (see Fig. 3.19(b)).

It can be deduced from Fig. 3.19(a) that only within a certain temperature range the Michelson contrast is above 94%. Outside of this range the cw-laser runs multi-mode, what reduces the instrumental contrast. For single longitudinal mode operation the instrumental contrast is around 95% under the condition of fiber-coupled near-field illumination of the interferometer with an angular distribution of the incident light of  $\pm 21$  mrad (i.e., a flat-top similar distribution of incident angles:  $-[21, +21]$  mrad). This high contrast verifies the performance of the field-widening function detailed in section 3.4.1. The reduced instrumental contrast of the FWFIMI compared to the theoretical value of one at  $\rho_{max} = 21$  mrad (see Fig. C.15 in appendix C.6) may be due to non-ideal imaging of the localization plane.

Fits for the experimental verification of the free spectral range ( $FSR$ ) are therefore only performed in the regime where the instrumental contrast is above 94% (see Fig. 3.19(a)).

The illumination function (see Fig. 3.19(c)) is obtained by a determination of the fringe maximum for every temperature (wavelength) step (see envelope in Fig. 3.19(b)).

The corrected 1D fringes (see Fig. 3.19(d)) are calculated by dividing the uncorrected fringes by this illumination function. Downhill-Simplex (DSA) fitting (see appendix C.8) is performed in order to get the phase shift for every wavelength step. The fit model used here is of the form

$$F(x) = w_0 \cdot (1 + w_1 \cos(0.96x + \arcsin(w_4 \sin(w_5 - 0.96x)) - w_2)) + w_3, \quad (3.21)$$

where  $w_4$  and  $w_5$  are additional parameters for skewness and kurtosis of the fringe shape.

The phase parameter  $w_2$ , which is shown in Fig. 3.19(a) in black, is of primary interest, here. Both the phase and the frequency shift measured with the wavemeter are linearly interpolated and the free spectral range is determined as the frequency shift, where the phase shift is closest to  $2\pi$  (see green squares in Fig. 3.19(a)). In this case  $FSR$  is determined to be 10.809 GHz, deviating from the theoretical value by approximately 1%.

Furthermore, it appears from Fig. 3.19(d), that the deviations during the fitting can be in the order of 20%. These deviations change with the position of the fringe, what implies the fringe shape is changing as a function of absolute fringe position. There are several



possible reasons for this behavior. Firstly, the cw-laser profile changes slightly as a function of time and temperature. This could lead to a variation of the near-field of the fiber, which is imaged on the CMOS camera. Secondly, there are parasitic interferences produced by the imaging lenses together with the CMOS camera's sensor glass (see Fig. 3.17).

Both effects may produce a change of the illumination function during the scanning of the laser frequency. Consequently, the fringe shape is artificially altered after division by the illumination function (see Fig. 3.19(c), blue line).

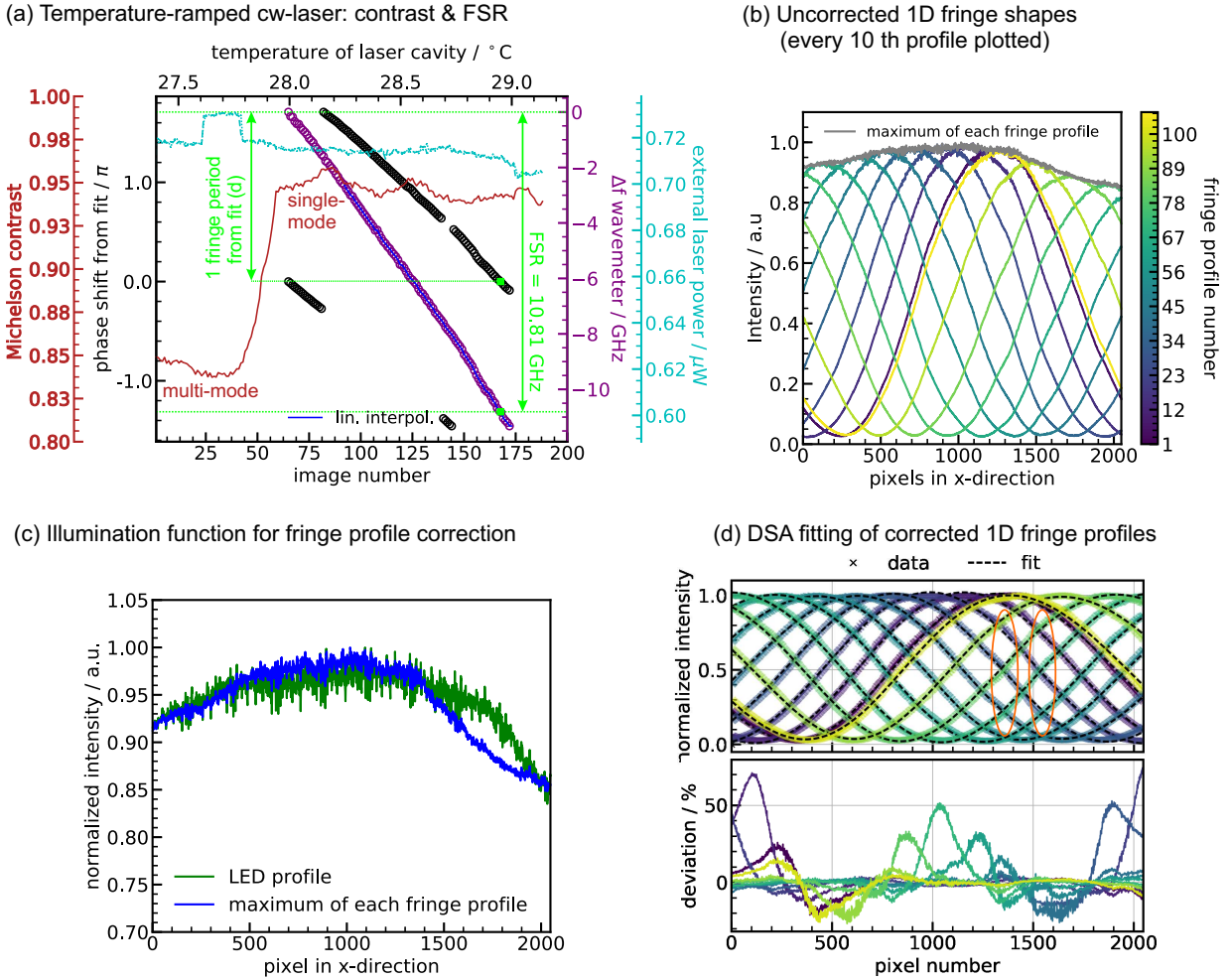


**Figure 3.19:** (a) Overview of temperature-ramped cw-laser: Contains Michelson contrast, phase shift extracted from fitting a cosine for every profile (shown in d), frequency shift measured with the wavemeter, and laser power measured externally with a power meter in a setup like shown in Fig. 3.17. (b) Raw 1D fringe profiles obtained by summing dark- and flat-field corrected CMOS frames along y-axis. (c) Illumination function used for correction of the fringe profiles (blue) and comparison with profile of a UV-LED (green). (d) Fitting of the corrected 1D fringe profiles with a fit model (see eq. 3.21) including fit parameters for skewness and kurtosis. For better readability only every 10th fitted fringe profile is shown.

The alternative for determining the illumination function by illumination with a UV-LED yields a profile shown in Fig. 3.19(c) (green line). The profile is clearly deviating from the profile produced by ramping the laser frequency. This is most likely due to the excitation of cladding modes or due to a different mean angle of incidence and spot sizes during coupling, and if the laser beam and the LED are not exactly co-linearly aligned.

Illuminating the interferometer with the LED in exactly the same way as with the laser

is difficult, as this would require the same angular and intensity distributions, as well as, precise co-alignment of both light sources. Furthermore the illumination function can be range-dependent. That is why, an LED based procedure could be used for the laser reference signal only. This emphasizes the challenge to illuminate the FWFIMI in the actual receiver setup.

From this experience, a procedure for determining the illumination function regularly during wind measurements (detailed in section 3.5.6) was developed and is therefore very similar to the frequency ramping described in this section. The major difference being the WALES/DELICAT transmitter (see section 3.6) and the assembled AEROLI receiver with a photomultiplier tube array as detector are used.

In this section the quasi-linear fringe of the manufactured FWFIMI has been characterized using a fiber-coupled illumination setup. The instrumental contrast is 95% for extended quasi-coherent light sources, i.e., for reference laser light from a UV cw-laser coupled into a 600  $\mu\text{m}$ -core fiber with its near-field being imaged on the FWFIMI. The free spectral range (FSR) was estimated by a quasi-linear frequency ramping of the cw-laser, obtaining an illumination function to correct the imaged fringe shapes. The estimated FSR deviates by 1% from the specified 10.7 GHz. The described experimental findings contributed to the implementation of a DWL receiver prototype.

The next section provides a detailed description of the receiver and of the AEROLI Doppler wind lidar setup built up in this work.

### 3.5.3 Receiver prototype and electronics

#### Receiver prototype

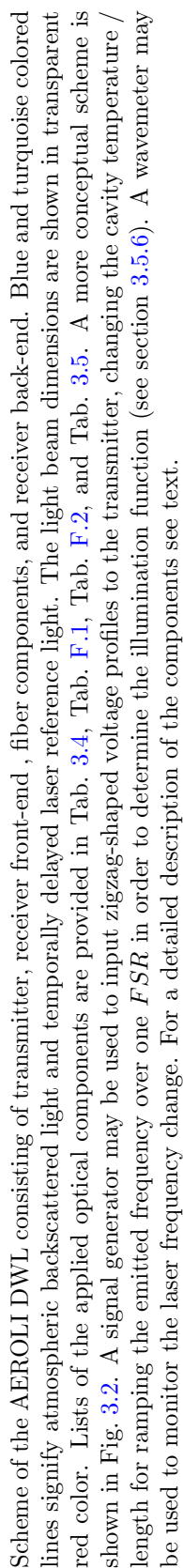
The DWL lidar and the receiver prototype consist of all of the components drawn schematically in Fig. 3.20.

The front-end part is a derivative of the DELICAT receiver (*Vrancken et al., 2016*), and contains a Newtonian telescope, the sunlight filter (IR), and lenses for collimation ( $L_{F1}$ ) and for coupling into multimode fibers ( $L_{F2}$ ).

Tab. 3.4 lists the optical components of the front-end part and important properties. A photograph of the front-end part of the receiver is shown in Fig. 3.21. A raytracing model of the front-end part is described in appendix D.1.

**Table 3.4: Optical components of the receiver front-end and properties.**

Component	Name	Properties
Newton telescope	DELICAT telescope	(see appendix F)
Lens $L_{F1}$	SPX017	$d = 25.4 \text{ mm}$ , EFL = 62.9 mm
Mirror $M_1$		
sunlight filter IF	Materion F-NB-0012489	FWHM of $0.5 \pm 0.1 \text{ nm}$
PBSC	PBSO-355-100	$d = 25.4 \text{ mm}$ , $Tp/Ts=500:1$
Lens $L_{F2}$	SPX014	$d = 25.4 \text{ mm}$ , EFL = 33 mm



Scheme of the AEROLI DWL consisting of transmitter, receiver front-end, fiber components, and receiver back-end. Blue and turquoise colored lines signify atmospheric backscattered light and temporally delayed laser reference light. The light beam dimensions are shown in transparent colored color. Lists of the applied optical components are provided in Tab. 3.4, Tab. F.1, Tab. F.2, and Tab. 3.5. A more conceptual scheme is shown in Fig. 3.2. A signal generator may be used to input zigzag-shaped voltage profiles to the transmitter, changing the cavity temperature / length for ramping the emitted frequency over one  $FSR$  in order to determine the illumination function (see section 3.5.6). A wavemeter may be used to monitor the laser frequency change. For a detailed description of the components see text.

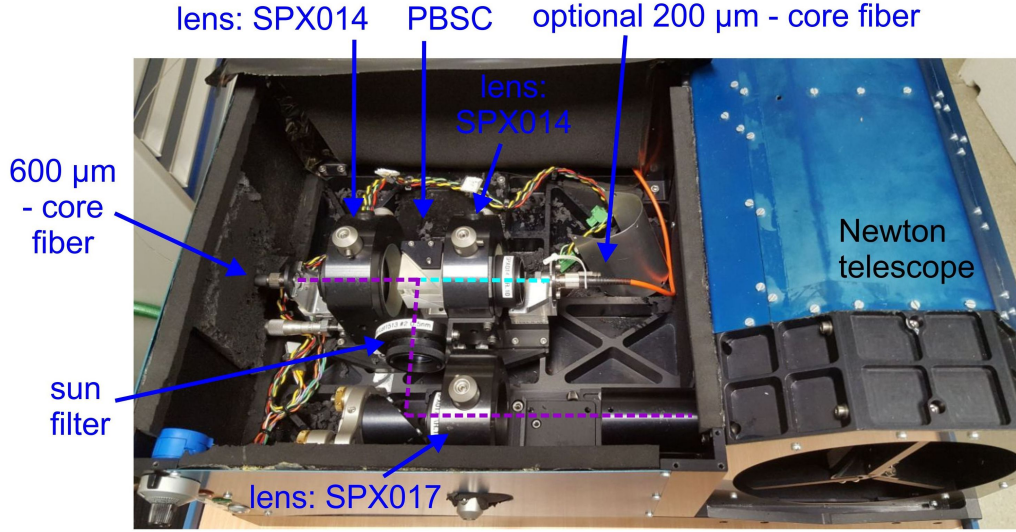


**Figure 3.21:** Front-end part of the receiver making use of the Newtonian telescope of DELICAT (Vrancken *et al.*, 2016). Turquoise: optional free-beam combination with reference light from a 200  $\mu\text{m}$ -core fiber.

Fiber components link the receiver front-end and the receiver back-end (see Fig. 3.20). The fibers and their properties are listed in appendix F (Tab. F.1 and Tab. F.2). Fiber S1 is applied to guide the atmospheric backscattered light to the high transmission port of the 3:1 fiber coupler. Other fibers ( $R_1$ ,  $R_1$ , and  $R_2$ ) connected by fiber couplers provide a time delay of laser reference light. This reference light is connected with one of the low transmission ports of the 3:1 fiber coupler. Both the atmospheric backscattered light and the reference light are guided through fiber  $S_F$ . The fiber  $S_F$  is applied for optical scrambling (see section 3.5.5), i.e., for the dampening of the influence of spatial characteristics of the input beam on the intensity distribution of the output cone of light of a fiber (Hunter and Ramsey, 1992) in order to decrease laser beam pointing biases (see section 4.3). Fiber  $S_F$  is a 600  $\mu\text{m}$  quadratic-core, multimode fiber. The fiber is vibrated for fiber speckle reduction using a vibration motor (VB), as this provides increased homogeneity of the illumination through increased diversity (see section 3.5.4).

The back-end part of the receiver consists of a lens  $L_1$  and another polarizing beam splitter (PBSC) to illuminate the FWFIMI with s-polarized light. The p-polarized part of the light is imaged on the DELICAT PMT, using lens  $L_3$ , for power measurements. The FWFIMI is fixed with an invar cage (see photograph of Fig. 3.16) inside a housing (with windows  $W_1$  and  $W_2$ ) for temperature stabilization at 40 °C. Pt-100 resistance thermometers are applied for feedback and for monitoring the temperature inside the housing. More details on the temperature stabilization are provided in section 3.4.2.

The windows  $W_1$  and  $W_2$  are tilted around the x-axis (see Fig. 3.20) by  $+1^\circ$  and  $-1^\circ$ , respectively, to decrease multiple interferences. A bi-convex lens  $L_2$  and a cylindrical lens ( $L_c$ ) are used for imaging the linear interference fringes of the atmospheric signal and of the reference signal onto the detector, i.e., the photomultiplier tube assembly / array (PMTA) (see appendix F). The back-end optics were selected based on raytracing designs. The respective raytracing models are described in appendix D.3.

The interferometer can be illuminated either with the far-field or the near-field of the optical scrambling fiber. In the far-field configuration the light is quasi-collimated, but still has an angular distribution of  $> \pm 1^\circ$ , due to the 600  $\mu\text{m}$  core of the scrambling fiber  $S_F$ .

The same is true for the near-field configuration, but the fiber core itself (end face of the fiber) is imaged onto the localization plane of the interferometer, which is again imaged onto the detector plane. Fig. 3.22 shows these two options, where each color is the light rays from a different location on the fiber core. In this work the near-field illumination configuration is chosen without the second additional cylindrical lens shown in Fig. 3.22.

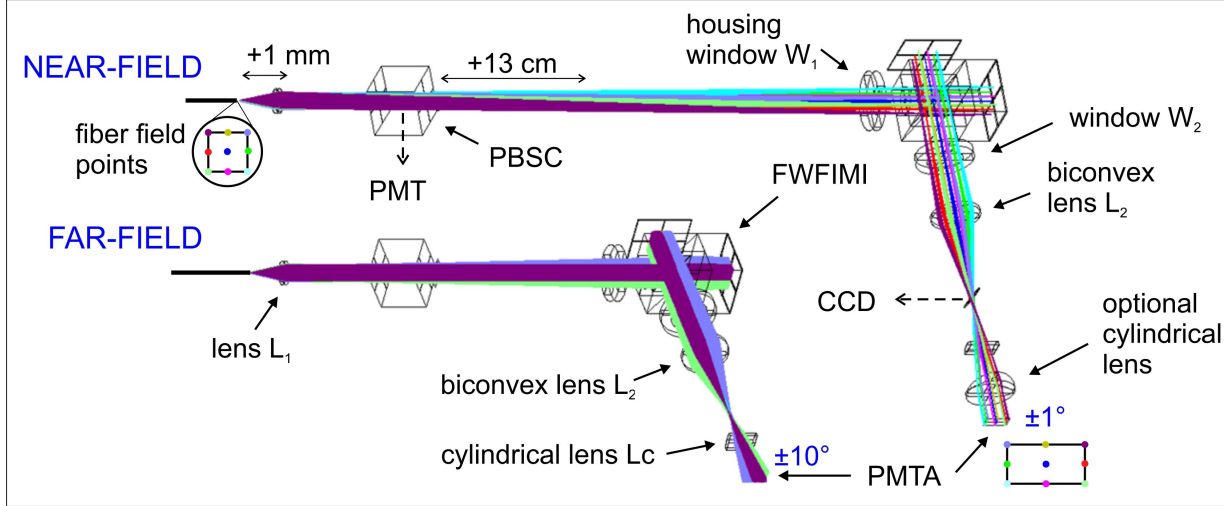


**Figure 3.22:** Zemax sequential raytracing models of alternative illuminations of the PMT array. (a) Far-field illumination of the PMT array with an angular distribution of  $\pm 10^\circ$  at the detector plane. (b) Near-field illumination with an additional cylindrical lens to decrease the angular distribution on the detector to  $\pm 1^\circ$ . The raytracing model is described in appendix D.3.

Tab. 3.5 lists the optical components of the back-end part and important properties. All optics, the FWFIMI, and the detector are fixed on a breadboard using a commercial cage system.

**Table 3.5: Optical and electronic components of the back-end receiver and properties.**

Component	Name	Properties
Lens $L_1$	A12-20FPX	$D = 12.5$ mm, EFL = 20 mm
PBSC	PBSO-355-100	$D = 25.4$ mm, $Tp/Ts=500:1$
Lens $L_3$	A12-20FPX	$D = 12.5$ mm, EFL = 20 mm
Windows $W_1, W_2$	FSW17AR.10	$D = 40$ mm, $d = 4$ mm, $\lambda/10$ , AR.10
Interferometer	FWFIMI	(see sections 3.4, 3.5.1, and appendix E)
Biconvex lens $L_2$	LB4096-UV	$D = 25.4$ mm, EFL = 50 mm
Cylindrical lens $L_c$	LJ4796-UV	$H = 10$ mm, $L = 15$ mm, $f = 25$ mm
PMTA	H7260-200	(see appendix F, <a href="#">Hamamatsu (2011)</a> )
Amplifier	TIA	(see 3.5.3, appendix F)
Digitizer boards	M2i4932-exp	(see appendix F, <a href="#">Spectrum (2015)</a> )

A photograph of the final back-end receiver is shown in Fig. 3.23. Fig. 3.24 provides a photograph, showing the assembled DWL transmitter and receiver. The DELICAT laser transmitter ([Vrancken et al., 2016](#)) being applied in the AEROLI DWL is described in section 3.6.



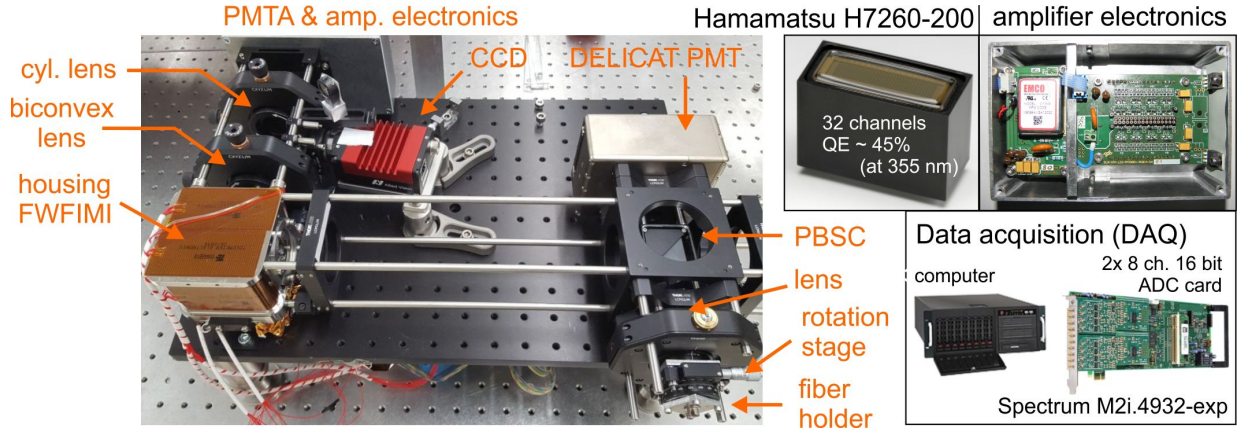


**Figure 3.23:** Photograph of the receiver back-end with photographs of the photomultiplier tube array, the amplifier electronics, and the data acquisition PC with two ADC cards installed.

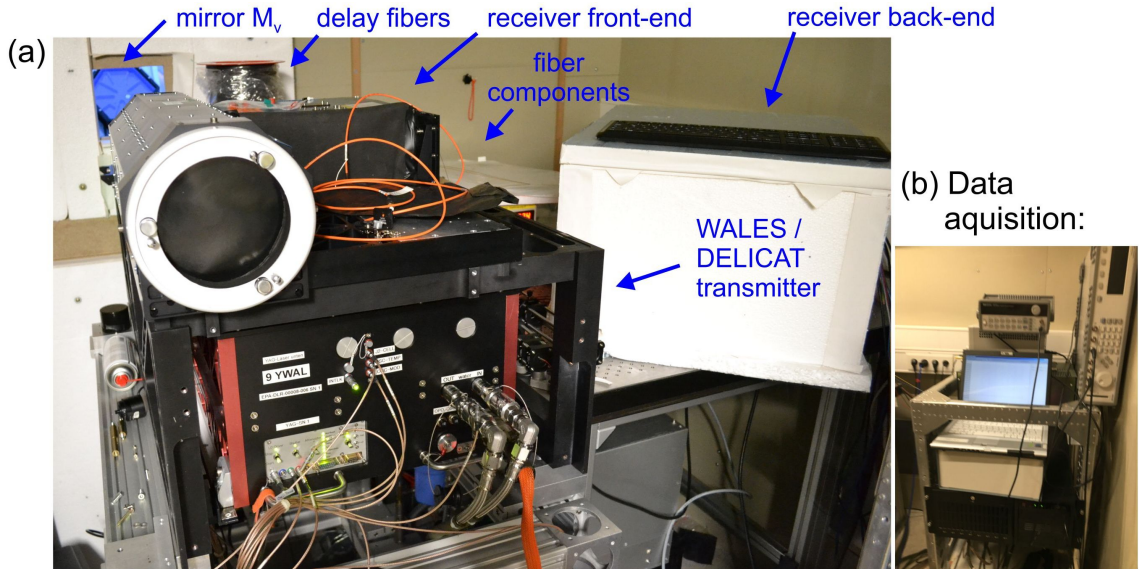


**Figure 3.24:** Photograph of assembled DWL transmitter (see section 3.6) and receiver with mirror  $M_V$  for vertical measurements (see chapter 5).

The decision was made to use the near-field illumination configuration as this would possibly allow higher optical scrambling, a quadratic flat-top light distribution, simplifying imaging and alignment, and because the required larger distance between the polarizing beam splitter cube (PBSC) and the interferometer facilitates adding a second detection arm in back-reflection (see appendix D.3) in future evolutions of the system. The configuration was realized without the additional lens for the reduction of the horizontal angular distribution (see Fig. 3.22(b)) in order to keep the setup as simple as possible. It was realized that the angular distribution, which would give rise to a varying response per channel of the PMTA (due to different angular responses of the detector elements, see appendix F), may be neglected, since it is contained in the illumination function (see section 3.5.6).

The photomultiplier tube array (PMTA) “H7260-200” by Hamamatsu, Japan (see appendix F) consists of 32 channels. The central 16 channels are connected to amplifier circuits. The remaining channels may be used for the tilted configuration (see appendix D.3) in the future.

## Electronics

This subsection describes how the amplifier electronics design influences the temporal shape of the detected signal and how its components can be tuned to yield optimum noise and bandwidth behaviour.

Each element (pixel) of the PMTA when illuminated produces a current, which has to be converted to a voltage and has to be amplified. A transimpedance amplifier (TIA) is used, that yields a very high-frequency response and therefore rise times in the order of one nanosecond (*Kovalev and Eichinger, 2005*). A simple TIA circuit using a photodiode as current source, an operational amplifier, a feedback resistor ( $R_L$ ), and a feedback capacitor ( $C_L$ ), is shown in Fig. 3.25(a).

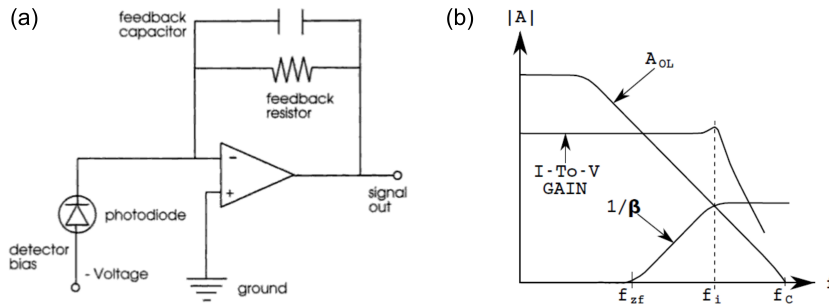


**Figure 3.25:** (a) Simplified transimpedance amplifier (TIA) circuit for a photodiode using an operational amplifier, a feedback resistor and a feedback capacitor. (b) Bode diagram showing I-to-V gain, open loop gain  $A_{OL}$  (see appendix C.7), and noise gain  $1/\beta$  (*Graeme, 1995*).

This circuit acts as a low-pass filter as depicted in the Bode plot of Fig. 3.25(b) (*Graeme, 1995*). Here the logarithmic gain is plotted over the logarithmic frequency. At low frequencies, the TIA acts like an ideal amplifier, where current is converted to voltage with  $U_a = -R_L \cdot I$  and the gain is given by the load resistance  $R_L$ .  $R_L$  is chosen in our case to be 2.21 k $\Omega$  (cf. real circuits, appendix F) in order to achieve maximum voltages of 1 V for realistic atmospheric photocurrents and a gain of  $3 \cdot 10^4$  to  $6 \cdot 10^6$  of the photomultiplier tubes (depending on the supply voltage of 500 V to 900 V) (*Hamamatsu, 2011*). The maximum electric currents after the PMT gain and before amplification are in the order of  $\approx 0.5$  mA per channel. The average anode current per channel should not exceed 6  $\mu$ A over an interval of 30 s (*Hamamatsu, 2011*), that is, the continuous (DC) voltage should not be above  $\approx 13.3$  mV. The feedback capacitance ( $C_L$ ) can be tuned to compensate for oscillations and ringing. The above Bode plot shows an ideally compensated case with a minimized gain spike at frequency  $f_i$ , where  $\beta$  is the inverse noise gain, and  $A_{OL}$  is the open loop gain of the operational amplifier (OPA4820 by Texas Instruments (*TI, 2008*), see  $A_0$  in eq. C.73). A higher value of  $C_L$  increases compensation but reduces the bandwidth of the amplifier. The desired bandwidth (of -3 dB) in our case is 1.55 MHz, provided that the maximum sampling rate of the digitizer (AD-converter) is 31.25 MHz (*Spectrum, 2015*), and that a laser pulse of 8 ns FWHM should be sampled with at least 3 to 5 sampling points over the FWHM. As may be shown through calculations the optimum value of  $C_L$  is then 47 pF (see circuit in Fig. F.4 of appendix F). For details on the compensation calculations the reader is referred to appendix C.7 and specialist literature (*Graeme, 1995*; *Tietze et al., 1991*). The impulse or pulse response  $h(t)$  of a delta-shaped input signal  $i(t)$ , i.e., the current of the PMT when illuminated with a short pulse, determines the output signal by  $o(t) = i(t) * h(t)$  in the temporal domain (where  $*$  means convolution).  $h(t)$  is



the inverse Fourier transform of the frequency response  $H(\omega)$  or transfer function of the amplifier, such that  $O(\omega) = I(\omega) \cdot H(\omega)$ .  $H(\omega)$  can be simulated with a simplified transimpedance amplifier model (see appendix C.7). The absolute value of the resulting  $H(\omega)$  in terms of frequency-dependent gain is called transimpedance function and is shown in Fig. 3.26(a).

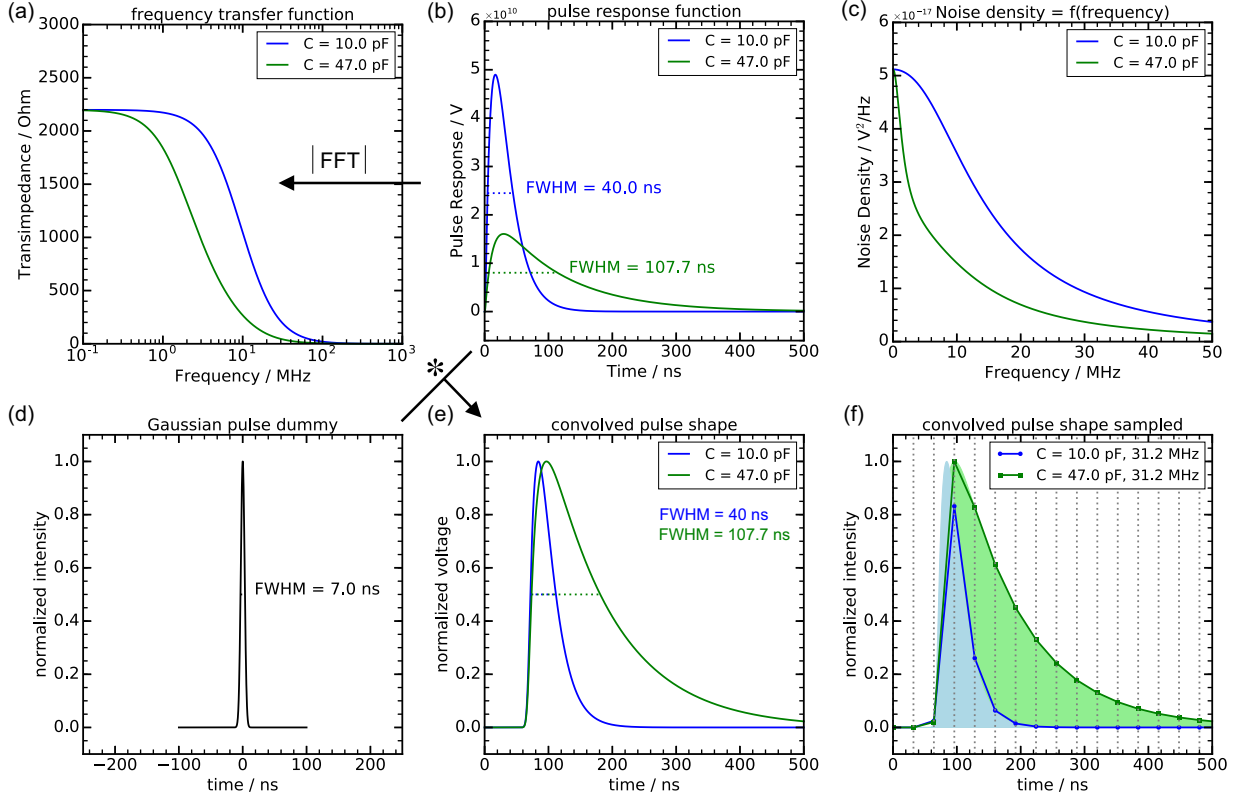


**Figure 3.26:** (a) Transimpedance function derived from frequency transfer function, (b) pulse response function, which is the Fourier transform of the frequency response, and (c) noise density for the TIA circuit using modeling assumptions (see appendix C.7) for  $C_L = 10$  pF and  $C_L = 47$  pF. (d) Reference pulse with Gaussian shape and given FWHM. (e) Convolved pulse shape obtained by a convolution of pulse response function and reference pulse. (f) Convolved pulse shapes sampled by AD-converter with a sampling rate of 31.25 MHz.

The simulated pulse response function is given in Fig. 3.26(b). Fig. 3.26(c) shows the noise density as a measure of the noise suppression due to different applied feedback capacitances (see appendix C.7). A Gaussian reference pulse dummy with FWHM of 8 ns (Fig. 3.26(d)) can be convolved with the pulse response function (b) to obtain the convolved pulse shape (Fig. 3.26(e)), which is sampled by the AD-converter with a sampling rate of 31.25 MHz (Fig. 3.26(f)).

The influence of the choice of  $C_L$  (determining the bandwidth of the frequency transfer function of the TIA circuit) on the sampling of a series of 8 ns long reference laser pulses recorded in the lab for both  $C_L = 10$  pF (a) and  $C_L = 47$  pF (b) is shown in Fig. 3.27. In case of  $C_L = 10$  pF the sampling rate is too low to adequately sample the pulse, what is apparent from the varying amplitude of the recorded voltages in Fig. 3.27(a). This variation is induced by the laser pulse timing jitter of the master oscillator, power amplifier (MOPA) transmitter (see section 3.6), which is not fully compensated by triggering the acquisition to each pulse signal. A smaller bandwidth of the frequency transfer function spreads the

signal in time allowing to sample the pulse without aliasing in case of  $C_L = 47$  pF, using the same sampling time of  $T_s = 32$  ns (see Fig. 3.27(b)).

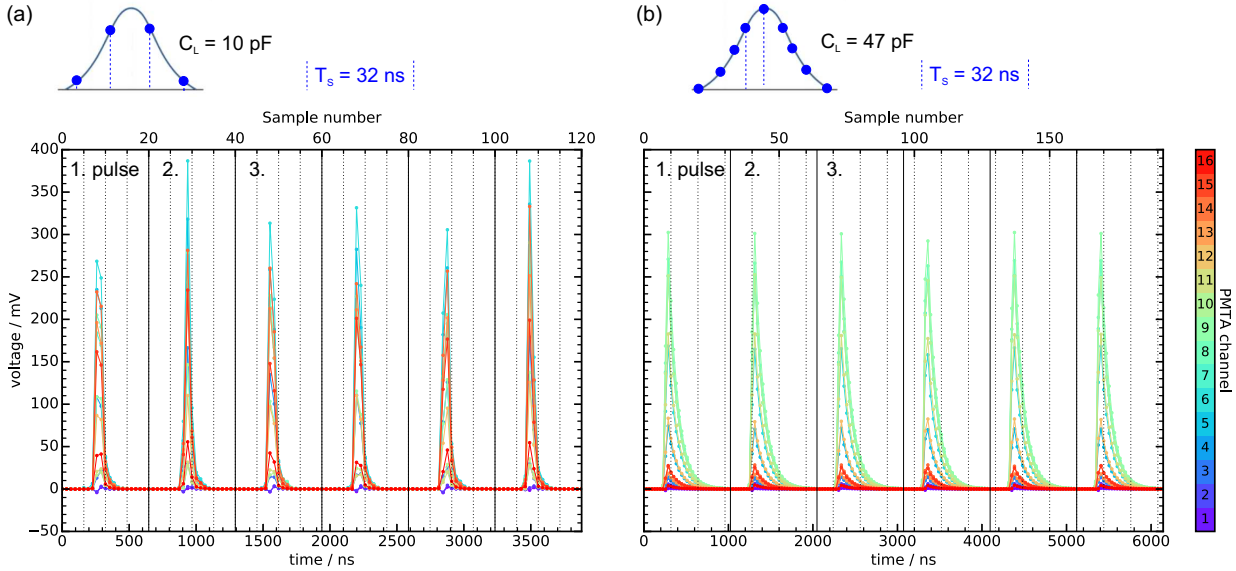


**Figure 3.27:** Recorded voltages as a function of time for two different capacitances  $C_L$  of the TIA circuit for a 8 ns long reference pulse using a sampling rate of 31.25 MHz. For  $C_L = 10$  pF the sampling rate is too low to adequately sample the pulse (left). Aliasing is suppressed by reducing the bandwidth of the TIA with  $C_L = 47$  pF (right). Color encoded are different channels of the PMT-array.

The TIA circuit introduces a voltage offset for zero signal, which is due to the operational amplifiers of each channel. This voltage offset varies from channel to channel, due to the individual circuit response of each channel's circuit (see Fig. 5.5) in section 5.2. This voltage offset has already been subtracted in Fig. 3.27.

The time-dependent voltages of the 16 center PMTA channels are converted to digital numbers using two analog-to-digital converter (ADC) boards. The 16 bit A/D board “Spectrum M2i.4932-exp” provides 8 channels with a maximum sampling rate of 30 MS/s (31.25 MHz), a bandwidth (-3 dB) > 30 MHz, and an effective number of bits (ENOB) based on the SNR of > 12.1 LSB (least significant bit). Both boards are synchronized using a Spectrum starhub ([Spectrum, 2015](#)). The input range is programmed to  $\pm 0.5$  V with a 100% input offset, obtaining a voltage range of 0 V to 1 V.

This section introduced the developed and built receiver prototype consisting of front-end, fiber components, back-end, and electronics. Amplifier electronics have been described with special focus on the anti-aliasing compensation of the transimpedance amplifier circuit using a higher feedback capacitance than originally intended.

The next sections are dedicated to the experimental characterization of scrambling fibers ( $S_F$ , fiber components in Fig. 3.20) (sections 3.5.4 and 3.5.5) and to the characterization of the receiver back-end illumination function (see section 3.5.6) and the temperature tuning of the FWFIMI (see section 3.4.2).

### 3.5.4 Fiber induced speckle / modal noise

The goal of this subsection is to characterize the fiber induced speckle of multimode fibers for applying them as fiber  $S_F$  in the fiber components part of the AEROLI DWL lidar (see Fig. 3.20).

Atmospheric speckle (see appendix C.1) are not the only source of noise induced by the temporal coherence of the laser light. Both the already speckled atmospheric signal and the laser reference signal, when coupled into a multimode fiber, produce thousands of propagating modes traveling with different phase velocities and phase delays due to different routes of propagation. All these individual field contributions interfere and give rise to another type of speckle, modulating the illumination function (see, e.g., [Goodman \(2007\)](#)). Its statistics depend on parameters like core diameter ([Imai, 1986](#)), fiber length ([Rawson and Goodman, 1980](#)), polarization, coupling to cladding modes ([Tremblay et al., 1981](#)), and the number of excited modes (depending on the coupling conditions, e.g., [Corbett et al. \(2007\)](#)). This speckle pattern may fluctuate due to laser frequency variations, temperature changes, and movements of the fiber, giving rise to so called “modal noise” (termed by [Epworth \(1978\)](#)), being influenced by an additional spatial filtering process. In our case the Michelson interferometer and the linear detector (truncation and summation by detector pixels) act as spatial filters.

Modal noise SNR has been modeled by [Goodman and Rawson \(1981\)](#) for a large set continuous wave (CW) modes. It is given by  $SNR = \rho\sqrt{(M+1)/(1-\rho^2)}$ , where  $\rho^2$  is the truncation (ratio of detector area  $A_d$  to fiber core end face area  $A_f$ ) and  $M$  is the number of propagating modes. The statistics of the intensity on a detector pixel  $k$  is described by a beta law, which resembles a gamma law with parameter  $M_k$  for  $\rho^2 \ll 1$  (see section C.1, eq. C.4).  $M_k$  is the number of speckle grains integrated by pixel  $k$ .

The values of parameter  $M_k$ , i.e.,  $SNR_k$  of detector pixel  $k$  in our case of a pulsed UV source cannot be calculated analytically, but have to be measured for different degrees of spatial averaging (within  $A_d$ ) and temporal averaging (for example by vibration and summation over single pulse frames, i.e., scrambling of the modal noise), in order to estimate the noise on the illumination function caused by the multimode fiber. This is done in the following for the multimode fiber used in our receiver (SQ, Ceramoptec, square core, 600  $\mu\text{m}$ , length = 10 m, NA = 0.22, see Tab. F.1) using the following relations ([C  zard, 2008](#)):

The energetic weight on a certain pixel is given by  $X_k = I_k / (\sum_{k=1}^{I_{pix}} I_k) = I_k / I_{tot}$  with  $I_k$  being the intensity on pixel  $k$ , and  $I_{tot}$  being the total intensity of all pixels, correcting for pulse-to-pulse energy variations of the laser. Detector noise is neglected here. A variable  $Y_k = X_k / \langle X_k \rangle$  then obeys a gamma law of mean 1 and variance  $1/M_k$  (see also eq. C.4 in appendix C.1). That is the speckle SNR being the inverse of the speckle contrast of pixel  $k$  is given by

$$SNR_k = \frac{1}{C_k} = \sqrt{M_k} = \frac{1}{\sqrt{\text{var}(Y_k)}} \quad (\text{method 1}). \quad (3.22)$$

This method requires a large number of images taken in a row in order to get a reliable statistic. In case of temporal averaging (scrambling of the modal noise) an alternative approach is to consider the speckle SNR within a certain region-of-interest (ROI) of an averaged speckle frame. The speckle pattern within this ROI (statistic over several pixels  $k$  of the camera) obeys again a gamma distribution (variation not in time, but in space).

The speckle SNR is again given by

$$SNR_{ROI} = \frac{1}{C_{ROI}} = \sqrt{M_{k_{ROI}}} = \frac{1}{\sqrt{\text{var}(Y_{k_{ROI}})}} \quad (\text{method 2}). \quad (3.23)$$

Methods of temporal scrambling of speckle noise ([Goodman, 2007](#)) are not new. Piezo-electric transducers have been used for instance to vibrate a fiber and thereby to reduce the speckle contrast (see, e.g., [Ha et al. \(2009\)](#)).

The experimental scheme for measuring fiber speckle and modal noise, using method 2, including temporal scrambling, is shown in Fig. 3.28.

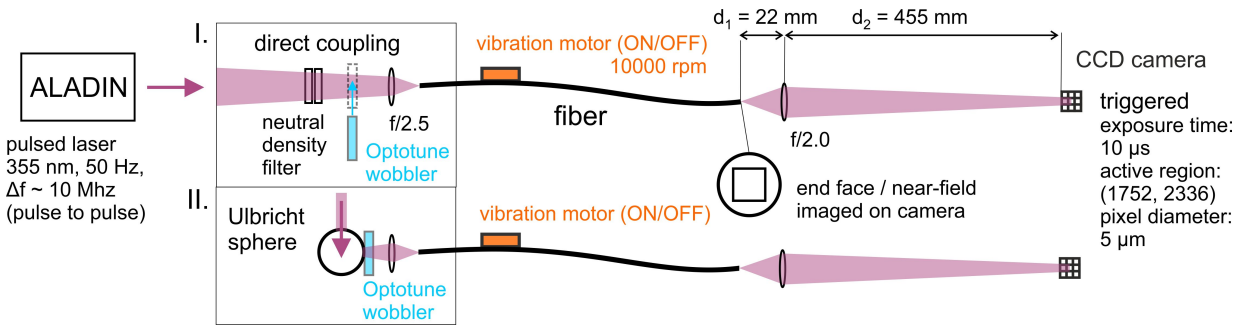


**Figure 3.28:** Measurement setup for fiber speckle and modal noise scrambling characterization.

The setup consists of the pulsed UV laser of A2D with a repetition rate of 50 Hz ([Lemmerz et al., 2017](#)). The pulses are coupled into the multimode fiber either in direct mode (Fig. 3.28, I.) with an optional Optotune wobbler (“LSR-C-4C-L”, ([Stadler et al., 2015](#))), or via an Ulbricht sphere (Fig. 3.28, II.). Using an integrating sphere is highly inefficient and, therefore, only an option for the laser reference signal. Another option with a high transmission efficiency, that could be used with the backscattered atmospheric signal, is to vibrate the fiber using an unbalanced vibration motor (10000 rpm). The speckle on the end face of the fiber are imaged onto a CCD camera (Allied Vision, C2, see appendix F) at a distance  $d = d_1 + d_2$  from the fiber, in order to obtain a magnified image of the near-field of the fiber for resolving individual speckle grains. The CCD camera runs on triggered mode with an exposure time of 10  $\mu$ s to ensure that each speckle pattern can be attributed to a single pulse.

In the following, the results of speckle SNR measurements using direct coupling without a wobbler with optional vibration of the multimode fiber (SQ, see scrambling fiber in Tab. F.1, or fiber A in appendix F.) are presented. Corresponding measurement results with the wobbler or with the Ulbricht sphere and for different multimode fibers are described in appendix G.

Method 2 (described above) is used to quantify the modal noise scrambling behavior. Fig. 3.29 contains the resulting speckle  $SNR_{ROI}$  without (a) and with vibration (b) for different regions-of-interest ( $ROI_1$ :  $100 \times 100$  pixels,  $ROI_2$ :  $400 \times 400$  pixels,  $ROI_3$ :  $1160 \times 1760$  pixels of the CCD) and different types of spatial averaging (different colors: none, line image, hypothetical 12 pixel detector) as a function of the number of averaged pulses.

The averaged frames are dark frame corrected and flat-field corrected prior to the speckle SNR determination. Increased speckle SNR without temporal averaging (single pulse) and without spatial averaging (see Fig. 3.29(a), blue lines) can be explained with mode mixing along the length of the fiber ([Goodman, 2007](#)).

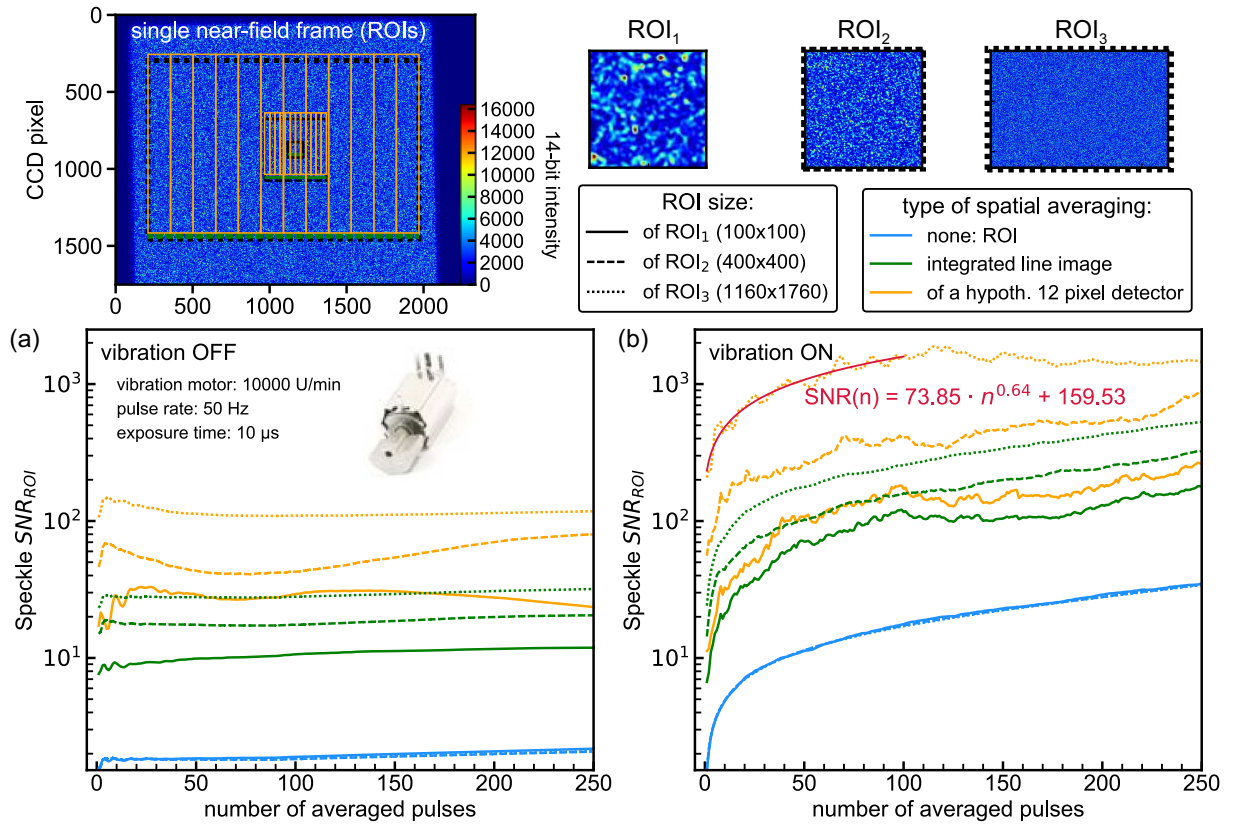


**Figure 3.29:** Speckle  $SNR_{ROI}$  as a function of the number of temporally averaged pulses  $n$  (determined with method 2) without (a) and with fiber vibration (b) using a vibration motor (photograph shown in inset) for different types of ROI (line styles: solid =  $100 \times 100$  pixel (ROI<sub>1</sub>), dashed =  $400 \times 400$  pixel (ROI<sub>2</sub>), and dotted =  $1160 \times 1750$  pixel (ROI<sub>3</sub>)) and spatial averaging (colors: blue = no spatial averaging, green: integration along vertical direction, and orange: hypothetical 12 pixel detector). Example: The orange dotted line provides the speckle SNR of a hypothetical 12 pixel detector on ROI<sub>3</sub>. A fit shows the dependence of the SNR on  $n$  (red line). Insets show a single near-field image on the CCD camera, and the location of the ROIs.

The blue lines in Fig. 3.29 show that without spatial averaging the size of the ROI (different line styles) has no effect on the determined value of  $SNR_{ROI}$ . Temporal averaging provides increased values of  $SNR_{ROI}$  (see Fig. 3.29(b)). The effect of spatial averaging is seen by the elevated values of  $SNR_{ROI}$  when the ROI pixel intensities are summed along the vertical direction (green color in Fig. 3.29) or when a hypothetical 12 pixel detector (its pixels being shown by orange rectangles) is assumed on the ROI area. The most realistic situation compared to the actual receiver is the combination ROI<sub>3</sub>–hypothetical 12 pixel detector (orange dotted line). In this case without temporal averaging ( $n = 1$  in Fig. 3.29(a)) the  $SNR_{ROI}$  is above 100.

When the fiber is vibrated  $SNR_{ROI}$  increases with  $n^{0.64}$  (as indicated by the red fitting curve in Fig. 3.29(b)). Temporal averaging by pulse summation increases the SNR to  $>500$  for 20 pulses.

Without vibration (Fig. 3.29(a)) temporal averaging of the speckle is far less effective and  $SNR_{ROI}$  as a function of the number of averaged pulses ( $n$ ) is almost constant. This is because the frequency stability of the laser ( $\approx 10$  MHz pulse-to-pulse) is too high for the speckle patterns to change significantly during an image run of 250 images at a repetition



rate of 50 Hz.

The reason for the high SNR achieved by spatial averaging lies in the small size of the speckle grains (see, e.g., Fig. 3.29, image of  $ROI_1$ ). The average grain size can be determined via autocorrelation of a single speckle frame ( $ROI_1$ ), e.g., along the vertical direction (see Fig. G.2(b) in appendix G). For each column of the frame an autocorrelation function is calculated and the mean of all columns is determined (one realization highlighted in blue). The mean speckle size is  $\approx 1.3 \mu\text{m}$ .

Further effects not estimated here are: 1. an already speckled input (see atmospheric speckle), 2. central obscuration for atmospheric light, and 3. the effect of the delay fiber (length: 320 m), which could increase the speckle SNR due to mode mixing in case of laser reference light ().

A comparison of the speckle characteristics of different core-shapes and diameters of multimode fibers is provided in appendix G. Circular-core fibers show a lower speckle SNR than quadratic-core fibers at the same number of averaged pulses. A possible explanation is the more static and highly correlated movement of speckle in circular fibers as explained by *Stürmer et al.* (2016).

In conclusion, the ratio of speckle grain size to the full detector size ( $1/R_f$ ) is roughly  $1/470$  for fiber SQ (fiber A, see appendix F), and roughly 18000 speckle grains are spatially averaged by one pixel of a linear detector with 12 pixels (summation in x- and y-direction as indicated by the orange rectangles in Fig. 3.29), what corresponds to a speckle SNR  $> 100$  (i.e., a speckle contrast  $C < 1\%$ ). Temporal averaging over varying speckle patterns (produced with fiber vibration) allows to improve these values, whereby the SNR increases with roughly  $n^{0.64}$ .

As follows from these findings, the studied fiber (SQ, fiberA see appendix F) provides a way to suppress atmospheric speckle noise (see appendix C.1), because the ratio of the fiber core diameter (or detector size) to the speckle grain size induced by the (600- $\mu\text{m}$ -core) fiber ( $R_f$ ) is much higher than for atmospheric speckle ( $R_f = 140 \text{ mm} / 2.3 \text{ mm} \approx 61$ , see Fig. C.2(a) in appendix C.1) and also higher compared to multimode fibers with smaller core sizes (e.g.,  $R_f \approx 156$  for a 200- $\mu\text{m}$ -core fiber, see Tab. G.1 in appendix G).

The quantitative influence of this speckle noise on the wind speed measurement accuracy is estimated using end-to-end simulations in sections 4.1, 4.2, and 4.6.

The next section describes scrambling gain measurements of the scrambling fiber ( $S_F$  in the fiber components part of the AEROLI DWL lidar, see Fig. 3.20).



### 3.5.5 Scrambling gain measurements of various fibers

Scrambling gain measurements provide information on the degree of removal of the spatial information of light coupled into a fiber due to mode-mixing during propagation within the multimode fiber (see, e.g., [Hunter and Ramsey \(1992\)](#)).

The so-called near-field scrambling gain ( $SG$ ) is defined as the ratio of the lateral shift  $\Delta x$  of the light spot on the fiber core (diameter  $D$ ) to the displacement  $\Delta S$  of the illumination function (with FWHM:  $F$ ) on the detector (see Fig. 3.30(b), definition by [Avila and Singh \(2008\)](#)).  $SG$  can be used as a figure-of-merit for the stability of the illumination function against laser beam pointing fluctuations (see appendix I).

The destruction of the spatial information is important for suppressing the influence of laser beam pointing fluctuations (see appendix I) on the accuracy of the wind speed measurements performed with the AEROLI DWL receiver (see section 3.5.3). Possible effects of laser beam pointing fluctuations on this accuracy are estimated in section 4.3.

The intention of this section is, therefore, to estimate and compare the optical scrambling properties of multimode fibers to be used (as  $S_F$ ) in the fiber components part of the AEROLI DWL (see Fig. 3.20).

Relatively large core multimode fibers (600  $\mu\text{m}$  core diameter) are studied, because these provide a large étendue, and therefore provide full overlap already close to the receiver (50 m up to distances of several hundred meters, see appendix D.1). These studies have to include the range-dependent spot sizes of the received light during coupling into the fibers (caused by the shift of the telescope focal spot position, see appendix D.1), because high optical scrambling should be obtained for all measurement ranges of the DWL. The results presented here were obtained in a Master thesis by [Unsinn \(2016\)](#).

A scheme of the test setup used in this work is shown in Fig. 3.30(a). The test setup consists of a UV-light source, i.e., cw-laser Zouk (1) or a UV-LED (2) (see appendix F), which are expanded and focused with an NA close to the  $NA = 0.22$  of the studied multimode fibers, having various core diameters, shapes, and lengths. The fibers are mounted on a xyz-translation stage, which shall simulate laser beam fluctuations (see appendix I), by stepping the fiber position laterally with minimum steps of 0.8  $\mu\text{m}$ . Optical scrambling can be studied in the far-field or near-field by imaging the respective information onto a rectangular camera sensor (CMOS: FLR (C1) or CCD: Allied Vision (C2), see appendix F). Advanced test setups for the measurement of near-field and far-field scrambling properties of fibers have been developed by various authors, e.g., by [Feger et al. \(2012\)](#) and by [Sutherland et al. \(2016\)](#).

The stability and measurement accuracy of such a setup depends on the quality of the components, such as xyz-stepping stages, cameras, and the frequential and positional stability of the light source ([Sutherland et al., 2016](#); [Unsinn, 2016](#)). The described setup is thus not perfect. The major limitations and possible improvements are described in appendix H.

The near-field imaging is performed with a magnification of 1.7, i.e., 3  $\mu\text{m}$  on the fiber exit-face correspond to 1 pixel of the CMOS camera (C1). The fiber input is centered in x-, y-, and z-direction relative to the incoming beam by taking an image for every position of the xyz-stage and by maximizing the total intensities (see appendix H, Fig. H.1(a)). A mask is applied, in order to cancel out the influence of background light in the image (see Fig. H.1(b)).

The shift  $\Delta S$  of the spot is determined from the shift of the center-of-mass along the lateral directions  $(\Delta X_{CM}, \Delta Y_{CM}) = (\frac{\sum I_i x_i}{I_i}, \frac{\sum I_i y_i}{I_i})$  of each near-field image:

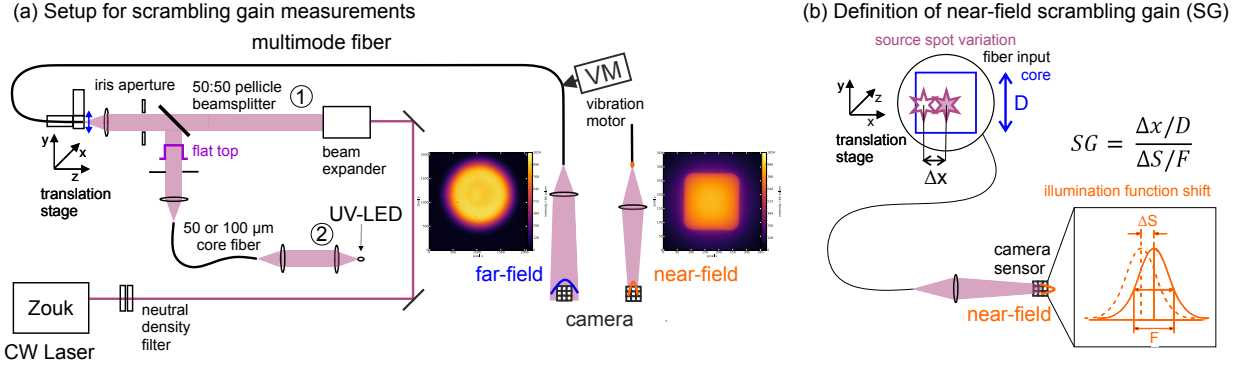


**Figure 3.30:** (a) Setup for scrambling gain measurements using either an expanded cw-laser beam (1) from a cw-laser Zouk or a collimated quasi-flat-top UV-LED (2) made small in focal spot by means of a 50 μm core fiber (see appendix F). The light is coupled into the respective multimode fiber, fixed on a xyz-translation stage. The fiber can be vibrated with a vibration motor in order to average out speckle in case of (1). A lens can be shifted for imaging of either the far-field or the near-field of the light exiting the fiber, onto the camera sensor (CMOS: FLIR or CCD: Allied Vision). The insets show exemplary the far-field and near-field of a 600 μm quadratic core fiber by Ceramoptec. (b) Definition of the near-field scrambling gain (SG) (defined by *Avila and Singh (2008)*).

$$\Delta S = \sqrt{\Delta X_{CM}^2 + \Delta Y_{CM}^2} \quad (3.24)$$

Despite the limitations of the setup, the following comparison of a circular- and a quadratic-core fiber allows an estimate of the scrambling performance. The quadratic-core fiber shows scrambling gain values which are in the order of 10 times higher than those of the circular-core fiber (see Fig. 3.31(a, b)).

The change of the scrambling gain with the in-coupling z-position is apparent (see Fig. 3.31(a, b) different colors). No clear trend is visible, however, and the variation may be attributed to the measurement precision of the setup. A shift of the fiber in z-direction by 1 mm increases the spot size of the light coupled into the fiber by  $\approx 400 \mu\text{m}$  assuming a coupling f-number of  $f/4.7$ .

Fig. 3.31(c) shows scrambling gains of the circular- and the quadratic-core fiber for two different input f-numbers ( $f/3.4$  and  $f/4.7$ ), i.e., opening diameters of the iris aperture in Fig. 3.30(a) of 9 mm and 5 mm, respectively. The input f-number does not alter the determined  $SG$  significantly.

Exemplary near-field images of the fibers for different x-shifts are shown in Fig. 3.31(d), confirming that circular-core step-index fibers provide a high degree of azimuthal scrambling (*Hunter and Ramsey, 1992*), i.e., the intensity profile of the output beam is symmetric. The circular-core images exhibit a changing annular intensity distribution ( $\Delta x/D = 0$ : mainly meridional rays excited,  $\Delta x/D = 0.5$ : mainly skew rays excited (*Lemke et al., 2012*)), i.e., a low degree of radial scrambling, whereas the quadratic-core images have a flat-top intensity distribution.

The flatness of the near-field in case of the quadratic-core fiber compared to the circular-core fiber may be understood, modeling a step-index fiber (homogeneous and ideal along z-direction) as a frictionless particle trapped within a 2D core shape (“dynamical billiard”) (*Stürmer et al., 2016*). In case of an ideally quadratic core all trajectories cover the whole cross section uniformly.

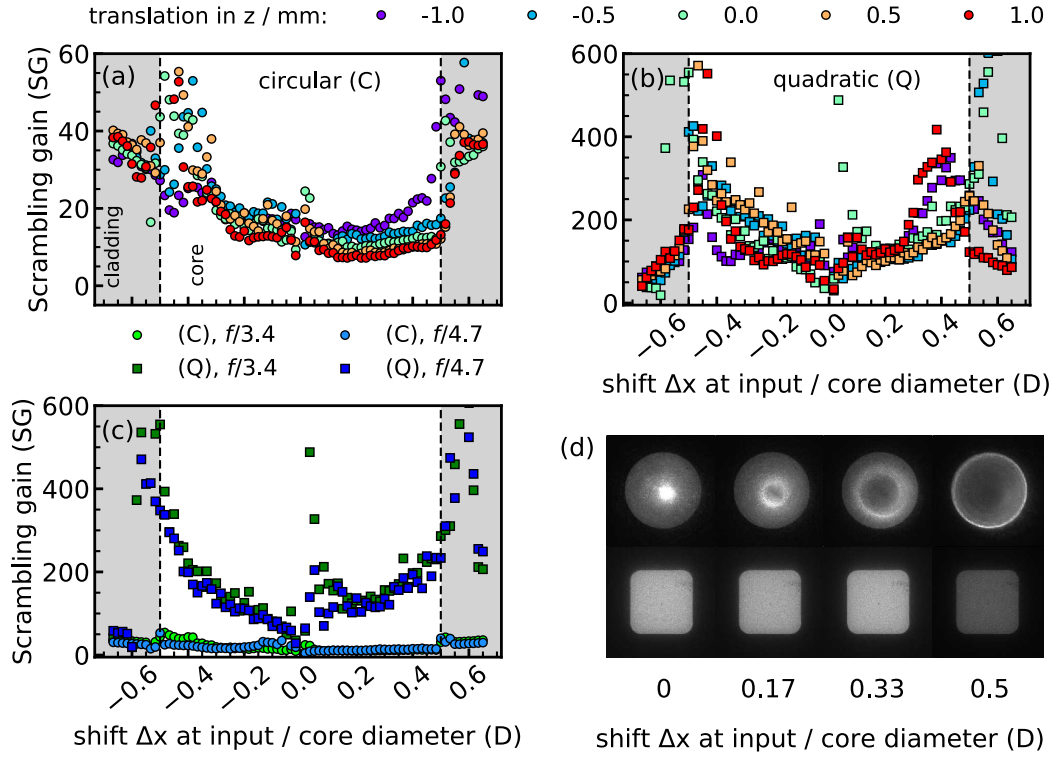


**Figure 3.31:** Comparison of scrambling gains ( $SG$ ) as a function of shift  $\Delta x/D$  at the fiber input for a circular-core fiber (C, UM22-600, see appendix F) (a) and a quadratic-core fiber (Q, fiber B, see appendix F) (b) for different z-shifts (spot sizes, colors) of the xyz-stage with vibration of the respective fibers using a vibration motor. Zouk laser as light source and CMOS camera (C1) as detector. The cladding region is highlighted in gray. (c)  $SG$  for different f-numbers of the incident light during coupling for both fibers (C) and (Q). (d) Near-field images taken at different shifts  $\Delta x/D$  for both fibers. The data was obtained by Unsinn (2016).

Fig H.3 in appendix H provides plots of the intensity profile (pixel intensities summed along the vertical (y) direction) as a function of  $\Delta x$  for both core shapes. The deviations of these summed intensities (for  $\Delta x \leq 20 \mu\text{m}$ , see Fig H.3, bottom) may be used as a measure of the optical scrambling and thus of the stability of the illumination function on the linear PMTA detector (see section 4.3).

Better optical scrambling using polygonal multimode fiber core shapes is a phenomenon registered in many experimental studies so far (e.g., by Avila (2012); Chazelas et al. (2012), especially for exoplanet detectors in astronomy and in combination with free-beam optical scramblers, e.g., Halverson et al. (2015)), what has also been explained through simulations (Allington-Smith et al., 2012).

Measurements with the UV-LED provided approximately the same values of  $SG$  for both the circular-core and the quadratic-core fiber compared to the UV laser. Measurements with and without vibration of the tested fibers yielded the approximately the same scrambling gains. Thus, modal noise did not influence the  $SG$  measurements significantly.

The optical scrambling gain may be improved by using a two-lens optical scrambler (TLS), which works by exchanging the near- and far-fields of two fibers (Hunter and Ramsey, 1992). A design of a TLS using a raytracing model is provided in appendix D.4. A prototype of this TLS design is applied for scrambling gain measurements in appendix H, Fig. H.5. The values of  $SG$  for combinations of TLS with circular-core fibers (Fig. H.5(a))

and with circular-core and quadratic-core fibers (Fig. H.5(b)) are five to eight times higher compared to the circular-core fiber alone. The disadvantages of the TLS-prototype are its high transmission losses ( $T < 60\%$ ) and the challenge of finding its optimum lens positions, influencing its  $SG$  (see Fig. H.5(b)). For these reasons, the TLS-prototype is not applied to the fiber components part of the AEROLI receiver prototype.

Far-field scrambling measurements of the fibers are provided Fig. H.4 in appendix H. The far-field is related to the angular distribution of the light illuminating the FWFIMI under near-field illumination conditions. The deviations as a function of  $\Delta x$  are higher at larger  $x$ -values from the center of the far-field distribution (see Fig. H.4, bottom).

Due to the higher optical scrambling in the near- and far-field, a 600  $\mu\text{m}$  quadratic-core multimode fiber (SQ, fiber A, see appendix F) is used as scrambling fiber  $S_F$  in the receiver prototype.

The quantitative influence of the optical scrambling on the wind speed measurement accuracy of the DWL is estimated using an end-to-end simulation in section 4.3.

### 3.5.6 Illumination function determination procedure

This section describes the routine used to determine the illumination function for characterizing the instrument and to correct the fringe prior to the mean wavelength estimation during the field-tests of section 5.

As shown in Fig. 3.19 of section 3.5.2, the illumination function  $\xi(x, y)$ , which is the 2D distribution of the intensity of the illumination on the detector without interference, modulates the linear fringe, i.e., the instrument function  $I_F$  (eq. 3.3) as a function of the positions  $x$  and  $y$  on the detector. In case of a linear detector  $\xi(x, y)$  becomes a 1D illumination function  $\xi(x)$  and the modified instrument function is given by  $I_{F_{ill}}(x) = \xi(x) \cdot I_F(x)$ . The goal of the illumination function determination procedure is to determine  $\xi(x)$  in order to correct the modulated fringe shape  $I_{F_{ill}}(x)$  and to obtain the corrected 1D fringe profiles ( $I_F(x)$ ).

C  zard (2008) simply blocked one mirror of his sequential Michelson interferometer in order to obtain the 2D illumination function. This is not possible in case of the monolithic FWFIMI, due to the non-accessibility of the mirrors.

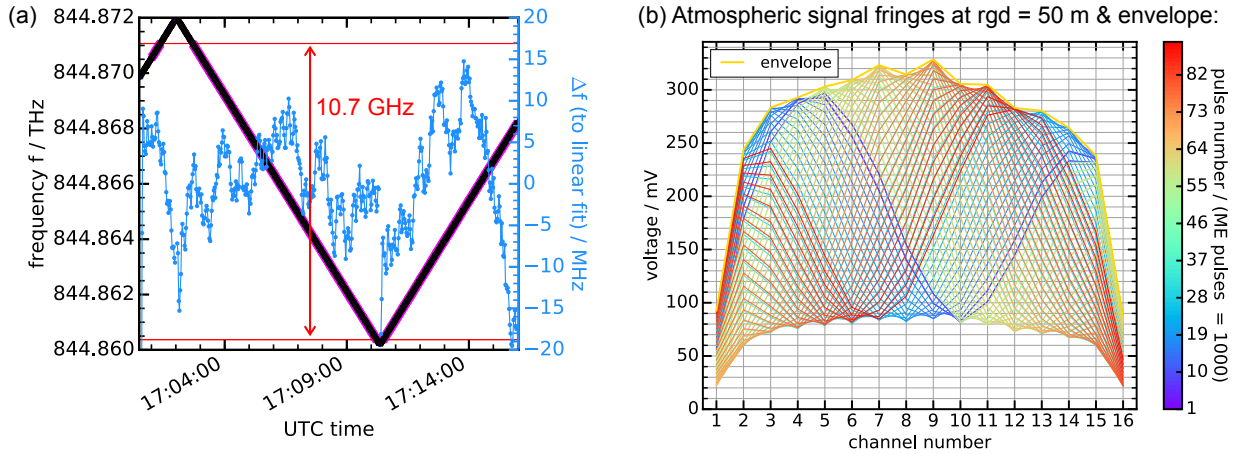
Here, the DELICAT laser is swept in frequency by changing the master oscillator temperature (similar to the cw-laser in Fig. 3.19), what is achieved by ramping the voltage of the MO TEC between zero and 10.7 V in a zigzag-profile using a signal generator (see the AEROLI DWL setup in Fig. 3.20).

Fig. 3.32(a) shows an exemplary (zigzag) frequency profile of the DELICAT laser measured with a wavemeter (WSU-10 by HighFinesse/  ngstrom), using the IR-reference output of the transmitter. The linear ramp is composed of frequency steps, whereby the step size is determined by the ramping frequency (here 1 mHz) and by the sampling rate of the wavemeter (here 0.5 Hz), which depends on the laser power and on the exposure time of the wavemeter. These measured frequency steps (here 40 MHz) are interpolated within a frequency range of 10.7 GHz (marked in red) in order to ensure that no reversal points of frequency lie within the interval, which is used for recording the interference fringes with the PMTA. In this way an increased exposure at these frequencies can be avoided.

Two separate illumination functions 1. of the laser illuminating the receiver (reference) and 2. of the atmospheric backscattered signal are determined. The atmospheric signal illumination function can be range dependent due to a range dependent angular distribution,

when the light is coupled into the scrambling fiber (see Fig. 3.1), and due to insufficient far-field scrambling (see appendix H). Measurement results of range-dependent illumination functions are shown in Fig. A.17 of appendix A.

The atmospheric illumination function is determined for every range gate as the normalized envelope of all the recorded laser power corrected interference fringes within this interval of interest (parts of the ramps marked in magenta). The deviation from linear fits ( $\Delta f$ ) is in the order of  $< 20$  MHz (blue axis in Fig. 3.32(a)). Fig. 3.32(b) shows exemplary fringes recorded with the PMTA, averaged over 1000 pulses, during the frequency ramp shown in Fig. 3.32(a). The determined envelope is highlighted in yellow.



**Figure 3.32:** (a) Exemplary frequency ramp taken during an illumination determination procedure on January 31, 2018. Intervals of interest marked in magenta. Deviations from linear fits are shown in blue. (b) Fringes recorded with the PMTA at a distance of  $50 \pm 15$  m, whereby the shown fringe signals have been averaged over 1000 ME pulses. Every color represents a fringe at a different time instant (pulse number) during the ramp shown in (a). The envelope (marked in yellow) is determined as the maximum signal of every channel during the one  $FSR$  frequency sweep.

After division by the illumination function the interference fringes of Fig. 3.32(b) resemble a quasi-cosine shape (as shown in Fig. A.13(c) of appendix A), which can be fitted with fitting models of the form of eq. 5.2 and eq. 5.3.

Examples of range-dependent illumination functions for a number of horizontal and vertical range gates and for laser reference fringes are provided in appendix A. The laser reference illumination function is determined in a similar way as for the atmospheric backscattered signal. Fig. A.13(b) in appendix A shows exemplary fringes of laser light backscattered by a hard target during a frequency ramp and the according envelope. Respective corrected reference fringe shapes are shown in Fig. A.13(d) and are discussed in appendix A.

Within this section a way to determine illumination functions of the backscattered light and of laser reference light in the receiver was presented. This routine is used in the wind speed retrieval algorithm during the evaluation of measurements with the AEROLI DWL (see section 5.2).

Long-term changes or inaccurately determined illumination functions may result in alterations of the corrected fringe shapes. As a consequence the determined wind speed can be offset (biased) by several m/s. An estimation of the quantitative influence of illumination function deviations on the measured wind speeds of the receiver is provided in section 4.4.



### 3.5.7 Interferometer temperature tuning and stability

In section 3.4.2 a theoretical temperature tuning rate ( $T_{\text{Trate}}$ ,  $R_T$ ) due to the compensated interferometer arm design of less than 700 MHz/K has been derived and specified. In Tab. 3.3 of section 3.5.2 the calculated  $T_{\text{Trate}}$  of the manufactured FWFIMI is 477 MHz/K. The aim of this section is to verify this rate through measurements by comparing the displacement of the fringe position with temperature measurements.

Temperature control is achieved by placing the interferometer within a temperature-stabilized compartment filled with air. The major components for temperature stabilization are shown in Fig. 3.33.

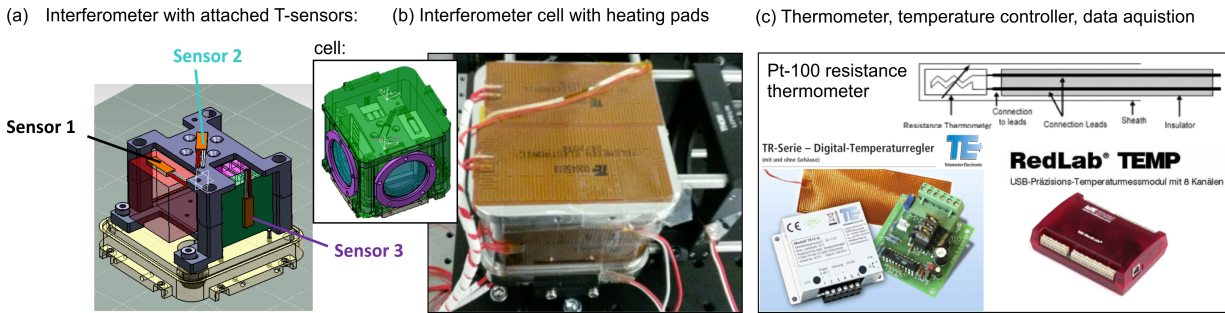


**Figure 3.33:** Setup for temperature stabilization of the interferometer.

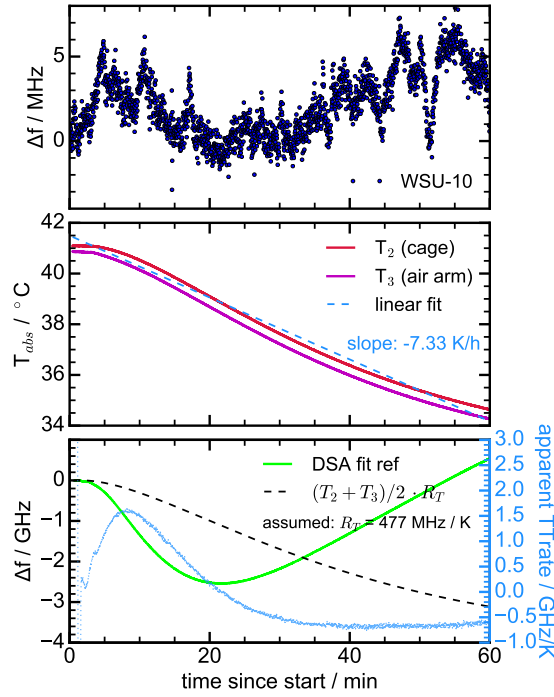
Three Pt-100 thermometers (IEC60751 class A with a measurement precision of 0.2 °C at 40 °C) are attached to the glass arm (sensor 1), the cage (sensor 2), and the backside of the mirror of the air arm (sensor 3). The compartment with fused silica glass windows has heating pads attached to the top, bottom, and two sides (see Fig. 3.33(b)). Additional Pt-100 thermometers are placed on the outside of the cell and on the surrounding optical table. Sensor 1 provides the feedback control signal. A simple two-point feedback control unit (TR-Serie, Telemeter Electronic, Germany) is used to control the current flow through the heating pads. A precision temperature measurement module with eight channels (RedLab TEMP) is used to acquire the temperature data (see Fig. 3.33(c)).

The cell is initially stabilized at 40 °C. The laser frequency is locked to the iodine line and is simultaneously measured with a wavemeter (WSU-10, HighFinesse/Ångstrom). The interferometer is illuminated with laser light using the measurement configuration described in section 3.5.3. Fig. 3.34 contains two exemplary trials to determine the “real” temperature tuning rate of the instrument, (a) during cooling, and (b) during temperature stabilization, i.e., during wind speed measurement.

Case (a) typically occurs when the instrument is shut down for transportation. The cooling rate of -7.3 K/h can be estimated by the slope of a linear fit (dashed blue, middle plot). The theoretical constant  $T_{\text{Trate}}$  of  $R_T = 477$  MHz/K would give frequency changes  $\Delta f$  represented by the black dashed line in the bottom plot. These changes do not follow the frequency changes obtained from Downhill-Simplex fits to the interference fringes of reference and optional atmospheric signal (see section 5.2). During cooling the fringe at first shifts to higher and lower frequencies (see Fig. 3.34(a), green line). In case of (b) the shift of both reference and signal fringe follows the temperature trend times a factor of roughly 10. The right y-axis shows the apparent time-varying temperature tuning rate based on calculating the gradient of fringe frequency shifts, assuming a linear dependence between absolute temperature and time. During cooling (Fig. 3.34(a)) and heating (not



(a) Temperature tuning rate during cooling



(b) Temperature tuning rate during temperature stabilization

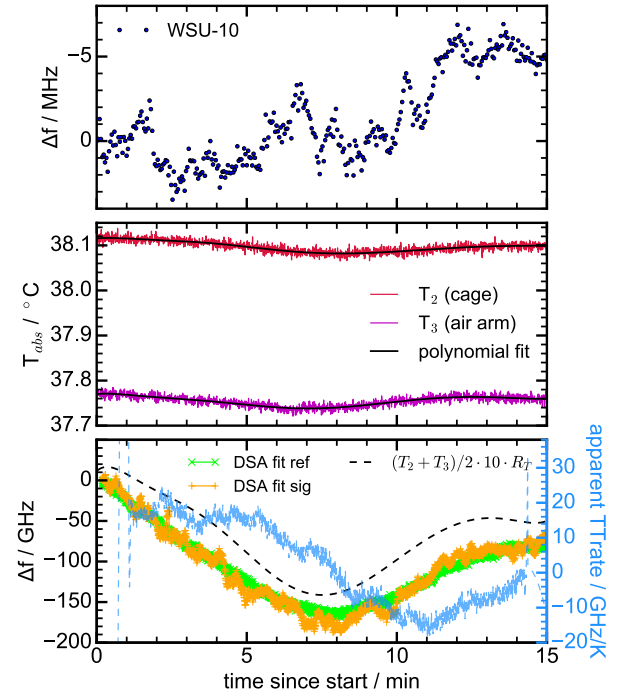


**Figure 3.34:** Temperature tuning rate during cooling on March 13, 2018 (a) and during stabilization on January 29, 2018 (b). All frequency changes are plotted: 1. of the laser (measured with wavemeter WSU-10, top), 2. fits to equivalent frequency changes of absolute temperatures measured with the Pt-100-sensors (middle), and 3. the interference fringe position as frequency change determined by Downhill-Simplex-Algorithm (DSA, Nelder-Mead) fits (see section 5.2) (bottom). The right y-axis shows the estimated temperature tuning rate determined from the DSA fit and from the linear fit to the absolute temperature (middle boxes).

shown here) the estimated TTrate reaches up to 1.5 GHz/K and 3 GHz/K, respectively. During stabilized measurements (Fig. 3.34(b)) the absolute value of the TTrate would be up to ten times higher then the theoretical TTrate (see black dashed line).

A plausible explanation is, that the measurement values provided by Pt-100 (sensor 2 and 3) cannot accurately show the ambient temperature dynamics (e.g., convection), during cooling, during heating, and during temperature feedback-control. That is, the instrument (air between the mirrors, glass) needs time to stabilize to the temperature measured by the sensors, which are located close to metal structures of the cage and the cell housing wall. Temperature gradients within the compartment may affect the fringe position.

To conclude, the temperature stabilization scheme is one of the items to be optimized in future evolutions of the system. However, the principle of comparing reference and atmospheric fringe in a differential measurement, allows being ignorant of the absolute temperature changes. Although they are large compared to typical Doppler shifts caused by wind ( $\approx 5.6$  MHz for 1 m/s), they change on different time scales (compare Fig. 3.34(b)). Temperature changes of this order of magnitude might however bias the illumination function correction, because it requires measurement durations of several minutes (see section 3.5.6), yielding a limitation to the ultimate performance.

### 3.6 Laser transmitter characteristics

This section describes the most important characteristics of the WALES/DELICAT transmitter used in this work.

The high power Nd:YAG laser was developed for the DLR WALES lidar system ([Wirth et al., 2009](#)). It is a MOPA (master oscillator, power amplifier) design with a monolithic Nd:YAG master resonator, running single-mode. This non-planar ring oscillator (NPRO) is diode-pumped and emits IR laser pulses of a duration (FWHM) of 8 ns at a rate of 4 kHz. The frequency is tunable either by temperature or mechanical stress. A small fraction of the IR radiation is frequency-doubled (SHG) for stabilizing the laser to the absorption line center of  $I_2$  inside an iodine cell, with an absolute frequency stability of 1 MHz (300 kHz on short time scales, i.e.,  $< 1$  min). The power amplifier (PA) stages work through passive Q-switching with a timing jitter of less than 0.5  $\mu$ s (at  $1\sigma$ ), and with pulse energies up to 400 mJ ([Wirth et al., 2009](#)). The repetition rate of the MOPA setup (100 Hz) is determined by the driver current cycle of the PA stages.

This pump laser is combined with a Third-Harmonic Generation (THG) unit developed for the DELICAT system ([Vrancken et al., 2016](#)). A schematic optical layout of the WALES/DELICAT transmitter with THG unit is shown in Fig. 3.35(a). A CAD-model of the THG unit is shown in Fig. 3.35(b).

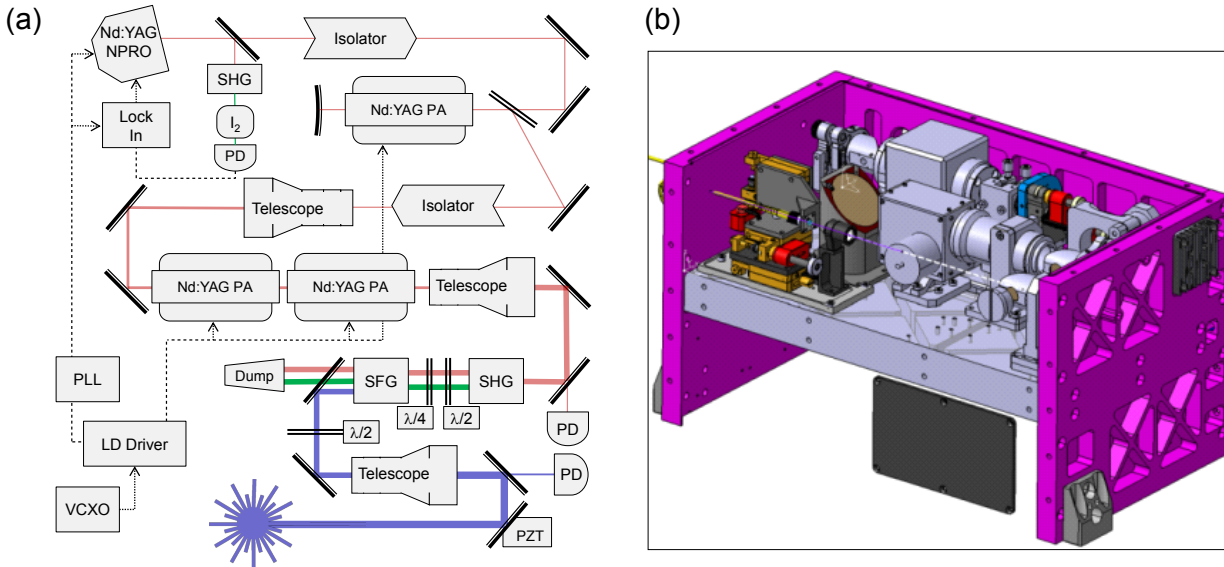


**Figure 3.35:** (a) Schematic optical layout of the DELICAT laser transmitter ([Vrancken et al., 2016](#)). (b) CAD-model of THG-unit with 3-axis piezo stage (modification by Patrick Vrancken, orange) for coupling UV light into a glass fiber (reference light path) and towards the internal powermeter.

The THG unit contains a KTP crystal for second-harmonic generation (SHG), that is used in type II configuration, while phase-matching is achieved by angle and temperature tuning. The SHG conversion efficiency is in the order of 55%. A set of two-wavelength zero-order waveplates with  $\lambda/4$  and  $\lambda/2$  is needed to adjust the polarization of the SHG and the fundamental, which both yield slightly elliptical polarization. In the next step, the beams are guided into a BBO crystal for sum frequency generation (SFG), whereby the phase matching is performed by angular tuning within a piezo-driven two-axes mount. The overall THG efficiency is up to 30%. A highly dichroic mirror is used to separate

the UV part from the infrared and green part, the latter two being fed into a dump. A motorized zero-order  $\lambda/2$  waveplate is used to rotate the polarization of the UV part.

The THG unit was modified for the purpose of this work. Before being expanded with a Galilean telescope, a small fraction is diverted and coupled into a multimode fiber, using a xyz-piezo stage (orange, Fig. 3.35(b)). This light guided into the multimode fiber is separated using a 98:1:1-splitter into 1. a high power reference (600  $\mu\text{m}$  output port), 2. a low power reference (600  $\mu\text{m}$  output port), and 3. another low power signal fed into a powermeter for internal laser power measurements. The required delayed laser reference beam path (1. or 2.) is used as internal reference for the DWL receiver.

The expanded beam has a waist diameter ( $2w_0$  at  $1/e^2$ ) of 13 mm, a divergence  $\Theta$  of 150  $\mu\text{rad}$ , and a beam quality factor ( $M^2$ ) of 4.3. A subsequent shutter system can be used to remotely block the beam (Vrancken *et al.*, 2016).

The laser transmitter is flight-proven and resilient to vibrations and ambient conditions. The laser is cooled through water-water-air cooling circuits (Vrancken *et al.*, 2016).

Table 3.6 summarizes several important properties of the laser transmitter.

**Table 3.6: WALES/DELICAT laser transmitter parameters** (Wirth *et al.*, 2009; Vrancken *et al.*, 2016).

Parameter	Value
Repetition rate	100 Hz
Pulse-to-pulse timing jitter (MOPA)	$< 0.5 \mu\text{s}$
Laser pulse energy (IR)	$< 310 \text{ mJ}$
Laser pulse energy (UV)	$< 85 \text{ mJ}$
Linewidth (IR, FWHM)	54 MHz
Frequency stability (IR)	$\leq 1 \text{ MHz}$
Pulse-to-pulse frequency jitter (IR)	300 kHz (RMS)
Pulse length (FWHM)	8 ns
Beam quality $M^2$ (UV)	4.3
Beam divergence $\Theta$	150 $\mu\text{rad}$
Beam diameter ( $2w_0$ )	13 mm

Laser beam pointing fluctuations of the WALES/DELICAT transmitter are estimated in appendix I. A  $3\sigma$  standard deviation of the laser beam tilt angle of approximately 48  $\mu\text{rad}$  is estimated. This order of magnitude should be taken into account when estimating the resulting bias of the wind speed (see section 4.3).

Chapter 3 described the development and design of a Doppler wind lidar receiver based on the fringe-imaging Michelson interferometer (FIMI) technique. Starting from requirements of the receiver for alleviation control of wake vortices and gusts, different direct-detection DWL were compared and the FIMI technique was found most suitable.

A monolithic field-widened fringe-imaging Michelson interferometer (FWFIMI) with partial temperature compensation was designed and specified with respect to fabrication tolerances. After fabrication its characteristics were investigated experimentally. The FWFIMI was integrated into a fiber-coupled receiver with suitable imaging optics, amplifier electronics, and a PMTA. The receiver's fiber components' speckle noise and scrambling gain performance were characterized, an illumination function determination procedure was de-

veloped, and the physical temperature tuning rate was estimated through measurements. The WALES/DELICAT transmitter was slightly modified, yielding a DWL prototype.

## 4 End-to-end simulation

This chapter provides an estimation of the performance of the DWL receiver using an end-to-end simulation. The following description is partly based on [Herbst and Vrancken \(2016\)](#).

The simulation includes different transmitter properties, atmospheric backscattering conditions (section 2.1), estimated losses of a receiver setup (section 3.5.3), and an ideal cosine-shaped instrument function of a FWFIMI (section 3.3.2) to simulate the light distribution of the interference pattern imaged on the linear detector. Light distributions are generated for laser reference light and Doppler-shifted signal light including analog detection noise. Mean wavelength estimators (see appendix C.8) are used to compare the fringe positions of reference and signal light in order to obtain the simulated radial wind speed. The illumination function being very specific for the receiver optics is not considered for the simulation of horizontal measurements (section 4.2). In the sections 4.3 and 4.4 random errors and biases induced by laser beam tilt fluctuations and illumination function fluctuations are estimated. Simulations of vertical measurements and comparisons with Cramér-Rao bound (CRB) calculations, and a measurement of chapter 5 are provided in section 4.5. Lidar system scaling for improved performance is studied in section 4.6 employing CRB calculations. Simulations of deviations from ideal cosine shape are considered in appendix C.8.

### 4.1 Prerequisites

Relevant prerequisites of the end-to-end simulations such as assumptions on laser energy and losses, the general simulation approach, mean wavelength estimators and their biases, the noise of the photomultiplier tube array, speckle noise, cross-talk, laser frequency jitter, and ADC quantization are described in the following.

The amount of emitted light depends on the laser (transmitter system) being used. Different existing and proposed transmitter systems are assumed. Their energy per pulse ( $E_L$ ), their repetition rate ( $R_L$ ), and power ( $P_L$ ) are listed in Tab. 4.1:

**Table 4.1: Laser transmitters for end-to-end simulations: energy per pulse  $E_L$ , repetition rate  $R_L$ , and power  $P_L$**

Transmitter	$E_L$ / mJ	$R_L$ / kHz	$P_L$ / W
WALES/DELICAT ( <a href="#">Vrancken et al., 2016</a> )	80	0.1	8
hypothetic HYPO	8	1	8
ESA MULTIPLY ( <a href="#">Binietoglou et al., 2016</a> )	1.5	4	6
AWIATOR ( <a href="#">Rabadan et al., 2010</a> )	0.17	18	3

The total number of backscattered photons  $n_p$  is calculated with the lidar equation (eq. 2.2) for different ranges, altitudes, and scattering ratios  $R_b$ . We estimate a total loss of signal photons before the detector of at least 92% in case of a fiber-coupled setup (see Fig. 3.3.1), and a total loss including a linear PMT array of approximately 97% (a total receiver efficiency  $\eta$  of 2.7%, see Tab. F.4). The factors  $\eta_R = 3\%$  and  $\eta_T = 97\%$  (of eq. 2.2) for the proposed setup are thus assumed. The backscattering coefficients  $\beta_{Ray}$  and  $\beta_{Mie}$  are obtained from a mid-latitude standard atmospheric model for different altitudes (see

Fig. 2.1).  $\beta_{Ray}$  and  $\beta_{Mie}$  are also used to calculate the light scattering spectra with the G3 model (Witschas, 2011).

The spectra are numerically convolved with the Michelson instrument function (eq. 3.1), using ideal values (determined in the section 3.3.1) to obtain the received spectrum and the received instrument function, i.e., interference pattern (cf.  $I_F$ , eq. 3.3). The instrumental interference contrast  $V$  with reference laser light is estimated with 95% (if not stated otherwise). All tolerances and all contrast reducing imaging properties (see chapter 3) are assumed to be contained in  $V$ . The additional atmospheric contrast factor  $G$  (see eq. 3.4) is introduced here by the numerical convolution. Strictly linear fringes with ideal cosine-shape are assumed, if not stated otherwise (see appendix C.8).

$I_F$  is normalized such that its integral is equal to the number of backscattered photons ( $n_p$ ).  $I_F$  is downsampled to simulate the detector elements of the linear detector (see, e.g., Fig. 4.1). The photocurrents per element are calculated from the number of photons, as described below.

### Mean Wavelength estimators, their systematic biases, and shot noise

The relative shift between the signal and reference light distributions can be determined with mean wavelength estimators. Several algorithms have been evaluated. The centroid method (CM) (Gagné et al., 1974) and a Gaussian correlation algorithm (GCA) (maximization of the correlation function with a Gaussian) (Paffrath, 2006) (see appendix C.8) produce large systematic errors, increasing linearly with wind speed (see appendix C.8). This phenomenon is referred to as 'slope error' and is very pronounced for the FWFIMI as is shown below. For large shifts (several hundred m/s in case of the AEROLI FWFIMI) parts of the lineshape are not fully imaged, and the systemic errors become nonlinear (edge bias).

A maximum likelihood function approach may be used as well (see appendix C.8 for a description).

Least-square fits are a simple alternative, that do not show slope error and edge bias.

Effects caused by the illumination function are neglected, here. The experimental illumination function has to be characterized and has to be included in the final fit model.

Here a "downhill simplex algorithm fit" (DSA, Nelder-Mead method) is applied. The DSA does not use derivatives and therefore converges very safely (see appendix C.8).

The fit function prior to downsampling has the form

$$f(p, \phi) = p_A (1 + p_V \cos(\phi + p_{\Delta\phi})) + p_B, \quad (4.1)$$

where  $p_A$ ,  $p_V$ ,  $p_{\Delta\phi}$ ,  $p_B$  are the fit parameters for amplitude, contrast, phase, and background, whereby  $p_B$  is optional. The quadratic sum of the data values minus the downsampled fit function  $f(p, \phi)$  is minimized with a Nelder-Mead simplex algorithm ((Nelder and Mead, 1965), implemented by Jones et al. (2001), see section C.8 for a full description). Wind speeds are determined differentially, dividing the difference of the shifts of the reference and the signal fringes  $p_{\Delta\phi}(Ref) - p_{\Delta\phi}(Sig)$  by the phase sensitivity  $S_e = 4\pi/(FSR \cdot \lambda_L)$  (see section 3.3.2).

Simulated (downsampled) fringe distributions (without noise) and the application of the GCA method (FWHM of Gaussian = 3 pm), of the CM method, and of the DSA method are depicted in Fig. 4.1.



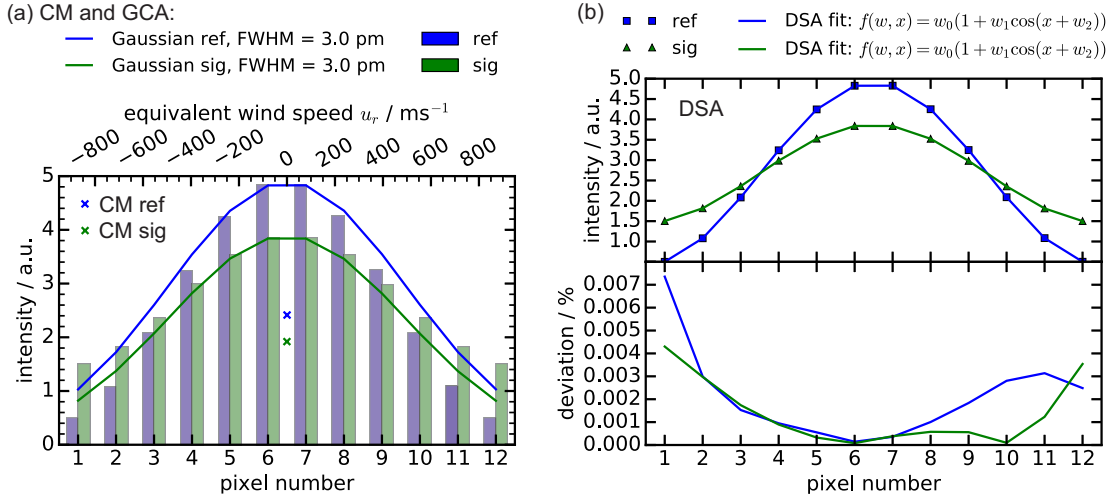


**Figure 4.1:** (a) Fringe distributions (bars) without noise and Gaussians (lines) with the highest correlation of the Gaussian correlation algorithms (GCA) with FWHM = 3 pm. Crosses: center of gravity of reference and signal (centroid method, CM). (b) Fringe distributions (symbols) without noise, Downhill-Simplex fits (lines) with cosine-shaped fit functions (prior to downsampling), and deviations between data and fits (below). The instrumental contrasts are  $V = 0.85$ , and  $V_{sig} = 0.66$ . The number of imaged fringe periods  $n$  is set to 1.

Fig. 4.1(a) illustrates that the FSR (one period) of the designed FWFIMI covers a wide range of possible wind speeds ( $\approx \pm 950$  m/s). The DSA method allows to determine fringe shifts in the simulations without noise with a precision of  $< 0.016$  m/s, i.e.,  $\approx 8 \cdot 10^{-6}$  of the  $FSR$ . The deviations shown in Fig. 4.1(b) (bottom) are of numerical origin. In case of CM and DSA systematic errors, i.e., offsets between simulated and determined wind speeds (biases), depending on the absolute fringe position, impede this order of accuracy.

Fig. 4.2(a) shows the systematic errors  $e$  for different mean wavelength estimators (CM, GCA, DSA) as a function of simulated wind speed, using fringe distributions without noise.

As detailed in appendix C.8, Fig. C.17, the slope error of the CM and GCA depends on the number of periods  $n$ , and on the contrasts  $V$  and  $V_{sig}$ . In case of the DSA method the slope is always zero. For this reason the DSA method is selected for the following end-to-end simulations.

In the next step artificially produced noise is added on each detector element  $k$ . The Poisson distribution of the noise can be approximated by a normal distribution, because of the large magnitude of the detected photons. The signal-to-noise (amplitude) ratio SNR for every detector element is  $i_{sig}/i_d$ , where  $i_{sig}$  is the photocurrent of the respective detector element, and  $i_d$  is the noise current. The same SNR is assumed for all detector pixels for both the laser reference fringe and the atmospheric signal fringe (case I) or only for the atmospheric signal fringe (case II). Case III contains a cosine-modulated SNR of the atmospheric fringe pixel signals, whereby the SNR at the maximum of the fringe is varied (see Fig. 4.2(b), inset) by setting  $\max(N_k) = SNR^2$ , calculating all  $N_k$ , and obtaining  $SNR_k = \sqrt{N_k}$ . Here  $N_k$  is an artificial cosine-shaped distribution on the pixels  $k$ .

Systematic bias plots with shot noise (case I) are shown in Fig. C.18 in appendix C.8. These are noisy versions of Fig. 4.2(a). When Gaussian shot noise is added the (wind-speed-independent) standard deviation of the systematic error ( $\sigma(e)$  during 50 simulation runs) is increased, and the systematic error  $e$  is fluctuating.

Fig. 4.2(b) shows  $\sigma(e)$  as a function of the shot noise signal-to-noise ratio per channel (SNR) (symbols) for the DSA method, compared to the calculated Cramér-Rao bounds

(CRB) (green line) for one fringe period being imaged on  $N_{pixel} = 12$  pixels. Eq. C.30 is used to calculate  $CRB(SNR)$  with  $N_c = 2/N_{pixel}$  by setting  $N_{tot}$  equal to  $SNR^2$  (because for shot noise:  $SNR \propto \sqrt{N_{tot}}$ ). A fit with fit parameters is shown (green line). A similar match of end-to-end simulations and CRB calculations is obtained for  $N_{pixel} = 3$  (fit parameter  $A \approx 620$ ) and  $N_{pixel} = 48$  ( $A \approx 125$ ).

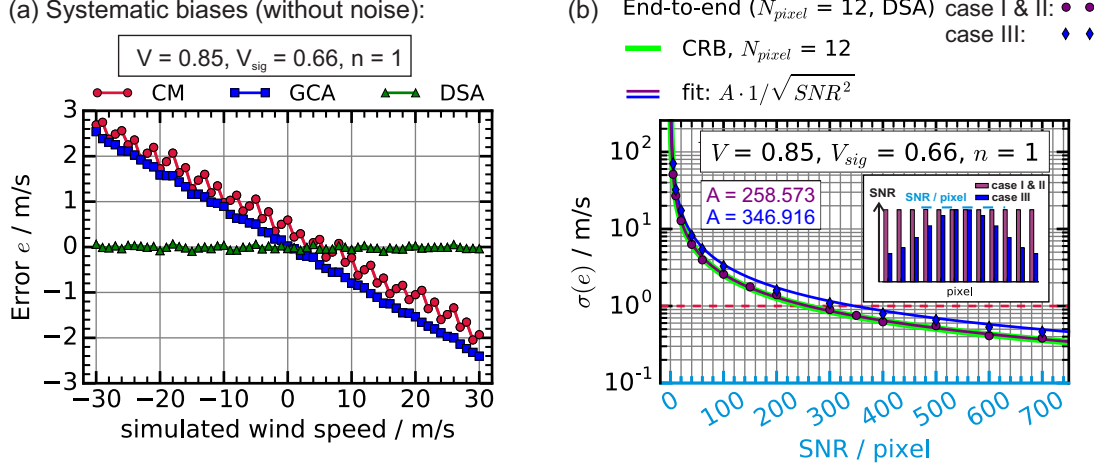


**Figure 4.2:** (a) Systematic biases of a FIMI simulated in end-to-end simulations (without noise) for the mean wavelength estimators: centroid method (CM), Gaussian correlation algorithm (GCA), and Downhill-Simplex Fit (DSA, Nelder-Mead). (b) Standard deviation of the error ( $e$ ) between simulated and determined wind speed as a function of shot noise SNR. Green: Cramér-Rao bound calculated with eq. C.30 (appendix C.3). Symbols: End-to-end simulation with results obtained like shown in Fig. C.18 in appendix C.8 (purple: constant SNR per pixel, i.e., case I & II, blue: cosine-modulated SNR, i.e., case III). Lines: Fit with  $A \cdot 1/SNR$ .

A  $1/SNR$  proportionality is observed, which is characteristic for shot-noise limited processes (see, e.g., the  $\kappa/N_{sd}$  term in eq. C.33 of appendix C.3). Slightly different results of the end-to-end simulations are obtained for the cases I & II, and III ( $A(I \& II) \approx 259$ ,  $A(III) \approx 347$ ). The noise behavior of the calculated Cramér-Rao bounds (green line) and the respective results of end-to-end simulations with the DSA method (I & II: purple) are in good accordance.

The goal of the next subsection is to model the noise of a linear photomultiplier tube array more realistically.

### Noise of the photomultiplier tube array

The total noise current  $i_k$  of every detector element  $k$  in analog detection mode is calculated with the standard equations for the thermal noise current  $i_T$ , the shot noise currents of the dark current  $i_{SD}$ , of the photocurrent  $i_{SL}$ , and for the solar background light current  $i_{SBG}$  (Hamamatsu, 2007):

$$i_k^2 = i_T^2 + i_{SD}^2 + i_{SL}^2 + i_{SBG}^2 = \left( \sqrt{4k_B \frac{T_{eq}}{R_{out}}} \cdot B \right)^2 + \left( \sqrt{2i_D \cdot e \cdot B \cdot F_{PMT}} \right)^2 + \left( G \sqrt{2eR_p P_k \cdot B \cdot F_{PMT}} \right)^2 + \left( G \sqrt{2eR_p \frac{P_{bgnd}}{N_{Pixel}} \cdot B \cdot F_{PMT}} \right)^2, \quad (4.2)$$

whereby  $k_B$  is Boltzmann's constant,  $T_{eq} = 10^{N_{fig}/10} \cdot T_0$  with  $N_{fig}$  being the noise figure

of the first amplifier in dB,  $T_0 = 290$  K is the temperature of the readout resistor,  $R_{out}$  is the resistance of the readout resistor, assumed to be equal to 1 M $\Omega$ , and  $B = 1/\Delta t = 7.5$  MHz is the minimum bandwidth of the receiver (Kovalev and Eichinger, 2005) with  $\Delta t = 2\Delta R/c$  being the duration of signal detection (133 ns for  $\Delta R = 20$  m).  $i_D$  is the anode dark current being dependent on the PMT polarization voltage  $U_{pol}$  (values can be found in the spec sheet of “H7260-200” (Hamamatsu, 2011)). The minimum value of  $U_{pol} = 500$  V is assumed.  $e$  is the electron charge.  $G$  is the gain of the PMT achieved through current amplification, whereby each dynode amplifies the incident electron current.  $G$  is dependent on  $U_{pol}$ , and is equal to  $3 \cdot 10^4$  for  $U_{pol} = 500$  V.  $R_p = QE \cdot e \cdot \lambda_L / (h \cdot c) \approx 0.13$  A/W is the responsivity of the “H7260-200” at  $\lambda_L = 355$  nm, whereby  $h$  is Planck’s constant.  $F_{PMT} = \rho / (\rho - 1) = 1.2$  is the so-called noise figure of the PMT.  $P_k$  is the signal optical power per pixel  $k$ , calculated by  $N_{ph_k} \cdot (hc/\lambda) / \Delta t$ ,  $N_{ph_k}$  is the number of photons per pixel  $k$ . The signal current  $i_{sig_k}$  per pixel  $k$  is obtained by  $R_p \cdot P_k \cdot G$ . The received solar background radiation power  $P_{bgnd}$  is given by

$$P_{bgnd} = P_{RadAtm} \cdot 10^6 \cdot A_{tel} \cdot 2\pi \cdot (1 - \cos(FOV/2)) \cdot FWHM \cdot \eta. \quad (4.3)$$

$\eta$  is the total efficiency of the receiver.  $P_{RadAtm}$  is the solar spectral radiance.  $P_{RadAtm} = 300$  W/(m<sup>2</sup>sr  $\mu$ m) at 354.8 nm is assumed (Hirschberger and Ehret, 2011). The FOV is set to 4 mrad (double angle). The full width at half maximum (FWHM) of the sunlight filter (IF) is assumed with 0.5 nm giving a transmission of 88%. Under these conditions  $i_{SBG}$  is in the order of a few tenth of  $\mu$ A.

Cross-talk between the detector elements can be included using typical cross-talk ratios of PMT arrays of 3%, 0.6%, 0.2%, 0.1% for the detector elements in a row next to a given detector element (see appendix F).

Fig. 4.3(a) contains the optical power  $\sum_k P_k$  as a function of range for an altitude of 10 km (assuming the atmospheric model presented in section 2.1.1,  $\eta = 2.7\%$ ,  $\Delta R = 20$  m, and the WALES/DELICAT laser transmitter, see Tab. 4.1). The respective signal current per pixel ( $i_{sig}$ ) and the noise currents of eq. 4.2 are shown in Fig. 4.3(b) for a number of PMTA detector elements  $N_{Pixel}$  of 12, assuming full overlap at all ranges.

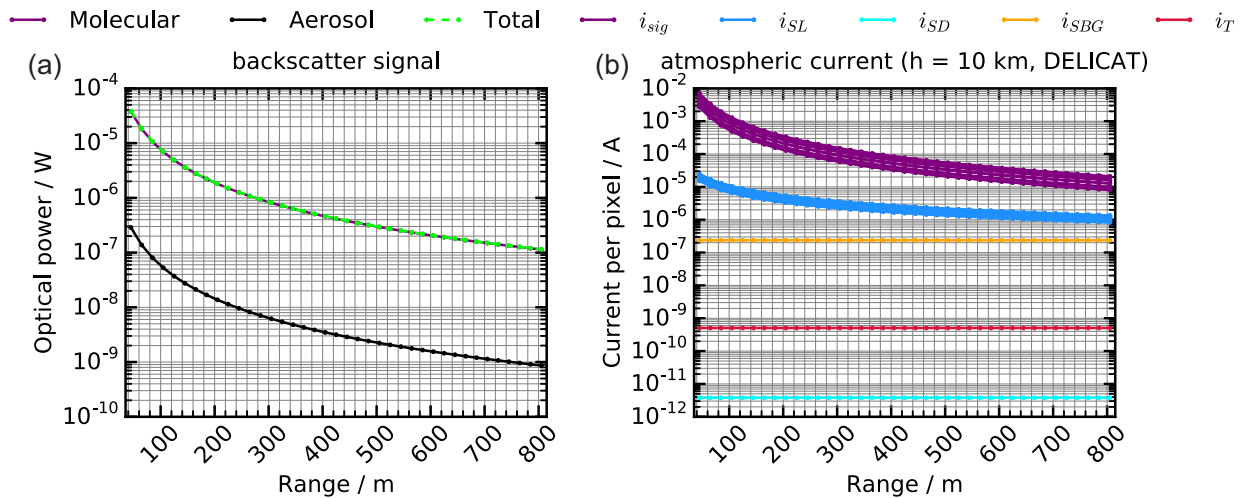


**Figure 4.3:** (a) Backscattered optical power as a function of range (with molecular and aerosol contribution indicated). (b) Atmospheric signal current ( $i_{sig}$ ) and noise currents of eq. 4.2 for every pixel  $k$  of the PMTA with shot noise of photocurrent ( $i_{SL}$ ), shot noise current of the dark current ( $i_{SD}$ ), shot noise of the solar background light current ( $i_{SBG}$ ), and thermal noise current ( $i_T$ ).

It may be deduced from Fig. 4.3(b) that the backscattered signal noise is clearly shot-noise dominated in the shown range of distances up to 800 m. The ratio of the number of received laser signal photons to the number of the received solar background photons ( $N_{tot}/B_{tot}$ ) is higher than 60 at a range of 800 m.

These noise contributions are added onto the noise-free signals per channel  $k$  of the photomultiplier tube array. The noise contribution due to speckle (modal noise) is described in the next subsection.

### Speckle noise

Another additional cause of noise are speckle. Speckle are produced due to the interference of backscattered light from the atmosphere (see appendix C.1) and by interference of many propagation modes of reference light in the multimode delay fiber (RF) and signal light in the multimode scrambling fiber (SF) (see section 3.5.4). Speckle render the illumination of the interferometer inhomogeneous and erratic. The speckle noise is defined here as an uncertainty of the number of photons per detector element  $k$  of the PMTA and is quantified with the speckle signal-to-noise ratio  $SNR_{sp} = \langle I_k \rangle / \sigma(I_k)$  (cf. eq. C.3), where  $I_k$  is the integrated intensity on pixel  $k$  of the PMTA (see section 3.5.4).

For coherent light, the average intensity  $\langle I \rangle$  is equal to the standard deviation  $\sigma_I$ . For partially coherent light,  $C$  reduces to  $1/\sqrt{M}$ , here  $M$  is the number of incoherently added speckle patterns (degrees of freedom), during the coherence time (see appendix C.1).  $M$  equals  $M_a \cdot M_f$ , where  $M_a$  is the number of atmospheric speckle patterns, and  $M_f$  the number of fiber speckle patterns (without spatial or temporal averaging). That is, speckle behave like a multiplicative noise.

In case of fiber-induced speckle,  $C$  is reduced due to mixing of the fiber modes during propagation and  $M$  depends on the vibration frequency of the vibration motor and the time of exposure of the detector, i.e.,  $\Delta t \approx 133$  ns ( $\Delta R = 20$  m), and has to be determined experimentally. Due to this very short time  $\Delta t$ ,  $M_f$  is assumed equal unity without spatial and temporal averaging. Taking into account spatial averaging by the PMTA pixels ( $k$ ) the number of speckle realizations averaged on a single pixel ( $M_k$ ) is at least 10000 without vibration for  $R_f = 470$  (see section 3.5.4).  $M_k$  relates to the speckle SNR by  $SNR_{sp} = \sqrt{M_k}$  (see section 3.5.4, eq. 3.23).

Every pulse is assumed to generate a new, arbitrary speckle pattern, due to the changing distribution of scatterers in the scattering volume during flight from pulse to pulse (signal) and due to vibrations of the fibers (laser reference, temporal averaging).

A simplified model is used to simulate speckle patterns.  $R_f$  was defined in section 3.5.4 as the ratio of the fiber-core diameter to the mean speckle grain size  $D_{sp}$ . Here  $R_f$  is a dimensionless quantity describing the ratio of the total detector width to  $D_{sp}$ . The actual speckle grain size depends on the laser beam waist diameter in front of the telescope, in our case  $w(R) > 20$  mm at  $R = 50$  m ( $R_f \approx 65$  for atmospheric free-beam speckle of  $D_{sp} = 2.3$  mm, see Fig. C.2), and on the multimode fiber core diameter (Rodriguez-Cobo *et al.*, 2012) (for fiber speckle). Numerical arrays of dimension  $R_f \cdot R_f$  with  $R_f = 48$  (fiber with a core diameter  $D_{core} \approx 100$   $\mu$ m) or  $R_f \approx 480$  ( $D_{core} \approx 600$   $\mu$ m) with a negative-exponential distribution according to eq. C.1 represent coherent speckle patterns in the model. Fiber speckle pattern properties are characterized in section 3.5.4. Larger fiber cores provide a higher  $R_f$ , and therefore a higher diversity (cf. section 3.5.4), and a larger potential for spatial averaging and speckle contrast reduction. The total speckle patterns for atmospheric signal are computed by the incoherent sum of  $M_{mol}$  and  $M_{aer}$  speckle

patterns.  $M_{mol}$  and  $M_{aer}$  are equal to  $M_a = \Delta R/d_c$  with  $d_c$  being the respective coherence lengths of the molecular and aerosol scattering fractions ( $d_{coh_{mol}} = 4.5$  cm,  $d_{coh_{aer}} = 1.5$  m, cf. appendix C.1).  $R_b$  is included by setting  $\langle \xi \rangle$  in eq. C.1 equal to the number of photons backscattered by molecules and aerosols, respectively. The total laser reference speckle patterns are modeled as incoherent sums of speckle patterns with  $M_f = 1$  for a single laser pulse.

The linear detector spatially integrates over the total speckle pattern (spatial averaging). All rows of the total speckle patterns are summed up and are downsampled to simulate the integration by the linear detector. The downsampled speckle distribution is normalized to unity and multiplied with the distribution of photons on the linear detector for every pulse, before the detector noise is included.

Simulated speckle patterns for  $R_f = 48$  and  $R_f = 480$ , under two different conditions: 1.:  $h = 1$  km,  $R_b = 6$  and 2.:  $h = 10$  km,  $R_b = 1$  are shown in Fig. 4.4. The respective speckle SNR is indicated without (top) and with spatial averaging over 12 pixels of a linear detector array (bottom). The lower plots show the resulting speckle noise for atmospheric signals and laser reference signals.

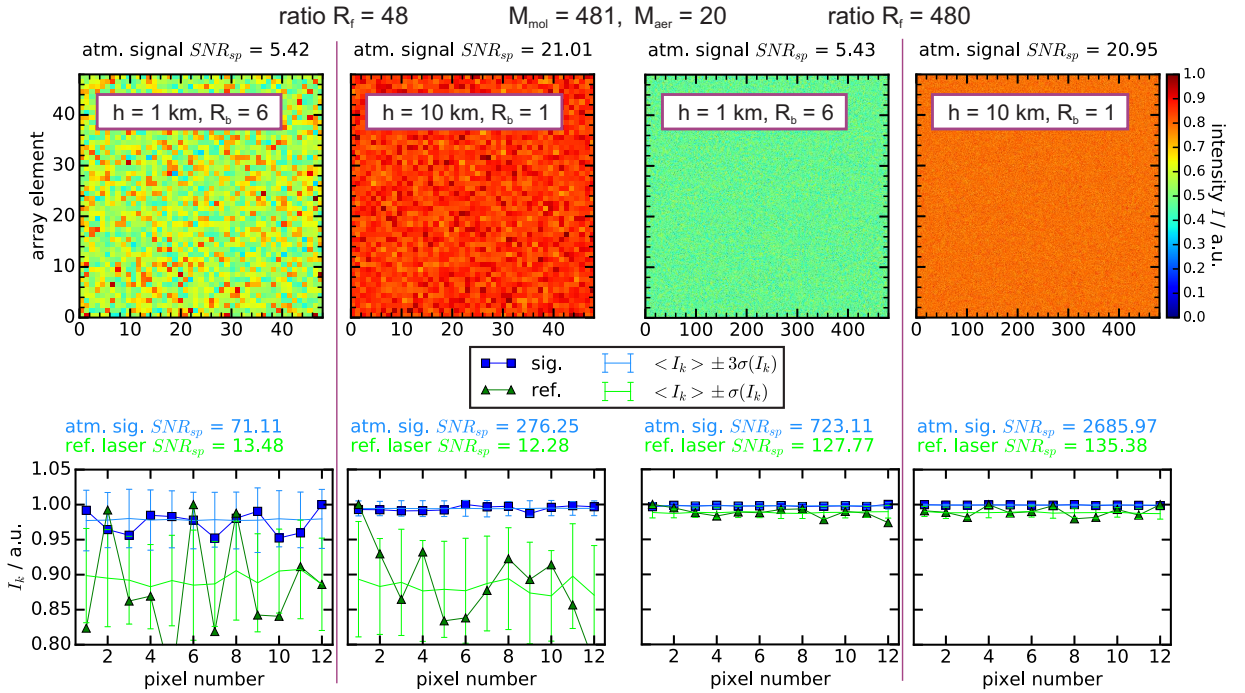


**Figure 4.4:** Top: Simulated speckle patterns with a fiber core diameter to speckle grain size ratio  $R_f = 48$  and  $R_f = 480$  under two different atmospheric conditions (1.:  $h = 1$  km,  $R_b = 6$ , 2.:  $h = 10$  km,  $R_b = 1$ ). Bottom: Respective speckle noise on a 12 pixel detector. 50 trials (their mean  $\bar{I}_k$ ) and the standard deviations ( $\sigma(I_k)$ ) are indicated as lines and error bars. One realization is additionally plotted for each case for atmospheric signal ( $M_{mol} = 481$ ,  $M_{aer} = 20$ ) and reference signal ( $M_f = 1$ ) (squares and triangles).

The dependence of the speckle noise SNR on the ratio  $R_f$  is linear (as can be seen by the fitting curves in Fig. 4.5(a)). Vertical red lines mark the ratios  $R_f$  of fibers with a core diameter of 90  $\mu\text{m}$  and 600  $\mu\text{m}$  (see Fig. 3.29(b) in section 3.5.4). The atmospheric speckle simulated in Fig. C.2(a) of appendix C.1 have a telescope aperture to speckle grain size ratio ( $R_f$ ) of 65 (marked by the orange line in Fig. 4.5(a)). The advantage of a higher  $SNR_{sp}$  using a fiber-coupled setup with a 600  $\mu\text{m}$ -core fiber is apparent.



A 600  $\mu\text{m}$ -core fiber provides a high diversity with a ratio  $R_f$  of approximately 480 (see Fig. G.2(b) in appendix G). The y-scale in Fig. 4.5(a) is logarithmic to show the almost one order of magnitude difference in speckle noise SNR between a frequency-broadened atmospheric return signal (blue symbols for  $R_b = 1$  and  $R_b \approx 6$ ) and a coherent reference signal with  $M_f = 1$  (green). Measurements in section 3.5.4 show, that indeed  $SNR_{ROI} \approx 100$  without temporal averaging and spatial averaging by a hypothetical 12 pixel detector (see orange dotted line in Fig. 3.29).

The dependence on the particle backscattering ratio  $R_b$  is negative exponential, as is shown in Fig. 4.5(b) for  $R_f = 480$ . This means, that highest speckle noise is obtained for high particle concentrations, while the high  $R_f$  ratio (high diversity for spatial averaging) still guarantees a high speckle SNR.

Another promising way to increase  $SNR_{sp}$  is the digital summation of several pulses for signal and reference light prior to evaluation, called “mean evaluation” (ME) in the following. In contrast to the evaluation of a single pulse, “pulse evaluation” (PE), ME reduces the effective measurement rate, but has the advantage of averaging both the speckle noise and the detector noise. ME requires thermomechanical stability of the setup over the short mean evaluation time, i.e., stability of the positions of the interference fringes during the time of digital summation.

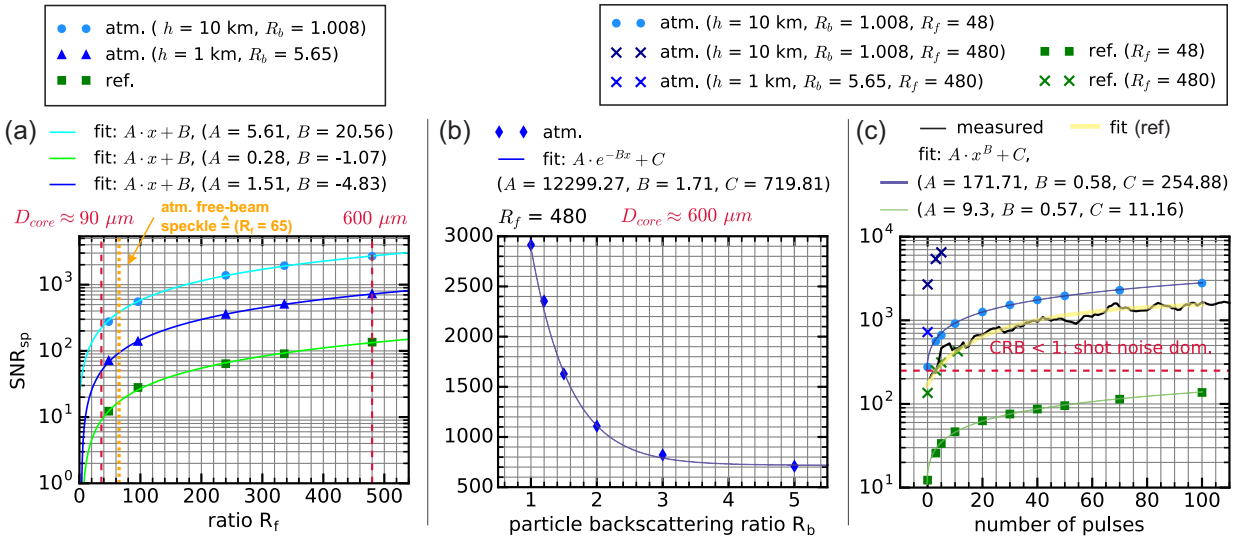


**Figure 4.5:** (a) Speckle noise SNR dependency on the fiber core diameter to speckle grain size ratio  $R_f$ . Red lines:  $R_f = 48$  and  $R_f = 480$  corresponding to  $D_{core} \approx 100 \mu\text{m}$  and  $D_{core} \approx 600 \mu\text{m}$  of a quadratic-core fiber (see Fig. 3.29 in section 3.5.4), orange line: corresponding  $R_f$  for atmospheric speckle in Fig. C.2(a). (b) Dependency on the particle backscattering ratio  $R_b$  for  $R_f = 480$ , and (c) on the number of averaged, uncorrelated speckle patterns produced by independent pulses for  $R_f = 48$  (symbols) and  $R_f = 480$  (crosses) for backscattered light (blue, atm.) and reference light (green, ref.). Black line: Measured dependence for fiber A and fit (yellow line, see  $SNR(n)$  in Fig. 3.29 in section 3.5.4).

Temporal averaging can be achieved by averaging over a number  $M_p$  of uncorrelated speckle patterns using independent laser pulses, translated air volumes, or mechanical scrambling. The WALES/DELICAT transmitter has a pulse-to-pulse frequency jitter distribution during less than 60 s of about 1 MHz in the UV (Wirth et al., 2009). This frequency variation alone is however not sufficient for temporal averaging of the speckle (cf. Fig. G.5), that is why an additional “scrambler”, such as a vibrating fiber (see section 3.5.4) is applied.



The approximate  $\sqrt{M_p}$  dependency in this case is shown in Fig. 4.5(c).  $SNR_{sp}$  for laser reference light with  $R_f = 480$  (green crosses) is in good accordance with the measured dependency for a 600  $\mu\text{m}$ -core fiber (fiber A) marked by a black line and a fit (yellow line) (cf.  $SNR(n)$  in Fig. 3.29). The other dependencies show, that in case of  $R_f = 480$  (i.e.,  $D_{core} \approx 600 \mu\text{m}$ ), speckle noise for a single pulse is only a problem for the laser reference light (green symbols), because the  $SNR_{sp}$  is  $< 300$ . In this case temporal averaging may be necessary, but as is apparent from Fig. 4.5(c) due to more efficient spatial averaging for  $R_f = 480$  than for  $R_f = 48$  (i.e.,  $D_{core} \approx 100 \mu\text{m}$ ) a lower number of pulses has to be averaged.

In case of free-beam atmospheric speckle (without applying a fiber-coupled setup)  $R_f$  is approximately 65, because in atmospheric speckle simulations for a telescope diameter of 15 cm a speckle grain size  $D_{sp}$  of  $\approx 2.3 \text{ mm}$  is obtained (see Fig. C.2(a), appendix C.1).

The here described model is employed in subsection 4.2 to include the influence of speckle noise during simulations of horizontal wind speed measurements.  $R_f = 48$  is used in these simulations because this array size is less computationally expensive than  $R_f = 480$ . Furthermore  $R_f = 48$  provides a conservative estimate of speckle noise in a free-beam setup (without fiber coupling).

### Cross-talk, laser frequency jitter, ADC quantization

The influence of crosstalk (cross-talk ratios CTR according to Tab. 4.2, ideal, and Fig. F.2, real), a pulse-to-pulse frequency jitter of 1 MHz, and quantization due to the analog-to-digital-converter (ADC) are shown in Fig. 4.6(a, b, c). In each case, the error  $e$  between the simulated and the determined wind speed (DSA method) is determined, and its mean value  $\bar{e}$  and standard deviation  $\sigma(e)$  are plotted as a function of range.

**Table 4.2:** Ideal CTR for pixels  $p_k$ , and their neighbors  $p_{k,j}$  for  $k = 1 \dots 12$  and  $j = -5 \dots 5$ .

pixel	$p_{k,-5}$	$p_{k,-4}$	$p_{k,-3}$	$p_{k,-2}$	$p_{k,-1}$	$p_{k,0}$	$p_{k,+1}$	$p_{k,+2}$	$p_{k,+3}$	$p_{k,+4}$	$p_{k,+5}$
CTR / %	0	0.1	0.2	0.6	3	100	3	0.6	0.2	0.1	1

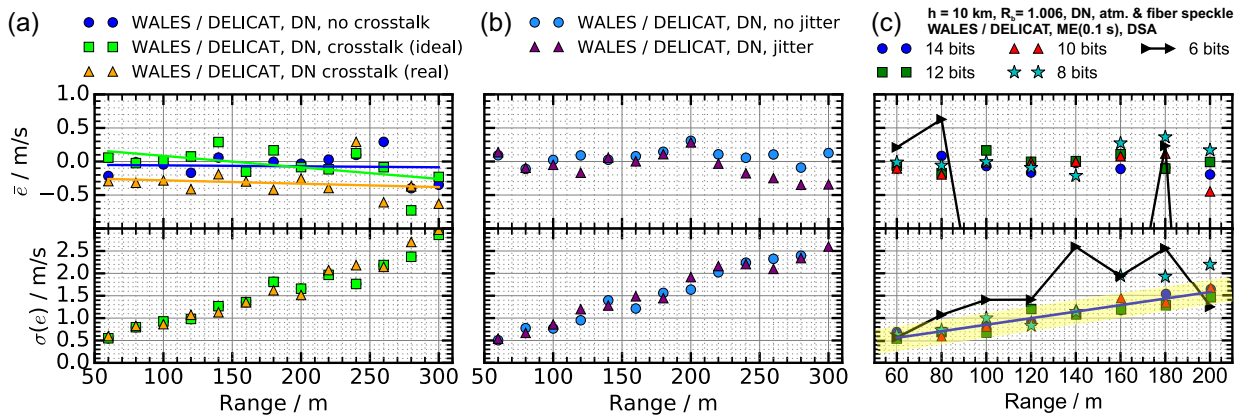


**Figure 4.6:** Mean and standard deviation of the error  $e$  between simulated and determined wind speed  $u_r$  in 50 trials: (a) Influence of crosstalk with the same cross-talk ratios for every pixel (ideal) and according to Fig. F.2 (real). (b) Influence of a laser frequency pulse-to-pulse jitter of 1 MHz. (c) Influence of different effective number of bits (ENOB) of the analog-to-digital converter (ADC).

$\sigma(e)$  increases linearly as a function of range. No visible bias of  $\bar{e}$  is obtained for the ideal CTR of Tab. 4.2. Slightly different cross-talk ratios for every pixel (real), can introduce a constant bias, i.e., an offset of  $\bar{e}$  (see Fig. 4.6(a)).

Frequency jitter with a standard deviation of  $\sigma(\Delta\nu) \approx 1$  MHz in the UV for the DELICAT transmitter (*Vrancken et al., 2016*), does not change the result (see Fig. 4.6(b)).

The ADC quantizes the analog signal. The resolution of the ADC is assumed to be 16 bits with an effective number of bits (ENOB) of 12 (see appendix F). Fig. 4.6(c) shows, that reduced ENOB values of 10 bits and 8 bits would not significantly change  $\sigma(e)$  compared to 14 bits. ENOB values of 6 bits result in a mismatch of  $\bar{e}$  and  $\sigma(e)$  compared to the other ENOB values and the measurement performance is thus reduced.

Furthermore, higher ENOB values allow for a higher dynamic range. In the present simulation, the reference photocurrent is set for optimum use of the quantization levels. The saturation level can be set to the expected maximum signal light current by adjustment of the PMT gain.

An experimental implementation of the lidar receiver (in a future airborne setup) should automatically adapt the amplification to the varying altitude  $h$  and scattering ratio  $R_b$ . In this case the signal currents could be adjusted to a lower saturation level for all signal strengths, what would guarantee a higher resolution at small signal strengths.

In this section important prerequisites for performing end-to-end simulations of wind speed measurements with a direct-detection DWL based on a fringe-imaging Michelson interferometer have been described. Downhill-Simplex fits with a cosine-shaped fit showed the lowest systematic biases. SNR values per pixel of approximately 300 are needed for a wind speed measurement precision higher than 1 m/s. Neglecting laser beam pointing fluctuations, and illumination function variations, the detection process can be considered shot-noise-limited. A model to simulate speckle noise was presented, showing good accordance with experimental speckle SNR measurements, and highlighting the advantage of using a fiber-coupled setup with large-core multimode fibers. Such a fiber-coupled setup allows to average out atmospheric speckle noise effectively. The effects of cross-talk, laser frequency jitter, and ADC quantization were modeled and their potentials to bias wind speed measurements were estimated.

## 4.2 End-to-end simulation of horizontal wind speed measurements

The prerequisites described above are used to estimate the performance of the AEROLI receiver prototype. The pixel dependent (shot noise) SNR is calculated for the two cases 1.  $h = 10$  km,  $R_b = 1$ , and 2.  $h = 1$  km,  $R_b \approx 6$ , and is plotted as a function of range in Fig. 4.7 for different transmitter types (described in 4.1) whereby full overlap is assumed for all ranges.

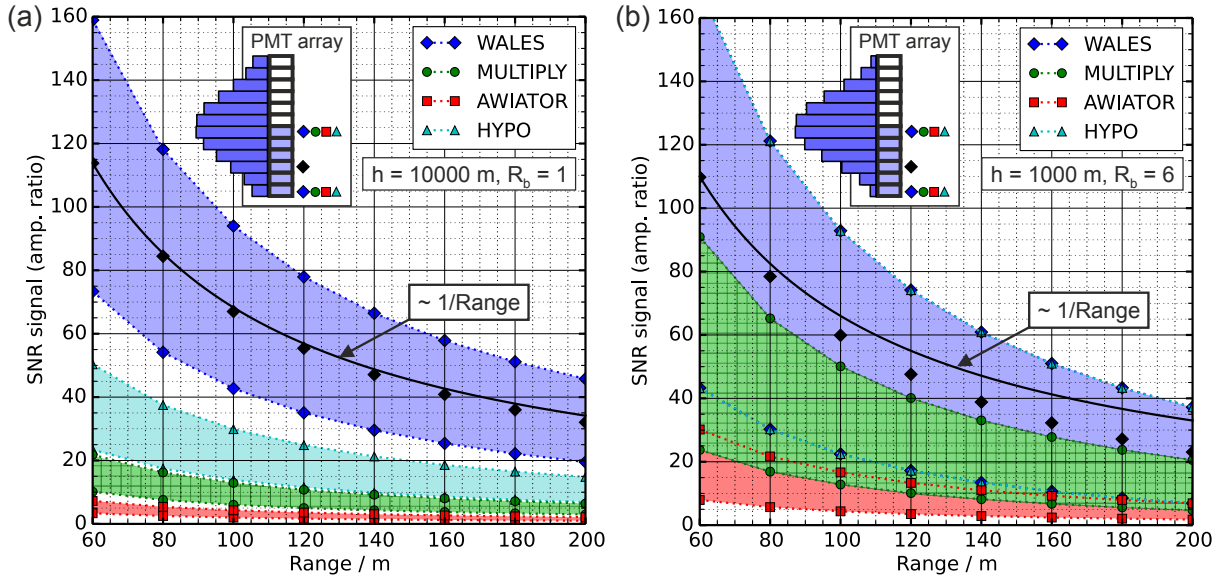


**Figure 4.7:** (a) Detector SNR of one pulse for  $h = 10000$  m,  $R_b = 1$  and (b)  $h = 1000$  m,  $R_b = 6$  in case of the laser transmitters: “WALES / DELICAT”, “MULTIPLY”, “AWIATOR”, and “HYPO”. Two curves are shown for every transmitter giving the SNR of one center and one edge pixel of the PMT array illuminated with a centered interference fringe. Colored areas mark the regions in between where the SNR values of the other pixels are located. Additional black squares mark the SNR of the third pixel in case of WALES / DELICAT (see inset). The solid black line marks a range dependence of the SNR proportional to  $1/\text{Range}$ . Figure taken from [Herbst and Vrancken \(2016\)](#).

Fig. 4.7 illustrates that the SNR depends on the considered position within the fringe, and is roughly proportional to  $1/\text{Range}$ , what is a consequence of the signal  $N_{sig}$  decreasing with  $1/R^2$ , and  $SNR = \sqrt{N_{sig}}$  in the shot noise limit. For  $h = 1$  km the dependence is  $1/R^{1.25}$ , what can be explained with additional extinction from aerosols.

For all four laser types (see Tab. 4.1), resulting standard deviations of the determined radial wind speeds  $\sigma(u_r)$  of fifty simulation runs are determined. Without averaging a multitude of pulses,  $\sigma(u_r)$  is higher than one m/s, even for the high pulse energies of WALES/DELICAT. Therefore, within each simulation run the signals are averaged for a time span of 0.1 s (“mean evaluation”, ME). Thus, different numbers of pulses are averaged, depending on the laser type. Here, the assumption is made, that every laser pulse produces a new set of uncorrelated speckle patterns. The different simulated scenarios are: 1. with shot noise only (top), 2. with atmospheric speckle (middle), and 3. with fiber speckle, jitter, and cross-talk for  $R_f = 48$  (bottom), and are shown in Fig. 4.8 for two atmospheric situations equivalent to cruise flight (UTLS,  $h = 10$  km,  $R_b = 1.006$ , left) and approach (boundary layer,  $h = 1$  km,  $R_b = 6$ , right).

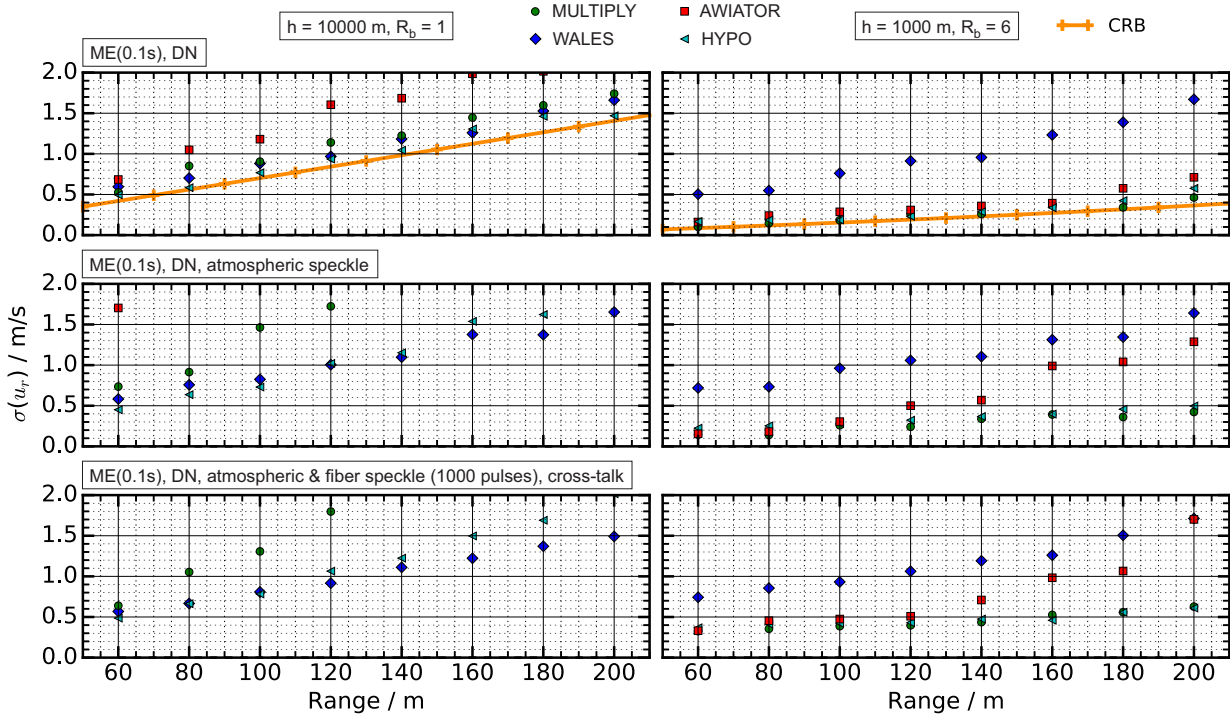


**Figure 4.8:** Results of the end-to-end simulation: The standard deviation  $\sigma(u_r)$  of the determined wind speed  $u_r$  as a function of range  $R$  for the transmitters “WALES / DELICAT”, “MULTIPLY”, “AWIATOR”, and “HYPO” (see Tab. 4.1) in case of weak backscattering signal ( $h = 10 \text{ km}$ ,  $R_b = 1$ ) and strong backscattering signal ( $h = 1000 \text{ m}$ ,  $R_b = 6$ ). The CRB calculated with eq. C.30 of appendix C.3 is shown for comparison (orange line). The results are taken from [Herbst and Vrancken \(2016\)](#).

With shot noise only, the standard deviation  $\sigma(u_r)$  increases linearly approximately (in the limits of the possible for fifty simulation realizations).  $\sigma(u_r)$  is in accordance with the calculation of the Cramér-Rao bound (CRB), using eq. C.30, whereby  $N_{tot}$  is the total number of received photons during the ME time span of 0.1 s (being independent of the transmitter type), including a receiver overall efficiency  $\eta$  of 2.7% (orange lines in Fig. 4.8).

For  $h = 1 \text{ km}$ ,  $R_b = 6$  the SNR is elevated, and therefore lower values of  $\sigma(u_r)$  are achieved in case of MULTIPLY, AWIATOR, and HYPO. In case of WALES the signal damping must be so strong that  $\sigma(u_r)$  is bigger. However, a small decrease of  $\sigma(u_r)$  is observed, what is probably due to the increased atmospheric contrast (see eq. 3.4).

When modeled atmospheric speckle are included, the following trends can be observed. For WALES and HYPO,  $\sigma(u_r)$  is below 1 m/s up to ranges of about 120 m. HYPO performs better mostly because the digital averaging allows more pulses during 0.1 s, while the SNR is better than for MULTIPLY and AWIATOR. HYPO seems to be closer to an optimal combination of pulse energy and repetition rate for averaging out detector and speckle noise than WALES.

At low signal strengths, the SNR per pulse of MULTIPLY and AWIATOR is very small, increasing  $\sigma(u_r)$  for these two transmitters. Especially when speckle noise is considered, these low values of SNR seem to reduce the measurement performance. Averaging in the presence of speckle seems to be less effective, requiring higher signal-to-noise ratios.

At high signal strengths, MULTIPLY and AWIATOR profit from higher SNR values for each pulse and from a higher number of pulses for averaging during measurement intervals of 0.1 s, such that WALES is outperformed ([Herbst and Vrancken, 2016](#)).

Fiber speckle are averaged out (see lower plots of Fig. 4.8) during time periods of 1000 pulses for every transmitter type.  $\sigma(u_r)$  seems not to be elevated in comparison to the case where only atmospheric speckle are considered. The assumed  $R_f = 48$  is a pessimistic approximation of the free-beam illumination case (i.e.,  $R_f \approx 65$  in case of atmospheric speckle as simulated in Fig. C.2(a)).

For  $R_f = 480$  (fiber-coupled case with  $D_{core} = 600 \mu\text{m}$ ) atmospheric speckle and fiber speckle may be spatially averaged out more efficiently, yielding shorter required time periods for the averaging (see appendix C.8, Fig. C.23).

Fig. 4.8 illustrates, that especially for strong signal situations it is advantageous to have higher repetition rate transmitters (e.g., “HYPO”), allowing for more effective averaging of detector noise (and speckle noise) during ME averaging, and for lower detector currents per pulse. When the combined performance at  $h = 10 \text{ km}$ ;  $R_b = 1$  and  $h = 1 \text{ km}$ ,  $R_b = 6$  is considered, “HYPO” appears to be the best choice within the considered transmitter types (*Herbst and Vrancken, 2016*).

A possible candidate for the high power UV pulsed transmitter are thin disc lasers, first experimented with in the early 1990s (*Giesen et al., 1994*), which are currently used in industrial material processing (*Speiser, 2016*) and are in particular developed at DLR. Thin disc lasers can have short pulses below 10 ns independent of the pulse repetition rate (up to 200 kHz), with fundamental mode beam quality, with output powers  $>20 \text{ W}$  at 343 nm, for instance (*Joosten et al., 2014*). Frequency stability comparable to the WALES/DELICAT transmitter would have to be ensured.

In Fig. C.19(a) of appendix C.8 the number of illuminated pixels ( $N_{pixel}$ ) of the linear detector is varied. The resulting values of  $\sigma(e)$  of the horizontal end-to-end simulations suggest that  $\sigma(e)$  is increasing for  $N_{pixel} < 12$ . It seems that lower values of  $V_{pix} = \text{sinc}(1/N_{pixel})$  at low  $N_{pixel}$  affect the result in a way similar to CRB calculations using eq. C.30 with  $V = V_{pix}$ . The end-to-end simulations are performed assuming a pitch loss factor of the PMTA depending on  $N_{pixel}$  (see eq. F.2 and Fig. C.19(b)). These results confirm that  $N_{pixel} = 12$  is a good choice.

Further studies exploring lidar system scaling for LoS update rates of 100 Hz (as possibly needed for wake vortex alleviation control (*Schwithal, 2017*), see appendix B.2) are provided in section 4.6.

This section was dedicated to the simulation of horizontal wind speed measurements considering shot noise and speckle noise. Different laser transmitter types were compared, yielding that temporal averaging in combination with the transmitter “HYPO” prospects best performance on all altitudes. Effects such as laser beam pointing fluctuations and illumination function variations were not considered. These phenomena are studied in the following sections.

## 4.3 Estimation of the random error due to laser beam pointing fluctuations

This section provides an estimation of the random wind speed error introduced by laser beam pointing fluctuations (see appendix I), in the case that a fiber-coupled setup (see Fig. 3.17) with a scrambling fiber (SQ, 10 m long 600  $\mu\text{m}$ -quadratic-core fiber, as studied in section 3.5.5) is employed.

This estimation consists of the following steps. 1. The raytracing model of the front-end



receiver (Fig. D.1 in appendix D.1) is used to estimate the equivalent lateral shifts of the backscattered light when coupling into the scrambling fiber for a range of laser beam tilt angles. 2. These lateral shifts are set in the experimental setup to determine the changes of the illumination function. 3. These changes of the illumination function are input into an end-to-end simulation.

Fig. D.6(a) and (b) in appendix D.1 illustrate that the lateral positional shift on the entrance surface of the fiber is in the order of 10  $\mu\text{m}$  for a tilt of 50  $\mu\text{rad}$ , and that the change of the mean incident angle on the fiber is below 1.8 mrad.

These estimated lateral shifts are set in the test setup. The test setup is similar to the scrambling gain measurement setup (see section 3.5.5), except that the near-field of the scrambling fiber is connected to the assembled receiver, whereby the PMTA is exchanged for a CMOS camera (as shown in Fig. 3.17). The fiber is illuminated with the UV-LED (broad source with respect to the FWFIMI) and a 2D illumination function (exemplary image in Fig. 4.9) is recorded for every position of the fiber. The translational precision  $\Delta x$  of the x-, y-, z-stage is multiples of 0.8  $\mu\text{m}$ . The small changes of the angles of incidence of 1.8 mrad cannot be set in this setup and are considered to be negligible here.

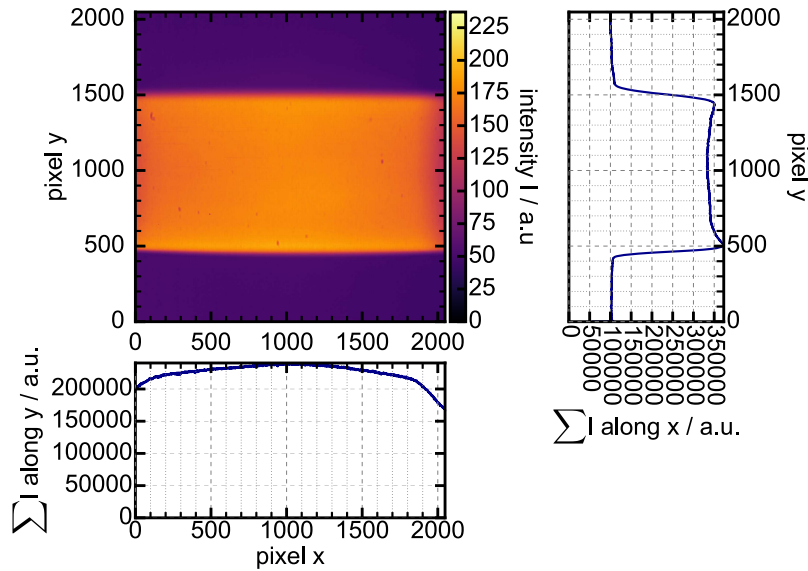


**Figure 4.9:** Exemplary 2D illumination function (image taken with the CMOS-camera) with the xyz-stage at location (0,0,0) of the focused UV-LED with respect to the fiber core center.

The illumination function deviations are introduced in the end-to-end simulation to estimate the random error due to laser beam tilt variations damped by the scrambling of the fiber (fiber A, SQ, see Tab. F.3). For this purpose a measured laser reference PMTA illumination function is multiplied with the downsampled fringe distributions of laser reference and atmospheric signal (without detector noise) and the change of the illumination function is modeled by multiplication of this PMTA illumination function with the measured fractional deviations of the 2D illumination functions recorded with the CMOS camera, which are summed along y, and downsampled (see Fig 4.10(a)).

In the next step, the altered fringe distributions are divided by the original PMTA illumination function (without the deviations). The modified fringe distributions are then employed in end-to-end simulations as described in section 4.1.

Fig. 4.10(b) shows the resulting error  $e$  between the simulated and the determined wind speeds of the laser beam tilt bias estimation simulations employing the DSA method. In



case of the GCA and CM method similar wind speed independent random errors plus the slope biases (described in section 4.1) are obtained.

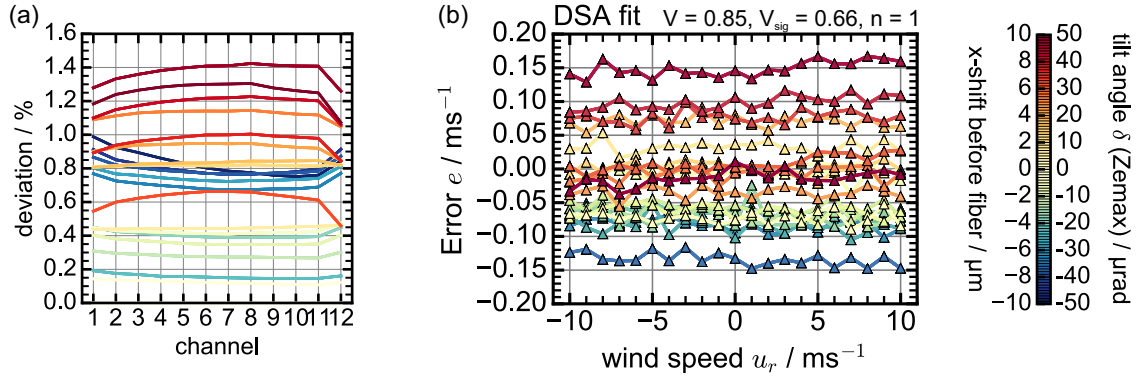


**Figure 4.10:** Laser beam pointing random error estimation using the measured deviations of the illumination function modifying the fringe shape for various laser beam tilt angles  $\delta$ . (a) Down-sampled CMOS images summed along y-direction to simulate the 1D illumination function of the PMT-array, given as deviations from the original image at (0,0,0) (see Fig. 4.9) for various x-positions ( $\pm 10 \mu\text{m}$  with  $\Delta x = 0.8 \mu\text{m}$  given by the positional accuracy of the xyz-stage). (b) Results using Downhill Simplex fitting (DSA). The error due to tilts of the laser beam is visible as a horizontal offset smaller  $0.15 \text{ m/s}$  for  $\delta < 50 \mu\text{rad}$ .

In case of the fiber-coupled setup with the SQ fiber the estimated random error is about  $0.05 \text{ m/s}$  for a random tilt of  $10 \mu\text{rad}$  and about  $0.15 \text{ m/s}$  for  $50 \mu\text{rad}$  ( $3\sigma$  of laser beam pointing fluctuation, see Fig. I.2 in appendix I).

The above results may be interpreted with respect to laser beam pointing induced random errors of other instruments. In a free-beam setup a tilt of  $1 \mu\text{rad}$  would shift the illumination function at the detector plane by  $\approx 6 \mu\text{m}$ , i.e.,  $\approx 0.9 \text{ m/s}$ . Airborne instruments like the ALADIN Airborne Demonstrator (A2D) where measurements are based on the double edge technique are comparably sensitive with an estimated bias of  $0.4 \text{ m/s}$  if the unconsidered noise of the alignment angle is in the order of  $1 \mu\text{rad}$  (Reitebuch, 2016; Lux et al., 2018).

Considering the measured beam pointing variation of  $50 \mu\text{rad}$  ( $3\sigma$ ) in appendix I, the above estimated fluctuating bias (of  $\pm 0.15 \text{ m/s}$ ) has to be considered as additional random measurement noise. A possible means of reducing this estimated random error further would be the usage of different fibers with higher scrambling gains (e.g., different polygonal shapes and fiber combinations (Halverson et al., 2015)) or applying a free-beam optical scrambler, like a two-lens optical scrambler (see, e.g., Hunter and Ramsey (1992)), used by Bruneau et al. (2015), e.g. Meanwhile, such a system, even if properly designed and aligned, adds additional losses. Appendix D.4 contains a raytracing design of a two-lens optical scrambler adapted for illumination (in and out) with  $600\text{-}\mu\text{m}$ -core fibers.

## 4.4 Estimation of biases due to illumination function deviations

In this section an estimation of the bias due to either an erroneous measurement of the illumination function or due to a long-term change of the illumination function is performed. For this purpose pseudo-ideal illumination functions of backscattered signal and laser reference are defined (“sig” and “ref” selected in Fig. 4.11(a), taken from real measurements

of section 5). Measured or changed illumination functions are then simulated as these pseudo-ideal ones plus Gaussian noise of standard deviation  $\sigma_{illum}$  (given as a fraction of the pixel value of the normalized pseudo-ideal illumination function). Simulated fringes of “true-cosine” shape are multiplied with the ideal illumination functions. Then, these fringes are corrected with the simulated (modified) illumination functions. Detection and speckle noise are neglected. One hundred simulation runs are carried out for each value of  $\sigma_{illum}$ . Furthermore, the maximum of the fringe is positioned in the middle of the PMTA.

Exemplary laser reference and atmospheric signal illumination functions are shown in Fig. 4.11(a) for  $\sigma_{illum} = 0.03$ . The mean and standard deviations of the simulated illumination functions are indicated by error bars. Illumination functions of an exemplary simulation run are shown as dashed lines. For every simulation run an offset error (bias)  $e$  between the simulated and the determined wind speeds using the GCA, DSA and CM method is obtained for a range of simulated wind speeds from -10 m/s to +10 m/s.

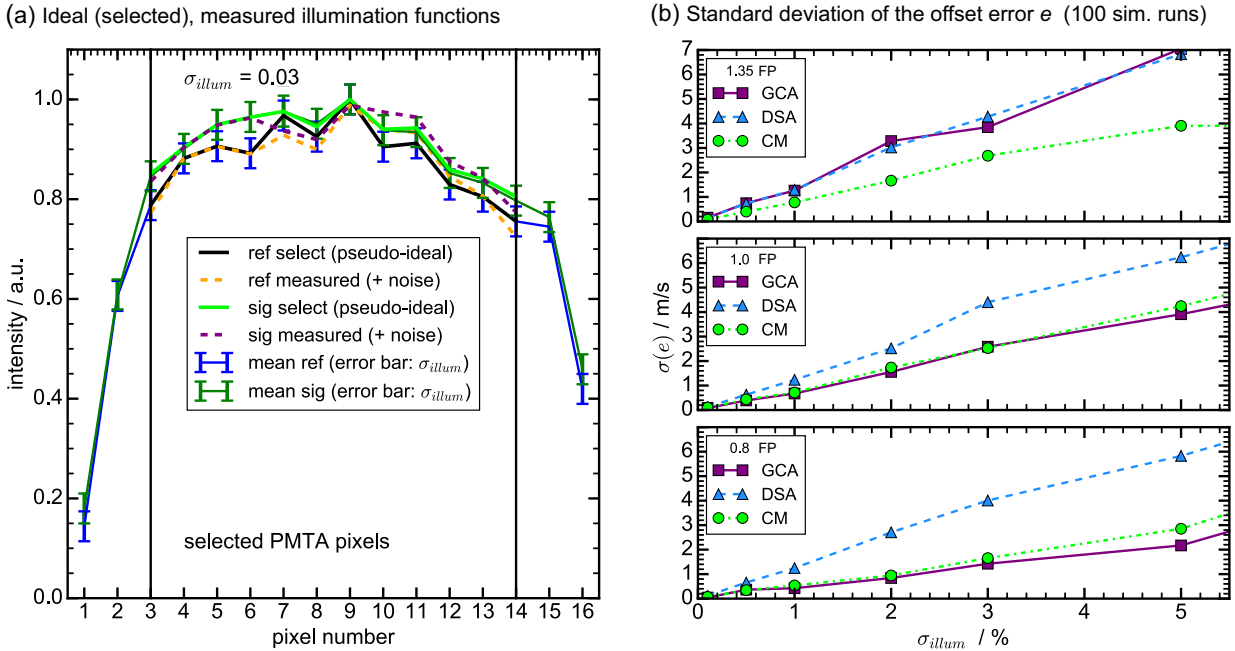


**Figure 4.11:** (a) Exemplary illumination functions: One time measured illumination functions represent pseudo-ideal ones. 12 pixels are selected for the simulation. Changed illumination functions are generated by adding Gaussian noise with a standard deviation  $\sigma_{illum}$  of the respective pixel value. (b) For 1.35 FP, 1.0 FP, and 0.8 FP (fringe periods) imaged on 12 pixels: Standard deviation  $\sigma(e)$  of the bias between the simulated and the determined wind speed  $u_r$  as a function of the standard deviation of the Gaussian noise ( $\sigma_{illum}$ ) added on the reference and signal pseudo-ideal illumination functions.

The dependence of the offset error  $e$  on the simulated wind speed is shown in Fig. 4.12(a) in case of  $\sigma_{illum} = 0.01$  for five different simulation runs (colored lines). The mean error  $e$  and its standard deviation  $\sigma(e)$  are indicated by black symbols and error bars.

Fig. 4.12(a) shows that the offset  $e$  may be dependent on the simulated wind speed  $u_r$  for a certain noise representation of the illumination function. The absolute value of the slope  $\Delta e / (20 \text{ m/s})$  of this dependence is distributed differently for different values of  $\sigma_{illum}$  as is shown in Fig. 4.12(b). This slope bias increases with  $\sigma_{illum}$ .

The standard deviation  $\sigma(e)$  of the mean offset biases  $e$  of the 100 simulation runs (see black error bars in Fig. 4.12(a)) is constant in the simulated wind speed range.

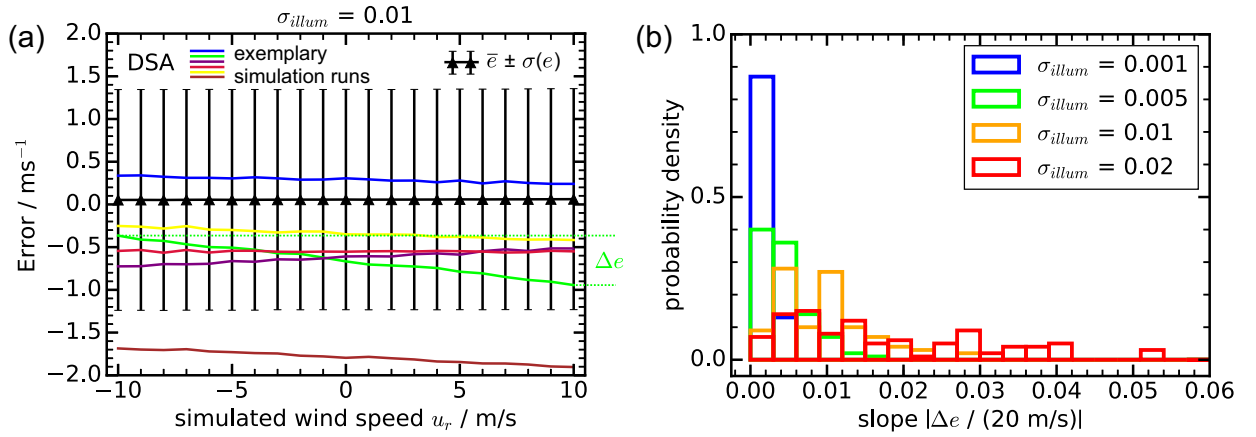


**Figure 4.12:** (a) Resulting error  $e$  as a function of the simulated wind speed  $u_r$  for exemplary simulation runs (different colors) in case of noise of the illumination function with  $\sigma_{\text{illum}} = 0.01$ . The mean error  $\bar{e}$  and its standard deviation  $\sigma(e)$  of all 100 simulation runs are indicated by black triangles and error bars. (b) Distribution of the absolute value of the slope  $\Delta e / (20 \text{ m/s})$  for different values of  $\sigma_{\text{illum}}$ .

This standard deviation of the constant offset bias for 100 realizations of Gaussian noise ( $\sigma(e)$ ) is shown in Fig. 4.11(b) as a function of  $\sigma_{\text{illum}}$  for the cases that 1.35 fringe periods (FP), 1.0 FP, and 0.8 FP are imaged on 12 pixels of the PMTA.

The standard deviation of the offset bias of the 100 simulation runs increases linearly for GCA, DSA, and CM methods. For one fringe period (FP) imaged on the 12 pixels (see Fig. 4.11(b) middle) values of  $\sigma(e) < 1 \text{ m/s}$  are only obtained for values of  $\sigma_{\text{illum}} < 1\%$  in case of DSA. Similar results are obtained for  $\text{FP} = 1.35$  and  $\text{FP} = 0.8$ . Except for  $\text{FP} = 1.35$  both the GCA method and the CM method show smaller values of  $\sigma(e)$  at the same  $\sigma_{\text{illum}}$  and a lower steepness of increase of  $\sigma(e)$  with  $\sigma_{\text{illum}}$  than the DSA method.

Seemingly, local alterations of the fringe shape (as introduced by the Gaussian noise of the illumination functions) have less influence on the outcome of the GCA and of the CM method. A possible explanation could be that both GCA and CM are more related to finding the maximum of the fringe than fitting the whole fringe profile (as in case of the DSA method). Nevertheless, both GCA and CM are biased with respect to the absolute fringe position (see slope bias in section 4.1) limiting their applicability compared to the DSA method.

The above results stress the need to accurately determine the illumination functions of both the laser reference and the atmospheric signal during repeated calibration runs in order to avoid the above biases. Moreover, the illumination function should be stable between these calibrations with comparable accuracy.

The accuracy of the illumination function determination and the stability should be on the order of 0.5% per illuminated pixel to limit the resulting offset bias ( $\sigma(e) < 0.6 \text{ m/s}$ ) and the mean of the slope bias ( $\Delta e / (20 \text{ m/s}) < 0.005$ ).

## 4.5 End-to-end simulation of vertical measurements with comparisons to CRB calculations and field-test measurements

This section provides end-to-end simulations of vertical, range-resolved, ground-based wind speed measurements and a comparison with CRB calculations, and with the measurement results presented in section 5.3.3.

A range gate length  $\Delta R = 30$  m, a mid-latitude standard atmospheric model (see Fig. 2.1, with  $h = 0$  equivalent to sea level), a realistic total AEROLI receiver efficiency of 2.7% (see Tab. F.4 in appendix F), and full overlap at all ranges are assumed.

Fig. 4.13 shows a comparison of end-to-end simulations and CRB calculations (using eq. C.30), for altitudes up to 900 m, for a LoS update rate  $r_{LoS}$  of 1 Hz, a solar background radiance of  $P_{RadAtm} = 300$  W/(m<sup>2</sup> sr  $\mu$ m) assuming a sunlight interference filter (see Tab. 3.2, eq. 4.3) is applied, and for different assumed concentrations of aerosols. The transmitter parameters in the simulation are adjusted to be similar to the parameters during vertical field-test measurements (see section 5.3.3), i.e.,  $E_L = 48$  mJ,  $R_L = 100$  Hz,  $P_L = 4.8$  W.

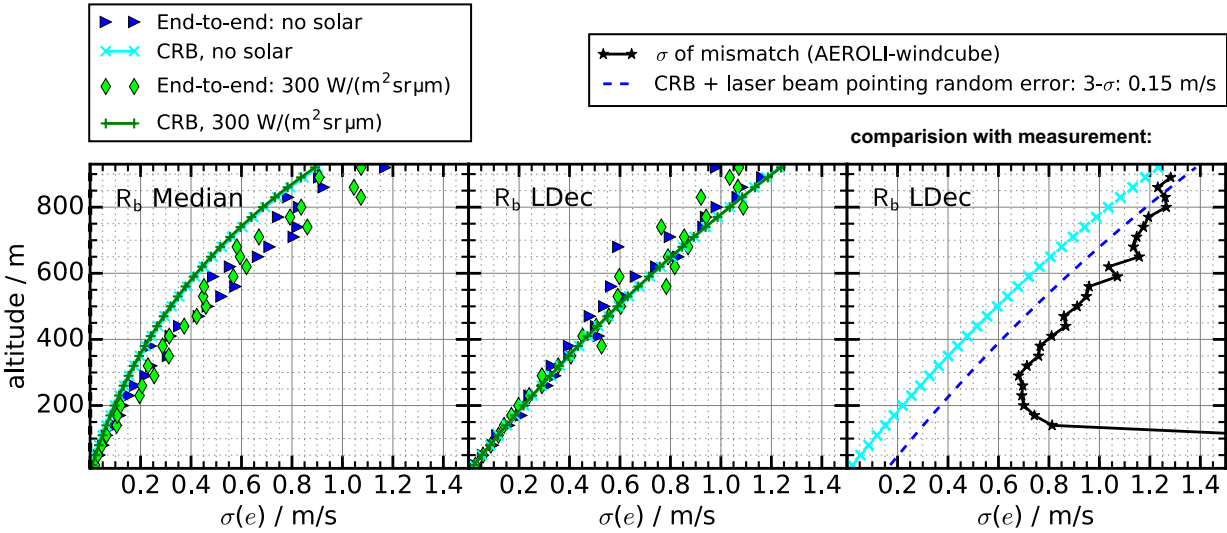


**Figure 4.13:** Comparison of vertical end-to-end simulations with standard deviation  $\sigma(e)$  of the error  $e$  between simulated and determined wind speed  $u_r$ , using the DSA method in 50 simulation runs, with the CRB calculation using eq. C.25 and eq. C.30 for a LoS update rate ( $r_{LoS}$ ) of 1 Hz, and a solar background radiance of 300 W/(m<sup>2</sup> sr  $\mu$ m). Left: Median values of the particle backscattering ratio ( $R_b$ ) applied in end-to-end simulations and CRB calculations. Middle: Lower decile of  $R_b$ . Right: Comparison of vertical measurements (see section 5.3.3), i.e., with the standard deviation ( $\sigma$ ) of the mismatch  $e$  between the AEROLI DWL receiver and the Leosphere Windcube 200s (black stars). The total random error with added random error due to unexpected laser beam pointing variation (see section 4.3) is shown as dotted blue line.

In case of median values of  $R_b$  a mismatch by a factor of  $1/\sqrt{2}$  exists between the (vertical) end-to-end simulation results and the CRB calculation.

Higher values of  $R_b$  at low altitudes reduce the standard deviation and together with extinction introduce deviations from expected linear behavior ( $\sigma(u_r) \propto R$ ). When only the lower decile of  $R_b$  is considered (Fig. 4.13 middle) linear behavior is visible.

In case of lower decile values of  $R_b$  there is good accordance between the results of the end-to-end simulation and the CRB calculation (Fig. 4.13 middle).

A solar background radiance of  $300 \text{ W}/(\text{m}^2 \text{ sr } \mu\text{m})$  ([Hirschberger, 2013](#)) does not influence the result (see Fig. 4.13(a)), because the ratio of detected backscattered signal photons to solar background photons is large, i.e.,  $N_{tot}/B_{tot} \approx 20$  at an altitude of 900 m, due to the application of the interference filter (see eq. 4.3). Realistic values of the downward diffuse radiance obtained by a 1-D UV radiative transfer model based on the Matrix Operator Method (see e.g., [Meerkötter and Degünther \(2001\)](#)) are on the order of  $50 \text{ W}/(\text{m}^2 \text{ sr } \mu\text{m})$  for a ground-based vertical LoS at a zenith angle of zero (sun zenith angle  $54^\circ$ , clear sky) and about  $140 \text{ W}/(\text{m}^2 \text{ sr } \mu\text{m})$  for a horizontal LoS at an altitude of 10 km (clear sky) at a wavelength of 355 nm ([Meerkötter, 2018](#)). Thus, the influence of solar background shot noise is negligible.

For comparison the standard deviation  $\sigma$  of the difference  $e$  between the AEROLI receiver measurements and the reference measurement made with a Windcube<sup>®</sup> 200S (see 5.3.3) is plotted (black stars). These measurements show a linear dependence on range (for altitudes above 300 m), as well. The estimated random error caused by laser beam pointing fluctuations (see section 4.3) is added to the CRB and the total random error is marked by a blue dashed line in Fig. 4.13. Further reasons for still existing deviations between the end-to-end simulation, the CRB calculation, and the measured standard deviations are discussed in sections 5.3.3 and 5.4.

The good accordance between end-to-end simulation and CRB calculation in case of lower decile values of  $R_b$  justifies an approach where CRB calculations are used to estimate the prospective performance of scaled lidar systems for improved performance.

## 4.6 Lidar system scaling for improved performance

This section is dedicated to plausible transmitter and receiver improvements for measurements at cruise flight altitudes, and for line-of-sight wind speed update rates ( $r_{LoS}$ ) of 100 Hz, possibly required for wake vortex alleviation and control ([Schwithal, 2017](#)).

Here a system parameter describing both the transmitter and the receiver, the Power-Aperture-Efficiency-Product ( $PAE$ ), is introduced:

$$PAE = P_L \cdot A_{tel} \cdot \eta, \quad (4.4)$$

where  $P_L$  is the transmitter optical power,  $A_{tel}$  is the opening area of the telescope, and  $\eta$  is the efficiency of the receiver. Realistic values for the AEROLI DWL are  $P_L = 8 \text{ W}$  (WALES/DELICAT, see section 3.6),  $A_{tel} = 13.5 \cdot 10^{-3} \text{ m}^2$  (opening diameter of 14 cm),  $\eta = 2.7\%$  (see Tab. F.4 in appendix F), and thus  $PAE = 3 \cdot 10^{-3} \text{ Wm}^2$ .

Altitude- and range-dependent Cramér-Rao bounds (CRB) for different values of  $PAE$  are calculated using eq. C.30 with an instrumental contrast  $V = 0.95$ , assuming lower decile values of  $R_b$ , using the atmospheric model provided in section 2.1.1 (Fig. 2.1) and the lidar equation (eq. 2.2). End-to-end simulations are carried out for comparison as described in section 4.2 assuming that speckle noise is completely suppressed.

A comparison of end-to-end simulations and CRB calculations for the exemplary case of  $PAE = 3 \cdot 10^{-3} \text{ Wm}^2$  is provided in Fig. 4.14(a). The end-to-end simulations consist of 400 simulation runs for every range and altitude, and the standard deviation of the difference



between the simulated wind speed and the determined wind speed ( $\sigma(e)$ ) using the DSA method is determined.

The slope of the standard deviation of the determined (estimated) wind speed (i.e., of the CRB) as a function of range  $R$  increases for higher altitudes, because the density of air and the concentration of aerosols are lower. Especially at cruise flight altitudes higher than 10 km, a  $PAE$  of  $3 \cdot 10^{-3} \text{ Wm}^2$  is not sufficient for several longitudinal measurement points with standard deviations below 1 m/s at a LoS update rate ( $r_{Los}$ ) of 100 Hz.

The results of the end-to-end simulation and the CRB calculations are matching to a high degree. The CRB calculation is very fast compared to the end-to-end simulation. That is why for lidar system scaling solely CRB calculations are applied. The  $PAE$  is increased stepwise and the CRB and its slope  $CRB/R$  are evaluated.

Fig. 4.14(b) shows the dependance of the CRB on the range  $R$  at an altitude of 10 km for hypothetical increased values of  $PAE$ , as obtained for example by higher receiver efficiencies  $\eta$ . The slope  $CRB/R$  is lower for higher values of  $PAE$ .

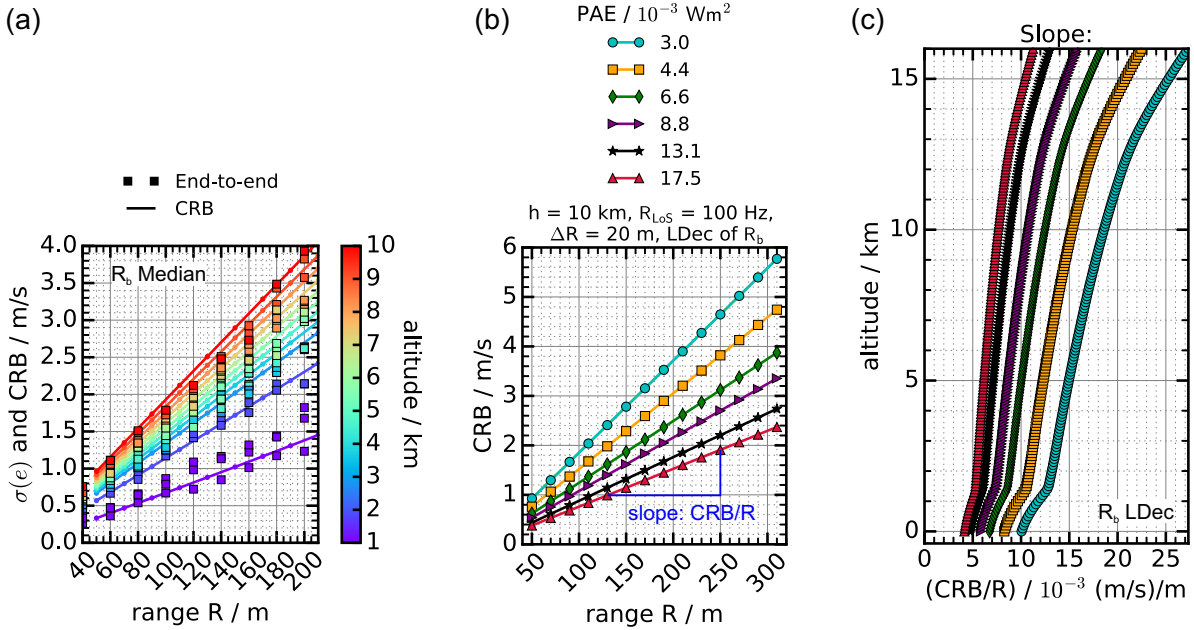


**Figure 4.14:** Calculation of CRBs of a FWFIMI with different Power-Aperture-Efficiency-Products ( $PAE$ ) with a range gate length  $\Delta R$  of 20 m, lower decile values of  $R_b$ , assuming a LoS update rate ( $r_{Los}$ ) of 100 Hz as needed for wake vortex alleviation, using eq. C.30. (a) Comparison of end-to-end simulations and CRB calculations of horizontal wind speed measurements at different altitudes. (b) Linear dependence of Cramér-Rao bounds (CRB) for different values of  $PAE$  at an altitude of 10 km. (c) Slope  $CRB/R$  as a function of altitude. The slope parameter  $CRB/R$  is shown for different values of the  $PAE$  (see legend of (b)).

Fig. 4.14(c) shows calculated slopes  $CRB/R$  for different values of  $PAE$  as a function of altitude. The slope decreases for higher  $PAE$  and increases for higher altitudes.

A  $PAE$  of  $8.8 \cdot 10^{-3} \text{ Wm}^2$ , i.e.,  $\eta = 8\%$  would suffice to obtain CRB values  $< 1 \text{ m/s}$  up to altitudes of 10 km for the first three ranges at a  $r_{Los}$  of 100 Hz. All three parameters of eq. 4.4 may be increased to achieve this threefold increase of the  $PAE$ .

In terms of power consumption and eye-safety higher laser powers are however problematic. Laser transmitters with higher repetition rates such as disc lasers may be employed.

Higher receiver efficiencies ( $\eta > 2.7\%$ ) may be realized by applying HR-coatings (e.g., on the primary telescope mirror), by improving the transmission in the fiber components



(scrambling) part of the receiver, by installing the FWFIMI in the tilted two-channel configuration ( $PAE = 6 \cdot 10^{-3} \text{ Wm}^2$ , doubled efficiency because the reflected interference pattern can be analyzed, see appendix D.3), or by using a hexagonal beamsplitter (doubled efficiency because unpolarized light can be used at the input of the interferometer as discussed in section 3.4.3).

The telescope aperture could be increased from 14 cm to 20 cm providing a  $PAE$  of  $6 \cdot 10^{-3} \text{ Wm}^2$ . However, the larger the aperture the bigger are the windows, mirrors, and scanner optics required, limiting the practicability of this approach aboard an aircraft.

The performance of such a scaled lidar system will not be impaired by atmospheric speckle noise (see section 4.1), provided that the ratio  $R_f$  and thereby the speckle SNR is high enough. This is shown by performing end-to-end simulations with  $R_f = 480$ . The resulting values of  $\sigma(e)$  for  $SNR_{sp}(atm) \approx 700$  and  $SNR_{sp}(ref) \approx 116$  (speckle ON) are compared in Fig. C.23 of appendix C.8 to results without speckle (OFF) for a LoS update rate of 100 Hz (WALES/DELICAT transmitter,  $PAE = 3 \cdot 10^{-3} \text{ Wm}^2$ ), assuming  $R_b = 8.5$  (upper decile) at  $h = 10$  m (ground level). It is assumed that every pulse creates a new uncorrelated speckle pattern and no temporal averaging is done ( $r_{LoS} = 100$  Hz). In this case no increase of  $\sigma(e)$  due to atmospheric speckle alone is observable. If the laser reference signal is averaged over 100 pulses  $\sigma(e)$  is reduced to the shot-noise-limited value.

The general conclusion is that DWL system scaling for improved system performance is possible by increasing the Power-Aperture-Efficiency-Product ( $PAE$ ). The value of  $PAE$  should be at least tripled in order to have at least three measurement points with  $\sigma(e)$  below 1 m/s on cruise-flight altitudes. The most feasible way to achieve this may be by increasing the AEROLI DWL receiver efficiency. Speckle may be averaged spatially in a scaled lidar system by using a multimode fiber with an  $R_f$  value of approximately 480 and with temporal averaging of the reference signal (see section 4.1 and section 3.5.4).

Within chapter 4 the prospective performance of a direct-detection DWL based on the FIMI technique was estimated, using a large variety of assumptions and models. The development of these models helped to improve the understanding of the measurement principle, providing guidelines and support for the receiver prototype design and improvement. An estimation of the systematic errors of mean wavelength estimators yielded that a fit with a cosine-shaped fit model minimizes these errors. The otherwise shot-noise limited detection process may however be aggravated by speckle noise, by cross-talk, by ADC-quantization, by laser beam pointing fluctuations, and inaccurate illumination function correction or temporal changes of the illumination function. A 600  $\mu\text{m}$  quadratic-core multimode fiber is shown to increase accuracy and precision, being otherwise more severely degraded due to speckle noise, due to laser beam pointing fluctuations, and due to illumination function variations. To conclude, the end-to-end simulations predict that the FIMI technique allows to measure wind speeds on all altitudes in the near-range in front of an aircraft, provided that these sources of random errors and biases are minimized. Performance may be increased to meet the requirements for wake vortex and turbulence alleviation control by a larger power-aperture-efficiency-product of the DWL. This may be achieved by an increase of the receiver efficiency.

The aim of the following chapter is to verify this prospective wind speed measurement performance of the AEROLI DWL prototype by performing first ground-based validation measurements of the FIMI technique.



## 5 Field-tests of the lidar receiver on the ground

Ground-based field-measurements with the DWL prototype AEROLI were carried out in January 2018 and March 2018. In section 5.1 important settings of AEROLI and the measurement setup are described. The development of the evaluation algorithm for the determination of the Doppler shift from positional shifts of the fringes are detailed in section 5.2. Section 5.3 provides the AEROLI measurement results of the speed of a moving hard target, of horizontal wind speed measurements, and of vertical wind speed measurements. The measurement results and their implications are discussed in section 5.4.

### 5.1 Doppler wind lidar receiver prototype and measurement setup

The DWL lidar prototype AEROLI is described in section 3.5.3 (see Fig. 3.20). Here special focus is put on summarizing the transmitter and receiver settings during the validation measurements, and on describing the measurement setups.

#### Transmitter and receiver settings

The WALES / DELICAT transmitter (see section 3.6) was adjusted to laser pulse powers of 48 mJ for most of the measurements avoiding saturation of the photomultiplier tubes of the PMTA of the receiver at short ranges. The maximum receiver efficiency of the AEROLI receiver is estimated in appendix F to be approximately 2.7%. The receiver efficiency can be additionally impaired due to incomplete overlap at very short measurement distances below 150 m. During most of the measurements the supply voltage of the photomultiplier tube array is set to the lowest possible voltage (500 V) giving an amplification of  $\approx 3 \cdot 10^4$  and an additional amplification of  $\approx 2000$  due to the transimpedance amplifier (see section 3.5.3). These settings ensure that the PMTA is not saturated.

#### Measurement setup

The test site is located at the DLR Oberpfaffenhofen apron. For horizontal measurements the line-of-sight (LoS) is one meter above the ground with a direction of  $213^\circ$  (southwest), as shown in Fig. 5.1(a). The AEROLI DWL is installed inside a specially equipped measurement container (power and air conditioning, C in Fig. 5.1(b)). The Windcube<sup>®</sup> 200S (Leosphere, France, W in Fig. 5.1(b)) is positioned next to the opened door of the container to allow parallel LoS directions of the two lidars (see Fig. 5.2).

For simulating various speeds of a hard target a belt sander can be installed at a distance of 50 m and test measurements are carried out (see section 5.3.1). The belt sander is mounted with the sandpaper at an angle of  $10^\circ$  with respect to the lidar line-of-sight (see Fig. 5.2, left).

Ultrasonic anemometers (Vaisala WXT520 - Svantek DAQ) are positioned at 50 m and 75 m distance as additional reference instruments for horizontal wind speed measurements.

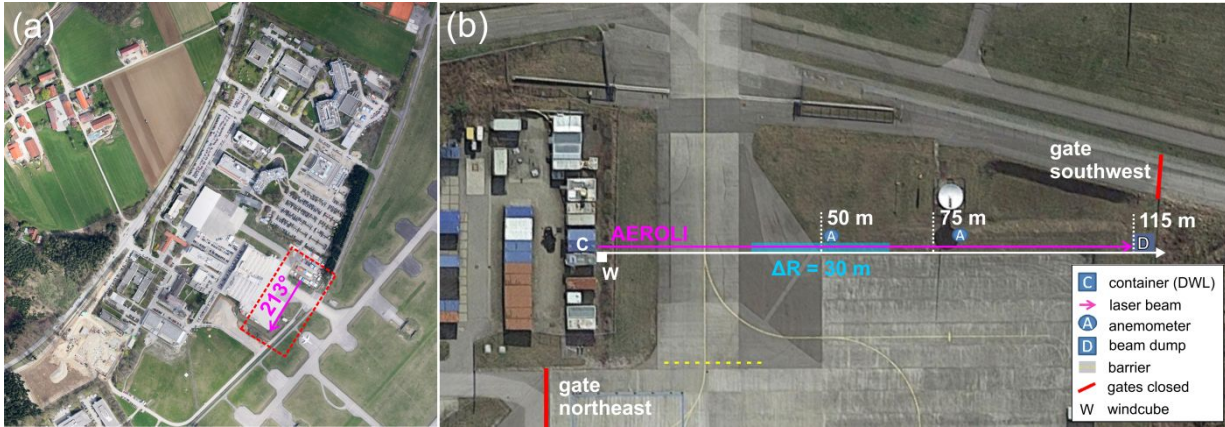


**Figure 5.1:** Test site for ground-based horizontal wind speed measurements with AEROLI and Windcube® 200S (W) at German Aerospace Center (DLR) Oberpfaffenhofen apron.

The high-power eye-harming AEROLI laser beam is directed into a beam dump (D) at a distance of 115 m. The WALES/DELICAT transmitter is operated under the eye-safe distance (nominal ocular hazard distance - NOHD, DIN EN 60825-1). Because some residual scattered light escapes the beam dump, it may be used as hard target reference during measurements, as well. Since the apron is used by various aircraft, security measures and warning signs are installed at the gates (red) and on the runway (yellow dotted line), in addition to temporary closures to these users.

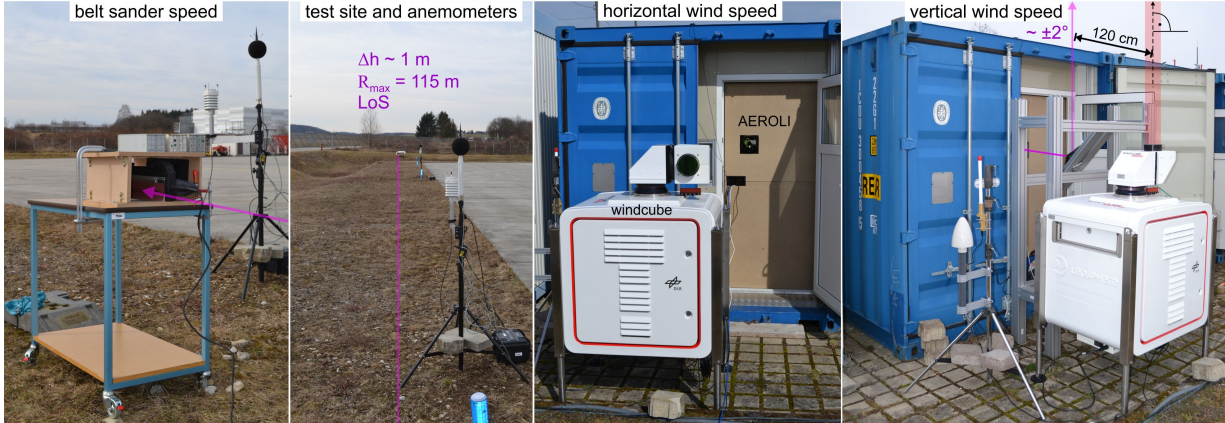


**Figure 5.2:** Photographs of measurement setups for hard target speed measurements, test site with anemometers, Windcube® 200S, and AEROLI for horizontal wind speed measurements and for vertical wind speed measurements.

In vertical configuration a high-power laser coated mirror allowing for the receiver telescope aperture is used at  $45^\circ$  to deflect the AEROLI laser beam (see also mirror  $M_v$  in Fig. 3.20). The vertical misalignment error with respect to the Windcube® vertical LoS is in the order of  $\pm 2^\circ$ . The Windcube® vertical LoS is ensured by the scanner precision and by an aluminum level. Both beams are separated by a distance of 120 cm in this case (see Fig. 5.2 right).

## 5.2 Development of a wind speed retrieval algorithm

### Data acquisition

The DELICAT data acquisition (DAQ) records the laser settings, power, and the signal of the DELICAT-PMT for acquiring the time-dependence of the backscattered signal power. The transmitter DAQ's absolute time may be synchronized to a GPS receiver.

The amplified voltages of each of the 16 PMTA channels are acquired with the receiver DAQ. The receiver DAQ consists of two synchronized digitizer boards (ADC-cards, see appendix F). The digitizer board computer time is synchronized to the transmitter DAQ computer using the network time protocol (NTP). The NTP Meinberg software allows to synchronize the computer times with sub-ms precision.

A timing diagram of the data acquisition of the AEROLI DWL is shown in Fig. 5.3.

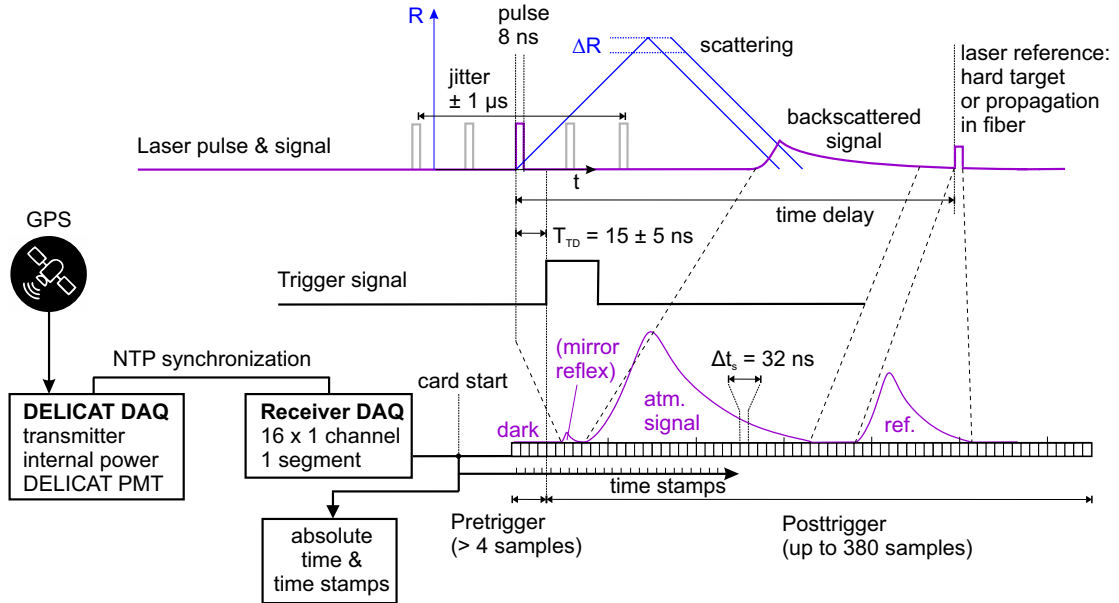


**Figure 5.3:** Timing diagram of the transmitter and receiver data acquisition (DAQ).

The passively Q-switching scheme of the WALES/DELICAT transmitter MOPA laser system entails a timing jitter ( $> 99.9\%$  of shots) of  $\pm 1 \mu\text{s}$ . Backscattered signals and a reference laser pulse either from a hard target or being delayed in a fiber are acquired. The digitizer boards are triggered to the rising edge of the laser pulse departure trigger signal. The trigger delay  $T_{TD}$  of  $15 \pm 5 \text{ ns}$  is the delay from the light pulse to the output connector.

A MATLAB routine is used to control the settings of the ADC-cards (see Tab. F.5) of the receiver, and to save the binary data to hard disc. The routine is built on code provided by Spectrum Instrumentation GmbH, Germany ([Spectrum, 2015](#)). A mode called “rec-std-multi” is used, storing all the data on the cards internal memory, and - after a defined number of acquisitions (segments) - shifting the data to the computer. Each segment is subdivided into a pretrigger region (at least 4 samples), where only dark signal is detected, and a posttrigger region which contains samples of the actual backscattered signal and the laser reference signal (up to 380 samples for vertical wind speed measurements). The maximum temporal resolution  $\Delta t_s$  of one sample is 32 ns, given by the maximum sampling rate of the ADC-cards (see appendix F).



## Evaluation steps

An overview of the steps of the wind speed retrieval algorithm developed in this work is shown in Fig. 5.4.

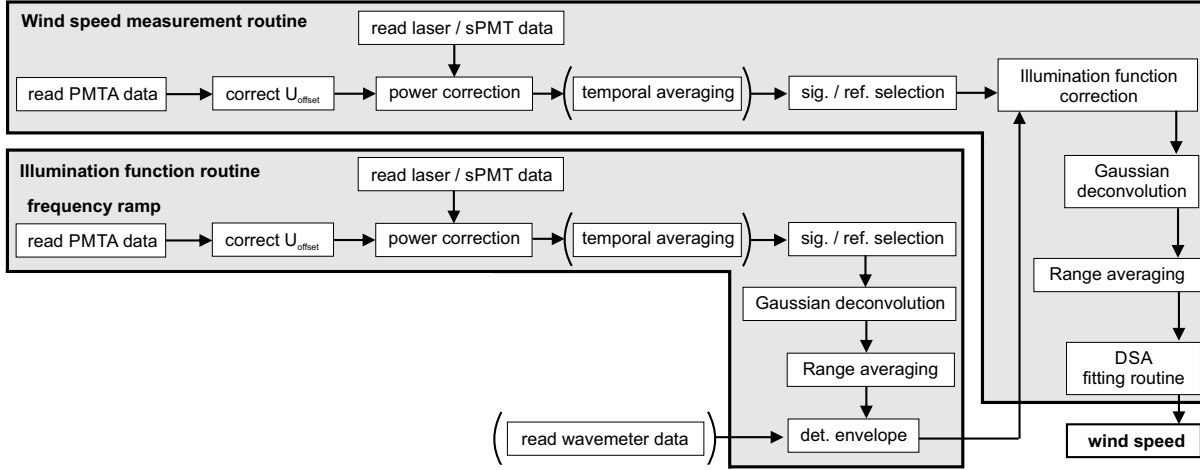


**Figure 5.4:** Steps of the wind speed retrieval algorithm.

The measurement consists of two evaluations: 1. a routine to determine the illumination function of the interferometer, and 2. the wind speed measurement routine with illumination function correction. In the following sections the steps of both routines, i.e., offset voltage correction, power correction, signal-reference selection, Gaussian deconvolution routine, range-averaging, illumination function correction, and the Downhill-Simplex fitting routine are described in detail.

## Offset voltage correction

The first step is to correct each individual channel for its dark offset voltage. The offset voltage varies from channel to channel due to tolerances of the electronic parts, such as the operational amplifiers and resistances.

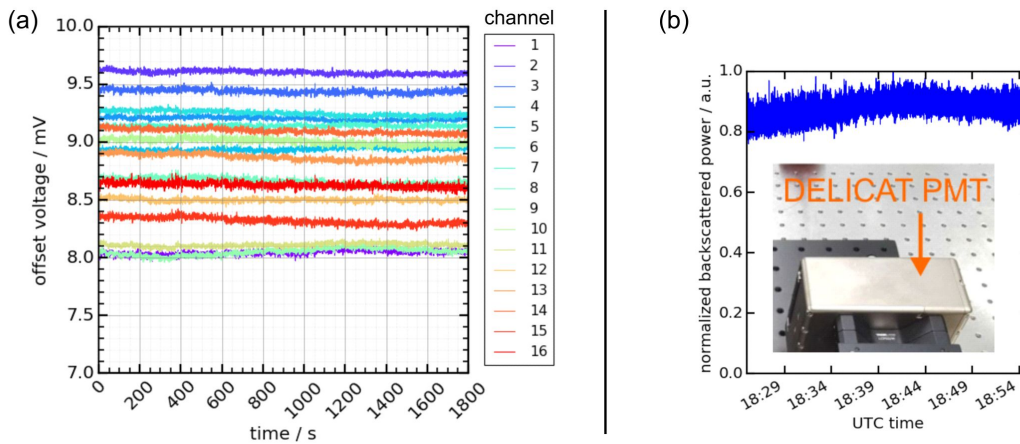


**Figure 5.5:** (a) Offset voltages of PMTA channels prior to correction. (b) Time-dependent, normalized backscattered laser power measured with the DELICAT-PMT.

This offset is temperature-dependent, and therefore difficult to calibrate ([Wirth, 2017a](#)), that is why the offset is determined online for each channel, taking a signal from the



pretrigger region (1. sample) of every pulse, and subtracting it from all subsequent samples. Fig. 5.5(a) shows exemplary offset voltages of the 16 channels of the PMTA during one measurement run.

### Power correction

Each pulse is corrected amplitude-wise by division by a normalized power coefficient. It is determined by using the DELICAT-PMT located in the transmitting ray path of the PBSC in the back-end receiver (see Fig. 3.20). This step is particularly important during the illumination function determination procedure (see section 3.5.6), because otherwise a power variation during a frequency ramp can falsify the determined envelope. The DELICAT-PMT may be however not fully synchronized to the AEROLI PMTA on an individual pulse basis because the applied routine of saving the start time of the receiver acquisition shortly after the start command may be affected by the computation time. Directly obtaining an absolute time reference to an external clock for every time stamp is not possible with the current digitizer hardware configuration. Only long term (time span of more than one second) variations of the laser power are therefore corrected. That is why a pulse-to-pulse variation of the backscattered power as a consequence of aerosol backscatter signal fluctuations, for example due to turbulent aerosol concentration fluctuations or laser beam pointing fluctuations, is not corrected. Fig. 5.5(b) provides the normalized power coefficient measured during one of the measurement runs on January 29, 2018.

### Temporal averaging

This (optional) step involves a summation of consecutive (power-corrected) pulse signals and determines the temporal resolution, i.e. the line-of-sight update rate ( $r_{LoS}$ ) of the AEROLI receiver.

### Gaussian deconvolution routine

This section describes a Gaussian deconvolution routine that allows increasing the spatial resolution of the AEROLI DWL for attributing the range gates to the signals of the AEROLI PMTA with the required range resolution of  $\Delta R = 30$  m.

The deconvolution routine used in this work is similar to the routine proposed for MERLIN (“Methane Remote Sensing LIDAR Mission”) (Wirth, 2017b). The pulse response of a reference laser pulse  $\tau_p = 8$  ns (as presented in section 3.5.3) is shown in Fig. 5.6(a). This pulse response is equivalent to the signal of a passive Q-switch laser pulse with long tail being detected with the PMTA and being amplified with the transimpedance amplifier. This temporally long pulse response is necessary for sufficient sampling (see Fig. 3.26(f)) by the ADC. However, the low bandwidth character of the amplifier spreads the atmospheric signal (response function), as well, reducing the longitudinal resolution (i.e.,  $\Delta R$  increases to  $\approx 100$  m).

In order to decrease this spread of the return signal, and in order to render it symmetric, it can be convolved with an appropriate kernel, such that the resulting response is of reduced width and Gaussian shaped. This procedure is henceforth called Gaussian deconvolution routine (GDR).

According to Wirth (2017b), the kernel has to be chosen, such that 1. the resulting FWHM is close to the required range resolution (in our case  $\approx 30$  m), 2. the temporal fall-

off is fast, 3. the shape is Gaussian, and 4. the frequency space cut-off should be at small frequencies and steep to avoid deterioration of the signal due to amplified high frequency noise.

Here, this can be achieved by deconvolving the response function to a Gaussian of FWHM of 118 ns ( $\Delta R \approx 18$  m). The respective deconvolution kernel  $D_k$  (Fig. 5.6(c)) is found by the inverse Fourier transform of the quotient of the Fourier transform of a Gaussian  $g$  with parameter  $\sigma$  of 50 ns (Fig. 5.6(e)) and the Fourier transform of the pulse response ( $p_r$ ) (Fig. 5.6(b)). The pulse response of the laser reference pulse ( $p_r$ , blue, Fig. 5.6(a)) is then convolved with the deconvolution kernel ( $D_k$ ) to obtain the resulting Gaussian ( $r$ ):

$$r = p_r * D_k = p_r * FFT^{-1} \left( \frac{FFT(g)}{FFT(p_r)} \right) \quad (5.1)$$

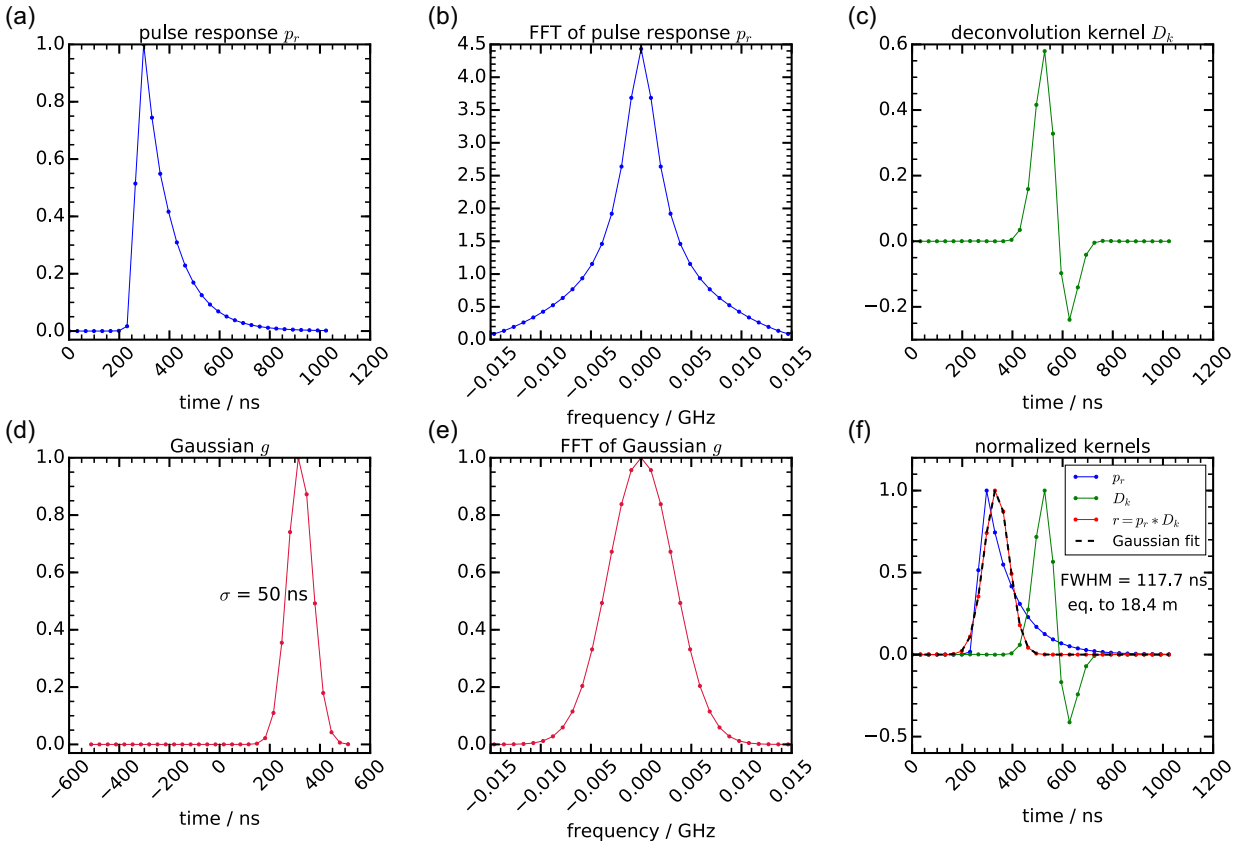


**Figure 5.6:** Gaussian deconvolution procedure. (a) Measured pulse response ( $p_r$ ) of a WALES/DELICAT laser pulse. (b) Fast Fourier transform (FFT) of  $p_r$ . (c) Deconvolution kernel  $D_k$ . (d) Gaussian function ( $g$ ) with  $\sigma = 50$  ns shifted by 320 ns. (e) FFT of  $g$ . (f) Normalized kernels and resulting deconvolved response  $r$  (Gaussian) with a FWHM of 117.7 ns.

The Gaussian  $g$  is shifted by 320 ns (see Fig. 5.6(d)) to make  $p_r$  and the deconvolved response's rising edge overlap (see Fig. 5.6(f)). A Gaussian fit yields a FWHM of the Gaussian  $r$  of 117.7 ns (see black dashed line in Fig. 5.6(f)).

An exemplary range-dependent signal of one of the array's photomultiplier tubes during vertical measurements (see 5.3.3) is shown in Fig. 5.7(a). The deconvolved signal is marked with a dotted line with cross markers.

Further examples of the application of the GDR to atmospheric signals are shown in section 5.3 in Fig. 5.8 and Fig. 5.10.

The Gaussian deconvolution routine thus provides a way to enhance the range resolution ( $\Delta R$ ) of the AEROLI DWL to approximately 30 m.

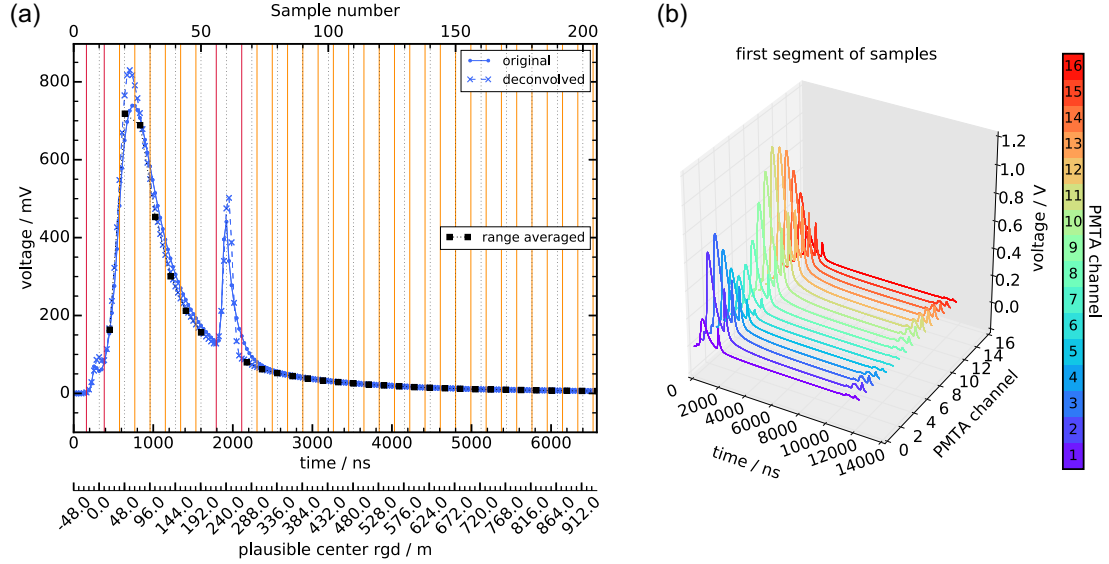


**Figure 5.7:** (a) Gaussian deconvolution for an exemplary atmospheric signal of a photomultiplier tube during vertical measurements. Each consecutive six measurements are averaged. These range-averaged regions are marked by vertical orange lines and the averaged value is represented by a black square. Reference light back-reflected from the mirror (at 0 m) and an additional pulse delayed by an optical fiber of length 320 m (at  $\approx 480/2$  m) are within red vertical lines. (b) Time-dependent voltages of all illuminated PMTA channels for one laser pulse.

### Weighted range averaging

The deconvolved signal width is larger than the interval between two measurement points separated by 32 ns for a sampling rate of 31.25 MHz of the analog-to-digital converter. A range-resolution  $\Delta R = \Delta t \cdot c/2$  of 30 m is equivalent to  $\Delta t \approx 200$  ns. Thus, six consecutive range-values are averaged ( $\Delta R \approx 27$  m) and weighted according to their amplitude normalized to the maximum within the six range-values. This weighting avoids too much weight to shorter ranges. The averaged segments are marked by vertical orange lines in Fig. 5.7(a). The range-averaged values are labeled by black squares. The time-dependent signal of all 16 PMTA channels for one pulse (segment) is shown in Fig. 5.7(b).

### Illumination function routine

The illumination function is determined by ramping the temperature of the oscillator of the WALES/DELICAT laser (see section 3.6), and by recording the envelope of the shifting interference fringe patterns for both the atmospheric signal light and the laser reference light as the fringe position shifts over one FSR. The procedure is described in section 3.5.6.

### Downhill-Simplex fitting

The corrected reference and atmospheric signal fringes formed by all 16 PMTA channels (see Fig. 5.7(b)) have a cosine-similar shape. The position of both fringes depends on the incident angular distribution (see appendix C.6 eq. C.60), on the temperature and thus the refractive index inside the interferometer housing (see section 3.4.2), and on the laser

frequency (see section 3.5.6). In case of the signal fringe additional frequency changes, due to the Doppler effect of molecules and aerosols moving with the wind, shift the fringe by  $\Delta\nu_D$ . These shifts are on the order of 5.6 MHz in case of a wind speed of 1 m/s (see eq. 2.3). For such precision (1 m/s), required precision is thus  $< 5.6$  MHz corresponding to a fraction of  $\approx 1/1900$  of the free spectral range (FSR = 10.69 GHz) of the FWFIMI. A precise fitting routine is thus required.

The end-to-end simulations of appendix C.8 show that lowest biases are obtained if a fit model of the form (similar to eq. C.97) is used:

$$f_1(\phi) = p_A \cdot (1 + p_W \cdot \cos(\phi + \arcsin(p_{Cu} \cdot \sin(p_{Sk} - \phi)) - p_{\Delta\phi})) \quad (5.2)$$

Alternatively, a simple cosine-shaped fit model is applied in this work as well.

$$f_2(\phi) = p_A \cdot (1 + p_W \cdot \cos(\phi - p_{\Delta\phi})) + p_B, \quad (5.3)$$

where  $p_A$ ,  $p_W$ ,  $p_{Cu}$ ,  $p_{Sk}$ ,  $p_B$  are the fit parameters for amplitude, contrast, kurtosis, skewness, and background.  $p_B$  is optional.  $\phi$  is the phase of the fringe varying within the interval  $N_{period} \cdot [-\pi ; +\pi]$  for a single frequency.  $p_{\Delta\phi}$  is the fit parameter for the phase shift being the primary parameter of interest. Under the presently set illumination conditions of the receiver, 1.2 fringe periods correspond to 13 pixels.  $N_{period}$  is set to 1.2 accordingly for  $N_{pixel} = 13$ . These 13 pixels are selected for the fitting from the center of the 16 channel PMTA data, because this is where the illumination function is assumed to be most stable. This kind of fringe-imaging gives a maximum instrumental contrast factor of  $V_{pix} = 98.6\%$  (see appendix C.6).

The Nelder-Mead algorithm (*Nelder and Mead, 1965; Jones et al., 2001*), described in chapter 4 and appendix C.8 is used to minimize the quadratic deviations between the data and the stepwise integrated fitting model. Stepwise integration is needed to account for the down-sampling due to the low number of illuminated pixels.

## 5.3 Validation measurements

### 5.3.1 Moving hard target speed measurements

First test measurements were performed on a moving hard target allowing to set known speeds independent of the current weather conditions.

Prior to the belt sander speed measurements both lidar laser beams were aligned onto the sanding paper. In case of AEROLI the laser spot was visible on the paper (see Fig. A.1(a) in appendix A). In case of the Windcube<sup>®</sup> the beam was scanned in order to find the optimum position. Fig. A.1(b) shows a scanning image of the belt sander arrangement at 50 m distance obtained by ranging with the Windcube<sup>®</sup>. The Windcube's carrier-to-noise ratio (CNR) is color encoded. The belt sander is positioned at 50 m distance with an angle relative to the line-of-sight of  $\approx 10^\circ$ , as can be seen in Fig. A.1(c).

The speed of the belt sander paper is 220 m/min to 350 m/min and can be continuously adjusted. Taking into account the inclination angle of the paper with respect to the LoS of  $10^\circ$ , the LoS hard target speed component is 3.6 m/s to 5.7 m/s.

During the measurements the Windcube<sup>®</sup> is scanned azimuthally ( $\pm 0.1^\circ$  in 2 s, i.e., with a scanning speed of  $0.1^\circ/\text{s}$ ) to ensure that the largest LoS component is measured, because the Windcube's laser beam spot is comparable or larger in size compared to the sand paper area. The measured sand paper speed therefore constantly oscillates between zero (area beside the sand paper) and the actual moving hard target speed, because only part of the laser beam spot may be incident upon the paper. The Windcube's accumulation time is set to 0.1 s.

The time-dependent signal voltages of the AEROLI PMTA channels (different colors) without GDR (see section 5.2) are shown in Fig. 5.8(a). A 3D view is depicted in Fig. 5.8(b).

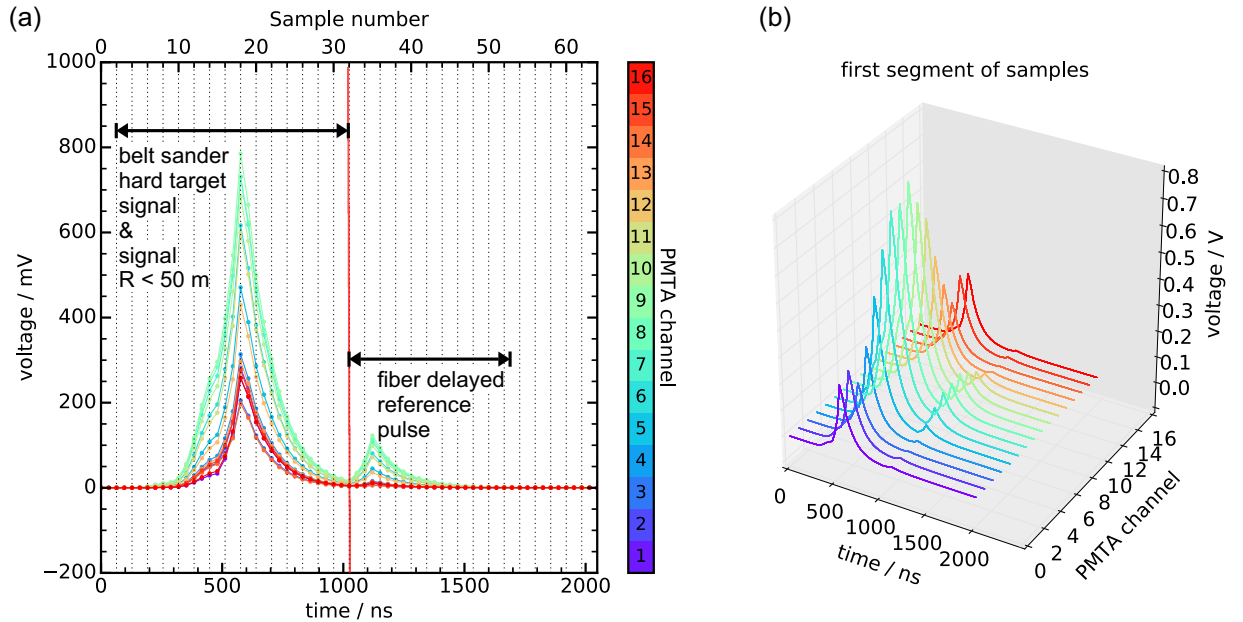


**Figure 5.8:** (a) Time-dependent signal voltages of each channel of the PMTA for moving hard target speed measurements on January 30, 2018. Signals originating from the hard target (belt sander) and from the fiber-delayed ( $L = 170$  m) reference laser pulse are indicated. (b) Time-dependent voltages of all PMTA channels of one laser pulse.

The first signal peak belongs to the hard target signal of the sand paper and to backscat-

tering signal of air in front of the belt sander. The reference laser pulse is delayed using an optical fiber of 170 m length (fiber R1 and fiber R2, see Fig. 3.20). Both signal peaks should have a FWHM of 8 ns, i.e., the pulse width of the laser, but they are broadened in time due to the pulse response of the amplifier circuits (see section 3.5.3).

Fringe shapes are depicted in Fig. A.2(a) in appendix A.

The maximum measured component of the Windcube® is the LoS speed (marked in blue) parallel to the AEROLI LoS speed (marked in black) in Fig. 5.9. Fig. 5.9 shows two measurement runs: (a) Belt sander turned on and off. (b) Belt sander speed varied in a pseudo-random way. The speed measured with the AEROLI DWL has to be multiplied by a factor of 1.7 in order to obtain the maximum speed measured with the Windcube®.

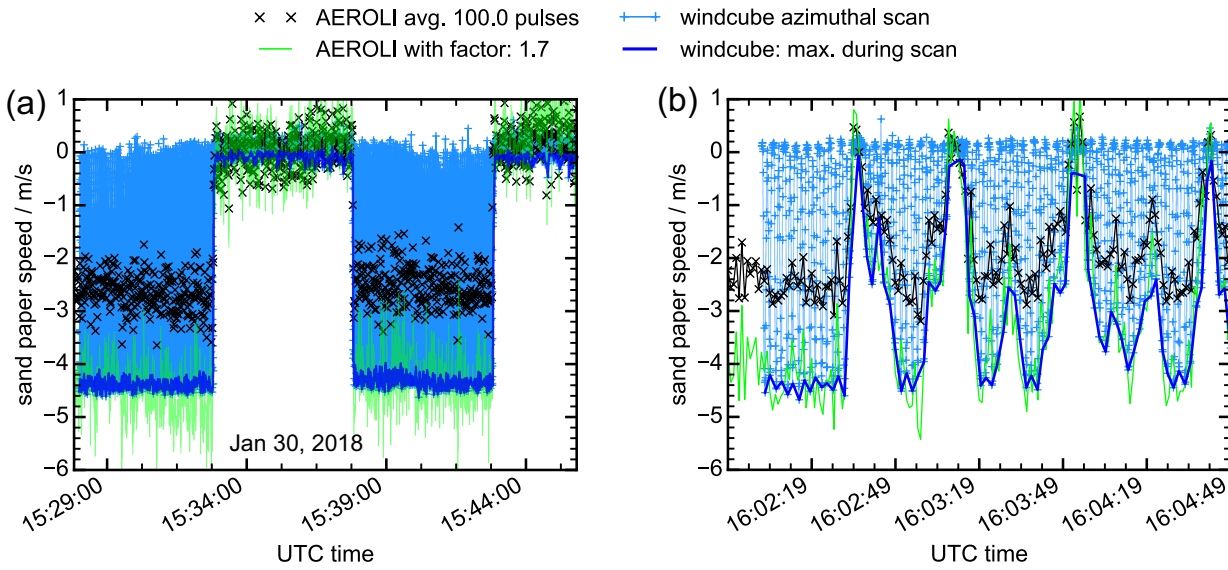


**Figure 5.9:** Results of belt sander speed measurements with the AEROLI receiver and the Leosphere Windcube® 200S on January 30, 2018. (a) Belt sander turned on and off in intervals of 5 min. (b) Belt sander speed changed by hand in a pseudo-random way.

The speed measured with the Windcube® at the maximum turning speed of the belt sander is lower than five m/s. This is possibly because the belt sander is rotating more slowly than specified or because a part of the beam is incident on non-moving parts.

Fluctuations of the speed determined with the Windcube® may be caused by hard target reflective speckle, non-optimal modal overlap of heterodyning, and by the azimuthal scanning. For a scanning speed of  $0.1^\circ/\text{s}$ , during an averaging time of 0.1 s, and the belt sander paper at a distance of 50 m with  $10^\circ$  inclination, the geometrical line-of-sight component of the scanning speed is  $\approx 0.1$  m/s.

The speed measured with AEROLI is relatively noisy, possibly due to hard target reflective speckle. These yield a high temporal coherence and therefore the spatial averaging of the scrambling fiber speckle (see section 3.5.4) is possibly insufficient for an adequate elimination of the overall speckle noise.

A possible explanation for the factor 1.7 is that the AEROLI return signal is a mixture of light scattered from the moving hard target and light backscattered by aerosols and molecules in the line-of-sight in front of the hard target.

The AEROLI DWL's spatial resolution is too low for unbiased moving hard target speed measurements. Nevertheless, the comparison with the Windcube® has shown that the AEROLI receiver is sensitive to moving hard target speeds smaller than 1 m/s.



### 5.3.2 Horizontal wind speed measurements

Horizontal wind speed measurements with the AEROLI DWL were undertaken on January 29, 2018. This section focuses on one measurement run from 19:19 to 19:34 (UTC), which yielded the best quality of referential Windcube<sup>®</sup> wind speed measurements. The aim is to evaluate the AEROLI DWL's wind speed measurement accuracy and precision. Further measurement runs are provided in appendix A.

The DELICAT transmitter was set to a pulse energy of 48 mJ, i.e., a power of 4.8 W. Laser beam and telescope axis were adjusted slightly cross-eyed with maximum signal at around 40 m, what is shown in Fig. 5.10(b). Total overlap may be achieved with the same setting of the front-end receiver optics but without squint at  $\approx 200$  m (overlap of  $\approx 40\%$  at  $R = 50$  m, see section 5.3.3). The PMTA voltage was set to 500 V. Reference light was provided by a hard target at 115 m distance. Both the AEROLI receiver and the Windcube<sup>®</sup> were aligned on this hard target to ensure parallel line-of-sights (see Fig. 5.1(b)).

Range-resolved measurements with the AEROLI DWL require an increase of the spatial resolution using the Gaussian deconvolution routine (GDR, procedure as described in Fig. 5.7 of section 5.2) and the consequent range averaging (section 5.2) into range gates with  $\Delta R = 30$  m, that can be compared to the range gates of the Windcube<sup>®</sup> ( $\Delta R = 25$  m). A comparison of wind speeds measured with the Windcube<sup>®</sup> and with ultrasonic anemometers ( $\Delta R = 0$  m) is provided and discussed in appendix A.

Exemplary range-dependent voltages of channel 2 of the AEROLI PMTA without and with GDR, and the attributed center range gate distances (rgd, black squares) obtained by range averaging are shown in Fig. 5.10(a). Fig. 5.10(b) provides the same normalized signal after correction of the  $1/R^2$  dependence.

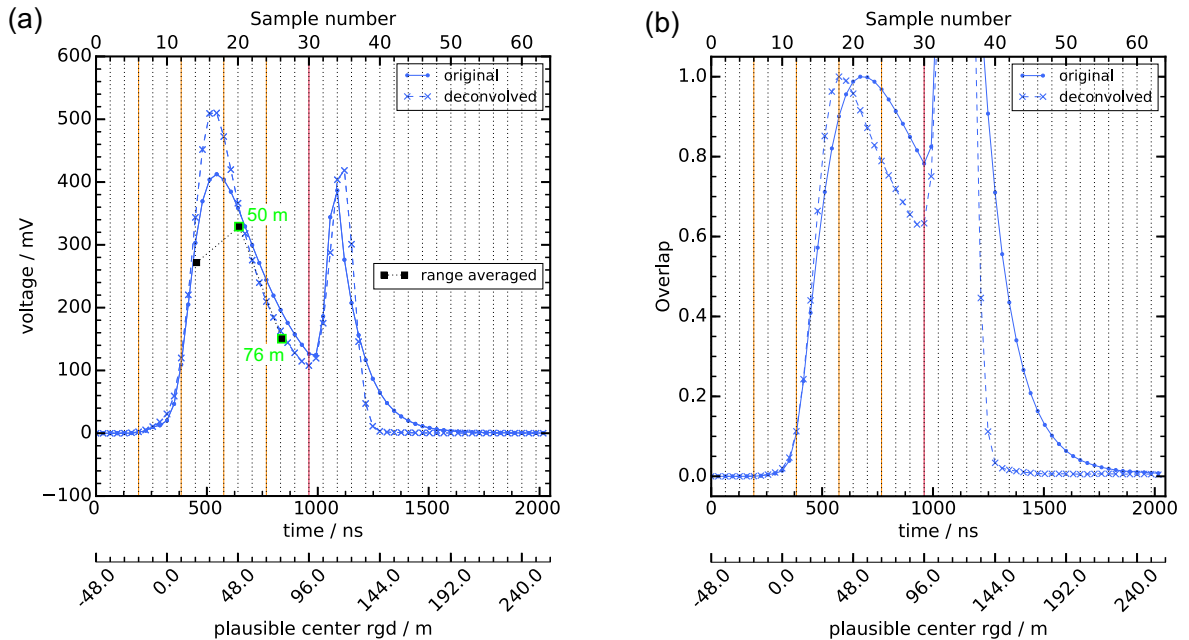


**Figure 5.10:** (a) Time-dependent voltages of PMTA channel two without and with Gaussian deconvolution with marked plausible center range gate distances (rgd). The maximum of the inference fringe was not located at channel 2. Black squares: Range-averaged over six consecutive samples giving a range resolution of  $\approx 30$  m. Each interval of six samples is marked by orange vertical lines. The reference signal peak of the hard target is located at an rgd of 115 m. (b) After correction of  $1/R^2$ -dependence: Maximum signal at  $\approx 40$  m, due to intentional squint of the laser beam relative to the telescope axis.

Two range gates with  $\Delta R = 30$  m are obtained at rgds of 50 m and 76 m (see green highlighted squares in Fig. 5.10(a)), which may be compared to the Windcube<sup>®</sup> measurement data starting at rgd = 40 m up to rgd = 90 m. At rgd > 90 m parts of the Windcube<sup>®</sup>'s range gates may involve a hard target signal of the ground or of the dump, being thus not suitable for wind speed measurements.

The fringe shapes (symbols) after illumination correction and Downhill-Simplex fits (lines) of atmospheric signal (Sig) and hard target laser reference (Ref) at different times are provided in Fig. 5.11.

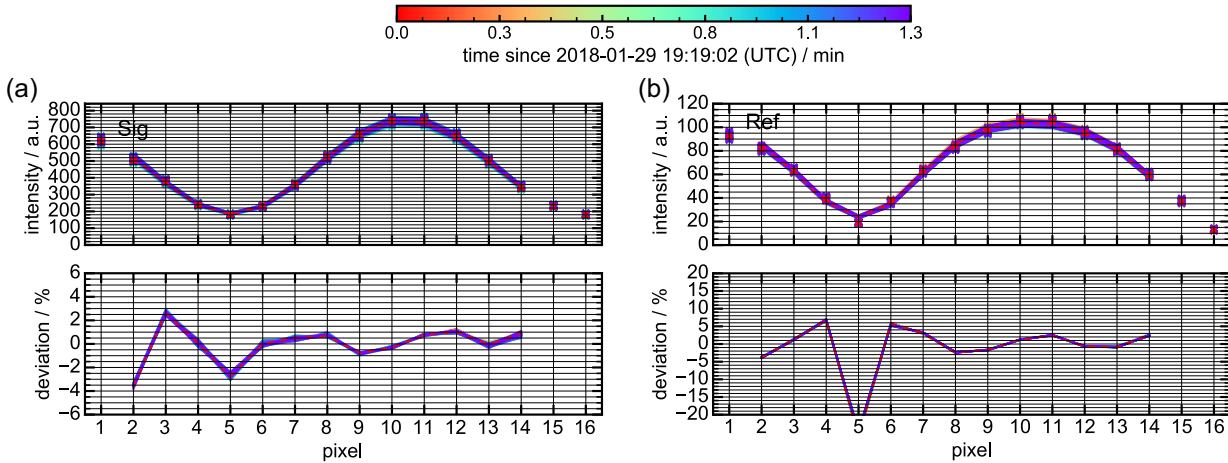


**Figure 5.11:** Fringe shapes and DSA fits for both the atmospheric signal (Sig) at rgd = 50 m and the hard target laser reference (Ref) during a measurement run on January 29, 2018 (first 200 measurement times). Symbols indicate the measured value. Each measurement is averaged over 40 pulses prior to DSA fitting. Lines indicate the fits (see eq. 5.2). (a): Sig, (b): Ref. The fractional deviation between the fringe data and the corresponding fit is shown below. Different colors correspond to different times. The first time is highlighted with a dashed red line.

The laser reference fringe appears to have a mesokurtic fringe shape with higher values of kurtosis ( $p_{Cu} \approx 0.4$ ) compared to the atmospheric return ( $p_{Cu} \approx -0.02$ , see Fig. A.11(b)), what may be explained by the mixture of signals backscattered from molecules/aerosols and from the hard target (beam dump).

A comparison of wind speeds determined by the AEROLI receiver from the positional shift of fringes (see Fig. 5.11) and by the Windcube<sup>®</sup> at rgds of 50 m and 76 m over time is shown in Fig. 5.12. During this measurement the DELICAT transmitter was locked to the iodine line. Apparent frequency changes induced by temperature changes ( $\approx 175$  MHz during 15 min) in the FWFIMI compartment and due to the locked laser ( $\approx 10$  MHz, i.e.,  $\approx 2$  m/s) are shown in Fig. A.7(b).

Fig. 5.12 displays phase shift independent, i.e., wind speed independent offset biases, that are constant over a measurement period of 10 min. These offset biases being dissimilar for different distances, are shown on the top of Fig. 5.12. The resulting values after correction by a subtraction of the mean are shown on the bottom of Fig. 5.12. During various measurement runs on the same day, this bias is time-dependent over the measurement period, for example from 18:25 - 18:55 (see Fig. A.6). The fringe shapes among themselves showed larger deviations in this case (see Fig. A.10(c)) compared to Fig. A.10(d), being a measurement with the DELICAT transmitter set to free-running mode. Free-running mode means that the laser frequency is not locked to the iodine line, allowing for larger frequency drifts (here  $\approx 60$  MHz during 30 min). The frequency is manually adjusted

before the measurement in this case such that the fringe maximum is centered on the PMTA.

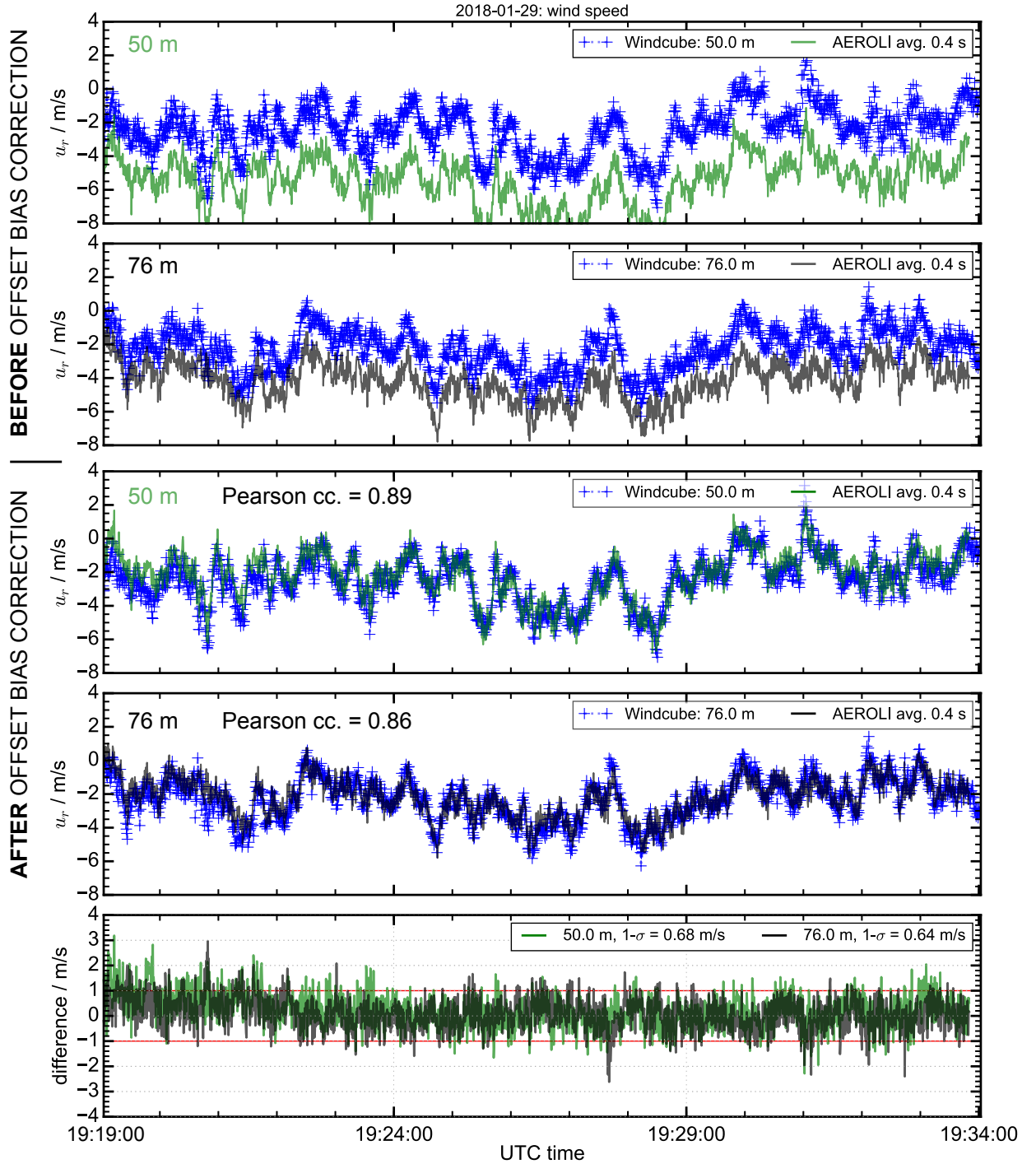


**Figure 5.12:** Horizontal wind speed measurements: time dependent radial wind speeds of Windcube® (blue) and AEROLI at an rgd of  $\approx 50$  m (green) and 76 m (black) before and after correction of the wind speed independent offset bias. The difference between the two instruments with averaging times of 0.5 s (Windcube®) and 0.4 s (AEROLI) is shown below. The  $1-\sigma$  standard deviation of the difference between both instruments during the measurement period of 15 min is below 0.7 m/s.

The offset bias itself seems to be a consequence of the limited measurement accuracy of the illumination function determination procedure (see section 3.5.6), as is shown in

appendix A. Fig. A.14 proves this, showing illumination functions obtained by averaging over different numbers of pulses during the frequency ramp. The selection of the averaging duration is arbitrary and therefore variations of the illumination function in this regard have to be treated as measurement uncertainties. These variations of the determined illumination function can induce offset biases in the order of several m/s, as shown in Fig. A.16(a). Furthermore the illumination functions of atmospheric signal and of hard target reference are not stable over the day (January 29, 2018), as is shown in Fig. 5.13.

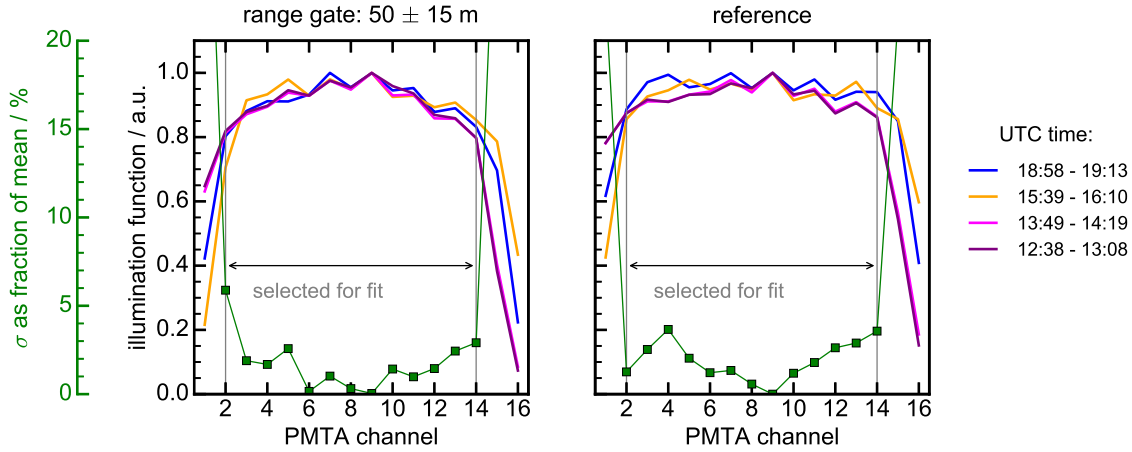


**Figure 5.13:** Comparison of signal and reference illumination functions obtained from different frequency ramps at different times on January 29, 2018. In all cases the number of averaged pulses of the recorded fringes is set to 10.

The illumination function variation results in varying offset biases as shown in Fig. A.16(b). This could be a consequence of long-term laser beam orientation drifts and of variations of its intensity profile. That is why, periodical illumination function determinations are necessary.

The short-term time-dependent drift of the bias is most likely, due to macroscopic fringe shifts (see green and orange lines in Fig. A.7(a, b)), because the air in the FWFIMI compartment is not in thermodynamic equilibrium due to insufficient temperature stabilization. An imperfectly determined illumination function in combination with those macroscopic fringe shifts, may alter the corrected fringe shape. This may lead to a time dependent offset bias. Further possible origins of these constant biases are discussed in appendix A and in section 5.4

The correction of the bias leads to a good accordance between AEROLI and Windcube<sup>®</sup> measurements, as can be seen in Fig. 5.12. The standard deviation of the difference  $e$  between AEROLI and Windcube<sup>®</sup> is less than 0.7 m/s for both ranges. Pearson correlation coefficients for both rgds between AEROLI and Windcube<sup>®</sup> are in the order of 0.86.

The aim in the following is to compare the LoS wind speed components measured by the AEROLI DWL and by the Windcube<sup>®</sup> more closely. Fig. 5.14(a) shows the approximately normally distributed differences between both instruments.

A scatter plot of the radial wind speeds  $u_r$  measured with AEROLI versus those of the Windcube<sup>®</sup> is shown in Fig. 5.14(b). After offset bias correction the centroids are close to the 1:1 line. Before offset bias correction an offset exists with respect to the 1:1 line (see linear regression lines in Fig. 5.14(b)). The right axis provides an estimate of the measurement standard deviation of AEROLI ( $\sigma(u_r)$ ), whereby the  $u_{r\text{Windcube}}$  are assumed to be the equal to the actual radial wind speeds, and  $\sigma(u_r)_{\text{AEROLI}}$  is evaluated in intervals

of  $u_r$ Windcube of  $\pm 0.1$  m/s.  $\sigma(u_r)_{AEROLI}$  is independent of wind speed and on the order of 0.7 m/s. Meanwhile, Leosphere specifies a wind speed measurement accuracy and probably a similar precision of the Windcube® 200S of  $<0.5$  m/s (Leosphere, 2016).

Thus, we may stipulate that both lidar systems yield a comparable measurement precision (random error) of about 0.5 m/s.

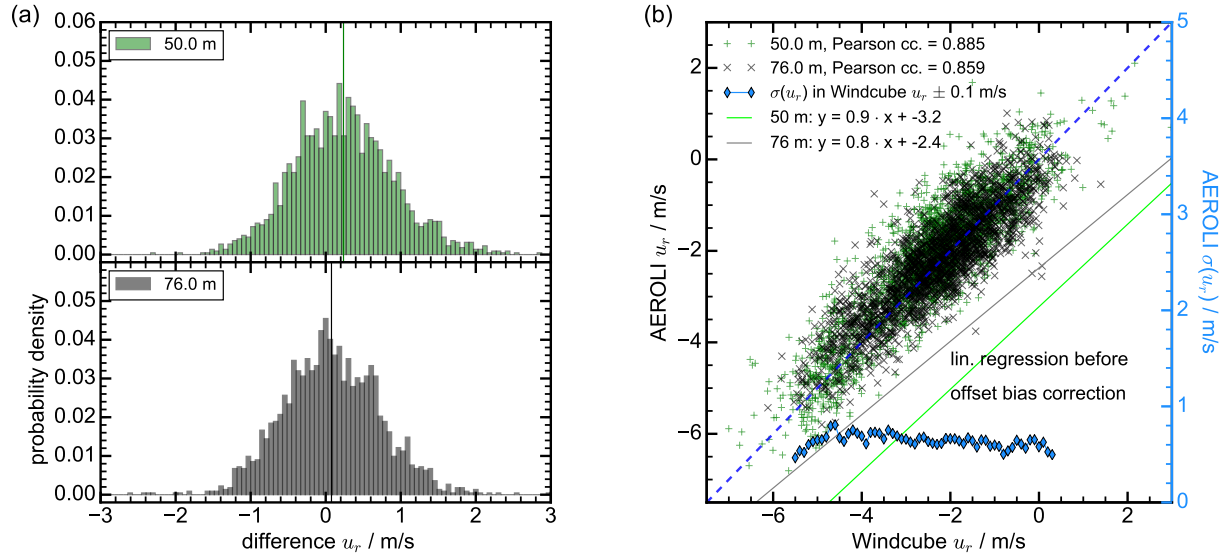


**Figure 5.14:** (a) Probability density of differences and standard deviations after offset bias correction shown in Fig. 5.12. (b) Radial wind speed of windcube versus AEROLI after offset bias correction, Pearson correlation coefficients, linear regression prior to offset bias correction, and standard deviation of  $u_r$ (AEROLI) in intervals of  $\pm 0.1$  m/s, assuming that  $u_r$ (Windcube) is equal to the absolute radial wind speed (right axis).

Another important aspect are the ambient atmospheric conditions and the related quality of the measurements of the Windcube® and of the AEROLI DWL, which are described in appendix A and which are summarized in the following.

The global fringe contrast  $W$  (see eq. 3.3) was on the order of 60% for atmospheric signals during the measurement run (19:19 - 19:34 UTC). Fig. A.4(b) of appendix A provides the signal and reference fringe contrasts (green) during all measurements on January 29, 2018. As shown during the laboratory test-measurements (see 3.5.2) and during measurements of the temperature tuning (see 3.4.2), the instrumental contrast  $V$  was in the order of 95%. Cézar *et al.* (2009a) showed theoretically, that the fringe contrast is influenced by both atmospheric temperature and by the particle backscattering ratio  $R_b$  (see the atmospheric contrast factor  $G$  given by eq. 3.4). This suggests, that the low value of  $G$  is a consequence of a low particle concentration. Fig. A.4(b) contains also absolute temperatures measured with the weather station MWS5 (by Reinhardt, Germany) installed on the roof-top of the building of the Institute of Atmospheric Physics. Using these temperature values, eq. 3.4 can be applied to estimate  $R_b$  values. These appear to be in the range of 1 - 1.3. These low particle concentrations could be a reason for the low CNR of the Windcube® (also shown in Fig. A.4(b)) during that day, which led to several noisy measurement runs with the Windcube® (see Fig. A.5, Fig. A.8, and Fig. A.9). The influence of solar background radiation (Fig. A.4(b), yellow) on the clear and sunny January 29, 2018 can be excluded,



because sunset occurred at 16:10 (UTC), as is shown in Fig. A.4(a). Humidity (Fig. A.4(b), blue) increased throughout the day and could play a role through ambient relative humidity (RH) enhancement of the particle scattering coefficient (see, e.g., [Zieger et al. \(2013\)](#)).

The AEROLI DWL wind speed measurements precision seems to be unaffected by the change in humidity and particle backscattering ratio  $R_b$ , in contrast to the Windcube® 200S measurement precision.

Another interesting aspect studied next is the dependence of the measurement precision of the AEROLI DWL on the temporal resolution of the measurements. The measurement precision of the AEROLI DWL is evaluated in the following as a function of the averaging time  $\Delta t$ , related to the LoS update rate by  $r_{LoS} = 1/\Delta t$ . Values of  $r_{LoS} > 45$  Hz combined with  $\sigma(u_r) < 1$  m/s are required according to [Schwithal \(2017\)](#) for alleviating wake vortices (see appendix B.2). The intent here is to study to what extent these requirements are fulfilled.

Fig. 5.16(a) provides a cut-out of 5 min of the last measurement of horizontal wind speeds  $u_r$  on January 29, 2018, applying various amounts of temporal averaging (ME), yielding different LoS update rates  $r_{LoS}$ . The values of  $u_r(AEROLI)$  are already corrected for the constant offset bias.

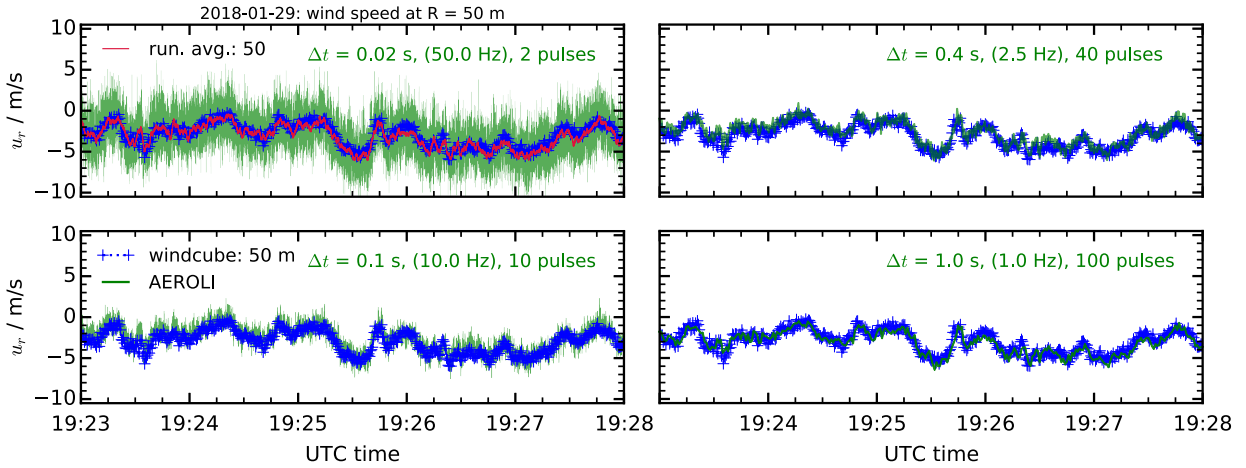


**Figure 5.15:** Windcube® and AEROLI radial wind speeds  $u_r$  as a function of time for different amounts of averaging times  $\Delta t$ , (LoS update rates), number of pulses. Red: running average over 50 measurement points of AEROLI.

The AEROLI wind speed measurements become increasingly noisy with shorter  $\Delta t$ , i.e., with higher  $r_{LoS}$ , and with a lower number of averaged pulses.

A way to quantify this decreasing measurement precision is to assume absolute accuracy of  $u_r(\text{Windcube})$  and to determine  $\sigma(u_r(AEROLI))$  within intervals of  $u_r(\text{Windcube}) \pm 0.1$  m/s, as shown in Fig. 5.16(a).

The AEROLI wind speed measurement standard deviation  $\sigma(u_r)$  in intervals of  $u_r$  of the Windcube  $\pm 0.1$  m/s is independent of wind speed (see Fig. 5.16(a)) and increases with the LoS update rate (see Fig. 5.16(b)), i.e., with shorter averaging times  $\Delta t = 1/r_{LoS}$ .

The determined values of  $\sigma(u_r(AEROLI))$  are compared to end-to-end simulations and CRB calculations for estimating their validity and origin.

End-to-end simulations are performed with a total receiver efficiency of 4% for various  $r_{LoS}$  without simulated speckle noise (green squares in Fig. 5.16(b)) and with the speckle model of section 4.1 with an image to speckle grain size ratio  $R_f$  of 48 (yellow rhombs in



Fig. 5.16(b)). Orange rhombs mark similar simulation results with an additional averaging time of the laser reference signal of 1 s.

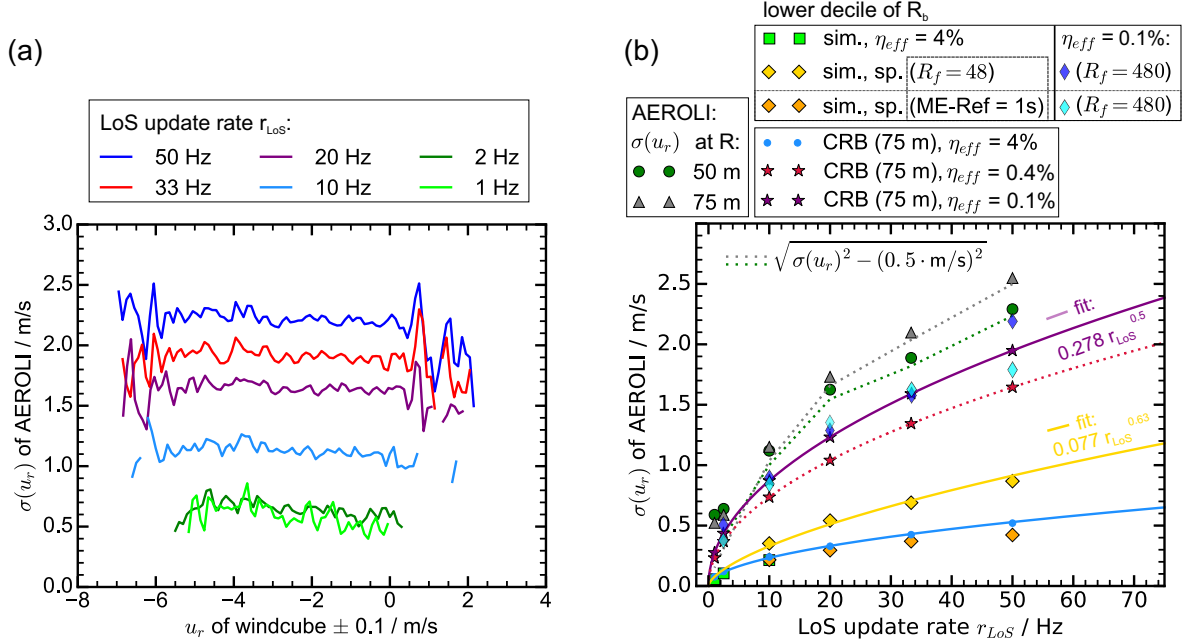


**Figure 5.16:** Standard deviation  $\sigma(u_r)$  of AEROLI for intervals of  $\sigma(u_r)$  of the Windcube<sup>®</sup>  $\pm 0.1$  m/s. (b) Mean  $\sigma(u_r)$  of AEROLI for different LoS update rates at ranges  $R$  of 50 m and 75 m. Dotted lines are corrected values of  $\sigma(u_r)$ , taking into account the measurement precision of the Windcube<sup>®</sup> of 0.5 m/s. This plot includes a comparison with end-to-end simulations (without (sim.) and with speckle noise (sim., sp.) considering  $R_f = 48$  and  $R_f = 480$ ) and CRB-calculations considering total receiver efficiencies of 4% (blue), 0.4% (red) and 0.1% (purple). Fitting curves demonstrate how shot-noise limited behavior ( $\sigma(u_r)r_{LoS}^{0.5}$ , purple line) and the influence of speckle noise with  $R_f = 48$  ( $\sigma(u_r)r_{LoS}^{0.63}$ , yellow line) should look like.

Fits in Fig. 5.16(b) indicate shot-noise behavior with  $\sigma(u_r) \propto r_{LoS}^{0.5}$ , i.e., the total number of received photons  $N_{tot}$  being proportional to  $1/r_{LoS}$  and how an influence of speckle ( $R_f = 48$ ) with  $\sigma(u_r) \propto r_{LoS}^{0.63}$  should look like. Similar simulations with  $\eta_{eff} = 0.1\%$  and  $R_f = 480$  are shown as blue rhombs. In this case a proportionality  $r_{LoS}^{0.5}$  is obtained, what indicates that speckle noise with  $R_f = 480$  does not increase  $\sigma(u_r)$  (see also Fig. C.23 in appendix C.8) compared to the case without speckle noise for LoS update rates smaller 30.

CRB calculations and end-to-end simulations are performed assuming an atmospheric model (see Fig. 2.1) with a low particle concentration, i.e., with the lower decile of the particle backscattering coefficients at an altitude of  $h = 0$  m (Vaughan, 1989). CRB values are calculated for  $R = 75$  m, for a total receiver efficiency of 4% (blue circles in Fig. 5.16(c)) and for 0.4% and 0.1% (violet and red stars in Fig. 5.16(c)), using eq. C.30 of appendix C.3.

The determined values of  $\sigma(u_r(\text{AEROLI}))$  are higher than anticipated by the end-to-end simulations and by the CRB calculations (see Fig. 5.16(c)). The detailed findings and possible explanations are described in the following.

Increasing the temporal averaging to a duration of 10 s in case of the laser reference fringe does not decrease the standard deviation  $\sigma(u_r)$  of AEROLI. If speckle played a role this should show (compare with end-to-end simulations yellow and orange rhombs in Fig. 5.16(b)). Thus, it can be concluded that the high values of  $\sigma(u_r)$  of AEROLI in cases of high LoS update rates are not solely the consequence of insufficiently temporally

averaged laser reference fiber speckle.

Furthermore, for a LoS update rate of  $r_{LoS} = 10$  Hz there is no difference between measurements taken with a vibration of the scrambling fiber using a vibration motor and without vibration, concerning the standard deviation  $\sigma(u_r)$  of the measurement. This suggests, that at this LoS update rate the detection process is shot-noise limited, because the speckle noise is reduced sufficiently by spatial averaging alone.

A plausible maximum efficiency  $\eta_{eff}$  of the receiver of 2.7% is estimated in appendix F (see Tab. F.4) with full overlap assumed at all distances. Using the amplifier gain, and the gain of the PMTA, the number of received photons can be estimated on the basis of the maximum detected voltage of 1 V during the measurement run. The estimated real detection efficiency during the measurements is approximately 0.4% (full overlap) and 0.1% (partial overlap). This may be explained with partial overlap, unsuitable polarization alignment, and a misalignment of the front-end receiver optics (see appendix F).

The results of CRB calculations assuming a reduced efficiency of 0.4% and 0.1% show more similarity with the determined standard deviation (see Fig. 5.16(b), purple solid and red dotted line).

At very small  $r_{LoS}$  of 1 Hz and 2.5 Hz the measurement accuracy of the Windcube<sup>®</sup> 200S (specified with 0.5 m/s for a fixed averaging time  $\Delta t$  of 0.5 s) seems to mask the probably lower  $\sigma(u_r)$  of the AEROLI receiver. Taking  $\sqrt{\sigma(u_r)^2 - (0.5\text{m/s})^2}$ , end-to-end simulations and measured  $\sigma(u_r)$  coincide for  $r_{LoS} < 2.5$  Hz (see green and gray dotted lines in Fig. 5.16(b)). Furthermore, the estimated laser beam pointing random error of 0.15 m/s (see section 4.3) is included in  $\sigma(u_r(\text{AEROLI}))$ .

The origin of the mismatch between CRB calculation / end-to-end simulation and the measured  $\sigma(u_r)$  at high  $r_{LoS}$  is unknown. The most likely reason is the low efficiency of the AEROLI receiver. Alternatively, aerosol concentration fluctuations in the turbulent atmosphere could contribute by creating additional intensity fluctuations of the backscattered light.

In summary the AEROLI DWL receiver was tested successfully during range-resolved horizontal wind speed measurements with a measurement precision of  $\approx 0.5$  m/s at an averaging time  $\Delta t$  of 0.4 s, being comparable to the Windcube<sup>®</sup> 200S, with a high temporal correlation between both measurements. AEROLI's measurement precision was insensitive to humidity and likely variations of the particle backscattering ratio  $R_b$  in contrast to the Windcube<sup>®</sup> 200S. AEROLI's accuracy is reduced by a range-dependent and wind speed independent offset bias, whereby its time dependence may be related to long term changes of the illumination function (e.g., due to laser beam orientation and profile variations) and to thermal gradients within the interferometer compartment aggravating the illumination function calibration. Lower averaging times (i.e., higher LoS update rates  $r_{LoS}$ ) yielded a measurement precisions of  $\sigma(u_r) > 1$  m/s at  $r_{LoS} > 45$  Hz. Thus, the tested AEROLI DWL receiver does not fulfill the currently required combination of  $\sigma(u_r)$  and  $r_{LoS}$  of OWIDIA for impact alleviation control of wake vortices. This is most likely due to a total receiver efficiency smaller than 0.4% during the validation measurements.

### 5.3.3 Vertical wind speed measurements

In this section the performance of the AEROLI DWL during long-range, range-resolved, vertical wind speed measurements is compared with results of the Windcube® 200S. The intention of performing range-resolved vertical wind speed measurements is to increase the number of measurement points and the maximum range. This allows to determine the range-dependent overlap function, which could not be evaluated during the horizontal wind speed measurements (see Fig. 5.10(b)) due to range limitations.

Fig. 5.7 shows the time dependent voltages for one pulse during a vertical measurement run on March 16, 2018. Every six consecutive voltage samples are assigned to an artificial range gate (interval between two vertical orange lines) by weighted-averaging (black squares). The reference pulse may be either constituted of a fiber-delayed pulse at a range gate distance (rgd) of 240 m, or just of the reflex from the “scanning” mirror ( $M_v$  in Fig. 3.20 in section 3.5.3) at  $\text{rgd} = 10$  m. A plausible center rgd value is attached to every consolidated range gate with  $\Delta R = 30$  m (6.5 m).  $\Delta R = 30$  m is approximately equal to the respective minimum range gate length due to the pulse response of the amplifier ( $\Delta R_{\min}$ ) obtained after the Gaussian deconvolution procedure.

The overlap function in Fig. 5.19(b) is obtained by multiplication with  $R^2$  and normalization to 0.88, i.e., the obstruction due to the secondary mirror of the Newton telescope.

Higher intensities and fluctuations starting at times of 10  $\mu\text{s}$  (altitudes of  $\approx 1500$  m) may be attributed to aerosol concentration fluctuations related to cloud cover and are not a characteristic of the overlap. Full overlap is reached at approximately 200 m.

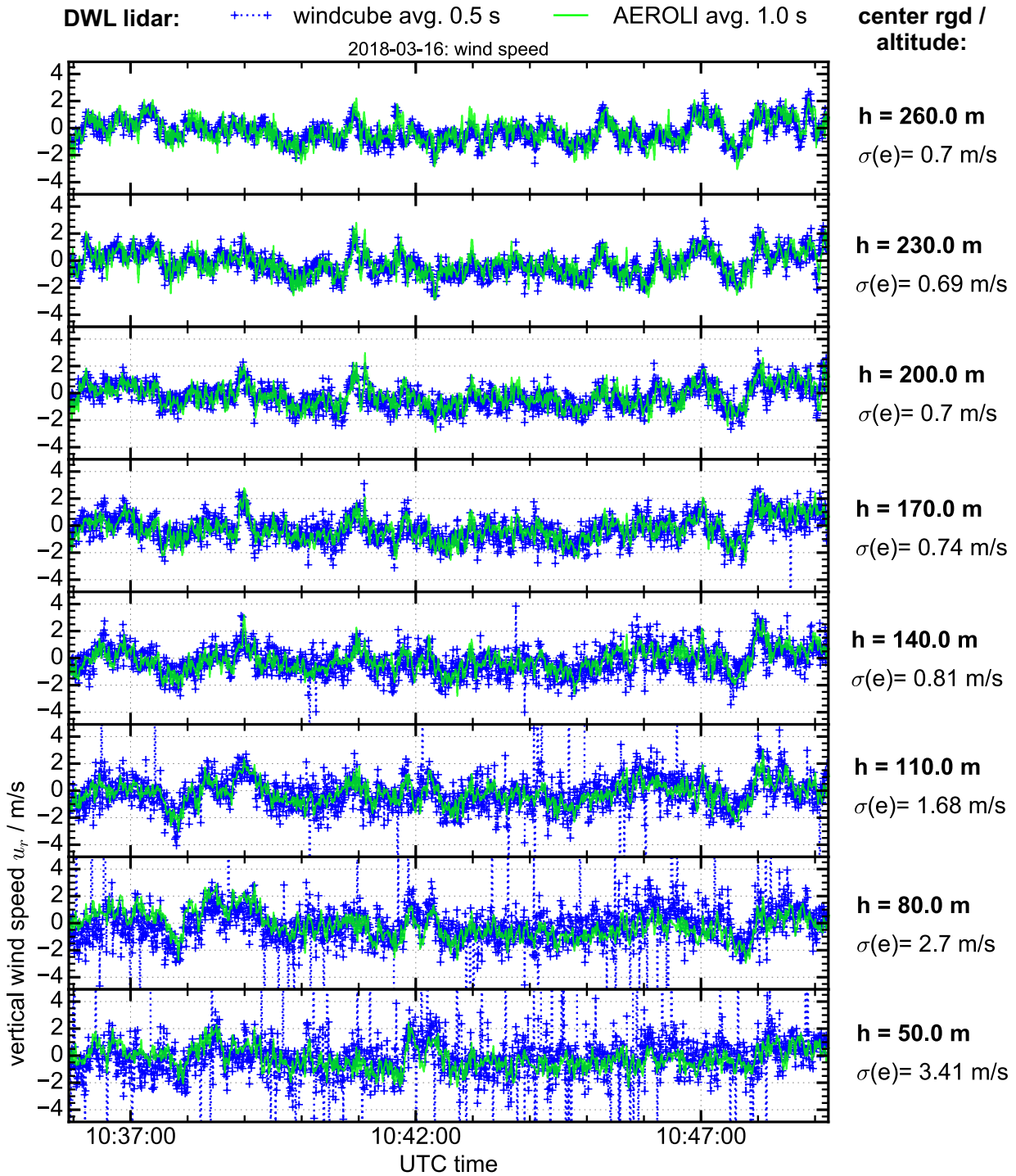
In the following long-range vertical wind speed measurements of the AEROLI DWL and the Windcube® 200S are presented. The determined vertical wind speeds over time shown in Fig. 5.17 were determined on March 16, 2018 at noon (11:45 local time). It was a partly cloudy day. Fig. 5.17 contains vertical wind speeds of AEROLI and Windcube® for altitudes ranging from 50 m to 260 m over time. The averaging time of the Windcube® was fixed to 0.5 s. The averaging time of AEROLI prior to evaluating the fringe positions is set to 1 s. Constant offset biases in case of AEROLI have been corrected by subtracting the mean radial wind speed  $\langle u_r \rangle$  during the total measurement time of roughly 13 min. The laser reference signal is provided by the reflex from mirror  $M_v$  (see Fig. 3.20).

The standard deviation of the difference  $e$  between the determined wind speeds of AEROLI and Windcube® decreases down to a value of 0.7 m/s with increasing altitude. This combined precision is approximately the same value as obtained during the horizontal wind speed measurements (see section 5.3.2).

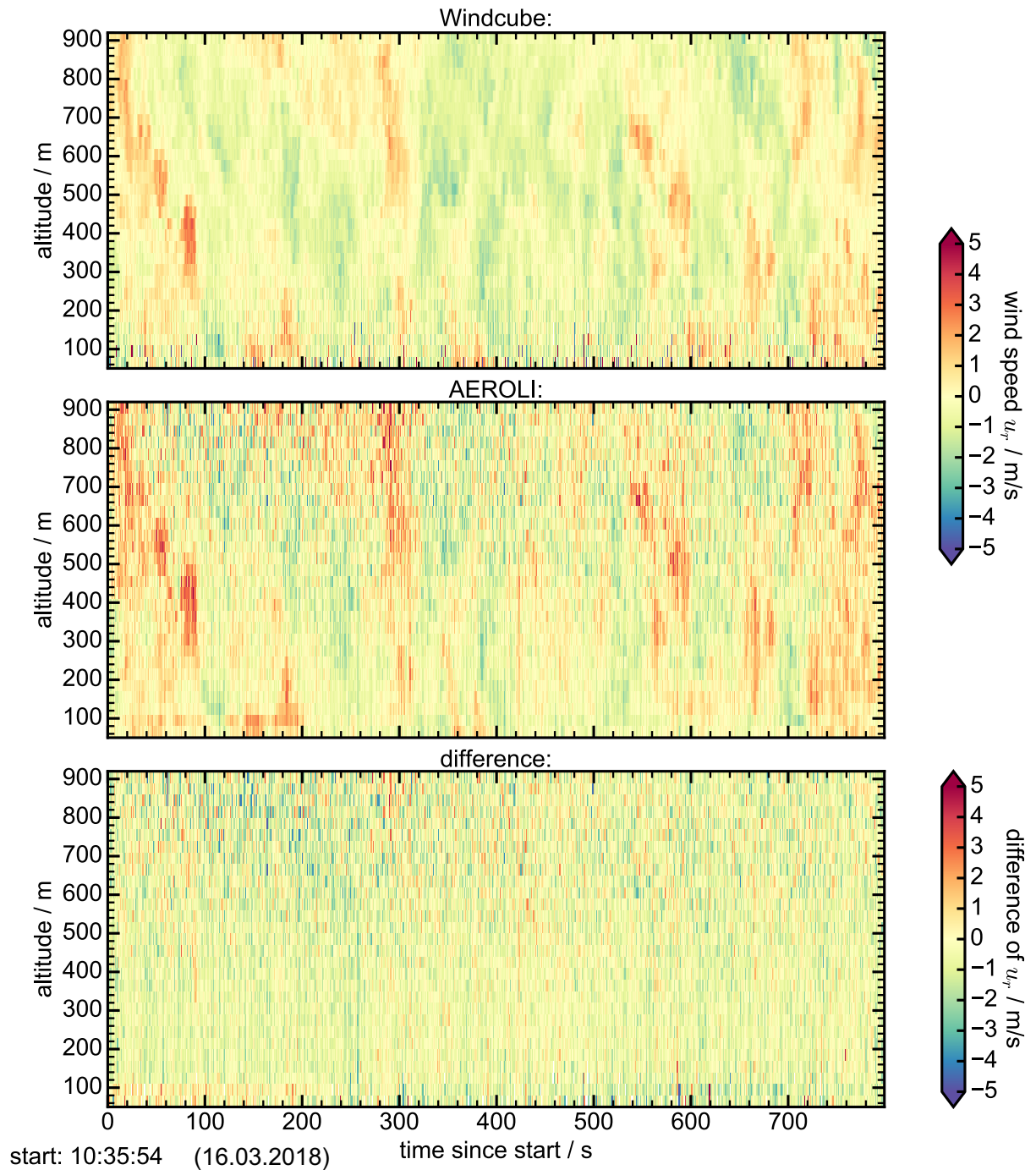
A similar increase of the combined precision with altitude was visible during different measurement runs on the same day. The results of another exemplary measurement run are shown in Fig. A.18 in appendix A. In this case a fiber-delayed laser pulse is used as reference signal. Vertical wind speeds of both DWLs over the full measurement range up to altitudes of 900 m are shown in Fig. 5.18. Again the AEROLI constant offset biases have been corrected. The wind speeds determined with the Windcube® are less noisy at higher altitudes. Possible reasons for this are discussed below.

Fig. 5.19(a) provides an overview of the altitude-dependent standard deviation  $\sigma(e)$  of the difference between the two lidar systems (black), and the corrected offset bias between AEROLI and windcube (green), before correction and after correction by subtraction of the temporal average AEROLI wind speeds  $\langle u_r \rangle$  over the whole measurement (see Fig. 5.18). The plot also provides the mean carrier-to-noise ratio (CNR) of the Windcube® as a function of altitude (blue triangles), and Pearson correlation coefficients of the interpolated

AEROLI and Windcube® wind speeds (red crosses).



**Figure 5.17:** Vertical wind speeds of AEROLI (green) and Windcube® (blue) at increasing altitude ( $h$ ) as a function of time. The averaging times of AEROLI and Windcube® are 1 s and 0.5 s, respectively. In case of AEROLI the constant offset bias is removed (see text). The standard deviation  $\sigma$  of the difference  $e$  between the AEROLI receiver and the Leosphere Windcube® 200S is given for every altitude.



**Figure 5.18:** Color-encoded radial wind speeds for altitudes up to 900 m of both Windcube® (top) and AEROLI (middle). Bottom: Difference between both instruments in m/s.



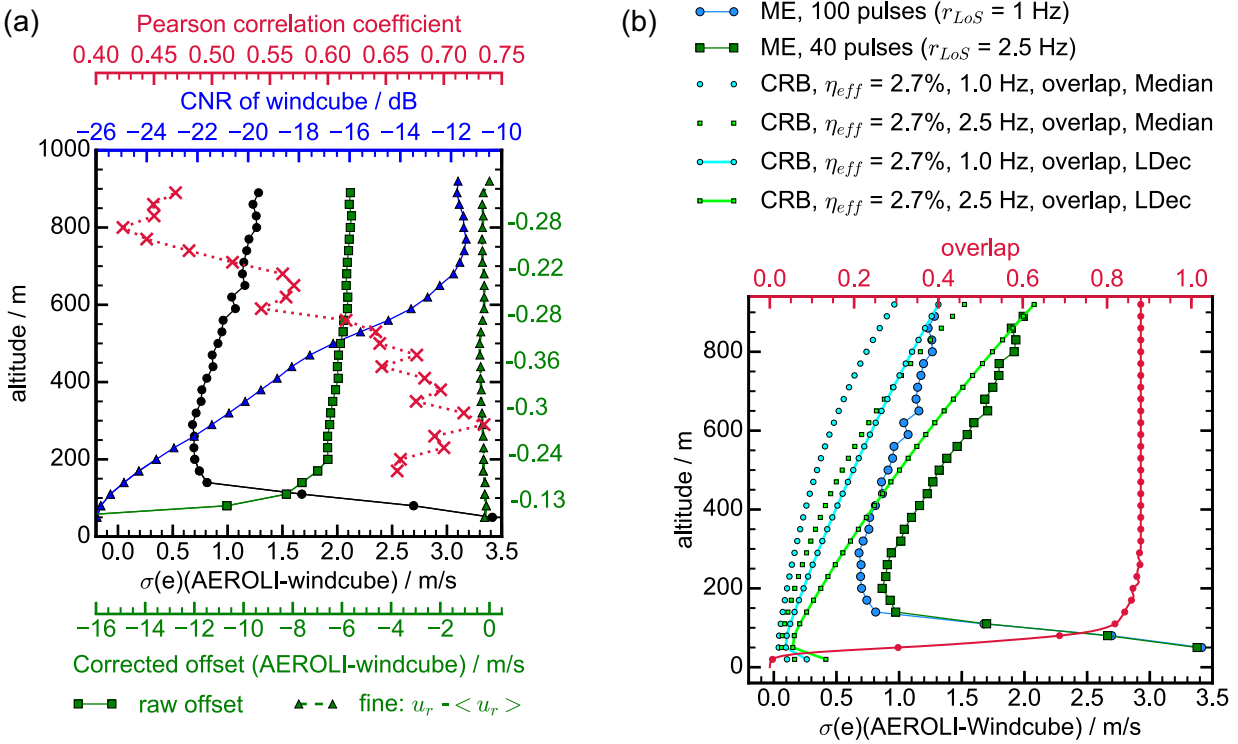


**Figure 5.19:** (a) Altitude / center range gate distance (rgd) dependent corrected offset (green squares), standard deviation of difference between AEROLI and windcube ( $\sigma(e)$ , black), CNR of the Windcube® (blue triangles), and Pearson correlation coefficient (red crosses). The range-dependent offset is corrected by subtracting the temporal average (over 13 min) of the AEROLI radial wind speed  $u_r$ . The offset after this correction is plotted with a green triangles with typical annotated values.  $u_r(\text{AEROLI})$  are obtained with  $r_{LoS} = 1$  Hz,  $u_r(\text{Windcube})$  with  $r_{LoS} = 2$  Hz. (b)  $\sigma(u_r)$  as a function of altitude for different  $r_{LoS}$  compared to CRB calculations assuming a reconstructed overlap (red), an atmospheric backscattering coefficient model (see Fig. 2.1) with median and lower decile (LDec) aerosol concentrations, and a receiver efficiency of 2.7%.

$\sigma(e)$  is very high at short ranges up to altitudes of 100 m, what is in accordance with increased noise of the Windcube® in Fig. 5.17 for these range gates. This is also where the CNR of the Windcube® is lowest. The CNR reaches a maximum at 700 m, i.e., at the location where the laser is focused, and thus where heterodyne optical mixing is most efficient due to optimum similarity between the modal shapes of the atmospheric signal light and the reference light (see section 2.2.1).

Data of the range-dependent random error of the radial velocity determined with the Windcube® 200S and its dependence on the CNR has not been published to the author's knowledge. The random error of the wind speed estimate of a coherent DWL is certainly connected to the CNR (see, e.g., eq. C.31 in appendix C.3 and eq. C.33 in appendix C.4), it depends however also on characteristics and settings of the individual coherent DWL (such as the adjustment of its focus, averaging duration, efficiency, the mean wavelength estimation algorithm, etc.) and on atmospheric conditions (e.g., on the turbulent energy dissipation rate (*Smalikho et al., 2013*) or the particle backscattering coefficient, see, e.g., *Beck and Kühn (2017)*). Precise knowledge of the range-dependent random error of the Windcube® 200S on that day would have been desirable, in order to get more precise results on the range-dependent random error of the AEROLI DWL. This could however not be achieved due to the reasons given above. Another possible approach could be dynamic filtering (*Beck and Kühn, 2017*) of the Windcube® 200S data instead of the here applied



common method of excluding estimated wind values if the CNR is below 29 dB.

The offset bias of the AEROLI DWL strongly varies in the near-range ( $R = [50 \text{ m}, 200 \text{ m}]$ ) and less in the far-range ( $R = [200 \text{ m}, 1160 \text{ m}]$ ) as indicated by the green squares in Fig. 5.19. The range-dependence of the offset bias in the near-range could be related to range-dependent illumination functions (see appendix A, Fig. A.17) and to the angular distribution of light illuminating the Michelson interferometer. As is shown in appendix D.1, Fig. D.4(c) and in Fig. 3.1(b) the angular distribution (i.e., the far-field intensity distribution with respect to the fiber) during coupling into the scrambling fiber is range-dependent and changes more strongly for short ranges. Due to incomplete far-field scrambling properties (see appendix H) of the used scrambling fiber, it is likely, that the far-field, i.e., the angular distribution, on the back-end receiver side of the fiber is also slightly range dependent. A related cause could be focal-ratio-dependent (i.e., range-dependent, see Fig. D.4(b)) focal-ratio degradation of the scrambling fiber. It is shown in appendix C.6, eq. C.59, Fig. C.12, that a difference of  $\approx 14 \text{ } \mu\text{rad}$  of the angular distribution is enough to induce a phase shift of 0.009 fringe periods, i.e., an equivalent wind speed of 16 m/s.

*Tucker et al.* (2018) report a similar effect in case of their aerosol backscatter direct-detection DWL (OAWL-P) system. Field angle differences between laser reference and atmospheric return varying with range have been identified as the cause of a range-dependent bias in the near-range (*Tucker et al.*, 2018).

This is true although the near-range illumination functions in case of AEROLI appear to resemble for these ranges, without any obvious range dependent trend (see Fig. A.17). The region in between range gate distances of 200 m and 260 m contains the optional fiber-delayed reference laser pulse (see Fig. 5.7, region between red vertical lines).

It should be noted, that a single illumination function at  $h = 260 \text{ m}$  ( $\Delta R = 30 \text{ m}$ ) is used to correct the fringes for altitudes higher than 260 m. If this is not done the offset bias can change abruptly from one range gate to the next, due to aerosol concentration fluctuations, and therefore backscattering signal fluctuations, which falsify the envelope of the interference fringes during the frequency ramping of the illumination function determination procedure (see Fig. A.17 in appendix A).

Subtraction of the temporal average  $\langle u_r(\text{AEROLI}) \rangle$  leaves relatively small offset values (green triangles in Fig. 5.19), which could also be related to the Windcube<sup>®</sup> with a specified accuracy of 0.5 m/s. The exact accuracies of the Windcube<sup>®</sup> at these ranges are dependent on the CNR, i.e., on the range, on the weather conditions, on the averaging duration, and on the mean wavelength estimator algorithm.

The Pearson correlation coefficient is maximum at an altitude of  $\approx 300 \text{ m}$ , that is when  $\sigma(e)$  is lowest and decreases with altitude as  $\sigma(e)$  increases.

Next the results of the vertical wind speed measurements are compared against CRB calculations. Respective CRB calculations and end-to-end simulations have been compared in section 4.5.

Fig. 5.19(b) provides the altitude-dependent standard deviation of the difference between AEROLI and Windcube<sup>®</sup> for LoS update rates of 1 Hz and 2.5 Hz of AEROLI. The LoS update rate of the Windcube<sup>®</sup> is 2 Hz throughout all measurements. CRB calculations using eq. C.30 of appendix C.3 together with the atmospheric models of Fig. 2.1, show a lower steepness of the increase of  $\sigma(u_r)$ , assuming 1. lower decile aerosol concentrations (*Vaughan et al.*, 1995), 2. an AEROLI receiver efficiency of 2.7%, and 3. a reconstructed overlap function (crimson in Fig. 5.19(b)), taking into account the obstruction by the secondary mirror of the telescope (obstruction ratio of 12%). Furthermore, there is an offset

of  $\sigma(u_r)$  between the CRB predictions (which only assume shot noise) and the AEROLI measurements of  $\approx 0.5$  m/s at low altitude, decreasing with higher altitude. Higher particle backscattering ratios (median values of  $R_b$  in the model ([Vaughan et al., 1995](#))) provide a lower steepness of increase of  $\sigma(u_r)$  with altitude. This mismatch between CRB calculations and  $\sigma(e)(AEROLI - Windcube)$  could be related to an increase of the measurement precision of the Windcube<sup>®</sup> with range because the laser of the Windcube<sup>®</sup> is focused at  $R = 700$  m.

This section showed that long-range, range-resolved, vertical wind speed measurements up to altitudes of 900 m can be performed with the AEROLI DWL. The highest combined precision and correlation of AEROLI and Windcube<sup>®</sup> measurement was achieved at an altitude of 300 m. The measurement precision of the AEROLI DWL at this distance was on the order of 0.5 m/s. To the best knowledge of the author the above measurement results represent the first long-range and range-resolved measurements of winds speeds using a fringe-imaging Michelson interferometer based Doppler wind lidar receiver. The range-dependent noise behavior, precision, and accuracy of the Windcube<sup>®</sup> differ fundamentally from AEROLI. The lack of information on the Windcube<sup>®</sup>'s range-dependent accuracy and precision aggravates a more precise analysis of AEROLI's performance.

## 5.4 Discussion and Outlook

### Discussion

The comparative field-tests show good accordance between LoS measurements with the AEROLI receiver and parallel, aligned measurements with the Leosphere Windcube® 200S in terms of relative precision and correlation. The horizontal measurements at close range provide proof that the FWFIMI is sensitive to wind speeds, and works according to theory. At close range a precision comparable to the Windcube® is reached for averaging times on the order of 0.5 s, with standard deviations of about 0.5 m/s.

A velocity-independent, range-dependent, and time-dependent offset (bias) remains (see Fig. 5.14(b)), which was subtracted during the comparison with the Windcube®. Possible reasons for the short-term time-dependence are variations of the illumination function or the insufficient determination of the illumination function. Reasons for the latter may be temperature fluctuations and convection in the interferometer compartment, inducing phase-shifts during calibration, i.e., during the ramping of the laser frequency, affecting the procedure. Furthermore, the illumination function is most likely subject to a long-term change related to a long-term drift of the laser beam orientation and profile.

A possible explanation for the range-dependence of this bias is a range-dependent angular distribution of the illumination function behind the scrambling fiber, introducing a range-dependent phase shift of the atmospheric signal interference pattern (see Fig. C.12) relative to the laser reference interference pattern. One major reason for range dependent signal illumination functions could be the excitation of cladding modes of the quadratic-core scrambling fiber (QSF). The spot-size on the fiber during coupling is range-dependent, as the focus of the telescope changes with range. The QSF core itself acts as the field-aperture (limiting the FOV of the telescope), which was not optimally set, as is proven by the partly incomplete overlap during vertical measurements at altitudes smaller 150 m (see Fig. 5.19(b)). This overlap deviates from the results of raytracing simulations with optimum adjustment (see appendix D.1).

Speckle in case of atmospheric signal light are effectively averaged out in time, due to limited coherence of molecular and aerosol scattering, and above all due to an artificial increase in diversity (see appendix C.4) when using a large-core multimode scrambling fiber, allowing very efficient spatial averaging of the speckle. Together both effects seem to cancel out the atmospheric signal speckle noise. In case of laser reference light, averaging on the order of 1 s, together with mechanical vibration of the scrambling fiber, allows to compensate the increased temporal coherence with additional temporal scrambling. In case of atmospheric signal light a mechanical vibration of the fiber seems to be not necessary (see section 4.1).

Another noise influence are unexpected beam pointing fluctuations, which are mitigated due to the relatively high near-field scrambling gain of the quadratic-core multimode scrambling fiber. The estimated  $3\sigma$  standard deviation of this random tilt error is  $<0.15$  m/s (see section 4.3).

Solar background shot noise is suppressed by the Materion interference filter. This is confirmed by CRB calculations, by end-to-end simulations assuming a radiance of  $300 \text{ W}/(\text{m}^2 \text{ sr } \mu\text{m})$  in Fig. 4.13 of section 4.5, and by daytime measurements.

The standard deviation of the radial wind speed  $\sigma(u_r)$  is proportional to range and follows  $1/SNR$ , what indicates a shot-noise influence on the detection process. This is confirmed by CRB calculations, end-to-end simulations, and by the vertical field-test measurements,

which showed a linear increase of  $\sigma(e)$ , i.e., of the standard deviation of the difference  $e$  between AEROLI and Windcube<sup>®</sup> with altitude, as well.

The major difference between the end-to-end simulations and the measurement is that the measured  $\sigma(e)$  is constantly offset to higher values. The steepness of the increase is also different from CRB calculations with an atmospheric model for particles backscattering coefficients (Vaughan *et al.*, 1995), if the lower decile is used, i.e., if a low particle concentration is assumed, together with a receiver efficiency of 2.7% and for ranges with full overlap.

Fig. 5.19 in section 5.3.3 showed a comparison of vertical measurement standard deviations and CRB calculations. These simulations together with the low instrumental contrast, due to the low atmospheric contrast factors, i.e., estimated low particle concentrations ( $R_b < 1.2$ ) during measurements (see appendix A), show that the AEROLI receiver seems to work independently of AEROSOL concentration and with standard deviations smaller 1 m/s, provided that the distance is short enough, and that sufficient averaging is possible, as is shown theoretically in section 4.6.

The AEROLI receiver is not sensitive to the particle backscattering ratio  $R_b$ , only to a combination of  $R_b$  and the atmospheric temperature  $T$ . The low atmospheric instrumental contrast of around 60%, which was measured most of the time suggests that the measurement mainly relied on Rayleigh scattering (see also Fig. A.4). The polarization of the emitted laser light should be s-polarized. This was not checked thoroughly during the measurements. This unknown transmitted polarization together with the polarizing beamsplitter in the front-end part of the receiver, which only guides s-polarized light into the fiber components, could explain the low aerosol scattering signal component, inducing a low atmospheric contrast factor  $G$  (see eq. 3.4), which decreases the global fringe contrast  $W$ , provided that a high number of particles with low depolarization ratio  $\delta_p$  participated to the backscattered signal.

In contrast, the Leosphere Windcube<sup>®</sup> 200S may have suffered from low particle concentrations, even for integration times of 0.5 s, as can be concluded from high standard deviations during January 29th, 2018 (see section A). The humidity of the air could have influenced the particle scattering coefficient. Relative humidity enhancement could explain the Windcube<sup>®</sup>'s higher measurement precision in the evening. However, no independent measurements of aerosol concentrations have been performed. Thus, the high standard deviation of the Windcube<sup>®</sup> could not be strictly related to the aerosol concentration. Moreover, the Windcube<sup>®</sup> was not optimized for short measurement ranges. Sun exposure seems not to correlate with the standard deviation of the Windcube<sup>®</sup>. Furthermore, the exact dependence of the measurement accuracy and precision of the Windcube<sup>®</sup> on the measurement distance and atmospheric conditions is not known.

A comparison of AEROLI with other existing direct DWL receivers in terms of accuracy, precision, and systematic errors is not necessarily conclusive, because these systems are developed for other purposes. The ALADIN Airborne Demonstrator (A2D) for example showed in latest airborne tests a systematic error of less than 0.5 m/s and random errors from 1.5 m/s (Mie channel) to 2.7 m/s (Rayleigh channel), with a range resolution on the order of hundreds of meters, ranges of several kilometers, and averaging times on the order of 14 seconds (Lux *et al.*, 2018). Bruneau *et al.* (2015) report for their high spectral resolution (HSR) equipped 3-wavelength-2-polarization-backscatter lidar LNG, based on a 4-channel Mach-Zehnder technique (Bruneau *et al.*, 2013), a wind velocity measurement precision in the range of 1 to 2 m/s with biases up to 1 m/s with averaging times on the order

of minutes. Ball Aerospace reported validation of their aerosol backscatter direct-detection DWL (OAWL-P) system (wavelength of 355 nm) based on a field-widened Mach-Zehnder interferometer during ground tests in 2011 versus a 9.355- $\mu\text{m}$  coherent detection DWL. With OAWL data accumulation times of 2 s and a range gate length of 30 m, correlation coefficients of 0.92 and measurement precisions between 1 m/s and 2 m/s were obtained at ranges of 500 m to 1 km ([Tucker et al., 2018](#)).

## Outlook

Vertical and horizontal test measurements with the AEROLI DWL should be carried out in atmospheric regions with lower air density and lower particle concentrations in order to verify the projected theoretical and simulated performances (see sections 3.3.2, 4.2). Ground-based measurements could be done on the Schneefernerhaus at the “Zugspitze” mountain at an altitude of 2650 m.

Moreover, CRB calculations could be undertaken with more accurate data on local particle concentrations.

Typical sources of bias like the determination of the illumination function, illumination function stability, and temperature stabilization should be optimized. For the determination of the illumination function, different frequency ramping profiles could be tested. Illumination function stability could be improved by better optical scrambling, using, e.g., a two-lens optical scrambler. Furthermore, the stability of the spatial profile of the transmitted laser beam should be characterized over time. The laser beam pointing and time-dependent profile should be recorded with a 2D camera in parallel to future test measurements in order to verify a relation between a likely long-term laser beam drift and the long-term change of the illumination function. Better temperature stabilization is required with lower thermal gradients within the compartment of the interferometer, such that the temperature tuning is minimized. This requires better isolation of the compartment and of the back-end receiver, and more advanced stabilization schemes including optimized heating rates (e.g., a proportional-integral-derivative (PID) controller) and more sensitive temperature probes. A possible way to reduce thermal gradients within the compartment may be to fill it with helium (thermal conductivity:  $\approx 0.15$  W/mK) instead of air ( $\approx 0.03$  W/mK).

The problem of range-dependent illumination functions behind the scrambling fiber may be reduced by applying a quadratic aperture to the front-face of the QSF (blocking the cladding) and adjusting the positions of optics in the front-end receiver. The primary challenge would be the precise alignment of this aperture, such that the overlap is not impeded. Furthermore, the far-field scrambling performance should be increased using different fibers, or by a two-lens optical scrambler, or by a mechanical squeezer (e.g., [Avila \(2012\)](#)). Alternatively, if the time-dependence of the bias is restricted the known range-dependent bias could be characterized and could be corrected online.

For feed-forward alleviation and control, the AEROLI receiver prototype should be optimized for efficiency. First of all the current AEROLI receiver overlap should be maximized for distances of 50 to 150 m by adjusting the front-end coupling optics positions. A more efficient way of coupling signal and reference light should be used, e.g., second generation fiber couplers. Moreover, the telescope primary mirror reflectivity should be optimized for UV wavelengths.

The FWFIMI receiver principle could be improved further by using the FWFIMI in tilted configuration with a second linear detector (see appendix D.3), improving the Cramér-Rao



bound (CRB) by a factor of  $\sqrt{2}$ . Using a hexagonal monolithic beamsplitter like [Harlander et al. \(2003\)](#) would allow to use UV beamsplitter coatings at  $30^\circ$  angle of incidence, with splitting ratios of 35/65 for unpolarized light. This method would render the need to repolarize the light behind the multimode fiber obsolete, thus giving another reduction of the CRB by  $\sqrt{2}$ . Such an advanced receiver principle is shown as a sketch in Fig. 5.20.

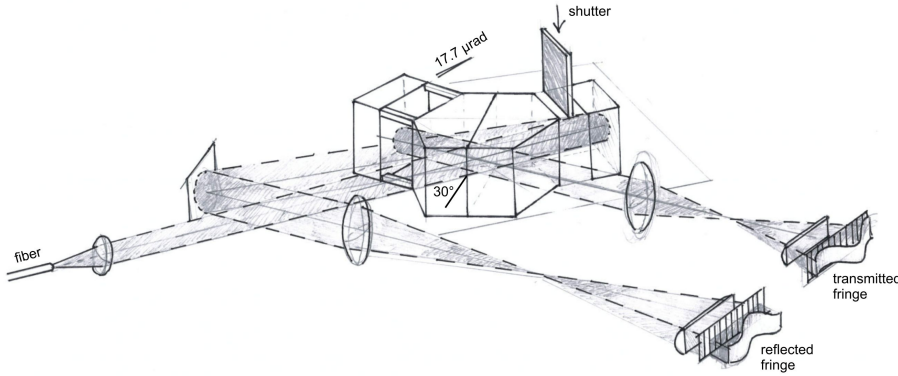


**Figure 5.20:** Advanced receiver concept including a hexagonal beamsplitter, a glass arm, and an air arm with inclined mirrors, and illumination at a mean angle of incidence of  $\approx 2^\circ$ . These measures would allow for illuminating with unpolarized light and for the detection of the back-reflected linear fringe with a second linear detector channel.

A fiber-coupled principle remains advisable in the future with respect to speckle noise reduction, tilt bias reduction, and illumination bias reduction, what means unavoidable losses due to attenuation, coupling and imaging of the light on the detector, such that an improved total receiver efficiency  $\eta < 16\%$  will not be surpassed. A threefold increase of the Power-Aperture-Efficiency-Product (see eq. 4.4) would allow for multiple LoS measurements (with  $\sigma(u_r) < 1$  m/s) at once, possibly lowering the requirements on the LoS measurement rate for impact alleviation control of wake vortices and gusts by increasing the total number of measurement points and measurement ranges.

The FWFIMI is designed for a high instrumental contrast at 532 nm, as well (see appendix E). A convenient method using this green mode for the determination of the backscattering ratio  $R_b$  is described in appendix J. This requires a modified THG-unit.

Adequate sampling of the reference laser pulse without the need for broadening the pulse response in the amplifier electronics could be achieved in several ways. A seeded laser would enable cw illumination of the reference fringe, provided the IR-seeder yields sufficient power for frequency-tripling. Alternatively, an actively Q-switched laser pulse could be sampled repeatably at identical time steps. Furthermore, a longer pulse duration pulse could be used. Otherwise, analog-to-digital converter cards with higher sampling rates are necessary to achieve a higher spatial resolution ( $\Delta R < 25$  m).

A higher pulse repetition rate would allow for faster averaging of shot noise and speckle. Lower energies per pulse would also reduce the signal in the near-range, what may be relevant in case of higher receiver efficiencies.

Scanner optics should be developed in order to cover several line-of-sight measurement directions for turbulence and wake vortex alleviation.

The turbulence and wake vortex alleviation algorithms should be optimized for a higher number of quasi-instantaneously obtained LoS measurement points, for a lower number of LoS directions, and for increased standard deviations or lower LoS update rates. The combined effect may be a reduction of the requirements on the lidar sensor.



## 6 Summary

Concepts for alleviation and control of wake vortices and gusts using wind field information obtained by Doppler wind lidars (DWL) are currently under development. These concepts impose high requirements (i.e., high accuracy, high spatial and temporal resolution, multiple close-range measurement points, multiple line-of-sights) on a future DWL sensor.

The aim of this work was to develop and test a lidar receiver concept for the monaxial measurement of wind speeds aiming at fulfilling these requirements. The first question investigated in this work was

### 1.1) What are the most promising state-of-the-art Doppler wind lidar receiver techniques for this application and how do they compare?

With coherent detection DWL relying on aerosol scattering not being guaranteed at cruise flight level the focus was laid on direct-detection DWL.

Multiple filter techniques with at least four channels or fringe-imaging techniques, not relying on a knowledge of the particle backscattering ratio, were studied with respect to their range-resolved measurement capabilities in the near-range in front of an aircraft. It turned out that full overlap at all measurement distances requires high étendue capabilities of the spectral analyzer. At the same time multiple quasi-simultaneous measurement points require fast linear photomultiplier tube arrays (PMTA) with high enough gains in the UV. Fizeau- and Fabry-Pérot-type fringe-imaging interferometer fringes were found unsuitable with respect to shape, stability, and contrast. Therefore, two-beam interferometer techniques such as the 4-channel Mach-Zehnder, its fringe-imaging version producing two linear fringes, or the fringe-imaging Michelson interferometer, which can all be compensated for wide angular distributions, were favored.

Based on these findings the selection process was started, which leads to the second question.

### 1.2) Which technique for wind measurements on cruising altitude is especially suited and realizable?

The fringe-imaging Michelson interferometer was recognized as a simpler, easier to realize alternative to Mach-Zehnder-based techniques, with minor to no concessions with respect to theoretical performance, depending on the realized concept. The selected concept is based on a Michelson interferometer with inclined mirrors to produce a linear fringe, and with field-widening and partial temperature tuning compensation. A monolithic design, based on the requirement of thermomechanical stability of the fringe position, seemed promising. Furthermore, linear fringe shape can be ideally combined with linear photomultiplier tube arrays to yield a high range-resolution. The concept needed stable illumination, therefore, a fiber-coupled based approach was envisioned. The concept performance was estimated using calculations.

In the next step the receiver concept was realized and characterized, answering the question:

### 2.1) Can such a Doppler wind lidar receiver prototype be built up and characterized?

Indeed, a monolithic Michelson interferometer was specified with respect to the ideal optical path length difference between the arms, mirror inclination angle, wavefront error, and fabrication tolerances, and was handed to an experienced industrial manufacturer for fabrication. The manufactured interferometer was integrated inside a compartment for protection and temperature stabilization. The interferometer was illuminated under different conditions and was characterized using 2D cameras. A concept to illuminate the interferometer with the near-field of a multimode fiber, and to image the linear fringe onto the linear photomultiplier tube array was developed and was realized using a steel cage system for mechanical stability.

The fringe characteristics and the temperature tuning rate were evaluated during tests in the laboratory. Measurements were undertaken to estimate the scrambling gain and the speckle characteristics of fibers, which lead to the selection of a quadratic-core 600  $\mu\text{m}$  multimode fiber. A routine to determine the illumination function by ramping the laser frequency was developed, and biases due to laser beam pointing fluctuations and due to limited illumination function determination accuracies were estimated, using a combination of measurements, end-to-end simulations, and Cramér-Rao bound calculations, which were also used to assess theoretical performance at cruise flight level.

The developed and built up receiver was installed inside a measurement container for testing purposes in order to evaluate the question:

### 2.2) To what extent can the lidar receiver concept be validated by first ground-based wind speed measurements?

This question was answered by performing ground-based test measurements in January and March 2018.

Horizontal wind speed measurements on the hangar apron of DLR Oberpfaffenhofen compared to coherent detection DWL (C-DWL, Windcube® 200S) proved that the instrument and the data retrieval method are sensitive to wind speeds  $< 1$  m/s, with high correlation coefficients of 0.89, and standard deviations on the order of 0.5 m/s for LoS-update rates of 2 Hz at close ranges of 50 m and 76 m. The C-DWL was verified against ultrasonic anemometer measurements. A range-dependent offset bias of AEROLI of several m/s due to angular distribution variations of the atmospheric backscattering illumination was identified. This bias is corrected manually. The illumination function varied over the day. Its change may be related to laser beam profile changes, and to convectional temperature gradients in the interferometer compartment, yielding macroscopic fringe shifts and deformations. For all these reasons the offset bias was temporally stable during  $< 10$  min.

Vertical wind speed measurements at a LoS-update rate of 1 Hz proved the range-resolved measurement capability with range gate lengths of  $\approx 30$  m in the boundary layer up to altitudes of 900 m with correlation coefficients up to 0.7 (compared to the C-DWL). Relative precisions of both lidar systems  $> 0.7$  m/s below altitudes of 300 m have to be attributed to increased measurement uncertainties of the C-DWL. The AEROLI receiver has a theoretical efficiency of  $< 2.7\%$  at distances larger than 200 m. The offset bias decreases as a function of altitude from up to 16 m/s down to 6 m/s. This could be explained with stronger varying angular distributions for the extreme near-ranges than for larger distances.

Summarizing, the direct-detection Doppler wind lidar receiver prototype “AEROLI” developed in this work was validated against coherent detection DWL wind speed measurements. These tests constitute, to the author’s knowledge, the first range-resolved wind speed measurements with a fringe-imaging Michelson Doppler wind lidar.

### 2.3) Which requirements with respect to wake vortex alleviation control does the receiver prototype fulfill?

It was demonstrated that the receiver fulfills the required sensitivity to wind speeds with a standard deviation of the measured wind speeds  $< 1$  m/s provided that the LoS-update rate is  $\leq 2$  Hz. Higher update rates reduce the time for averaging of shot noise, leading to increased standard deviations, which are above the ones predicted with Cramér-Rao bound calculations and end-to-end simulations. Further end-to-end simulations including atmospheric speckle, ruled out speckle as the primary reason for the increased standard deviation. The conclusion was drawn, that only  $\approx 17\%$  of the predicted backscattered signal actually fell on the detector, increasing  $\sigma(u_r)$ , and reducing the receiver efficiency to  $< 0.4\%$ . This signal loss together with systematic biases are held responsible for increased values of  $\sigma(u_r)$ . The combination of measurement accuracy and update rate does not meet the requirements for wake vortex alleviation and control (i.e.,  $\sigma(u_r) < 1$  m/s and  $r_{LoS} > 45$  Hz to 100 Hz), today.

## Outlook

The major advantage of the AEROLI receiver principle compared to the FIFPI technique used in AWIATOR ([Rabadan et al., 2010](#)) is the use of a fast linear photomultiplier tube array, allowing for range-resolved quasi-simultaneous measurements on a single detector.

Cramér-Rao calculations and end-to-end simulations show that the principle would work at cruise flight level and for a pure molecular signal, however the prevailing lower molecular densities would decrease measurement precision by a factor between 2 and 3 compared to ground-based measurements.

It is thus advisable to increase the receiver efficiency in the near-range and to perform further longer range vertical measurements in low-aerosol concentration atmospheric environments, such as from the Schneefernerhaus on the Zugspitze mountain, to confirm the theoretical findings.

Overall, the performance requirements for the Doppler wind lidar in a wake vortex alleviation control scheme are not yet fulfilled, but there is a high potential for the here developed technique, as soon as the receiver is improved with respect to efficiency and reduced systematic biases, and when its performance has been verified experimentally in low-particle concentration atmospheric environments.

Moreover, a suitable laser transmitter, e.g., a UV disc laser, with approximately ten times the repetition rate, and similar average powers ( $> 8$  W) could be developed for further improving on the noise and speckle averaging, and thereby on the precision and accuracy of the wind speed measurement.

The problem of required illumination calibration remains, which should be addressed with a suitable procedure in the future, provided that sufficient stability of the illumination cannot be achieved. Calibration and measurement could be performed at the same time, for instance by ramping the laser in frequency continuously, or by using a periodic calibration using a shutter installed within one of the interferometer arms.

Furthermore, lidar parameter studies with respect to wake vortex and gust / turbulence alleviation should be refined, considering a higher number of longitudinal measurement points on a single detector, in order to find out if the requirements on the Doppler wind lidar sensor can be reduced. For this purpose a more accurate lidar model emulating the end-to-end simulations of this work should be implemented in the alleviation and control simulations.

Provided that these issues are solved the AEROLI receiver or its successors could be tested aboard the novel DLR flight test aircraft “iSTAR”, a Falcon 2000LX twin-jet within an approximate timeframe of five years. In the end, a direct-detection DWL receiver based on the fringe-imaging Michelson interferometer concept could also be envisioned for a future Doppler wind lidar satellite mission succeeding ADM Aeolus, for instance.

# A Background on field-test measurements of the AEROLI receiver

This chapter provides background information on field-test measurements of chapter 5.

## Moving hard target speed measurements

Fig. A.1 shows how the line-of-sights of the AEROLI DWL and the Windcube<sup>®</sup> 200S are aligned on the belt sander paper. In case of AEROLI the laser beam spot is visible to the eye (Fig. A.1(b)). In case of the Windcube<sup>®</sup> a scan is performed and a CNR-map is recorded (see Fig. A.1(b)).

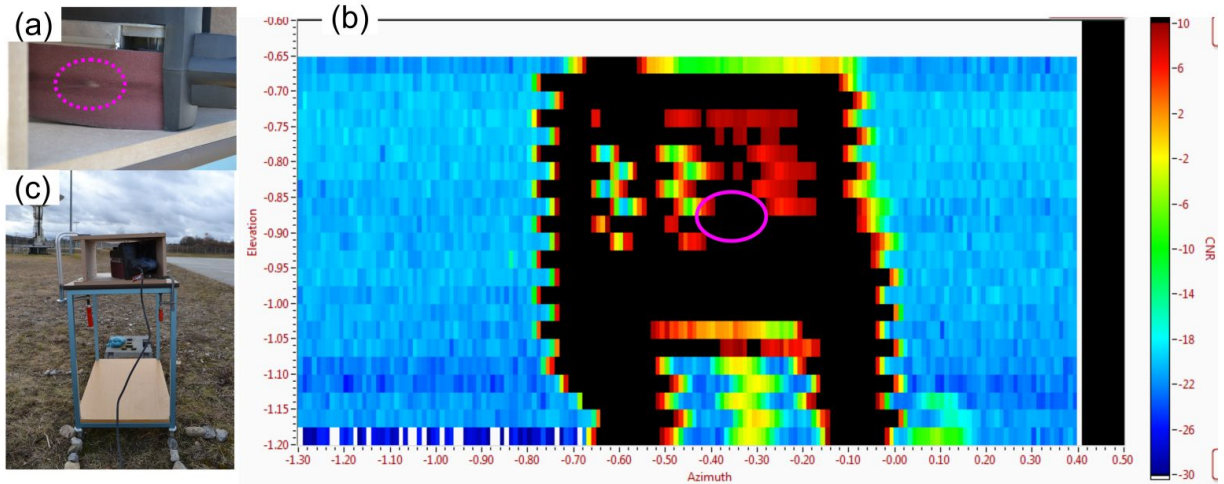


**Figure A.1:** (a) Laser spot of AEROLI transmitter on the belt sander. (b) CNR-map generated by scanning the Windcube<sup>®</sup> over the belt sander (with supposed position of the sanding paper marked in violet). (c) Photograph of the belt sander located at 50 m distance from the lidar sensors.

Fringe data (crosses) of both backscattered light (sig) and laser reference light (ref, fiber-delayed laser pulse) for different times during a measurement run are shown in Fig. A.2(a). The fitting curves using the DSA method with fit model eq. 5.3 are shown as lines. The respective fractional deviations between fringe data and fit are shown below. The fit parameters determined from the DSA fits are shown as a function of time in Fig. A.2(b). The respective determined belt sander paper speeds of the same measurement run are shown in Fig. 5.9(a).

Fit parameter  $p_{\Delta\phi}$  is influenced by the long-term changes of the temperature within the interferometer cell. Steps of  $p_{\Delta\phi}(\text{sig})$  indicate when the belt sander was switched off and on. The phase offset between backscattered signal (sig) and laser reference (ref) during times when the hard target was not moving (e.g., from 15:28 to 15:33) may be the consequence of different angular distributions of the backscattered signal illumination and the laser reference illumination of the FWFIMI, introducing different phase shifts (see eq. C.59).

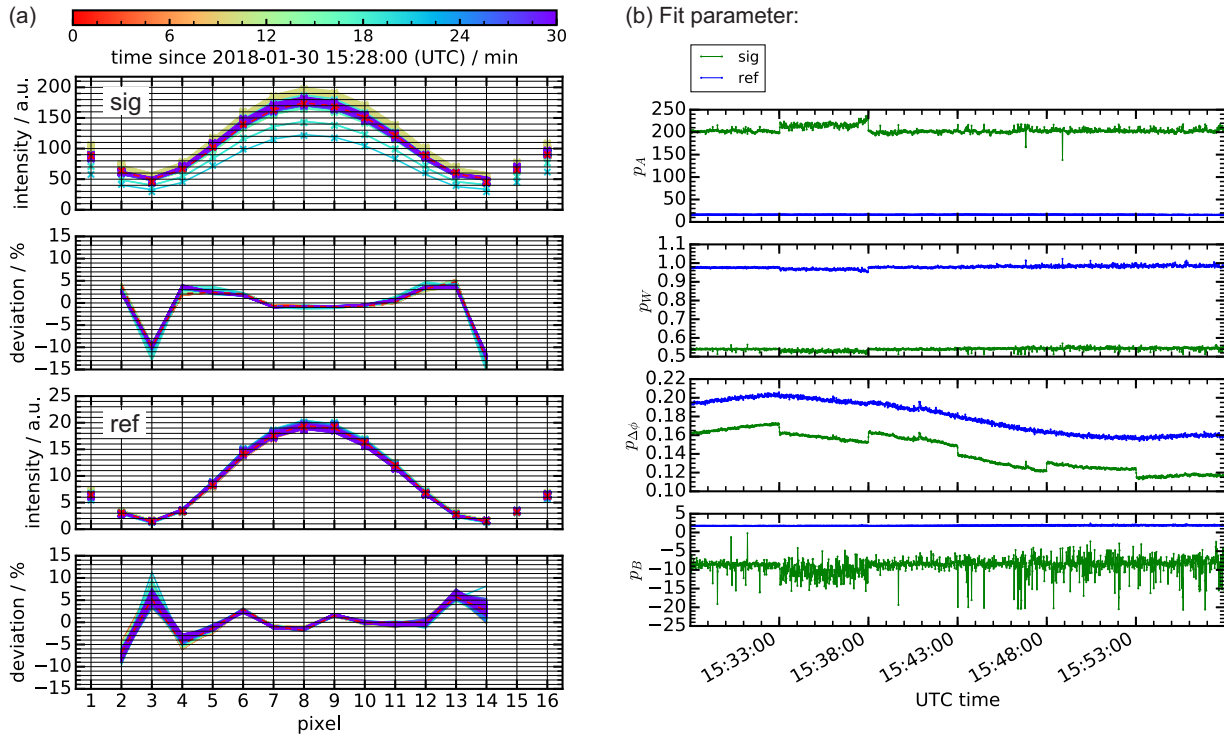


**Figure A.2:** (a) Fringe data (crosses), fitting curves (lines), and their fractional deviation per PMTA channel of backscattered light (sig) and of laser reference light (ref) during a hard target speed measurement run. The measurement time is color-encoded. The first measurement at 15:28 is marked with a dashed red line. (b) Temporal dependence of the values of the fit parameters of the DSA fitting routine using fit model eq. 5.3 for both backscattered light (sig, green) and laser reference light (ref, blue).

## Horizontal wind speed measurements

### 1. Anemometer versus Windcube<sup>®</sup>

Anemometer measurements were carried out during all lidar measurements. The ultrasonic anemometers (Vaisala WXT520, Svantek DAQ) provide point measurements in contrast to the range gate lengths ( $\Delta R = 25$  m) of the Windcube<sup>®</sup> 200S and of the AEROLI receiver ( $\Delta R \approx 30$  m). The Windcube<sup>®</sup> wind speeds were verified against anemometer measurements on July 17, 2017. Fig. A.3 shows these measurements, with a Topsonic DAQ anemometer at  $R = 67$  m and the Svantek 181 (DAQ) at  $R = 75$  m. Both the Windcube<sup>®</sup> data and the anemometer data are shown without and with smoothing. Smoothing is performed with a rolling mean with a window of 20 observations for the Windcube<sup>®</sup> ( $\Delta t = 0.5$ s) and the Svantek instruments ( $\Delta t = 1$ s). The Topsonic anemometer provided measurements every 10 s and is not smoothed.

After smoothing the measurements of the Windcube<sup>®</sup> and of the Topsonic at 67 m and the Svantek 181 at 75 m fit together. In case of Windcube<sup>®</sup> versus Svantek 181 the Pearson correlation coefficient is 0.92 and the standard deviation of the difference  $e$  between the estimated wind speeds of the anemometer and the coherent DWL is 0.5 m/s.

Minor deviations can be attributed to the different measurement rates in case of Topsonic versus Windcube<sup>®</sup>, and to the point measurements of the anemometers in general. Topsonic instruments provide a too low temporal resolution for an adequate reference measurement. In case of  $R = 92$  m no Windcube<sup>®</sup> wind speeds could be obtained because



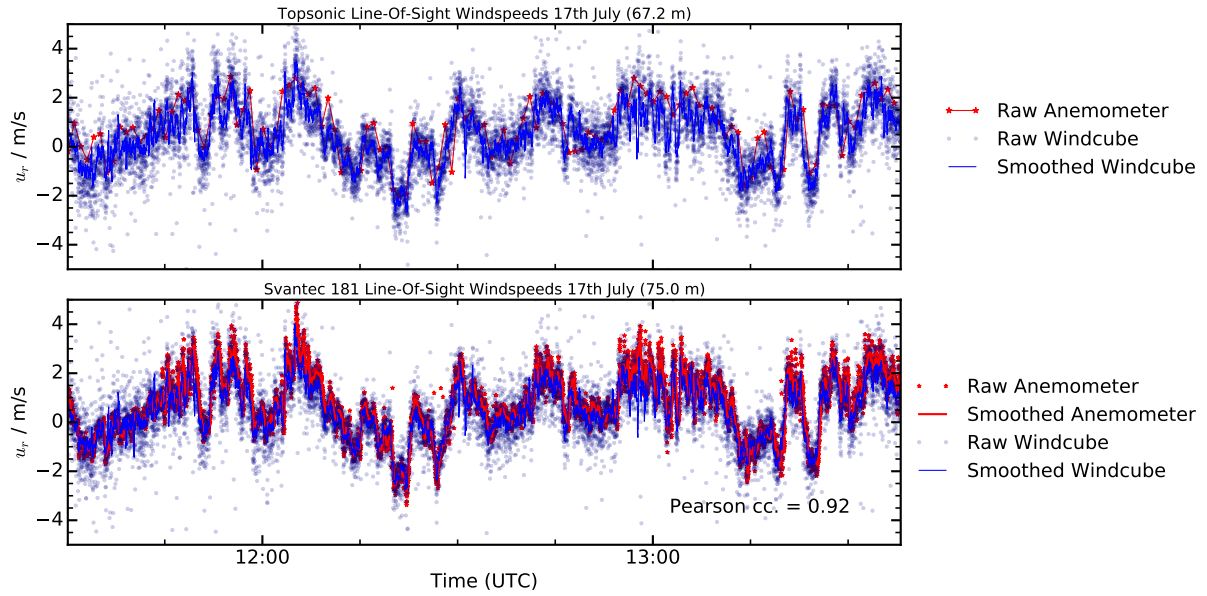


**Figure A.3:** Windspeed measurements with a Windcube® 200S and ultrasonic anemometers (Vaisala WXT520, Topsonic DAQ, Svantec 181 DAQ) on July 17, 2017. Windcube® and Svantec are smoothed using a running mean with a window of 20 observations.

part of its range gate already hit the hard target positioned at  $R \approx 115$  m.

The decision was made that the Windcube® measurements are reliable and can be compared to AEROLI measurements more conveniently than anemometer measurements, because of the approximately equal range gate lengths, providing the same degree of spatial averaging over the wind speed field. That is why, during the field-test measurements comparing AEROLI and Windcube® 200S measurements, which are treated in chapter 5.3 and in the following, anemometer measurements are not evaluated further.

## 2. Further measurements with AEROLI and Windcube®

The following section of the appendix provides additional horizontal wind speed comparisons between AEROLI and Windcube® carried out on January 29, 2018.

For this purpose the weather conditions during the day are evaluated. Solar data obtained from “www.suncalc.org” by Torsten Hoffmann is shown in Fig. A.4(a). Fig. A.4(b) shows the CNR of the Windcube® as a function of time over the day and measurement conditions (temperature, pressure, solar global radiation, and humidity) measured with a weather station (MWS 5) located at a linear distance of  $\approx 300$  m from the measurement location on the roof of the Institute of Atmospheric Physics building.

Additionally the global contrasts of AEROLI (atmospheric signal and laser reference obtained from the fit and from determination of the Michelson contrast (MC)), and plausible values of the particle backscattering ratio  $R_b$  calculated based on the weather station temperatures and on the determined contrasts are included. For this calculation eq. 3.4 is used, assuming a free-spectral range (FSR) of 10.69 GHz and an instrumental contrast (V) of 0.9. This estimation of  $R_b$  is quite error-prone because the actual instrumental contrast during the measurements is unknown. The actual value of  $R_b$  could be higher. The contrast of the laser reference (green crosses in Fig. A.4(b)) is not equivalent to the instrumental contrast. This is because the laser reference fringe stems from a hard tar-

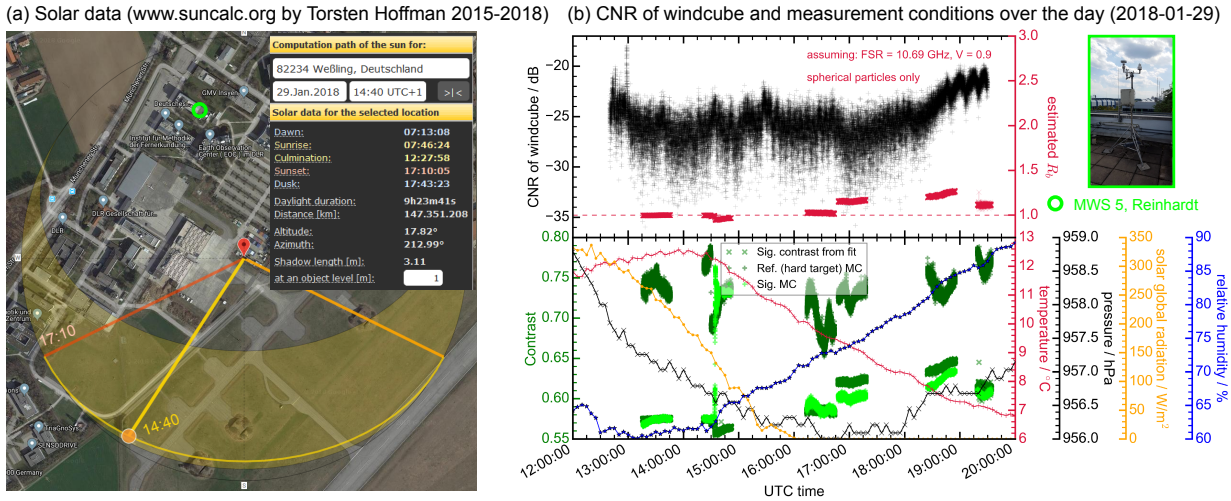


**Figure A.4:** (a) Solar data (www.suncalc.org by Torsten Hoffmann), (b) CNR of Windcube® and measurement conditions over the day (January 29, 2018) provided by the weather station (MWS 5, Reinhardt) on the roof of the Institute of Atmospheric Physics building. Particle backscattering ratios  $R_b$  (crimson) are estimated using eq. 3.4 based on temperature data provided by MWS 5.

get return which is superimposed with backscattering signal from air in front of the hard target. This superposition reduces the contrast of the reference fringe to about 70%.

The first observation is, that the Windcube's CNR goes down to -30 dB over the day until after sunset. January 29th, 2018 was a sunny blue sky day with sunset at 17:10 (local time). The sun was shining in measurement direction around 13:40 UTC. However, both the Windcube® and AEROLI are designed for daytime measurement capability and the observation of high measurement noise of the Windcube® after sunset (see Fig. A.5) seems to exclude the solar radiation from affecting the measurements. The contrast is especially low during mid day and increases slightly to the evening. A low concentration of aerosols could be the cause of the low CNR values and the relatively high measurement noise of the Windcube®, which is shown in the following measurements (see, e.g., Fig. A.5).

In all following measurements of this section  $u_r$  values of the Windcube® stemming from measurements with a CNR < -29 dB are excluded. This fixed CNR-threshold filtering is a common approach, although more intelligent, dynamic data filtering (see, e.g., Beck and Kühn (2017)) may be applied.

Fig. A.5 shows a measurement on January 29, 2018 with high noise of the Windcube®, i.e., relatively low CNR of down to -34 dB.

$u_r$ (Windcube) yields some outliers even though values stemming from CNR < -29 dB have been excluded (Fig. A.5 top). After applying a median filter with a threshold of 3 m/s, the measurements of both instruments show good correlation (Fig. A.5 middle). The standard deviation of the difference is greater than 1 m/s, also because many noisy spikes of the Windcube® are not properly filtered out.

In contrast, Fig. A.6 shows another measurement on January 29, 2018 with low noise of the Windcube®, i.e., relatively high CNR of > -28 dB (see Fig. A.4).

As is especially visible at 18:49 (UTC), the radial wind speeds ( $u_r$ ) measured by the coherent detection DWL and AEROLI seem to drift apart, while the finer features are well reproduced. This behavior suggests a velocity independent offset bias, which may be constant on time scales of 10 min.

A possible reason could be a long-term change of the illumination function of either the signal, the reference, or both. It was shown in section 4.4 that a change of the illumination function can induce a bias.

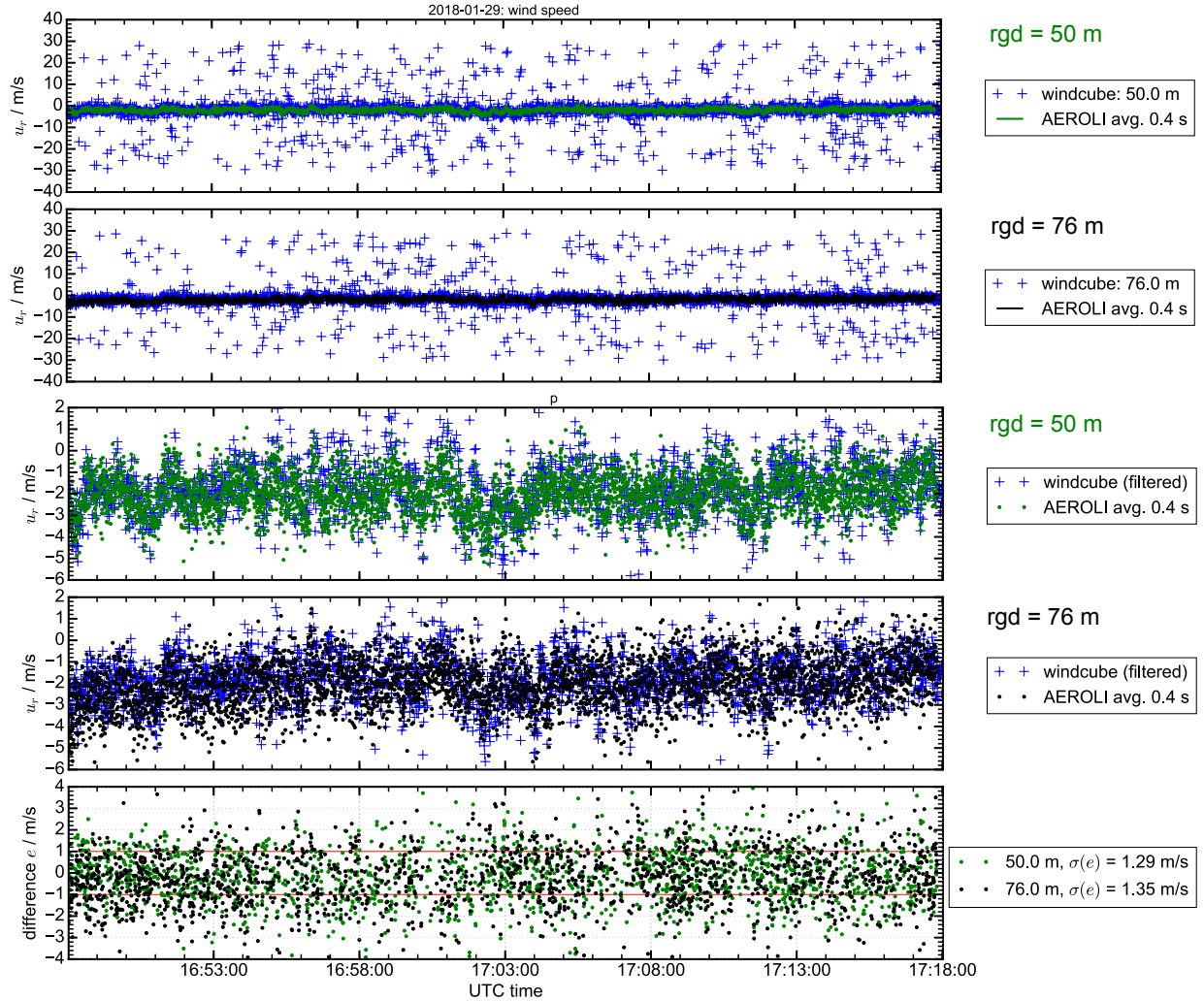


**Figure A.5:** Horizontal radial wind speed of AEROLI with laser locked to the iodine line and of Windcube® shortly after sunset (on January 29, 2018 at 16:10 UTC). The relatively noisy Windcube® data (filtered such that CNR >-29 dB, top) is then median filtered (bottom), whereby the mean of the last 10 measurements is compared against a threshold of 3 m/s. If this threshold is exceeded, the corresponding data is rejected.

Changes of the fringe position due to temperature tuning can affect the differential character of the measurement (see green lines in Fig. A.7(a)), when temperature-induced shifts are large enough (e.g., visible with the eye). Because if the illumination function is slightly different, this changes the macroscopically shifted fringes (both reference and signal) in a different way than for an nonshifted pair. Alternatively, the same effect can be induced if the fitting model does not exactly match the fringe shape. This is the case for reference fringes obtained from a mixture of atmospheric backscattering and hard target reflection with different contrast factors producing a mesokurtic fringe shape with a large positive kurtosis (see Fig. A.7(b)).

Fig. A.7(a) shows that there is a macroscopic shift in fringe position by 300 MHz (i.e.,  $1/36 \cdot \text{FSR}$ , equivalent to a radial wind speed  $u_r$  of 60 m/s). This shift of the fringe position

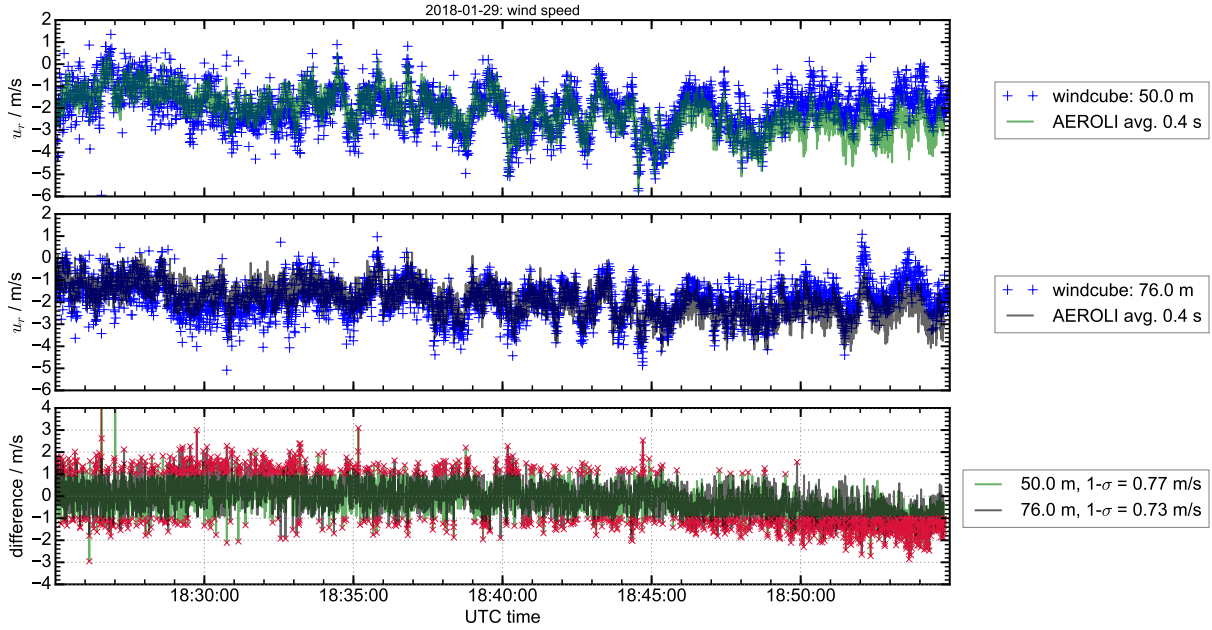


**Figure A.6:** Horizontal radial wind speed of AEROLI with free-running laser (centered interference fringe maximum) and Windcube®. This is the first measurement on January 29, 2018, comprising a low noise of the Windcube®.

cannot be explained with frequency shifts of the free-running laser (see Fig. A.7(a), blue line).

Fig. A.7(b) shows the same kind of plot for a measurement run with less time dependence (drift) of the bias. The resulting wind speeds of this measurement run are shown in section 5.3.2 (Fig. 5.12).

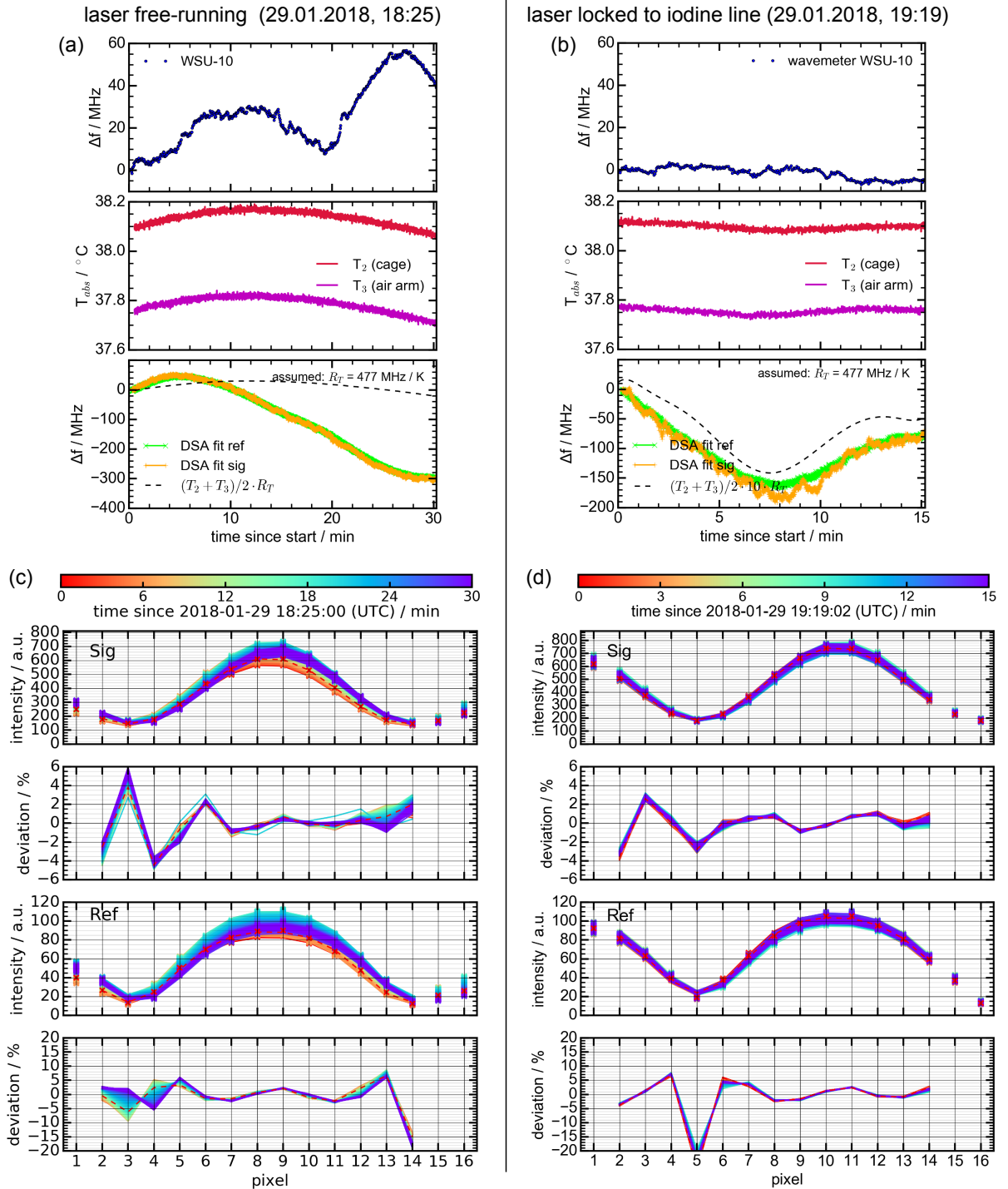
In this case with less drift there is a macroscopic shift (200 MHz) of the fringes, as well. However, it is not as large as in the previously shown case, and the fringe shapes and deviations between data and fit at different times resemble more closely (compare Fig. A.7(c) and (d)).

Consequently, it is very likely that biases as seen in Fig. A.6 can be avoided by improving on the temperature stabilization of the interferometer, and on the stability of the illumination functions. Furthermore, the laser should be locked to the iodine line (as in Fig. A.7(b)) to avoid additional fluctuations of the fringes position.

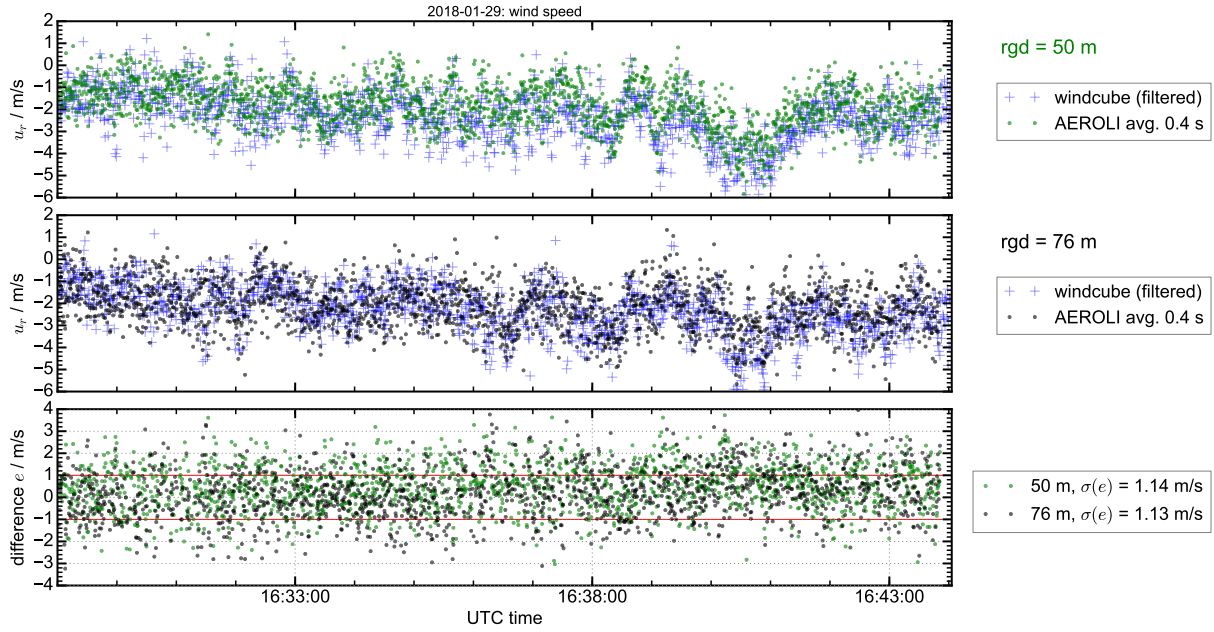
Another horizontal measurement (with the laser of the AEROLI DWL being locked to the iodine line) shortly after sunset is shown in Fig. A.8. Almost no temporal drift of the difference  $e$  between both lidars is visible.

Fig. A.9 shows another example of a daytime measurement on January 29, 2018, whereby the sun was shining along the measurement direction ( $213^\circ$ ) at 13:40. Again the AEROLI DWL laser was locked to the iodine line. The resulting wind speed values of AEROLI correlate well with the Windcube®'s values after threshold filtering. In case of the measurement of Fig. A.9, a drift of  $u_r$  is apparent between both instruments. This drift may again be due to temperature fluctuations in the interferometer cell or due to long-term changes of the illumination function. These changes of the illumination function could also be related to a gradual drift of the laser beam orientation, which was not tracked during the test measurements. It is clearly not caused by frequency variations of the laser itself.





**Figure A.7:** Measurement on January 29, 2018: (a) The laser was not locked to the iodine line (see also Fig. A.6). (b) Laser locked to the iodine line (see also Fig. 5.11). Frequency measured with wavemeter (top). The temperature within the FWFIMI cell (middle). Bottom: Temperature tuning given as frequency change and frequency shift of laser reference (green) and atmospheric signal (orange). (c, d) Time-dependent fringe shapes (points), fits (lines), and deviations between data and fits for the atmospheric signal at  $R = 50$  m and for the hard target reference of a measurement with time dependent bias. Different fringes at different times are shown in different colors.



**Figure A.8:** Horizontal radial wind speed of AEROLI with laser locked to the iodine line and of Windcube® shortly after sunset (Measurement on January 29, 2018 at 16:10 UTC, 17:10 local time). The relatively noisy Windcube® data is median filtered, whereby the mean of the last 10 measurements is compared against a threshold of 3 m/s. If this threshold is exceeded, the corresponding data is rejected.

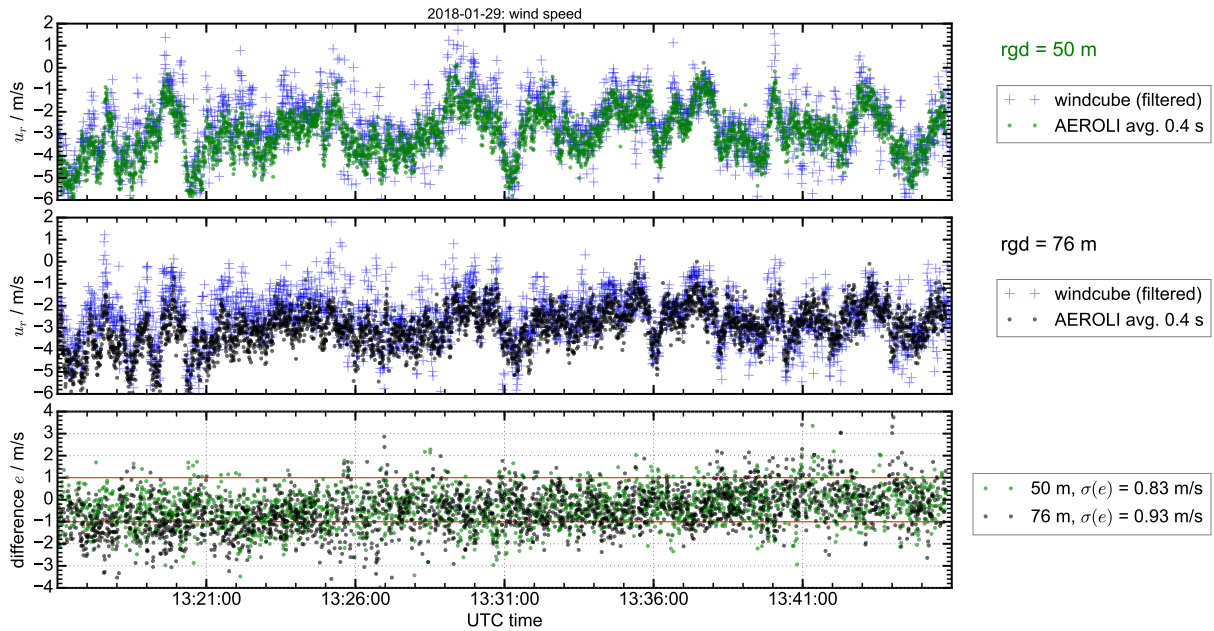


**Figure A.9:** Horizontal radial wind speed of AEROLI with laser locked to the iodine line and of Windcube® in the sunny, blue sky afternoon (measurement on January 29, 2018). At 13:40 (UTC) the sun is located exactly in measurement direction (at  $213^\circ$  azimuth), and at an altitude of  $17.8^\circ$ . The relatively noisy Windcube® data is median filtered, whereby the mean of the last 10 measurements is compared against a threshold of 3 m/s. If this threshold is exceeded, the corresponding data is rejected.



### 3. Analysis of fit routine and parameters

In the following the results obtained with different fit models for measurement runs without and with the laser being locked to the iodine line are compared and analyzed.

Fig. A.10(a, b) provides a comparison of wind speeds determined with the DSA method with two different fit models (see eq. 5.2 and eq. 5.3) for the measurement runs shown also in Fig. A.6 and Fig. 5.12.

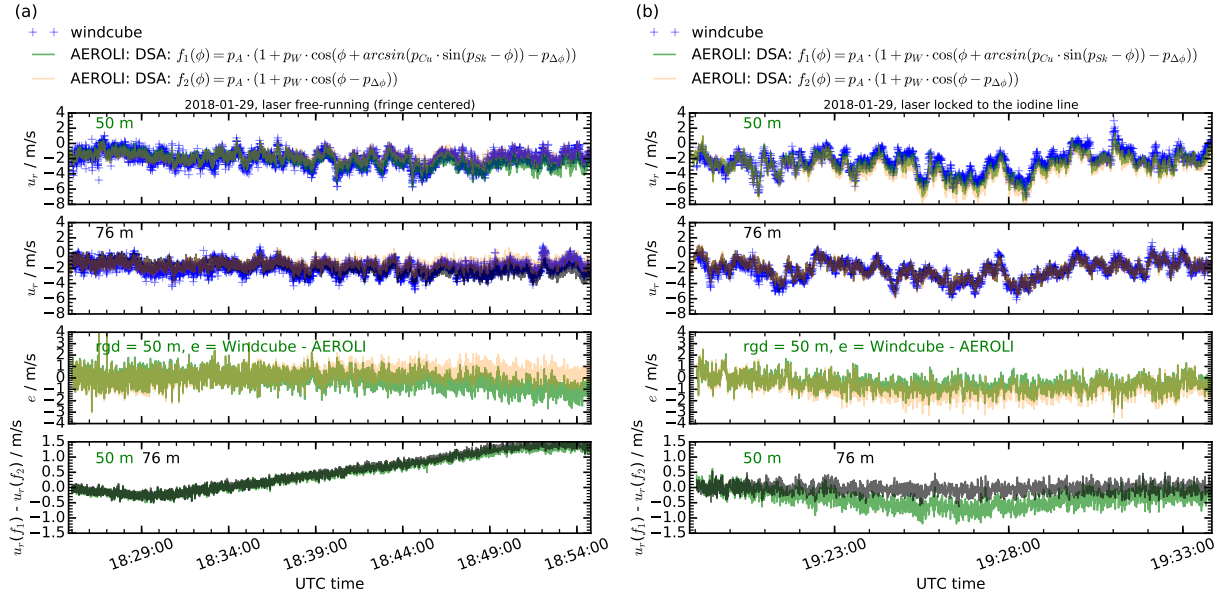
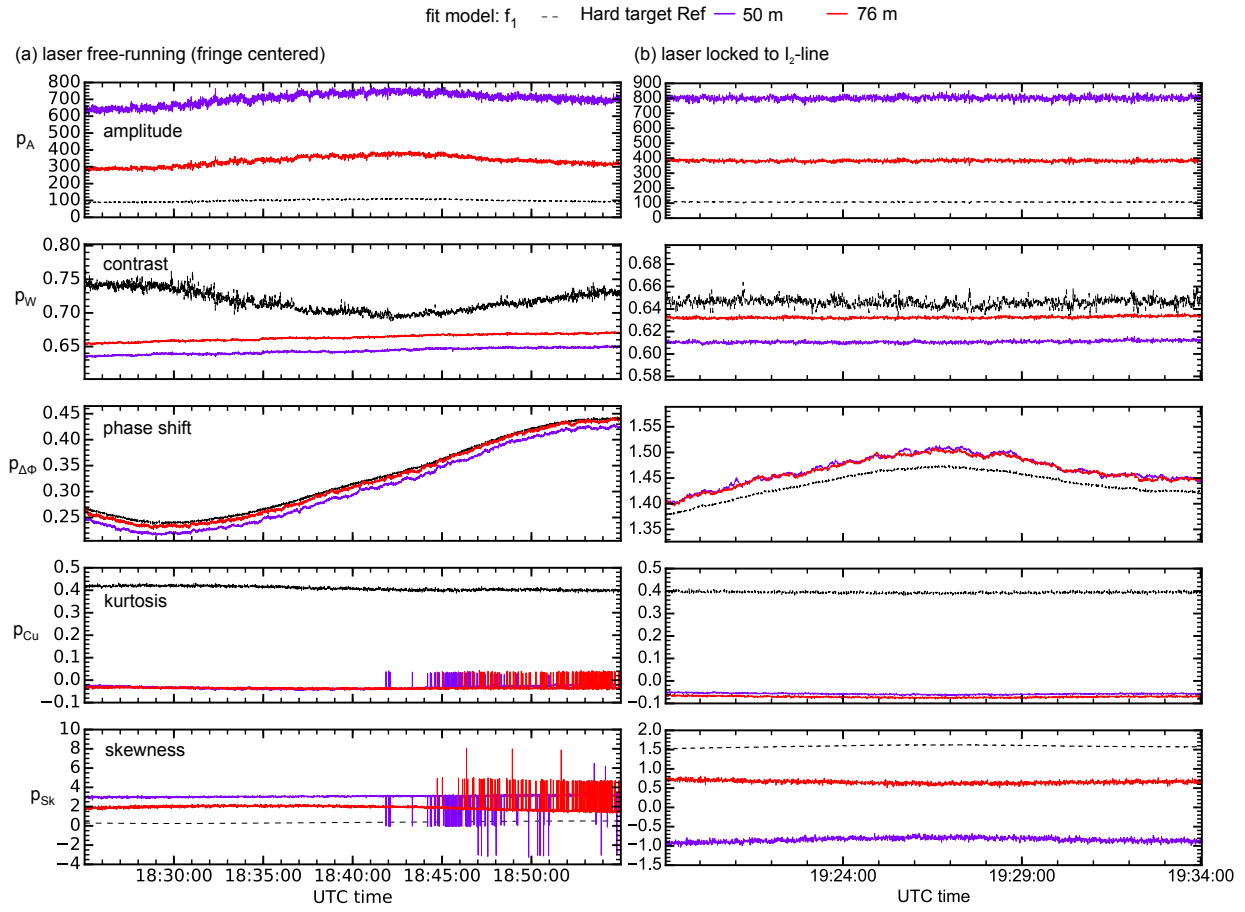


**Figure A.10:** Resulting wind speeds during measurements on January 29, 2018: (a) Same measurement run as in Fig. A.6 and Fig. A.7(a) with the free-running laser and centered fringe. (b) Same measurement run as in Fig. 5.12 and Fig. A.7(b) with laser locked to the iodine line. Top: Resulting  $u_r$  for rgds of 50 m and 76 m in case of a DSA fit model  $f_1$  including skewness and kurtosis (green, see eq. 5.2) and in case of a simple cosine fit model  $f_2$  (orange, see eq. 5.3). The respective difference between Windcube® and AEROLI for these rgds is shown below. Bottom: Difference of the resulting  $u_r(f_1) - u_r(f_2)$  as a function of time.

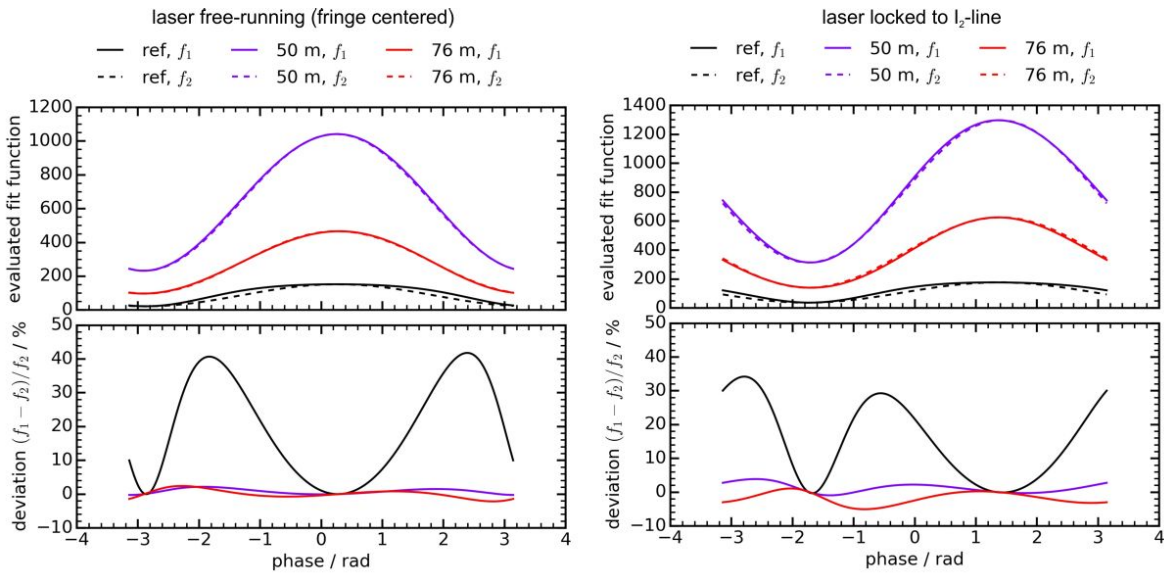
A significant discrepancy  $u_r(f_1) - u_r(f_2)$  is visible at a distance of 50 m in case of Fig. A.10(a, b). The more complex model ( $f_2$ ) seems to deviate less relative to the coherent DWL measurements than model ( $f_1$ ) in case of Fig. A.10(b). However, in case of Fig. A.10(a) the situation is reversed. This could be explained with a higher variation of the fringe shape in case of Fig. A.10(a). This result suggests that a fit model of type  $f_1$  may be preferable in comparison to type  $f_2$ . However, no clear trend is visible and further studies considering different fit models should be undertaken, once a better temperature stabilization and illumination function correction routine have been developed.

Fig. A.11(a, b) provides all fit parameters of the complex fit model ( $f_1$ ) during that same measurement runs with the laser in free-running mode and with the laser stabilized to the iodine line (the same as in Fig. A.10(a, b)).

The according fringe-shapes for the fit models  $f_1$  compared to the fit model  $f_2$  at the same phase, prior to downsampling are shown in Fig. A.12 for one measurement time.



**Figure A.11:** Variation of the fit parameters using fit model  $f_1$  as a function of time for the two different measurement runs shown in Fig. A.10(a, b). Black dashed: laser reference fringe of the light scattered back from the hard target. Purple / Red: Atmospheric signal fringe from the respective range gate distance (rgd).



**Figure A.12:** Fringe shapes of fit model  $f_1$  compared to  $f_2$  at the same phase for a particular instant of time for both measurement runs.

In case of the free-running laser measurement parameters for amplitude ( $p_A$ ) show a long-term drift (Fig. A.11(a)) not being visible for the measurement with the laser being locked to the iodine line (Fig. A.11(b)). The contrast parameter ( $p_W$ ) shows the largest drift in case of the hard target reference fringe of the free-running laser measurement (black line, Fig. A.11(a)), while being constant in Fig. A.11(b). The phase shift parameter ( $p_{\Delta\phi}$ ) follows a long-term drift in both cases. This drift can be attributed to shifts of the laser reference and atmospheric signal fringes when there are temperature fluctuations and gradients within the interferometer cell. Finer short term features are induced by the Doppler shift of the backscattered light. The kurtosis parameter ( $p_{Cu}$ ) is equal to 0.4 for the laser reference fringe (black line) compared to slightly negative values for the atmospheric signal fringes. This elevated kurtosis of the reference fringe shows also in Fig. A.12 and may explain the different results obtained with the fit models  $f_1$  and  $f_2$  in Fig. A.10. Different skewness parameters in Fig. A.11(a) and (b) suggest that the fringe shape is dependent on the absolute position of the fringe in case of reference and signal fringes. Theoretically, this should not be the case if the illumination is constant for both frequencies of the illumination and if the illumination function was determined correctly. It can be concluded that the different fringe shape parameters may be a consequence of deviations of the determined illumination function from the actual illumination function.

### Influence of illumination function variations

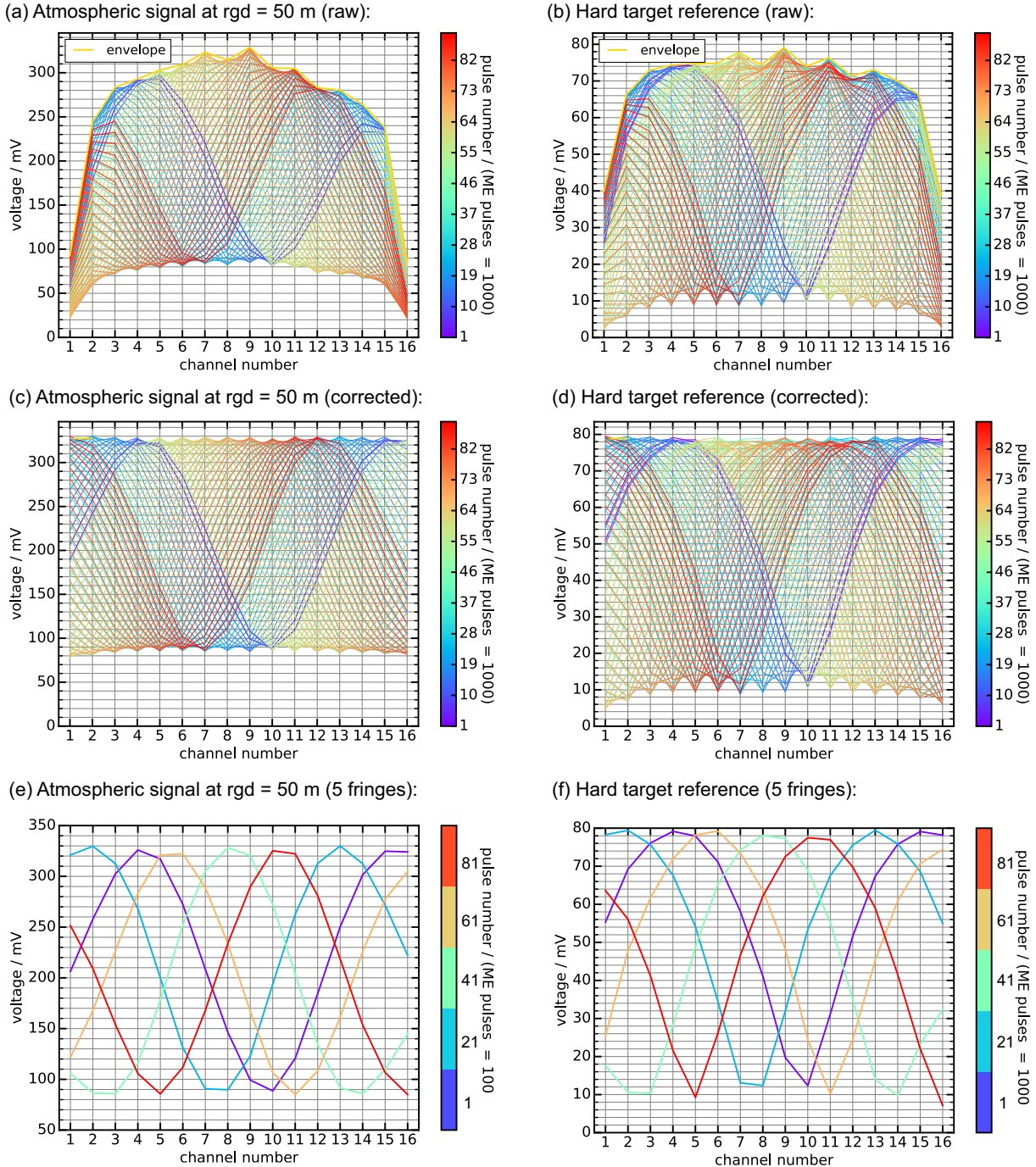
This section provides experimental studies of the precision of the illumination function procedure during the field-test measurements and of the influence on the offset bias studied theoretically in section 4.4.

Fig. A.13 shows atmospheric signal fringes at  $\text{rgd} = 50$  m and hard target reference fringes taken during an exemplary frequency ramp in an illumination function determination procedure performed on January 31, 2018 (see section 3.5.6) before (a, b) and after (c, d) correction with the determined illumination function for a number of averaged pulses (ME) of 1000.

The higher intensities at low and high channel numbers of the envelope in Fig. A.13(b) indicate that the angular distribution of the reference light seems to be more flat-top compared to the signal light. The fringe contrast is higher but not ideal, i.e., 85% not 95%, because the hard target reference light is a mixture of atmospheric scattering and hard target signal. The corrected reference fringes do not resemble ideal cosine functions (see Fig. A.13(d)). The fringes appear to be broader at higher intensities and slimmer at lower intensities, i.e., they have an increased kurtosis ( $Cu$ ) (see, e.g., Fig. C.21 for an illustration of fringe shapes with different amounts of kurtosis). This may be explained with a mixture of signal scattered from the atmosphere and the hard target signal in case of the laser reference. The corrected atmospheric signal fringes are very similar to ideal cosine-shaped fringes with a fringe contrast of  $\approx 66\%$ , which may be attributed to a low particle backscattering ratio  $R_b$ .

Next the influence of the illumination determination function correction procedure on the offset bias is studied. Fig. A.14 provides illumination functions of a frequency ramp taken on January 29, 2018 from 18:58 to 19:13 (UTC), which was also used as illumination function for the field-test measurements of that day. The different colors have the meaning of different numbers of pulses averaged when recording the fringes prior to taking the envelope, whereby different illumination functions, which are the normalized envelopes, are the result. The standard deviations of these envelopes is shown in green as a fraction

of the mean. A variation of the number of averaged pulses (ME) between 10 and 100 induces a change of the illumination function per PMTA channel of up to 1% of the mean for atmospheric signal illumination functions. Referring to the end-to-end simulations of section 4.4, such a variation of the illumination function can induce biases on the order of 1 m/s (standard deviation of the simulated biases).



**Figure A.13:** Recorded fringe shapes during illumination function determination (frequency ramp): (a) Uncorrected atmospheric signal fringes. (b) Raw uncorrected hard target laser reference fringes. (c) Atmospheric signal fringes after correction with the envelope of (a, yellow). (d) Hard target laser reference fringes after correction with the envelope of (b, yellow line). (e) Five exemplary fringes of c). (f) Five exemplary fringes of d). The fringes were recorded on January 31, 2018.



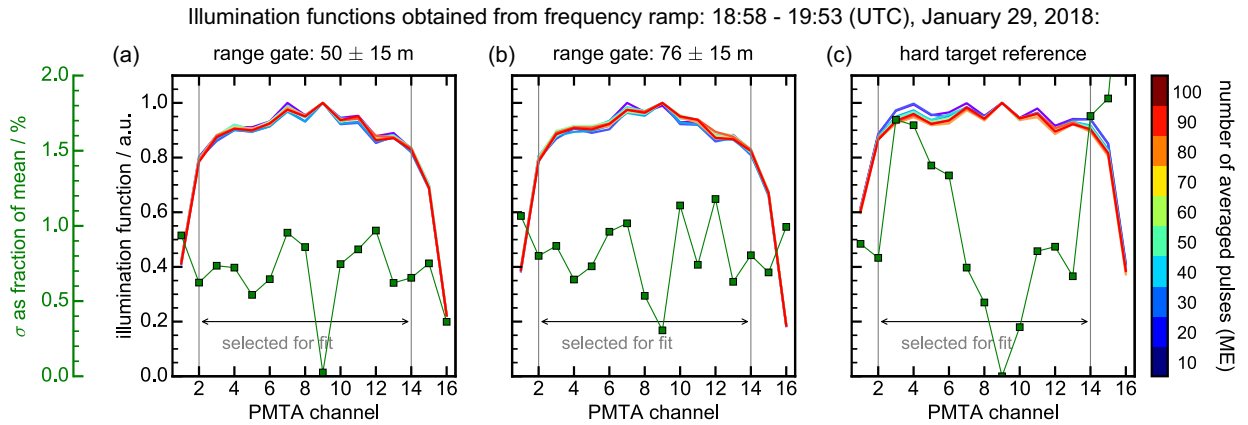


**Figure A.14:** Horizontal field-test illumination functions determined by ramping the DELICAT laser frequency and determining the envelope of the recorded fringes, using the procedure described in section 3.5.6. Illumination functions are shown for different numbers of averaged pulses (ME), shown in different colors, during envelope determination for two range gates:  $50 \pm 15$  m (a) and  $76 \pm 15$  m (b), and for the hard target laser reference (c). The green axis shows the standard deviation  $\sigma$  as a fraction of the mean in % of these different illumination functions.

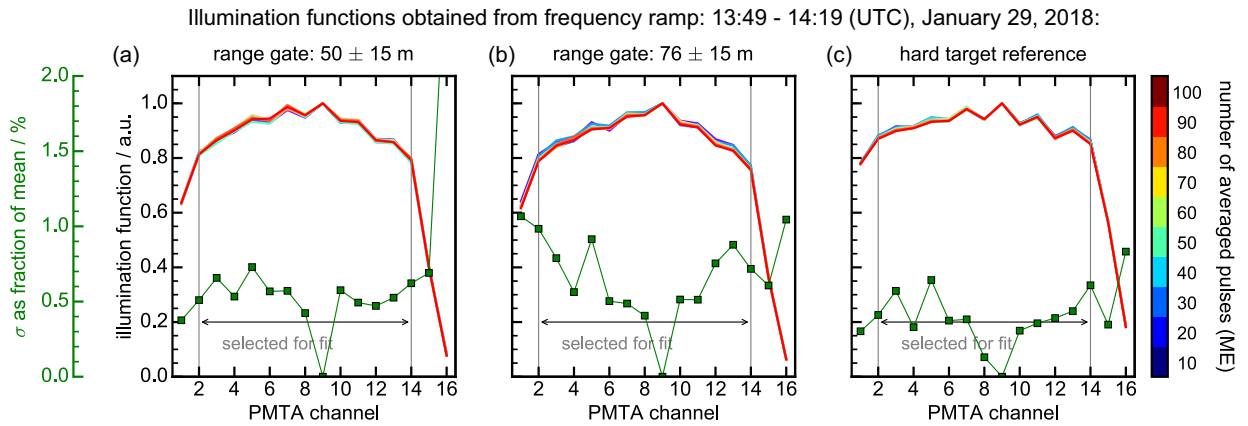


**Figure A.15:** Horizontal field-test illumination functions determined by ramping the DELICAT laser frequency and determining the envelope of the recorded fringes, using the procedure described in section 3.5.6. Illumination functions are shown for different numbers of averaged pulses (ME), shown in different colors, during envelope determination for two range gates:  $50 \pm 15$  m (c) and  $76 \pm 15$  m (b), and for the hard target laser reference (c). The green axis shows the standard deviation  $\sigma$  as a fraction of the mean in % of these different illumination functions.

Similar results are obtained for different illumination function determination runs on the same day. Fig. A.15 shows another set of illumination functions determined at 13:49 (UTC) of the same day.

A comparison of signal and reference illumination functions determined at four different times on January 29, 2018, is shown in Fig. 5.13 of section 5.3.2. The standard deviations as fractions of the mean are on the order of 2% up to 5% in the region selected for DSA fitting (see gray vertical lines in Fig. 5.13). Both the atmospheric signal illumination functions and the reference illumination functions appear to shift on a time scale of hours, while illumination functions taken shortly after each other (see the magenta and the purple curve in Fig. 5.13) are closely resembling

Now, these different illumination functions are applied to correct the fringe shapes of



the horizontal measurement run described in section 5.3.2, in order to evaluate how such a variation of the illumination function changes the phase-shift-independent offset bias. Fig. A.16(a) shows offset biases obtained for different numbers of pulses averaged during the frequency ramp of the illumination function determination procedure, i.e., for the different illumination functions shown in Fig A.14. Fig. A.16(b) provides offset biases according to Fig. 5.13.

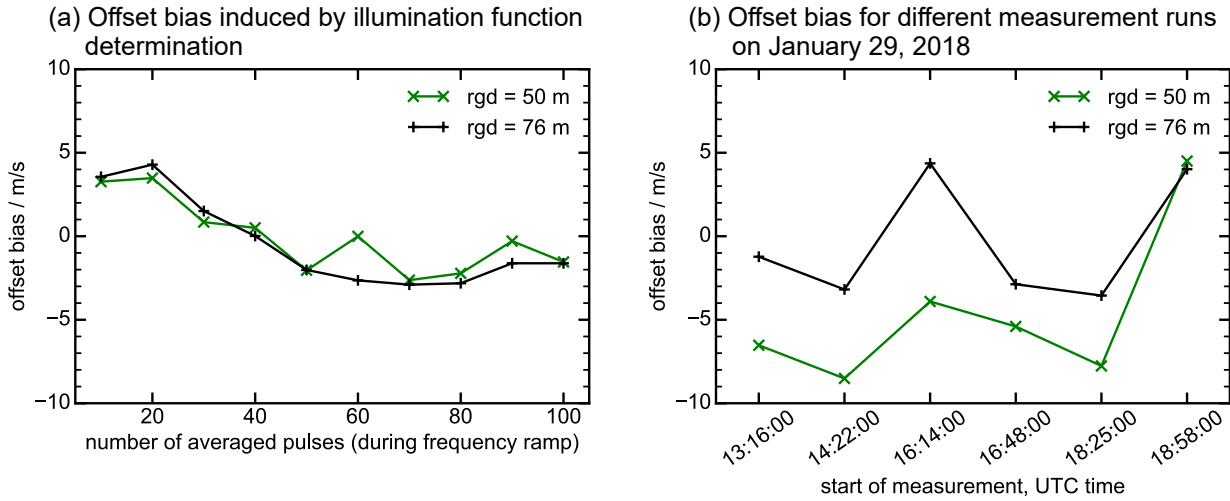


**Figure A.16:** (a) Offset bias of horizontal wind speed measurements at 19:19 - 19:49 (UTC) on January 29, 2018, for different determinations using the same illumination function with a different number of averaged pulses (ME) during the frequency ramp (see Fig A.14). (b) Offset bias for different measurement runs on January 29, 2018, using the illumination functions shown in Fig. 5.13.

Comparing the results of Fig. A.16(a) to the end-to-end simulations of section 4.4, the determined offset bias is up to four times higher than the simulated one for similar fractional changes of the illumination functions. Nevertheless, the offset bias is quasi-independent of the wind speed, which is in accordance with the results of section 4.4. The offset biases in Fig. A.16(b) are of the same order of magnitude, although the illumination functions are visibly shifted (see Fig. 5.13). It is likely that the shift of the illumination functions is compensated by the different illumination function determinations (see Fig. 5.13) if the time span between illumination function determination and wind speed determination is short. The remaining fluctuation of the offset bias is most likely due to the measurement error of the illumination function determination procedure itself (similar to Fig. A.16(a)).

## Vertical measurements and illumination function analysis over distance

This section provides background information on section 5.3.3 and additional vertical measurements.

Fig. A.17 shows range-dependent illumination functions at different altitudes (range gate distances = rgd), determined with the illumination function procedure described in section 3.5.6 at 9:22 (1.) and at 12:37 (2.) on March 16, 2018.

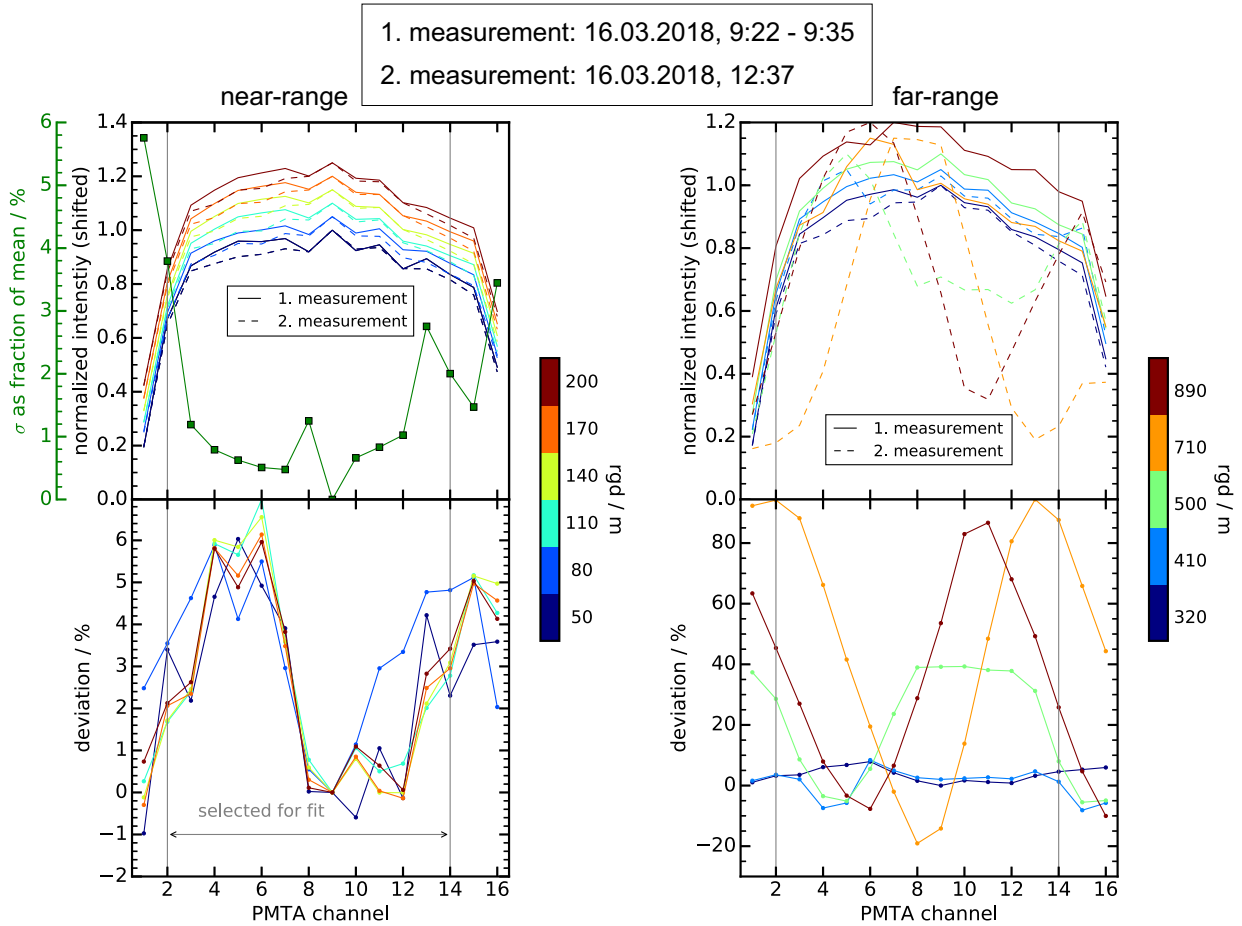


**Figure A.17:** Two sets of range-dependent illumination functions determined with the illumination function determination procedure in the near-range (range gate distances, rgd: 50 m to 200 m) and in the far-range (rgd: 260 m to 1160 m) with  $\Delta R = 30$  m. The respective PMTA channel-dependent intensities are normalized and shifted with respect to each other for better visibility. The green axis shows the standard deviation as a fraction of the mean between the first 6 illumination functions. The lower plots show the channel-dependent deviation between the illumination functions of the 1. and 2. measurement at 9:22 and at 12:37 on March 16, 2018, respectively. The PMTA region used for DSA fitting and wind speed determination is marked by two vertical gray lines.

The variation of the illumination function with range is on the order of a few percent with respect to the mean intensity, with higher deviations at the edges of the PMTA. It depends on how well the fiber core is aligned and imaged on the photomultiplier tube array (PMTA), i.e., if cladding modes illuminate the PMTA or not. A center region of the PMTA, stemming from the core region of the fiber shows the smallest deviations. In the near-range and up to range gate distances (rgd) of  $\approx 400$  m, the deviations between the two measurements are on the order of a few percent. At larger distances in the far-range, fluctuations of backscattering due to clouds can severely degrade the illumination

function determination, as was the case during measurement number two (see Fig. A.17 right:  $\text{rgd} = 500$  m,  $\text{rgd} = 710$  m, and  $\text{rgd} = 890$  m). That is why calibration should be performed in clear-sky environments.

The first set of range-individual illumination functions (9:22) of March 16, 2018, is used to correct the vertical wind speed measurements. Fig. A.18 provides the first six range gates of a vertical wind speed measurement run from 9:45 to 9:57 (UTC).

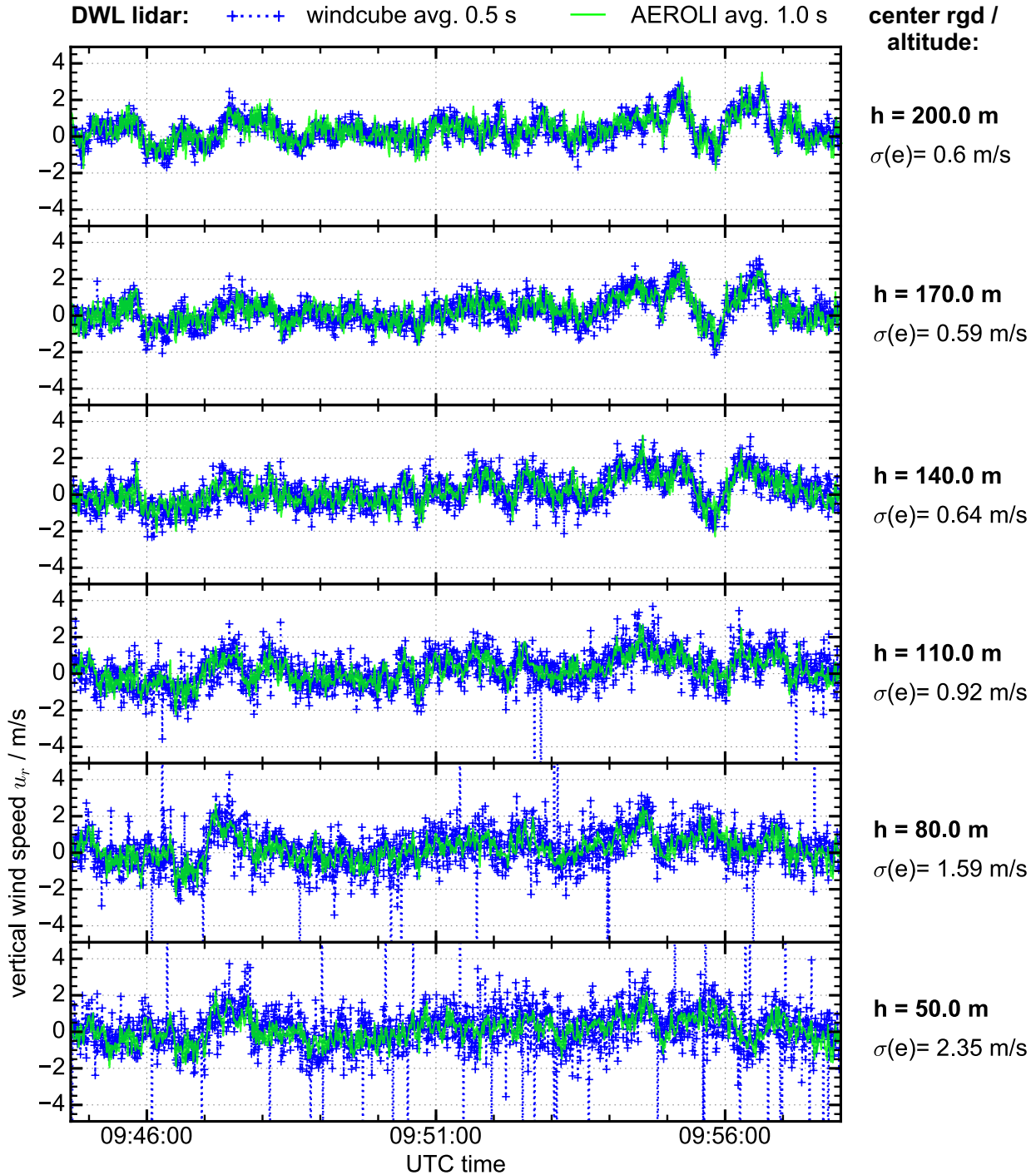


**Figure A.18:** Vertical wind speeds of AEROLI (green) and Windcube® (blue) at increasing altitude ( $h$ ) as a function of time. The standard deviation  $\sigma$  of the mismatch  $e$  between the AEROLI receiver and the Leosphere Windcube® 200S is given for every altitude.

The offset bias is corrected using  $u_{r_{corr}} = u_r - \langle u_r \rangle$ . The reference fringe is provided by fiber-delayed laser pulse. During this measurement run the standard deviations of the Windcube<sup>®</sup> are smaller (the minimum CNR is -27 dB at 150 m compared to -29 dB for Fig. 5.17), leading to a reduced standard deviation of the error  $e$  between  $u_r$ (AEROLI) and  $u_r$ (Windcube) in comparison to Fig. 5.17.

$\sigma(e)$  decreases as a function of altitude  $h$ . As described in section 5.3.3 this reduction of the combined precision of AEROLI and Windcube<sup>®</sup> may be a consequence of both shot noise of AEROLI and of a range dependence of the measurement precision of the Windcube<sup>®</sup> 200S. This interpretation is very likely due to visible noisy spikes of the Windcube<sup>®</sup>'s measurement values at short ranges where the CNR is lowest. The exact dependence of  $\sigma(u_r)$  of the Windcube<sup>®</sup> on its CNR is however not known to the author.

The results of this section of the appendix on background information of the field-test measurements of the AEROLI receiver are summarized in the following.

Drifts of the wind speeds measured with AEROLI with respect to the wind speeds measured with a Windcube<sup>®</sup> 200S occur on a different time scale than wind speed fluctuations. This time scale may range from several minutes to hours, and is most probably related to instabilities of the laser orientation and to intensity profile of the AEROLI DWL. These long-term variations together with temperature fluctuations of the interferometer cell may thus be the cause of illumination function variations, which produce a time-dependent offset bias, because the fringe shapes may become dependent on the fringe position and on the measurement time. The according time dependent shift is thus also dependent on the choice of fit model. The reference fringe shows increased kurtosis due to a mixture of light scattered by molecules and aerosols and the hard target signal. A fit model including parameters for skewness and kurtosis seems to be better suited, however further studies are required. The illumination function routine itself may yield a certain bias related to the measurement precision of the illumination function. The bias depends for example on the number of averaged pulses during the frequency ramp. Long-term changes of the atmospheric signal illumination function and of the laser reference illumination function were indeed observed. Vertical oriented long-range illumination function determinations indicate that the illumination function may also be slightly range-dependent. The combined measurement precision of AEROLI and Windcube<sup>®</sup> 200S seems to depend also largely on the range-dependent CNR of the Windcube<sup>®</sup> 200S and thus on atmospheric conditions.





## B Lidar parameters

### B.1 Parameters of the Green-Wake project

The project “Green-Wake” (Demonstration of lidar based Wake Vortex Detection System incorporating an Atmospheric Hazard Map) was a EC project from 2008 to 2012, building on the results of the DWL tested during the AWIATOR project, with the goal of developing a lidar system for wake vortex and wind sheer detection and mitigation. Like AWIATOR the lidar sensor was based on a direct-detection DWL, i.e., on a fringe-imaging Fabry-Pérot interferometer (FIFPI). Two intensified 2D s-CMOS detectors allow for two independent interference ring structures to be imaged and thus for two range gates. Two receivers are necessary because the s-CMOS detectors do not provide enough speed and gain for range-resolved detection.

The requirements on wake vortex detection, which were defined within the project, are summarized in table B.1 (*Rees, 2014*).

**Table B.1: Required system parameters for the Doppler wind lidar sensor specified in the Green-Wake project (*Rees, 2014*)**

Parameter	Value
minimum range	50 m
maximum range	200 m
minimum number of measurement points	100
scanning area	120 m $\times$ 50 m
range resolution	2 range bins
full field-of-view update rate	2.5 Hz
require LoS velocity accuracy in a single integration	1 m/s
operating altitude (max)	flight level 400 ( $> 12,100$ m)
maximum atmospheric density	all conditions
range of velocity	$\pm 25$ m/s
receiver optics	200 mm

*Rees (2014)* claims that those requirements were almost met by the “Green-Wake” UV Imaging lidar. To the author’s knowledge, however, no peer-reviewed publication exists to the present day, which proves this. The results of *Schwithal (2017)*, presented next, suggest that the requirements defined in “Green-Wake”, although they are a helpful guideline, are not sufficient for wake vortex alleviation and control.

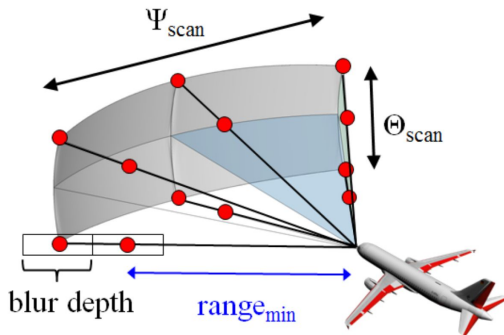
### B.2 Results of the OWIDIA lidar sensitivity parameter study

The results and assumptions of a lidar parameter study for wake vortex alleviation carried out by *Ehlers and Fezans (2015)* and *Schwithal (2017)* are summarized here for quick reference. The concept underlying these simulations was introduced in Fig. 2.7 of section 2.3.3. The conclusions drawn from this parameter study are used in section 3.1 to define requirements for the lidar receiver prototype to be developed in this work.

*Schwithal* (2017) assumes that the lidar sensor contains a separate receiver for every range gate, and that the signal has to be split amongst these receivers, like in the Green-Wake project. Bearing this primary assumption in mind, *Schwithal* (2017) assumes that the standard deviation of the line-of-sight wind speed is proportional to  $\sqrt{N_{range\ bins}}$ . This is a deficit inherent to the 2D detectors used in AWIATOR and Green-Wake, which are necessary due to the non-transformed two-dimensional ring-like interference pattern of fringe-imaging Fabry-Pérot interferometers and the lack of fast, high gain two-dimensional detector arrays. That is why the performance of configurations with multiple range gates along one line-of-sight, which is possible with the receiver of this work, is underestimated. Nevertheless the study provides worthwhile guidelines for lidar receiver design.

Fig. B.1(a) contains a scheme of important geometric lidar parameters (*Ehlers and Fezans*, 2015): minimum measurement range ( $range_{min}$ ), lateral and vertical scan angle range ( $\Psi_{scan}$ ,  $\Theta_{scan}$ ), the number of measurement points (MP) along the measurement axis (range bins), the number of horizontal MP axes, the blur depth (i.e., range gate length  $\Delta R$ ), and the full screen update rate. Fig. B.1(b) shows the values of these parameters studied by *Ehlers and Fezans* (2015) and *Schwithal* (2017). For different combinations of these parameters the influence on the performance of the OWIDA system was evaluated by checking the reduction of the maximum bank angle, which is the main disturbance during a wake vortex encounter. Overall performance was considered for lateral encounter angles of  $5^\circ$ ,  $10^\circ$ , and  $15^\circ$ .

(a) Exemplary lidar geometry:



(b) Lidar parameters for sensitivity study:

Parameter	Range of values
minimum measurement range $range_{min}$ [m]	60; 90; 120; (150)
lateral Scan angle range $\Psi_{scan}$ [°]	+/-16; +/-30; +/-40
vertical Scan angle range $\Theta_{scan}$ [°]	+/-10
# MP along measurement axis, $N_a$ (2 in Fig. 8)	1; 3; 5
# horizontal MP axes, $N_h$ (3 in Fig. 8)	3; 5; 7; 9
blur depth [m]	15; 30
full screen update rate [Hz]	5;10

**Figure B.1:** (a) Scheme of an exemplary lidar geometry with important geometric lidar parameters for wake vortex alleviation. (b) Ranges of lidar parameter values in the sensitivity study carried out by *Ehlers and Fezans* (2015) and *Schwithal* (2017).

*Schwithal* (2017) found that, while MP density does not obviously correlate with the OWI execution, the initial LoS wind speed standard deviation of the lidar sensor, if it is too high ( $> 0.87$  m/s in some cases), impedes the activation criterion from being passed during some encounter scenarios, and the OWI is not executed. *Schwithal* (2017) considered a wake vortex circulation of  $341 \text{ m}^2/\text{s}$  and concluded that the ratio of vortex circulation to reference standard deviation should be above 200 for the OWI to perform with her applied activation criterion (standard deviations  $> 120\%$  of the reference standard deviation). This criterion is considered very simple and should be enhanced in her view, which would possibly allow a wider range of sensor configurations. Maximum performance was achieved if the standard deviation was below 1 m/s with only very few exceptions.

Fig. B.2 shows lidar sensor configurations studied by *Schwithal* (2017) (in a “detailed study of selected parameters sets”) at various encounter altitudes and geometries. It contains simulated reductions of the maximum bank angle  $\Delta\phi_{max}$  for different encounter angles

$\psi_{WV}$ , geometries (number of horizontal measurement points  $N_h$ , number of longitudinal measurement points  $N_a$ ), lateral field-of-views  $\psi_{scan}$ , and ranges of 60 m, 75 m, and 90 m. All configurations use  $\pm 10^\circ$  vertical scanning with three vertical measurement points. Color encoded are different blur depths and full scan update rates (pink: 15 m / 5 Hz, green: 15 m / 10 Hz, black: 30 m / 5 Hz). Especially promising sensor sets are highlighted. These “best” configurations show a reduced maximum bank angle with a factor  $\Delta\phi_{max}$  small compared to 1.

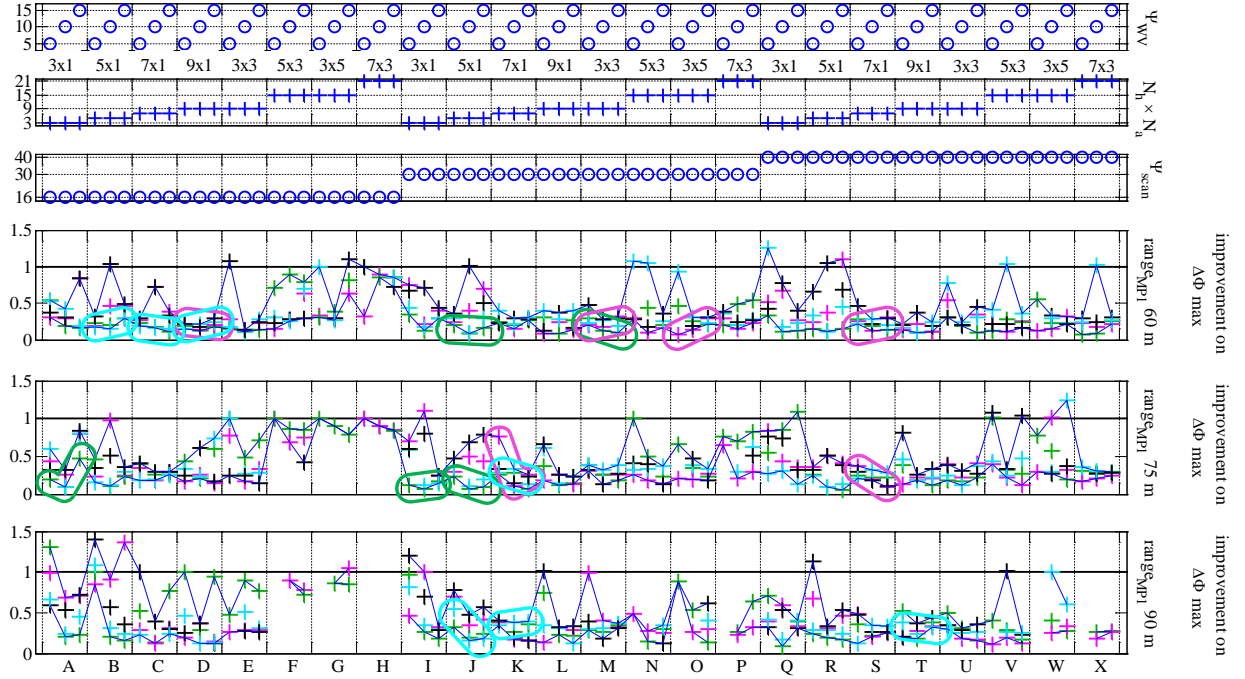


**Figure B.2:** Results of a parameter study carried out by [Schwithal \(2017\)](#). Color code: red: blur depth of 15 m and full scan update rate of 5 Hz, green: 15 m and 10 Hz, black: 30 m and 5 Hz, blue: 30 m and 10 Hz. Some promising configurations with a low bank angle after alleviation ( $\Delta\Phi < 1$ ) are marked for further study.

In her work [Schwithal \(2017\)](#) summarizes several requirements in terms of sensor characteristics for a lidar-based wake impact alleviation system. First of all there is a tradeoff between high spatial resolution and low measurement noise for sensor configurations using the OWIDIA system.

Secondly, the range gate length ( $\Delta R$ ) and the full scan update rate are of only minor importance and their optimum values will depend on the number of measurement axis and range gates. Though a larger blur depth (30 m) is certainly helpful in terms of lidar sensor noise reduction, the primary effect in Schwithal’s study appears to have been a reduction of the density of measurement points (MP), because the MP were spaced at distances of the range gate length  $\Delta R$ .

The number of lateral measurement axes has to be adjusted to the above tradeoff.

In general three, four, or even five vertical measurement axes provided good performance. Four or five vertical axes allowed alleviation with the first measurement point at 60 m, 75 m, and 90 m. Configurations with only three vertical axes required the first measurement point at 60 m. A short minimum measurement distance ( $\text{range}_{\min} = \text{range}_{\text{MPI}} = 60$  m) is certainly advantageous from a lidar sensor development perspective due to the  $1/\text{range}$  decrease of shot-noise limited signal-to-noise ratio. Cruise flight speeds of approximately

250 m/s imply however that in many cases the aircraft might be already in contact with the wake vortex while a future wake vortex detection and alleviation system like OWIDIA senses and reacts to it. [Schwithal \(2017\)](#) explains this contradictory situation by stating that at the beginning the effects of the wake vortex being still very small, could be compensated by the basic control system. OWIDIA's main benefit as explained by [Schwithal \(2017\)](#) seems to be when the aircraft is exposed to the strongest wake-induced disturbances close to the vortex cores. For  $\text{range}_{\min} = 60$  m Schwithal identified sensor configurations D, K, L, S, and T in Fig. B.2 as well performant, i.e., with good bank angle reduction for all combinations of blur depth and full scan update rate, high MP density, and low standard deviation of the LoS velocity. These configurations (including also B and C), however require a relatively high number of measurement axes, which have to be provided by scanning the laser beam.

From the perspective of DWL sensor design, scanning operations, which increase the number of measurement axes and measurement noise, because less time for signal averaging along one line-of-sight direction is available, are less favorable. From the OWIDIA perspective a higher total scan update rate increases MP density and the measurement noise level. Sensor configuration studied by [Schwithal \(2017\)](#) with a high density of measurement points require a total scan update rate of 5 Hz. Sensor configurations with a low density of MP seem to require a larger total scan update rate of 10 Hz, because the MP are then spaced closer together in flight direction.

Based on [Schwithal \(2017\)](#) configurations with only three vertical and three horizontal axes ( $N_h \times N_a = 9$ , Fig. B.2 columns: E, M, U), and three longitudinal range gates achieve better performance than with only one longitudinal range gate (columns: A, I, Q). Especially configuration M shows a very good reduction of the maximum bank angle. [Schwithal \(2017\)](#) explains this very good alleviation performance by a favorable distribution of measurement points within the scanned volume, and with relatively low measurement noise, due to a small number of measurement axes.

In the studies of [Schwithal \(2017\)](#), five range gates do not improve performance. These results rely, however on the assumption, that each additional range gate will increase measurement noise for all other points, which is not the case for the lidar sensor developed in this work. In our case an increase of the number of longitudinal range gates comes at no cost, and the respective alleviation performance based on this changed precondition should be evaluated, because sensors may be realized more easily in this way. This makes the results of Schwithal concerning configurations with more than one range gate the more promising, because the potential is currently underestimated.

An increase of the scanning FOV decreases the MP density locally, while increasing the overall measurement volume.

[Schwithal \(2017\)](#) states that in total many configurations allowed a reduction of the maximum bank angle of more than 70% for all lateral encounter angles ( $\Psi_{wv}$ ) and up to 90% for some encounter angles.

[Schwithal \(2017\)](#) marked especially promising configurations in Fig. B.2 for further study. Her notation convention is given in Fig. B.3. Fig. B.4 provides a table with the geometrical and temporal parameters of selected configurations using this notation.

Fig B.5 summarizes the alleviation performance of these selected configurations for a range of encounter altitudes of -45 m to 45 m, using refined performance criteria: 1. The average reduction of  $\Phi_{max}$ , 2. the number of incidences where the OWIDIA system caused an increase of  $\Phi_{max}$ , 3. the sum of the absolute maximum bank angle increases of all



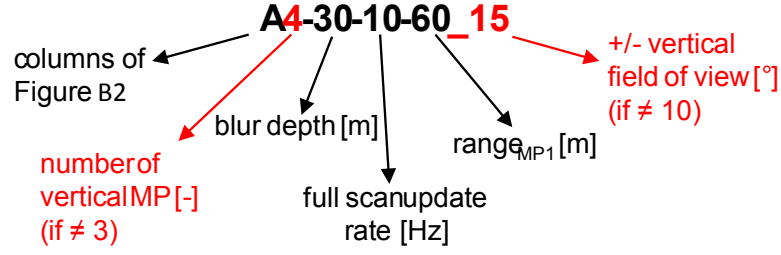


Figure B.3: Notation of sensor configuration used by [Schwithal \(2017\)](#).

Sensor configuration [-]	Number of vertical axes [-]	Number of horizontal axes [-]	Number of MP along axis [-]	Total number of MP [-]	range <sub>MP1</sub> [m]	Vertical field of view $\Theta_{\text{scan}}$ [°]	Lateral field of view $\Psi_{\text{scan}}$ [°]	Blur depth [m]	Full scan update rate [Hz]	Single axis update rate [Hz]
B-30-10-60	3	5	1	15	60	+/-10	+/-16	30	10	150
C-30-10-60	3	7	1	21	60	+/-10	+/-16	30	10	210
D-15-5-60	3	9	1	27	60	+/-10	+/-16	15	5	135
D-30-10-60	3	9	1	27	60	+/-10	+/-16	30	10	270
J-15-10-60	3	5	1	15	60	+/-10	+/-30	15	10	150
M-15-5-60	3	3	3	27	60	+/-10	+/-30	15	5	45
M-15-10-60	3	3	3	27	60	+/-10	+/-30	15	10	90
O-15-5-60	3	3	5	45	60	+/-10	+/-30	15	5	45
S-15-5-60	3	7	1	21	60	+/-10	+/-40	15	5	105
A-15-10-75	3	3	1	9	75	+/-10	+/-16	15	10	90
I-15-10-75	3	3	1	9	75	+/-10	+/-30	15	10	90
J-15-10-75	3	5	1	15	75	+/-10	+/-30	15	10	150
K-15-5-75	3	7	1	21	75	+/-10	+/-30	15	5	105
S-15-5-75	3	7	1	21	75	+/-10	+/-40	15	5	105
J-15-10-90	3	5	1	15	90	+/-10	+/-30	15	10	150
J-30-10-90	3	5	1	15	90	+/-10	+/-30	30	10	150
K-30-10-90	3	7	1	21	90	+/-10	+/-30	30	10	210
T-30-10-90	3	9	1	27	90	+/-10	+/-40	30	10	270

Figure B.4: Sensor configurations selected by [Schwithal \(2017\)](#). The table lists the geometrical and temporal parameters of the configurations.

encounters ( $\sum \Phi_{\text{max}}$ ), 4. the maximum increase of the bank angle ( $\max(\Phi_{\text{max}})$ ), and 5. the number of cases when the OWI could not identify a wake vortex.

[Schwithal \(2017\)](#) states that only the configurations D-30-10-60, J-15-10-60, and S-15-5-60 (marked with red boxes) never induced an increase of the maximum bank angle independent of the encounter altitudes. The configurations D-15-5-60 and M-15-10-60, marked with dashed boxes in Fig. B.5, exhibit only a minor bank angle impairment of  $0.1^\circ$  and  $1^\circ$  at one specific altitude offset, which is negligible. M-15-10-60 is the only suitable configuration with a LoS velocity standard deviation above 0.5 m/s, and its performance is again explained by a larger measurement domain and a good spatial distribution of measurement points in vertical direction.

[Schwithal \(2017\)](#) also considered an increase of the amount of vertical scanning axes to four and five and observed an improved alleviation performance and increased robustness of the bank angle reduction for encounter at different altitudes, while an increase from four to five is not worthwhile. An increase of the vertical scanning VOV was also studied, and [Schwithal \(2017\)](#) concluded from her findings, that the benefit is not very large.

[Schwithal \(2017\)](#) studied the influence of increased measurement noise, as well. Depending on the sensor configuration, an increase of noise, more or less impairs wake impact alleviation performance. Small deviations are not critical, while an increase of noise by 50% (to 1.44 m/s for a M4-15-5-60 configuration) can already provoke a significant increase



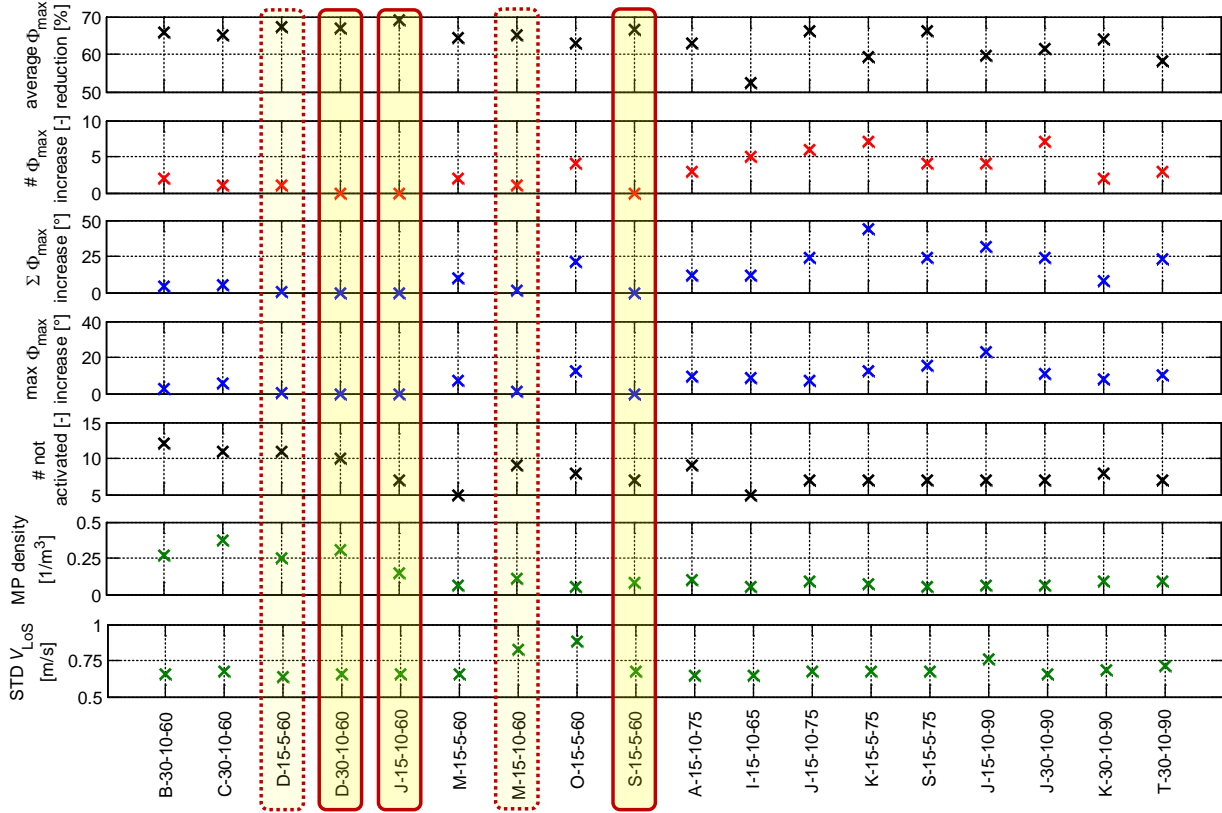


**Figure B.5:** Alleviation performance of selected configurations for a large range of encounter altitudes ([Schwithal, 2017](#)).

of the bank angle for some encounter scenarios. Therefore, as low as possible lidar sensor measurement noises are desirable.

It should be evaluated if a high number of range gates ( $> 3$ ), along one measurement axis within 60 m and 300 m would be beneficial, and if this would lower the requirement on the standard deviation of the radial wind speed determination, or on the number of measurement axes. This study should be carried out with the special assumption, that an increase of the number of longitudinal MP does not increase the measurement noise of any MP. The study should also include an adjusted activation criterion ([Schwithal, 2017](#)).

[Fezans and Joos \(2017\)](#) did not explicitly perform a lidar parameter sensitivity study for their concept of gust and turbulence alleviation control. Such a study appears to be aggravated by the current lack of a model to produce a large set of representative wind fields to test the routines, and by the large parameter space to be explored in such a study, which requires optimized computational routines currently under development. Judging from selected parameters in [Fezans et al. \(2017\)](#), i.e., a total scan update rate of 13 Hz, ten measurement ranges between 65 m and 300 m, with an opening of the scanning cone of  $\pm 40^\circ$ , and LoS air speed velocity measurement standard deviations of the lidar sensor in the order of 1.5 m/s, the requirements are probably similarly high, to say the least.

The conclusions drawn from this section for the design of a Doppler wind lidar receiver are summarized in section 3.1.

# C Theoretical background

## C.1 Speckle

### Speckle phenomena and statistics

This section introduces the phenomenon of “speckle”. The interested reader finds detailed descriptions in [Goodman \(1975\)](#), [Goodman \(2007\)](#), and [Goodman \(2015\)](#).

Speckle are a phenomenon which results from coherent light being shown on multiple dielectric inhomogenities on a rough surface or within a volume (atmosphere), and when it interferes, the light received by collection optics is modulated spatially, in phase, and in intensity.

Each light ray contributing to this interference pattern (or speckle pattern) can be constructed as a random walk in the complex space (see Fig.C.1(a)). These random walks obey the central limit theorem, that is the total field at location  $\vec{r}$  is Gaussian complex and of zero mean. An example are atmospheric speckle in the plane of reception of a lidar telescope (see Fig.C.1(b)), when the light of a laser beam is scattered within a scattering volume at distance  $z = z_s$ . In this case every emitted field  $d\vec{E}_{emitt}(\vec{\rho}, z)$  in the plane of scattering is random and obeys Gaussian complex statistics.

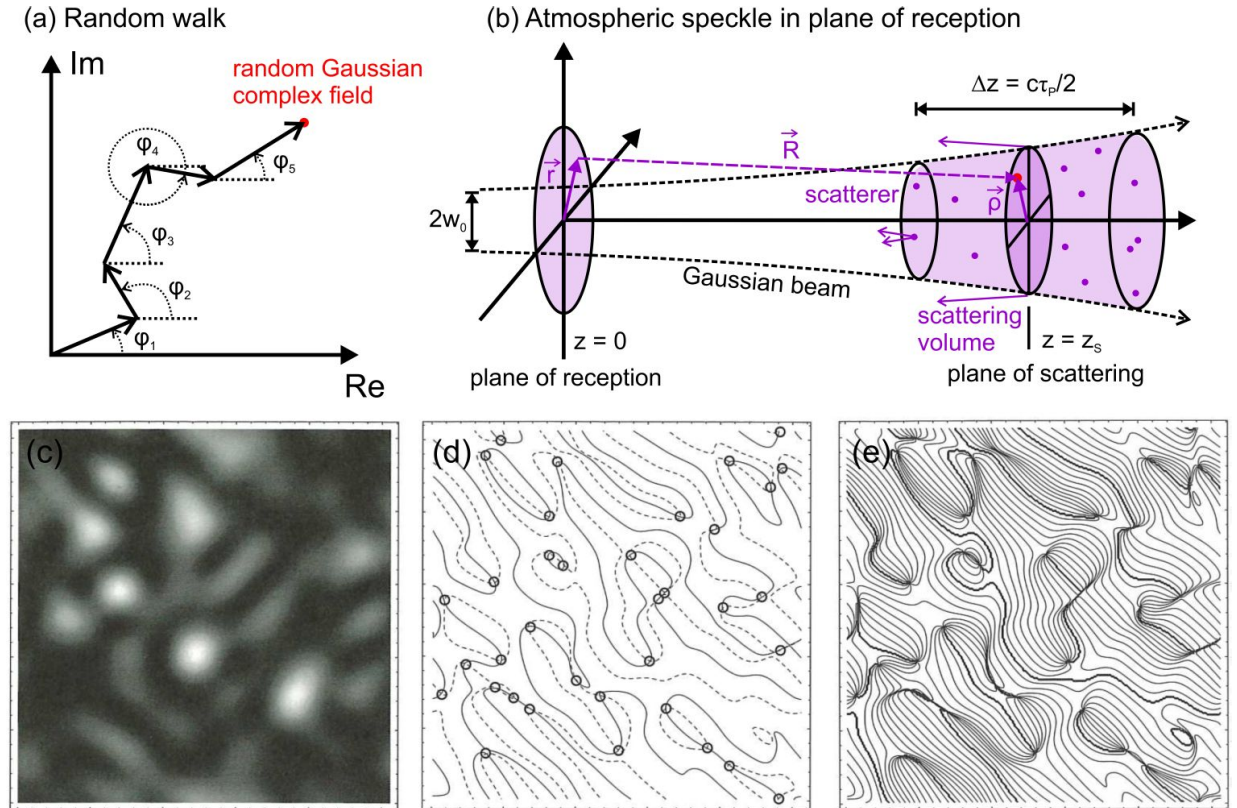


**Figure C.1:** (a) Random walk in complex plane. (b) Backscattering into receiver plane scheme for simulating atmospheric speckle. (c) Example of a speckle pattern intensity. (d) Corresponding values of the real and imaginary part of the complex field. (e) Corresponding phase with obvious vortices around locations of zero intensity. (b) inspired by [Cézar \(2008\)](#), (c) to (e) taken from [Goodman \(2007\)](#).

The probability density of the illuminance  $\xi$  at a location  $\vec{r}$  in the plane of reception,

assuming polarized, perfectly coherent light, is thus given by an exponentially negative distribution with mean  $\langle \xi \rangle$  and variance  $\langle \xi \rangle^2$ :

$$P_{\vec{r}}(\xi = \xi_0) = \frac{1}{\langle \xi \rangle} \exp \left( -\frac{\xi_0}{\langle \xi \rangle} \right), \quad (\text{C.1})$$

where  $\xi_0$  is the incident illuminance, related to the incident intensity  $I_0$  by  $\xi_0 = I_0/r^2$ . Important properties of these so-called fully developed speckle are that the phases of the contributing phasors are uniformly distributed and that the standard deviation  $\sigma_\xi$  obeys

$$\sigma_\xi = \sqrt{\langle \xi^2 \rangle - \langle \xi \rangle^2} = \sqrt{2\langle \xi \rangle^2 - \langle \xi \rangle^2} = \sqrt{\langle \xi \rangle^2}, \quad (\text{C.2})$$

using the relation  $\langle \xi^n \rangle = n! \langle \xi \rangle^n$  for the  $n$ th moment, and is equal to the mean  $\langle \xi \rangle$  for polarized, perfectly coherent light. This means that the speckle contrast

$$C = \frac{1}{\text{SNR}} = \frac{\sigma_\xi}{\langle \xi \rangle} \quad (\text{C.3})$$

is 1, where SNR is the speckle signal-to-noise ratio. This is not the case for light scattered by molecules and aerosols due to its limited coherence length  $d_c$  (as is shown later in section C.1).

An exemplary (simulated) speckle intensity pattern obeying these statistics is shown in Fig. C.1(c). The corresponding values of the real part and imaginary part of the field are shown in Fig. C.1(d). Circles mark locations where both real and imaginary part are zero (locations of zero intensity, i.e., so-called optical vortices). It can be seen in Fig. C.1(e) that these optical vortices are characterized by a circulation of phase.

The spatial resolution of any detector recording a speckle pattern is limited, what means, that every detector pixel  $k$  spatially integrates over a part of the speckle pattern. The integration over the surface of one pixel is equivalent to the summation of exponentially-negative distributed random variables. The resulting distribution obeys a gamma density function of order  $M_k$ :

$$P(N_k = n_k) = \frac{M_k^{M_k}}{\Gamma(M_k)} \frac{n_k^{M_k-1}}{\langle N_k \rangle^{M_k}} \exp \left( -M_k \frac{n_k}{\langle N_k \rangle} \right) \quad (\text{C.4})$$

where  $M_k$  is the number of speckle grains integrated spatially within the pixel  $k$ , and  $n_k$  is the number of photoelectrons detected by pixel  $k$ .

Furthermore,  $M$  different speckle patterns can be summed incoherently by accumulation in time. In this case, the resulting speckle pattern is again obtained by  $(M-1)$  convolutions of the exponentially negative statistics (of varying speckle patterns), which results in a gamma law with parameter  $M$ :

$$P_{\vec{r}}(\xi = \xi_0) = \frac{M^M}{\Gamma(M)} \frac{\xi_0^{M-1}}{\langle \xi \rangle^M} \exp \left( -M \frac{\xi_0}{\langle \xi \rangle} \right) \quad (\text{C.5})$$

with mean  $\langle \xi \rangle$  and variance  $\langle \xi \rangle^2/M$ , whereby  $M$  is the number of speckle patterns.  $\Gamma(M)$  is the gamma function given by  $\Gamma(M) = (M-1)!$ .

In these cases (eq. C.4 and eq. C.5) the speckle contrast (see eq. C.3) is given by  $C = 1/\sqrt{M}$ .  $M$  is also referred to as Goodman's diversity parameter.

### Atmospheric speckle simulation

The term “atmospheric speckle” is used in the following to describe complex interference patterns ([Goodman, 1965](#)) in the reception plane of a lidar. They are produced, when a coherent laser pulse is scattered in all directions by an ensemble of scatterers (hard target reflective speckle ([Nelson et al., 2000](#)), aerosols, air molecules ([Goodman, 2007](#)) and when the received light interferes. They fluctuate in time due to air turbulence (time scale smaller than 10 ms to 20 ms) ([Beavers et al., 1989](#)). In the following the atmosphere is treated as instantaneously frozen.

The formulae and derivations underlying this simulation are based on [C  zard \(2008\)](#). The fundamental scheme of the simulation is shown in Fig. C.1(b).

The light is backscattered from a volume of length  $\Delta z = c \cdot \tau_p/2$ , where  $c$  is the speed of light, and  $\tau_p$  is the pulse length of 7 ns. Points in the emitting plane at  $z = z_s$  (like the red dot in Fig. C.1(b)) are emitting a field  $E_s$ . The received field  $E_{pup}$  in the pupil of reception at  $z = 0$  is then given by the Kirchhoff integral

$$E_{pup}(\vec{r}, t_0) = \iint_{scatt. plane} \frac{1}{j\lambda} \frac{1 + \cos(\vec{u}_z, \vec{R})}{2} \frac{e^{-jkR}}{R} E_s(\vec{\rho}, t_0 - z_s/c) d\vec{\rho}, \quad (C.6)$$

whereby  $\vec{u}_z$  is the unit vector along  $z$ , and the vectors  $\vec{R}$ ,  $\vec{\rho}$ , and  $\vec{r}$  are defined in Fig. C.1(b).  $e^{-jkR}/R$  are spherical waves and the vector  $\vec{R}$  is given by:  $\vec{R} = z_s \vec{u}_z + (\vec{\rho} - \vec{r})$ .

In case of a distance  $z_s \approx 50$  m to hundreds of meters, the factor  $\cos(\vec{u}_z, \vec{R})$  is approximately one and  $\vec{R}$  depends on  $\vec{\rho}$  and  $\vec{r}$ , only.  $\vec{R}$  can be expanded to 3rd order:

$$R = z_s + \frac{|\vec{\rho} - \vec{r}|^2}{2z_s} + \frac{|\vec{\rho} - \vec{r}|^4}{4z_s^3} \quad (C.7)$$

The 3rd order of eq. C.7 is negligible compared to  $\lambda$ , and eq. C.6 can be approximated by a Fresnel integral:

$$E_{pup}(\vec{r}, t_0) = \frac{1}{j\lambda z_s} e^{-jkz_s} e^{-jk \frac{r^2}{2z_s}} \iint_{scatt. plane} E_s(\vec{\rho}, t_0 - z_s/c) e^{-jk \frac{\rho^2}{2z_s}} e^{jk \frac{\vec{r} \cdot \vec{\rho}}{z_s}} d\vec{\rho} \quad (C.8)$$

As the light is backscattered from many scattering planes within the scattering volume the total field received in the reception plane, using:  $\tilde{E}(z(t)) = \sqrt{2/c} \cdot E(t)$ , is given by

$$E_{pup}(\vec{r}, t_0) = \int_{z_0}^{z_0 - c\tau_p/2} \iint_{plane_z} \frac{1}{j\lambda z} e^{-jkz} e^{-jk \frac{r^2}{2z}} \sqrt{c/2} \cdot d\tilde{E}_{emitt}(\vec{\rho}, z) e^{-jk \frac{\rho^2}{2z}} e^{jk \frac{\vec{r} \cdot \vec{\rho}}{z}} d\vec{\rho}, \quad (C.9)$$

whereby  $d\tilde{E}_{emitt}(\vec{\rho}, z)$  is the infinitesimal Gaussian complex field emitted by the cylindrical volume element  $dV$  of length  $dz > \lambda/2$  in the plane  $z$ . The field is Gaussian complex, because the location of the scattering centers within the volume  $dV$  is random, and thus the phase emitted by these scatterers is random and equally distributed between 0 and  $2\pi$ . Using these assumptions the emitted field at a location  $(\vec{\rho}, z)$  (e.g., red dot in Fig. C.1(b)) is given by

$$d\tilde{E}_{emitt}(\vec{\rho}, z) = A \cdot |\tilde{E}_{inc}(\vec{\rho}, z)| h(\vec{\rho}, z) dz, \quad (C.10)$$

with a coefficient  $A$ , which is a function of the backscattering coefficient  $\beta$ , and a Gaussian complex variable  $h(\vec{\rho}, z)$ .  $h$  is a centralized variable, i.e.,  $\langle h(\vec{\rho}, z) \rangle = 0$  and of variance equal to one. The covariance is assumed to be given by  $\delta(\vec{\rho} - \vec{\rho}')\delta(z - z')$ , that is without spatial correlation. Using these assumptions the field in the reception pupil can be expressed by eq. C.11.

The instantaneous electric field of a laser pulse at time  $t_0$  in the reception plane of the lidar spanned by vectors  $\vec{r}$  can be calculated with equation C.11, derived by [C  zard \(2008\)](#), which represents an integral over Fresnel integrals in cylindrical coordinates in the pupil planes spanned by vectors  $\vec{\rho}$  along the line-of-sight axis  $z$ :

$$E_{pup}(\vec{r}, t_0) = \int_{z_0}^{z_0 - c\tau_p/2} \iint_{plane_z} \sqrt{\frac{c}{2}} \frac{|A|}{\lambda z} e^{-jk \frac{r^2}{2z}} |\tilde{E}_{inc}(\vec{\rho}, z)| h(\vec{\rho}, z) e^{jk \frac{\vec{r} \cdot \vec{\rho}}{z}} d\vec{\rho} dz, \quad (C.11)$$

whereby  $z_0 = 100$  m is the distance from the telescope,  $c$  is the speed of light,  $\tau_p = 7$  ns is the pulse length, and  $\lambda = 355$  nm is the laser wavelength.  $\tilde{E}_{inc}(\vec{\rho}, z)$  is the incident electric field of a Gaussian beam of waist  $w_0$ , and of divergence  $\Theta = 150$   $\mu$ rad at the scattering location  $z_0$ .  $h(\vec{\rho}, z)$  is a Gaussian complex random variable, which is responsible for atmospheric speckle in equation C.11. It describes the random walk in the complex plane, given the assumption that the central limit theorem applies. The statistics of the total field intensity (speckle pattern) at a position  $\vec{r}$  are given by an exponentially negative distribution (see eq. C.1). The speckle intensity in the receiver plane  $r$  is obtained by  $E_{pup}(\vec{r}, t_0) \cdot E_{pup}(\vec{r}, t_0)^*$ . Terms of eq. C.9 which do not depend on  $\vec{r}$  are contained in  $h(\vec{\rho}, z)$  in eq. C.11. Equation C.11 can be solved numerically.

The obtained speckle intensity patterns for a Gaussian beam waist  $2w_0 = 13$  mm with a beam quality factor  $M^2 = 4.3$ , i.e.,  $2w_{100\text{ m}} = 19.8$  mm, is shown in Fig. C.2(a), assuming a diameter of the Newton telescope's secondary mirror in the reception plane of 6 cm and a diameter of its primary mirror of 15 cm. Fig. C.2(b) shows the same simulation for the hypothetical case:  $2w_{100\text{ m}} \approx 2$  mm.

Fig. C.2 shows that the speckle grain size  $D_{sp}$  is proportional to  $1/w_0$ , what can be explained with the help of the Van Cittert-Zernike theorem ([Goodman, 1975](#)). It says that the wider the source is in terms of   tendue (spatial spectrum), the lower is the degree of spatial coherence between two points, which are illuminated incoherently by this source, i.e., the smaller the speckle grain size. According to [C  zard \(2008\)](#) the underlying assumption of applicability of the central limit theorem is valid, due to very fast convergence of the field backscattered by an ensemble of aerosols towards Gaussian complex behavior, which can already be seen with a number of aerosols exceeding six, what was shown by [Valla \(2005\)](#).

It is interesting to discuss the influence of the degree of temporal coherence of the backscattered light on the speckle pattern contrast ( $C$ ).

The width of the Rayleigh spectrum (HW at  $1/e$ ) is given by  $\gamma = \sqrt{2}\sigma_{Ray}(T)$ , where  $\sigma_{Ray}(T)$  is the standard deviation in Hz of the Rayleigh spectrum at the atmospheric temperature  $T$  (see section 2.1.1).

For a Gaussian-shaped spectrum the coherence time  $\tau_{coh}$  is given by  $\tau_{coh} = \frac{2}{\pi\gamma}$  (i.e., the value at  $1/e$  of the Fourier transform of the spectrum) and is approximately 0.3 ns.



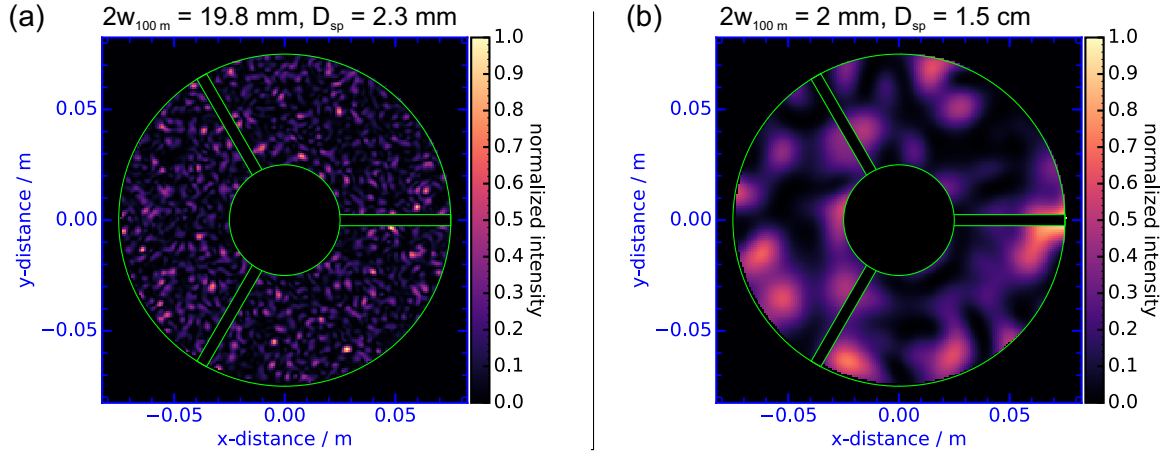


**Figure C.2:** Simulated instantaneous atmospheric speckle pattern at the reception plane for a Gaussian intensity scattering source, 100 m from the telescope (obscuration marked by green lines). With Gaussian beam waist (diameter)  $2w_0 = 13$  mm (beam quality factor  $M^2 = 4.3$ , i.e.,  $2w_{100\text{ m}} = 19.8$  mm) (a) and for the hypothetical case:  $2w_{100\text{ m}} = 1.98$  mm (b). The mean speckle grain size  $D_{sp}$  is determined by an autocorrelation of the simulated patterns (cf. Fig. G.2) in appendix G.

The length in the atmosphere, which can be identified with a coherent wave train (coherence length  $d_c$ ) is given by  $d_c = c\tau_{coh}/2$ . In case of molecules it is in the order of  $d_c^{mol} \approx 4.5$  cm. In the case of aerosols the coherence time is determined by the spectral width of the laser, linked to the pulse duration  $\tau_p = 7$  ns. The according coherence length is thus  $d_c^{aer} \approx 1.5$  m.

The coherence length has an influence on the number of speckle patterns  $M$ , which are incoherently summed within the range gate of length  $\Delta z_{eff}$  of the lidar:  $M = \frac{\Delta z_{eff}}{d_c}$ . The statistics of the sum of  $M$  incoherently added speckle patterns are obtained by  $(M - 1)$  convolutions of the exponentially negative statistics, and are thus given by eq. C.5, and  $M$  is Goodman's diversity parameter. The speckle contrast  $C$  of the total speckle pattern is given by eq. C.3, i.e., by  $C = 1/\sqrt{M}$ .

Simulated total speckle patterns produced by incoherent summation of  $M$  speckle patterns are shown in Fig. C.3, whereby  $C$  is determined from the simulated speckle patterns by  $\sigma(I_k)/\langle I_k \rangle$  with  $I_k$  being the intensity and  $\sigma(I_k)$  its standard deviation at the  $k^{\text{th}}$  point of the simulation mesh (200 x 200 points) of a total speckle pattern.

A practical value of  $\Delta z_{eff}$  is 5 m, which is set by the integration time of the detector, i.e., in our case by the sampling rate of the analog-digital converter. In this case  $M_{aer}$  is 5 and  $M_{mol}$  is in the order of 111. The above simulation results show that for pure molecular scattering the illumination at the location of the spider of the telescope would be quasi-homogeneous, i.e.,  $C = 10\%$ . This is not the case for scattering by aerosols ( $M < 5$ ) with a speckle contrast smaller than 45%. It should be noted here, that Rayleigh scattering at UV wavelengths dominates Mie scattering even at low altitudes. As can be seen in section 2.1.1 (Fig. 2.1), the median value of the particle backscattering ratio  $R_b$  is smaller than 1.5 above an altitude of 1500 m.

The atmospheric speckle are therefore considered to be averaged out in case of low aerosol concentrations in the atmosphere and the illumination is quasi-homogeneous. As described in appendix C.4 this is also a feature of the high diversity, i.e., of a high number of degrees of freedom for the spatial averaging of noise, in Rayleigh (direct-detection) receiver systems (Henderson et al., 2005). Atmospheric speckle thus represent an additional noise source

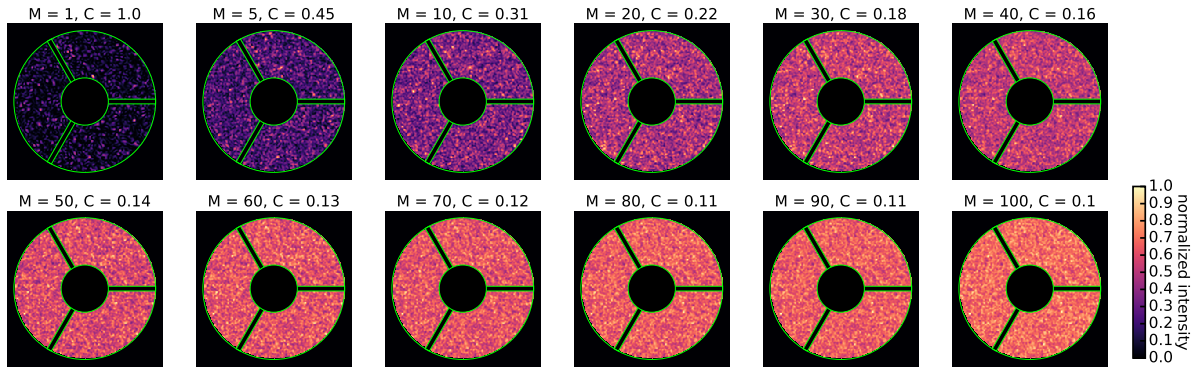


**Figure C.3:** Incoherent summation of simulated atmospheric speckle patterns at the reception plane for a Gaussian scattering source 100 m in front of the plane of reception (telescope) for different values of Goodman's diversity parameter  $M$  and according speckle contrasts  $C$ .

(being modeled in section 4.1), especially at low altitudes (higher aerosol concentrations).

When the light received by the telescope is coupled into a multimode fiber another type of “speckle” (so-called modal noise or fiber speckle) arises in the illumination exciting the fiber. The total speckle noise signal-to-noise ratio  $SNR_t$  is given by  $\sqrt{M_a \cdot M_f}$ , where  $M_a$  is the number of incoherently added atmospheric speckle patterns and  $M_f$ , is the number of fiber speckle patterns (see section 3.5.4 for an experimental study). Due to the multiplicative character of speckle noise, and ways of spatial and temporal averaging (vibration of the fiber and the averaging of multiple pulses, increasing diversity, see section 3.5.4) in a fiber-coupled setup (see section 3.3.1), it is possible to significantly reduce the influence of “speckle noise” during the measurement process (see section 5).

The turbulence-induced fluctuation and modulation of speckle (produced if the target is larger than the correlation width of the irradiance) is one of the reasons for “scintillation”, i.e., intensity fluctuation of the backscattered radiation ([Andrews et al., 2001](#)), and is not treated here.

## C.2 Cramér-Rao lower bound of an ideal multichannel spectral analyzer

The Cramér-Rao Lower Bound (CRLB) or Cramér-Rao Bound (CRB) in general is the minimal variance of an estimation procedure for signal parameters. That is, it gives the theoretically highest precision of the determination of a signal parameter from a data pool. The CRB determination is equivalent to maximizing a Likelihood-function. A precise description of Cramér-Rao bounds can be found for example in [McDonough and Whalen \(1995\)](#).

The intension here is to recount the derivation of the CRB of an ideal spectral analyzer with multiple channels (see [Cézard et al. \(2009a\)](#)) as a reference to the reader. The underlying assumption is that the signal is shot-noise limited. That is, the probability to obtain  $\sigma_k$  photoelectrons on a detector element  $k$  of a spectral analyzer with a total number of  $M$  channels, obeys a Poisson statistic:

$$P(S_k = \sigma_k) = \frac{\langle S_k \rangle^{\sigma_k} e^{-\langle S_k \rangle}}{\sigma_k!}, \quad (\text{C.12})$$

where  $S_k$  is the random variable and  $\langle S_k \rangle$  is its mean being equal to its variance.

As detailed by [Cézard \(2008\)](#), the wind speed  $u_r$  is one of the parameters  $\theta_i$ , which form the parameter vector  $\vec{\theta}$  (other influencing parameters which influence the contrast and shape of the fringe are the density  $\rho$ , the temperature  $T$ , and the particle backscattering ratio  $R_B$ ). The maximum precision of an ideal spectral analyzer (ISA) of  $M$  channels, measuring these parameters can be determined with a calculation of the Cramér-Rao bounds of these parameters. The Cramér-Rao bounds are obtained from the diagonal elements of the inverse Fisher information matrix of the measurement system:

$$\epsilon_{\theta_i} = (F^{-1})_{ii}^{1/2}, \quad (\text{C.13})$$

where the Fisher matrix is given by

$$F_{ij} = -E \left[ \frac{d^2 \ln (\Lambda(\vec{\theta}))}{d\theta_i d\theta_j} \right], \quad (\text{C.14})$$

i.e., it is the negative expectation value  $E[X]$  of the second order derivatives of the log-likelihood function of the signal. The likelihood function  $\Lambda(\vec{\theta})$  is a measure of the probability to obtain one realization of a photon distribution  $(\sigma_1, \sigma_2, \dots, \sigma_k, \dots, \sigma_M)$  in case of applied parameter vector  $\vec{\theta}$ .  $\Lambda(\vec{\theta})$  is a function of joint probabilities:

$$\Lambda(\vec{\theta}) = P \left( S_1(\vec{\theta}) = \sigma_1 \dots S_k(\vec{\theta}) = \sigma_k \dots S_M(\vec{\theta}) = \sigma_M \right) \quad (\text{C.15})$$

If the  $M$  channels are statistically independent, that is if each channel is a different detector element (without cross-talk), this likelihood function is a product of the individual Poissonian probabilities:

$$\Lambda(\vec{\theta}) = \prod_{k=1}^M P \left( S_k(\vec{\theta}) = \sigma_k \right) \quad (\text{C.16})$$

The Fisher matrix is obtained in the following form by inserting eq. C.12 into eq. C.16 and by calculating eq. C.14:

$$F_{ij} = \sum_{k=1}^M \frac{1}{\langle S_k \rangle} \frac{d\langle S_k \rangle}{d\theta_i} \frac{d\langle S_k \rangle}{d\theta_j} \quad (\text{C.17})$$

Assuming that the spectral analyzer consists of a large number of channels  $M$ , with only minor differences between neighboring channels, the integral form of the Fisher matrix can be written in the form:

$$F_{ij}(\vec{\theta}) = \int_{-\infty}^{+\infty} \frac{1}{S(\nu)} \frac{dS(\nu, \vec{\theta})}{d\theta_i} \frac{dS(\nu, \vec{\theta})}{d\theta_j} d\nu, \quad (\text{C.18})$$

whereby  $S(\nu)$  is the density of photoelectrons per channel.

An ideal spectral analyzer is constituted of an infinite amount of channels, which sample the spectrum with Dirac-type transmission functions. Under this condition the spectrum of the incident lidar signal  $S(\nu)$  can be inserted into eq. C.18 to obtain  $\epsilon_{u_r}$  by eq. C.13. The spectrum  $S(\nu)$  is considered to be pure Rayleigh:

$$S(\nu) = \frac{N_{ISA}}{\gamma_R(T)\sqrt{\pi}} e^{-\left(\frac{\nu - \nu_c(u_r)}{\gamma_R(T)}\right)^2}, \quad (\text{C.19})$$

whereby  $N_{ISA} = K\eta\rho^*$  is the total number of photoelectrons detected by the ideal spectral analyzer with the overall photoreceiver efficiency  $\eta$ ,  $\rho^* = \rho/\rho_0$  is the local molecular concentration  $\rho$  normalized to sea level concentration  $\rho_0$ , and  $K$  is a factor, giving the number of received photons obtained at sea level.  $K\eta$  includes all energetic factors ( $\beta$ ,  $\eta_R$ ,  $\eta_T$ ,  $E_L$ ,  $\alpha$ ,  $O(R)$ , see lidar equation eq. 2.2).  $\nu_c(u_r)$  is the central frequency of the peak.

In this way the Cramér-Rao lower bound (CRLB) of an ideal spectral analyzer, i.e., the theoretically lowest possible standard deviation of the measured wind speed  $u_r$ ,  $\epsilon_{u_r}$  is obtained as the first diagonal element of the inverse Fisher matrix (*Gagné et al.* (1974); *Rye and Hardesty* (1993), see, e.g., *Bruneau* (2001)):

$$\epsilon_{(u_r)ISA} = \frac{\gamma}{\sqrt{2N_{ISA}}}, \quad (\text{C.20})$$

with  $\gamma = \sqrt{2k_B T/m}$  (in case of molecules, Knudsen regime) being the most probable thermal velocity of the scatterers.  $m$  is the molecular mass given by  $m_{\text{air}}/N_A$ .  $m_{\text{air}}$  is the mean mass of dry air (per mol), and  $N_A$  is Avogadro's constant. Eq. C.20 is the lowest theoretical bound for both coherent and direct receiver techniques (*Henderson et al.*, 2005). As is apparent from eq. C.20, the performance increases proportional to  $\sqrt{N_{ISA}}$ , what is characteristic for a photon noise limited measurement process. The magnitude of the random thermal molecular velocity  $\gamma$ , is on the order of 400 m/s, while for aerosols  $\gamma$  is on the order of 1 m/s. That is why, a Rayleigh receiver requires  $10^5$  times the number of photons than required for a pure Mie receiver. For an absolute measurement error (standard deviation) of the wind speed of 1 m/s, thus 80000 Rayleigh scattering photons ( $T = 273$  K) are needed in case of an ideal spectral analyzer (ISA), in which case  $\epsilon_{(u_r)ISA} \approx 1$  m/s.

## C.3 Cramér-Rao bounds of real Doppler wind lidar receivers

### FIMI and direct-detection techniques

A “real” physical (unbiased) spectral analyzer (like the fringe-imaging Michelson interferometer (FIMI)) mixes the photons in the spatial and in the frequency domain, including losses, and therefore underperforms compared to the ISA. In case of the FIMI, the density of the photoelectrons per channel  $S(x)$  is given by the convolution of the number density of photoelectrons per channel for monochromatic light (related to the transmission function  $I(x, \nu)$ , eq. 3.1) and the Rayleigh spectrum  $I_{mol}(\nu)$ . It is assumed that the illumination function is rectangular, homogeneous, and that the detector channels are independent (no cross-talk).  $S(x)$  is then written in terms of phase as  $S(\phi)$ :

$$S(\phi) = \frac{1}{2\pi n} \frac{N_{tot}}{4} \left[ 1 + V \cdot e^{-\left(\frac{\pi OPD_{0\mu}}{c}\right)^2 T_0} \cos(S_e u_r + \phi) \right] \quad (C.21)$$

with the number of imaged fringe periods  $n$  set to one.  $N_{tot} = K\eta\rho_R^*$  is the number of signal photons on the detector, whereby  $K$  is the number of received photons.  $\eta$  are all losses in the back-end receiver, except for the losses due to the polarizing beam splitter and half of the light being reflected by the FWFIMI (factor of 1/4 in eq. C.21). The factor  $\mu$  is defined as  $1/\lambda_L \cdot \sqrt{8k_B/m}$ .  $S_e = d\phi/du_r = 4\pi OPD_0/(c\lambda_L)$  is the fringe phase sensitivity.

$\epsilon_{u_r} = (F_{11})^{-1/2}$  (i.e., eq. C.13 and inserting eq. C.21 into eq. C.18 with  $\theta_1 = u_r$ ) for pure a molecular backscattering signal is calculated (see Cézar (2008)):

$$\epsilon_{u_r} = \frac{1}{S_e} \cdot \sqrt{\frac{4}{N_{tot}}} \left( 1 - \sqrt{1 - V^2 \cdot e^{-2\left(\frac{\pi OPD_{01\mu}}{c}\right)^2 T_0}} \right)^{-\frac{1}{2}} \quad (C.22)$$

Cézar (2008) considered two Michelson interferometers sharing the signal, in this case the following penalty factor  $\kappa_{u_r}$  for one of the Michelson interferometers (1), considering an instrumental contrast  $V$ , was obtained:

$$\kappa_{u_r} = \frac{\epsilon_{(u_r)FIMI}}{\epsilon_{(u_r)ISA}} = \frac{1}{\sqrt{2}} \frac{d_c}{OPD_{01}} \left( 1 - \sqrt{1 - V^2 \exp \left[ -8 \left( \frac{OPD_{01}}{d_c} \right)^2 \right]} \right)^{-\frac{1}{2}} \quad (C.23)$$

Here  $d_c = 2c/(\pi\mu\sqrt{T_0})$  is the coherence length of the signal.  $T_0$  is set to 273 K. The minimum value of  $\kappa_{u_r}$ , at a fixed optical path difference  $OPD_{01} = 2.8$  cm, is 4.35. If only one Michelson interferometer is used at normal incidence without a prior polarizing beamsplitter,  $\kappa_{u_r}$  is reduced by a factor  $\sqrt{2}$ , or 2 at oblique incidence using two detectors for both the transmitted and reflected light of the FIMI (see section 3.3.2).

Cézar (2008) also studied the dependence of  $\kappa_{u_r}$  on the particle backscattering ratio  $R_b$ , on absolute atmospheric temperature  $T$  and on the total number of solar background photons  $B_{tot}$ . For this purpose eq. C.21 was modified, such that those parameters are included:



$$S(\phi) = \frac{1}{2\pi n} \left( \frac{B_{tot}}{4} + \frac{N_{tot}}{4} R_b [1 + W \cos(S_e \cdot u_r + \phi)] \right) \quad (C.24)$$

$B_{tot}$  is the number of solar background photons, and  $W = V \cdot G$  is the total contrast of the interference fringe with  $G$  being an atmospheric contrast factor, and  $V$  being the instrumental contrast (see eq. 3.4). The same is done here for a single FIMI. Again the CRB value (eq. C.13) is determined inserting eq. C.24 in the Fisher integral (eq. C.18).  $F_{11}$  turns out to be:

$$F_{(11)FIMI} = -\frac{1}{4} S_e^2 (B_{tot}(-1 + \Upsilon) + R_b N_{tot} [-1 + \Upsilon + GV\Upsilon]) \quad (C.25)$$

whereby  $\Upsilon$  is given by

$$\Upsilon = \sqrt{-1 + \frac{2(B_{tot} + R_b N_{tot})}{B_{tot} + R_b N_{tot} + R_b G V N_{tot}}}. \quad (C.26)$$

In eq. C.25 and eq. C.26, the atmospheric contrast factor  $G$  is defined as (see eq. 3.4):

$$G = \left( 1 - \frac{1}{R_b} + \frac{e^{-\frac{\mu^2 OPD_0^2 \pi^2 T}{c^2}}}{R_b} \right). \quad (C.27)$$

Fig. C.4(a) shows the global fringe contrast  $W = G \cdot V$  as a function of the absolute atmospheric temperature  $T$ , and of the particle backscattering ratio  $R_b$ , assuming an instrumental contrast  $V$  of 0.97. Fig. C.4(b) shows  $R_b$  as a function of a (measured) global fringe contrast  $W(T, R_b)$  for two different temperatures. This approach is used in section A to estimate values of  $R_b$  based on determined global fringe contrasts, referential atmospheric temperatures, and known instrumental contrasts.

For completeness the more compact expressions of  $F_{11}$  and of the CRB of a FIMI without solar background ( $B_{tot} = 0$  in eq. C.25) are given:

$$F_{(11)FIMI} = \frac{S_e^2 N_{tot} R_b}{4} \left( 1 - \sqrt{1 - G^2 V^2} \right) \quad (C.28)$$

$$\epsilon_{(u_r)FIMI} = \frac{1}{\sqrt{F_{(11)FIMI}}} = \frac{1}{S_e \sqrt{R_b}} \sqrt{\frac{4}{N_{tot}}} \cdot \frac{1}{\sqrt{1 - \sqrt{1 - G^2 V^2}}}, \quad (C.29)$$

which simplify to the expressions for pure Rayleigh scattering (eq. C.22) if the particle backscattering ratio  $R_b$  is set to one.

Then all parameters except for the one under study are fixed, and the resulting value of CRB is compared to the value of CRB at the conditions of optimization (eq. C.22), i.e., a normalized factor of performance ( $P_F = \epsilon_{(u_r)FIMI} / \epsilon_{(u_{r,opt.fixed})FIMI}$ ) is obtained. The results of this sensitivity study are shown in Fig. 3.4(b) of section 3.3.2.

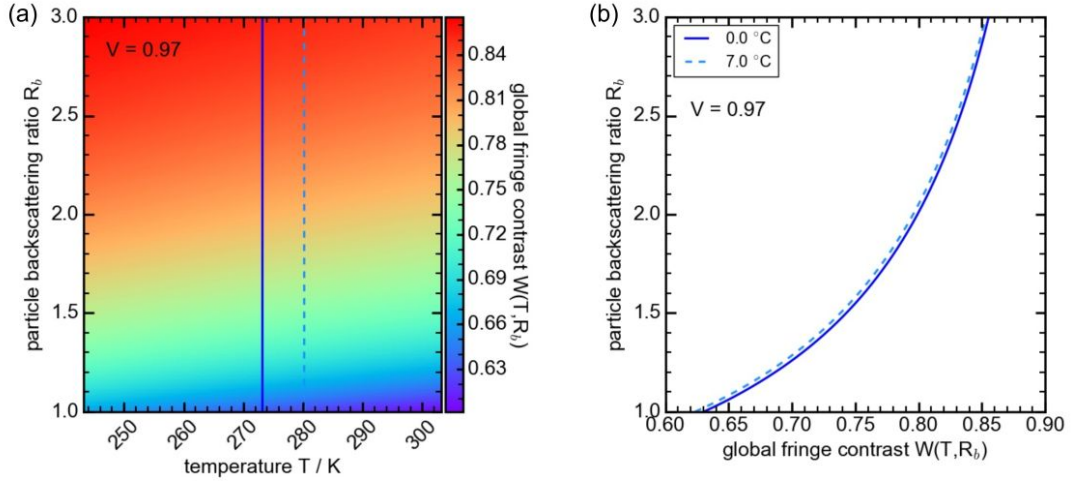


**Figure C.4:** (a) Global fringe contrast  $W$  as a function of absolute temperature  $T$  and of the particle backscattering ratio  $R_b$  for an instrumental contrast  $V = 0.97$ . (b) Values of  $R_b$  for different global fringe contrasts  $W$  making assumptions on  $V$  and on  $T$ .

Comparing results of CRB calculations using eq. C.29 with end-to-end simulations of sections 4.2 and 4.5 assuming a photomultiplier tube array (PMTA) as detector, in order to get similar results the factor  $N_c = 3$  has to be inserted into eq. C.29:

$$\epsilon_{(u_r)FWFIMI_{corr}} = \frac{1}{\sqrt{F_{(11)FIMI}}} = \frac{1}{S_e \sqrt{R_b}} \sqrt{\frac{4 \cdot N_c}{N_{tot}}} \cdot \frac{1}{\sqrt{1 - \sqrt{1 - G^2 V^2}}} \quad (\text{C.30})$$

The origin of this factor  $N_c = 3$  remains unknown. The penalty factor of the FIMI with respect to an ideal spectral analyzer for the measurement of wind speeds ( $\kappa_{(u_r)FIMI}$ ) is obtained by dividing eq. C.29 by eq. C.20 and is given by eq. 3.5 in section 3.3.2 for  $R_b = 1$ .

Similar penalty factors have been derived for other direct-detection DWL receivers. The according values of  $\kappa_{u_r}$  for different spectral analyzers are shown in table C.1.

**Table C.1: Penalty factors of wind speed measurements for various direct-detection Doppler wind lidar receiver concepts with respect to an ideal spectral analyzer (ISA)**

Technique (Interferometer)	Abbreviation	$\kappa_{u_r}$	Author
Dual-channel Fabry-Pérot	(DFP)	2.4	( <a href="#">McKay, 1998</a> )
Fringe-imaging Fabry-Pérot	(FIFPI)	3.1	( <a href="#">McGill and Spinhirne, 1998</a> )
Fringe-imaging Fizeau	(FIFI)	2 – 4	( <a href="#">McKay, 2002</a> )
Dual-channel Mach-Zehnder	(DMZ)	1.65	( <a href="#">Bruneau, 2001</a> )
Four-channel Mach-Zehnder	(QMZ)	2.3	( <a href="#">Bruneau, 2001</a> )
Fringe-imaging Mach-Zehnder	(FIMZ)	2.3	( <a href="#">Bruneau, 2002</a> )
Dual fringe-imaging Michelson	(FIMI)	4.4	( <a href="#">Cézard, 2008</a> )
Single normal-incidence FIMI	(FWFIMI)	4.4	(see section 3.3.2)
Single oblique-incidence FIMI	(FWFIMI)	3.1	( <a href="#">Herbst and Vrancken, 2016</a> )
Single oblique-incidence FIMI (PM)	(FWFIMI)	2.3	( <a href="#">Herbst and Vrancken, 2016</a> )

The penalty factor  $\kappa_{u_r}$  of the FIMI technique may be reduced by illuminating the FW-FIMI at oblique mean angles of incidence (i.e.,  $2^\circ$ ) and by using a hexagonal beamsplit-

ter, allowing for two detector channels and an illumination with unpolarized light (Single oblique-incidence FIMI (PM) in Tab. C.1, see Fig. 5.20).

### Coherent technique

For coherent detection receivers, using the result of [Van Trees \(1971\)](#), the following CRB for the velocity estimate variance (assuming a fixed-velocity zero-depth hard target, an infinite coherence time, and a Gaussian pulse) can be derived ([Henderson, 2013](#)):

$$\text{var}(u_r)_{CNR} \geq \left(\frac{\lambda}{2}\right)^2 \frac{2 \cdot \sigma(\nu_s)^2}{M_e} \left( \frac{1}{CNR_n} + \frac{1}{CNR_n^2} \right) \quad (\text{C.31})$$

The total diversity  $M_e$  is the combined number of independent pulses, range gates, frequencies, detectors and polarizations.  $\lambda$  is the wavelength and  $\sigma(\nu_s)$  is the single frequency spectrum standard deviation width. Assuming a Gaussian spectral shape,  $\sigma(\nu_s)$  is related to the coherence time  $\tau_c$  by  $\tau_c = 1/(\sqrt{2}\pi\sigma(\nu_s))$ .  $CNR_n$  is the narrowband CNR, given by  $\eta_r N_{SC}(t)$ , where  $N_{SC}$  is the number of photons accumulated within the coherent integration time, and  $\eta_r$  is the coherent receiver efficiency. In the limit of high  $CNR_n$  values,  $\text{var}(u_r)_{CNR}$  is twice the CRLB of an ideal spectral analyzer, which is explained by ([Henderson et al., 2005](#), p. 552) with the need to measure both in-phase and quadrature components of a signal for signal phase determination. For  $CNR_n \gg 1$  shot noise is dominant and results in  $1/CNR_n$  behavior. For  $CNR_n \ll 1$  the coherent receiver noise is dominant and results in  $1/CNR_n^2$  behavior, with one detected noise photon per coherent integration time.  $\kappa_{u_r}$  of a coherent detection receiver without speckle is thus two at optimized  $CNR_n$  (factor two in the numerator of eq. C.31). This limit is however typically not reached due to random speckle noise, what is considered in the next section C.4.

## C.4 Influence of speckle on performance

([Henderson et al., 2005](#), p. 558) considered the following approximate composite model (sum variance model) for the radial velocity measurement precision of a coherent receiver, combining the Cramér-Rao lower bound variance estimate without speckle  $\text{var}(u_r)_{CNR}$  (see appendix C.3, eq. C.31) with the estimated variance due to speckle saturation  $\text{var}(u_r)_{sat}$  (derived by [Doviak and Zrnic \(1984\)](#), and valid according to simulations ([Henderson et al., 2005](#))) if the diversity  $M_e > 5$  and if the measurement time is short compared to the signal coherence time):

$$\begin{aligned} \text{var}(u_r) &\sim \text{var}(u_r)_{CNR} + \text{var}(u_r)_{sat} \\ &= \left(\frac{\lambda}{2}\right)^2 \frac{2\sigma(\nu_s)^2}{M_e} \left( \frac{1}{CNR_n} + \frac{1}{CNR_n^2} \right) + \left(\frac{\lambda}{2}\right)^2 \frac{\sigma(\nu_s)^2}{2M_e} \end{aligned} \quad (\text{C.32})$$

$\text{var}(u_r)_{sat}$  is caused by random phase variations with time of the speckle-modulated signal and limits performance at high  $CNR_n$ , which is the narrowband carrier-to-noise ratio.  $M_e$  is the diversity,  $\sigma(\nu_s)^2$  is the frequency variance of the incident signal.

For a coherent detection system the total effective number of noise counts  $N_{nd}$  is equal to the total diversity  $M_e$ , and  $N_{sd} = M_e CNR_n$  is the total number of detected photons. The

noise floor of one photon per diversity mode is ascribed to zero-point energy fluctuations of the vacuum ([Henderson, 2013](#)). The diversity parameter  $M_e$  is used as a measure of the number of independent pulses, independent coherence times within a range gate, independent range gates, independent polarizations, independent spatial samples, detectors, etc., i.e., everything which provides uncorrelated samples ([Henderson, 2013](#)).

Using this, [Henderson et al. \(2005\)](#) also found a general composite model valid for both coherent and direct-detection receivers:

$$\text{var}(u_r) \sim \left(\frac{\lambda}{2}\right)^2 \sigma(\nu_s)^2 \left[ \frac{\kappa N_{nd}}{N_{sd}^2} + \frac{\kappa}{N_{sd}} + \frac{1}{2M_e} \right], \quad (\text{C.33})$$

where  $\kappa \geq 2$  for coherent receivers, and  $\kappa > 2$  for real direct-detection, is a constant, which depends on the design and efficiency of the receiver. [Henderson et al. \(2005\)](#) proved the validity of his model at high diversity against Monte Carlo simulations, which allow predictions at low diversity ([Frehlich and Yadlowsky, 1994](#)). The first term in eq. C.33 are all noise contributions except shot noise, which is the middle term. The last term models the speckle fluctuations of the signal. [Henderson \(2013\)](#) defines three regimes for weak, moderate and strong signal.

According to [Henderson et al. \(2005\)](#) the decoupling of diversity and noise in direct-detection receivers represents the key fundamental difference between a direct-detection receiver and a coherent receiver.

In a coherent receiver a single spatial mode is required for optical mixing with the local oscillator field. That is why the diversity of a single pulse in a single range gate is 1. Diversity can only be increased by independent pulses, range gates, frequencies, polarizations, and detector pixels, which should be averaged incoherently. However, because  $N_{nd} = M_e$ , i.e., one detected noise photon per diversity mode, every increase of the total diversity also increases the noise. Coherent systems are optimized for  $CNR_n \approx 1$  and it is ensured that the number of averaged pulses or range gates is high enough (diversity is high enough) to meet the velocity precision requirement ([Henderson, 2013](#)). When the range resolution is fixed, the product of pulse energy and square root of the pulse repetition rate should also be constant, which leads to high transmitter power requirements, if higher repetition rates are needed.

For a direct-detection receiver  $N_{nd}$ , and  $M_e$  are not coupled in this way, because noise can be limited to less than one detected photon per diversity mode ([Henderson, 2013](#)). The diversity can be maximized to improve performance. Large étendues possible with direct-detection allow for large mode diversity, what becomes apparent in the fine speckle grain size of atmospheric speckle patterns in the receiver plane (see Fig. C.2). Spatial averaging within a range gate increases the diversity, as well (what becomes apparent by reduced speckle contrasts in Fig. C.3). Additionally, multiple pulses allow temporal averaging (see section 3.5.4). Guidance through large-core multi-mode fibers with small speckle grain size increasing diversity further, and a low number of pixels allows spatial averaging (see section 3.5.4). Limited-diversity, however, will result in performance saturation as in the case of coherent detection.

As is shown in section 4.1 the atmospheric return in the AEROLI receiver may be shot-noise limited, because  $M_e = N_p \cdot M_k \cdot M_{mol/aer} \cdot M_f$  is very large, even though we are situated in the strong signal regime with  $N_{sd} \gg N_{nd}$ . The only means to increase performance further seems to be by optimizing the receiver efficiency or the transmitter power.

## C.5 Plane wave propagation in fringe-imaging interferometers

This chapter describes a plane wave propagation method for estimating fringe-shapes and instrumental contrasts in fringe-imaging interferometers such as the Fabry-Pérot (FIFPI), the Fizeau (FIFI), and the Michelson interferometer (FIMI). The major results of this study are discussed in Fig. 3.1(c) of section 3.2.

### Fringe-imaging Fabry-Pérot interferometer

A scheme of a FIFPI illuminated with a monochromatic, divergent, flat-top angular distribution, extended source, which is collimated by a lens with focal length  $f_1$ , is shown in Fig. C.5(a).

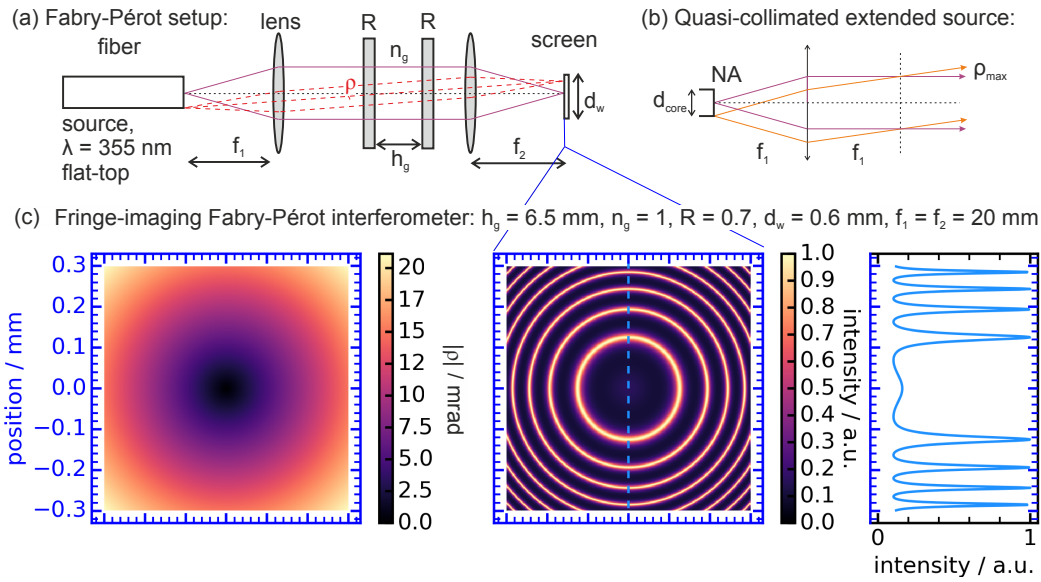


**Figure C.5:** (a) Scheme of a fringe-imaging Fabry-Pérot interferometer. Fringes of equal inclination (so-called Haidinger fringes) are formed at infinity when the FIFPI is illuminated with an extended light source. The annular fringes are imaged onto a screen positioned at the focal distance of a lens behind the the FPI (see, e.g., [Hecht \(2008\)](#)). (b) Scheme of a quasi-collimated extended source represented by a multimode fiber core. (c) Absolute value of angle of incidence ( $\rho$ ) as a function of position  $x$  and  $y$  (left), concentric interference fringe pattern (middle), and intensity distribution at the cross-section marked by the blue dashed line (right).

The exemplary FIFPI is set with a length of the gap between the mirrors of  $h_g = 6.5$  mm. The refractive index of this gap ( $n_g$ ) is set to 1. The reflectivity of the mirrors ( $R$ ) is 0.7. Concentric interference rings are formed on a screen in the focal plane of a second lens with focal length  $f_2$ .

The transmitted intensity distribution of this annular interference pattern has an Airy shape (see, e.g., [Hernandez \(1986\)](#); [Vaughan \(1989\)](#)):

$$I_{\text{FPI}} = I_0 \frac{1}{1 + F \sin^2(0.5 \cdot \delta)}, \quad (\text{C.34})$$

whereby  $I_0$  is the maximum intensity behind the FPI on the screen.  $F = \pi\sqrt{R}/(1 - R)$  is



the reflectivity finesse, and  $\delta$  is the geometrical phase difference defined by  $4\pi n_g h_g \cos(\rho)/\lambda_L$ , with  $\rho$  being the angle of incidence, and  $\lambda_L$  being the wavelength of light.

The maximum angle of incidence ( $\rho_{\max}$ ) in case of quasi-collimated light exiting a multimode fiber of core diameter  $d_{\text{core}}$  (see Fig. C.5(b)) is given by

$$\rho_{\max} = \arctan\left(\frac{\sqrt{2} \cdot d_{\text{core}}}{2 \cdot f_1}\right), \quad (\text{C.35})$$

whereby  $f_1$  is the effective focal length of the collimating lens, and the factor  $\sqrt{2}$  is inserted in case of quadratic core shapes. Considering  $f_1 = f_2 = 20$  mm and a quadratic core of diameter  $d_{\text{core}} = 600$   $\mu\text{m}$ , and a numerical aperture (NA) of 0.22,  $\rho_{\max}$  is about 21 mrad.

For an angular distribution of the light incident on the FIFPI and imaged on the screen as depicted in Fig. C.5(c) (left), four complete rings and eight fringe orders are obtained (see Fig. C.5(c) (right)) for these settings. The FIFPI thus acts like a filter with maximum transmission at the angles  $\rho_p$ , representing the  $p$ th order rings for a given wavelength  $\lambda_L$  of the incident light:

$$m \cdot \lambda_L = 2 \cdot n_g \cdot h_g \cdot \cos(\rho_p) \quad (p = 0, 1, 2, \dots) \quad (\text{C.36})$$

For an angular distribution of  $[-21, 21]$  mrad, there is no significant reduction of the contrast compared to smaller angular distributions.

### Fringe-imaging Fizeau interferometer

Background information on the basics of multi-beam interference in Fizeau interferometers can be found in [Born and Wolf \(1980\)](#). Following the formalism by [Novak et al. \(2011\)](#), the angles  $\alpha$  and  $\beta$  are defined as the incident angles parallel and normal to the direction of the inclination angle  $\theta$  between two mirrors of reflectivity  $R$ . A scheme of a Fizeau interferometer is shown in Fig. C.6.

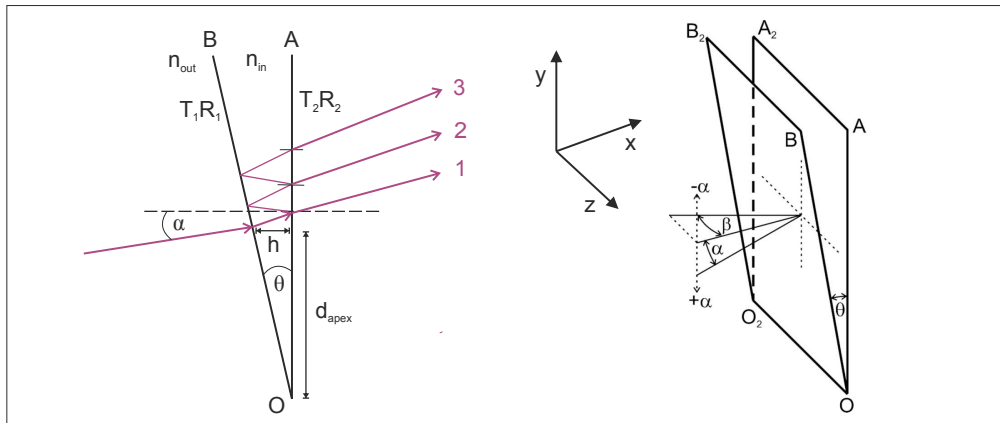


**Figure C.6:** Scheme of Fizeau interferometer with incident angles  $\alpha$  and  $\beta$  (partly taken from [Novak et al. \(2011\)](#)).

The phase term  $\delta_p$  including the initial wave vector (within the mirrors)  $\vec{k}_0$  in terms of  $\alpha$  and  $\beta$  is given by:

$$\delta_p = \frac{2\pi}{\lambda} [y \cos(\beta) \sin(2p\theta + \alpha) + z \sin(\beta)]. \quad (\text{C.37})$$

whereby  $p$  is the  $p$ th order of reflection. The wave vector after  $2p$  reflections is

$$\vec{k}_{2p} = (R_\theta R_x R_{-\theta} R_x)^p \vec{k}_0, \quad (\text{C.38})$$

whereby  $R_\theta$  is the rotational matrix for a rotation by  $\theta$ , and  $R_x$  is the matrix of reflection. The transmitted amplitude of the electric field of the  $p$ th order reflected ray is

$$E_p = E_0 T R^p e^{-j\delta_p}. \quad (\text{C.39})$$

The intensity along the wedge (at  $x = 0$ , see Fig. C.6) is then the absolute value squared of the sum of all  $p$ th order reflection amplitudes, whereby the first  $p_{max}$  orders are given by

$$p_{max} = \frac{\ln \left( \frac{\zeta}{2} \frac{1 - \sqrt{R_1 R_2}}{1 + \sqrt{R_1 R_2}} \right)}{\ln (\sqrt{R_1 R_2})}. \quad (\text{C.40})$$

$p_{max}$  orders should be evaluated to obtain a certain relative accuracy of  $\zeta$  (Rogers, 1982):

$$I_{out} = |E_{out}|^2 = \left| |E_{in}| \cdot (1 - R) \cdot \sum_{p=1}^{p=p_{max}} R^p \cdot e^{j\delta_p} \right|^2 \quad (\text{C.41})$$

The resulting intensity profiles  $I_{out}$  are converted to 2D images, which are shown in Fig. C.7 for different flat-top angular distributions of  $\alpha$ .

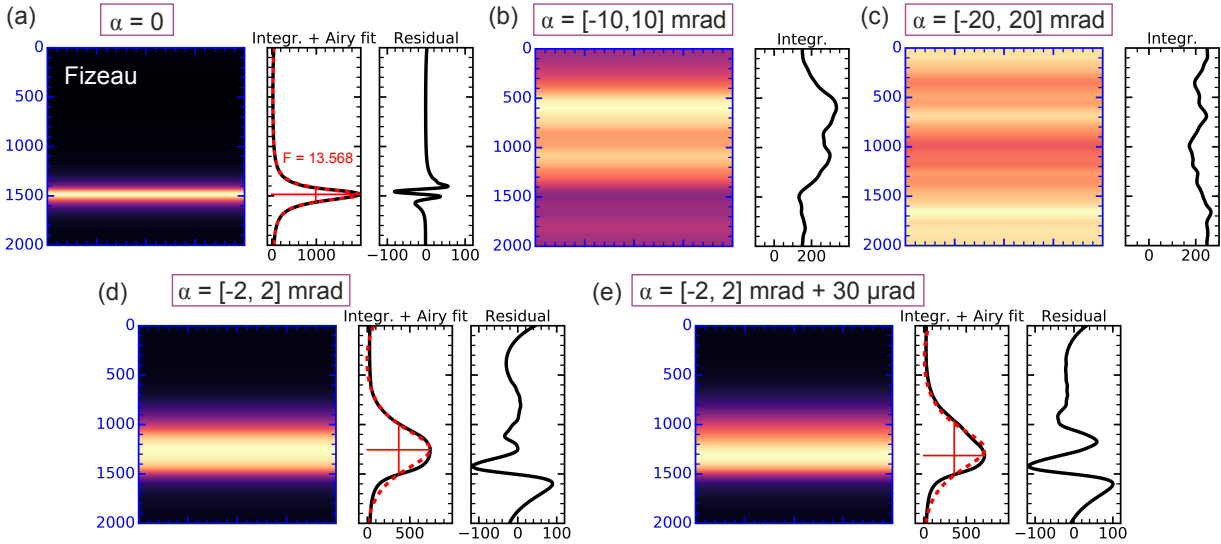


**Figure C.7:** Results of the plane wave propagation simulation of a fringe-imaging Fizeau interferometer: intensities, integrated fringe shapes and Airy fits for different flat-top angular distributions (0,  $[-10, 10]$  mrad,  $[-20, 20]$  mrad,  $[-2, 2]$  mrad) (a, b, c, d) and with a mean incident tilt angle of  $30 \mu\text{rad}$  (e). Mirror inclination angle  $\theta = 17.75 \mu\text{rad}$ , mirror reflectivity  $R = \sqrt{R_1 R_2} = 0.8$ , plate distance  $h = 15$  mm, wavelength  $\lambda = 354.84$  nm, error factor  $\zeta = 0.001$ , and size of detector is 10 mm.

The Fizeau parameters (i.e., inclination angle  $\theta$ , reflectivity  $R$ , mirror separation distance  $h$ , and illuminated aperture diameter  $d_w$ ) are chosen in such a way that a close to ideal Airy-shape (without secondary maxima) is obtained for collimated light.

Tab. C.2 lists the chosen values of the parameters of the Fizeau interferometer, and the finesse  $F$  obtained from an Airy fit.

**Table C.2: Fizeau interferometer parameters.**

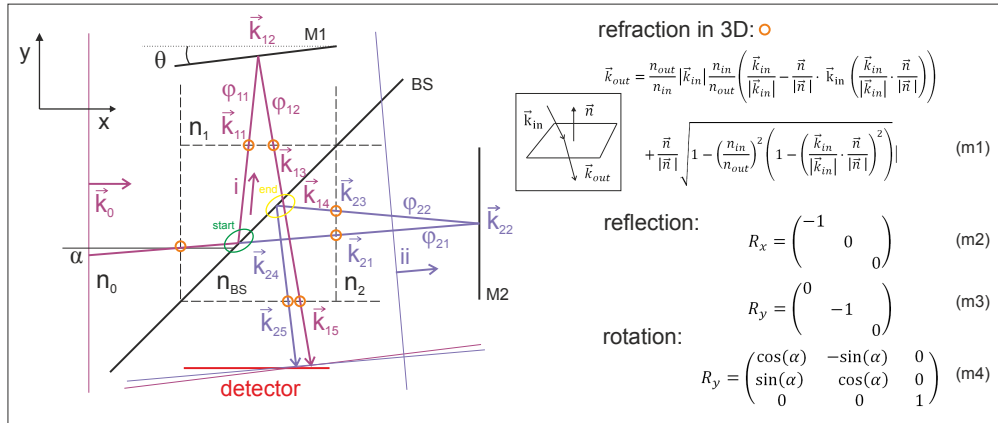
Parameter	$\theta$	$R$	$h$	$d_w$	finesse $F$ (fit)
Value	17.75 $\mu\text{rad}$	0.8	7.5 mm	10 mm	13.6

Fig. C.7 contains Airy fits to the profiles and the respective residuals.

The finesse  $F$  and contrast decrease as the light becomes more wide-angled. A tilt of the angular distribution of  $[-2, 2]$  mrad by 30  $\mu\text{rad}$  changes the fringe shape visibly (see Fig. C.7, bottom). For angular distributions of  $[-10, 10]$  mrad no useful fringe is obtained.

### Fringe-imaging Michelson interferometer

Plane wave propagation can be calculated in a similar way for the FIMI with the major difference, that the FIMI is a two-beam interferometer. A scheme is provided in Fig. C.8. Plane waves are propagated in the arms  $i$  and  $ii$ . The wave vectors at each step, the refractive indices of the regions, and the location where refraction occurs (orange circles), are indicated. The formula for refraction in vector form (eq. m1 in Fig. C.8) is provided on the right hand side, together with transformation matrices for reflection (eq. m2, eq. m3 in Fig. C.8) and rotation by an angle  $\alpha$  (eq. m4 in Fig. C.8).



**Figure C.8:** Scheme of fringe-imaging Michelson interferometer with a plane wave incident at an angle  $\alpha$  and formulas for refraction, reflection, and rotation of the coordinate system in 3D. Indicated in green is the plane where the propagation is started (due to symmetry considerations) and where the intensity is calculated (yellow).

$\varphi_{11}$  and  $\varphi_{12}$  are defined here as the phase shifts induced by the propagation of the plane wave in arm 1 of the interferometer. The wave is propagated by taking the scalar product of the respective wave vector  $\vec{k}$  with the coordinate vector ( $\vec{y}$  for arm 1 and  $\vec{x}$  for arm 2). The intensity of the interference pattern at the last plane of propagation is then given by

$$I_{out} = |E_1 + E_2|^2 = \left| e^{j(\varphi_{11} + \varphi_{12})} \cdot e^{j(\vec{k}_{14} \cdot \vec{r})} + e^{j(\varphi_{21} + \varphi_{22})} \cdot e^{j(\vec{k}_{24} \cdot \vec{r})} \right|^2, \quad (C.42)$$

whereby  $\vec{k}_{14}$  and  $\vec{k}_{24}$  are obtained by calculating all vectors  $\vec{k}$  (see Fig. C.8), which depend on each other through refraction, reflection, and rotation operations.

The parameters of the FIMI and of the FWFIMI are chosen according to considerations of section 3.4. Tab. C.3 lists the parameters during the plane wave propagation simulation.

Table C.3: Michelson interferometer parameters.

Parameter	$\theta$	$FSR$	$d_w$	$d_1$	$d_2$
FIMI (no comp.)	17.75 $\mu$ rad	10.7 GHz	10 mm	10 mm	38 mm ( $n_2 = n_1$ )
FWFIMI (comp.)	17.75 $\mu$ rad	10.7 GHz	10 mm	11.076 mm	16.360 mm

The resulting interference pattern (at the yellow marked locations in Fig. C.8, which is not the plane of localization, see section 3.4.4) are shown in Fig. C.9(a, b, c) for different flat-top angular distributions of  $\alpha$ .

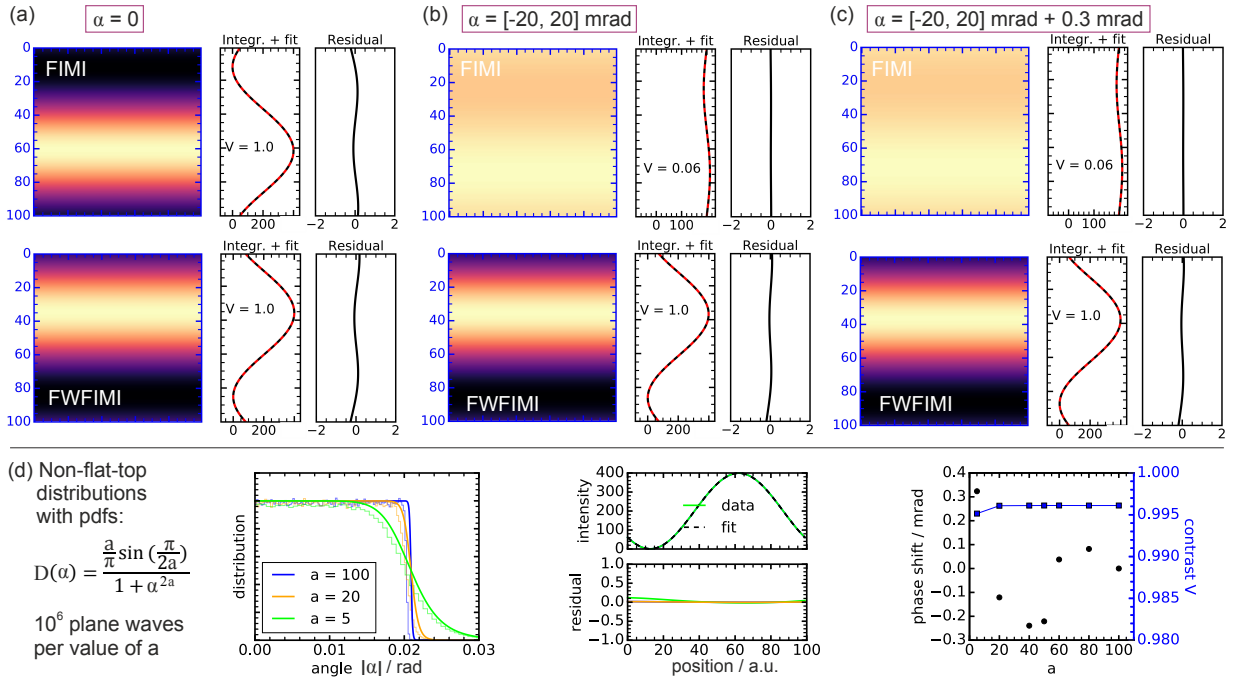


**Figure C.9:** Results of plane wave propagation simulations in fringe-imaging Michelson interferometers (FIMI: top and FWFIMI: bottom): intensities, integrated fringe shapes, and cosine fits for different flat-top angular distributions (0,  $[-20, 20]$  mrad, and with a mean incident tilt angle of 300  $\mu$ rad) (a, b, c). Mirror inclination angle  $\theta = 17.75 \mu$ rad, wavelength  $\lambda_L = 354.84$  nm,  $FSR = 10.7$  GHz,  $d_{1opt} = 11.076$  mm, and  $d_{2opt} = 16.360$  mm (in case of FWFIMI). (d) Non-flat-top distributions of  $\alpha$  (left), cosine fits (middle), phase and instrumental contrast (right) for different values of  $a$  in  $D(\alpha) = (a/\pi) \sin(\pi/(2a))/(1 + \alpha^{2a})$ .

The Michelson interferometer without field-widening compensation (FIMI) is impaired by a severe reduction of the instrumental contrast  $V$  for  $\alpha = [-20, 20]$  mrad. The field-widened FWFIMI (with parameters similar to section 3.4.1 for the arm lengths  $d_1$ ,  $d_2$ , and their refractive indices  $n_1$ ,  $n_2$ ) is not affected (with  $V \approx 1$ ). A change of the mean tilt angle to 300  $\mu$ rad yields phase-shifted (by 130 mrad) cosine-shaped fringes (see Fig. C.9(c)). In case of symmetric non-flat-top distributions of  $\alpha$  of the form  $(a/\pi) \sin(\pi/(2a))/(1 + \alpha^{2a})$  with  $a < 100$  (see Fig. C.9(d)) phase shifts of several hundred  $\mu$ rad are obtained.

In the above procedure plane waves of infinite extend normal to single wave vectors are used, and this method is thus not useful for estimating deviations of the mirrors from ideal planarity. For this purpose a raytracing procedure is applied (see section D.2).

The next section describes a versatile analytical model, which can be used to estimate the instrumental contrast  $V$  of different fringe-imaging Michelson interferometers.

## C.6 Analytical model of interference in Michelson interferometers

For a traditional sequential Michelson interferometer with inclined mirrors illuminated by a wide-field source a geometrical model following [Fortunato \(1997\)](#) and [C  zard \(2008\)](#) is presented here in order to visualize the advantage of a monolithic design in terms of field-widening (see section 3.4.1). This model approach is compared to raytracing simulations in appendix D.2. As we will see in the course of this section a monolithic design can make use of a cubic beamsplitter, which for symmetry reasons achieves a higher efficiency of compensation than a beamsplitter plate. This allows to illuminate the interferometer with larger angular distributions (of  $\rho_{\max} = \pm 20$  mrad) without a loss of contrast.

The (original) Michelson interferometer ([Michelson, 1891](#)) is a two-beam interferometer, whereby the beamsplitter provides a division of amplitude, and in its simplest form, two perpendicular plane mirrors allow recombination of a collimated beam of intensity  $I_0$ . A scheme of this simplest form is shown in Fig. C.10(a).

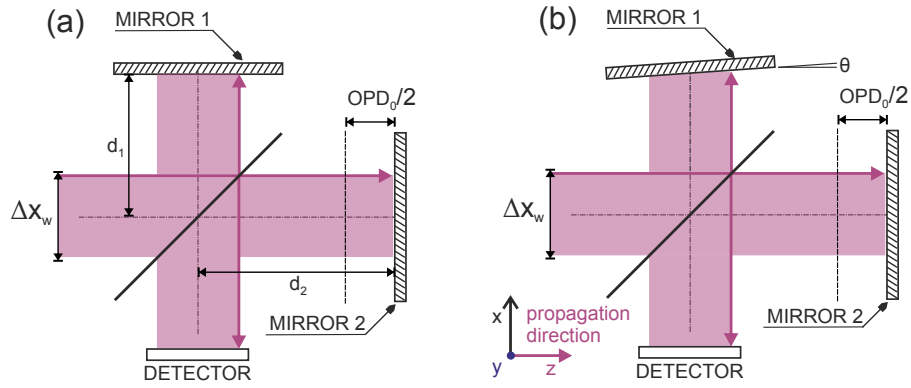


**Figure C.10:** (a) Scheme of a Michelson interferometer in simplest form. (b) Scheme of a Michelson interferometer with inclined mirrors.

If the reflectivity of the beamsplitter (BS) is given by  $R$  and the transmission by  $T$ , the intensities within the arms are given by  $I_1 = RI_0$  and  $I_2 = TI_0$  with  $R + T = 1$ . Considering a phase difference of  $\phi$  between the arms, the intensity at the detector can be written in terms of the incident field  $E_0$  as:

$$I_d = \left| \sqrt{R}E_0 + \sqrt{T}E_0 e^{j\phi} \right|^2 = I_0 \cdot [1 + V_{BS} \cos(\phi)] \quad (\text{C.43})$$

whereby  $V_{BS} = 2\sqrt{RT}$  is the contrast factor of the beamsplitter. For a 50/50 beamsplitter  $V_{BS}$  is exactly 1. For a beamsplitter with 60/40 it is  $\approx 98\%$ . A (lossless, thin) symmetric BS introduces a phase difference  $\phi_{BS}$  of  $\pm\pi/2$ , which is considered to be contained in  $\phi$ , i.e.,  $\phi$  is 0 or  $\pi$ , the intensity is zero at the detector and equal to one at the location of the incident light, e.g. ([H  nault, 2015](#)).  $\phi$  is related to the fixed optical path difference  $OPD_0 = 2d = 2(d_1 - d_2)$  by  $\phi = 2\pi/\lambda \cdot OPD_0 + 2 \cdot \phi_{BS}$ .  $\phi_{BS}$  is omitted in the following.

When the mirrors are inclined by an angle  $\theta$  with respect to each other as shown in Fig. C.10(b), the phase becomes dependent on the location  $x$  (along an axis  $x$  perpendicular to the rotation axis  $y$  of the inclination) on the detector:

$$\phi = \frac{2\pi\nu}{c}(OPD_0 - 2\theta x) \quad (\text{C.44})$$



That is, those frequencies  $\nu_m$  (of the collimated light) are transmitted, which correspond to constructive interference, i.e., which fulfill the equation:  $(OBD_0 - 2\psi x)\nu_m/c = m$  with  $m = 0, 1, 2, \dots$ , and a linear cosine-shaped fringe is obtained for monochromatic light (see eq. 3.1). The spectral resolution  $R_e = FSR/\Delta\nu_{min}$  is  $N \cdot m = 2 \cdot OPD_0/\lambda \approx 160000$ .

As this fringe is imaged onto a detector with rectangular pixels of width  $\Delta a$ , every pixel signal is an integrated subsection of the fringe, that is, the pixels become the channels of a spectral analyzer and the signal  $S_i$  per pixel  $i$ , assuming a rectangular shaped, homogeneous illumination, is given by:

$$S_i = \int_{x_i - \Delta a/2}^{x_i + \Delta a/2} I(x, \nu) dx = FI_0 \Delta a^2 [1 + V_{pix} \cos(\frac{2\pi\nu}{c}(OPD_0 - 2\theta x_i))]. \quad (C.45)$$

whereby  $V_{BS}$  is assumed to be 1, and  $V_{pix} = \text{sinc}(1/P)$  is the instrumental contrast factor due to finite number of pixels of the detector, with  $P = \Delta x_w/\Delta a$  being the number of pixels of the detector with width  $x_w$ . For  $P = 12$ ,  $V_{pix}$  is approximately 99%, and for  $P = 4$ ,  $V_{pix}$  is approximately 90%. The detector is neglected in the following.

The situation becomes more complicated when the incident (extended) light source has an angular distribution, i.e., if its étendue (throughput)  $E = \iint \cos(\psi) dA d\Omega$  [m<sup>2</sup>sr] is greater than zero, whereby  $\cos(\psi) dA$  is the projected area of the source with  $\psi$  being its tilt, and  $\Omega$  is the solid angle into which it is radiating. In this case the instrumental contrast  $V$  of the linear fringe is reduced and becomes dependent on the longitudinal position of the detector (localization), as is shown in the following.

A scheme of the geometrical model of a Michelson interferometer for wide-field (extended) sources is shown in Fig. C.11.

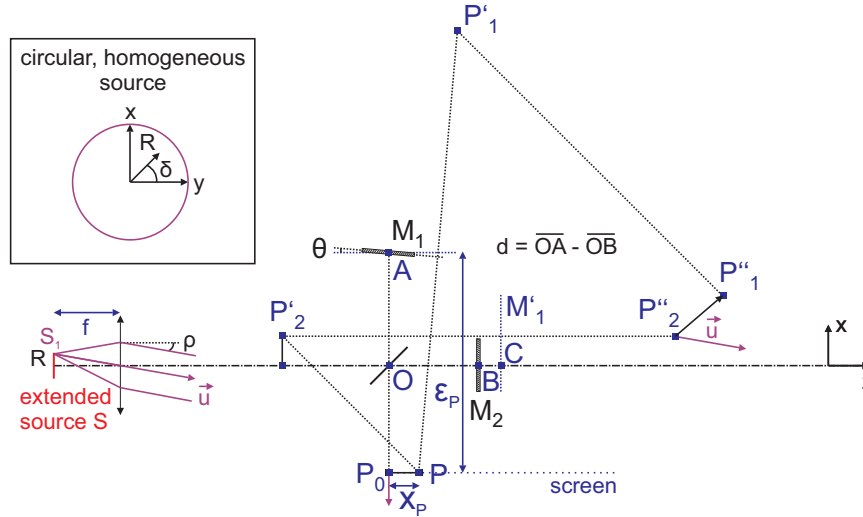


**Figure C.11:** Geometrical, analytical model of a Michelson interferometer with inclined mirrors (based on Fortunato (1997), using notations of Cézar (2008)).

At the beginning a collimated point source  $S_1$  is assumed, where a lens is placed at distance of its focal length  $f$  such that the angle illuminating the interferometer is given by:  $\rho = R/f$ . The difference between the arm lengths defined by an (initially) infinitely thin beam splitter at point O and the respective mirrors  $M_1$  and  $M_2$  at the points A and B is denoted  $d = \overline{OA} - \overline{OB}$ . Mirror  $M_1$  is inclined by the angle  $\theta$  with respect to the optical axis. For incident light (plane wave), which is traveling in direction  $\vec{u}$ , the direction cosines

$(\alpha, \beta, \gamma)$  can be used to relate this direction to a Cartesian coordinate system  $(x, y, z)$ :  $\vec{u} = \alpha\vec{u}_x + \beta\vec{u}_y + \gamma\vec{u}_z$ .

The rotationally symmetric collimated light beam is described in terms of polar coordinates  $(R, \delta)$  in the xy-plane. This beam is split by the beam splitter in two beams, which are recombined at the exit of the interferometer (point P). The optical path length difference between these beams at point P can be expressed in terms of the two image points of P along the respective optical pathways of the interferometer ( $P_1''$  and  $P_2''$  in Fig. C.11):

$$\Delta_p = \overrightarrow{P_1''P_2''} = \alpha(x_2 - x_1) + \beta(y_2 - y_1) + \gamma(z_2 - z_1) \quad (\text{C.46})$$

For simplification it can be considered that mirror  $M_1$  is inclined only along one axis. Therefore mirror  $M_1$  is considered to be rotated around the y-axis (only), and therefore  $y_1 = y_2$ . The optical path length difference between the beams in terms of  $(x_1, z_1)$  and  $(x_2, z_2)$  at point P can be expressed by taking account of the transversal distance  $x_p$  of P with respect to the optical axis and its longitudinal position  $\epsilon_p = \overline{AP_0}$ :

$$\Delta_p = \alpha(2\theta\epsilon_p) + \gamma(2d - 2\theta x_p) \quad (\text{C.47})$$

In paraxial approximation, i.e., if the point source is at small distance  $R$  from the optical axis,  $\gamma$  is in good approximation  $\gamma = 1 - (\alpha^2 + \beta^2)/2$ . Using the relations between polar angular coordinates and Cartesian:  $\rho^2 = \alpha^2 + \beta^2$  and  $\alpha = \rho \sin \delta$ ,  $\Delta_p$  can be written as:

$$\Delta_p(\rho, \delta) = \Delta_p^0 + \Delta_p^1(\rho, \delta) = (2d - 2\theta x_p) + [(2\epsilon_p\theta)\rho \sin(\delta) + (-d + \theta x_p)\rho^2]. \quad (\text{C.48})$$

The first term  $\Delta_p^0$  describes the fringes parallel to the y-axis, with a distance between the fringes of  $\Delta x_i = \lambda/(2\theta)$  along the x-axis. The term  $\Delta_p^1$  shows that the optical path difference at point P is a function of the angular coordinates of the point source, as well. This term will lead to the summation of a number of dephased fringe patterns in point P for an extended point source with some étendue (see “extended source” in Fig C.11). As a result the fringe contrast will be smaller than one.

The illumination received at point P is given by

$$\xi_p = L(\rho, \delta) d\rho d\delta [1 + \cos(k\Delta_p(\rho, \delta))], \quad (\text{C.49})$$

with  $k = 2\pi/\lambda$ .  $L(\rho, \delta)$  is the angular illumination density in  $[\text{W}/\text{m}^2/\text{sr}]$ , which characterizes the source after collimation. If the source is no point source, but extended, the collimated beam incident on the interferometer has some étendue.

$$\xi_p = \iint_S L(\rho, \delta) d\rho d\delta + Re \left\{ e^{jk\Delta_p^0} \iint_S L(\rho, \delta) e^{jk\Delta_p^1(\rho, \delta)} d\rho d\delta \right\}. \quad (\text{C.50})$$

The first term is the total illumination at point P without interference ( $\xi^{tot}$ ).

A complex contrast factor  $\tilde{V}_P$  can be introduced:

$$\tilde{V}_P = \frac{1}{\xi^{tot}} \iint_S L(\rho, \delta) e^{jk\Delta_p^1(\rho, \delta)} d\rho d\delta = V_p e^{j\Phi_p}. \quad (\text{C.51})$$

Eq. C.50 can thus be expressed as

$$\xi_p = \xi_p^{tot} [1 + V_p \cos(k\Delta_p^0 + \Phi_p)]. \quad (\text{C.52})$$

This shows that an extended source in comparison to a point source has two effects:

1. A change of the contrast of the fringe ( $V_p$ ) and 2. a phase shift of the fringe ( $\Phi_p$ ).

In case of a homogenous disc source the total illumination at point P, in absence of interference, can be expressed as

$$\xi^{tot} = \int_0^{\rho_{\max}} \left( \int_0^{2\pi} L_0 \rho d\delta \right) d\rho = L_0 \pi \rho_{\max}^2. \quad (C.53)$$

Here  $\rho_{\max}$  is the half-angle of the quasi-collimated source, and  $L_0$  is defined by the total power  $P_{tot}$  emitted by the source via conservation of energy relation  $L_0 \pi \rho_{\max}^2 S_{col} = P_{tot}$ , where  $S_{col}$  is the surface of the collimated beam. Previous assumptions are applied to write the complex contrast in a simplified form:

$$\tilde{V}_P = \frac{1}{\pi \rho_{\max}^2} \int_0^{\rho_{\max}} \rho e^{-jk(d-\theta x_{P_0})\rho^2} \left( \int_0^{2\pi} e^{jk2\epsilon_p \theta \rho \sin(\delta)} d\delta \right) d\rho \quad (C.54)$$

Within this expression C.54 a 0th order (1st kind) Bessel function of the form

$$J_0(z) = \frac{1}{2\pi} \int_0^{2\pi} e^{-jz \sin(\delta)} d\delta \quad (C.55)$$

can be found, which changes expression C.54 to

$$\tilde{V}_P = \frac{2}{\rho_{\max}^2} \int_0^{\rho_{\max}} \rho e^{-jk(d-\theta x_P)\rho^2} J_0(2k\theta\epsilon_p\rho) d\rho \quad (C.56)$$

This Bessel function  $J_0$  describes fringe localization (see section 3.4.4).  $J_0$  is maximum when  $\epsilon_P = 0$ , i.e., when  $P_0 = A$  (in Fig. C.11). It defines a plane close to the inclined mirror  $M_1$ . This is the so-called localization plane where the contrast of the fringes is maximum. The contrast reduction as a function of distance from the localization plane for the FWFIMI is shown in section 3.4.4. Here  $V_{loc}(\epsilon_p)$  is given by  $|2 \cdot J_1(2k\theta\epsilon_p\rho_{\max}) / (2k\theta\epsilon_p\rho_{\max})|$ .

In the following, the fringe localization term  $J_0(2k\theta\epsilon_p\rho)$  in eq. C.56 is neglected and the expression for the complex contrast (eq. C.56) is reduced to:

$$\tilde{V}_P = \frac{2}{\rho_{\max}^2} \int_0^{\rho_{\max}} \rho e^{-jk(d-\theta x_P)\rho^2} d\rho \quad (C.57)$$

Eq. C.57 can be again simplified by neglecting the mirror inclination term  $\theta x_P$ , which is in fact very small. The contrast  $V_{wf}$  and the phase shift  $\Phi$  are thus homogenous in the detection plane, and are given by:

$$V_{wf} = \left| \text{sinc} \left( \frac{d \cdot \rho_{\max}^2}{\lambda} \right) \right| \quad (C.58)$$

$$\Phi = -k \frac{d \cdot \rho_{\max}^2}{2} \quad (C.59)$$

The phase shift  $\Phi$  could provide a bias to the differential measurement, provided that the angular distributions of the signal and the reference are different. As shown in Fig. C.12 a difference of  $\rho_{\max}$  of 50  $\mu\text{rad}$  introduces a phase shift of about  $64 \cdot 10^{-3} \pi$ , which is equivalent to a Doppler shift induced by a radial wind speed  $u_r$  of about 60 m/s (assuming

an  $FSR$  of 10.69 GHz and a wavelength  $\lambda_L$  of 354.84 nm). This equivalent  $u_r$  is estimated by eq. C.60 and is shown in Fig. C.12 (blue axis):

$$u_r = \frac{\Delta\Phi}{2\pi} \cdot FSR \cdot \frac{\lambda_L}{2}. \quad (C.60)$$

One can assume that this phase shift  $\Delta\Phi$  between reference and signal is constant during a measurement. The maximum field angle of the signal entering the Michelson may however be range-dependent, such that a range-dependent bias may be introduced.

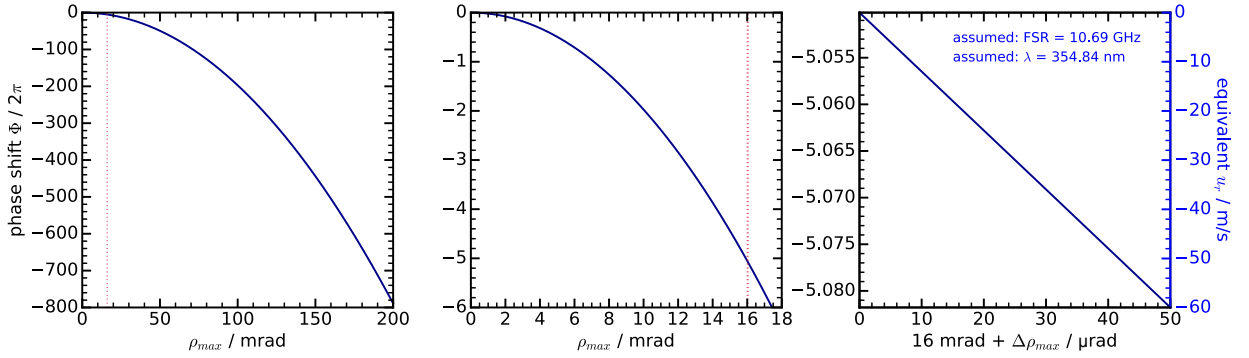


**Figure C.12:** Phase shift  $\Phi$  induced by the étendue of the light incident on a Michelson interferometer for different maximum angular distribution angles  $\rho_{\max}$ . Blue axis: Bias of  $u_r$ .

Fig. C.15 shows the contrast term  $V$  as a function of the maximum angular distribution of the light incident on such an uncompensated Michelson interferometer.

Assuming an angular distribution  $[0, \rho_{\max}]$  with  $\rho_{\max} = 1^\circ$  (i.e., 17.5 mrad, approximately as provided by quasi-collimated light behind a 600  $\mu\text{m}$  round-core multimode fiber, i.e., 15 mrad, see eq. C.35 without factor  $\sqrt{2}$ ), the contrast  $V$  in the localization plane would be zero. Eq. C.58 thus provides an explanation for the need of a field-widening compensation (see section 3.4.1).

The principle of field-widening is shown at first with a simplified model of a MI with an infinitely thin beamsplitter made of air. Then complexity is stepwise increased, considering an extended beamsplitter plate as well as cubic beamsplitters made of glass and monolithic interferometers (see section 3.4.1).

Fig. C.13 shows a scheme of a Michelson interferometer with an infinitely thin beamsplitter and with two arms with lengths  $d_1$  and  $d_2$  and refractive indices  $n_1$  and  $n_2$ , whereby the assumption is made that  $n_2 > n_1$ .

In terms of the model presented at the beginning of this chapter the path difference at point P, using paraxial approximation (to the 4th order), can be written as

$$\Delta_p = 2(d - \theta x_p) - (d - \theta x_p)\rho_0^2 - \frac{1}{4}(d - \theta x_p)\rho_0^4. \quad (C.61)$$

For compensation at least the 2nd order term should be made very small. This can be achieved by inserting a glass plate of well-defined thickness  $e$  into the longer arm of the interferometer. Such a glass plate with refractive index  $n_c$  is shown in Fig. C.13(b). A ray of light crossing the plate with an incident angle  $i$  is refracted under an angle  $r$ . The glass plate has the effect of moving the apparent position of the source of the returning ray closer to the origin of the ray (see blue lines in Fig. C.13(b)). The path length difference between a ray crossing the space to and fro with and without a glass plate is given by

$$\Delta_c = 2e(n_c \cos(r) - \cos(i)). \quad (C.62)$$

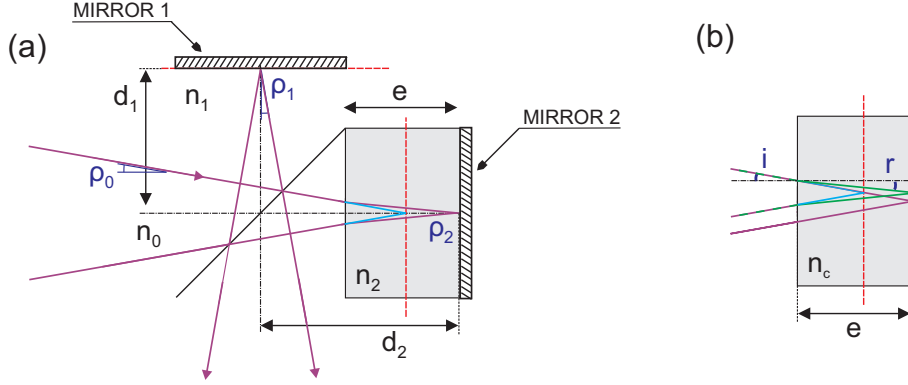


**Figure C.13:** (a) Michelson interferometer with an infinitely thin beamsplitter and with a compensation plate of thickness  $e$ . (b) Compensation plate of thickness  $e$ . Blue lines mark the apparent compensated light ray. Purple lines mark the ray without plate. The respective virtual mirror plane is marked with a red dotted line (depiction inspired by [Title \(2013\)](#)).

The term  $\cos(i)$  is actually the direction cosine  $\gamma$  of the collimated beam in the model. In paraxial approximation  $\cos(i)$  is  $\gamma \approx 1 - (\rho_0^2)/2 - (\rho_0^4)/8$ .

$\Delta_c$  is expressed in terms of the incident angle  $\rho_0$  using Snell's law ( $n_c \sin(r) = \sin(i)$ ):

$$\Delta_c = e \left( 2(n_c - 1) + \rho_0^2 \frac{n_c - 1}{n_c} + \frac{\rho_0^4 n_c^3 - 1}{4 n_c^3} \right) \quad (\text{C.63})$$

The optical path difference at point P upon inserting  $\Delta_c$  in the longer arm of the interferometer, ignoring the inclination term  $\theta x_p$  in the 4th order term, turns out to be

$$\Delta_p = 2(d - \theta x_p + e(n_c - 1)) + \rho_0^2 \left( e \frac{n_c - 1}{n_c} - d + \theta x_p \right) + \frac{\rho_0^4}{4} \left( e \frac{n_c^3 - 1}{n_c^3} - d \right). \quad (\text{C.64})$$

The 2nd order term can be made quasi zero by adjusting the position of the mirror such that  $d = d_{opt} = e(n_c - 1)/n_c$ . The 0th order term of  $\Delta_p$  is  $\Delta_p^0 = \Delta_0 = 2d_{opt}(1 + n_c)$ . Thus the optimum arm length difference  $d$  and optimum glass plate thickness  $e$  are:

$$d_{opt} = \frac{\Delta_0}{2} \frac{1}{n_c + 1}; \quad e_{opt} = \frac{\Delta_0}{2} \frac{n_c}{n_c^2 - 1} \quad (\text{C.65})$$

A variation of  $\Delta e_{opt} < 1$  mm has no great effect on the contrast and performance of a compensated Michelson interferometer. It is however very sensitive with respect to the optimal mirror position. The instrumental contrast factor  $V_{wf}$  as a function of  $\Delta d = d_{opt} - d$  and of  $\rho_{max}$  is given by the following expression:

$$V_{wf}(d, \rho_{max}) = \frac{2}{\rho_{max}^2} \left| \int_0^{\rho_{max}} \rho e^{jk \left[ \rho^2 (d_{opt} - d) + \frac{\rho^4}{4} \left( (d_{opt} - d) + d_{opt} \frac{n_c + 1}{n_c^2} \right) \right]} d\rho \right| \quad (\text{C.66})$$

A further complication is met in reality if a beamsplitter plate is used, which is not infinitely thin and shows some refractivity. As shown by [Fortunato \(1997\)](#) (and [C  zard \(2008\)](#)) the optical path difference introduced by a beamsplitter plate with a thickness  $h$  and with a refractive index  $n_s$  is

$$\Delta_S = \sqrt{2}h \left[ (2n_s^2 - 1)^{1/2} - 1 \right] + \alpha^2 \frac{h}{\sqrt{2}} \left[ 1 - (2n_s^2 - 1)^{-3/2} \right] + \beta^2 \frac{h}{\sqrt{2}} \left[ 1 - (2n_s^2 - 1)^{-1/2} \right], \quad (\text{C.67})$$



whereby  $\alpha$  and  $\beta$  in eq. C.67 are the direction cosines.

As a consequence, the combined effect of a compensation plate and of a beamsplitter plate complicates the expression of the total optical path difference (derived in Cézard (2008) with neglected term  $\theta x_P$ ):

$$\begin{aligned} \Delta = & 2d + 2e(n_c - 1) + \sqrt{2}h \left[ (2n_s^2 - 1)^{1/2} - 1 \right] \\ & + \alpha^2 \left( \frac{h}{\sqrt{2}} \left[ 1 - (2n_s^2 - 1)^{-3/2} \right] - \left( d - e \frac{n_c - 1}{n_c} \right) \right) \\ & + \beta^2 \left( \frac{h}{\sqrt{2}} \left[ 1 - (2n_s^2 - 1)^{-1/2} \right] - \left( d - e \frac{n_c - 1}{n_c} \right) \right) \end{aligned} \quad (\text{C.68})$$

In eq. C.68 the terms of the direction cosines  $\alpha$  and  $\beta$  are different. That is, no optimal values  $d_{opt}$  and  $e_{opt}$  can be found which would compensate both terms at the same time. A compromise is to minimize the average of both terms, what however decreases the efficiency of the field-widening compensation. Cézard (2008) derived an expression for the ideally compensated instrumental contrast  $V_{wf-comp}$  (see eq. C.58) in this case:

$$\begin{aligned} V_{wf-comp} = & \left| \text{sinc} \left( \frac{d_{comp} \cdot \rho_{\max}^2}{\lambda} \right) \right| = \\ = & \left| \text{sinc} \left( \frac{\left( \frac{h}{2\sqrt{2}} \left[ (2n_s^2 - 1)^{-1/2} - (2n_s^2 - 1)^{-3/2} \right] \right) \rho_{\max}^2}{\lambda} \right) \right| \end{aligned} \quad (\text{C.69})$$

The advantage of a monolithic interferometer is that the orientation and position of the interferometer mirrors and beamsplitter are stabilized against thermomechanical variations. Furthermore, it is convenient to optically contact a symmetric cubic beamsplitter to the arms. Due to its symmetry the field-widening compensation is not diminished (as in the above considered case of an inherently unsymmetric beamsplitter plate, eq. C.69). Fig. C.14 shows schemes of a compensated sequential Michelson interferometer with a glass plate (a) and of a field-widened monolithic FIMI with a cubic beamsplitter (b).

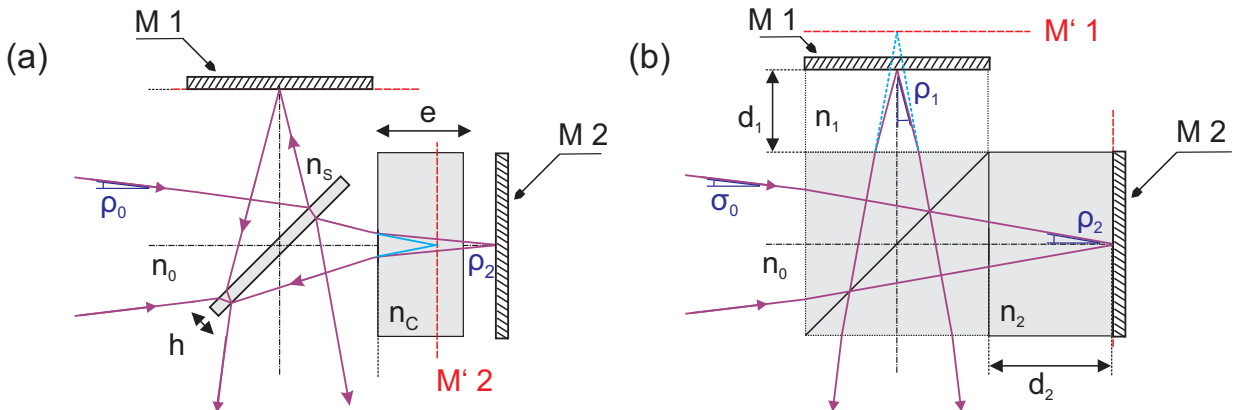


**Figure C.14:** (a) Michelson interferometer with plate beamsplitter of thickness  $h$  and compensation plate of thickness  $e$ . (b) Monolithic Michelson interferometer with ideal field-widening. The respective virtual mirror plane of compensation is marked with red dotted lines. (depiction inspired by Title (2013)).

In case of a monolithic Michelson interferometer with ideal field-widening (FWFIMI)

with a symmetric cubic beamsplitter and arm lengths  $d_1$  and  $d_2$ , eq. C.66 changes to

$$V_{wf}(d_1, d_2, \rho_{\max}) = \frac{1}{(+\rho_{\max} + \theta_t)^2} \left| \int_0^{\rho_{\max} + \theta_t} \rho e^{jk[(\rho^2 - \sin^2(\theta_t)) \cdot \Omega_t + (\rho^2 - \sin^2(\theta_t))^2 \cdot \Psi_t]} d\rho \right| \\ + \frac{1}{(-\rho_{\max} + \theta_t)^2} \left| \int_{-\rho_{\max} + \theta_t}^0 \rho e^{jk[(\rho^2 - \sin^2(\theta_t)) \cdot \Omega_t + (\rho^2 - \sin^2(\theta_t))^2 \cdot \Psi_t]} d\rho \right|, \quad (\text{C.70})$$

whereby  $\Omega_t$  and  $\Psi_t$  are given by:

$$\Omega_t = - \left( \frac{d_1}{\sqrt{n_1^2 - \sin^2(\theta_t)}} - \frac{d_2}{\sqrt{n_2^2 - \sin^2(\theta_t)}} \right) \quad (\text{C.71})$$

$$\Psi_t = -\frac{1}{4} \left( \frac{d_1}{(n_1^2 - \sin^2(\theta_t))^{\frac{3}{2}}} - \frac{d_2}{(n_2^2 - \sin^2(\theta_t))^{\frac{3}{2}}} \right) \quad (\text{C.72})$$

$\theta_t$  is the central incident angle (Cheng et al., 2015), which is unequal zero in case of an oblique illumination configuration of the FWFIMI (see Fig. 3.6).

Fig. C.15 provides the instrumental contrasts of the uncompensated case (eq. C.58), the compensated case assuming an ideal beamsplitter (eq. C.66,  $d = d_{\text{opt}}$ ), the maximum achievable contrast in case of a real beamsplitter plate of thickness  $h$  and refractive index  $n_s$  (eq. C.69), and the case of a better compensated monolithic Michelson interferometer (FWFIMI) with an ideal, symmetric cubic beamsplitter (eq. C.70, eq. C.71, eq. C.72).

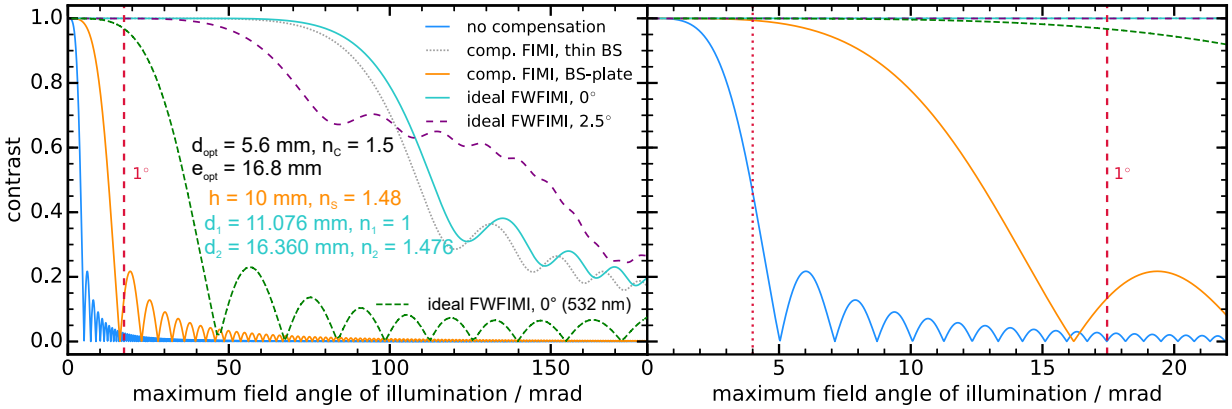


**Figure C.15:** Instrumental contrast factor  $V_{wf}$  as a function of the maximum incidence field angle ( $\rho_{\max}$ ) for different degrees of compensation. The sequential FIMI is compensated with the values used by Cézard (2008) ( $OPD_0 = 2d = 28$  mm,  $e_{\text{opt}} = 16.8$  mm,  $d_{\text{opt}} = 5.6$  mm) and the beamsplitter is either considered to be infinitely thin (gray) or with a thickness  $h$  of 10 mm, and a refractive index  $n_s$  of 1.48 (orange). For the monolithic FWFIMI with a symmetric cubic beamsplitter ideal values of section 3.4.1 are inserted (cyan, solid): mean incident angle  $\theta_t$  of  $0^\circ$ , purple (dashed):  $2.5^\circ$ .  $V_{wf}$  is lower in case of  $\lambda_L = 532$  nm (green, dashed line) because of optimized field-widening for  $\lambda_L = 355$  nm.

The ideal FWFIMI yields the best field-widening compensation and thus the highest instrumental contrast of one at angles  $\rho_{\max} \approx 1^\circ$  (in Fig. C.15). This level of compensation is needed for illumination with light from 600- $\mu\text{m}$ -core fibers.

As was shown by Title and Ramsey (1980), the compensation can be improved to higher order terms, introducing glass blocks in both interferometer arms, what is however not needed in our case.

A comparison of the previously recounted analytic model with raytracing simulations is provided in appendix D.2.

Appendix J describes a method using 355-532-nm illumination for estimating  $R_b$ .

## C.7 Current amplifier model

This section explains the transimpedance amplifier model used in section 3.5.3 (see Fig. 3.26) to calculate the optimum feedback capacitance and resistance. The model was developed by Wirth (2017a) and the following description is based on Wirth (2017b).

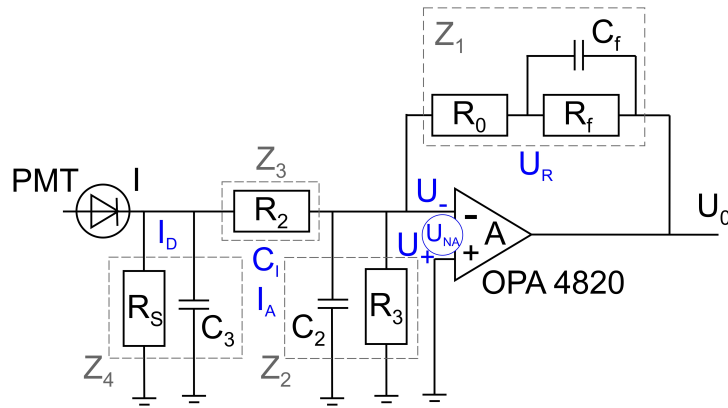


**Figure C.16:** Transimpedance amplifier model based on an IDL routine by Martin Wirth (Wirth, 2017a).

Here a current  $I_0 = 1$  nA is the input current from the photomultiplier tube.  $R_s = 1$  G $\Omega$  and  $C_3 = 5$  pF are the shunt resistance and the capacitance of the photomultiplier tube, including the wiring (2.2 pF).  $R_2$  is an input matching resistor, which is set to zero in the following, because the offset voltage of the amplifier is not compensated.  $R_3 = 10$  M $\Omega$  and  $C_2 = 1.4$  pF are the resistance and the capacitance of the operational amplifier (OPA 4820).  $U_-$  and  $U_+$  are the input voltages of the OPA.  $U_{NA} = 6$  nV is the amplifier input equivalent offset and noise voltage.  $A$  is the open loop differential gain of the OPA.

Here  $A$  is given by

$$A(f) = A_0 \cdot \frac{1 - i \frac{f}{f_1}}{1 + i \frac{f}{f_0}} \cdot e^{-i \cdot 2\pi f \tau}, \quad (\text{C.73})$$

which describes the single pole fall-off, which for OPA 4820 starts at a relatively low frequency  $f_0 = 12$  kHz and which is followed by a 2nd pole near the transit frequency  $f_1$  of 1 GHz. The overall propagation delay  $\tau$  is 15 ns, and  $A_0$  is 2500.  $R_f$  is a feedback resistor.  $C_f$  is the feedback capacity.  $R_0$  is the load resistance. The output voltage  $U_0$  is given by  $U_0 = A \cdot (U_+ - U_- + U_{NA}) = -A \cdot (U_- - U_{NA})$ . According to Kirchoff's first law the current at the negative input of the OPA is:  $I_D + I_A + I(C_I) + I(C_f) + I(R_f) = 0$ . From this follows that  $U_0$  expressed as a function of resistances and capacitances (Wirth, 2017b) is

$$U_0 = -\frac{Z_F A}{A + \frac{Z_f}{Z_p}} \cdot \left( I_D + I_A - \frac{U_R}{R_f} - \frac{U_{NA}}{z_p} \right), \quad (\text{C.74})$$

where  $G = -\frac{Z_f \cdot A}{A + \frac{Z_f}{Z_p}}$  is the transimpedance gain (units  $\Omega$ ),  $Z_f = (\frac{1}{Z_{C_f}} + \frac{1}{R_f})^{-1}$  is the feedback impedance, and  $Z_p = (\frac{1}{Z_{C_l}} + \frac{1}{Z_{C_f}} + \frac{1}{R_f})^{-1}$  is the total input impedance.

In the above circuit model, the following impedances  $Z_1$ ,  $Z_2$ ,  $Z_3$ , and  $Z_4$  can be defined, using the complex impedance of a capacity  $Z_{C_x} = 1/(i \cdot 2\pi f C_x)$ :

$$Z_1 = \left( \frac{1}{R_f} + i \cdot 2\pi f C_f \right)^{-1} + R_0 + i \cdot 2\pi f \cdot I_0 \quad (\text{C.75})$$

$$Z_2 = \left( \frac{1}{R_3} + i \cdot 2\pi f C_2 \right)^{-1} \quad (\text{C.76})$$

$$Z_3 = R_2 \quad (\text{C.77})$$

$$Z_4 = \left( \frac{1}{R_S} + i \cdot 2\pi f C_3 \right)^{-1} \quad (\text{C.78})$$

In our case the frequency transfer-function (see Fig. 3.26(a)) is given by the product of the amplifier transimpedance gain function  $G(f)$  and an additional filter transfer function  $g(f)$ :

$$\tilde{G}(f) = \left| -\frac{\frac{Z_4}{Z_4 + Z_3}}{\left( \frac{1}{A} \left( \frac{1}{Z_1} + \frac{1}{Z_2} + \frac{1}{Z_3 + Z_4} \right) + \frac{1}{Z_1} \right)} \cdot g(f) \right|, \quad (\text{C.79})$$

where  $g(f) = \frac{1}{1 + 2\pi f \tau}$  is a low-pass filter with  $\tau = 75$  nHz.  $R_f$  and  $C_f$  can be tuned in order to get optimal noise and bandwidth behavior with an optimally flat transimpedance gain  $G$ . In this case a good starting value for  $C_f$  (Wirth, 2017b) is

$$C_f = \sqrt{\frac{C_I}{\pi R_f A_0 f_0}}, \quad (\text{C.80})$$

whereby  $C_I$  is the total input capacity. The optimized values in our case are  $R_f = 2.21$  k $\Omega$  and  $C_f = 47$  nF. The 3 db bandwidth of the transimpedance stage is approximately given by

$$f_{-3dB} \approx \sqrt{A_0 \cdot \frac{f_0}{2\pi C_I R_F}}. \quad (\text{C.81})$$

The pulse response function is obtained as the inverse Fourier transform of the complex transimpedance  $t$  (see Fig. 3.26(b)).

Amplifier noise can be modeled by splitting the output voltage  $U_0$  (see eq. C.74) into a part which is proportional to the current from the PMT ( $I_D$ ) and the noise term  $U_{0N}$ . The noise components of the noise term are caused by the voltage/current offset, by the noise voltage and the noise current of the amplifier ( $U_{NA}$ ,  $I_A$ ), and by the feedback resistor noise ( $U_R$ ):

$$U_0 = U_{0D} + U_{0N} = \tilde{G} \cdot I_D + \tilde{G} \cdot \left( I_A - \frac{U_R}{R_F} - \frac{U_{NA}}{Z_P} \right) \quad (\text{C.82})$$

The interested reader finds background information on noise in amplifiers in ([Graeme, 1995](#)) (p. 87 ff.). According to [Wirth \(2017b\)](#) the spectral noise density  $u_0$  of  $U_0$  can be used to describe the random process of the amplifier output, because the noise sources (amplifier noise and resistor thermal noise) are modeled as stationary Gaussian random processes in the time domain. In the frequency domain the quantities are thus also described by a Gaussian random process, and the fluctuations at different frequency bins are uncorrelated ([Wirth, 2017b](#)).

The spectral noise density (see Fig. 3.26(c)) is then obtained by taking the ensemble mean of the output variation:

$$\begin{aligned} u_0 = \langle \Delta U_0^2 \rangle &= |\tilde{G}|^2 \cdot \left( \langle |\Delta I_A|^2 \rangle + \frac{\langle |\Delta U_R|^2 \rangle}{R_F^2} + \frac{\langle |\Delta U_{NA}|^2 \rangle}{|Z_P|^2} \right) \\ &= |\tilde{G}|^2 \cdot \left( i_A^2 + \frac{4 \cdot k_B \cdot T}{R_F} + \frac{u_A^2}{|Z_P|^2} \right) \end{aligned} \quad (\text{C.83})$$

where  $i_A$  is the spectral noise current input density and  $u_A$  is the equivalent input voltage noise density of the amplifier. The noise density of a resistor is given by  $u_R^2 = 4 \cdot k_B \cdot T \cdot R$  (Nyquist formula), whereby  $k_B = 1.308 \cdot 10^{-23}$  J/K is Boltzmann's constant.

An important property of the spectral noise density (shown in Fig. 3.26(c)) is that it is not constant over frequency (no white noise). The reduced bandwidth of the amplifier (due to increased feedback capacitance  $C_f$ ) reduces the underlying quadratically increasing noise term ([Wirth, 2017b](#)).

## C.8 Mean wavelength estimators

Finding the energetic centroid of a signal (mean wavelength), which is a measure of wind velocity in case of DWL receivers, is done using mean wavelength estimators. Mean wavelength estimators have been studied for Doppler Radar ([Frehlich and Yadlowsky, 1994](#)), Doppler Sodar ([Reitebuch, 1999](#)), coherent detection DWL ([Frehlich and Yadlowsky, 1994](#)), and for direct-detection DWL, such as the fringe-imaging Fizeau interferometer of the Mie receiver of the ALADIN instrument of ADM Aeolus ([Paffrath, 2006](#)), and a fringe-imaging Michelson concept ([Cézard et al., 2009a](#)).

A similar treatment and test of mean wavelength estimators (MWE) in case of the AEROLI receiver (FWFIMI) is described in section 4.

This section is dedicated to providing background information on the mean wavelength estimators used in section 4. In the following, descriptions provided by [Paffrath \(2006\)](#) and by [Cézard et al. \(2009a\)](#) are made use of.

### Centroid method (CM)

The centroid method (CM) is a commonly used algorithm for the determination of the center of gravity. For the analysis of spectral lines it can be written in the form ([Gagné et al., 1974](#)):

$$\lambda_m = \frac{\sum_{i=k}^{i=k+m} \lambda_i \cdot I_i}{\sum_{i=k}^{i=k+m} I_i} \quad (\text{C.84})$$

Where  $\lambda_m$  is the resulting wavelength,  $m$  is the number of pixels,  $\lambda_i$  is the wavelength at the center of pixel  $i$ , and  $I_i$  is the intensity at pixel  $i$ . The wind speed is then calculated using  $u_r = c\Delta\lambda_m/(2\lambda_L)$ , whereby  $c$  is the speed of light, and  $\lambda_L$  is the wavelength of the laser.

### Gaussian correlation algorithm (GCA)

The Gaussian correlation algorithm (GCA) is described by [Paffrath \(2006\)](#). It is assumed that the signal on the detector has a Gaussian line shape (which is not the case for both the FIFI and the FIMI). The signal  $I$  and a suitable Gaussian function  $W(\lambda)$  maximum position are compared by calculating the pixel index, where their cross-correlation function  $C$  has its maximum, i.e., where its first derivative  $C'$  is equal to zero.

The Gaussian function  $W$  is defined in the form

$$W(\lambda) = \frac{\sqrt{8\ln(2)}}{\sqrt{2\pi} \cdot \Delta\lambda_{FWHM}} e^{-\frac{4\ln(2) \cdot \lambda^2}{\Delta\lambda_{FWHM}^2}} \quad (\text{C.85})$$

with  $\lambda_{FWHM}$  being the full width half maximum of the Gaussian. The correlation function of the signal  $I_i$  and the Gaussian function  $W(\lambda_i)$  at pixel  $i$  is:

$$C(\lambda_0) = \sum_{i=1}^{i=i_{max}} I_i \cdot W(\lambda_i - \lambda_0) \quad (\text{C.86})$$

where  $i_{max}$  is the maximum index used during the calculation and  $\lambda_0$  is the center wavelength. The maximum is found by setting the first derivative to zero:

$$C'(\lambda_0) = \sum_{i=1}^{i=i_{max}} I_i \cdot W'(\lambda_i - \lambda_0) = 0 \quad (\text{C.87})$$

The derivative is calculated and the equation is rearranged to yield  $\lambda_0$ . In an iterative algorithm the value of  $\lambda_0$  is stepwise increased, setting it equal to  $\lambda_n$ , increasing  $n$  in every step. The iterative algorithm takes the form:

$$\lambda_{n+1} = \frac{\sum_{i=1}^{i=i_{max}} I_i \cdot \lambda_i \cdot W(\lambda_i - \lambda_n)}{\sum_{i=1}^{i=i_{max}} I_i \cdot W(\lambda_i - \lambda_n)} \quad (\text{C.88})$$

### Downhill Simplex algorithm method (DSA)

The downhill simplex algorithm (DSA) was developed by [Nelder and Mead \(1965\)](#). A compact overview is provided in [Press et al. \(1992\)](#). The algorithm works by determining the minimum (or maximum) of a function, which depends on more than one independent variable, using simple geometrical bodies (simplex). The simplex is multidimensional (e.g., a tetrahedron) and as the method progresses the minimum gets enclosed by the simplex, which is transformed from step to step. The simplest simplex body with  $n + 1$  corners within an  $n$ -dimensional geometry is a triangle ( $n = 2$ ). The corners are analyzed at every step and the “worst” corner is replaced. An initial simplex has to be chosen, which is then stepwise transformed by reflection, expansion, contraction, and multiple contraction. Compared to other algorithms, the DSA requires only function evaluations (no derivatives), and convergence is more likely, however longer processing times are possible.



In this work, the open-source python toolbox “scipy” with the implementation of the Nelder-Mead algorithm “optimize.fmin” ([Jones et al., 2001](#)) is used. The python package “multiprocessing” is applied to run several optimization tasks on multiple CPU cores in parallel.

A cosine-shaped fit function is defined with the parameter vector  $\vec{p}$  components  $p_A$  (amplitude),  $p_W$  (global fringe contrast),  $p_{\Delta\phi}$  (phase shift), and  $p_B$  (background):

$$f(x) = p_A \cdot (1 + p_W \cdot \cos(x + p_{\Delta\phi})) + p_B, \quad (\text{C.89})$$

where  $x$  covers a range of  $[-n\pi, +n\pi]$ .  $n$  is the number of imaged fringe periods.  $f(x)$  is a continuous function with thousands of points. The simulated fringe data has a resolution given by the number of illuminated pixels  $N_{pix} = 12$  of the linear detector. That is why the fit function  $f(x)$  has to be stepwise integrated (downsampled). The downsampled version  $f_p(x)$  is fit to the data  $y$  by minimization of the sum of the quadratic deviations  $\sum_k (y_k - f_p(\vec{p}, x))^2$  over all pixels  $k$ .

The DSA can also be parallelized at the parameter level (e.g., [Lee and Wiswall \(2007\)](#)) and python toolboxes exist for massive parallelization using graphic cards (see, e.g., the “Multi-threaded Optimization Toolbox (MOT)” by Robbert Harms).

### Maximum likelihood estimator (MLE)

This approach is the method of choice of [C  zard et al. \(2009a\)](#), because it is asymptotically unbiased and because it reaches the minimal standard deviation (CRB, see section C.3). [Paffrath \(2006\)](#) describes the MLE method for a FIFI-based receiver. Here the description is adjusted to the fringe-imaging Michelson interferometer (FIMI).

Suppose that  $N_{Mic}(i)$  are the observed number of detected photoelectrons at the FIMI-based receiver at pixel index  $i$ , and  $\langle N_i(\vec{\theta}) \rangle$  is the theoretical, mean intensity distribution for the parameter vector  $\vec{\theta} = (u_r, \rho^*, T, R_b)$ . The maximum likelihood estimator (MLE) method then tries to find that vector  $\theta_{max}$ , which maximizes the global probability to obtain the observed data ( $N_{Mic}(i)$ ). This probability is called likelihood function  $\Lambda$  of the signal. With statistical independence of the pixels,  $\Lambda$  takes the form

$$\Lambda(\vec{\theta}) = \prod_i^{i_{max}} p(N_i(\vec{\theta})) = N_{Mic}(i), \quad (\text{C.90})$$

whereby  $p$  is a probability density function.

According to [C  zard et al. \(2009a\)](#), the supposed mean number of photoelectrons per pixel  $i$ ,  $\langle N_i(\vec{\theta}) \rangle$ , for a fringe-imaging Michelson, is given by

$$\langle N_i(\vec{\theta}) \rangle = A_i \rho \cdot R_b \left[ 1 + W(T, R_b) \cos \left( \frac{d\phi}{du_r} u_r + \phi_i \right) \right] + B_i, \quad (\text{C.91})$$

where  $A_i$ ,  $B_i$ ,  $R_b$ ,  $W(T, R_b)$  are parameters for the signal amplitude, the solar background, the particle backscattering ratio, and the global fringe contrast.  $W$  has a new contribution due to pixel-wise integration (see  $V_{pix}$ ) and is given by  $V \text{sinc}(1/P) G(OPD_0)$ , where  $V$  is the instrumental contrast,  $P$  is the number of pixels, and  $G$  is the atmospheric contrast factor given by eq. C.27. The parameter of primary interest is the radial wind speed  $u_r$ , which could of course also be written in terms of Doppler-shifted wavelength.  $\phi_k = 2\pi/\lambda_L(OPD_0 - 2\theta x_i)$  is the fringe phase on pixel  $i$  at zero air speed, whereby  $\theta$  is

the angle of inclination of the mirrors, and  $x_i$  is the pixel position on the linear detector. The fringe phase sensitivity  $S_e = d\phi/du_r$  is given by  $4\pi OPD_0/(c\lambda_L)$ .

Under optimal (shot-noise limited) measurement conditions, the propability to observe  $N_{Mic}(i)$  signal photons obeys a Poisson statistic:

$$p(N_i = N_{Mic}(i)) = \langle N_i \rangle^{N_{Mic}(i)} \frac{e^{-\langle N_i \rangle}}{N_{Mic}(i)!} \quad (C.92)$$

Applying logarithmic calculus on eq. C.90 the log-likelihood function  $\Lambda_{ln}(\vec{\theta})$  is obtained, which can be maximized more easily:

$$\Lambda_{ln}(\vec{\theta}) = \ln \left( \prod_{i=0}^{i_{max}} p(N_i(\vec{\theta})) \right) = \sum_{i=0}^{i_{max}} \ln(p(N_i(\vec{\theta}))) \quad (C.93)$$

Inserting eq. C.92 into eq. C.93 the log-likelihood function becomes:

$$\Lambda_{ln}(\vec{\theta}) = \sum_{i=0}^{i_{max}} N_{Mic}(i) \cdot \ln(\langle N_i(\vec{\theta}) \rangle) - \sum_{i=0}^{i_{max}} \ln(N_{Mic}(i)!) - \sum_{i=0}^{i_{max}} \langle N_i(\vec{\theta}) \rangle \quad (C.94)$$

The second term contains only measured intensities and is thus constant ( $C$ ). The third term is the total signal intensity  $n_s$ . Thus, eq. C.94 is written as

$$\Lambda_{ln}(\vec{\theta}) = \sum_{i=0}^{i_{max}} N_{Mic}(i) \cdot \ln(\langle N_i(\vec{\theta}) \rangle) - C - n_s. \quad (C.95)$$

The final expression of  $\Lambda_{ln}(\vec{\theta})$  is obtained by inserting eq. C.91 into eq. C.95, for which no analytical solution exists, but which can be solved using iterative calculus, for example the Newton method:

$$\vec{\theta}_{i+1} = \vec{\theta}_i - H_f^{-1}(\vec{\theta}_i) \cdot \text{grad}_f(\vec{\theta}_i), \quad (C.96)$$

where  $H_f$  is the Hessian matrix, and  $\text{grad}_f$  is the gradient function of  $\Lambda_{ln}(\vec{\theta})$ .

### Gauss-Newton method (GNM)

Alternatively, the Gauss-Newton method (GNM), which is for example described in [Nocedal and Wright \(1999\)](#), could be used to minimize the sum of the quadratic deviations between the fit model (eq. C.89) and the data, which should be faster than the DSA method. In comparison to the Newton method the GNM does not require the calculation of the Hessian, only the Jacobian.

Within this work only the CM method, the GCA method, and the DSA method are tested. The MLE method or the GNM method could be used for a faster online determination of wind speeds.

### Systematic biases of the mean wavelength estimators in case of a FIMI

This section recounts results on systematic biases of the CM method, of the GCA method, and of the DSA method in addition to section 4.1.

Fig. C.17 shows systematic biases of a FIMI for different contrasts  $V$  and  $V_{sig}$  of the simulated laser reference fringe and the simulated atmospheric signal fringe, and for different number of cosine fringe periods  $n$ .

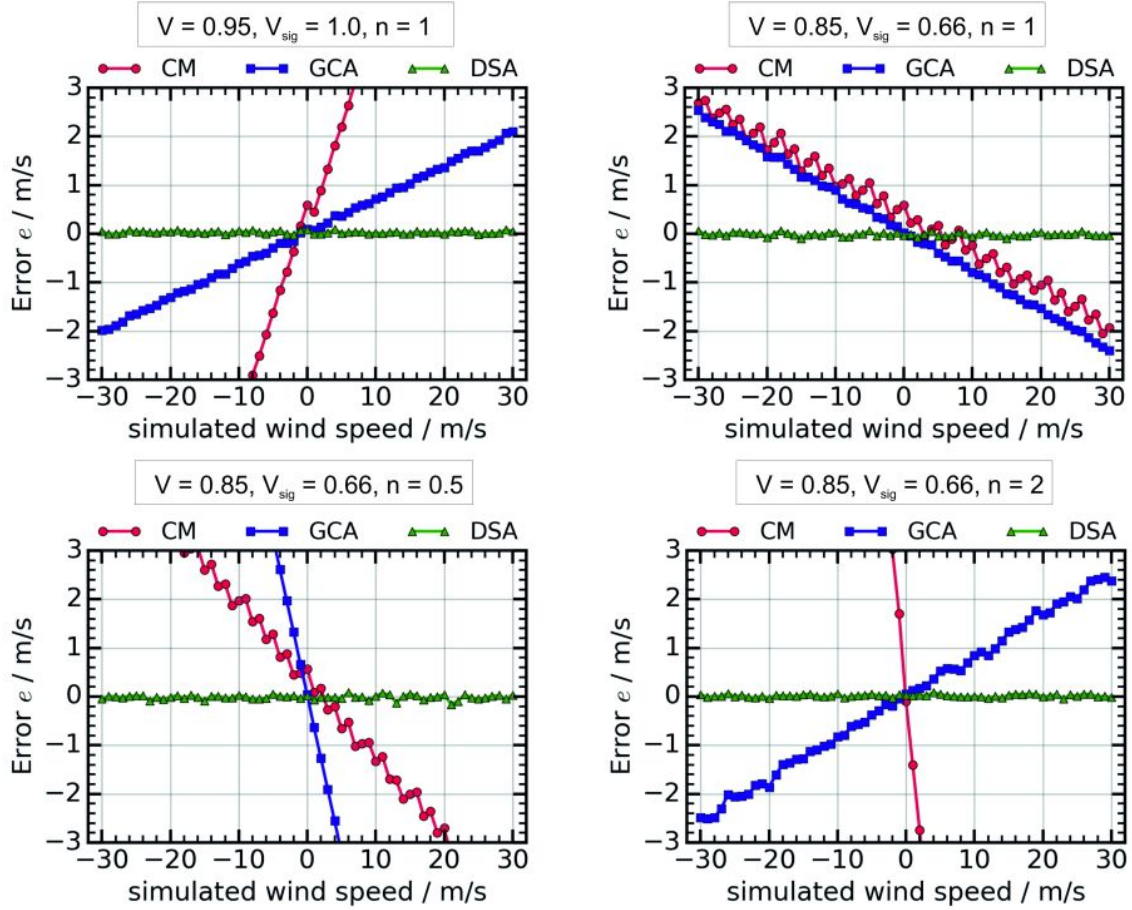


**Figure C.17:** Systematic bias simulation for a fringe-imaging Michelson interferometer with ideally cosine-shaped fringe for different contrasts  $V$  and  $V_{sig}$ , and number of fringe periods  $n$  without noise, using the mean wavelength estimators CM, GCA, and DSA.

The slope of the bias  $e$  is dependent on the choice of  $V$ ,  $V_{sig}$ , and on the number of fringe periods  $n$  in case of CM and GCA. The DSA method results indicate no slope bias for the same settings.

The same simulations are repeated adding noise of a specific SNR onto the simulated fringe distributions ( $V = 0.85$ ,  $V_{sig} = 0.66$ ,  $n = 1$ ). This is done by adding signals of a respective normal distribution to every channel of the 12 pixel fringe distribution. Then the CM, GCA, and DSA method are used to determine the respective fringe shift. This is repeated 50 times in a row, with different noise realizations, respectively. The resulting errors  $e$  between the simulated and determined wind speeds are shown in Fig. C.18 as a function of wind speed. The respective mean value  $\bar{e}$  and standard deviation  $\sigma(e)$  of the 50 trials are shown on the right side.

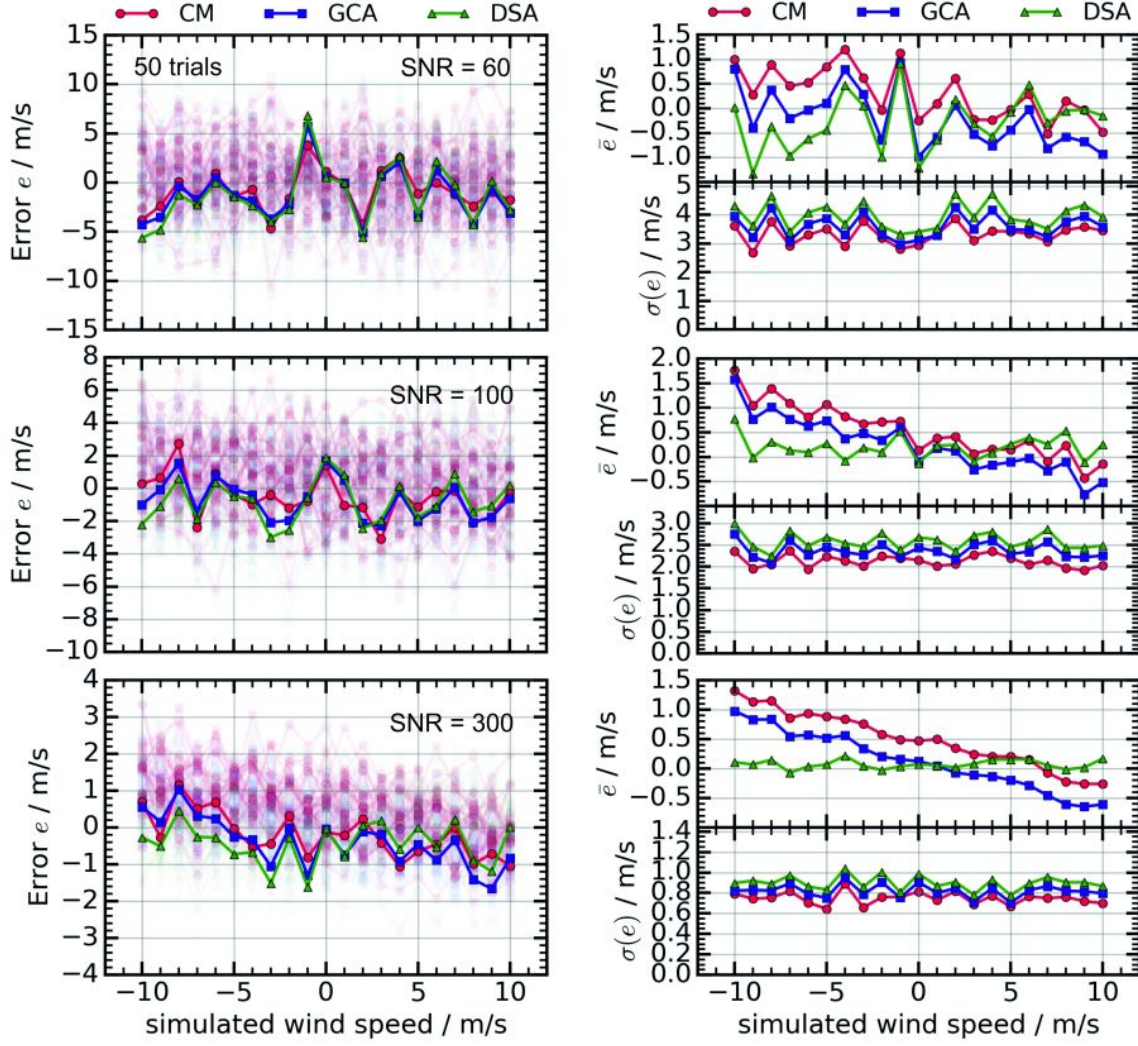


**Figure C.18:** Systematic bias simulation with added noise of different SNR on the cosine-shaped reference and signal fringe distributions ( $V = 0.85$ ,  $V_{sig} = 0.66$ ,  $n = 1$ ), whereby the results of 50 trials are shown on the left side. The error  $e$  between the determined and simulated wind speeds are shown as a function of the wind speed (one trial is highlighted). On the right side the respective mean error and standard deviation of the error  $e$  are shown.

The resulting mean value of  $\sigma(e)$  in case of the DSA method is shown in Fig. 4.2(b) as a function of the SNR.

### Dependence on the number of illuminated pixels

The dependence of  $\sigma(e)$  of end-to-end simulations of horizontal wind speed measurements on the number of illuminated pixels  $N_{pixel}$  is shown in Fig. C.19(a) (green rhombs). Therein one fringe period ( $n = 1$ ) on those illuminated pixels is assumed. Two hundred simulation runs are performed for each  $N_{pixel}$ -setting, whereby the DSA method is applied. The end-to-end simulations includes the pitch loss factor ( $F_{loss}$ ) of the PMTA depending on  $N_{pixel}$  (see eq. F.2, Fig. C.19(b)).  $\sigma(e)$  increases as  $N_{pixel}$  decreases. CRB calculations using eq. C.30 with  $V = V_{pix} = \text{sinc}(1/N_{pixel})$  yield slightly different results for a range of  $N_{pixel}$  of 3 to 30 and for the same total signal (black line in Fig. C.19).



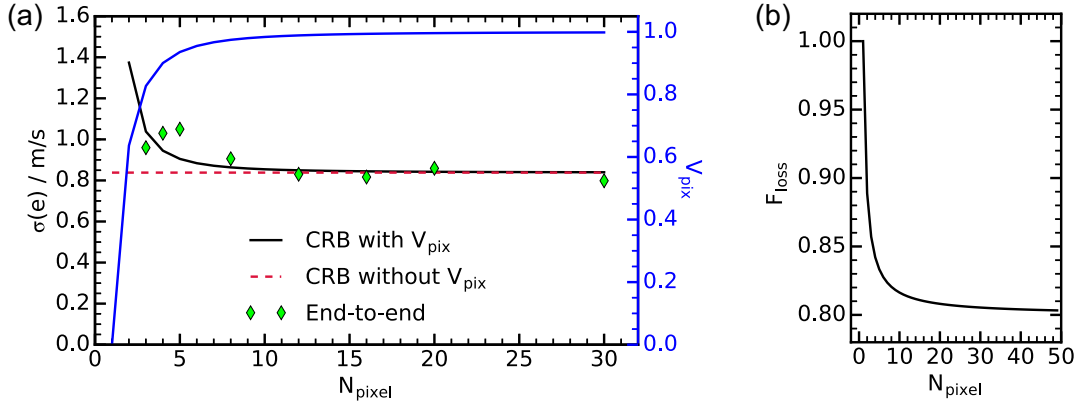


**Figure C.19:** Dependence of the standard deviation of the difference  $e$  between simulated and determined wind speeds ( $\sigma(e)$ ) on the number of illuminated pixels  $N_{pixel}$ . Comparison of CRB calculations using  $V = V_{pix}$  in eq. C.30 of appendix C.3 (black line) and end-to-end simulations at the same range, altitude, and atmospheric parameters. (b) Pixel factor  $F_{loss}$  as a function of the number of pixels  $N_{pixel}$ .

### Systematic biases for deformed fringe shapes

The influence of the real fringe shape deviating from an ideal cosine shape can be simulated using a modified fringe model with two additional parameters  $Cu$  and  $Sk$ , where  $Cu$  is the kurtosis and  $Sk$  is the skewness of the fringe:

$$f(\phi) = A \cdot (1 + V \cdot \cos(\phi + \arcsin(Cu \cdot \sin(Sk - \phi)))) \quad (C.97)$$

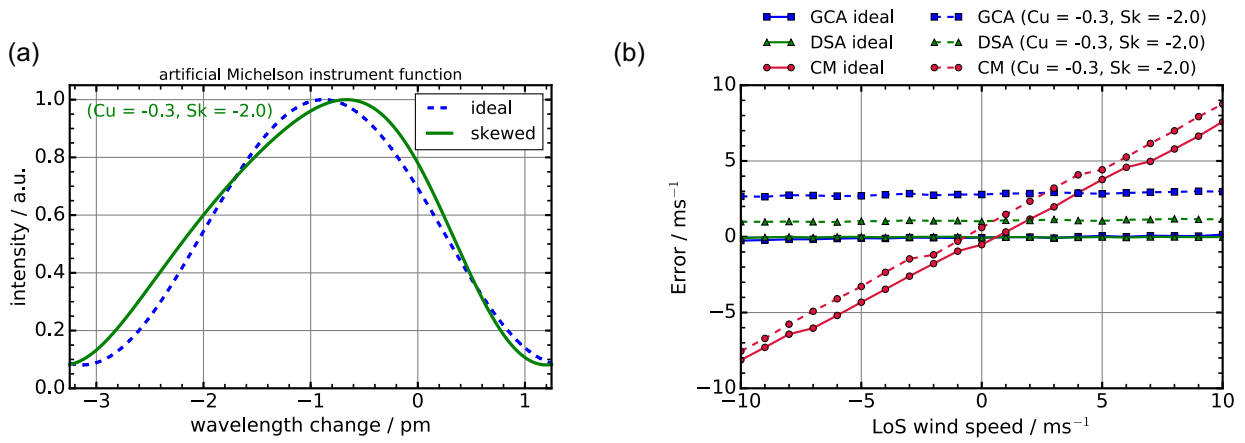
The parameters  $Cu$  and  $Sk$  are varied between  $[-0.3, 0.3]$  and  $[-2.0, 2.0]$ . The instrumental contrasts  $V$  and  $V_{sig}$  are set to 0.95.

Fig. C.20(a) shows an exemplary fringe shape ( $Cu = -0.3$ ,  $Sk = -2$ ). The same procedure as described in section 4.1 is used to simulate the instrument function without detection noise. Fringe shifts according to wind speeds in the range  $[-10, 10]$  m/s are simulated, and the wind speed is determined from the relative shift of the reference and signal fringes with the GCA method using a FWHM of 3 pm for the Gaussian, the DSA method using an ideal cosine fit model ( $p_{Cu} = 0$ ,  $p_{Sk} = 0$  in eq. C.97), and the centroid method. The resulting systematic errors  $e$  are shown exemplarily for  $Cu = -0.3$ ,  $Sk = -2$  in Fig. C.20(b).

An overview of wind speed dependent biases for the GCA, DSA and CM method in a parameter field of skewness ( $Sk$ ) and kurtosis ( $Cu$ ) is provided in Fig. C.21.

Fig. C.22(a) shows the mean of the bias (of lines shown in Fig. C.21) color encoded for the DSA method. The respective slope of the bias is shown in Fig. C.22(b).

These plots provide an idea of the change of the fringe shape as the parameters  $Cu$  and  $Sk$  are varied. Apparently, kurtosis alone, will introduce no mean bias in case of both DSA and GCA. In model eq. 5.2 a variation of the skewness ( $Sk$ ) does not change the fringe shape if the kurtosis  $Cu$  is equal to 0. Moreover, there is a symmetry, such that  $Cu < 0$  and  $Sk > 0$  gives the same result in terms of mean error as  $Cu > 0$  and  $Sk < 0$ . The velocity independent bias (mean error) in case of the DSA method is smaller than for the GCA method. The velocity dependent bias (slope) is symmetric with respect to parameter  $Sk$ , such that lowest and highest velocity dependence is reached for a high absolute value of parameter  $Cu$  (in case of GCA). In case of DSA small values of  $Cu$  only introduce a small velocity dependent bias independent of parameter  $Sk$  (see Fig. C.22(b)). This is



**Figure C.20:** (a) Exemplary ideal cosine and skewed fringe ( $Cu = -0.3, Sk = -2$ ). (b) Systematic bias of determined wind speed in simulation ( $Cu = -0.3, Sk = -2$ ) using GCA, DSA, and CM method.

because the model of the form of eq. 5.2 allows skewness only if  $Cu$  is unequal 0.

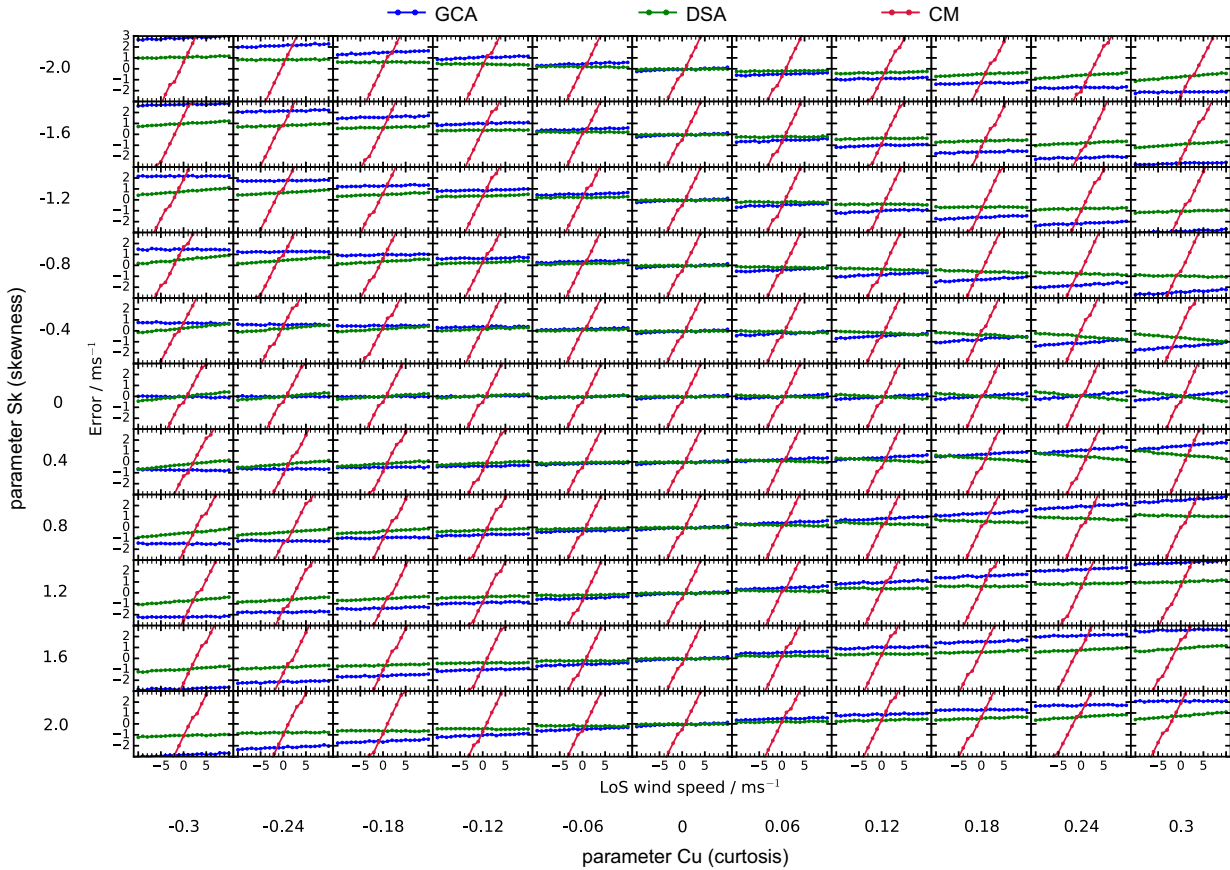


**Figure C.21:** Overview of wind speed dependent biases due to deformed fringe shapes with skewness ( $Sk$ ) and kurtosis ( $Cu$ ) for Gaussian correlation algorithm (GCA), Downhill-Simplex (DSA) fit with fitparameters fixed to  $p_{Sk} = 0$  and  $p_{Cu} = 0$ , and centroid method (CM).

The results of Fig. C.22 may be considered in terms of typical kurtosis and skewness values obtained during the field-test measurements (see Fig. A.11) in appendix A. Typical experimental values of  $Cu$  and  $Sk$  are  $[-0.05, -0.02, 0.4]$  and  $[-1, 0.75, 3]$ . The mean error (in Fig. C.22(a)) for these ranges of  $Cu$  and  $Sk$  is in the order of up to  $\pm 0.3$  m/s (1 m/s



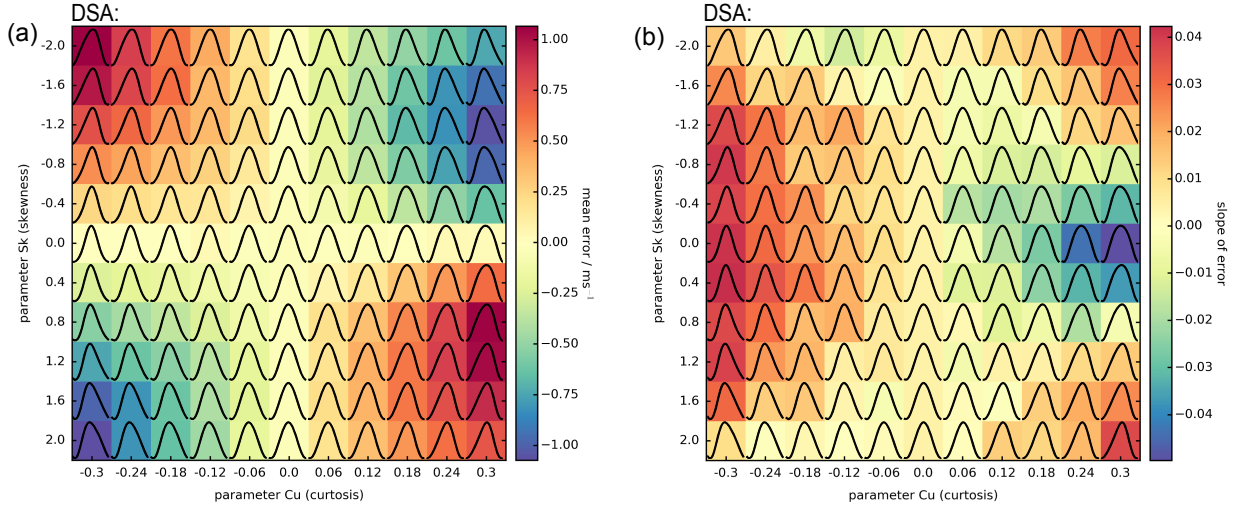


**Figure C.22:** Mean error (a) and slope of the bias (b) due to deformed fringe shapes with skewness ( $Sk$ ) and kurtosis ( $Cu$ ) for GCA. The mean error is a measure of the velocity independent bias. The slope is a measure of the velocity dependent bias.

in case of  $Sk = 2$  and  $Cu = 0.3$ ) and the slope of the error (in Fig. C.22(b)) is up to  $\pm 0.01$ . Above results show, that for a deformed fringe shape, which exhibits skewness and kurtosis, the best choice, in terms of bias reduction, is a Downhill-Simplex fit method with a fit model that allows for a variation of the fit parameters  $p_{Cu}$  and  $p_{Sk}$ .

In this case the bias obtained (independent of the skewness and kurtosis of the actual fringe shape) would be the one shown in Fig. C.21 for  $Cu = 0$  and  $Sk = 0$ .

### Influence of speckle

In this subsection further results of end-to-end simulations involving simulated speckle noise are shown. The results of Fig. C.23 are discussed in section 4.6 and show that for a scaled lidar system with a LoS update rate of 100 Hz, atmospheric speckle noise alone (green symbols) does not increase the measurement uncertainty ( $\sigma(e)$ ) in case of  $R_f = 480$  compared to the case without speckle noise (black circles).

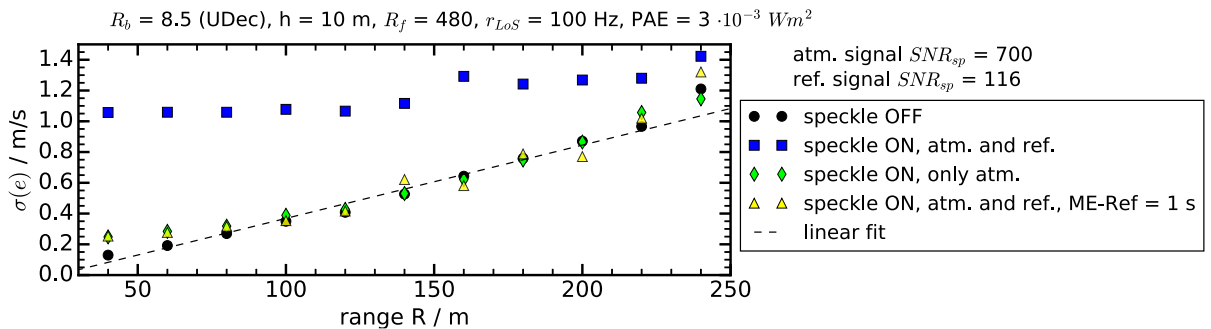


**Figure C.23:** Influence of speckle on  $\sigma(e)$  for a scaled lidar system with an LoS update rate of 100 Hz (WALES/DELICAT transmitter). The simulated speckle noise distributions are created with the model of section 4.1 assuming  $R_f = 480$ ,  $R_b = 8.5$  (upper decile,  $h = 10$  m).

In the case that speckle noise of the laser reference is involved (blue squares in Fig. C.23)  $\sigma(e)$  is visibly increased and the dependence on the range  $R$  is reduced. This effect of the laser reference speckle noise may be mitigated by temporal averaging over 100 laser reference pulses (ME-Ref, yellow triangles in Fig. C.23).



# D Raytracing models and simulations

## D.1 Receiver front-end

This section describes a raytracing model of the front-end part of the AEROLI receiver.

Fig. D.1 shows a 3D view of the receiver front-end modeled in ZEMAX and the corresponding Lens Data Editor.

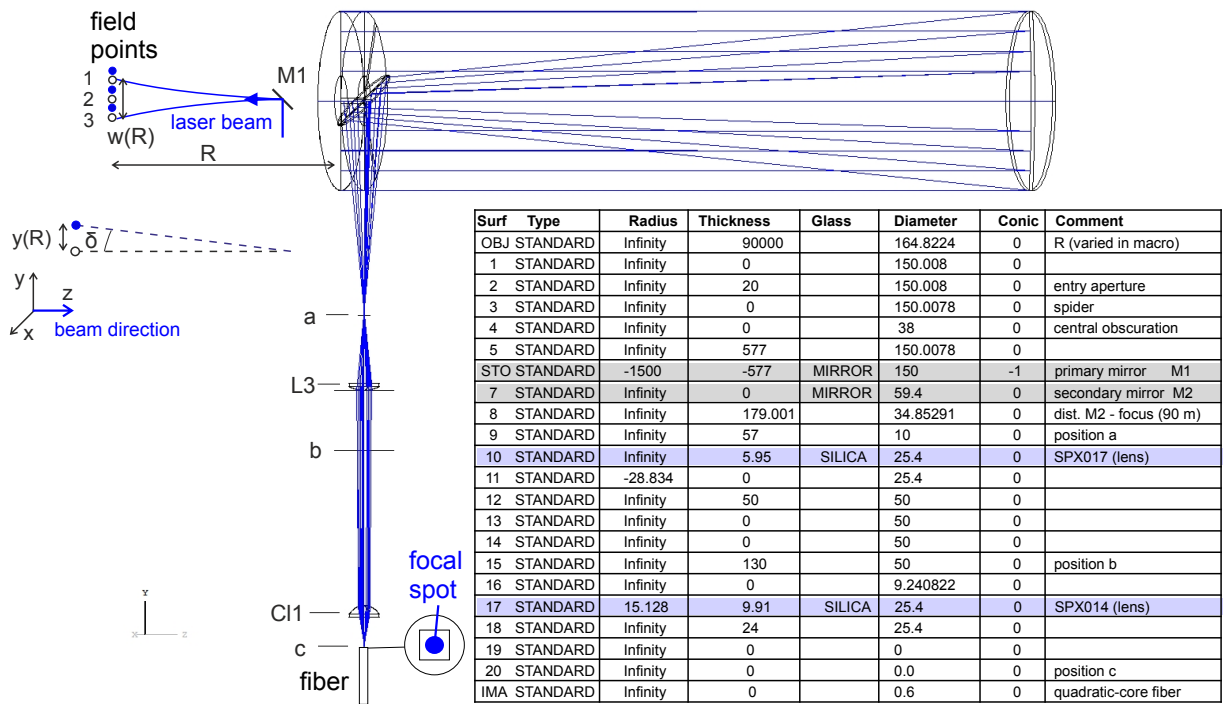


**Figure D.1:** Sequential raytracing model of the receiver front-end. Multiple field points are defined in front of the telescope. Schematically drawn fiber with symbolized focal spot. Right: Lens Data Editor (Lens unit: mm).

Mirror  $M1$  is used to send the laser beam into the atmosphere. If mirror  $M1$  is unstable with respect to rotation around the  $x$ -axis the laser beam can be misaligned by an angle  $\delta$  and the laser spot at distance  $R$  is shifted by a distance  $y(R)$ . Lens  $L3$  is used to quasi-collimate the light received by the Newton telescope. A field diaphragm can be inserted at position  $a$  to limit the FOV of the telescope. In a free-beam setup an interferometer could be installed at position  $b$ . In a fiber-coupled setup the lens  $Cl1$  is used to couple the light into a multimode fiber at position  $c$ .

The overlap function  $O(R) = A_{eff}/A_r$  describes losses of the light collection efficiency due to imperfect coincidence between the telescope's FOV and the laser beam or due to obstacles inside the telescope, where  $A_r$  is the telescope area and  $A_{eff}$  the effective telescope area. The total-overlap distance  $R_{min}$  is reached when  $O(R_{min}) = 1$ . For  $R_{min} = 40$  m, the respective necessary field-of-view (FOV) is obtained from the equations of [Stelmaszczyk et al. \(2005\)](#) for the overlap function without obstruction by the secondary telescope mirror. A FOV (full angle) of 4 mrad is thus required.

Fig. D.2 shows calculated GC form factors with marked range  $R$  of full overlap for a receiver field-of-view (RFOV) of 4 mrad (a) and for 0.8 mrad (b).

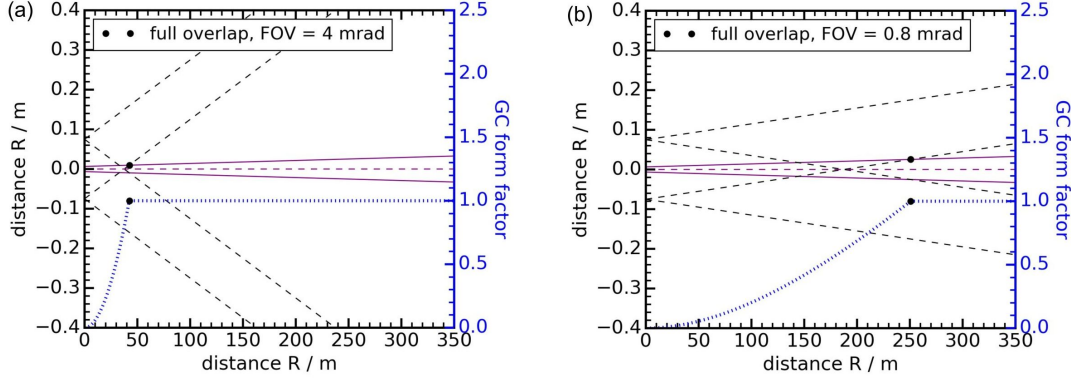


**Figure D.2:** Simple model of the overlap factor using the equations of [Stelmaszczyk et al. \(2005\)](#). A transmitter FOV of 150  $\mu\text{rad}$  is assumed and eq. D.1 is used. The receiver and transmitter field of views are shown as black dotted line and purple line for a RFOV of 4 mrad (a) and 0.8 mrad (b). The calculated GC form factor is marked in blue.

The RFOV is limited by the diameter of the field diaphragm ( $d_s$ ) in the focus of the telescope (position  $a$ ), i.e.,  $\text{RFOV} = d_s/f_t$ , where  $f_t$  is the focal length of the telescope primary mirror for an infinitely distant light source. The light beam direction angular distribution with maximum angle  $\rho$  in front of the primary mirror is magnified due to the angular magnification  $\gamma$  of the telescope.  $\gamma = d_t/d_c = f_t/f_c = \tan(\rho')/\tan(\rho)$ . Where  $f_c$  is the focal length of the collimating (ocular) lens and  $d_c$  is the diameter of the “collimated” beam behind the collimating lens.  $\rho$  and  $\rho'$  are the angles before the primary mirror and after the collimating lens. In our example  $f_t$  is 750 mm,  $f_c$  is 63 mm,  $d_c$  is 11.4 mm and thus  $\gamma$  is 12.

If the fiber would be positioned at the focus of the primary mirror (position  $a$ ), the necessary core diameter would be 3 mm. However, applying the lenses  $L3$  and  $Cl1$  changes the f-number of the beam, and thereby allows to use fibers with a smaller core diameter, which are positioned at position  $c$  (see Fig. D.1).

The angular distribution at the interferometer is a consequence of the shift of the focal spot position of the telescope as a function of range ( $R$ ). Because the distance between the collimating lens and the focal spot is fixed, as is  $f_c$ , ideal collimation is only possible for exactly one value of  $R$ . The collimating lens (CL) is fixed such, for example, that light coming from  $R = 90$  m is collimated, because light shall be collected from close distance. In this case the distance between the secondary mirror and the focal spot is 179 mm. To model this, three point sources (1, 2, 3) are defined at distance  $R$  in front of the telescope, which are located in the middle and at the edges of the laser illumination area with radius  $w(R)$ .

The telescope tubus opening is defined as the entrance pupil. The marginal rays of each point source are traced and the direction cosines are determined at a surface  $b$  behind the collimating lens. All raytracing simulations are carried out with the software ZEMAX. The points  $a$ ,  $b$ , and  $c$  mark the positions of the focus of the telescope, the location of the FIMI (free-beam setup), and the location of the entrance of the scrambling fiber (fiber-coupled setup), respectively.

The telescope and the front-end receiver are modeled to resemble to the optical components used in the AEROLI receiver (see section 3.5.3). A model is used to define the

locations of the point sources. The model assumes a Gaussian beam. The point sources are defined at the edges and middle of the waist at location  $R$ :

$$w(R) = w_0 \sqrt{1 + \frac{R^2}{z_R^2}} = w_0 \sqrt{1 + \left( \frac{R \lambda_L M^2}{\pi w_0^2} \right)^2}, \quad (\text{D.1})$$

whereby  $w_0 = DL/2 = 6.5$  mm is the initial waist (radius) of the laser beam, and  $z_R = \pi w_0 / \lambda_L$  is the Rayleigh length. The DELICAT transmitter laser beam has a divergence, or transmitter FOV (TFOV) of 150  $\mu\text{rad}$  and a beam quality  $M^2 = 4.3$ . Another approximate model is used to account for realistic laser beams, which may be tilted by an angle  $\delta$  with respect to the telescope axis. The location of the central point source is given by  $y_c = y_2 = DTL + \tan(\delta \cdot R)$ , whereby  $DTL$  is the lateral distance between laser and telescope. The point sources  $(y_1, y_3, y_4, y_5)$  on the edge of the beam are calculated by:

$$\begin{aligned} y_1 &= y_c - \frac{\left( \frac{DL}{2} + \tan\left(\frac{TFOV}{2}\right) \cdot \cos(\delta) \cdot R \right)}{\cos(\delta)} \\ y_3 &= y_c + \frac{\left( \frac{DL}{2} + \tan\left(\frac{TFOV}{2}\right) \cdot \cos(\delta) \cdot R \right)}{\cos(\delta)} \\ y_4 &= \frac{DL}{2} + \tan\left(\frac{TFOV}{2}\right) \cdot \cos(\delta) \cdot R \\ y_5 &= -\frac{DL}{2} - \tan\left(\frac{TFOV}{2}\right) \cdot \cos(\delta) \cdot R \end{aligned} \quad (\text{D.2})$$

The receiver FOV (RFOV) is determined by the fiber core diameter. A GC form factor including  $\approx 86\%$  obstruction by the secondary mirror of the telescope is obtained, by tracing the rays from the five point sources  $(y_1, y_2, y_3, y_4, y_5)$  through the setup for different distances  $R$ , evaluating the number of rays traced through surface c, using a macro written in the Zemax Programming Language (ZPL).

Fig. D.3 shows the resultant geometric compression (GC) form factors as function of distance ( $R$ ) for a Gaussian beam (eq. D.1) and for the approximation model (eq. D.2) (a), for different core diameters and shapes (b), and for different positions of lens L3 (c).

The selected solution used in the AEROLI receiver is a 600  $\mu\text{m}$  circular-core fiber, which is used to guide the received light to the 3:1 splitter, and then to the quadratic-core scrambling fiber. The GC form factor determination in the above model does not take into account limitations of the maximum angle of incidence on the fiber, which has a numerical aperture (NA) of 0.22. The marginal ray angles at position c are smaller than  $\pm 12.71^\circ$  only starting from a distance of  $R = 70$  m, what is shown in Fig. D.4(a) and (b). This means that the estimated overlap functions can only be trusted starting from  $R = 70$  m. Fig. D.4(c) shows the ray angles which are obtained after the collimating lens L3 at the initial position of  $d_{a-L3} = 57$  mm, which can amount to  $\pm 1^\circ$  for a distance of  $R = 50$  m. This angular distribution is slightly different to the one shown in Fig. 3.1(b), due to different lenses being used in the model (see Fig. D.1).

One way to mitigate this issue is to shift lens L3 by 3 mm in positive z-direction, which reduces the angles at position c for short ranges  $R$ , as can be seen in Fig. D.5(c), at the cost of overlap at large ranges (see Fig. D.3(c), green line). Another way is to increase the RFOV, using a fiber core diameter of 800  $\mu\text{m}$ .

The same front-end raytracing model can be used to estimate the influence of laser beam

tilt by an angle  $\delta$ . Fig. D.6(a) shows the influence of the laser beam tilt angle  $\delta$  on the shift of position of the focus of the signal light beam at position  $c$ . Fig. D.6(b) shows the according influence on the chief ray angle (for sources 1, 2, and 3 in Fig. D.1).

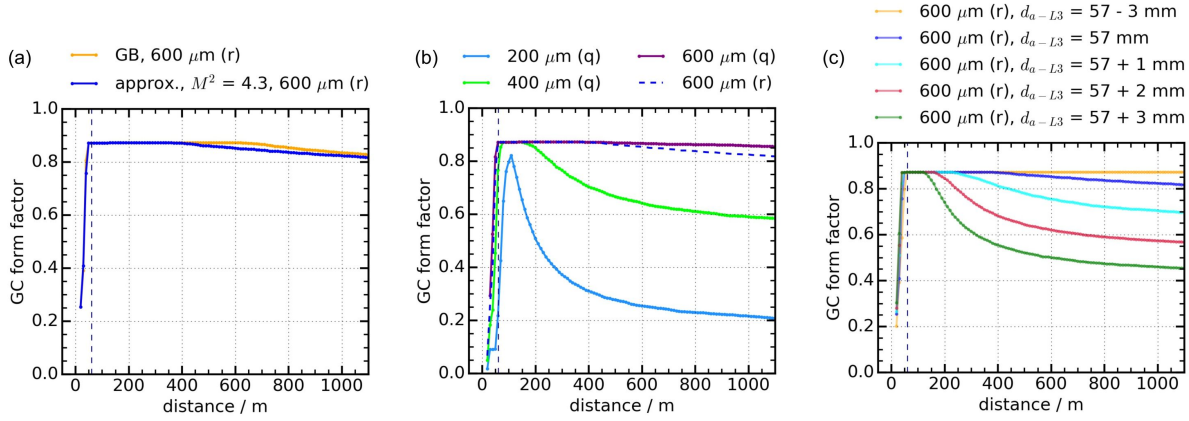


**Figure D.3:** Estimated overlap factor (geometric compression form factor) using the raytracing model shown in Fig. D.1. (a) Comparison between Gaussian and approximate model. (b) GC form factor for different core diameter and shapes (quadratic: q, circular: r). (c) GC form factor for a 600  $\mu\text{m}$  circular-core fiber with different distances  $d_{a-L3}$ .

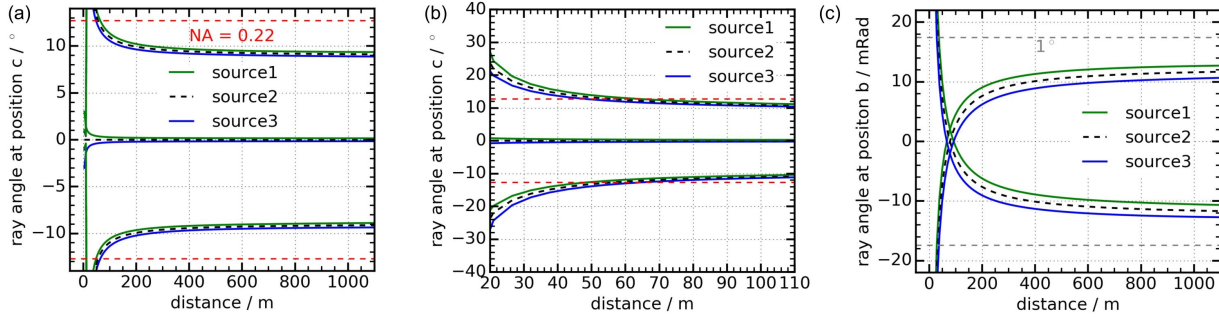


**Figure D.4:** Marginal and chief ray angles as a function of range  $R$  using the raytracing model shown in Fig. D.1. (a) Ray angles at position  $c$ . (b) Zoomed view of ray angles at position  $c$ . (c) Ray angles at position  $b$ .

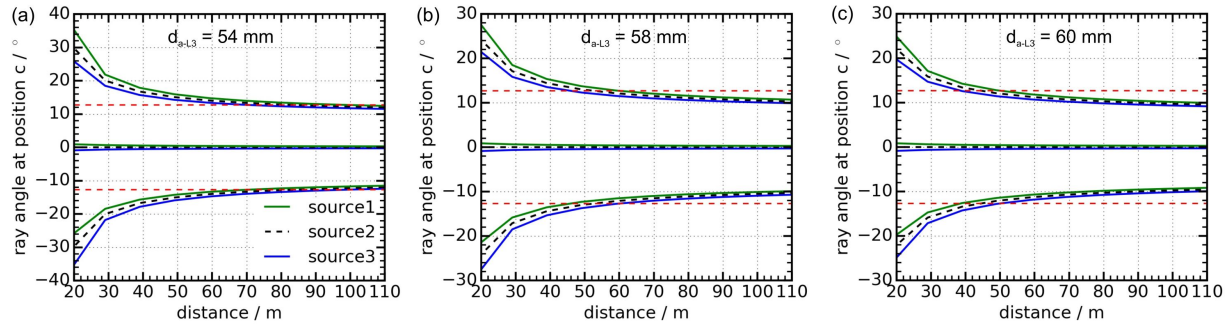


**Figure D.5:** Marginal and chief ray angles as a function of range  $R$  at position  $c$  using the raytracing model shown in Fig. D.1. Different distances  $d_{a-L3}$  between the focal spot position  $a$  for  $R = 90\text{m}$  and lens  $L3$  are evaluated. (a):  $d_{a-L3} = 54\text{ mm}$ . (b):  $d_{a-L3} = 58\text{ mm}$ . (c):  $d_{a-L3} = 60\text{ mm}$ .



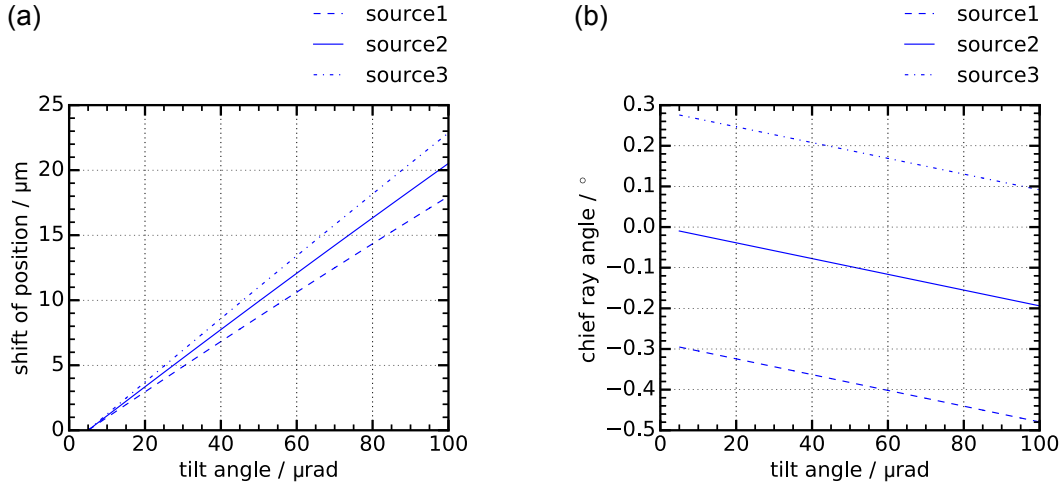


**Figure D.6:** (a) Shift of position of the light rays from sources 1, 2, and 3 as a function of the laser beam tilt angle  $\delta$  as obtained from the front-end receiver raytracing model (see Fig. D.1). (b) Chief ray angles of light rays from these sources as a function of angle  $\delta$ .

The position of the focus and the chief ray angle are proportional to the tilt angle and are dependent on the location of the sources (1, 2, 3 in Fig. D.1). A tilt angle of 50  $\mu\text{rad}$  causes a shift of the focus by 10  $\mu\text{m}$  (see Fig. D.6(a)). The chief ray angles for this tilt angle of 50  $\mu\text{rad}$  are shifted by  $-0.1^\circ$  (see Fig. D.6(b)).

Above results of Fig. D.6 are used in section 4.3 to estimate the systematic bias on the determined wind speed for a fluctuation of the laser beam tilt angle  $\delta$ .

## D.2 Monolithic fringe-imaging Michelson interferometer

Layouts of the sequential and non-sequential raytracing models (in ZEMAX) of the monolithic, field-widened, fringe-imaging Michelson interferometer (FWFIMI) are provided in Fig. D.7(a, b).

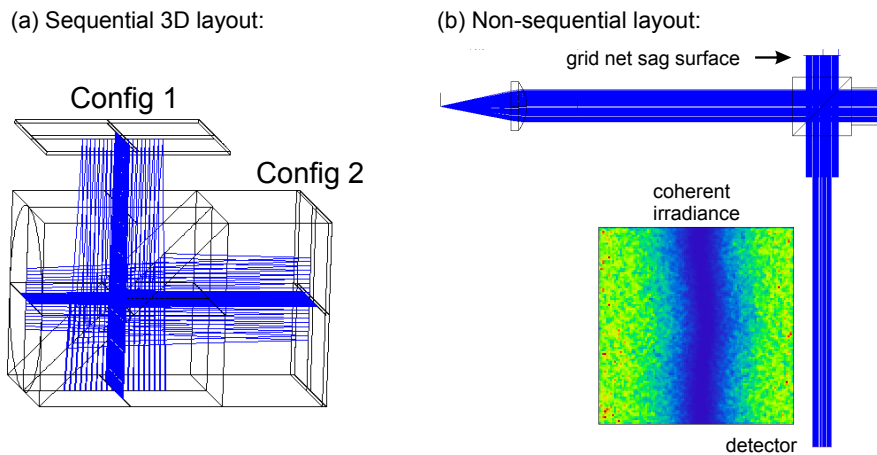


**Figure D.7:** Layouts of sequential (a) and non-sequential (b) raytracing models of the monolithic, field-widened, fringe-imaging Michelson interferometer (FWFIMI).

The “Sequential Lens Data Editor” (sequential model) and the “Non-sequential Component Editor” (non-sequential model) data are shown in Fig. D.8.

Sequential Lens Data Editor (Prescription Data, Config 1):

Surf	Type	Radius	Thickness	Glass	Diameter	Tilt About X	Comment
OBJ	STANDARD	Infinity	[300] varied		0	0	location of source
1	STANDARD	Infinity	0		30	0	
STO	STANDARD	Infinity	15	HOMOSILJ	150	0	surface stop & beamsplitter
3	COORDBRK	-	0		-	45	coordinate break
4	STANDARD	Infinity	0	MIRROR	42.42	0	beamsplitter
5	COORDBRK	-	0		-	45	coordinate break
6	STANDARD	Infinity	-15	HOMOSILJ	30	0	beamsplitter
7	STANDARD	Infinity	-11.076		0	0	length air arm (1)
8	STANDARD	Infinity	0	HOMOSILJ	30	0	
9	STANDARD	Infinity	0		30	0	
10	STANDARD	Infinity	0		30	0	
11	COORDBRK	-	0		-	-1.000E-003	inclination of air arm mirror
12	STANDARD	Infinity	0	MIRROR	30	0	air arm mirror
13	COORDBRK	-	0		-	+1.000E-003	inclination of air arm mirror
14	STANDARD	Infinity	0		30	0	
15	STANDARD	Infinity	11.076		30	0	length air arm (1)
16	STANDARD	Infinity	15	HOMOSILJ	30	0	beamsplitter
17	COORDBRK	-	0		-	-45	coordinate break
18	STANDARD	Infinity	0	HOMOSILJ	42.42	0	beamsplitter
19	COORDBRK	-	0		-	45	coordinate break
20	STANDARD	Infinity	15	HOMOSILJ	30	0	beamsplitter
21	STANDARD	Infinity	[-41.079]		30	0	distance: FWFIMI to detector
IMA	STANDARD	Infinity	-		30	0	detector

Config 2:

Thickness	Glass	Tilt About X	Comment
300		0	ocation of source
0		30	
15	HOMOSILJ	0	surface stop & beamsplitter
0		45	coordinate break
0	HOMOSILJ	0	beamsplitter
0		-45	coordinate break
15	HOMOSILJ	0	beamsplitter
0		0	
16.360	HOMOSILJ	0	length glass arm (2)
0		0	
0		0	
0		0	coordinate break
0	MIRROR	0	glass arm mirror
0		0	coordinate break
-16.360	HOMOSILJ	0	length glass arm (2)
0		0	
-15	HOMOSILJ	0	beamsplitter
0		45	coordinate break
0	MIRROR	0	beamsplitter
0		45	coordinate break
15	HOMOSILJ	0	beamsplitter
-41.079		0	distance: FWFIMI to detector
-		0	detector

Non-sequential component editor:

Object Type	Comment	X Position	Y Position	Z Position	Tilt About X	Tilt About Y	Material	Layout Rays	Analysis Rays	Power	Cone Angle
1 Source Point	Source	0.000	0.000	0.000	0.000	0.000	-	200	1000000	1.0000	12.71
								Radial Aperture	Thickness		
2 Even Asphere Lens	A12-20FPX x2	0.000	0.000	35.9548	0.000	0.000	C79-80	12.5000	8.0000		
								Max. Aperture	Interpolate	Radius	
3 Standard Surface	mirror air arm	0.000	26.075	195.000	90.000	1.0943E-003	MIRROR	9.5000	-	0.0000	
4 Grid Sag Surface	net surface sag	0.000	26.075	195.000	90.000	1.0943E-003	MIRROR	-	1		
								Scale	Is Volume?		
5 Polygon Object	Prism45.POB	0.000	0.000	180.000	0.000	0.000	HOMOSILJ	15.0000	1		
6 Polygon Object	Prism45.POB	0.000	0.000	210.000	180.000	0.000	HOMOSILJ	15.0000	1		
								X1/Y1 Half Width	Z Length		
7 Rectangular Volume	glass arm (2)	0.000	0.000	210.000	0.000	0.000	HOMOSILJ	9.5000	16.363		
								X1/Y1 Half Width	X, Y Pixels		
8 Detector Rectangle	detector	0.000	-173.822	195.000	90.000	0.000	ABSORB	5.0000 I	100, 100		

**Figure D.8:** Sequential and non-sequential raytracing models of the FWFIMI. Top: Sequential Lens Data Editor (Prescription Data). “Config 1” and “Config 2” are defined with the Multi-Configuration Editor (see Fig. D.9(a)). Elements marked by green rectangles may be varied using ZPL macros during the simulations. Bottom: Non-sequential component editor data (exported from ZEMAX). The grid sag surface (see Fig. 3.13(b)) is imported to model the realistic fringe shape.

In case of the sequential model, coordinate breaks are used to define the beamsplitter and the mirror inclination. Fig. D.9(a) shows the multi-configuration editor settings, which are applied to define two configurations: “Config 1” and “Config 2”. These settings are needed to model both arms of the interferometer (see Fig D.7).

The non-sequential model is applied in section 3.4.3 and section 3.5.2 to estimate the influence of wavefront errors on the deformation of the quasi-linear interference fringe. A deviation from planarity being a radial curvature (see Fig. 3.10) is obtained by adjusting the property “Radius” of “surface 3” in Fig. D.8. In another simulation the net sag deviation of the two mirrors from planarity, as obtained by measurements with scanned collimated laser beams carried out by LightMachinery Inc (see Fig. 3.13(b)), is inserted as grid sag surface data, and the coherent irradiance, for collimated light incident on the Michelson interferometer, is evaluated at the location of the detector. For this purpose “surface 4” in the Non-sequential component editor of Fig. D.8 is inserted and “surface 3” (planar mirror) is ignored. The resulting coherent irradiance on the detector is shown in Fig. 3.14 in section 3.5.2.

The sequential raytracing model can be used for interference fringe simulations using plane waves as inspired by *Harlander (2015)*. The sequential model is applied in section 3.4.4 in combination with a Zemax Programming Language (ZPL) macro for a simulation of fringe localization. The model can be used to estimate the instrumental contrast as a function of the incident angular distribution, as well. For these purposes the thicknesses

of “surface 21” and “surface OBJ” (in Fig. D.8) are varied, respectively.

A description of these simulations and of the modeling of interference using plane waves is provided in the following.

### Plane wave calculation of interference fringes

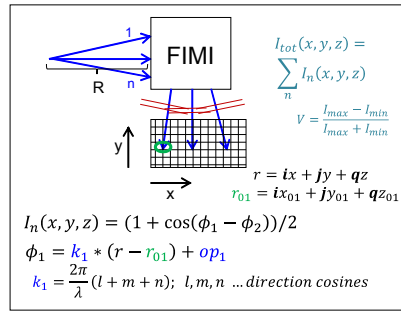
A ZPL macro is used to vary the maximum angular distribution of the rays incident on the Michelson interferometer or to vary the distance of the detector (see section 3.4.4).

Within the macro the calculation is performed at first for configuration 1 and then for configuration 2 (see Fig. D.9(a)).

(a) Mult-Configuration Editor:

Active	: 1/2	Config 1	Config 2
GLSS	4	MIRROR	HOMOSILJ
THIC	6	-15.000	15.000
THIC	7	-11.076	0.000
THIC	8	0.000	16.360
PRAM	5/3	45.000	-45.000
PRAM	17/3	-45.000	45.000
PRAM	13/3	1.000E-003	0.000
PRAM	11/3	-1.000E-003	0.000
GLSS	14		HOMOSILJ
GLSS	18	HOMOSILJ	MIRROR

(b) Interference contrast simulation using plane waves:



(c) Variation of the angular distribution:

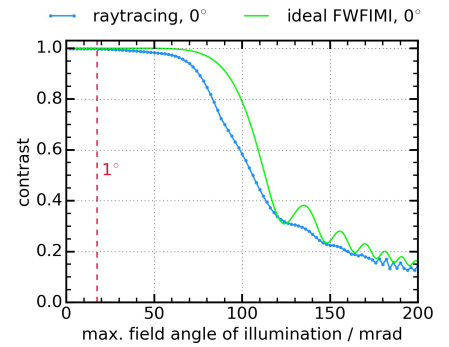


**Figure D.9:** (a) Multi-Configuration Editor for a sequential raytracing model of the monolithic, fringe-imaging Michelson interferometer (FWFIMI). (b) Scheme of the procedure for simulating a linear fringe for varying angular distributions. (c) Results obtained from the model with a mean angel of incidence of  $0^\circ$  using a ZPL macro to vary the distribution and to calculate the Michelson contrast (blue dotted). The results are compared to the analytical model results for an ideal FWFIMI (see Fig. C.15, ideal FWFIMI,  $0^\circ$ ) (green).

For every angular distribution an array of rays is traced and the traversed optical path length ( $OPD_1$ ) is determined. The phase  $\phi_1$  of a plane wave from arm 1 (configuration 1) is evaluated at the position  $x, y, z$  of a detection grid for every ray:

$$\phi_1 = \vec{k}_1 \cdot (\vec{r} - \vec{r}_{01}) = k_{x1}(x - x_{01}) + k_{y1}(y - y_{01}) + k_{z1}(z - z_{01}) + OPD_1. \quad (D.3)$$

whereby  $\vec{k}_1 = \mathbf{i}k_{x1} + \mathbf{j}k_{y1} + \mathbf{q}k_{z1}$  is the wave vector of the exit ray hitting the detector from arm 1, with  $k_{x1} = (2\pi/\lambda_L)l$ ,  $k_{y1} = (2\pi/\lambda_L)m$ , and  $k_{z1} = (2\pi/\lambda_L)n$ .  $l, m, n$  are the direction cosines of a ray returned from ZEMAX.  $\vec{r}_{01} = \mathbf{i}x_{01} + \mathbf{j}y_{01} + \mathbf{q}z_{01}$  is the vector to the  $x, y, z$  positions of the exit ray from arm 1 and  $\vec{r} = \mathbf{i}x + \mathbf{j}y + \mathbf{q}z$  is the vector giving the coordinates at the detector.  $OPD_2$ ,  $\phi_2$ ,  $\vec{k}_2$ , and  $\vec{r}_{02}$  are similarly defined for arm 2 (configuration 2). In the next step, the interference pattern at the detection grid locations  $(x, y, z)$  is determined for every ray:

$$I(x, y, z) = (1 + \cos(\phi_1 - \phi_2)) / 2. \quad (D.4)$$

The interference patterns  $I_n(x, y, z)$  of the  $n$  different rays are then superimposed incoherently in the plane of the detection grid defined by  $(x, y, z)$  to yield the total interference pattern  $I_{tot}(x, y, z)$  for a certain angular distribution. The detection grid is positioned in the plane of localization by defining a negative distance ( $z < 0$ ) for the last surface in the lens editor. The Michelson contrast  $V = (I_{max} - I_{min}) / (I_{max} + I_{min})$  is determined for every

angular distribution. The resultant contrast curve as a function of the varied maximum angular distribution of the rays is shown in Fig. D.9(c) for  $n = 10$  rays in x-direction, i.e., along the direction of optical path length variation caused by the inclination of the mirrors of the interferometer. Here optimum design values of the field-widening compensation of section 3.4.1 are used. The resultant instrumental contrast curve for a mean incident angle of  $0^\circ$  is compared to the result of the analytical model of section C.6 (see also Fig. C.15).

It can be seen that there are some deviations between the above raytracing model results and the results obtained with the analytical model of section C.6. However, there is good accordance in the important angular distribution range ( $\rho_{\max} \approx 1^\circ$ ).

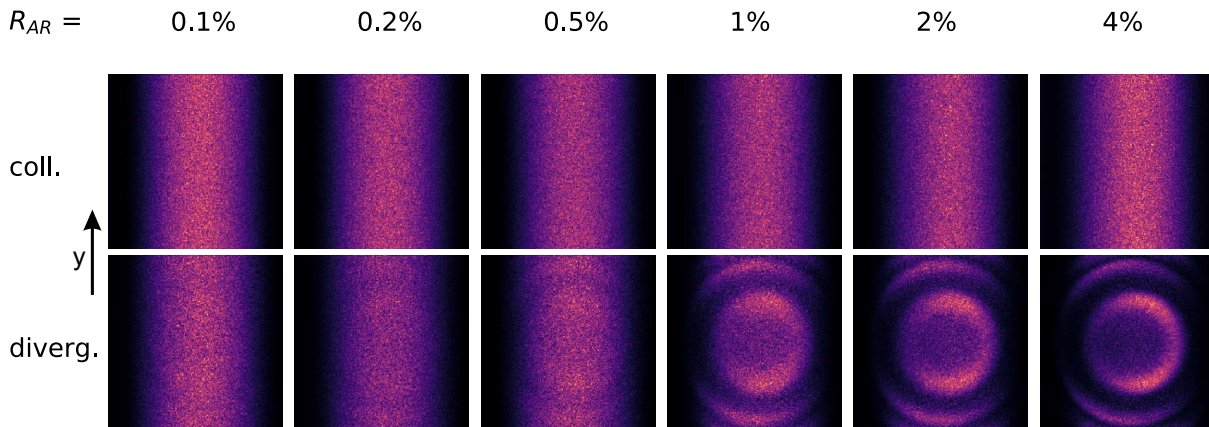
### Multiple reflections with AR-coatings on the beamsplitter surfaces

The non-sequential raytracing model (shown in Fig. D.7(b) and in Fig. D.8 bottom) is applied here to estimate the influence of multiple reflections on the instrumental contrast as described in section 3.4.3.

The coating reflectivity  $R_{AR}$  of objects 5 and 6 (see Fig. D.8, i.e., surfaces A, B, C, D of the FWFIMI in Fig. 3.6) is varied and non-sequential coherent raytracing is performed. The detector is defined with  $300 \times 300$  pixels and a diameter of 5 mm. The arm lengths, refractive indices and mirror inclination angle of the FWFIMI are set to the specified values (see appendix E). The relative intensity setting is adjusted to  $1 \cdot 10^{-7}$  to allow for multiple reflections, and  $4 \cdot 10^6$  rays are traced for each  $R_{AR}$  setting. The fringe shape and contrast depend on the illumination conditions. Therefore, simulations are run with a collimated beam of diameter larger than 5 mm from a point source, and with divergent light from the same point source by shifting the lens by 2 mm - towards the source.

The simulated interference patterns recorded on the detector for these two different illumination conditions and for varying values of  $R_{AR}$  are shown in Fig. D.10.

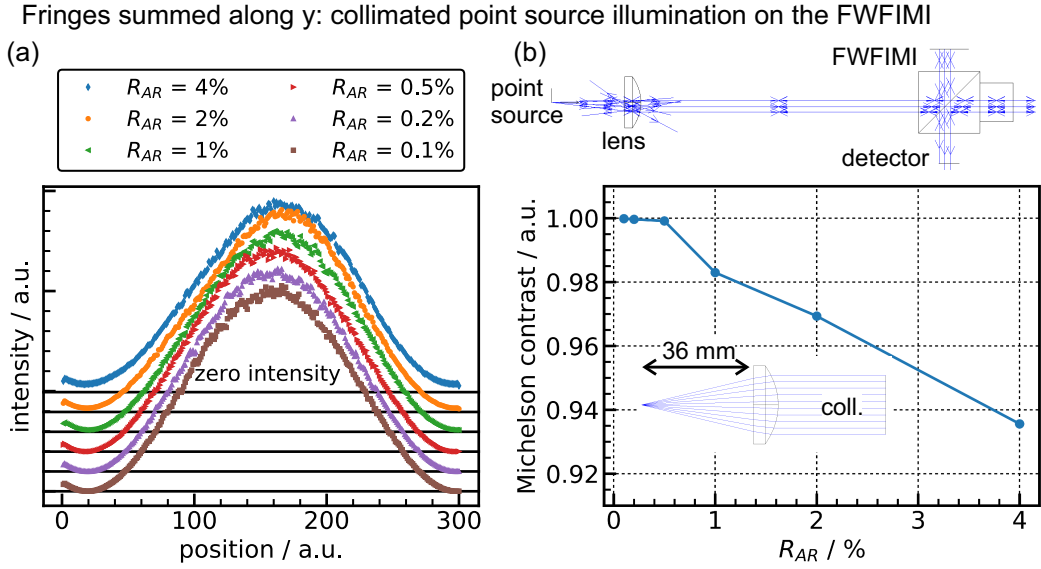
**Non-sequential raytracing with varying  $R_{AR}$  of the beamsplitter of the FWFIMI (obtained fringe patterns)**



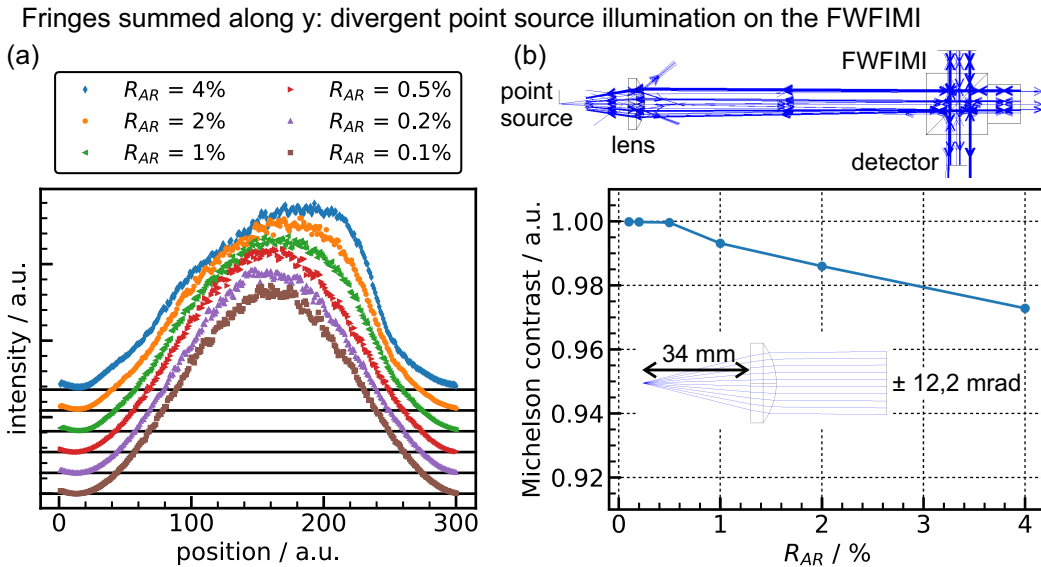
**Figure D.10:** (a) Fringe patterns obtained by non-sequential raytracing with illuminations from a collimated point source and a divergent point source on the FWFIMI for different reflectivities  $R_{AR}$  of the surfaces of the beamsplitter.

Fig. D.11 provides fringe profiles (summation along  $y$ ) and Michelson contrasts of the patterns shown in Fig. D.10 for a collimated point source. Respective profiles and Michelson contrasts for divergent light (maximum angles:  $\pm 12.2$  mrad) are shown in Fig. D.12.

As discussed in section 3.4.3 the Michelson contrast decreases as  $R_{AR}$  increases. More severe are the changes of the integrated fringe shapes in both cases for high values of  $R_{AR}$ .



**Figure D.11:** (a) Fringes shapes obtained by non-sequential raytracing with illumination from a collimated point source on the FWFIMI for different reflectivities  $R_{AR}$  of the surfaces of the beamsplitter. These fringe shapes are obtained by summation along the y-direction in the fringe patterns of Fig. D.10. The profiles are shifted with respect to each other as indicated by the black horizontal lines, which mark the respective levels of zero intensity. (b) Michelson contrasts of the fringe profiles in (a).



**Figure D.12:** (a) Fringes shapes obtained by non-sequential raytracing with illumination from a divergent point source on the FWFIMI for different reflectivities  $R_{AR}$  of the surfaces of the beamsplitter. A divergent light source is obtained by shifting the collimating lens 2 mm towards the point source. (b) Michelson contrasts of the fringe profiles in (a).

The next section is dedicated to raytracing simulations of the integration of the FWFIMI into the receiver back-end.



## D.3 Receiver back-end

### Normal incidence configuration

This section provides background on the sequential raytracing model of the back-end part of the receiver shown in Fig. 3.22 (section 3.5.3).

Fig. D.13 shows a detailed scheme of a sequential raytracing model of the back-end part of the AEROLI receiver for the case of the near-field of a quadratic-core multimode fiber ( $d = 600 \mu\text{m}$ ,  $\text{NA} = 0.22$ , no focal ratio degradation) being imaged on the FWFIMI and on a linear detector array under normal mean incidence angle. Fig. D.13 contains a view of the lens data editor and of the field data settings, which are necessary to model the illumination with the near-field of a fiber.

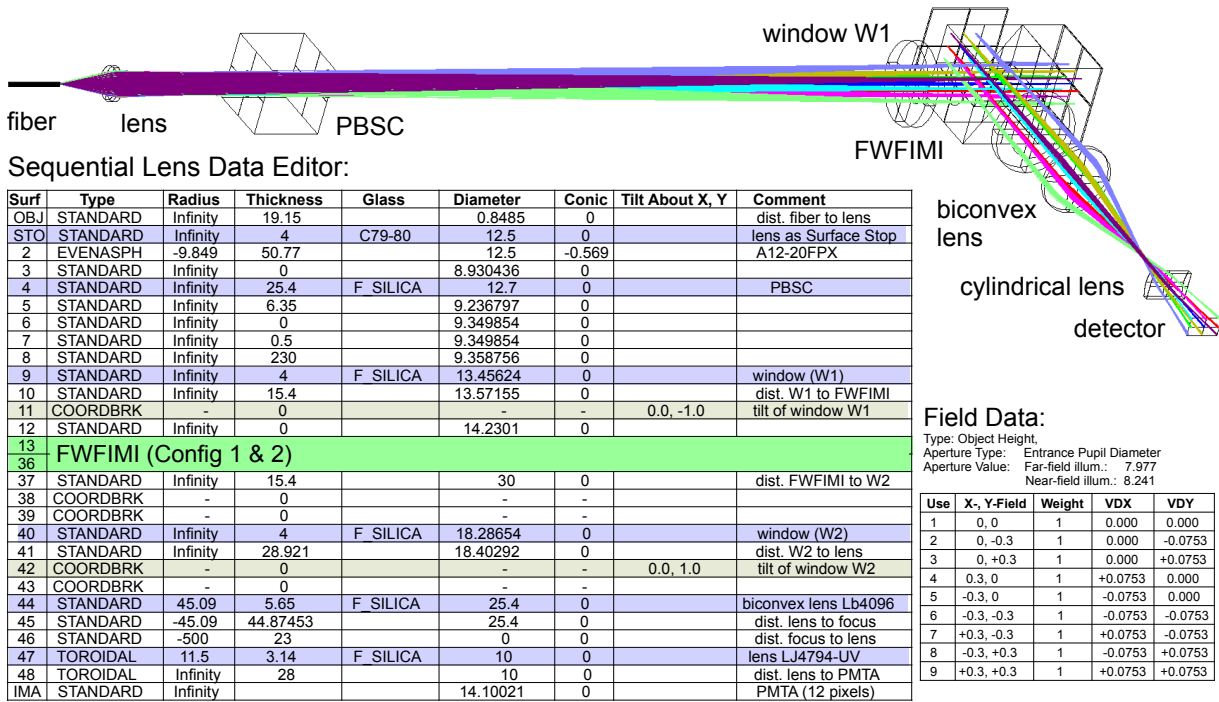


**Figure D.13:** Sequential raytracing model of the back-end part of the AEROLI receiver in case of illumination with the near-field of a 600- $\mu\text{m}$ -quadratic-core multimode fiber with a numerical aperture of 0.22 (see field data), neglecting focal ratio degradation at normal mean angle of incidence. Top: Layout, Left: Sequential Lens Data Editor (simplified: the FWFIMI sequential raytracing model is omitted here (green), see Fig. D.8), Right: Field data.

Surfaces 13 to 36 in Fig. D.13 (green) contain the lens data of the FWFIMI shown in Fig. D.8, which is omitted here for the sake of brevity.

Nine point sources in the center, in the corners, and on the edges of the quadratic-core of the fiber are defined (see Fig. D.13, right). The surface stop is set to the position of the collimating lens. The aperture entrance pupil diameter is adjusted to 8.241 mm in order to obtain maximum angles of the light cones of  $12.71^\circ$  ( $\text{NA}: 0.22$ ). The values of VDX, VDY are optimized (to 0.0753 mm, using a ZPL macro) such that the rays of the eight point sources are parallel to the rays of the central point source.

A far-field illumination configuration (shown in Fig. 3.22) can be obtained by shifting fiber, lens, and PBSC closer to the FWFIMI. The PBSC is substituted by a block of glass for convenience. The distance between fiber and lens would be reduced from 19 mm to 18 mm in order to obtain quasi-collimation for imaging the far-field onto the FWFIMI. In



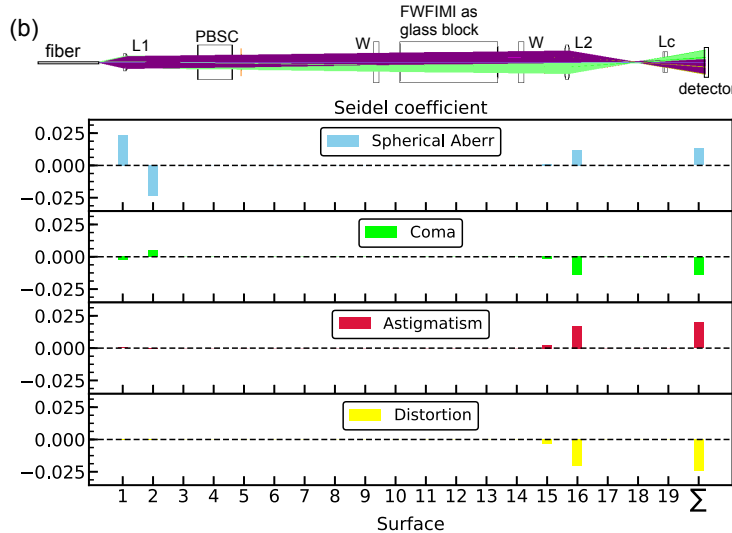
this case the aperture entrance pupil diameter should be slightly adjusted to 7.977 mm in order to obtain again a numerical aperture of the light source (fiber) of 0.22. All optics before the PBSC are shifted to a distance of 97 mm (instead of 230 mm, “Surf 8” in Fig. D.13) before the interferometer container. The maximum marginal angle ( $\rho_{max}$ ) in this case is approximately 21 mrad (compare with eq. C.35).

### Aberrations of the back-end receiver

For a study of the aberrations of the above receiver, the FWFIMI model is replaced by a block of glass. The modified raytracing setup is shown in Fig. D.14(a). The cylindrical lens “LJ4794-UV” (Lc) in Fig. D.14(b) is omitted. The Seidel coefficients obtained in this case are shown in Fig. D.14(b).

(a) Sequential Lens Data editor

Surf	Type	Radius	Thickness	Glass	Diameter	Conic	Comment
OBJ	STANDARD	Infinity	17.97742		0.8485281	0	dist. fiber to lens
STO	STANDARD	Infinity	4	C79-80	12.5	0	surface stop, lens
2	EVENASPH	-9.849	50.77		12.5	-0.569	A12-20FPX
3	STANDARD	Infinity	0		10.22334	0	
4	STANDARD	Infinity	25.4	F SILICA	12.7	0	PBSC
5	STANDARD	Infinity	6.35		10.94299	0	
6	STANDARD	Infinity	0		11.20858	0	
7	STANDARD	Infinity	0.5		11.20858	0	14x7 aperture
8	STANDARD	Infinity	97.2		11.2295	0	
9	STANDARD	Infinity	4	F SILICA	15.30014	0	window W1
10	STANDARD	Infinity	15.4		15.48052	0	
11	STANDARD	Infinity	72	F SILICA	16.51941	0	FWFIMI as block
12	STANDARD	Infinity	15.4		21.15616	0	
13	STANDARD	Infinity	4	F SILICA	22.64526	0	window W2
14	STANDARD	Infinity	28.921		22.83388	0	
15	STANDARD	45.09	5.65	F SILICA	25.4	0	lens LB4096
16	STANDARD	-45.09	44.87453		25.4	0	
17	STANDARD	-500	23		0	0	
18	TOROIDAL	11.5	3.14	F SILICA	10	0	LJ4794-UV (omitted)
19	TOROIDAL	Infinity	28		10	0	
IMA	STANDARD	Infinity	-		20	0	PMTA (12 pixels)



(c) Grid distortion (near-field)

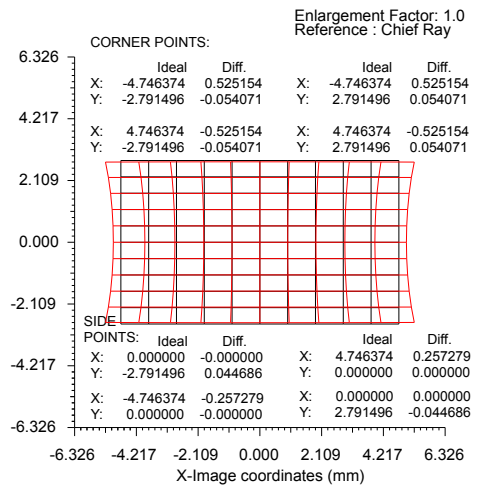


**Figure D.14:** (a) Modification of the sequential raytracing model for the aberration study (far-field configuration). (b) Layout of the raytracing model and Seidel diagram with Seidel coefficients in mm. The cylindrical lens (Lc) is omitted in the analysis due to rotational asymmetry. (c) Grid distortion in case of near-field illumination (see Fig. D.13).

Spherical aberration of the rays at the aspheric lens L1 and at the biconvex lens L2 is caused by the numerical aperture of 0.22 of the fiber. Further occurring aberrations are coma, astigmatism, and distortion, related to the extended source represented by the core

of the multimode fiber (point sources 2 to 9). The grid distortion of the near-field configuration (see Fig. D.13) is shown in Fig. D.14(c). The distortion  $D_x = x(\text{Diff})/x(\text{Ideal}) \cdot 100$  in x-direction depends on the location of the field points (e.g., on the sides or corners of the grid). The linear fringe at the localization plane is thus deformed due to distortion by lenses L2 and Lc.

Aberrations are uncritical if they solely modify the near-field illumination function, i.e., the image of the core of the multimode fiber. In this case the illumination function correction routine described in section 3.5.6 is sufficient to obtain a quasi-cosine fringe shape.

### Tilted configuration with two detectors

This subsection provides a sequential raytracing model of the back-end part of the AEROLI receiver for the (far-field) illumination of the FWFIMI with a tilted mean incident angle of  $2^\circ$ , which allows to detect the back-reflected light and the according linear fringe.

As was described in section 3.4.1, the FWFIMI is field-widening compensated for a mean incident angle of  $2.5^\circ$ , as well, what makes such a setup realizable. An additional quadratic aperture is inserted behind the PBSC, and additional mirrors and lenses could be used to image the second interference fringe on the same 32 channel PMTA or on another physically separated array.

The raytracing layout of a possible tilted configuration in the sequential mode of ZEMAX is shown in Fig. D.15.

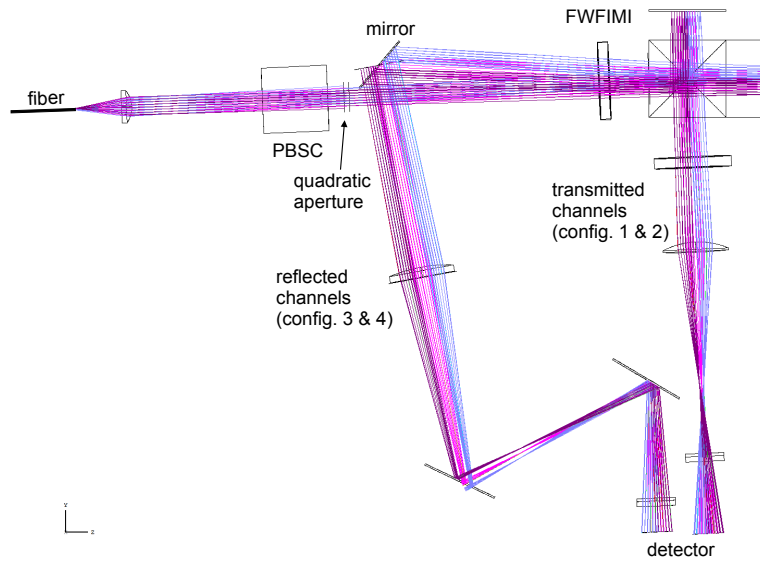


**Figure D.15:** Sequential raytracing model of the back-end part of the AEROLI receiver for a mean tilt angle of  $2.5^\circ$ . The backreflected ray path is modeled with two additional configurations in the multi-configuration editor. Far-field of the fiber illuminates the FWFIMI.

The layout consists of four different configurations, i.e., transmission and reflection for the air arm and the glass arm, respectively. The four different configurations are defined with the Multi-Configuration Editor of ZEMAX. The Multi-Configuration Editor and Lens Data Editor settings are not shown here for the sake of brevity.

## D.4 Design of a two-lens optical scrambler

This section provides a raytracing model of a proposed two-lens optical scrambler for the exchange of the near- and far-fields of two fibers to be used in the AEROLI receiver. This principle was first thought of by [Hunter and Ramsey \(1992\)](#). It is used for example by [Halverson et al. \(2015\)](#) or [Bruneau et al. \(2015\)](#) to increase the near-field and far-field scrambling of their fibers for the purposes of exoplanet detection and for wind speed measurements, respectively. These free-beam optical scramblers can also work with one single lens of very short focal length (e.g., ball lenses fixed between both fibers), e.g., [Avila \(2012\)](#). Many prototypes on double-scramblers exist, for example the one by [Avila and Singh \(2008\)](#); [Barnes and MacQueen \(2010\)](#), which more or less also minimize losses due to focal-ratio degradation (FRD).

FRD describes a degradation of the incident f-ratio along the fiber to faster output f-numbers (more spread out in angle), with the main cause being microscopic fiber bends, high stresses at the fiber termination, and polishing errors ([Bispo dos Santos et al., 2014](#)).

Fig. D.16 shows the layout of the designed two-lens scrambler and the corresponding lens data editor (Zemax). The optimal distances were obtained by using a ZPL macro. The design does not take into account the focal ratio degradation of the 600- $\mu\text{m}$ -core multimode fibers, because their FRD and its dependence on the coupling f-number ( $f/\# > 2.2$ ) have not been measured systematically in this work.

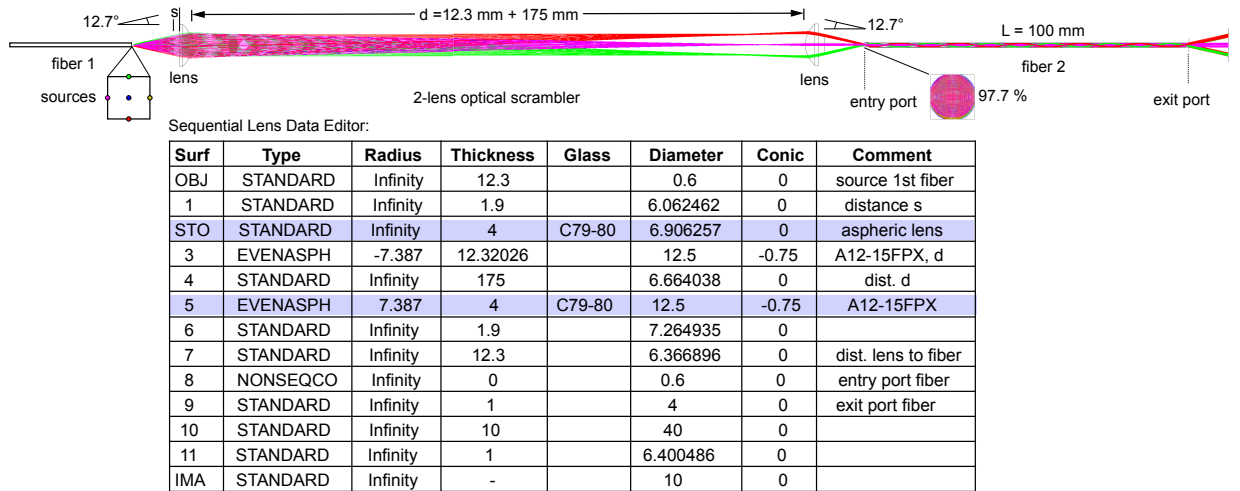


**Figure D.16:** Raytracing model of a two-lens (double) scrambler designed for UV wavelengths and with minimal losses due to vignetting. Exchange of the near- and far-field of two fibers.

Five point sources are defined at the location of the core of the first fiber. Field angles are set such, that the opening cone angle is  $12.71^\circ$  equivalent to a numerical aperture of 0.22, neglecting focal ratio degradation. Within the macro the distances  $s$  and  $d$  are varied sequentially in loops in order to obtain the optimal distances of the lenses with minimum losses ( $\approx 97\%$ ) due to vignetting and with parallel angles of inclination of the individual sources at the second fiber. The determined optimum values are shown in Fig. D.16, assuming fibers with a numerical aperture of 0.22. “Fiber 2” is modeled with a Non-Sequential Component (see entry port and exit port). The lenses A12-15FPX (Asphericon, Germany) are anti-reflection coated for ultraviolet wavelength of 355 nm ( $R < 0.2\%$ ). Nevertheless, there are additional losses due to Fresnel reflection losses at the uncoated fiber surfaces (4–8%). [Halverson et al. \(2015\)](#) summarized the efficiencies of multiple

fiber double-scrambler systems, whereby the efficiency of recently designed systems varies between 70% and 87%.

The here designed two-lens optical scrambler is constructed using a commercial cage system and its optical scrambling gains are measured in [appendix H](#).

# E Specifications and test sheets of the Michelson interferometer

Specifications of a monolithic, field-widened and temperature-compensated Michelson interferometer for fringe-imaging

## A/B - Cubic beam splitter:

Pos.	Requirement	Value	Comment/tolerance
Material:			
1.	Substrate	Synthetic silica glass	Heraeus Homosil 101 (see annex for details)
Form:			
2	Composed of right-angle Triangular prisms		See drawing DLR-IPA.LI-LBO-DDD.01.01
2.1	Edge lengths ( $d_3$ ) distance A1 to B3 and A3 to B1, respectively	30 mm (optical path length difference $d_{3x}, d_{3y}, d_{3z} < 10 \mu\text{m}$ )	( $\pm 100 \mu\text{m}$ ), at 22 °C center thickness
2.2	Wedge angle Between B1 and A2: Between A2 and A1: Between A3 and B2: Between B2 and B3: In y-direction	45° 45° 45° 45° 0°	( $\pm 50 \mu\text{Rad}$ ) ( $\pm 25 \mu\text{Rad}$ ) * <sup>1</sup> ( $\pm 25 \mu\text{Rad}$ ) * <sup>1</sup> ( $\pm 25 \mu\text{Rad}$ ) * <sup>1</sup> See 3.5 Parallelism
Surfaces / Coatings:			
3.1.	Coating- AR-coating  Beamsplitter-Coating	Surfaces: A1, A3, B1 R(354-356 nm, 532 nm, AOI: -3 to 3°) < 0.1 % (ISO 9211-2) Surfaces: A2, B2 R(355 nm, 532 nm) = 50% $\pm$ 2% for s-polarized light at 45° $\pm$ 2°	(T = 99.9 %) Angle of incidence (AOI) relative to optical axis in air, (beamsplitter prisms A and B are optically contacted), dual coating
3.2	Coating-Damage threshold	CW: 35 W/cm <sup>2</sup>	
3.3	Contour accuracy per surface / surface irregularity (flatness)	Surfaces: A1, A3, B1, B3 3/ 0.1 (0.1/-) $\bar{h} = 633 \text{ nm}$ (ISO 10110)	< $\bar{h}/20$ (19 mm clear aperture) * <sup>2</sup>
3.4	Wavefront deformation	3/- RMSi < 5 nm (ISO 10110)	< $\bar{h}/20$ P-V surface
3.5	Parallelism / Wedge		

**Vermerk/Mitteilung**

	x-direction:	Surfaces: A2 to A3, B2 to B3 4/ 0.086' (ISO 10110)	( $\pm 25 \mu\text{Rad}$ with respect to wedge angle) * <sup>1</sup>
	y-direction:	Surfaces: A2 to A3, B2 to B3 4/ 0.086' (ISO 10110)	( $\pm 25 \mu\text{Rad}$ with respect to wedge angle) * <sup>1</sup>
3.6	Surface error	Surfaces: A1, A3, B1, B3 5/1 x 0.01 C 1x0.005 L 1x0.001 E 0.5 (ISO 10110)	Scratch-Dig 5/1 (MIL-O-13830A) Coating Scratches Edge chips

**D - Glass arm:**

Pos.	Requirement	Value	Comment/tolerance
Material:			
1.	Substrate	Synthetic silica glass	Heraeus Homosil 101 (see annex for details)
Form:			
2.1	Edge length ( $d_i$ ) distance D1 to D2	16.360 mm	( $\pm 10 \mu\text{m}$ ), at 22 °C center thickness
2.2	Wedge angle Between D1 and D2 (in x- and y-direction)	0° (can be adjusted for fine-tuning of the net wedge angle and net surface deformation) * <sup>2</sup>	( $\pm 25 \mu\text{Rad}$ ) * <sup>1</sup> See 3.5 Parallelism
Surfaces / Coatings:			
3.1	Coating- HR-mirror coating AR coating	Surface: D2 $R > 99.8\%$ at 354.84 nm, 532 nm Surface D1 not coated	
3.2	Coating- Damage threshold	CW: 35 W/cm <sup>2</sup>	
3.4	Contour accuracy per surface	Surfaces: D1, D2 3/ 0.1(0.1/-) $\bar{h} = 633 \text{ nm}$ (ISO 10110)	$< \bar{h}/20$ (19 mm clear aperture) * <sup>2</sup> D1 is optically contacted to B3
3.5	Wavefront deformation	3/- RMSi $< 5 \text{ nm}$	$< \bar{h}/20$ P-V surface
3.6	Parallelism / Wedge x-direction  y-direction:	Surfaces: D1 to D2 4/ 0.086' (ISO 10110) Surfaces: A2 to A3, B2 to B3 4/ 0.086' (ISO 10110)	( $\pm 25 \mu\text{Rad}$ wedge angle) * <sup>1</sup> ( $\pm 25 \mu\text{Rad}$ with respect to wedge angle) * <sup>1</sup>
3.7	Surface errors	Surfaces: D1, D2 5/1 x 0.01 C 1x0.005 L 1x0.001 E 0.5 (ISO 10110)	Scratch-Dig 5/1 (MIL-O-13830A) Coating Scratches Edge chips



## Vermerk/Mitteilung

**C - Air arm mirror plate:**

Pos.	Requirement	Value	Comment/tolerance
Material:			
1.	Substrate	Synthetic silica glass	Heraeus Homosil 101 (see annex for details)
Form:			
2.1	Thickness	to be specified by manufacturer	No requirement center thickness
2.2	Wedge angle	0°	See 3.5 Parallelism
2.3	Clear aperture (surface C1):	19 mm	(± 0.5 mm)
Surfaces / Coatings:			
3.1	Coating- HR – mirror coating	Surface: C1 R > 99.8% at 354.84 nm, 532 nm	
3.2	Coating- Damage threshold	CW: 35 W/cm <sup>2</sup>	
3.4	Contour accuracy per surface	Surface: C1 3/ 0.1(0.1/-) $\bar{h} = 633$ nm (ISO 10110)	< $\bar{h}/20$ (19 mm clear aperture) * <sup>2</sup>
3.5	Wavefront deformation	3/- RMSi < 5 nm	< $\bar{h}/20$ P-V surface
3.6	Parallelism / Wedge	To be specified by manufacturer	No requirement center thickness
3.7	Surface errors	Surface: C1 5/1 x 0.01 C 1x0.005 L 1x0.001 E 0.5 (ISO 10110)	Scratch-Dig 5/1 (MIL-O-13830A) Coating Scratches Edge chips

**E - Spacers :**

Pos.	Requirement	Value	Comment/tolerance
Material:			
1.1	Substrate	Calcium fluoride (CaF <sub>2</sub> ), Synthetic silica glass (Composite CTE of 15.5·10 <sup>-6</sup> 1/K) * <sup>3</sup>	Corning, Inc. or Helma (see annex for details) (± 5·10 <sup>-7</sup> 1/K)
1.2	Glue:	UV hardened epoxy (CTE < 300·10 <sup>-6</sup> 1/K)	Norland 61, Norland Products Inc. or similar
1.3	Glue layers thickness	Each layer ≤ 40 μm	Typical: 20 μm
Form:			
2.1	Edge Length (d <sub>2</sub> ) Between A3 and C1	11.076 mm	(± 10 μm), at 22 °C Center thickness optimized for 2° tilt
2.2	Wedge angle Between A3 and C1 (around y-axis)	17.8 μRad * <sup>1</sup> = net wedge angle of the device * <sup>1</sup> To be determined by the	(± 1 μRad) * <sup>1</sup>

**Vermerk/Mitteilung**

		manufacturer	
2.3	Spacer struts cross-section & dimensions	To be determined by the manufacturer	Rectangular cross section
2.4	Spacing	To be determined by the manufacturer	Spacing between the struts
2.5	Clear aperture	19 mm	

**Net values for wedge angle and surface figure:**

\*<sup>1</sup> A net value of the wedge angle (between C1 and D2) of  $90^\circ + 17.8 \mu\text{Rad}$  with  $\pm 1 \mu\text{Rad}$  tolerance is required. This may either be achieved by conforming to individual specifications A/B – 3.6, D – 3.6 and E – 2.2; Or by compensating on surface D2.

The tolerance for the net parallelism perpendicular to the wedge angle (between C1 and D2, y-direction in sketch) is  $0^\circ \pm 1 \mu\text{Rad}$ .

\*<sup>2</sup> A net contour accuracy for the four surface combinations (paths r\*r, t\*t, r\*t, t\*r) of  $\lambda/20$  at 633 nm over 19 mm clear aperture is required. This may either be achieved by conforming to individual specifications A/B – 3.4, D – 3.4 and C – 3.4; Or by compensating on surface D2. The net contour accuracy of  $\lambda/20$  means, that the bending and distortion (h) of the interference fringe, divided by the fringe width (s) of the observed fringe pattern of the interferometer at 633 nm, is equal to or smaller than 1/20. The linear interference fringe is to be oriented in the y-z plane in parallel to the y-axis (see drawing), by adjusting the net wedge angle around the x- and y-axis.

\*<sup>3</sup> A reduced coefficient of linear thermal expansion (CTE) of  $15.5 \cdot 10^{-6} \text{ 1/K} \pm 5 \cdot 10^{-7} \text{ 1/K}$  is achieved by composite spacers (CaF<sub>2</sub> and synthetic silica glass glued together). The reduced thermal expansion ensures a temperature tuning rate at 40 °C (const. density), which is as close as possible to 0 and smaller than 700 MHz/K. The dimensions of the different materials of the composite spacer, in order to achieve the tuned CTE, are determined by the manufacturer.

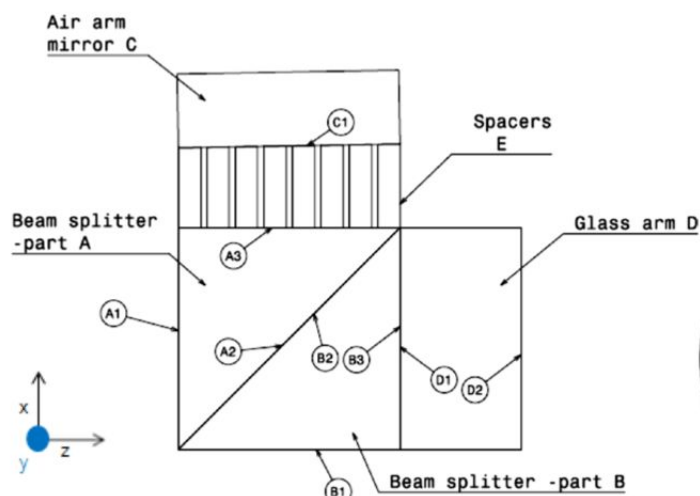
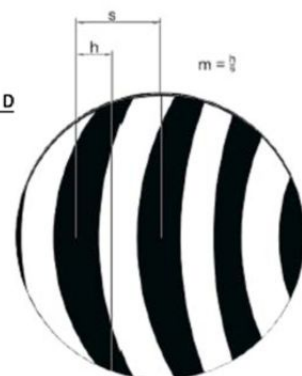


Figure: Appellation of parts and optical surfaces.



Aimed fringe pattern in y-z-plane.

## Vermerk/Mitteilung



## General / Conditions of use:

Pos.	Requirement	Value	Comment/tolerance
1.	Direction of use:	0° or 2° ± 22 mrad (arm lengths are optimized for 2°)	Angle with respect to beamsplitter entrance surface normal in air (z-axis, see drawing)
2.	Working wavelength	354.84 nm	
3.	Power density	CW: 35 W/cm <sup>2</sup>	
4.	Illumination	10 – 15 mm beam diameter, central, 10 mm beam diameter of illumination gives 1 FSR	Entrance surface: A1
5.	Clear aperture	19 mm	
6.	General goals:  Temp. tuning rate at 40 °C: (const. density) Optical path length difference (OPD) at 22 °C:  OPD variation over 20 K range:  Free spectral range (FSR):  Control measurements: Net angle of inclination of the mirrors:  Net surface irregularity:	  Illumination at 354.84 nm produces one linear fringe with contrast of almost 1 < 700 MHz / K * <sup>3</sup>  26.149 mm  < 2 %  10.7 GHz  17.8 ± 1 µRad * <sup>1</sup>  < h/20, h = 633 nm over 19 mm clear aperture * <sup>2</sup>	  Achieved by composite spacers * <sup>3</sup>    Dispersion corrected by arm lengths Control measurements required at Reference wavelength of 633 nm
7.	Temperature range	10 – 50 °C (storage) 40 °C (aimed operation temp.)	
8.	Pressure	0 – 1200 hPa	

## Description:

1. Beam splitter A/B, fused silica, optically contacted, dielectric coating, s-polarized, nominal 50% ± 2% reflectivity at incident angles ± 2° with respect to beamsplitter entrance surface normal.
2. Glass arm D optically contacted to beam splitter cube.
3. Air arm C spaced with calcium fluoride composite spacers E, cemented in place with UV cure epoxy. Tilt adjusted to approximately 17.8 µRad. \*<sup>1</sup>
4. Input/exit surfaces A1, A3, B1 are AR coated.
5. Dielectric HR mirrors on mirror faces. All coatings are dual coatings for 355 nm and 532 nm.
6. Aimed properties are verified in control measurements at specified wavelength at room temperature.
7. Glass arm mirror surface D2 is available for fine-tuning of the net wedge angle and of the wavefront deformation properties (net curvature), if an unexpected fringe shape is obtained during the control measurements.

## LightMachinery

Work order: 81396

Test Report

Product Part Number: OP-7728

Serial number: 1

Description: Michelson interferometer, field widened, 355, temperature compensated

Date: 2016 June 20

ID	requirement	Measured value	specification	notes
Cubic Beam splitter wo 81392				
1	substrate	Heraeus Homosil 101	Heraeus Homosil 101	
2	Composed of right-angle triangular prisms	OK		
2.1	Edge lengths (d3) distance A1 to B3 and A3 to B1	30.0 mm		caliper
2.1.1	Path matching	Less than 200 nm path difference	Less than 10 $\mu$ m path difference within cube	The beam splitter was inspected under illumination from a tungsten filament. The zero order interference fringe was observed between the faces facing the air arm and the glass arm before final assembly.
2.2	Wedge angle Between B1 and A2 Between A2 and A1 Between A3 and B2 Between B2 and B3 In y-direction	OK	45° 45° 45° 45° 0°	

3.1.1	AR coatings on A1, A3, B1	0.1% R at 355 nm <1.5% R at 532 nm	<0.1%R at 355 nm, normal incidence $\pm 3^\circ$	<0.2% R 350-360 nm, measured at normal incidence. Shift calculated at less than 1.5 nm over $\pm 5^\circ$ input angle range. Coating curves attached. Calculated off axis performance also included.
3.1.2	Beam splitter coating	48% T at 355 nm 52% T at 532 nm		Measured at 45° in contact with fused silica, s-polarization only
3.2	Coating damage threshold		>35W/cm <sup>2</sup> continuous	Not tested, e-beam evaporated coating, by similarity
3.3	Contour accuracy on A1, A3, B1, B3	0.057, 0.066, 0.033, 0.050 waves at 633	3/0.1—0.050 waves at 633 nm	Interference from other faces increases surface measurements, actual values are better. Zygo interferometer traces attached.
3.4	Wavefront deformation	5.7, 7.6, 3.8, 5.1 nm RMS	5 nm RMS	Interference from other faces increases surface measurements, actual values are better. From Zygo measurement

Glass arm, WO 81395 #2

1	material		Heraeus Homosil 101	
2.1	Arm length	16.363 mm	16.360 mm	At room temperature. Heidenain Certo length gauge
2.2	Wedge angle	OK	0°	
3.1	HR coating on D2	99.9% R at 355 nm, 97%R at 532 nm		>99.8%R 345-365 nm, coating curve attached



# LightMachinery

## Test Report

3.2	Coating damage threshold		>35W/cm <sup>2</sup> continuous	Not tested, e-beam evaporated coating, by similarity
3.4	Surface accuracy of D1 and D2	0.028, 0.050 waves at 633 nm	3/0.1 at 633 nm—equivalent to 0.05 waves	Before optical contacting. Zygo measurements attached.
3.5	Wavefront deformation			Not measured
3.6	Parallelism	<0.2"	D1 to D2 < 5"	HeNe laser inspection
3.7	Surface quality	OK	D1, D2 (ISO 10110) 5/1 x 0.01 C 1x0.005 L 1x0.001 E 0.5	Visual inspection

### Air arm mirror wo 81394 #2

1	Material	Heraeus Homosil 101	Heraeus Homosil 101	
2.1	Thickness	8.0 mm		caliper
2.2	Wedge	0°	0°	
2.3	Clear aperture	19 mm dia	19 mm dia	Flat to 0.022 wave (at 633 nm) before final correction, Zygo measurement
3.1	Coating on C1	99.8%R at 355 nm 95%R at 532		99.8% R 340-360 nm
3.2	Coating damage threshold		>35W/cm <sup>2</sup> continuous	Not tested, e-beam evaporated coating, by similarity
3.4	Contour surface accuracy C1	Flat to 0.022 wave (at 633 nm) before final correction		Zygo measurement
3.5	Wavefront deformation	0.044 wave (at 633 nm) before final correction		Zygo measurement
3.6	Parallelism	<10 µm wedge		
3.7	Surface quality	OK	D1, D2 (ISO 10110) 5/1 x 0.01 C 1x0.005 L 1x0.001 E 0.5	Visual inspection

### Spacers wo 81393

1.1	Materials	Calcium fluoride, fused silica		Helma Lithotec IR grade Corning HPFS 7980
1.2	Glue	Norland 61	Norland 61 or similar	
1.3	Glue layer thickness	<5 µm	<40 µm for each layer	
2.1	Spacer thickness	9.004 mm of CaF2		Heidenhain Certo gauge
2.2	Wedge angle	12 µrad		Wedge less than design, corrected in surface of air arm mirror. Zygo measurement
2.3	Spacer thickness	11.075 mm	11.076 mm	Measured at approximately 23°C. Calculated CTE of approximately 15.6 ppm/°C

## LightMachinery

### Test Report

2.4	Post configuration	20 posts		Pitch of cuts between posts is 5.0 mm, posts either square 4.5 mm x 4.5 mm (corners), or rectangular 4.0 mm x 4.5 mm.
2.5	Clear aperture	21 mm square		

Instrument performance				
1	Direction of use	0-2° tilt		phase uniformity over field of view not significantly affected by tilt over this range of input angles.
2	Working wavelength	355 nm		No significant change in coating performance over $\pm 5$ nm
3	Power density			
4	Illumination		10-15 mm beam diameter	
5	Clear aperture	19 mm	19 mm diameter	
6.1	Optical path difference	26.165 mm at 22°C, 26.166 mm at 40°C		Calculation
6.2	Free spectral range	10.69 GHz		At 355 nm, calculated
6.3	Net wedge	19.1 $\mu$ rad	17.8 $\pm 1$ $\mu$ rad	Measurements 6.3, 6.4.1, 6.4.2, 6.4.3 all based on a grid of intensity measurements performed at normal incidence with six different wavelengths near 355 nm. The local phase was calculated for each point, and the net wave front calculated from the phase measurements. The phase at each point is compared to nearest neighbours to resolve phase variations greater than $2\pi$ . Data file "Interferometer with New FJP mirror 31 May 2016.xlsx" sent separately
6.4.1	Net surface irregularity over 10 mm diameter	13 nm PV, 2.8 nm RMS		
6.4.2	Net surface irregularity over 15 mm diameter	15 nm PV, 3.0 nm RMS		
6.4.3	Net surface irregularity over 19 mm diameter	39 nm PV, 4.3 nm RMS	31.5 nm PV	26.5 nm PV with removal of two data points at the edge of the clear aperture; 4.0 nm RMS with the removal of these two points
6.5	Temperature tuning rate	477 MHz/°C		At constant pressure, by calculation
7	Temperature range	10-50°C		Strength of cement will be the limiting factor outside this range. Even within this range, very rapid temperature changes may damage the calcium fluoride spacers. $dT/dt$ of 10°C/hr has been tested without issue for this construction method. Higher temperature tuning rates have not been evaluated.
8	Pressure		0-1200 hPa	Changing pressure will cause the interferometer to tune, but will not affect the mechanical performance of the interferometer



# F Equipment

## Ultra-violet light emitting diode

A UV-LED “EOLD-355-525” (Epigap Optronic GmbH, Germany) is used in section 3.5.2 in an attempt to determine the illumination function of reference light on the PMTA. It has a peak wavelength of 353 to 360 nm ([EPIGAP, 2011](#)).

## Continuous wave laser

The cw-laser “Cobolt™ Zouk 0355-05-01-0010-50” provided by Cobolt AB, Sweden runs at a wavelength of 355 nm ([CoboltAB, 2016](#)).

## DELICAT telescope

The telescope used in the front-end part of the AEROLI receiver is a Newtonian telescope with a focal length of the primary mirror of 750 mm (out of a “Celestron OmniXLT150”, 6” - F/5 telescope with a diameter of 150 mm). This primary mirror with reflective Al-coating is not optimized for UV light with a reflectivity of  $\approx 85\%$  at a wavelength of 355 nm. The secondary mirror provides an obstruction of a diameter of 38 mm, and is optimized for the UV. The opening aperture of the telescope is 140 mm wide, such that, taking into account also the obstruction by the spider, the total obstruction ratio is 12% ([Vrancken et al., 2016](#)).

## Fibers of the receiver

This section lists the fiber components used in the AEROLI receiver (see Fig. 3.20), for characterizations of fiber speckle (section 3.5.4), and of the (near-field) scrambling gain (see section 3.5.5).

The 3:1 custom-built end face coupler (MM-Koppler 1x3, Laser Components) consists of three parallel oriented, laterally colliding 600- $\mu\text{m}$ -core fibers, aligned with respect to a fourth “combiner”-fiber (600  $\mu\text{m}$ ). The (theoretical) splitting ratio (94:3:3) of the three input ports / fibers is determined by the overlap of the areas of the cores of the three fibers with the “combiner”-fiber. The arrangement can be used in both ways as a coupler or as a splitter. Due to manufacturing tolerances the actual measured transmission ratio (60:2:2 if used as coupler) deviates from the specified theoretical ratio.

Tab. F.1 and Tab. F.2 list all the fiber components of the AEROLI receiver and their properties.

**Table F.1: Fiber components used in the AEROLI receiver (see Fig. 3.20)**

Component	Name	Manufacturer
fiber S1	FG600AEA	Thorlabs
3:1 coupler	MM-Koppler 1x3	Laser Components
Scrambling fiber	SQ WF 600x600/990/1400N (Optran WF)	CeramOptec (CO)
Delay fiber (R1)	FG105ACA-CUSTOM	Thorlabs
Delay fiber (R2)	FG400AEA-CUSTOM-MUC	Thorlabs

**Table F.2: Fiber properties of components used in the AEROLI receiver (see Fig. 3.20)**

Component	Core	NA	length	connector	attenuation ( $a_{int}$ )
fiber S1	600 $\mu\text{m}$ (circular)	0.22	3 m	FC/PC	60 dB/km
3:1 coupler	600 $\mu\text{m}$ (circular)	0.22	1 m	FC/PC	40%
Scrambling fiber	600 $\mu\text{m}$ (quadratic)	0.22	10 m	FC/PC	60 dB/km
Delay fiber (R1)	105 $\mu\text{m}$ (circular)	0.22	150 m	FC/PC	60 dB/km
Delay fiber (R2)	400 $\mu\text{m}$ (circular)	0.22	20 m	FC/PC	60 dB/km

The transmission after losses due to internal absorption can be calculated by

$$T_f = 10^{-a_{int}[dB/m]L/10}, \quad (\text{F.1})$$

whereby  $L$  is the length of the fiber.

### Fibers in speckle noise and scrambling measurements

Tab. F.3 lists all the fibers tested in sections 3.5.4 and 3.5.5. All the tested fibers exhibit a numerical aperture (NA) of 0.22 and are equipped with FC/PC connectors.

**Table F.3: Fibers tested in speckle noise and optical scrambling measurements.**

Fiber	Name	core diam.	shape	length
A	SQ WF 600x600/990/1400N (CO)	600 $\mu\text{m}$	quadratic, sharp edges	10 m
B	SQ WF 600x600/990/1400N (CO)	600 $\mu\text{m}$	quadratic, round edges	2 m
C	UM22-600 (Thorlabs)	600 $\mu\text{m}$	circular	2 m
C2	FVP600660710 (Polymicro)	600 $\mu\text{m}$	circular	1 m
C3	M133L02 (Thorlabs)	200 $\mu\text{m}$	circular	2 m
D	OCT-WF95/178/207P (CO)	90 $\mu\text{m}$	octagonal	3 m

### Cameras

Two 2D-area cameras are used in this work. For imaging of the fringe and for scrambling gain measurements (section 3.5.5) a CMOS camera (C1, “GS3-U3-41C6M-C”, USB 3.0 camera by FLIR, formerly Point Grey, Canada) with a monochrome 1” sensor (“CMOSIS CMV4000-3E5”, ams Sensors Belgium, formerly CMOSIS) with a microlens array and with a cover glass is applied.

For the fiber speckle characterization (section 3.5.4) a CCD camera (C2, AV “Prosilica GT2300-MOD” by Allied Vision, U.S.A.) with a 4.1 MP (16 mm diagonal) interline CCD sensor (“KAI-04050 Truesense” by ON Semiconductor, U.S.A.) with the “AAA-JP-BA” option, i.e., no microlens, no coatings, and a taped clear cover glass, which can be removed by hand in a cleanroom. The cover glass of the CCD sensor was removed prior to the fiber speckle measurements. Both cameras were selected with respect to maximum sensor area and quantum efficiency in the UV at 355 nm.

## Photomultiplier tube array

The photomultiplier tube array (PMTA) is of type “H7260-200” (Hamamatsu, Japan). It has 32 channels (anodes) with a width of  $\Delta x = 0.8$  mm and a height of 7 mm arranged linearly next to each other with a gap of 0.1 mm between two neighbor anodes, i.e., a channel pitch  $\Delta x_p$  of 1 mm (Hamamatsu, 2011). The -200 type has a slightly higher quantum efficiency of  $\approx 45\%$  at 355 nm. The gain at the minimum supply voltage of 500 V is  $\approx 3 \cdot 10^4$ . The peak wavelength is 400 nm and the photocathode material is Ultra BiAlkali (UBA). The rise and transit time spread are  $\approx 0.6$  ns and 0.18 ns, respectively. Complete specifications can be seen in Hamamatsu (2011).

Fig. F.1 provides the dependence of the response on the incident angle and the anode uniformity of the “H7260-200” at 355 nm.

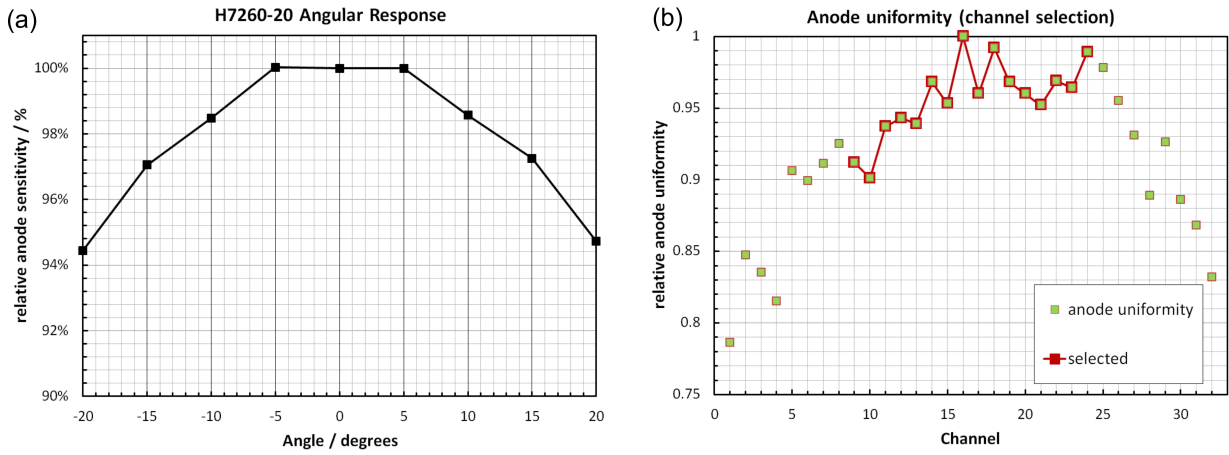
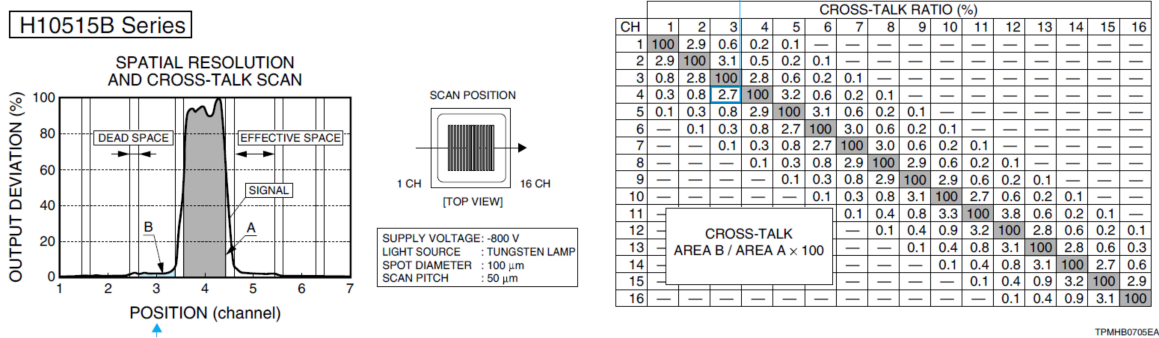


**Figure F.1:** Angular response at a supply voltage of 800 V (a) (provided by C. Dille, Hamamatsu Germany, 2016) and anode uniformity (b) of Hamamatsu H7260-200 at 355 nm (test sheet of bought PMTA).

The geometrical loss factor due to the gaps of with  $\Delta x_G = 0.2$  mm, i.e., a pitch  $\Delta x_p$  of 1 mm between the channels amounts to 0.8, for  $N_{pixel} = 12$ , calculated using eq. F.2:

$$F_{loss} = \frac{N_{pixel} \cdot (\Delta x_p - \Delta x_G)}{N_{pixel} \cdot (\Delta x_p - \Delta x_G) + (N_{pixel} - 1) \cdot \Delta x_G} \quad (\text{F.2})$$

The cross-talk between the PMTA channels is non-negligible. Typical values are provided in Hamamatsu (2011) (see Fig. F.2).



\* H7260 series is equivalent to H10515B series.

**Figure F.2:** Typical cross-talk ratios of Hamamatsu H7260-200 (Hamamatsu, 2011).

Fig. F.3 contains information on the dimensions of H7260 (a), the circuitry of one PMT (b) and an exemplary cathode uniformity curve.

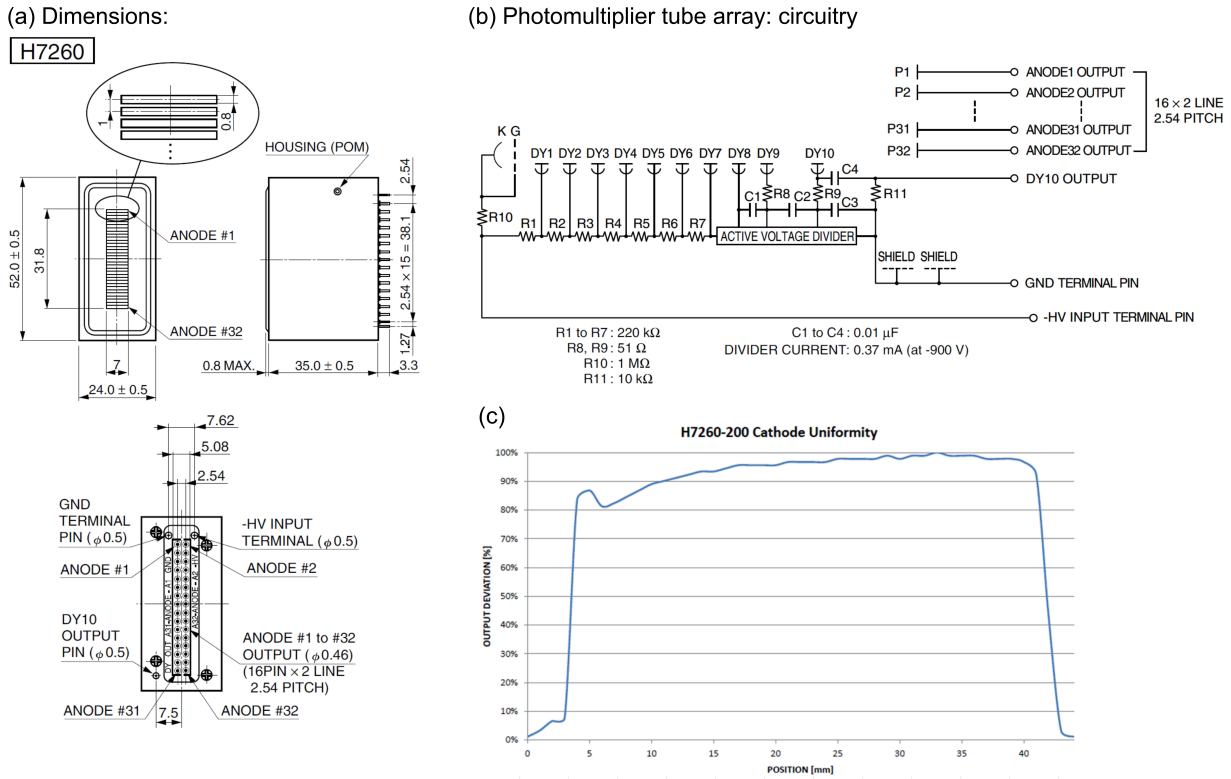


**Figure F.3:** (a) Dimensions of photomultiplier tube array (PMTA). (b) Circuitry of one channel (taken from [Hamamatsu \(2011\)](#)). (c) Exemplary cathode uniformity (C. Dille, Hamamatsu Germany, 2016).

## Amplifier circuit

The amplifier circuit was developed by Martin Wirth and was built by Philipp Roßi. Fig. F.4 shows an exemplary circuit scheme of the amplifier circuit for one channel of the photomultiplier tube array (PMTA).

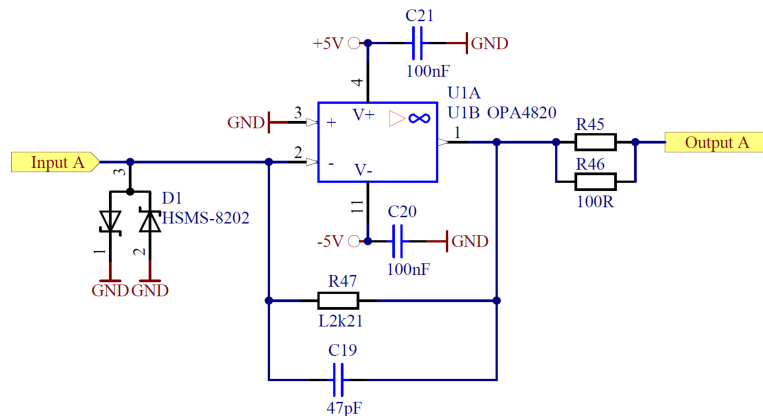


**Figure F.4:** Exemplary part of the current amplifier circuit for one channel of the PMTA ([Roßi, 2017](#)).

Because of the voltage divider circuit (see R45, R46) the effective output voltage of the 50Ω termination is half of the converted voltage with an amplification factor of 2.21 kΩ.

### AEROLI receiver efficiency estimation

The efficiencies of the components of the AEROLI receiver prototype (of the setup in Fig. 3.2) are listed in Tab. F.4.

The total estimated efficiency of the AEROLI receiver during the validation measurements is  $\approx 2.7\%$ , assuming total overlap and no losses due to focal-ratio-degradation (FRD). If a different primary mirror optimized for UV wavelengths and a more efficient, free-beam way to combine the backscattered signal light and the laser reference light would be used, a receiver efficiency of  $\approx 4\%$  could realistically be achieved.

The atmospheric signal can be estimated taking into account the gain of the amplifier circuit of  $R_L = 2210\Omega$ , divided by 2 due to voltage division, and the PMT gain of  $3 \cdot 10^4$  at a supply voltage of 500 V (Hamamatsu (2011), see section 3.5.3). Assuming the maximum detected voltage per channel was in the order of 1 V, the current after PMT gain (before amplification) would have been in the order 0.5 mA. Using  $P = I/(G \cdot R_e)$ , the maximum optical power per channel, including all losses, is  $\approx 2.34 \cdot 10^{-7}$  W. Using  $N_{ph-max} = P \cdot \Delta t \cdot \lambda/(h \cdot c)$ , the maximum number of photons per channel, including all losses, is  $\approx 70000$ .

The number of photons on the  $i$ th channel is estimated using an analytical expression for the stepwise integration of the fringe when it is imaged onto the PMTA:

$$N_i = \frac{A}{\sqrt{2}} [1 + W \cdot \cos((a_i + b_i) \cdot \Gamma/2) \cdot \text{sinc}((b_i - a_i) \cdot \Gamma)] \quad (\text{F.3})$$

Whereby  $\Gamma = S(\pi - \theta \frac{FSR}{\Delta\nu_{D(u_r=1\text{m/s})}})$ .  $a_i$  and  $b_i$  are the borders of pixel  $i$  defined by:  $a_i = i - D_{u_r}/N_{pix} - u_r - D_{u_r}/2$  and  $b_i = (i + 1) - D_{u_r}/N_{pix} - u_r - D_{u_r}/2$  with  $D_{u_r} = FSR/\Delta\nu_{D(u_r=1\text{m/s})}$ , where  $FSR = 10.7$  GHz is the free spectral range,  $\Delta\nu_{D(u_r=1\text{m/s})}$  is the Doppler shift in Hz caused by a radial wind speed of 1 m/s, and  $D_{u_r} \approx 1898$  m/s is the width of the  $n = 1$  period fringe imaged onto the PMTA in terms of radial wind speed.  $S = 4 \cdot OPD_0/(c\lambda_L)$  is the phase sensitivity,  $\theta$  is the angle of inclination between the mirrors of the Michelson interferometers (see section 3.3.2), and  $N_{pix} = 12$  is the number of illuminated PMTA channels.  $W$  is the global fringe contrast, which is set to 0.66 for the estimation. For  $N_{ph-max} = 70000$  by using eq. F.3, and summing over all channels  $i$ , a total number of photons  $N_{tot}$  of  $\approx 400000$  is obtained. Using this number of photons in the CRB calculation (eq. C.30) a CRB of  $\approx 1.4$  m/s is calculated.

Assuming the maximum voltage per channel is  $\approx 1$  V (see Fig. 5.10), which was the case during the horizontal field-test measurement shown in Fig. 5.16,  $N_{ph-max}$  is 70000 for one pulse with an IR pulse energy of 160 mJ, and the according CRB is  $\approx 2.8$  m/s. These numbers fit well to the standard deviations obtained for different LoS update rates in Fig. 5.16.

However,  $N_{ph-max} = 70000$  is different from  $N_{ph-max} \approx 400000$  ( $N_{tot} \approx 18 \times 10^6$ ) obtained by using the atmospheric model of section 2.1.1 assuming an altitude above sea level of  $h = 0$  m and the lower decile of the aerosol backscattering coefficients at a distance of  $R = 50$  m, considering full overlap ( $N_{tot} \approx 16.7 \times 10^6$  for  $h = 500$  m), together with a plausible receiver efficiency of 2.7% (see Tab. F.4).

Taking into account the overlap function determined during the vertical measurements (see Fig. 5.19(b)) with an overlap of 30% at 50 m, the efficiency is further reduced. It seems like only  $\approx 17\%$  of the anticipated photons hit the PMTA detector during the field-test measurement, such that the total receiver efficiency was on the order of 0.4% at full overlap and  $< 0.1\%$  at  $R = 50$  m with  $< 30\%$  overlap included.

**Table F.4: AEROLI receiver component efficiencies in logical order**

Component	transmission
Front-end part	
Newtonian telescope (primary mirror)	0.85
Obstruction ratio (secondary mirror)	0.88
Range-dependent overlap	1
Sunlight filter (Materion)	0.88
First collimating lens after telescope	0.9975
Polarizing beamsplitter (PbSO-355-50)	0.9925
Coupling lens into signal fiber	0.9975
Fiber components	
Signal fiber coupling (Fresnel reflection)	0.9624
FRD losses	1
Fiber internal transmission	0.87
Fiber coupling (Fresnel reflection)	0.9624
Fiber couplers / splitters	0.6
Back-end part and Michelson interferometer (FWFIMI)	
Collimator lens after signal fiber	0.9975
Repolarization to s-polarization	0.5
Polarizing beamsplitter (PbSO-355-50)	0.9925
AR-coated window 1 of interferometer compartment	0.9975
AR-coated window 2 of interferometer compartment	0.9975
Reflectivity AR entrance	0.999
Reflectivity of mirror arm 1	0.998
Reflectivity of mirror arm 2	0.998
Normal incidence / one detector	0.5
Imaging lens 1	0.9975
Imaging lens 2	0.9975
Imaging lens 3	0.9975
Geometric loss factor of PMTA (for 12 pixels)	0.80
Quantum efficiency of PMTA	0.45
Total	0.027



Possible reasons for this overall detection efficiency of  $\approx 0.4\%$  could be related to the laser transmitter and the front-end part of the receiver. One possible reason could be, that the laser beam was polarized not exactly parallel to the s-polarized part of the light, which is coupled into the fiber 3:1-coupler via the polarizing beam splitter cube (PbSO-355-50) in the front-end part (see “PBSC” in Fig. 3.21). In this case, a certain part of the aerosol backscattering signal and of the total backscattering signal would have been transmitted by the PBSC, not reflected and not coupled into the fiber linkage parts of the receiver. The alignment between laser beam polarization and PBSC was not checked upon prior to the measurements, and cannot be checked belatedly, because at the time of this writing, the setup is disassembled. Moreover, the narrow-band dielectric 355-nm-coating ( $R \approx 100\%$  at  $45^\circ$ ) of the secondary mirror of the Newtonian telescope may yield lower reflectivities at larger angles of incidence (i.e., at  $45^\circ + [-5.3^\circ, 5.3^\circ]$ ), what could have reduced the receiver efficiency and could have caused additional vignetting. A further reason could be a misalignment of the fiber coupling optics of the front-end receiver (Fig. 3.21), such that only a fraction of the rightly polarized light would have been coupled into the fiber parts. Furthermore, during the horizontal wind speed measurements, the laser beam was not optimally aligned with respect to the telescope axis, which could have caused a smaller overlap compared to the vertical measurements.

It should be considered as well, that the atmospheric backscattering coefficient model can be quite unrealistic compared to the real backscattering coefficients during the measurements, especially as the values obtained by *Vaughan et al. (1995)* were obtained at altitudes above sea level.

Another possible reason could be the damage of the scrambling fiber, which occurred during speckle contrast measurements on December 5th, 2017 (see section 3.5.4), when part of the polymer cladding was hit by the ALADIN laser and melted, whereby no apparent loss of transmission was visible directly afterwards.

It might be worthwhile to note, that between alignment in the lab and measurement in January 2018 the setup was stored for half a year inside the measurement container, because of the unavailability of the DELICAT transmitter, which was on a measurement campaign during this period, and that, within this period the front-end part of the receiver served as burrow for a mouse (see Fig. F.5). This caused some damage to cables of the temperature stabilization and some scratches on the primary mirror of the telescope, which was not completely repaired prior to the field-test measurements.



**Figure F.5:** Left: Mouse using front-end part of the receiver as burrow. Right: scratches on the Newtonian telescope’s primary mirror.

### Digitizer boards and settings

The 16 bit A/D board “Spectrum M2i.4932-exp” provides 8 channels with a maximum sampling rate of 30 MS/s (31.25 MHz), a bandwidth (-3 dB)  $> 30$  MHz, and an effective number of bits (ENOB) based on the SNR of the signal after the analog to digital conversion of  $> 12.1$  LSB (least significant bit). The boards thus output 16 bits, however, the noise generated by the conversion, reduces the achieved SNR to that of an ideal analog-to-digital converter (ADC) with 12.1 bits.

Both boards are synchronized using a Spectrum starhub ([Spectrum, 2015](#)).

The ADC board settings shown in Tab. F.5 are controlled with a MATLAB routine.

**Table F.5: Settings of the digitizer boards**

Setting	Value
Mode	rec-std-multi
Loops (number of pulses)	$> 1$
segment size	$> 64$ samples
trigger mode	SPC-TM-POS
pretrigger samples	$> 4$ samples
input range	$\pm 500$ mV
input offset	-500 mV
sampling rate	$31.25 \cdot 10^6$
timestamp mode	SPC-TSMODE-STARTRESET

The trigger mode is set to “SPC-TM-POS”, i.e., for detection of rising edges of the external TTL signal from the transmitter.

The time stamp mode “SPC-TSMODE-STARTRESET” means that the internal counter of the boards is reset at every card start and all the time stamps are in relation to this start event. The absolute computer time at each card start event is saved in an ASCII file.

The so-called “Refclock” mode would allow to directly obtain an absolute time reference to an external clock or a GPS receiver.

The recording mode “rec-std-multi” applied in section 5.2 prohibits online wind speed evaluations and limits the maximum recording time due the internal memory of the ADC board (8 channels) being limited to  $256 \cdot 10^6$  samples. This means that in case of vertical measurements (380 samples per segment per channel) the maximum continuous recording time (without temporal averaging of the raw data) is 14 min.

In the long run, the “rec-fifo-multi”-mode should be implemented, making use of a FIFO-buffer, such that the data can be saved and manipulated package-wise, parallel to an acquisition run. This mode would allow also longer measurement times during vertical (long-range) wind speed measurements, e.g., for monitoring long-term (possibly overlap-dependent) temporal velocity offset drifts.

## G Further fiber speckle measurements

This sections contains further measurements and background information about the speckle SNR measurements of section 3.5.4.

### Different temporal speckle scrambling techniques and fiber-core shapes

Fig. G.1 provides a comparison of the speckle SNR for the different speckle reduction techniques and coupling conditions shown in Fig. 3.28 using two different 600- $\mu\text{m}$ -core fibers (A and B, see Tab. F.3). The speckle SNR is evaluated over  $\text{ROI}_3$  ( $1160 \times 1760$  pixels) without spatial averaging (Fig. G.1(b), orange rectangle) and with spatial averaging provided by a 12 pixel hypothetical detector (Fig. G.1(c), averaging over green rectangles).

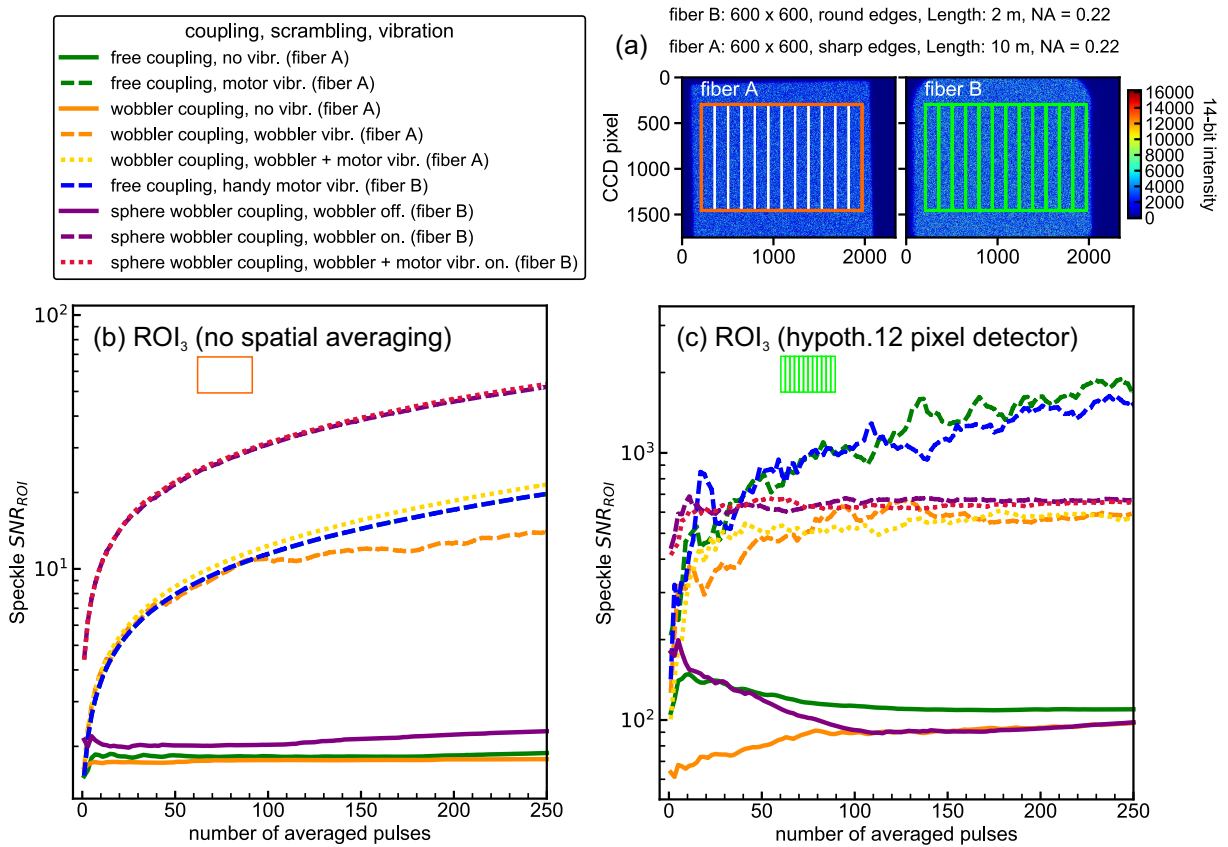


**Figure G.1:** (a) Near-field images of fibers A and B with indicated  $\text{ROI}_3$ . (b) Comparison of speckle SNR (method 2) for different coupling (free and Ulbricht sphere) and modal noise scrambling techniques (vibration motor, Optotune wobbler) as a function of the number of averaged pulses for the 600  $\mu\text{m}$  quadratic-core fibers A and B. Considering  $\text{ROI}_3$  for calculating the speckle SNR (as indicated by the orange rectangle). (c) Same as (a) with spatial averaging within each pixel of a 12 pixel hypothetical detector (green rectangles).

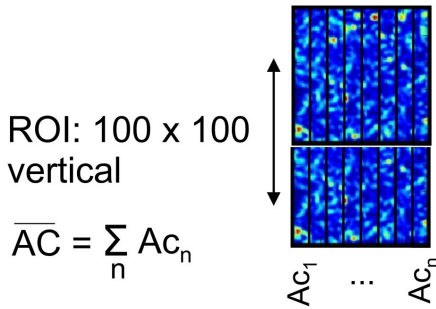
The Optotune wobbler's diffuser causes an excitation of cladding modes due to increased angular diversity before coupling. The SNR is lower for a low number of pulses and reaches a plateau below an SNR of 600. The comparison shows that the Optotune wobbler in free-coupling mode ("wobbler coupling") is not a more efficient scrambler than the vibration

motor (“free coupling, motor”). Only in combination with the Ulbricht sphere better scrambling is achieved by the wobbler for low numbers of averaged pulses ( $< 30$ ) at the cost of high losses due to scattering in the Ulbricht sphere (“sphere wobbler coupling” in Fig. G.1).

This can be explained with better spatial averaging because of the smaller speckle grain size due to the speckled input provided by the Ulbricht sphere.

The mean speckle size on the fiber end face is determined via a Gaussian fit to the mean vertical autocorrelation function (evaluation of 500 different frames, see Fig. G.2(a)) with one pixel being equivalent to approximately  $0.3 \mu\text{m}$ , calculated by the known width of the fiber core in the magnified near-field image with a magnification of 17.4 (see Fig. G.2(b) for fiber A).

(a) Speckle size determination:



(b) Result:

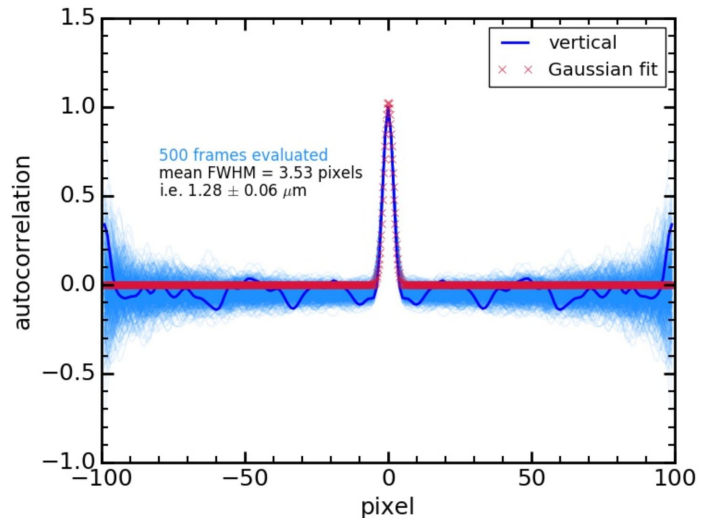


**Figure G.2:** (a) Principle of speckle size determination. (b) Speckle size determination by taking the mean vertical autocorrelation function of 500 near-field frames of a  $600 \mu\text{m}$  quadratic-core multimode fiber (fiber A). One mean vertical autocorrelation function is highlighted (bold blue line). A Gaussian fit (red crosses) is applied to determine the FWHM.

The speckle grain size is  $1.29 \mu\text{m}$  with direct coupling (fiber B) and  $0.84 \mu\text{m}$  with Ulbricht sphere coupling (see Fig. G.3(a, b)).

Speckle grain size determination measurements of a  $200 \mu\text{m}$  circular-core fiber and of an octagonal  $90 \mu\text{m}$  fiber are shown in Fig. G.3(c, d) for comparison.

Tab. G.1 summarizes the determined speckle grain sizes  $D_{sp}$  and the ratios  $R_f$  (of the fiber core diameter to the speckle grain size) of the tested fibers.

**Table G.1: Speckle grain sizes and ratios  $R_f$  of the tested fibers.**

Fiber	core diameter	shape	speckle grain size $D_{sp}$	ratio $R_f$
SQ, fiber A	$600 \mu\text{m}$	quadratic	$1.28 \mu\text{m}$	469
SQ, fiber B	$600 \mu\text{m}$	quadratic	$1.29 \mu\text{m}$	468
fiber C3	$200 \mu\text{m}$	circular	$1.28 \mu\text{m}$	156
fiber D	$90 \mu\text{m}$	octagonal	$2.45 \mu\text{m}$	37

Method 2 can be used to compare the speckle contrasts within  $\text{ROI}_1$  ( $100 \times 100$  pixels) for an octagonal-, a circular-, and two quadratic-core fibers (A and B) without spatial

averaging as a function of temporal scrambling, i.e., of the number of averaged pulses (see Fig. G.4).

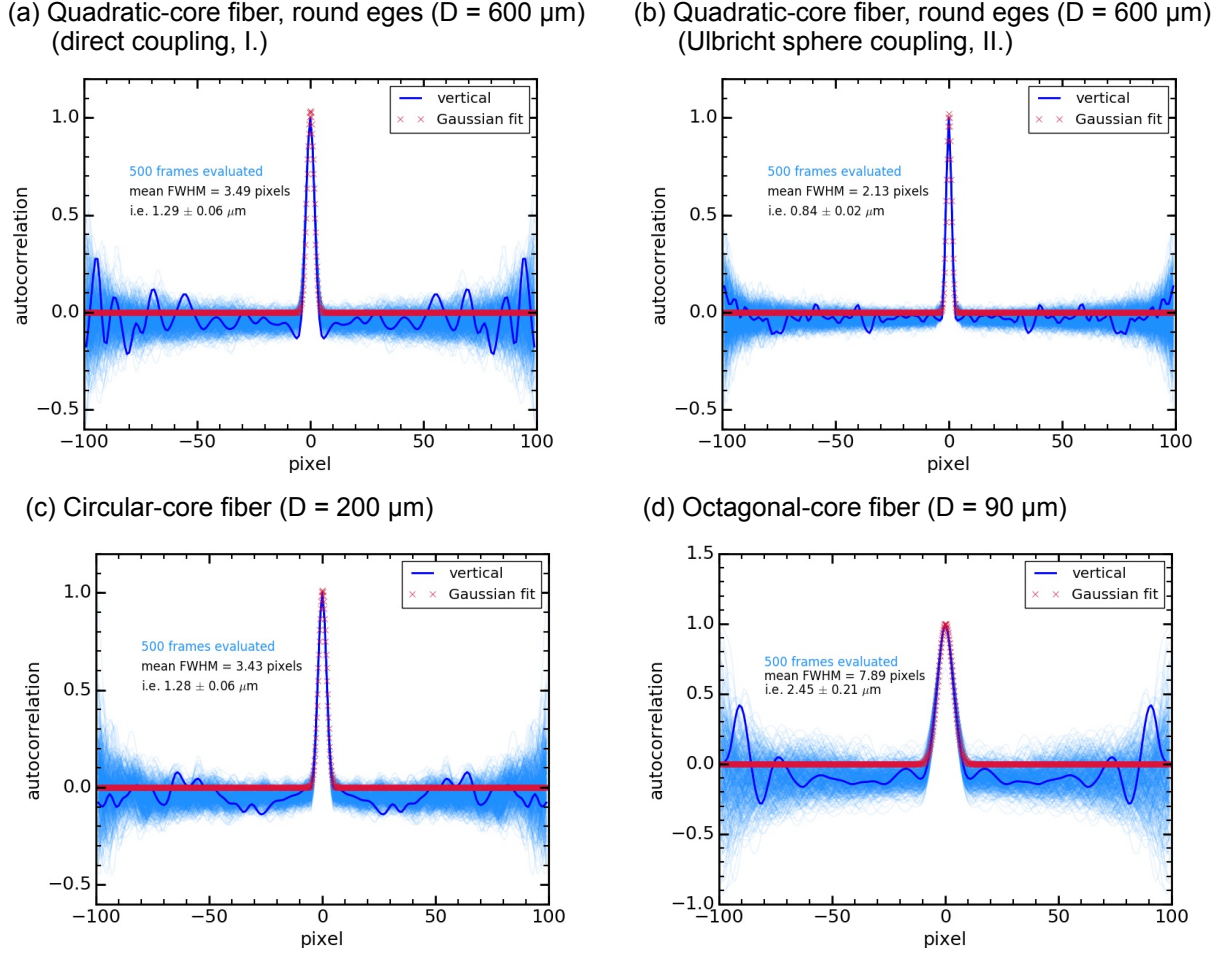


**Figure G.3:** Speckle grain size determination for a quadratic core fiber (a) direct coupling (I.), (b) Ulbricht sphere coupling (II.) and for a circular-core fiber (c) and a octagonal-core fiber (d).

The near-field frames are dark frame corrected, flat-field corrected, and masked prior to the speckle contrast evaluation (see Fig. G.4).

Without vibration the variation of the speckle pattern is only visible during long observation durations. This variation may be caused by temperature effects and by a change of the ALADIN laser frequency on a scale of minutes or hours.

Fig. G.5 shows the same region-of-interest ( $\text{ROI}_1$ :  $100 \times 100$  pixel) of CCD images taken for subsequent pulses without and with vibration. Fiber vibration in combination with pulse averaging (vibration ON) reduces the speckle contrast (temporal averaging). This reduction is independent of the ROI size (without spatial averaging), and is less pronounced in case of the circular-core fiber. The speckle pattern in case of a circular core is more static and highly correlated from frame to frame at comparable agitation levels (*Stürmer et al., 2016*) compared to polygonal core shapes. That is, better temporal modal noise scrambling behavior seems to be a further advantage of polygonal core shapes.

In conclusion, a combination of 600- $\mu\text{m}$ -quadratic-core fibers being vibrated with a motor with direct coupling seems to provide better results in terms of spatial averaging (highest ratio  $R_f$  of approximately 470) and temporal averaging (highest speckle SNR) than smaller core sizes, circular-core shapes, and different speckle reduction techniques.



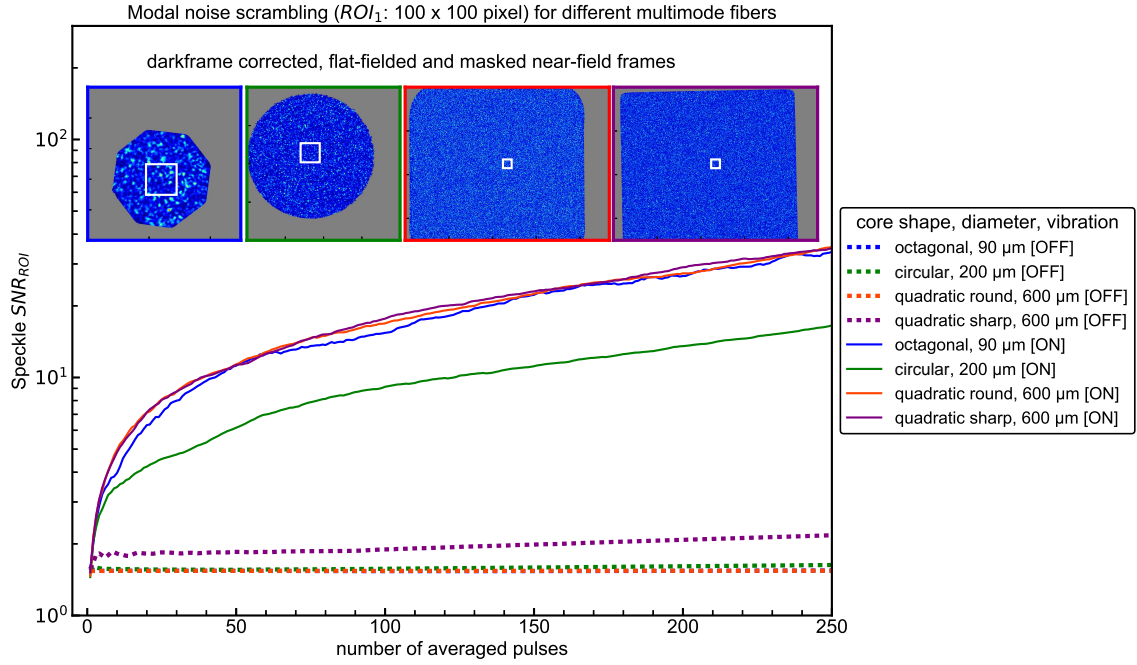


**Figure G.4:** Modal noise scrambling (temporal averaging by vibration motor vibration pulse averaging, no spatial averaging) comparison for different core shapes: octagonal, round, quadratic.

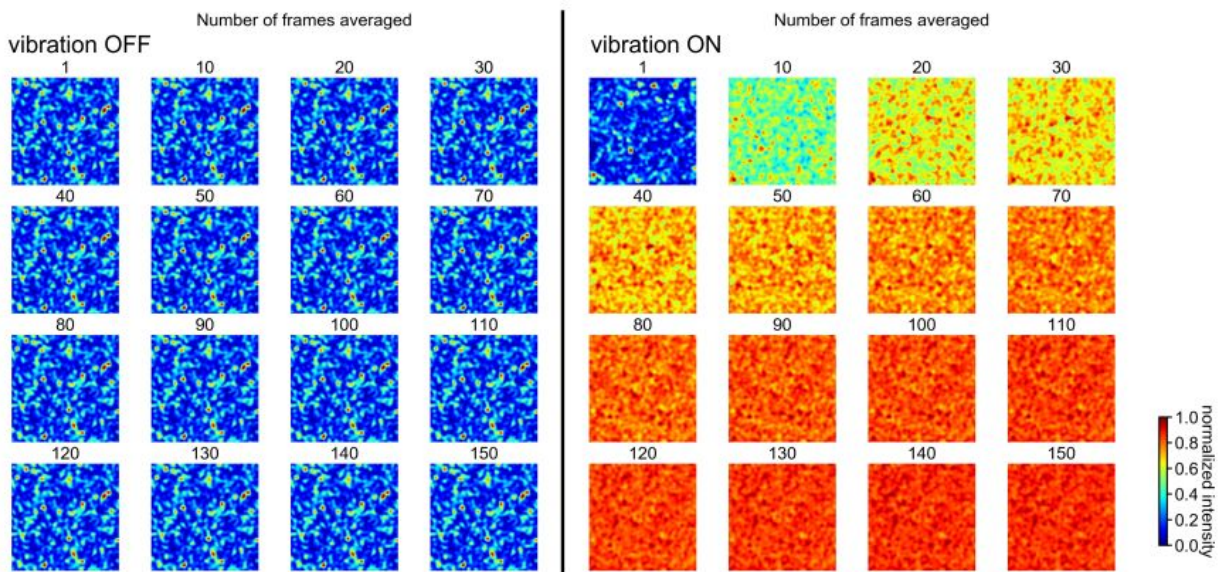


**Figure G.5:** Speckle patterns with temporal averaging (scrambling) without and with vibration for a 600  $\mu m$  quadratic-core fiber.



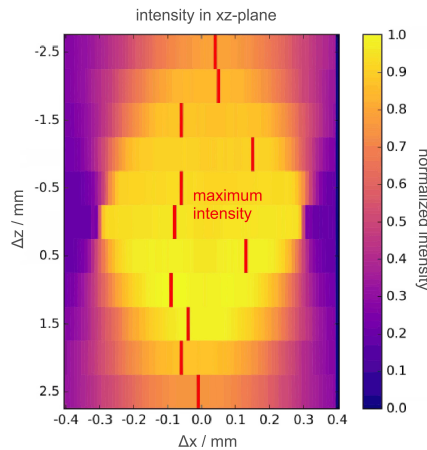
# H Near-field and far-field scrambling measurements

This section provides some background on how the scrambling gain measurements of section 3.5.5 are performed and additional near-field and far-field optical scrambling measurements.

## Background

Prior to each scrambling gain measurement the respective fiber is centered in x-, y-, and z-direction with respect to the focused light source. Fig. H.1(a) shows the total intensities of near-field images taken during the procedure for finding central x-, y-, and z-alignment of the fiber with respect to the input light beam. The application of a mask prior to the determination of the center-of-mass is shown in Fig. H.1(b). The near-field image of a circular-core fiber in Fig. H.1(b) was saturated, what should be avoided.

(a) Finding center position



(b) Masking of near-field frame (in case of 600  $\mu\text{m}$  round-core fiber)

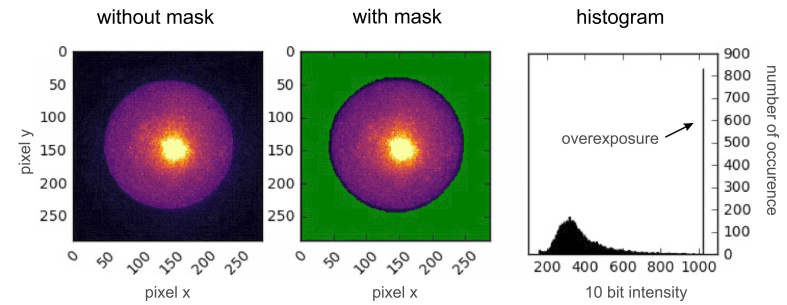


**Figure H.1:** (a) Normalized total intensity of near-field frames at different shifts  $\Delta x$ ,  $\Delta z$ . The fiber input is centered at the location with the sharpest edge between core and cladding ( $\Delta z$ ) and in x- and y-direction (highest intensity). (b) The near-field images with application of a mask (green) to remove the background. Overexposure is visible in the histogram (*Unsinn, 2016*).

The LED and laser intensity profiles of the collimated beams before coupling are different, as is shown in Fig. H.2. From this follows that the angular distribution during the coupling of the respective light into a fiber is different, what may affect the scrambling gain measurements. During the measurements however no decisive difference between the obtained values of SG using both sources were observed.

Using a cw-laser provides the advantage of having a very small focal spot on the entrance surface of the fiber. The disadvantages are its instability with respect to frequency, beam drift, and fluctuation (air flow in the laboratory), and its high temporal coherence, which gives rise to speckle at the end face of the multimode fibers, which have to be averaged out, in order to retrieve meaningful information from the measurements, by vibrating the fiber (see section 3.5.4). These vibrations may introduce measurement errors, when the vibration reaches the end face of the fiber. The influence of speckle is however limited if the ratio  $R_f$  (fiber core size to speckle grain size) is large (as in the case of a 600- $\mu\text{m}$ -core fiber of section 3.5.5). Furthermore, the coherent light can introduce interferences, for instance

with the sensor cover glass of a camera ([Unsinn, 2016](#)), which may fluctuate when the xyz-stage is shifted.

Furthermore, advisable dark frame correction, and flat-field correction were not performed during the scrambling gain measurements.

For these reasons a properly shaped UV-LED (small focal spot size) with a spectral maximum close to 355 nm light source should be preferred (see appendix F for details on the selected UV-LED and its spectral characteristics). A camera with a high bit depth and without microlenses attached to the sensor protection glass and with a removable sensor glass would be preferable (see appendix F for more information about the selected CMOS camera (C1) and on how the sensor glass of the alternative CCD camera (C2) can be removed).

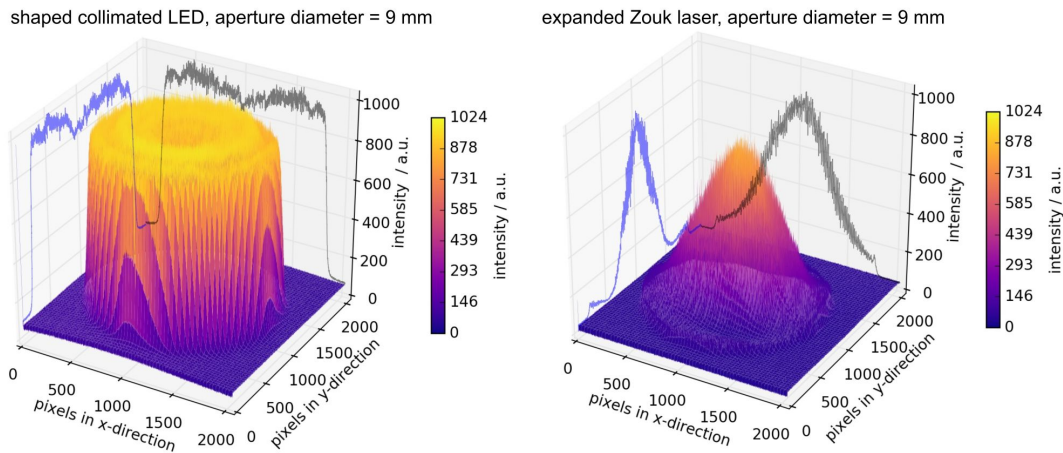


**Figure H.2:** Collimated and shaped LED beam intensity profile versus expanded, cw-laser (Zouk) profile. These intensity profiles represent the optical far-field, i.e., the angular distributions coupled into the test fibers during optical scrambling measurements ([Unsinn, 2016](#)).

### Near-field scrambling

The scrambling gain (SG, see Fig. 3.30(b)) does not take into account purely rotationally symmetric changes of the illumination behind the fiber. Here, another way of estimating and comparing the optical scrambling in the near-field is applied. For this purpose the 2D near-field intensity distributions are summed along the camera sensor's vertical axis in order to obtain 1D illumination function profiles.

Intensity profiles (summed along the camera sensor vertical axis, y-direction) for different shifts  $\Delta x$  of the xyz-stage of the setup in Fig. 3.30(a) for a circular-core fiber (C) and a quadratic-core fiber (fiber B, see Tab. F.3) are shown in Fig. H.3(a, b).

The circular-core fiber profiles are clearly offset from the quasi-rotational shape as  $\Delta x$  increases. The profile shape is quite inadequate for illuminating a linear detector with approximately the same intensity on each pixel.

In case of the quadratic-core fiber a tilt of the quasi-flat-top profile shape is visible as  $\Delta x$  increases. The profile is not perfectly flat-top because fiber B has round corners (see Fig. 3.31(d)). Dust particles on the surface (also visible in Fig. 3.31(d)) are the reason for the bump of intensity around pixel 120.

For laser beam pointing fluctuations only relatively small shifts of approximately 10  $\mu\text{m}$  of the light spot during coupling have to be taken into account for a laser beam tilt angle

( $\delta$ ) of 50  $\mu\text{rad}$  (see appendix D.1, Fig. D.6(a)). On the bottom of Fig. H.3 the fractional deviation of profiles for these relatively small shifts of  $< \pm 20 \mu\text{m}$  are shown.

These fractional deviations are slightly smaller ( $< 2\%$ ) for the quadratic-core fiber compared to the circular-core fiber (up to 5%) at the edges of the core region. This comparison indicates that the quadratic-core fiber B is the better choice for the application.

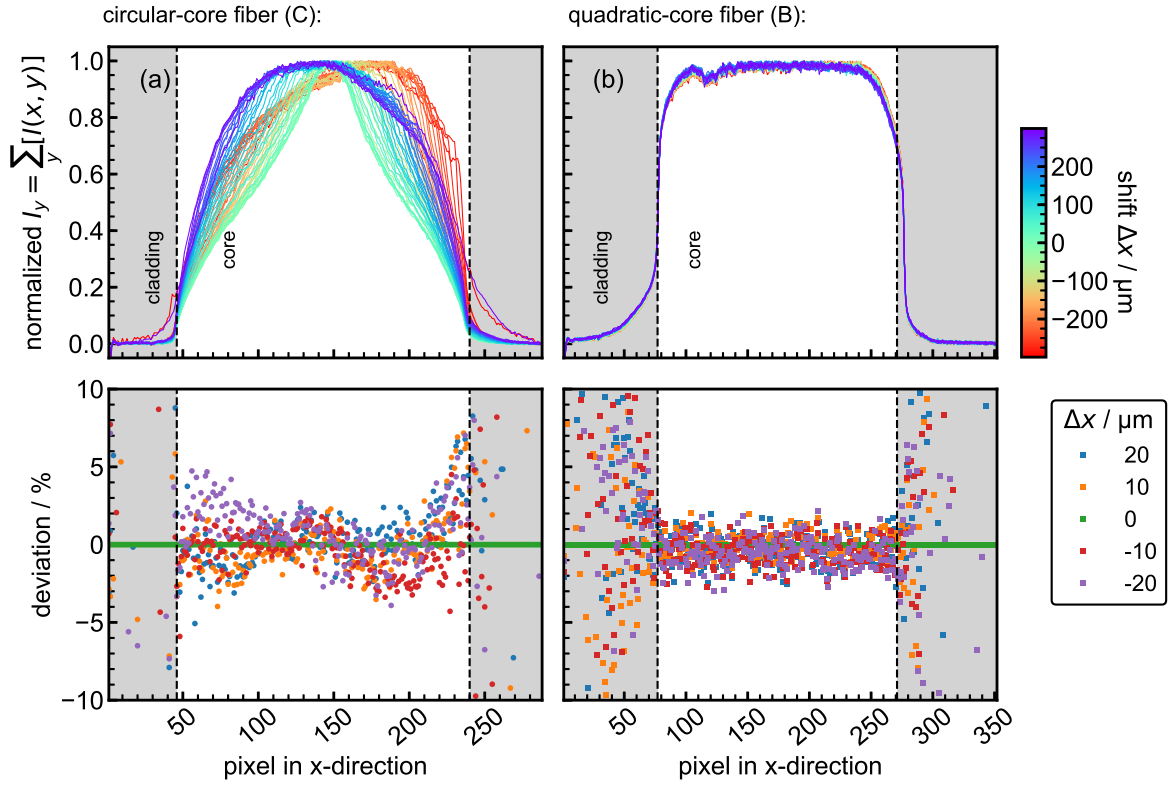


**Figure H.3:** Top: Near-field intensity profiles obtained by summing all vertical pixel intensities (normalized) for different shifts  $\Delta x$ : (a) Circular-core fiber (C), (b) Quadratic-core fiber (fiber B, see Tab. F.3) for  $\Delta z = 0$  and  $f/4.7$ . Bottom: Deviations of the profiles with respect to the centered position ( $\Delta x = 0$ ) for different values of  $\Delta x$ . Exposure time: 1 ms.

### Possible improvements

The measurement scheme applied above and in section 3.5.5 could be improved by averaging over multiple frames per position (xyz of stage), longer exposure times, applying dark-frame and flat-field correction, a higher magnification of the near-field image (to have higher pixel resolution), a microscope objective for imaging (reducing optical aberrations), avoiding overexposure, a better rotational alignment of the core of the quadratic fiber, and using a properly shaped UV-LED (with small focal spot on the fiber entrance) instead of the Zouk laser. A camera without microlens array (see camera C2 in appendix F) and with UV-AR coating should be used. Additionally, studies of the effect of tilts of the incident beam during coupling on the illumination function behind the fiber should be carried out, because tilts on the order of  $0.1^\circ$  occur during laser beam pointing fluctuations (see Fig. D.6(b)).

### Far-field scrambling

During far-field scrambling gain measurements the quasi-collimated light exiting the test fiber is imaged onto the CMOS-camera sensor. Due to different angular distributions of the LED and of the laser (see Fig. H.2) the near- and far-field behind the test fiber look different for both sources and for the same fiber. There is no numerical criterion such as the scrambling gain  $G$  available in the far-field.

Far-field profiles summed along the x- and along the y-direction of a circular-core 600- $\mu\text{m}$  test fiber, and the respective fractional changes as a function of the x-shift of the fiber relative to the previously centered lateral position of the cw-laser are shown in Fig. H.4.

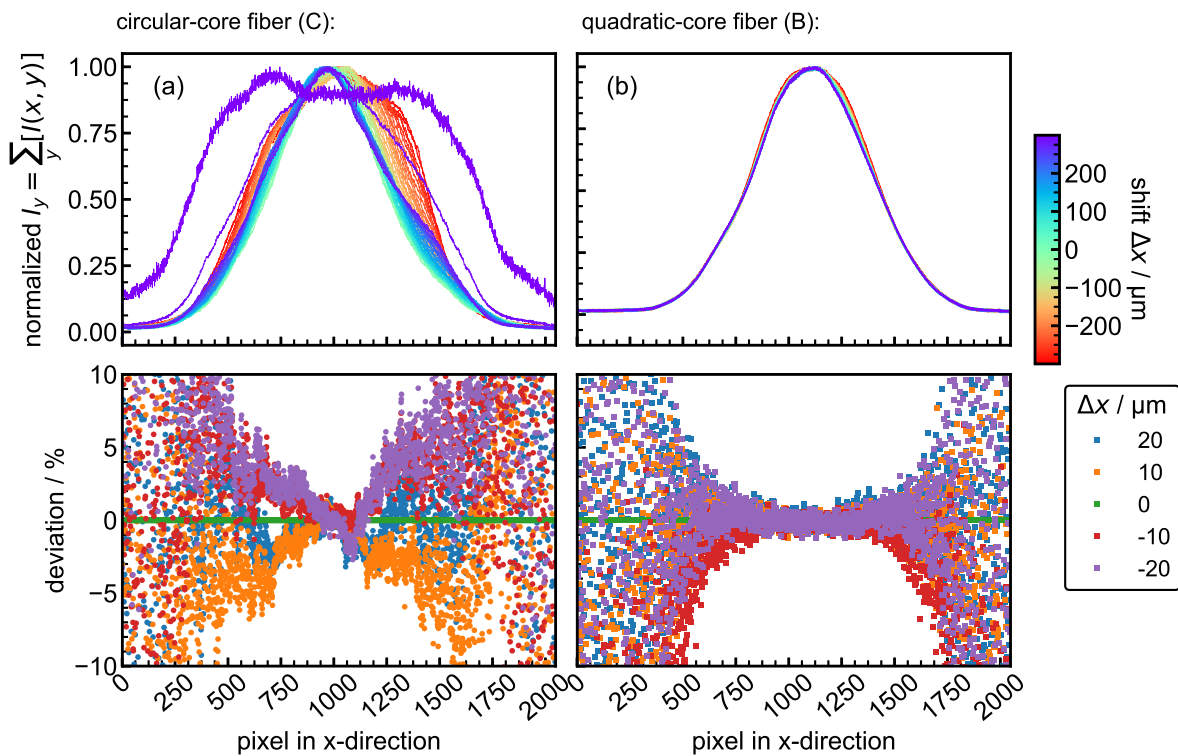


**Figure H.4:** Top: Far-field intensity profiles obtained by summing all vertical pixel intensities (normalized) for different shifts  $\Delta x$ : (a) Circular-core fiber (C), (b) Quadratic-core fiber (B) for  $\Delta z = 0$  and  $f/3.4$ . Bottom: Deviations of the profiles with respect to the centered position ( $\Delta x = 0$ ) for different values of  $\Delta x$ . Exposure time: 30 ms.

In case of the quadratic-core fiber the central region of the illuminated CMOS-camera sensor shows smaller fractional changes for similar x-shifts compared to the circular-core fiber. The quadratic-core fiber-shape was not rotationally aligned with respect to the camera sensor axes (x...horizontal, y...vertical).

In conclusion, the discussed near- and far-field scrambling measurements of circular- and quadratic-core fibers with core diameters of 600  $\mu\text{m}$  suggest that quadratic-core fibers are the better choice in terms of the suppression of illumination function changes due to laser beam pointing fluctuations.

## Near-field and far-field scrambling of a two-lens optical scrambler

A way to increase the optical scrambling may be to apply a two-lens optical scrambler (TLS) between two fibers. The design of the two-lens optical scrambler tested here is provided in appendix D.4. This two-lens scrambler was built using a commercial cage system and was tested with the setup of section 3.5.5.

Results of scrambling gain measurements of the two-lens-scrambler with two circular-core fibers (a) and with a circular-core and a quadratic-core fiber (b) are shown in Fig. H.5. The exposure time was set to 5 ms. Near-field images for both fiber combinations are depicted on the bottom as a function of the shift  $\Delta x$  of the xyz-stage (in Fig. H.5).

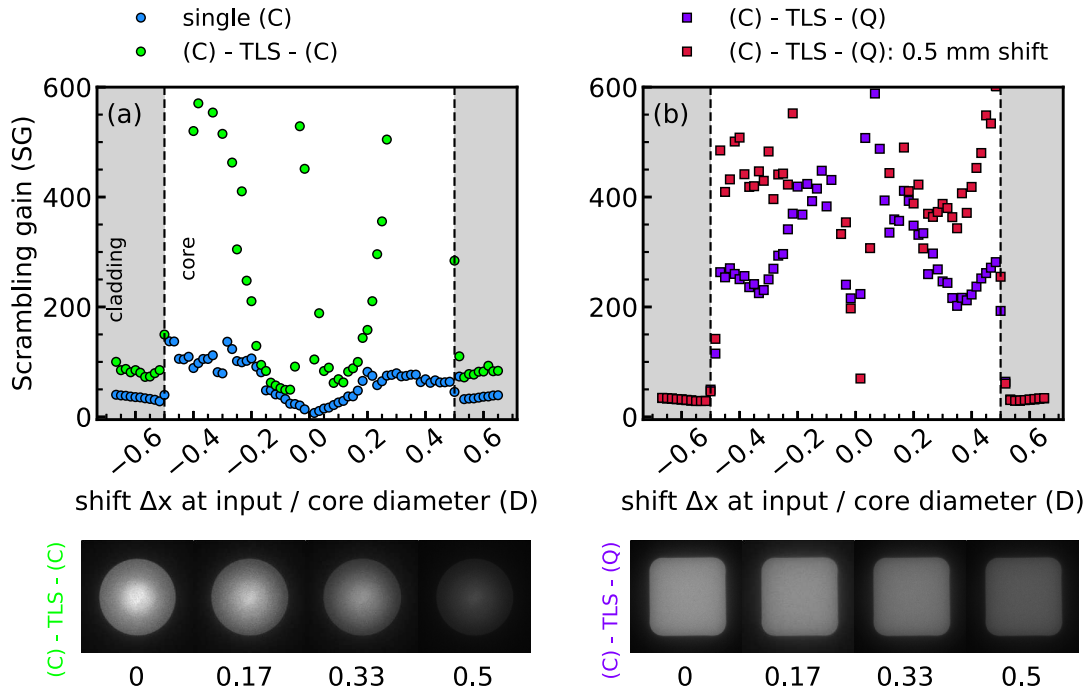


**Figure H.5:** (a) Comparison of scrambling gains (SG) as a function of shift  $\Delta x$  at the fiber input for a circular-core fiber (C2) and a combination of circular-core fiber (C2), two-lens scrambler, and circular-core fiber (C2, see Tab. F.3), i.e.,  $C = C2$ ,  $(C) - \text{TLS} - (C)$ . Below near-field images of the exit face of the second circular-core fiber of this combination are shown for different shifts  $\Delta x/D$ . (b) Scrambling gains (SG) as a function of shift  $\Delta x$  for a combination of a circular-core fiber (C2), two-lens scrambler, and a quadratic-core fiber (Q), i.e.,  $(C) - \text{TLS} - (Q)$ , for different positional shifts of  $C$  and  $Q$  relative to the fibers positions (red).

The resulting scrambling gains and near-field images indicate that the application of a two-lens-scrambler improves optical scrambling. In case of the two circular-core fibers (Fig. H.5(a)) the scrambling gain is increased above all at the edges of the core over three-fold and the annular structure of near-field images for different  $\Delta x$  is more resembling (compared to Fig. 3.31(d)). Fig. H.5(b) shows an increase of the scrambling gain compared to the quadratic-core fiber alone (see Fig. 3.31(b)), as well.

Fig. H.5(b) also shows that the optical scrambling is dependent on the distances of the lenses of the two-lens-scramblers relative to the fibers.

Near- and far-field profiles of the  $(C) - \text{TLS} - (Q)$  combination are shown in Fig. H.6(a) and (b). The exposure time was set to 5 ms for near-field images and to 120 ms for far-field images. In both cases the circular-core fiber (C) was vibrated. The quadratic-core

fiber was aligned parallel with respect to the camera sensor orientation and its input and output surfaces were cleaned prior to the measurements.

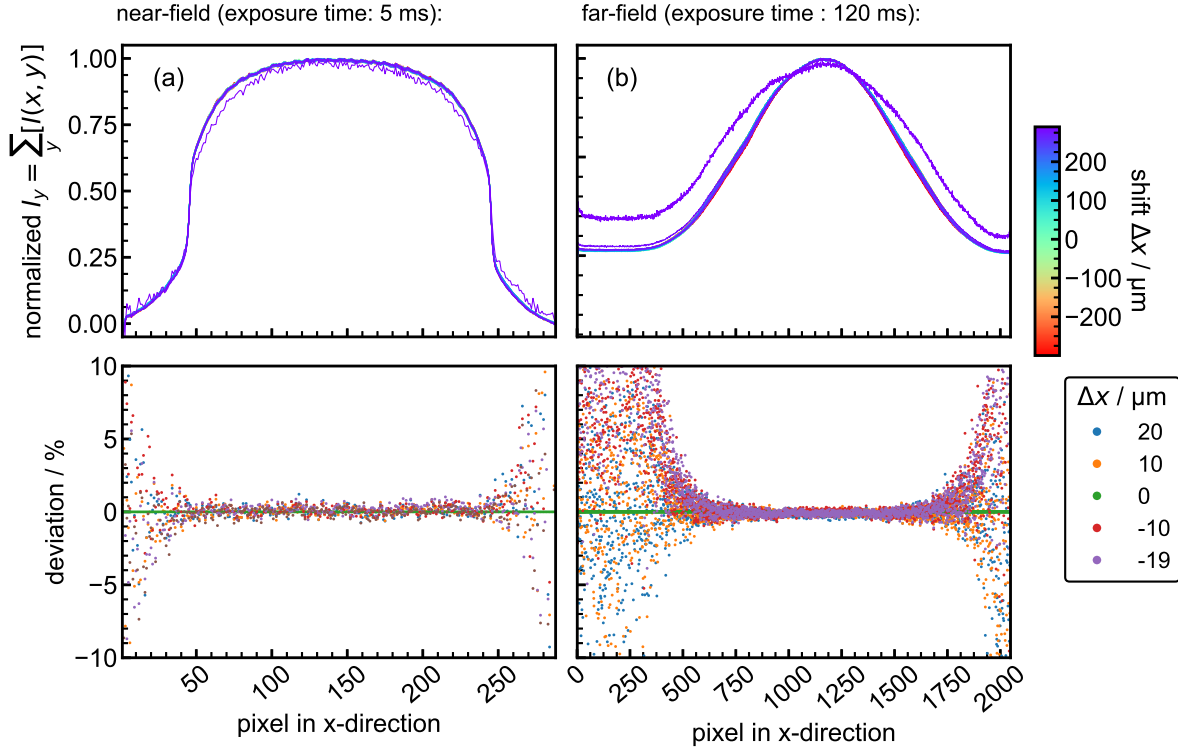


**Figure H.6:** Top: (a) Near-field intensity and (b) far-field intensity profiles of the (C) – TLS – (Q) combination for different shifts  $\Delta x$  of the xyz-stage. Bottom: Deviations of the profiles with respect to the centered position ( $\Delta x = 0$ ) for different values of  $\Delta x$ .

Compared to the single Q fiber in Fig. H.3(b) and Fig. H.4(b) the near- and far-field profile deviations for  $\Delta x = 10 \mu\text{m}$  are flatter ( $< 1\%$ ) over a broader range of pixels in x-direction. For larger shifts (top of Fig. H.6) the profiles show close resemblance. The more round edges of the near-field profile of the (C) – TLS – (Q) combination compared to the single Q fiber are visibly not caused by light coupled into the second cladding. The efficiency of the two-lens scrambler fiber combination with the distance settings used during the measurements was only 25%. Thus, the distance settings of the (C) – TLS – (Q) were not optimized for maximum efficiency.

The highest transmission of the (C) – TLS – (C) was 60% with an efficiency of the 2-lens-scrambler of 75% and with a transmission of 87% through a single C fiber.

A major problem of the assembled two-lens-scrambler is the manual adjustment in the cage system, which is very imprecise and does not provide feedback. This makes it harder to set the lenses to the optimum distances determined in appendix D.4 and therefore limits the scrambling performance and efficiency.

The next section provides an estimation of physical laser beam pointing fluctuations of the WALES/DELICAT transmitter.



# I Estimation of laser transmitter beam pointing fluctuations

Laser beam pointing fluctuations can be induced by an unstable transmitter (so-called laser-induced beam jitter), being in the order of  $30 \mu\text{rad}$  to  $40 \mu\text{rad}$  (RMS) for real-world laser systems ([Blaunstein et al., 2010](#)). Another source of laser beam pointing fluctuations are turbulent eddies of size larger than the beam size. This phenomenon is also called beam wander and is of the same or less order of magnitude. The interested reader finds related information in [Blaunstein et al. \(2010\)](#) and [Andrews and Philipps \(2005\)](#). Ignoring in the following as to why beam pointing fluctuations occur, after backscattering they lead to angle-of-arrival fluctuations at the receiver aperture, translating into lateral shifts of the focal spot of the telescope and lateral shifts of the laser spot during fiber-coupling, affecting the illumination function, and generating a fluctuating wind speed measurement bias (random error).

An estimation of this bias is performed using end-to-end simulations in section 4.3. In the following, measurements are presented to estimate the magnitude of laser beam pointing fluctuations.

In this work laser beam pointing variation is estimated using a white paper screen at a distance  $R = 50 \text{ m}$  in front of the transmitter and receiver optics taking a sequence of frames of the laser beam fluorescent spot on the screen with a CMOS camera (Nikon 3100 camera, with a frame rate of  $23.98 \text{ Hz}$ ) at an angle of  $30^\circ$ . Each Frame is unwarped in perspective (using The OpenCV Library for Python) as shown in Fig. I.1.

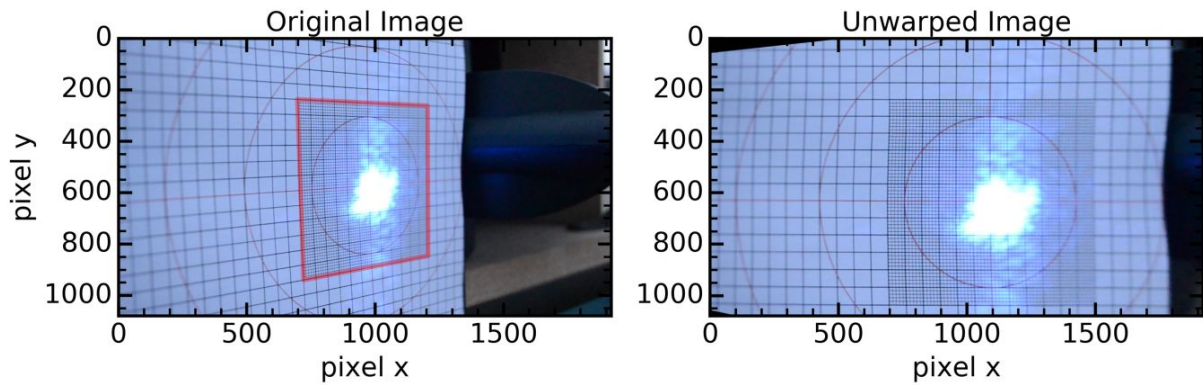


**Figure I.1:** Left: Original Frame, Right: Unwarped frame: correction of perspective using OpenCV in Python programming language.

Afterwards the same region of interest (ROI) is selected for every frame and all intensity values below 75% of the maximum intensity are masked (see Fig. I.2(a)).

In the next step the center of mass ( $CM_x, CM_y$ ) in pixels is determined in horizontal (x) and vertical direction (y), and the fluctuation around its mean ( $\Delta CM_x, \Delta CM_y$ ) = ( $CM_x - \langle CM_x \rangle$ ), ( $CM_y - \langle CM_y \rangle$ ) is determined. Fig. I.2(c) shows the temporal evolution of  $\Delta CM_x$  and  $\Delta CM_y$ . The standard deviations  $\sigma(\Delta CM_x)$  and  $\sigma(\Delta CM_y)$  are in the order of 1 mm. Fig. I.2(d) shows the respective Fourier decompositions, i.e., the frequencies of the fluctuation during the measurement time of 2 min.

The described method is too imprecise to draw further conclusions about the origin of the beam fluctuation and to make any expressions about the realization of turbulence.

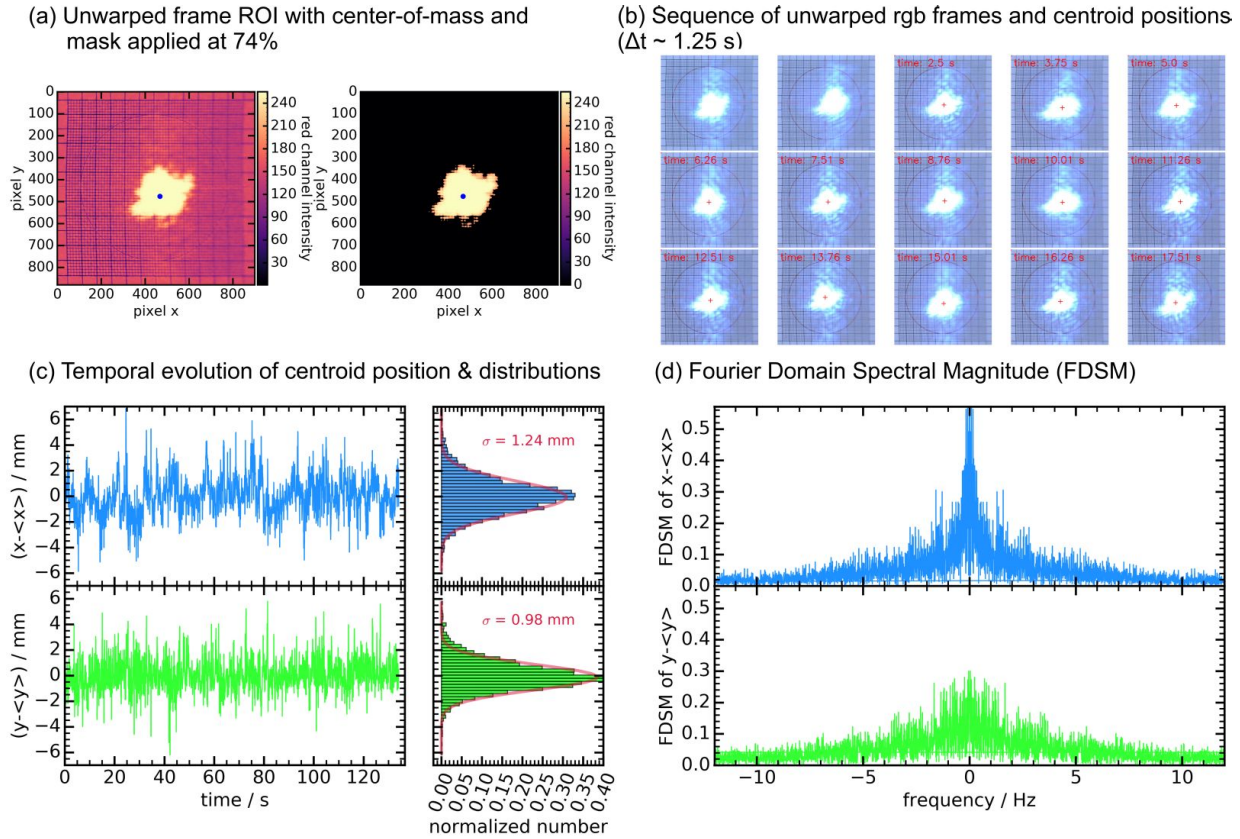


**Figure I.2:** (a) Unwarped frame region-of-interest with 75% mask applied prior to the center-of-mass determination. (b) Sequence of unwarped ROI frames at a distance of 60 m. (c) Temporal evolution of the horizontal and vertical components of the shift of the centroid with respect to the ensemble averaged position. (d) Fourier Domain Spectral Magnitude (FSDM) of horizontal (x) and vertical (y) time series.

The according standard deviation tilt angle of the laser beam is in the order of  $\approx 48 \mu\text{rad}$  ( $3\sigma$ ) during the two minute time series. This value is roughly equivalent to the typical value of 5% to 10% of the divergence value given by laser manufacturers and the divergence of the used laser.

Nevertheless, the measured  $\sigma(\delta)$  can be compared to plausible values that would be obtained due to turbulence. A formula for the root-mean-square (rms) angle-of-arrival (standard deviation) due to turbulence, is given in [Andrews and Philipps \(2005\)](#) (p. 201, eq. 84):

$$\sqrt{\langle \beta_a^2 \rangle} = \sqrt{\frac{2.91}{D^{1/3}} C_n^2 \cdot R}, \quad (\text{I.1})$$

where  $D$  is the diameter of the receiver,  $C_n^2$  is the refractive index structure parameter, and  $R$  is the distance of horizontal propagation. Assuming a constant conservative daytime value of  $C_n^2$  near the ground of  $5 \cdot 10^{-13} \text{ m}^{-2/3}$ , a diameter  $D$  of 140 mm, and  $R = 50 \text{ m}$ ,  $\sqrt{\langle \beta_a^2 \rangle}$  amounts to approximately  $40 \mu\text{rad}$  ( $3\sigma$ ).

The here estimated value of  $\beta_{\text{total}} = \sigma(\delta) \approx 48 \mu\text{rad}$  ( $3\sigma$ ) appears to represent the order of magnitude of laser beam pointing fluctuations, which should be taken into account when estimating the resulting wind speed bias of AEROLI (see section 4.3).

## J Proposed green-UV dichroic mode for determining $R_b$

This section describes a convenient method for estimating the particle backscattering ratio  $R_b$  using dichromatic illumination of the FWFIMI at 355 nm and 532 nm. This mode may allow to estimate  $R_b$  in future validation measurements of AEROLI in low particle concentration environments.

The FWFIMI was fabricated with beamsplitter and AR coatings suitable for UV and green illumination.  $R_{BS}(532 \text{ nm})$  is 48%,  $R_{AR}(532 \text{ nm})$  is  $< 1.5\%$ , and  $R_{HR}(532 \text{ nm})$  is 97% (glass arm mirror) and 95% (air arm mirror) (see appendix E).

$R_{AR}(532 \text{ nm})$  of  $< 1.5\%$  may cause reductions of the instrumental contrast of about 1% to 2% (see appendix D.2).  $R_{HR}(532 \text{ nm})$  does not affect the instrumental contrast, however, reduces overall efficiency.

Although the field-widening contrast factor  $V_{wf}$  was optimized for  $\lambda_L = 355 \text{ nm}$ , partial compensation with  $V_{wf} \approx 0.96$  is achieved at  $\lambda_L = 532 \text{ nm}$  (see Fig. C.15). This is also apparent from plane wave propagation simulations (see appendix C.5), as shown in Fig. J.1(a) for an incident flat-top angular distribution of  $[-20, 20]$  mrad with  $\lambda_L = 532 \text{ nm}$ . The number of imaged fringe periods at 532 nm is about 0.67.

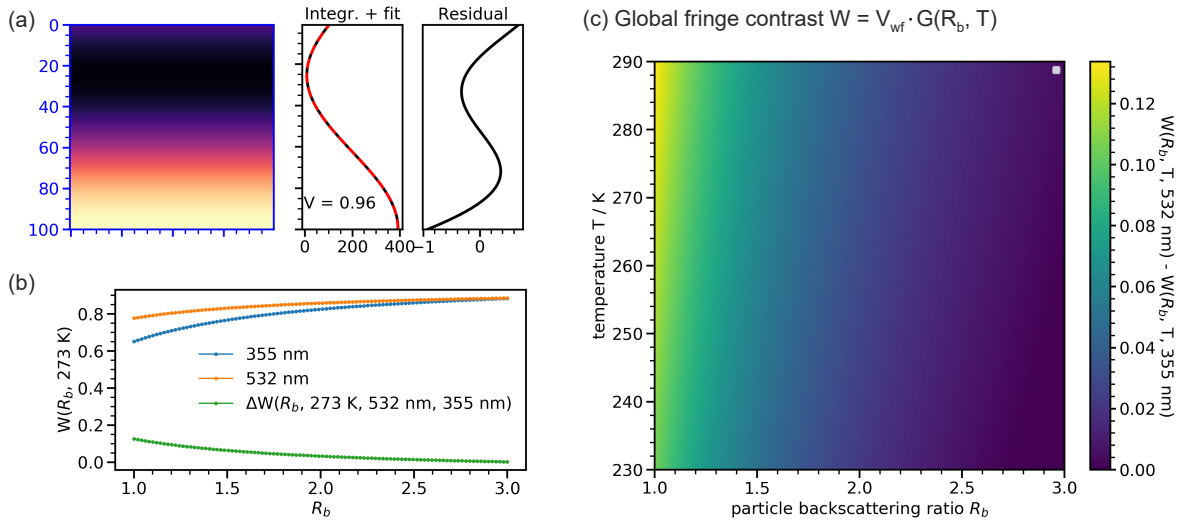


**Figure J.1:** (a) Simulated FWFIMI linear fringe for  $\rho = [-20, 20]$  mrad using the plane wave propagation method (see appendix C.5). (b) Global fringe contrasts, and  $\Delta W(R_b, 273 \text{ K}) = G(R_b, 273 \text{ K}, 532 \text{ nm}) \cdot V_{wf}(532 \text{ nm}) - G(R_b, 273 \text{ K}, 355 \text{ nm}) \cdot V_{wf}(355 \text{ nm})$  as a function of  $R_b$  using eq. 3.4. (c)  $\Delta W(R_b, T)$  as a function of  $R_b$  and  $T$ .

The proposed procedure for estimating  $R_b$  relies on measuring the atmospheric contrasts  $G(R_b, T)$  of both the UV- and the green-backscattering spectrum. The global fringe contrast  $W(R_b, 273 \text{ K}) = V_{wf} \cdot G(R_b, 273 \text{ K})$  as a function of  $R_b$  for  $\lambda_L = 532 \text{ nm}$  and  $\lambda_L = 355 \text{ nm}$  is calculated using eq. 3.4 and is shown in Fig. J.1(b). The difference  $\Delta W = G(R_b, 273 \text{ K}, 532 \text{ nm}) \cdot V_{wf}(532 \text{ nm}) - G(R_b, 273 \text{ K}, 355 \text{ nm}) \cdot V_{wf}(355 \text{ nm})$  shows a hyperbolic dependence on  $R_b$  with  $0.185 \cdot 1/R_b - 0.06$ . The dependence on the atmospheric temperature  $T$  is linear with  $5 \cdot 10^{-4} \cdot T - 0.01$  (for  $R_b = 1$ ) and  $3.3 \cdot 10^{-4} \cdot T - 0.026$  (for  $R_b = 1.5$ ).  $\Delta W$  is shown in Fig. J.1(c) as a function of both  $R_b$  and  $T$ .

A five percent change of  $\Delta W$  will allow to discern  $R_b = 1$  and  $R_b = 1.5$  situations with small dependence (about  $< 3\%$ ) on  $T$  within a 60 K range. However, at constant altitude the temperature variation will be much smaller (few K), e.g., for  $\Delta T = 1$  K the according  $\Delta W$  is  $< 0.05\%$

The proposed method may also help to reduce  $\sigma(u_r)$  by performing phase measurements in a UV-green parallel mode, i.e., by applying a prism or dichroic mirror behind the FWFIMI to image the UV- and the green fringe on two different vertically-stacked photomultiplier tube arrays or laterally shifted on the same PMTA with 32 channels.

End-to-end simulations at a wavelength of 532 nm with  $N = 0.67$  and  $N = 1$  imaged fringe periods using the methodology of chapter 4 are compared to results at 355 nm in Fig. J.2(a). The assumptions are that  $N_{\text{pixel}} = 12$ ,  $h = 10$  km,  $R_b = 1.008$ ,  $V_{355\text{nm}} = 0.95$ ,  $V_{532\text{nm}} = 0.95 \cdot 0.96$ ,  $\eta_{\text{THG}} = 0.3$ ,  $\eta_{\text{SHG}} = 0.55$ ,  $QE_{355\text{nm}} = 0.45$ , and  $QE_{532\text{nm}} = 0.2$ .

Fig. J.2(a) also contains simulation results for unpolarized illumination at 355 nm, yielding an instrumental contrast factor  $V_{\text{BS}}$  of  $(99.9\% + 44\%)/2$  (instead of 99.9% for s-polarization, see section 3.4.3, eq. 3.19) due to a reflectivity of the beamsplitter of the FWFIMI of 5% for p-polarized light. In case that the PBSC of the receiver back-end is omitted the available signal incident on the FWFIMI is doubled.  $r_{\text{Los}} = 10$  Hz is assumed.

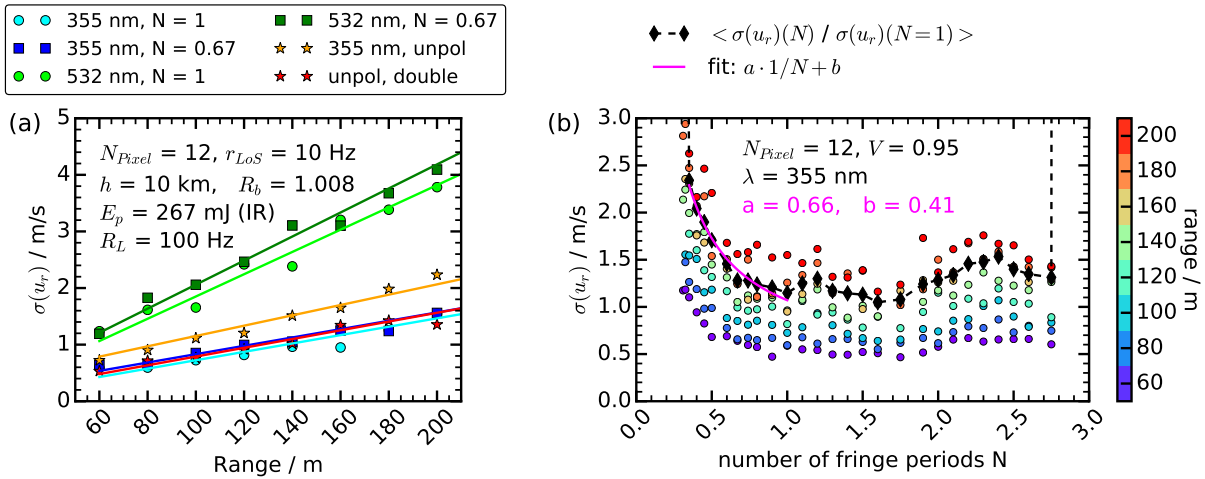


**Figure J.2:** (a) Standard deviation  $\sigma(u_r)$  of 100 end-to-end simulation runs at  $\lambda = 532$  nm versus  $\lambda = 355$  nm for different numbers of imaged fringe periods ( $N$ ) and for unpolarized light. (b)  $\sigma(u_r)$  of 100 end-to-end simulation runs at  $\lambda = 355$  nm as a function of  $N$  with  $r_{\text{Los}} = 10$  Hz.

The precision of  $u_r$  is dependent on  $N$  by  $a \cdot 1/N + b$  up to  $N = 1$  (see fit in Fig. J.2(b)).  $N = 0.67$  yields a factor of 1.4. The reduced precision in case of  $\lambda = 532$  nm is also a consequence of the non-optimal choice of  $FSR$ , which would be 7 GHz for green light (see eq. 3.5,  $\kappa_{(u_r)FIMI} = 5$  at 10.7 GHz). Further reasons are the reduced receiver efficiency of 1.2% at 532 nm and  $\beta_{\text{mol}}(532\text{nm}) < \beta_{\text{mol}}(355\text{nm})$ . The usage of unpolarized light results in an approximate  $\sqrt{2}$  increase of  $\sigma(u_r)$  due to  $V_{\text{BS}}$  (cf. Fig. 3.4(b)). Assuming twice the signal ('double unpol' in Fig. J.2(a)) provides an additional factor of  $1/\sqrt{2}$  (see eq. C.29).

Pulses at a wavelength of 532 nm could be provided by the DELICAT transmitter (see section 3.6) with a modified THG-unit, such that the SHG-532-nm-light is not blocked anymore, expanded, and guided in parallel to the exiting UV-light. For tests of the green-mode alone no further modifications of the receiver would be necessary in case of nightly measurements. Optimized AR-coatings on all receiver optics may be required. The number of illuminated pixels could be adjusted to image more than 0.67 fringe periods, if required.

# Bibliography

- Airbus (2007), Flight operations briefing notes - adverse weather operations - optimum use of the weather radar, *Airbus Customer Services*, available at [http://www.smartcockpit.com/docs/Optimum\\_Use\\_Of\\_The\\_Weather\\_radar.pdf](http://www.smartcockpit.com/docs/Optimum_Use_Of_The_Weather_radar.pdf), visited on 8.08.2018.
- Allington-Smith, J., G. Murray, and U. Lemke (2012), Simulation of complex phenomena in optical fibres, *Mon. Not. R. Astron. Soc.*, 427, 919–933, doi:10.1111/j.1365-2966.2012.21776.x.
- AMS (2018), gust, *American Meteorological Society, Glossary of Meteorology*, available at <http://glossary.ametsoc.org/wiki/Gust>, visited on 8.08.2018.
- Andrews, L. C., and R. L. Philipps (2005), *Laser Beam Propagation through Random Media*, 2nd ed., SPIE, doi:10.1117/3.626196.
- Andrews, L. C., R. L. Phillips, and C. Y. Hopen (2001), *Laser Beam Scintillation with Applications*, SPIE PRESS, doi:10.1117/3.412858.
- Avila, G. (2012), FRD and scrambling properties of recent non-circular fibres, *Proc. SPIE, Ground-based and Airborne Instrumentation for Astronomy IV*, 8446, 8446, doi:10.1117/12.927447.
- Avila, G., and P. Singh (2008), Optical fiber scrambling and light pipes for high accuracy radial velocities measurements, *Proc. SPIE, Advanced Optical and Mechanical Technologies in Telescopes and Instrumentation*, 7018, doi:10.1117/12.789509.
- Banakh, V., and I. Smalikho (2013), *Coherent Doppler Wind Lidars in a Turbulent Atmosphere*, Artech House, ISBN: 978-1-60807-667-3.
- Banakh, V. A., I. N. Smalikho, E. L. Pichugina, and W. A. Brewer (2010), Representativeness of measurements of the dissipation rate of turbulence energy by scanning Doppler lidar, *Atmospheric and Oceanic Optics*, 23(1), 48–54, doi:10.1134/S1024856010010100.
- Barnes, S. I., and P. J. MacQueen (2010), A high-efficiency fibre double-scrambler prototype, *Proc. SPIE, Ground-based and Airborne Instrumentation for Astronomy III*, 7735, 773567, doi:10.1117/12.857945.
- Bauer, T., D. Vechtel, F. Abdelmoula, and T. Immisch (2014), In-Flight Wake Encounter Prediction with the Wake Encounter Avoidance and Advisory System, *6th AIAA Atmospheric and Space Environments Conference, Atlanta, Georgia, USA*, doi:10.2514/6.2014-2333.
- Baynes, J., and P. Tyrdy (2014), Rockwell Collins multiscan threattrack TM weather radar, *Rockwell Collins multiscan threattrack TM weather radar*, available at <https://www.rockwellcollins.com/Products-and-Services/Commercial-Aviation/Flight-Deck/Surveillance/Weather-Radar/WXR-2100-MultiScan-Threat-Track-weather-radar.aspx>, visited on 8.08.2018.



- Beavers, W. I., D. E. Dudgeon, J. W. Beletic, and M. T. Lane (1989), Speckle Imaging through the Atmosphere the Earthbound View, *The Lincoln Laboratory Journal*, 2, 207–228.
- Beck, H., and M. Kühn (2017), Dynamic Data Filtering of Long-Range Doppler LiDAR Wind Speed Measurements, *Remote Sensing*, 9(6), doi:10.3390/rs9060561.
- Behrendt, A., S. Pal, V. Wulfmeyer, A. Valdebenito, and G. Lammel (2011), A novel approach for the characterization of transport and optical properties of aerosol particles near sources i. measurement of particle backscatter coefficient maps with a scanning UV lidar, *Atmos. Environ.*, 45, 2795–2802, doi:10.1016/j.atmosenv.2011.02.061.
- Bennett, F. D., and G. D. Kahl (1953), A Generalized Vector Theory of the Mach-Zehnder Interferometer, *Journal of the Optical Society of America*, 43(2), 71–78, doi:10.1364/JOSA.43.000071.
- BFU (2017), Interim report BFU17-0024-2X, *German Federal Bureau of Aircraft Accident Investigation*, available at [https://www.bfu-web.de/EN/Publications/Interim\\_Reports/IR2017/IR2\\_17\\_0024\\_CL600-A380.pdf?\\_\\_blob=publicationFile](https://www.bfu-web.de/EN/Publications/Interim_Reports/IR2017/IR2_17_0024_CL600-A380.pdf?__blob=publicationFile), visited on 8.08.2018.
- Biniotoglou, I., I. Serikov, D. Nicolae, V. Amiridis, L. Belegante, A. Boscornea, B. Bruggmann, M. Costa Suros, D. Hellmann, P. Kokkalis, H. Linne, I. Stachlewska, and S.-N. Vajaiac (2016), MULTIPLY: Development of a European HSRL Airborne Facility, *Living Planet Symposium, ESA Special Publication*, 740, ISBN: 978-9292213053.
- Bispo dos Santos, J., A. Cesar de Oliveira, J. Gunn, L. Souza de Oliveira, M. Vital de Arruda, B. Castilho, C. D. Gneiding, F. F. Ribeiro, G. Murray, D. J. Reiley, L. Sodré, and C. Mendes de Oliveira (2014), Studying focal ratio degradation of optical fibers for Subaru's Prime Focus Spectrograph, *Proc.SPIE*, 9151, doi:10.1117/12.2056460.
- Blaunstein, N., S. Arnon, A. Zilberman, and N. Kopeika (2010), *Applied Aspects of Optical Communication and Lidar*, CRC Press Taylor & Francis Group, doi:10.1201/9781420090451-c3.
- Born, M., and E. Wolf (1980), *Principles of Optics: Electromagnetic Theory of Propagation, Interference and Diffraction of Light*, 7 ed., Cambridge University Press, ISBN: 978-0521642224.
- Breitsamer, C. (2011), Wake vortex characteristics of transport aircraft, *Progress in Aerospace Sciences*, 47(2), 89–134, doi:10.1016/j.paerosci.2010.09.002.
- Bruneau, D. (2001), Mach-Zehnder interferometer as a spectral analyzer for molecular Doppler wind lidar, *Appl. Opt.*, 40(391399), doi:10.1364/AO.40.000391.
- Bruneau, D. (2002), Fringe-imaging Mach-Zehnder interferometer as a spectral analyzer for molecular Doppler wind lidar, *Appl. Opt.*, 41, 503–510, doi:10.1364/AO.41.000503.
- Bruneau, D., and J. Pelon (2003), Simultaneous measurements of particle backscattering and extinction coefficients and wind velocity by lidar with a Mach-Zehnder interferometer: principle of operation and performance assessment, *Appl. Opt.*, (42), 1101–1114, doi:10.1364/AO.42.001101.



- Bruneau, D., F. Bouzon, J. Spatazza, F. Montmessin, J. Pelon, and B. Faure (2013), Direct-detection wind lidar operating with a multimode laser, *Applied Optics*, 52(20), 4941–4949, doi:10.1364/AO.52.004941.
- Bruneau, D., J. Pelon, F. Blouzon, J. Spatazza, P. Genau, G. Buchholtz, N. Amarouche, A. Abchiche, and O. Aouji (2015), 355-nm high spectral resolution airborne lidar LNG: system description and first results, *Appl. Opt.*, 54, doi:10.1364/AO.54.008776.
- Bucholtz, A. (1995), Rayleigh-scattering calculations for the terrestrial atmosphere, *Appl. Opt.*, 34, 2765–2773, doi:10.1364/AO.34.002765.
- Burnham, D. C., and J. N. Hallock (1982), Chicago monostatic acoustic vortex sensor system., *Report No. DOT-TSC-FAA-79-103.IV*, July, p. 206 pp.
- Cézard, N. (2008), Etude de faisabilité d’un lidar Rayleigh-Mie pour des mesures à courte portée de la vitesse de l’air, de sa température et de sa densité, Ph.D. thesis, Département d’Optique Théorique et Appliquée de l’ONERA, dissertation, available at <https://pastel.archives-ouvertes.fr/pastel-00004485/document>, visited on 8.08.2018.
- Cézard, N., A. Dolfi-Bouteyre, J.-P. Huignard, and P. H. Flamant (2009a), Performance evaluation of a dual fringe-imaging Michelson interferometer for air parameter measurements with a 355 nm Rayleigh-Mie lidar, *Appl. Opt.*, 48(23212332), doi:10.1364/AO.48.002321.
- Cézard, N., C. Besson, A. Dolfi-Bouteyre, and L. Lombard (2009b), Airflow Characterization by Rayleigh-Mie Lidars, *AerospaceLab*, <hal-01180643>, pp. 1–4.
- Chan, P. W., and Y. F. Lee (2012), Application of Short-Range Lidar in Wind Shear Alerting, *Journal of Atmospheric and Oceanic Technology*, 29(2), 207–220, doi:10.1175/JTECH-D-11-00086.1.
- Chazelas, B., F. Pepe, and F. Wildi (2012), Optical fibers for precise radial velocities: an update, *Proc.SPIE*, 8450, 8450 – 8450 – 9, doi:10.1117/12.926188.
- Cheng, Z., D. Liu, J. Luo, Y. Yang, Y. Zhou, L. Duan, L. Su., L. Yang, Y. Shen, K. Wang, and J. Bai (2015), Field-widened Michelson interferometer for spectral discrimination in high-spectral-resolution lidar: theoretical framework, *Opt. Express*, 23, 12,117–12,134, doi:10.1364/OE.23.012117.
- CIAIAC (2011), Wake Turbulence Encounter in High-Level Airspace Involving an AIRBUS A320 Aircraft Registration EC-JDK, Operated by Vueling, in Route Between Barcelona and Santiago de Compostela on 28 May 2006, *Comisión de Investigación de Accidentes e Incidentes de Aviación Civil, Rept. IN-029/2006*, Madrid, Feb.
- CoboltAB (2016), Cobolt 05-01 Series, *OWNERS MANUAL, D0106-B*, June.
- Collis, R. T. H., and P. B. Russell (1976), *Laser Monitoring of the Atmosphere, Topics in Applied Physics*, vol. 14, chap. Lidar measurement of particles and gases by elastic backscattering and differential absorption, pp. 71–151, Springer.

- Corbett, J., T. Butterley, and J. R. Allingthorn-Smith (2007), Fibre modal power distributions in astronomy and their application to OH-suppression fibres, *Mon. Not. R. Astron. Soc.*, 378, 482–492, doi:10.1111/j.1365-2966.2007.11765.x.
- Cornman, L. B., C. S. Morse, and G. Cuning (1995), Real-time estimation of atmospheric turbulence severity from in-situ aircraft measurements, *Journal of Aircraft*, (1), 171–177, doi:10.2514/3.46697.
- Crow, S. C. (1970), Stability Terminal Theory for a Pair of Trailing Vortices, *AIAA Journal*, 8.12, 2172–2179, doi:10.2514/3.6083.
- Crow, S. C., and E. R. Bate (1976), Lifespan of trailing vortices in a turbulent atmosphere, *Journal of Aircraft*, 13.7, 476–482, doi:10.2514/3.44537.
- Dolfi-Bouteyre, A., B. Augere, M. Valla, D. Goular, D. Fleury, G. Canat, C. Planchat, T. Gaudo, C. Besson, A. GILLIOT, J. Cariou, O. Petilon, J. Lawson-Daku, S. Brousmiche, S. Lugan, L. Bricteux, and B. Macq (2009a), Aircraft Wake Vortex Study and Characterization with 1.5- $\mu\text{m}$  Fiber Doppler Lidar, *AerospaceLab*, (1), 1–13.
- Dolfi-Bouteyre, A., G. Canat, M. Valla, B. Augere, C. Besson, D. Goular, L. Lombard, J.-P. Cariou, A. Durecu, D. Fleury, L. Bricteux, S. Brousmiche, S. Lugan, and B. Macq (2009b), Pulsed 1.5 $\mu\text{m}$  LIDAR for Axial Aircraft Wake Vortex Detection Based on High-Brightness Large-Core Fiber Amplifier, *IEEE J. Sel. Top. Quantum Electron.*, doi:10.1109/JSTQE.2008.2010463.
- Dors, I., J. P. McHugh, G. Y. Jumper, and J. Roadcap (2011), Velocity spectra and turbulence using direct detection lidar and comparison with thermosonde measurements, *Journal of Geophysical Research: Atmospheres*, 116(D1), doi:10.1029/2010JD014606.
- Douxchamps, D., S. Lugan, Y. Verschueren, L. Mutuel, and B. Macq (2009), On-board axial detection of wake vortices using a 2- $\mu\text{m}$  LiDAR, *IEEE J. Quantum Electron*, 15(2), 441–450.
- Doviak, R. J., and D. S. Zrnic (1984), *Doppler Radar and Weather Observations*, Equation 6.22b, Academic Press, New York,.
- Durand, Y., R. Meynart, M. Endemann, E. Chinal, D. Morançais, T. Schröder, and O. Reitebuch (2005), Manufacturing of an airborne demonstrator of ALADIN: the direct detection Doppler wind lidar for ADM-Aeolus, *Proc. SPIE 5984*, doi:10.1117/12.627789.
- Ehlers, J., and N. Fezans (2015), *Advances in aerospace guidance, navigation and control*, chap. Airborne Doppler LiDAR sensor parameter analysis for wake vortex impact alleviation purposes, pp. 433–453, Springer, Toulouse, doi:10.1007/978-3-319-17518-8.
- Ehlers, J., D. Fischenberg, and D. Niedermeier (2015), Wake Impact Alleviation Control Based on Wake Identification, *JOURNAL OF AIRCRAFT*, 52, doi:10.2514/1.C033157.
- EPIGAP (2011), Product Data Sheet: EOLD-355-525, *Rev. 01*.
- Epworth, R. E. (1978), The Phenomenon of Modal Noise in Analogue and Digital Optical Fibre Systems, *Fourth European Conference on Optical Communication*, B. Catania, ed. (Istituto Internazionale delle Comunicazioni Via Pertinace, Villa Piaggio, Genova, Italy, 1978, pp. 492501.

- EUROCONTROL (2006), EUROCONTROL and Joint Aviation Authorities and Federal Aviation Administration and Airbus, Safety Case for Wake Vortex Separation Criteria for A380-8000, *Edition 2.0, 16 November*.
- Evans, J. K. (2014), An updated examination of aviation accidents associated with turbulence, wind shear and thunderstorm, *AMA-RPT No. 14-14, NF1676L-20566 (Analytical Mechanics Associates, Inc.)*.
- FAA (2014), Advisory Circular - Aircraft Wake Turbulence, *AC 90-23G. Federal Aviation Administration*.
- FAA (2018), Turbulence: Staying Safe, *Federal Aviation Administration*, available at [https://www.faa.gov/travelers/fly\\_safe/turbulence/](https://www.faa.gov/travelers/fly_safe/turbulence/), visited on 8.08.2018.
- Feger, T., A. Brucalassi, F. U. Grupp, F. Lang-Bardl, R. Holzwarth, and R. Hopp, U. Bender (2012), A testbed for simultaneous measurement of fiber near and far-field for the evaluation of fiber scrambling properties, *Proc.SPIE*, 8446, 8446 – 8446 – 14, doi:10.1117/12.925624.
- Fezans, N., and H.-D. Joos (2017), Combined Feedback and LIDAR-based Feedforward Active Load Alleviation, *Submitted to the 2017 AIAA Aviation/Atmospheric Flight Mechanics conference, 5 - 9 June 2017, Denver, Colorado, USA*, doi:10.2514/6.2017-3548.
- Fezans, N., J. Schwithal, and D. Fischenberg (2017), In-flight remote sensing and identification of gusts, turbulence, and wake vortices using a Doppler LIDAR, *CEAS Aeronaut J*, doi:10.1007/s13272-017-0240-9.
- Fischenberg, D. (2013), Online Wake Identification Algorithms Using Forward Looking LIDAR Sensor Measurements, *Institute report IB 111-2013/11.DLR*.
- Fortunato, G. (1997), L'interféromètre de Michelson, quelques aspects théoriques et expérimentaux, *Bulletin de l'Union des Physiciens*, 91, 15–56.
- Frehlich, R., and R. Sharman (2004), Estimates of Turbulence from Numerical Weather Prediction Model Output with Applications to Turbulence diagnosis and data assimilation, *Monthly Weather Review*, 132(10), 2308–2324, doi:10.1175/1520-0493(2004)132<2308:EOTFNW>2.0.CO;2.
- Frehlich, R. G., and M. J. Yadlowsky (1994), Performance of Mean-frequency Estimators for Doppler Radar and Lidar, *J. Atmos. Ocean. Technol.*, 11(5), 1217–1230, doi:10.1175/1520-0426(1994)011<1217:POMFEF>2.0.CO;2.
- Gagné, J.-M., J.-P. Saint-Dizier, and M. Picard (1974), Méthode dechantillonnage des fonctions déterministes en spectroscopie: application à un spectromètre multicanal par comptage photonique, *Appl. Opt.*, 13(3), 581–588, doi:10.1364/AO.13.000581.
- Gerz, T. S., F. Holzäpfel, and D. Darracq (2002), Commercial aircraft wake vortices, *Progress in Aerospace Sciences*, 38, 181–208, doi:10.1016/S0376-0421(02)00004-0.
- Ghosh, G. (1997), *Handbook of Thermo-Optic Coefficients of Optical Materials With Applications*, 1st ed., Academic Press of USA.

- Giesen, A., H. Hügel, A. Voss, K. Wittig, U. Brauch, and H. Opower (1994), Scalable concept for diode-pumped high-power solid-state lasers, *Applied Physics B*, 58(5), 365–372, doi:10.1007/BF01081875.
- Ginevsky, A. S., and A. I. Zhelannikov (2009), *Vortex wakes of Aircrafts*, Springer, ISBN: 978-3-642-01760-5.
- Goodman, J. (2007), *Speckle Phenomena in Optics: Theory and Applications*, 1 ed., Englewood: Roberts and Company, ISBN: 0-9747077-9-1.
- Goodman, J. W. (1965), Some effects of target-induced scintillation on optical radar performance, *Proceedings of the IEEE*, 53, 1688–1700, doi:10.1109/PROC.1965.4341.
- Goodman, J. W. (1975), *Laser Speckle and Related phenomena*, chap. Statistical Properties of Laser Speckle Patterns, pp. 9–75, Springer-Verlag, ISBN: 3-540-07498-8.
- Goodman, J. W., and E. G. Rawson (1981), Statistics of modal noise in fibers: a case of constrained speckle, *Optics Letters*, 6, 324–326, doi:10.1364/OL.6.000324.
- Goodman, W. J. (2015), *Statistical Optics*, 2nd ed., John Wiley & Sons, ISBN: 978-1-119-00945-0.
- Graeme, J. G. (1995), *Photodiode Amplifiers - Op Amp Solutions*, McGraw-Hill, ISBN: 978-0070242470.
- Gross, H., H. Zügge, M. Peschka, and F. Blechinger (2007), *Handbook of Optical Systems, Volume 3: Aberration Theory and Correction of Optical Systems*, Wiley, ISBN: 9783527403790.
- Groß, S., V. Freudenthaler, M. Wirth, and B. Weinzierl (2015), Towards an aerosol classification scheme for future earthcare lidar observations and implications for research needs, *Atmos. Sci. Lett.*, 16, 77–82, doi:10.1002/asl2.524.
- Grund, C. J., J. Howell, R. Pierce, and M. Stephens (2009), Optical autocovariance direct detection lidar for simultaneous wind, aerosol, and chemistry profiling from ground, air, and space platforms, *Proc. SPIE 7312, Advanced Environmental, Chemical, and Biological Sensing Technologies VI*, 73120U (30 April 2009), doi:10.1117/12.824204.
- Ha, W., S. Lee, Y. Jung, J. K. Kim, and K. Oh (2009), Acousto-optic control of speckle contrast in multimode fibers with a cylindrical piezoelectric transducer oscillating in the radial direction, *Optics Express*, 17(20), 17,536, doi:10.1364/OE.17.017536.
- Halverson, S., A. Roy, S. Mahadevan, L. Ramsey, E. Levi, C. Schwab, F. Hearty, and N. MacDonald (2015), An efficient, compact, and versatile fiber double scrambler for high precision radial velocity instruments, *The Astrophysical Journal*, 806(61), doi:10.1088/0004-637X/806/1/61.
- Hamamatsu (2007), *PMT Handbook, version 3*, Hamamatsu Photonics.
- Hamamatsu (2011), Data sheet: Linear Array Multianode PMT Assembly and Module, *Hamamatsu Photonics KK, Electron Tube Division*.

- Hansen, G. (1941), Die Sichtbarkeit der Interferenzen beim Michelson- und Twyman-Interferometer, *Zeitschrift für Instrumentenkunde*, (61), 411.
- Hardesty, M., S. Tucker, S. Baidar, and M. Beubien (2018), Airborne tests of an OAWL Doppler lidar: Results and potential for space deployment, *EPJ Web of Conferences, ILRC 28*, 176, doi:110.1051/epjconf/201817602004.
- Harlander, J. M. (2015), St. Cloud State University, St. Cloud, Minnesota, *personal communication*.
- Harlander, J. M., and C. Englert (2013), Design of a real-fringe DASH interferometer for observations of thermospheric winds from a small satellite, in *Imaging and Applied Optics, OSA Technical Digest (online)*, paper FW1D.2, doi:10.1364/FTS.2013.FW1D.2.
- Harlander, J. M., F. L. Roesler, R. C. Englert, J. G. Cardon, R. R. Conway, C. M. Brown, and J. Wimperis (2003), Robust monolithic ultraviolet interferometer for the SHIMMER instrument on STPSat-1, *Applied Optics*, 42(15), 2829–2834, doi:10.1364/AO.42.002829.
- Harris, M., R. Young, R. I. Köpp, F. Dolfi, and J.-P. Cariou (2002), Wake vortex detection and monitoring, *Aerospace Science and Technology*, 6(5), 325–331, doi:10.1016/S1270-9638(02)01171-9.
- Hecht, E. (2008), *Optics*, 4th ed., Addison Wesley, ISBN: 978-0805385663.
- Hénault, F. (2015), Quantum physics and the beam splitter mystery, *Proc. SPIE 9570*, doi:10.1117/12.2186291.
- Henderson, S. W. (2013), Review of Fundamental Characteristics of Coherent and Direct Detection Doppler Receivers and Implications to Wind Lidar System Design, *17th CLRC*.
- Henderson, S. W., P. Gatt, D. Rees, and M. Huffaker (2005), *Laser Remote Sensing*, chap. Wind Lidar, pp. 469–779, Taylor and Francis Group, ISBN: 978-0824742560.
- Herbst, J., and P. Vrancken (2016), Design of a monolithic Michelson interferometer for fringe imaging in a near-field, UV, direct-detection Doppler wind lidar, *Applied Optics*, 55(25), doi:10.1364/AO.55.006910.
- Hernandez, G. (1986), *Fabry-Perot Interferometers*, Cambridge University Press, ISBN: 978-0521368124.
- Hilliard, R. L., and G. G. Shepherd (1966), Wide-Angle Michelson Interferometer for Measuring Doppler Line Widths, *JOSA*, 56(3), 362–369, doi:10.1364/JOSA.56.000362.
- Hirschberger, M. (2013), Beiträge zur Erfassung von Wirbelschleppen mit Lidar: Simulation und Analyse rückgestreuter Signale zur Windfeldbestimmung vor Flugzeugen., *Dissertation, LMU München: Fakultät für Mathematik, Informatik und Statistik*.
- Hirschberger, M. C., and G. Ehret (2011), Simulation and high-precision wavelength determination of noisy 2D Fabry-Pérot interferometric rings for direct-detection Doppler lidar and laser spectroscopy, *Appl. Phys. B*, 103(207222), doi:10.1007/s00340-011-4391-9.
- Hoblitt, F. M. (1988), *Gust Loads on Aircraft: Concepts and Applications*, American Institute of Aeronautics and Astronautics, Washington DC, doi:10.2514/4.861888.

- Holzäpfel, F. (2003), Probabilistic Two-Phase Wake Vortex Decay and Transport Model, *Journal of Aircraft*, 40, 323–331, doi:10.2514/2.3096.
- Holzäpfel, F. (2005), Aircraft Wake Vortex Evolution and Prediction, *Habilitation, Technical University Munich*.
- Holzäpfel, F. (2006), Probabilistic Two-Phase Aircraft Wake-Vortex Model: Further Development and Assessment, *Journal of Aircraft*, 3, 700–708, doi:10.2514/1.16798.
- Holzäpfel, F., A. Stephan, T. Heel, and S. Körner (2016), Enhanced wake vortex decay in ground proximity triggered by plate lines, *Aircr. Eng.*, 88, 206–214, doi:10.1108/AEAT-02-2015-0045.
- Hoogstraten, M., H. G. Visser, D. Hart, V. Treve, and F. Rooseleer (2015), Improved Understanding of En-Route Wake Vortex Encounters, *Journal of Aircraft*, 52(3), 981–989, doi:10.2514/1.C032858.
- Hunter, T. R., and L. W. Ramsey (1992), Scrambling Properties of Optical Fibers and the Performance of a Double Scrambler, *Publications of the Astronomical Society of the Pacific*, 104, 1244–1251, doi:10.1086/133115.
- IATA (2015), Air Passenger Market Analysis, *International Air Transport Association*, available at <https://www.iata.org/publications/economics/Reports/pax-monthly-analysis/passenger-analysis-dec-2015.pdf>, visited on 8.08.2018.
- ICAO (2008), Guidance on A380-800 Wake Vortex Aspects, *Tech. rep. REC/OPS/SEP - 08-0294.SLG*, International Civil Aviation Organization.
- ICAO (2010), Meteorological Service for International Air Navigation Int. Civ.
- ICAO (2016), Procedures for Air Navigation Services - Air Traffic Management, *Tech. rep. Doc 4444*, 16th edition.
- Imai, M. (1986), Statistical Properties of Optical Fiber Speckles, *Bulletin of the Faculty of Engineering, Hokkaido University*, No. 130.
- Inokuchi, H., H. Tanaka, and T. Ando (2009), Development of an Onboard Doppler Lidar for Flight Safety, *J. Aircr.*, 46(4), 1411–1415, doi:10.2514/1.41738.
- Inokuchi, H., M. Furuta, and T. Inagaki (2014), High Altitude Turbulence Detection Using an Airborne Doppler Lidar, *29th Congress of the International Council of the Aeronautical Sciences (ICAS)*, St. Petersburg, Russia, 712 September.
- Inokuchi, H., T. Akiyama, and S. Machida (2016), Development of an Onboard Safety Avionics System using a Doppler Lidar, *18th Coherent Laser Radar Conference (CLRC)*, June 26 - July 1.
- Jones, E., T. Oliphant, P. Peterson, et al. (2001), SciPy: Open Source Scientific Tools for Python, URL: <http://www.scipy.org/>.
- Joosten, S. M., R. Busch, S. Marzenell, C. Ziolk, and D. Sutter (2014), High power UV from a thin-disk laser system, *Proc.SPIE*, 8959, 8959 – 8959 – 5, doi:10.1117/12.2039414.



- Kameyama, S., T. Ando, K. Asake, Y. Hirano, and S. Wadaka (2007), Compact all-fiber pulsed coherent Doppler lidar system for wind sensing, *Appl. Opt.*, *46*(11), 1953–1962, doi:10.1364/AO.46.001953.
- Keane, M., D. Buckton, M. Redfern, C. Bollig, C. Wedekind, F. Kpp, and F. Berni (2002), Axial Detection of Aircraft Wake Vortices Using Doppler Lidar, *Journal of Aircraft*, *39*(5), 850–861, doi:10.2514/2.3005.
- Kolmogorov, A. N. (1941), The Local Structure of Turbulence in Incompressible Viscous Fluid for Very Large Reynolds Numbers, *Doklady Acad Sci. USSR*, *31*, 301–305.
- König, R., and K.-U. Hahn (1990), Load Alleviation and Ride Smoothing Investigations Using ATTAS, In: *Proceedings of the 17th congress of the international council of the aeronautical sciences, Stockholm, Sweden*,.
- Köpp, F. (1994), Doppler lidar investigation of wake vortex transport between closely spaced parallel runways, *AIAA Journal*, *32*(4), 805–810.
- Köpp, F., S. Rahm, and I. Smalikho (2004), Characterization of Aircraft Wake Vortices by 2- $\mu$ m Pulsed Doppler Lidar, *J. Atmos. Ocean. Technol.*, *21*, 194–206.
- Köpp, F., S. Rahm, I. Smakikho, A. Dolfi, J.-P. Cariou, and M. Harris (2005), Comparison of Wake-Vortex Parameters Measured by Pulsed and Continuous-Wave Lidars, *Journal of Aircraft*, *42*(4), 916–923, doi:10.2514/1.8177.
- Kovalev, V. A., and W. E. Eichinger (2005), *Elastic Lidar: Theory, Practice, and Analysis Methods*, John Wiley & Sons, Inc., ISBN: 9780471643173.
- Kristensen, L., P. Kirkegaard, and T. Mikkelsen (2012), *Determining the Velocity Fine Structure by a Laser Anemometer in VAD operation*, DTU Wind Energy, Denmark.
- Kundu, P. K., and I. M. Cohen (2004), *Fluid Mechanics*, Elsevier Academic Press, San Diego, CA, ISBN: 978-0124059351.
- Lane, T. P., R. D. Sharman, S. B. Trier, R. G. Fovell, and J. K. Williams (2012), Recent Advances in the Understanding of Near-Cloud Turbulence, *Bulletin of the American Meteorological Society*, *93*(4), 499–515, doi:10.1175/BAMS-D-11-00062.1.
- Lee, D., and M. Wiswall (2007), A Parallel Implementation of the Simplex Function Minimization Routine, *Comput Econ*, *30*, 171–187, doi:10.1007/s10614-007-9094-2.
- Lemke, U., R. Allington-Smith, and J. Stürmer (2012), Understanding incomplete scrambling in fibres: Experimental investigations, *Proceedings of SPIE*, *8450*, doi:10.1117/12.926148.
- Lemmerz, C., O. Lux, O. Reitebuch, B. Witschas, and C. Wührer (2017), Frequency and timing stability of an airborne injection-seeded Nd:YAG laser system for direct-detection wind lidar, *Applied Optics*, *56*(32), 9057–9068, doi:10.1364/AO.56.009057.
- Leosphere (2016), Windcube 100s/200s/400s weather climate brochure, *Leosphere*.

- Liu, D., C. Hostetler, I. Miller, A. Cook, and J. Hair (2012), System analysis of a tilted field-widened Michelson interferometer for high spectral resolution lidar, *Opt. Express*, 20, 1406–1420, doi:10.1364/OE.20.001406.
- Liu, Z., and T. Kobayashi (1996), Differential Discrimination Technique for Incoherent Doppler Lidar to Measure Atmospheric Wind and Backscatter Ratio, *Opt. Rev.*, (3), 4752, doi:10.1007/s10043-996-0047-0.
- Liu, Z., W. Chen, T. Zhang, J. Hair, and C. She (1997), An incoherent Doppler lidar for ground-based atmospheric wind profiling, *Applied Physics B*, 64(5), 561–566, doi:10.1007/s003400050215.
- Liu, Z., B. Liu, Z. Li, Z. Yan, S. Wu, and Z. Sun (2007), Wind measurements with incoherent Doppler lidar based on iodine filters at night and day, *Applied Physics B*, 88(2), 327–335, doi:10.1007/s00340-007-2674-y.
- Looye, G., T. Lombaerts, and T. Kier (2012), Design and flight testing of feedback control laws, *Research Report 2012-02 (The DLR Project Wetter und Fliegen, German Aerospace Center)*, pp. 162–170, doi:10.1109/TCST.2006.880203.
- Lux, O., C. Lemmerz, F. Weiler, U. Marksteiner, B. Witschas, S. Rahm, A. Schäfler, and O. Reitebuch (2018), Airborne wind lidar observations over the North Atlantic in 2016 for the pre-launch validation of the satellite mission Aeolus, *Atmospheric Measurement Techniques*, 11(6), 3297–3322, doi:10.5194/amt-11-3297-2018.
- Mahadevan, S., J. Ge, C. DeWitt, J. C. van Eyken, and G. Friedman (2004), Design of a stable fixed delay interferometer prototype for the ET project, *Proc. SPIE*, 5492, 615–623, doi:10.1117/12.550447.
- Mariscal, J.-F., D. Bruneau, J. Pelon, M. Van Haecke, F. Blouzon, F. Montmessin, and H. Chepfer (2018), High spectral resolution lidar based on quad mach zehnder interferometer for aerosols and wind measurements on board space missions, *EPJ Web of Conferences 176, ILRC 28, 176*, doi:10.1051/epjconf/201817602017.
- McDonough, R. N., and A. D. Whalen (1995), *Detection of Signals in Noise*, 2nd ed., Academic Press, Inc., ISBN: 978-0127448527.
- McGill, M. J., and J. D. Spinhirne (1998), Comparison of two direct-detection Doppler lidar techniques, *Opt. Eng.*, 37, 2675–2686, doi:10.1117/1.601804.
- McKay, J. A. (1998), Modeling of direct detection Doppler wind lidar. I. The edge technique, *Applied Optics*, 37, 6480–6486, doi:10.1364/AO.37.006480.
- McKay, J. A. (2002), Assessment of a multibeam Fizeau wedge interferometer for Doppler wind lidar, *Appl. Opt.*, 41, 1760–1767, doi:10.1364/AO.41.001760.
- Measures, R. M. (1992), *Laser Remote Sensing*, Wiley, Florida, ISBN: 0-89464-619-2.
- Meerkötter, R. (2018), personal communication, *Institute of Atmospheric Physics, German Aerospace Center (DLR)*.

- Meerkötter, R., and M. Degünther (2001), A Radiative Transfer Case Study for 3-d cloud effects in the UV, *Geophysical Research Letters*, 28(9), 1683–1686, doi:10.1029/2000GL011932.
- Melgosa Farrés, M., X. Prats Menéndez, S. Ruiz Navarro, J. Tarragó, J. Busto, and M. Steen (2017), A novel framework to assess the wake vortex hazards risk supported by aircraft in en-route operations, A: *SESAR Innovation Days*. "Proceedings of the 7th SESAR Innovation Days". Belgrade, pp. 1–6.
- Michelson, A. A. (1891), Visibility of Interference-Fringes in the Focus of a Telescope, *Philos. Mag. Ser. 5*, 31(190), 256–259, doi:10.1086/120291.
- Mie, G. (1908), Beiträge zur Optik trüber Medien, speziell kolloidaler Metallösungen, *Annalen der Physik, Vierte Folge, Band 25*, (3), 377–445, doi:10.1002/andp.19083300302.
- Miles, R. B., W. R. Lempert, and J. N. Forkey (2001), Laser Rayleigh scattering, *Meas. Sci. Technol.*, 12, R33, doi:10.1088/0957-0233/12/5/201.
- Miller, I. (2018), LightMachinery Inc., *personal communication*,.
- Mishchenko, M. I. (2014), Directional radiometry and radiative transfer: The convoluted path from centuries-old phenomenology to physical optics, *Journal of Quantitative Spectroscopy and Radiative Transfer*, 146, 4 – 33, doi:10.1016/j.jqsrt.2014.02.033.
- Münster, C. (2011), Modellierung, Identifizierung und Bewertung eines analytischen Modells für gekrümmte Wirbelschleppen (English title: Modeling, Identification, and Evaluation of an Analytical Model of Curved Vortices, *DLR Technical Report IB-111-2011/09, Braunschweig, March*.
- Nelder, J. A., and R. Mead (1965), A Simplex Method for Function Minimization, *Comput. J.*, 7, 308–313, doi:10.1093/comjnl/7.4.308.
- Nelson, D. H., D. L. Walters, E. P. MacKerrow, M. J. Schmitt, C. R. Quick, W. M. Porch, and R. R. Petrin (2000), Wave optics simulation of atmospheric turbulence and reflective speckle effects in CO2 lidar, *Applied Optics*, 39(12), 1857–1871, doi:10.1364/AO.39.001857.
- Nocedal, J., and S. Wright (1999), *Numerical Optimization*, Springer Series in Operations Research, ISBN: 978-0-387-40065-5.
- Novak, O., I. S. Falconer, R. Sangines, M. Lattemann, R. N. Tarrant, D. R. McKenzie, and M. M. M. Bilek (2011), Fizeau interferometer system for fast high resolution studies of spectral line shapes, *Rev. Sci. Instrum.*, 82, doi:10.1063/1.3525102.
- NTSB (1994), Brief of Accident LAX94FA073, *National Transportation Safety Board, Washington, D.C., Oct.*
- NTSB (2001), B733 Wake Turbulence During Cruise, Santa Barbara CA, 2 sept., *Rept. LAX99LA291, National Transportation Safety Board, Washington, D.C., May*.

- NTSB (2004), In-Flight Separation of Vertical Stabilizer American Airlines Flight 587 Airbus Industrie A300-605R, N14053 Belle Harbor, New York November 12, 2001,, *Accident Rept. NTSB/AAR-04/04, National Transportation Safety Board Aircraft, Washington, D.C.*
- Paffrath, U. (2006), Performance assessment of the Aeolus Doppler wind lidar prototype, Ph.D. thesis, Phd thesis, TU München, DLR-FB2006-2012 (DLR Forschungsbericht).
- Press, H. W., B. P. Fannery, S. A. Teukolsky, and W. T. Vetterling (1992), *Numerical Recipes in C: The Art of Scientific Computing*, 2 ed., Cambridge University Press, ISBN: 978-0521431088.
- Rabadan, G. J., N. P. Schmitt, T. Pistner, and W. Rehm (2010), Airborne Lidar for Automatic Feedforward Control of Turbulent In-Flight Phenomena, *J. Aircr.*, 47, 392–403, doi:10.2514/1.44950.
- Rahm, S., I. Smalikho, and F. Köpp (2007), Characterization of aircraft wake vortices by airborne coherent Doppler lidar, *J. Aircraft*, 44(3), 799–805, doi:10.2514/1.24401.
- Rawson, E. G., and J. W. Goodman (1980), Speckle in Optical Fibers, *SPE Vol. 243 Applications of Speckle Phenomena*, doi:10.1117/12.959282.
- Rees, D. (2014), UV Imaging Lidar for Wake Vortex Detection - The Green-Wake Project, *WakeNet Europe 2014 Workshop, Bretigny, France*, available at [http://www.wakenet.eu/fileadmin/user\\_upload/Workshop2014/Presentations/WakeNetEurope\\_Workshop2014\\_502\\_Rees.pdf](http://www.wakenet.eu/fileadmin/user_upload/Workshop2014/Presentations/WakeNetEurope_Workshop2014_502_Rees.pdf), visited on 8.08.2018.
- Reichler, T. (2009), *Climate Change: Observed Impacts on Planet Earth*, chap. Changes in the Atmospheric Circulation as Indicator of Climate Change, Elsevier, doi:10.1016/B978-0-444-53301-2.00007-5.
- Reitebuch, O. (1999), SODAR-Signalverarbeitung von Einzelpulsen zur Bestimmung hochaufgelöster Windprofile, *Ph.D thesis, Fraunhofer Institute for Atmospheric Environmental Research, Garmisch-Partenkirchen, Shaker Verlag, Aachen, 175 p.*
- Reitebuch, O. (2016), personal communication, *Institut für Physik der Atmosphäre (IPA), German Aerospace Center (DLR), Oberpfaffenhofen, Münchner Str. 20, 82234 Wessling, Germany.*
- Rodriguez-Cobo, L., M. Lerner, C. Galindez, and J. M. Lopez-Higuera (2012), Speckle characterization in multimode fibers for sensing applications, *Proc. SPIE*, 8413, doi:10.1117/12.978217.
- Rogers, J. R. (1982), Fringe shifts in multiple-beam Fizeau interferometry, *JOSA*, 72(5), 638–643, doi:10.1364/JOSA.72.000638.
- Rooseleer, F., and V. Treve (2018), RECAT-EU - European Wake Turbulence Categorization and Separation Minima on Approach and Departure, *Eurocontrol, Edition 1.2.*
- Roßi, P. (2017), Documentation sheet, *DLR-IPA-LID-PMTARR1-DOC1A.*

- Rossow, V. J., and K. D. James (2000), Overview of Wake-Vortex Hazards During Cruise, *Journal of Aircraft*, 37(6), 960–975, doi:10.2514/2.2723.
- Rye, B. J., and R. M. Hardesty (1993), Discrete spectral peak estimation in incoherent backscatter heterodyne lidar. I: Spectral accumulation and the CramerRao lower bound, *IEEE Trans. Geosci. Remote Sens.*, 31, 16–27, doi:10.1109/36.210440.
- Sathe, A., and J. Mann (2013), A review of turbulence measurements using ground-based wind lidars, *Atmospheric Measurement Techniques*, 6(11), 3147–3167, doi:10.5194/amt-6-3147-2013.
- Schmitt, N. P., W. Rehm, T. Pistner, P. Zeller, H. Diehl, and P. Navé (2007), The AWIATOR airborne LIDAR turbulence sensor, *Aerosp. Sci. Technol.*, 11, 546–552, doi:10.1016/j.ast.2007.03.006.
- SCHOTT (2007), Refractive Index and Dispersion, *SCHOTT Technical Information*, TIE-29.
- SCHOTT (2008), Temperature Coefficient of the Refractive Index, *SCHOTT Technical Information*, TIE-19.
- Schumann, U., and R. Sharman (2014), Aircraft Wake-Vortex Encounter Analysis for Upper Levels, *Journal of Aircraft*, 52(4), 1277–1285, doi:10.2514/1.C032909.
- Schwiesow, R. L., and S. D. Mayer (1995), Coherent Optical Signal Processing for a Doppler Lidar Using a Michelson Interferometer, *Coherent Laser Radar Conference (Keystone, CO)*, *OSA Technical Digest Series* 19.
- Schwithal, J. (2017), Lidar-based Wake Identification and Impact Alleviation, Ph.D. thesis, Doctoral Thesis, Technical University Braunschweig, DLR-Forschungsbericht 2017-59, ISSN: 1434-8454.
- Schwithal, J., and N. Fezans (2016), Institut für Flugsystemtechnik (FT), German Aerospace Center (DLR), Lilienthalplatz 7, 38108 Braunschweig, Germany, *personal communication*.
- SESAR (2015), European ATM Master Plan, *Edition 2015*.
- Shangguan, M., H. Xia, C. Wang, J. Qiu, S. Lin, X. Dou, Q. Zhang, and P. J.-W. (2017), Dual-frequency Doppler lidar for wind detection with a superconducting nanowire single-photon detector, *Opt. Lett.*, (42), 3541–3544, doi:10.1364/OL.42.003541.
- Sharman, R. (2016), *Aviation Turbulence*, chap. Nature of Aviation Turbulence, pp. 3–30, Springer International Publishing, Cham, doi:10.1007/978-3-319-23630-8\_1.
- Simon, J., and S. Comastri (2004), Zero fringe visibility in the classical localization plane of a two-beam interferometer, *J. Opt. Soc. Am. A*, 21, 1488–1495, doi:10.1364/JOSAA.21.001488.
- Smalikho, I., F. Köpp, and S. Rahm (2005), Measurement of Atmospheric Turbulence by 2- $\mu\text{m}$  Doppler Lidar, *Journal of Atmospheric and Oceanic Technology*, 22(11), 1733–1747, doi:10.1175/JTECH1815.1.

- Smalikho, I. N., V. A. Banakh, E. L. Pichugina, and A. Brewer (2013), Accuracy of Estimation of the Turbulent Energy Dissipation Rate from Wind Measurements with a Conically Scanning Pulsed Coherent Doppler Lidar. Part II. Numerical and Atmospheric Experiments, *Atmospheric and Oceanic Optics*, 26(5), 411–416, doi:10.1134/S1024856013050151.
- Spectrum (2015), *M2i.49xx M2i.49xx-exp fast 16 bit transient recorder, A/D converter board for PCI-X, PCI bus and PCI Express bus Hardware Manual*, Spectrum Instrumentation GmbH, Germany.
- Speiser, J. (2016), Thin disk lasers: history and prospects, *Proc.SPIE*, 98930L, doi:10.1117/12.2231529.
- Stadler, D., M. Suter, M. Ventura, and D. Niederer (2015), Speckle reduction with reluctance force-based oscillating diffusors, *The 4th Laser Display and Lighting Conference (LDC15), Yokohama, Japan, Apr. 22 - Apr. 24*.
- Stelmaszczyk, K., M. Dell’Aglia, S. Cudzynski, T. Stacewicz, and L. Wöste (2005), Analytical function for lidar geometrical compression formfactor calculations, *Appl. Opt.*, 44, 1323–1331, doi:10.1364/AO.44.001323.
- Storer, L. N., P. D. Williams, and M. M. Joshi (2017), Global Response of Clear-Air Turbulence to Climate Change, *Geophysical Research Letters*, 44, 9976–9984, doi:10.1002/2017GL074618.
- Strauss, L., S. Serafin, S. Haimov, and V. Grubisic (2015), Turbulence in breaking mountain waves and atmospheric rotors estimated from airborne in situ and Doppler radar measurements, *Quarterly Journal of the Royal Meteorological Society. Royal Meteorological Society (Great Britain)*, 141(693), 3207–3225, doi:10.1002/qj.2604.
- Stürmer, J., C. Schwab, S. Grimm, A. Kalide, A. P. Sutherland, A. Seifahrt, K. Schuster, J. L. Bean, and A. Quirrenbach (2016), Optimal non-circular fiber geometries for image scrambling in high-resolution spectrographs, *Proceedings Volume 9912, Advances in Optical and Mechanical Technologies for Telescopes and Instrumentation II*, doi:10.1117/12.2234552.
- Sutherland, A. P., J. Stürmer, K. R. Miller, A. Seifahrt, and J. L. Bean (2016), Characterizing octagonal and rectangular fibers for MAROON-X, *Proc.SPIE*, pp. 9912 – 9912 – 10, doi:10.1117/12.2231707.
- Tenti, G., C. D. Boley, and R. C. Desai (1974), On the Kinetic Model Description of Rayleigh-Brillouin Scattering from Molecular Gases, *Can. J. Phys.*, 52, 285–290, doi:10.1139/p74-041.
- TI (2008), OPA4920, *Texas Instruments, SBO317D, September 2004 - revised August 2008*.
- Tietze, U., C. Schenk, and E. Gamm (1991), *Electronic Circuits - Handbook for Design and Application*, 2nd ed., Springer, Heidelberg, ISBN: 978-3-540-78655-9.
- Title, A. M. (2013), *Observing Photons in Space: A Guide to Experimental Space Astronomy*, chap. Imaging Michelson interferometers, pp. 349–361, Springer, ISBN: 9781461478034.



- Title, A. M., and H. E. Ramsey (1980), Improvements in birefringent filters. 6: Analog birefringent elements, *Appl. Opt.*, *19*, 2046–2058, doi:10.1364/AO.19.002046.
- Tremblay, Y., B. S. Kawasaki, and K. O. Hill (1981), Modal noise in optical fibers: open and closed speckle pattern regimes, *Appl. Opt.*, *20*, 1652–1655, doi:10.1364/AO.20.001652.
- TSB (2008), Encounter with wake turbulence, *Aviation Investigation Report, Airbus A319-114-C-GBHZ*, The Transportation Safety Board of Canada, p. 44.
- Tucker, S. C., C. Weimer, and R. M. Hardesty (2016), The Athena-OAWL Doppler Wind Lidar Mission, *EPJ Web of Conferences*, *ILRC 27*, *119*, doi:10.1051/epjconf/201611901002.
- Tucker, S. C., C. S. Weimer, S. Baidar, and M. Hardesty (2018), The Optical Autocovariance Wind Lidar. Part I: OAWL Instrument Development and Demonstration, *Journal of Atmospheric and Oceanic Technology*, *35*(10), 2079–2097, doi:10.1175/JTECH-D-18-0024.1.
- Tvaryanas, A. P. (2003), Epidemiology of turbulence-related injuries in airline cabin crew, 1992-2001, *Aviat. Space Environ. Med.*, *74*, 970–976.
- Unsinn, K. (2016), Untersuchung von Scrambling- und Speckleeigenschaften von Glasfasern für ein Lidarempfangssystem, *Masterarbeit, DLR Oberpfaffenhofen, Hochschule München*.
- Valla, M. (2005), Etude d'un lidar Doppler impulsif à laser Erbium fibré pour des mesures de champ de vent dans la couche limite de l'atmosphère, *doctoral thesis, ENST, Paris*.
- Van Trees, H. L. (1971), *Detection, Estimation, and Modulation Theory, Part III: Radar-Sonar Signal Processing and Gaussian Signals in Noise.*, John Wiley & Sons, Inc., ISBN: 978-0-471-10793-4.
- Vaughan, J. M. (1989), *The Fabry-Pérot Interferometer: History, Theory, Practice and Applications*, Hilger, Philadelphia, ASIN: B078RR4XBK.
- Vaughan, J. M., D. W. Brown, C. Nash, S. B. Alejandro, and G. G. Koenig (1995), Atlantic atmospheric aerosol studies: 2. compendium of airborne backscatter measurements at 10.6  $\mu\text{m}$ , *J. Geophys. Res.*, *100*, 1043–1065, doi:10.1029/94JD01817.
- Vinnichenko, N. (1980), *Turbulence in the Free Atmosphere*, 1 ed., Springer US, doi:10.1007/978-1-4757-0100-5.
- Von Kármán, T. (1948), Progress in the Statistical Theory of Turbulence, *Proceedings of the National Academy of Sciences of the United States of America*, *34*(11), 530–539.
- Vrancken, P. (2016), *Aviation Turbulence - Processes, Detection, Prediction*, chap. Airborne Remote Detection of Turbulence with Forward-Pointing LIDAR, pp. 443–464, Springer, doi:10.1007/978-3-319-23630-8.22.
- Vrancken, P. (2018), Institut für Physik der Atmosphäre (IPA), German Aerospace Center (DLR), Oberpfaffenhofen, Münchner Str. 20, 82234 Wessling, Germany, *personal communication*.

- Vrancken, P., M. Wirth, G. Ehret, H. Barny, P. Rondeau, and H. Veerman (2016), Airborne forward-pointing UV Rayleigh lidar for remote clear air turbulence detection: system design and performance, *Applied Optics*, 55(32), 9314–9328, doi:10.1364/AO.55.009314.
- Wan, X., J. Ge, and Z. Chen (2011), Development of stable monolithic widefield Michelson interferometers, *Appl. Opt.*, 50, 4105–4114, doi:10.1364/AO.50.004105.
- Wang, L., F. Gao, J. Wang, Q. Yan, B. Chang, and D. Hua (2017), Design and experimental verification of a novel Mie Doppler wind lidar based on all-fiber Mach-Zehnder frequency discriminator, *Optics Communications*, 389, 5 – 9, doi:10.1016/j.optcom.2016.11.075.
- Ward, E. W., Z. Pasturczyk, W. A. Gault, and G. G. Shepherd (1985), Multiple reflections in a wide-angle Michelson interferometer, *Appl. Opt.*, 24(11), 1589–1598, doi:10.1364/AO.24.001589.
- Weinstock, J. (1981), Energy Dissipation Rates of Turbulence in the Stable Free Atmosphere, *Journal of the Atmospheric Sciences*, 38(4), 880–883, doi:10.1175/1520-0469(1981)038<0880:EDROTI>2.0.CO;2.
- Weitkamp, C. (2005), *LIDAR: Range-Resolved Optical Remote Sensing of the Atmosphere*, Springer Science+Business Media Inc, ISBN: 978-0-387-25101-1.
- Werner, C. (2005), *Lidar, Springer Series in Optical Sciences 102*, chap. Doppler wind lidar, Springer, ISBN: 978-0-387-25101-1.
- Wildmann, N., N. Vasiljevic, and T. Gerz (2018), Wind turbine wake measurements with automatically adjusting scanning trajectories in a multi-Doppler lidar setup, *Atmospheric Measurement Techniques*, 11(6), 3801–3814, doi:10.5194/amt-11-3801-2018.
- Williams, P. D., and M. M. Joshi (2013), Intensification of winter transatlantic aviation turbulence in response to climate change, *Nature Climate Change*, 3, 644, doi:10.1038/nclimate1866.
- Wirth, M. (2017a), personal communication, *Institute of Atmospheric Physics, German Aerospace Center (DLR)*.
- Wirth, M. (2017b), MERLIN Algorithm Theoretical Basis Document: Top level algorithms for primary L1/2 products, MLN-PLDP-ATBD-90001-PI, 1. Rev, 2. August.
- Wirth, M., A. Fix, A. Mahnke, H. Schwarzer, F. Schrandt, and E. G. (2009), The airborne multi-wavelength water vapor differential absorption lidar WALES: system design and performance, *Appl. Phys. B*, doi:10.1007/s00340-009-3365-7.
- Witschas, B. (2011), Analytical model for Rayleigh-Brillouin line shapes in air, *Applied Optics*, 50, 267–270, doi:10.1364/AO.50.000267.
- Witschas, B. (2012), *Atmospheric Physics: Background-Methods-Trends*, chap. Light scattering on molecules in the atmosphere, p. 6983, Springer, doi:10.1007/s00340-008-3075-6.
- Witschas, B., O. Reitebuch, C. Lemmerz, P. G. Kabelka, S. Kondratyev, Z. Gu, and W. Ubachs (2016), The Measurement of Tropospheric Temperature Profiles using Rayleigh-Brillouin Scattering: Results from Laboratory and Atmospheric Studies, in *EPJ Web of Conferences 119, ILRC 27*, doi:10.1051/epjconf/201611927004.

- Wriedt, T. (2012), *The Mie Theory: Basics and Applications*, chap. Mie theory: a review, pp. 53–71, Springer, ISBN: 978-3-642-28738-1.
- Wu, J., J. Wang, and P. B. Hays (1994), Performance of a circle-to-line optical system for a Fabry-Pérot interferometer: a laboratory study, *Appl. Opt.*, *33*, 7823–7828, doi:10.1364/AO.33.007823.
- Wyant, J. (1978), Fringe localization, *Applied Optics*, *17*, 1853–1853, doi:10.1364/AO.17.001853.
- Zeng, J., and B. Moulin (2010), Adaptive Feedforward Control for Gust Load Alleviation, *J. Guid. Control Dyn.*, *33*(3), 862–872, doi:10.1002/2017GL074618.
- Zieger, P., R. Fierz-Schmidhauser, E. Weingartner, and U. Baltensperger (2013), Effects of relative humidity on aerosol light scattering: results from different european sites, *Atmospheric Chemistry and Physics*, *13*(21), 10,609–10,631, doi:10.5194/acp-13-10609-2013.



## Acknowledgments

This work was mainly financed by the DLR project “Land-Based and Onboard Wake Systems” (L-bows) and partly by “CleanSky2-NACOR”.

First of all, I would like to thank all my colleagues at the Institute of Atmospheric Physics of the German Aerospace Center (DLR) in Oberpfaffenhofen for providing their knowledge, guidance and support. Special thanks go to Dr. Patrick Vrancken for supervising my work, for his contributions to the developed Doppler Wind Lidar receiver, and for his assistance in first ground-based wind speed measurements. Thanks also to Christian Lemmerz, who helped me perform speckle characterization measurements, and for his guidance, and to Dr. Benjamin Witschas for reviewing my publication and for his insights on fringe-imaging interferometers. Thank you also to Dr. Martin Wirth for providing his knowledge and for designing the transimpedance amplifier of the AEROLI receiver, which was built by Philipp Röfi and colleagues. In addition I would like to thank Dr. Norman Wildmann for taking his time setting up the institute’s coherent Doppler Wind Lidar (Windcube®200S) for reference wind speed measurements and to Dr. Arthur Schady for explaining the usage of the institute’s ultrasound anemometers. Furthermore, I would like to thank Dr. Gerhard Ehret and Dr. Frank Holzäpfel for their support. I would also like to thank Pau Gomez Kabelka, a former doctoral candidate colleague, for fruitful discussions.

Many thanks to my dissertation chairman Prof. Dr. Markus Rapp and to assessor Prof. Dr. em. Wolfgang Zinth for supervising my thesis at the Department of Physics of the Ludwig-Maximilians-Universität München.

Moreover, I would like to express my gratitudes to Dr. Jana Schwithal and Dr. Nicolas Fezens of the DLR Institute of Flight Systems in Braunschweig, for providing information and explanations on their alleviation and control routines. I would like to thank Dr. Volker Freudenthaler of the Ludwig-Maximilians-Universität München for an eye-opening discussion on lidar overlap and its simulation using ZEMAX.

I would also like to thank some colleagues from other institutions. Foremost, I would like to thank Dr. Nicolas Cézard of the Optics and Associated Techniques Department of the French Aerospace Lab (ONERA) at Palaiseau, France, for the insight he provided in his dissertation and during discussions, on speckle and on the fringe-imaging Michelson interferometer. I would also like to thank Dr. Didier Bruneau of the Laboratoire atmosphères, milieux et observations spatiales (LATMOS) for discussing the receiver principle with me. Much thanks go also to Ian Miller of LightMachinery, Inc. in Canada, who provided know-how on the design of monolithic Michelson interferometers, and whose team built the monolithic Michelson interferometer of the AEROLI receiver as an industrial supplier. Thank you also to Dr. Gerardo Avila of the European Southern Observatory in Garching for taking his time, showing me around in his lab, and for his explanations on the measurement of optical scrambling in fiber-coupled spectrometers. Thank you as well to Dr. John M. Harlander of St. Cloud State University (Minnesota) for providing information on plane wave calculations in ZEMAX for the simulation of interference fringes.